DOT/FAA/AR-06/24

Air Traffic Organization
Operations Planning
Office of Aviation Research and
Development
Washington, DC 20591

The Evaluation of Cold Dwell Fatigue in Ti-6242

January 2007

Final Report

This document is available to the U.S. public through the National Technical Information Service (NTIS), Springfield, Virginia 22161.

U.S. Department of Transportation
Federal Aviation Administration

NOTICE

This document is disseminated under the sponsorship of the U.S. Department of Transportation in the interest of information exchange. The United States Government assumes no liability for the contents or use thereof. The United States Government does not endorse products or manufacturers. Trade or manufacturer's names appear herein solely because they are considered essential to the objective of this report. This document does not constitute FAA certification policy. Consult your local FAA aircraft certification office as to its use.

This report is available at the Federal Aviation Administration William J. Hughes Technical Center's Full-Text Technical Reports page: actlibrary.tc.faa.gov in Adobe Acrobat portable document format (PDF).

Technical Report Documentation Page

1. Report No.	2. Government Accession No.	3. Recipient's Catalog No.
DOT/FAA/AR-06/24		

4. Title and Subtitle	5. Report Date
THE EVALUATION OF COLD DWELL FATIGUE IN Ti-6242	January 2007
	6. Performing Organization Code
7. Author(s)	8. Performing Organization Report No.
Somnath Gosh[1], Mike Mills[2], Stan Rokhlin[3], Vikas Sinha[2], Wolé Soboyejo,[4] and Jim Williams[2]	

9. Performing Organization Name and Address		10. Work Unit No. (TRAIS)
[1]Department of Mechanical Engineering The Ohio State University Columbus, OH 43210	[2]Department of Materials Science and Engineering The Ohio State University Columbus, OH 43210	
[3]Department of Industrial, Welding and System Engineering The Ohio State University Columbus, OH 43210	[4]Department of Mechanical and Aerospace Engineering Princeton University Princeton, NJ 08544	

12. Sponsoring Agency Name and Address	13. Type of Report and Period Covered
U.S. Department of Transportation Federal Aviation Administration Air Traffic Organization Operations Planning Office of Aviation Research and Development Washington, DC 20591	Final Report
	14. Sponsoring Agency Code ANE-110

15. Supplementary Notes

The Federal Aviation Administration Airport and Aircraft Safety R&D Division COTR was Joseph Wilson.

16. Abstract

The primary objective of this research was to develop a fundamental understanding of the mechanical and metallurgical factors that cause early crack initiation under dwell-fatigue conditions in Ti-6Al-2Sn-4Zr-2Mo (+Si) alloy. Materials examined in this study have the representative lamellar and globular alpha/beta microstructures.

The study combined experiment with detailed solid mechanics analysis to produce a semiquantitative understanding of the processes that lead to fatigue crack initiation under dwell-loading conditions. Time-dependent flow behavior was incorporated into the constitutive relations used to model the material behavior during dwell loading. A variety of state-of-the-art experimental methods were used to support the analytical work and to provide detailed characterization information regarding the nature of dwell-initiated fatigue cracks.

The key analytical finding was that significant internal load redistribution occurs from soft to hard regions when time dependence is incorporated into the analysis. Here, soft and hard refer to the orientation dependence of the flow stress in the hexagonal alpha phase. Detailed examinations of the dwell-fatigue crack origins show that they lie close to but do not coincide with the basal planes. The precise orientation of these cracks was determined experimentally. Very small cracks were located using acoustic microscopy and microradiography. These cracks were excised and characterized in detail, including the local orientation dependence of the flow stress of regions surrounding the crack. The size of the hard regions where the crack initiates were measured using a quantitative technique.

Experts in the field have suggested that hydrogen has an influential role in dwell fatigue. Consequently, the effect of variation in hydrogen content on dwell fatigue was examined by testing hydrogen-charged specimens. The results indicated that for the continuous alpha phase microstructure, the dwell-fatigue life is higher for higher hydrogen contents, especially for hydrogen contents $\geq$ 150 ppm.

This report describes the detailed associated information obtained during the course of this research, including the novel experimental methods used to obtain them. It also contains a number of appendices which contain more detailed data and results.

17. Key Words	18. Distribution Statement
Ti-6Al-2Sn-4Zr-2Mo alloy, Dwell fatigue, Orientation imaging, Focused ion beam techniques, In situ crack detection, Solid mechanics modeling	This document is available to the public through the National Technical Information Service (NTIS) Springfield, Virginia 22161

19. Security Classif. (of this report)	20. Security Classif. (of this page)	21. No. of Pages	22. Price
Unclassified	Unclassified	375	

Form DOT F 1700.7 (8-72) Reproduction of completed page authorized

ACKNOWLEDGEMENTS

The Ohio State University investigator team gratefully acknowledges the advice and guidance from our partners and collaborators from industry, university, and government.

In particular, we thank Andy Woodfield (GE Aircraft Engines), Jim Hall (Honeywell Engines), Jack Schirra (Pratt & Whitney), and Amit Chatterjee (Rolls Royce). We also thank Mike Uchic and Dennis Dimiduk (Air Force Materials Lab), Jonathan Spowart (UES Incorporated), and Dave Furrer (Ladish Company). We appreciate and value the input provided by the Federal Aviation Administration (FAA) Rotor Integrity Sub-Committee, Chaired by Bill Knowles (Honeywell). Ricardo Schwarz (Los Alamos National Lab) oversaw the hydrogen charging and was the source of valuable technical discussion regarding hydrogen effects. Our FAA sponsor representatives, Tim Mousakis and Joe Wilson, have provided invaluable advice and guidance.

The objective of this program was to assist our partners in understanding dwell fatigue. Without the diversity of inputs from the aforementioned sources this task would have been much more difficult.

TABLE OF CONTENTS

		Page
EXECUTIVE SUMMARY		xiii
1.	INTRODUCTION	1
2.	APPROACH, RESULTS, AND DISCUSSION	1
2.1	Constitutive Data	1
2.1.1	Compression Testing of Ti-6A1 Single Crystals	2
2.1.2	Anisotropy and Tension-Compression Asymmetry in the Room Temperature Deformation of α/β Colonies in Ti-6242	2
2.1.3	Observations of Room Temperature Recovery in Single Colony Crystals	4
2.1.4	Size Effects Associated With Ti-6242 Single Colonies	6
2.2	Influence of Microstructure on Dwell-Fatigue Susceptibility	8
2.2.1	Microtexture Analysis	9
2.2.2	Normal Fatigue and Dwell-Fatigue Test Results	10
2.3	Early Crack Detection	12
2.3.1	Samples and Mechanical Testing	12
2.3.2	In Situ Dwell-Fatigue Crack Monitoring and Secondary Crack Localization	12
2.3.3	Crack Growth Rate Measurements, Interruptive Tests	13
2.3.4	Effect of Dwell Time on Sample Fatigue Life	15
2.4	Secondary Crack Characterization	16
2.5	Contributions of Normal Fatigue and Static-Loading Deformation/Damage Processes to the Dwell-Fatigue Failure	20
2.5.1	Rupture Lives and Strain Accumulation	20
2.5.2	Fractography and Failure Modes	21
2.6	Crystallographic Orientation of Fracture Facets at the Initiation Site	21
2.7	Crystallographic Orientation of the Regions Below the Dwell-Fatigue Fracture Surface	24

2.8 Influence of Hydrogen Content 29

2.9 Long Crack Growth Rates 32

2.10 Computational Modeling of Ti-6242 34

2.10.1 Summary of Experiments 35
2.10.2 Computational Modeling of Ti-6242 35
2.10.3 Polycrystal Simulations 37
2.10.4 Polycrystalline Simulations 38

3. CONCLUSIONS 39

4. REFERENCES 43

APPENDICES

A—Constitutive Data

B—Influence of Microstructure on Dwell-Fatigue Susceptibility of Ti-6242 Alloy

C—Early Crack Detection

D—Secondary Crack Characterization

E—Understanding the Contributions of Normal-Fatigue and Static-Loading to the Dwell-Fatigue in a Near-Alpha Titanium Alloy

F—Determination of Crystallographic Orientation of Dwell-Fatigue Fracture Facets in Ti-6242 Alloy

G—Crystallography of Fracture Facets in a Near-Alpha Titanium Alloy

H—Observations on Crystallographic Orientations of the Regions Below the Dwell-Fatigue Fracture Surface in Ti-6242 Alloy

I—Influence of Hydrogen Content on the Dwell-Fatigue Behavior of Ti-6242 Alloy

J—Effects of Microstructure on Normal-Fatigue and Dwell-Fatigue Crack Growth in Ti-6242

K—Deformation and Creep Modeling in Polycrystalline Ti-6A1 Alloys

L—A Crystal Plasticity Based Model of Polycrystalline Ti-6242

LIST OF FIGURES

Figure		Page
1	Compression Stress-Strain Curves of the Various Orientations for Ti-6A1 Single Crystals	2
2	Plot of CRSS Versus Slip System for the Bulk Compression, Microtensile and Microcompression Samples	3
3	Stress-Strain Curves for β-Processed Ti-6A1-4V With Coarse and Fine Lath Spacings and Nominally the Same Grain and Colony Sizes, and α Phase Volume Fraction Showing Clear Lath Spacing Effect	4
4	Strain Versus Time Plot From a Room Temperature Creep Test of a Single Colony Ti-6242 Compression Sample Oriented to Maximize the Resolved Shear Stress on the a_3 Basal Slip System	5
5	Strain Versus Time Plot From a Room Temperature Creep Test of a Single Colony Ti-6242 Compression Sample Oriented to Maximize the Resolved Shear Stres on the a_2 Basal Slip System	5
6	Microcompression Testing From Specific Microstructure Region From Ti-6242 (a) OIM Image of Pancake 2 Region Having a Local Region (Arrow) for Which the Schmid Factor for Basal Slip is Maximized (Red), (b) 20-μm-Diameter Compression Pillar Machined From the Region Arrowed in (a), (c) Enlarged SEM Image Showing Transmission of Slip Traces Across β Laths, the Operative Slip System is a a_2 Basal, and (d) Comparison of Flow Curves for a a_2 Colony Crystal (Bulk and Microcompression) Versus the 20-μm Pancake 2 Pillar	7
7	Plot of Stress Versus Sample Size Showing Both Yield Stress and Limit for a Series of a_1 Basal Single Colony Crystals	8
8	Optical Micrographs of the Forgings Tested in This Research (a) Forging No. 1, α/β-Forged; (b) Forging No. 2 α/β-Forged; (c) Forging No. 3, β-Forged; and (d) 1970s-1980s Vintage Material, α/β-Forged	9
9	Analysis of Microtexture in the Three α/β-Forged Microsturctures (a) Orientation Map of Forging No. 1, (b) Orientation Map of Forging No. 2, and (c) Orientation Map of 1980s Vintage Material	10
10	Radiographic Matching of the Locations of Two Cracks With Ultrasonic Monitoring (a) Peak Amplitudes of the Reflected Ultrasonic Signals From Initiated Cracks, (b) Obtained Positions of the Cracks Matched With Crack Sites Obtained From the Microradiographic Images, and (c) Sample Geometry of the Test Specimen	13
11	Microradiographic Images of the Primary Crack in the Sample 2-SR2-3	14

12	Comparison of Dwell-Fatigue (Squares) and Cyclic-Fatigue (Circles) Crack Growth Rates	15
13	(a) An SEM Image of a Secondary Crack Lying on the Basal Plane and (b) the Corresponding OIM of the Same Crack, Indicating the Locations TEM Foils Were Extracted	17
14	TEM Images Taken From the Crack Tip in Region 1, Showing Lots of a-Type and c+a-Type Activity	18
15	TEM Images Taken in Bright Field and Weak-Beam Dark Field From the Wake of the Crack	19
16	Crystallographic Orientation of Normal-Fatigue Fracture Facet at the Initiation Site	22
17	Crystallographic Orientation of Dwell-Fatigue Fracture Facet at the Initiation Site	23
18	Crystallographic Orientation of Three Different Dwell-Fatigue Fracture Facets at the Initiation Site	23
19	Crystallographic Orientation of Static-Loading Fracture Facet at the Initiation Site	24
20	Dwell-Fatigue Fracture Surface With the Faceted Initiation Site Circumscribed by a Dotted Curve	25
21	Orientations Images for the Entire Polished Surface at Five Different Depths Below the Reference Plane (a) After First Serial Sectioning Step (44 μm Below the Reference Plane); (b) After Second Serial Sectioning Step (83 μm Below the Reference Plane); (c) After Third Serial Sectioning Step (115 μm Below the Reference Plane); (d) After Fourth Serial Sectioning Step (155 μm Below the Reference Plane); and (e) After Fifth Serial Sectioning Step (187 μm Below the Reference Plane)	27
22	Variation in Fatigue Life With Hydrogen Content for Normal-Fatigue and Dwell-Fatigue Test Conditions	31
23	Comparison of Normal-Fatigue and Dwell-Fatigue Crack Growth Rate Data for Pancake 1 Material	33
24	Comparison of Normal-Fatigue and Dwell-Fatigue Crack Growth Rate Data for Pancake 2 Material	33
25	Comparison of Normal-Fatigue and Dwell-Fatigue Crack Growth Rate Data for Pancake 3 Material	34
26	Microstructure of Ti-6242 After Forging in the α+β Regime	35

27	Calibration of bcc Parameters Single Colony Ti-6242 Sample	36
28	Experimental and Simulation Pole Figures Used in Polycrystalline Simulations	38
29	Matching the Misorientation Distribution (a) Experimental Misorientation Distribution, (b) Initial Misorientation Distribution for the Mesh, and (c) Final Misorientation Distribution for the Mesh	38
30	Orientation Distribution Used in the Polycrystalline Simulation Model	39
31	(a) Constant Strain Tension, (b) Constant Strain Compression, (c) Compression Creep Test, and (d) Tension Creep Test	39

LIST OF TABLES

Table		Page
1	Summary of Normal-Fatigue and Dwell-Fatigue Tests	11
2	Summary of Normal-Fatigue and Dwell-Fatigue Tests	20
3	Comparison of Dwell-Fatigue and Static-Load Tests	21
4	Normal-Fatigue Response at the Peak Stress ~ 95% of Yield Strength for Different Hydrogen Contents	30
5	Dwell-Fatigue (Hold Time = 2 Minutes) Response at the Peak Stress ~ 95% of Yield Strength for Different Hydrogen Contents	30

LIST OF ACRONYMS

3D	Three-dimensional
BF	Bright field
bcc	Body centered cubic
CDF	Cold dwell fatigue
CRSS	Critical resolved shear stress
EBSD	Electron backscatter diffraction
EBSP	Electron backscattered diffraction patterns
EDM	Electrical discharge machine
FIB	Focused ion beam
GA	Genetic algorithm
hcp	Hexagonal close packed
ISDG	Interferometric strain/displacement gauge
LVDT	Linear variable displacement transducer
Ni	Nickel
OIM	Orientation imaging microscopy
OSU	Ohio State University
RF	Radio frequency
SEM	Scanning electron microscope
TEM	Transmission electron microscope
Ti	Titanium
TMP	Thermomechanical processing
UTS	Ultimate tensile strength
YS	Yield strength

EXECUTIVE SUMMARY

There is a failure mode in titanium (Ti) alloys known as dwell fatigue. This mode is manifested by significant reductions in fatigue life, as measured by the number cycles to failure, when the load is held at maximum value instead of continuously cycled. This failure mode is most prevalent in high-temperature alloys such as Ti-6Al-2Sn-4Zr-2Mo (+Si), IMI-829, and IMI-834, all of which contain a relatively low volume fraction of the body-centered-cubic β-phase. Dwell fatigue is most prevalent at temperatures below 300˚C; thus it is sometimes also called cold dwell fatigue. This failure mode has been documented in aircraft engine rotors, but the methods for incorporating this possible failure mode into life calculations are less well developed. The consequences of a rotor failure can be severe, so conservative assumptions and field inspections are currently in use to prevent such an occurrence during service. There is a real need to better understand cold dwell fatigue phenomena to better determine its effect on life.

This project was aimed at providing a fundamental understanding of the factors that promote the occurrence of dwell fatigue in the Ti alloy, Ti-6242. It incorporates detailed materials characterization, analysis and testing, solid mechanics modeling and sensitive in situ monitoring to detect crack formation in the earliest possible stages. Significant progress was made in the ability to model time-dependent stress redistribution and in understanding the fundamental aspects of dwell crack initiation.

Ti-6Al single crystals and single colony Ti-6242 specimens were prepared and tested to measure the magnitude of anisotropy in flow properties. These data were needed for use in the high-fidelity solid mechanics models developed and used in this project. These results were critical for developing the computational model for deformation behavior of Ti-6242 and also for modeling the time-dependent internal stress-redistribution under an externally applied load. Influence of key microstructural variables, including the degree of microtexture and the size of the microtextured regions, on the dwell-fatigue susceptibility was evaluated through experiments. An in situ ultrasonic crack monitoring system was used to detect the early stages of crack initiation and to measure the rate of small crack growth. The crystallographic orientation of the crack initiation site fracture facets was determined. The orientation is generally close to the basal plane but always misaligned to some extent (5º-20º), the degree of misalignment being dependent on the type of loading (continuous cycling, dwell fatigue or static loading). The growth rates of long cracks under continuous cycling and dwell-loading conditions were also measured for the different microstructural and loading conditions examined in this study. The rate of long crack growth was not significantly affected by the loading method (i.e., dwell versus no dwell). From this, it was concluded that the principle reason for the reduction in dwell-fatigue life is earlier crack initiation under dwell conditions.

Serial sectioning and electron backscattered diffraction experiments were used to evaluate the microtextured region size effects associated with the dominant dwell-fatigue crack initiation site. The results indicate that the largest near-basal-oriented microtextured region in the sampled volume of material corresponds to the faceted initiation site on the fracture surface.

1. INTRODUCTION.

The titanium (Ti) alloy Ti-6242 is the workhorse for compressor rotor spools. In work conducted in several laboratories around the world, a significant debit in the fatigue capability (reduced lifetimes) of these alloys has been found when comparing results obtained from continuous cycling and holding at maximum load (dwell fatigue) conditions. Because the magnitude of the life debit decreases with increasing temperature, the phenomenon has been called cold dwell fatigue. The least well understood aspects of this phenomenon are the variations in fatigue capability. These variations in behavior appear to be closely linked to variations in microstructure. In particular, there is a real need to develop an understanding of dwell time fatigue-microstructure relations and dwell time crack initiation. This is not a new phenomenon, but the details of the interaction between microstructure, loading history, hydrogen content, and fatigue strength (life) are not understood in a fundamental sense.

This research project was undertaken to provide a better understanding of the factors that cause dwell fatigue. The project involved metallurgy, solid mechanics, and nondestructive evaluation experts from The Ohio State University and Princeton University. A team of Ti experts from General Electric (GE) Aircraft Engines, Rolls-Royce, and Honeywell was also formed, and the results of the research were communicated to them on a regular basis.

In this program, the experimental investigation was carried out on both the single crystal/single colony and polycrystalline materials. Both the elastic and plastic properties of the single crystal/ single colony material were experimentally measured. The mechanical properties of the polycrystalline material along with the details of their microtexture were also experimentally determined. All these experimental results are utilized in the development of the finite element method-based models.

2. APPROACH, RESULTS, AND DISCUSSION.

2.1 CONSTITUTIVE DATA.

To model a given microstructure, the crystal plasticity modeling required a sound understanding of the constitutive response of the individual components of the microstructure. The microstructure of most critical concern, pancake 2, consists of globular alpha surrounded by regions of colony microstructure. The first step in the development of the crystal plasticity model for deformation in Ti alloys was the modeling of single phase α (hcp) Ti-6wt%Al. The α phase is the principal constituent in near-α alloys such as Ti-6242. The second step was to model the two-phase colony microstructure, consisting of α and β (bcc). However, the symmetry of slip systems was broken with the addition of the β phase, leading to an anisotropy in the mechanical behavior. Therefore, it is critical to characterize the constitutive behavior of the colonies as a function of the operative slip system. This information can then be incorporated into the crystal plasticity modeling for creep and load shedding.

2.1.1 Compression Testing of Ti-6Al Single Crystals.

The results of the constant strain rate tests are shown in figure 1. As can be seen, the yield and flow strengths for the prism and basal orientations are very similar, while the [0001] orientation has a much larger yield strength. Slip line analysis using scanning electron microscope (SEM) has confirmed that single basal and prism slip systems were dominant for these two crystal orientations, while for the [0001] orientation, multiple <c+a> slip occurs on several first-order pyramidal planes. This information was used to calibrate the crystal plasticity model, as described in section 2.10.

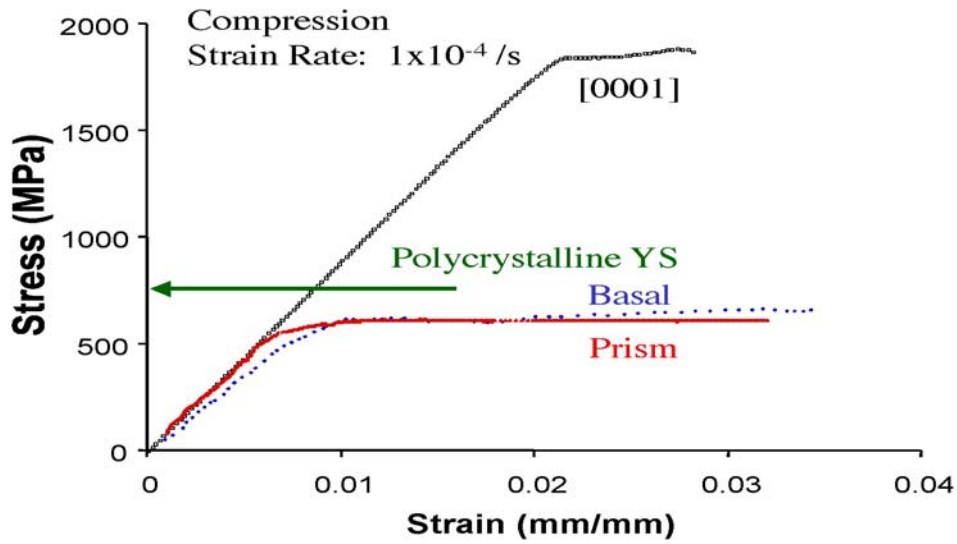

Figure 1. Compression Stress-Strain Curves of the Various Orientations for Ti-6Al Single Crystals

2.1.2 Anisotropy and Tension-Compression Asymmetry in the Room Temperature Deformation of α/β Colonies in Ti-6242.

Figure 2 summarizes the results for the bulk compression, microtensile, and microcompression tests on Ti-6242 single colony crystals. In all cases, the imposed strain rate is 1×10^{-4} s^{-1}. There is significant anisotropy in the critical resolved shear stress (CRSS) values, depending on the a-type slip vector that is active, and between basal and prism systems. The CRSS values are small for a_1 slip on both basal and prism planes, with the latter having the smallest value tested (250 MPa). The a_2 basal system has a significantly larger CRSS value compared to the other a-type systems. Quite unexpectedly, the a_3 basal system has a relatively small CRSS value. Insight into this remarkable result was provided by the transmission electron microscopy (TEM) observations on the single colony compression samples summarized in the second paragraph of section 3 and described in detail in appendix A (for example, figure A-19). The anisotropy is, in general, less pronounced for the prism slip systems. The [0001] orientation has a significantly larger CRSS value compared to all of the a-type slip systems, consistent with the fact that <c+a> slip must be activated in this orientation. Thus, the CRSS for the [0001] orientation is between

17% and 40% larger than for a-type slip systems. The 0.2% offset yield strengths of 670 MPa, 824 MPa, and 765 MPa were measured for the a_1, a_2, and a_3 basal slip orientations for Ti-6242, respectively. The corresponding values for CRSS are 330 MPa, 405 MPa, and 375 MPa.

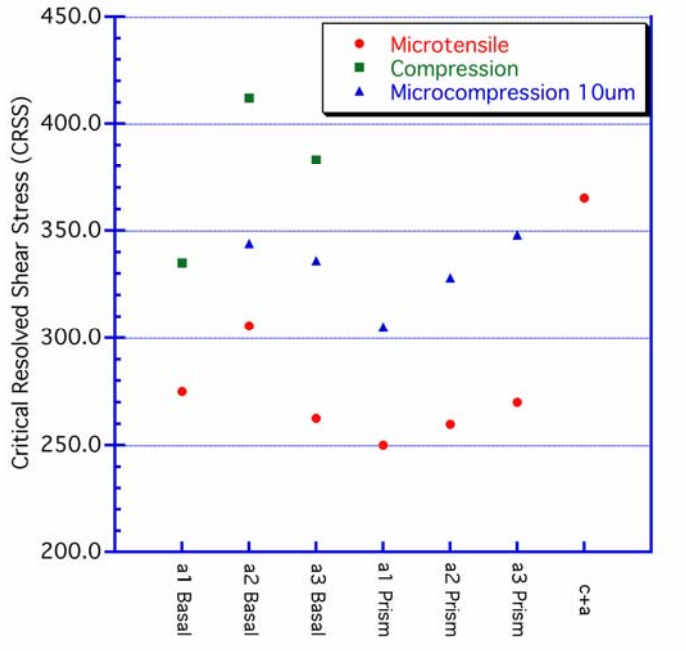

Figure 2. Plot of CRSS Versus Slip System for The Bulk Compression, Microtensile, and Microcompression Samples

TEM investigations of the dislocation mechanisms active during deformation of single α/β colonies oriented for basal slip were performed to provide insight into the observed anisotropy in constant strain rate behavior and to explain the role of the α/β interface. A detailed discussion of these results is provided in reference 1. A synopsis of these observations is provided in appendix A.

This single colony crystal data also clearly demonstrates that there is a significant asymmetry in the flow characteristics of the crystals in tension versus compression—the former exhibiting lower strengths for all orientations. The source of this asymmetry may be due to the β phase characteristics, since it is known that slip via a/2<111> dislocations can exhibit tension-compression asymmetry due to dislocation core effects. On the other hand, there are also significant dislocation core effects for both a-type and <c+a> dislocations in the α phase. Indeed, a tension-compression asymmetry has been documented for a Ti-Al binary alloy deformed in the [0001] direction [2]. However, no such single crystal tests have been preformed to date for basal or prism a-type slip systems. On the basis of these considerations, the crystal plasticity modeling allows for both α and β phases to exhibit asymmetry in the response in both tension and compression.

An important difference between the single colony crystals and the transformed β regions of the actual polycrystalline microstructure is the scale of the α and β lath structure—about 10-μm lath spacing in the former and only about 1 μm in the latter. This difference is due to the very slow effective cooling rate experienced by the single colonies during crystal growth. Therefore, the single colony crystals are expected to be significantly softer than the transformed β counterparts. The effect of the lath spacing on strength is shown in figure 3. Direct measurement of the lath spacing effect is problematic using the single colony crystals; however, an excellent estimate has been obtained of the effect by measuring the flow curve response for β-processed material with subsequent, carefully controlled cooling and hold times. The unique thermomechanical processing was performed courtesy of Dr. Lee Semiatin (Air Force Wright Laboratories) on Ti-6Al-4V. Nevertheless, the results are expected to be extendable to all transformed β structures.

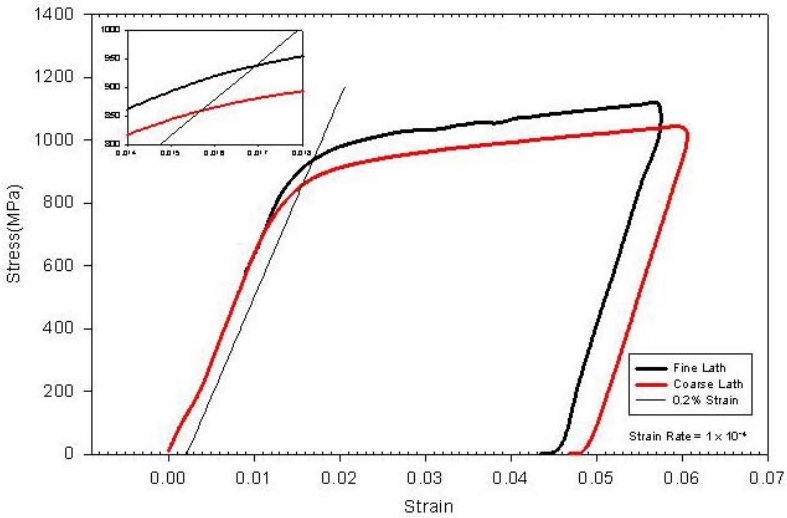

Figure 3. Stress-Strain Curves For β-Processed Ti-6al-4v With Coarse And Fine Lath Spacings And Nominally The Same Grain And Colony Sizes, And α Phase Volume Fraction Showing Clear Lath Spacing Effect

2.1.3 Observations of Room Temperature Recovery in Single Colony Crystals.

Creep testing on oriented single α/β colonies of Ti-6242Si has provided dramatic insight into a phenomenon that was previously unknown to occur in Ti alloys prior to the present work—the recovery of strain hardening at room temperature [3]. Figure 4 shows the strain-time curve for an a_2 basal sample deformed at a stress level of 640 MPa, corresponding to 84% of the observed 0.2% offset yield strength. An exhaustive primary creep behavior was observed during the initial portion of the creep test, indicative of rapid strain hardening. The sample was subsequently unloaded for 24 hours. Upon reloading, a creep rate of 1.4×10^{-7} s^{-1} was observed. This corresponds to over a two order of magnitude increase in creep rate upon reloading. The extrapolated power law primary creep behavior of the initial loading portion of the test is shown in figure 4 to demonstrate the large effect of the unloading/reloading sequence on the accumulated creep strain.

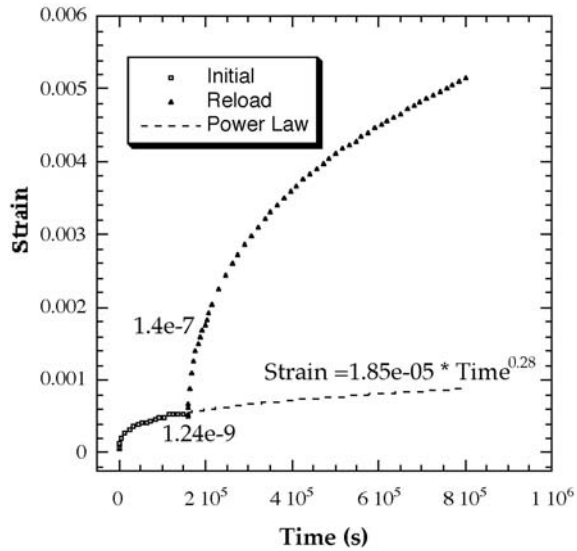

Figure 4. Strain Versus Time Plot From a Room Temperature Creep Test of a Single Colony Ti-6242 Compression Sample Oriented to Maximize the Resolved Shear Stress on the a_3 Basal Slip System

A similar test of an a_2 basal creep provided a notably different result, as shown in figure 5. This test was performed at a stress level of 640 MPa, corresponding to 78% of the 0.2% offset yield strength. An exhaustive primary creep behavior was observed during the initial portion of the creep test, to a minimum creep rate of 4.4×10^{-9} s^{-1}. The sample was then unloaded for 24 hours, then reloaded. The sample then resumed power law (exhaustive) creep behavior at a rate of 1.70×10^{-8} s^{-1}. Thus, the unloaded period had little effect on the creep rate or accumulated creep strain observed for the a_2 basal orientation compression sample.

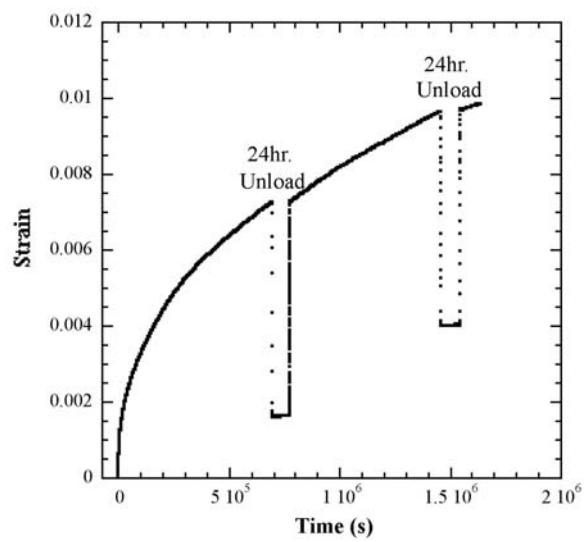

Figure 5. Strain Versus Time Plot From a Room Temperature Creep Test of a Single Colony Ti-6242 Compression Sample Oriented to Maximize the Resolved Shear Stress on the a_2 Basal Slip System

The recovery phenomenon is dependent upon the operative slip system for the colony crystals. It is also observed for polycrystalline Ti-6242 deformed in compression and tension [4]. The detailed deformation mechanisms associated with the phenomenon are described in the appendix A; however, present evidence indicates that it is associated with the presence of frequent internal barriers to slip, leading to a high density of pileup structures. For instance, for the a_3 basal slip orientation, large planar arrays of a-type dislocations are observed in the α phase, piled up at the entrance α/β interface. In contrast, these extended pileups are absent for the a_2 basal slip-orientated sample. Therefore, it is postulated that large pileups of a-type dislocations exist in the α phase, which stimulate the activation of fresh dislocation sources, even when the sample is under no macroscopically applied stress. The precise mechanism by which relaxation of these pileups leads to the activation of new sources in the α phase is yet be elucidated. It is likewise possible that these large local stress concentrations may also cause preferential diffusion of hydrogen to these regions. The theories of hydrogen-induced plasticity postulated by Birnbaum, et al. [5] would then suggest that enhanced, localized plasticity in these regions may be promoted by the locally elevated hydrogen levels.

It is believed that these preliminary recovery results have important implications for the development of local stress and strain distributions during alternating loading conditions. In particular, the effect of length of time in the unloaded state has not been explored in detail previously, and yet could have significant effect on local recovery processes as a function of individual grain or colony orientation. Characterization of these recovery effects is presently the focus of an Air Force Office of Scientific Research (AFOSR)-sponsored program.

2.1.4 Size Effects Associated With Ti-6242 Single Colonies.

The recent confluence of several capabilities has made possible the direct determination of the flow behavior of different regions of the complex polycrystalline microstructure of interest to the dwell fatigue issue in Ti-6242. The Focused Ion Beam (FIB) allows small-scale mechanical test samples to be milled on a polished section of a microstructure. Presently, pillars have been machined in the range of sizes from 5 to 25 micrometers using FIB. An example of such a pillar machined into a microtextured region of pancake 2 is shown in figure 6. Orientation Imaging Microscopy (OIM) can be used to ascertain the local orientation of various regions of the structure, and thus the anisotropy of the flow behavior can be assessed in situ. The particular pillar of figure 6(a) has an orientation for which a_2 basal slip should be activated. A nanoindentor with a tip that was intentionally flattened is then used to test the pillars under constant displacement rate conditions. The resulting stress-strain curve for the pancake 2 pillar is shown in figure 6(d), along with curves for a microcompression pillar tested from the a_2 basal colony crystal, and finally the bulk a_2 basal compression test. The remarkable features to note are that (1) the proportional limit and yield strength of the pancake 2 pillar are somewhat larger than those for the single colony crystal and (2) the strengths measured for both microcompression tests are substantially larger than those for the bulk sample. Feature 1 indicates that the a_2 colony crystal is only slightly softer than a similarly oriented microtextured region, providing validation for the colony crystal data as input into the crystal plasticity modeling. Nevertheless, feature 2 complicates the vision of using the microcompression technique to directly provide the required constitutive input.

Therefore, these important size effects have been further explored by focusing on the a_1 basal single colony crystals and fashioning pillars over a range of sizes. The results shown in figure 7 demonstrate that the proportional limts for a_1 basal orientation in bulk and microcompression are in good agreement, while the yield strength of the latter is about 100 MPa higher. Thus, the discrepancy between bulk and microcompression is much smaller for the a_1 basal case than it is for the a_2 basal case shown in figure 6(d). At present, it is not fully understood why the size effect should depend on the operative slip system, although it is notable that the size effect is large for the orientation that has the highest strength, even in the bulk case. Truncating the sample size may limit the buildup of local stress concentrations at the α–β interfaces, or within the β laths, and necessitate larger applied stress to initiate deformation. TEM investigations have been initiated to determine whether or not the deformed microstructures in the pillars are similar to those in bulk samples and to explore whether or not there are any obvious surface-related pileup structures that can explain the larger strengths for small sample sizes. The preliminary results of these investigations of FIB-extracted TEM foils from the pillars are described in appendix A.

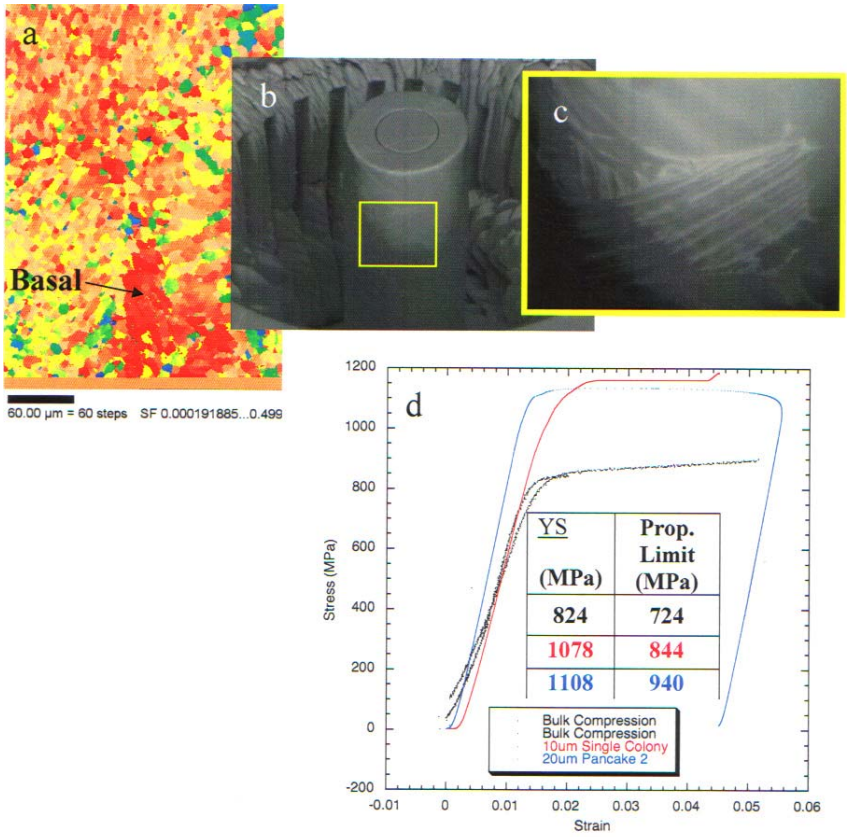

Figure 6. Microcompression Testing From Specific Microstructure Region From Ti-6242 (a) OIM Image of Pancake 2 Region Having a Local Region (Arrow) for Which the Schmid Factor for Basal Slip is Maximized (Red), (b) 20-µm-Diameter Compression Pillar Machined From the Region Arrowed in (a), (c) Enlarged SEM Image Showing Transmission of Slip Traces Across β Laths, the Operative Slip System is a_2 Basal, and (d) Comparison of Flow Curves for a_2 Colony Crystal (Bulk and microcompression) Versus the 20-µm Pancake 2 Pillar

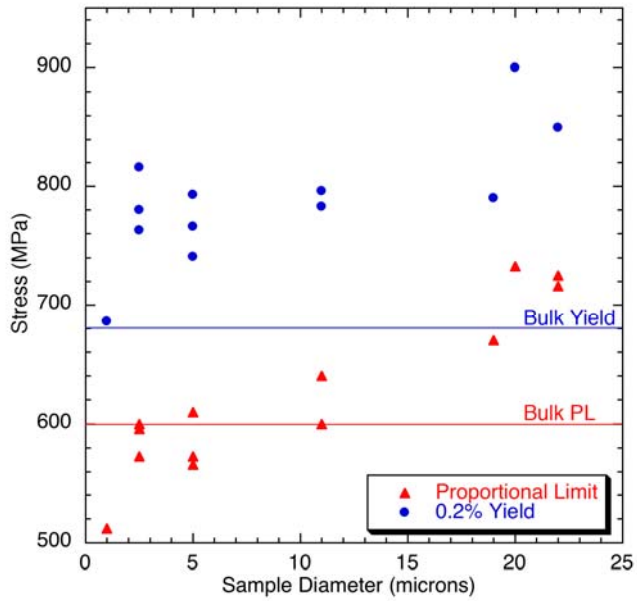

Figure 7. Plot of Stress Versus Sample Size Showing Both Yield Stress and Limit for a Series of a_1 Basal Single Colony Crystals (The lines indicate the properties measured on bulk samples.)

2.2 INFLUENCE OF MICROSTRUCTURE ON DWELL-FATIGUE SUSCEPTIBILITY.

In the current program, four different microstructural conditions of Ti-6242 alloy have been examined: three of these are α/β-forged and the fourth one is β-forged. Two of the α/β-forged Ti-6242 alloys were supplied by Ladish Co. and the third α/β-forged alloy was taken out of the field-returned (retired) impellers. The β-forged material was again supplied by Ladish Co. The thermomechanical processing (TMP) parameters for the three (two α/β-forged and one β-forged) Ladish pancakes represent the current or prior industrial forging practice for aircraft engine compressor components. The TMP parameters for the four microstructures are described in detail in appendix B. The optical micrographs of the four microstructures are shown in figure 8.

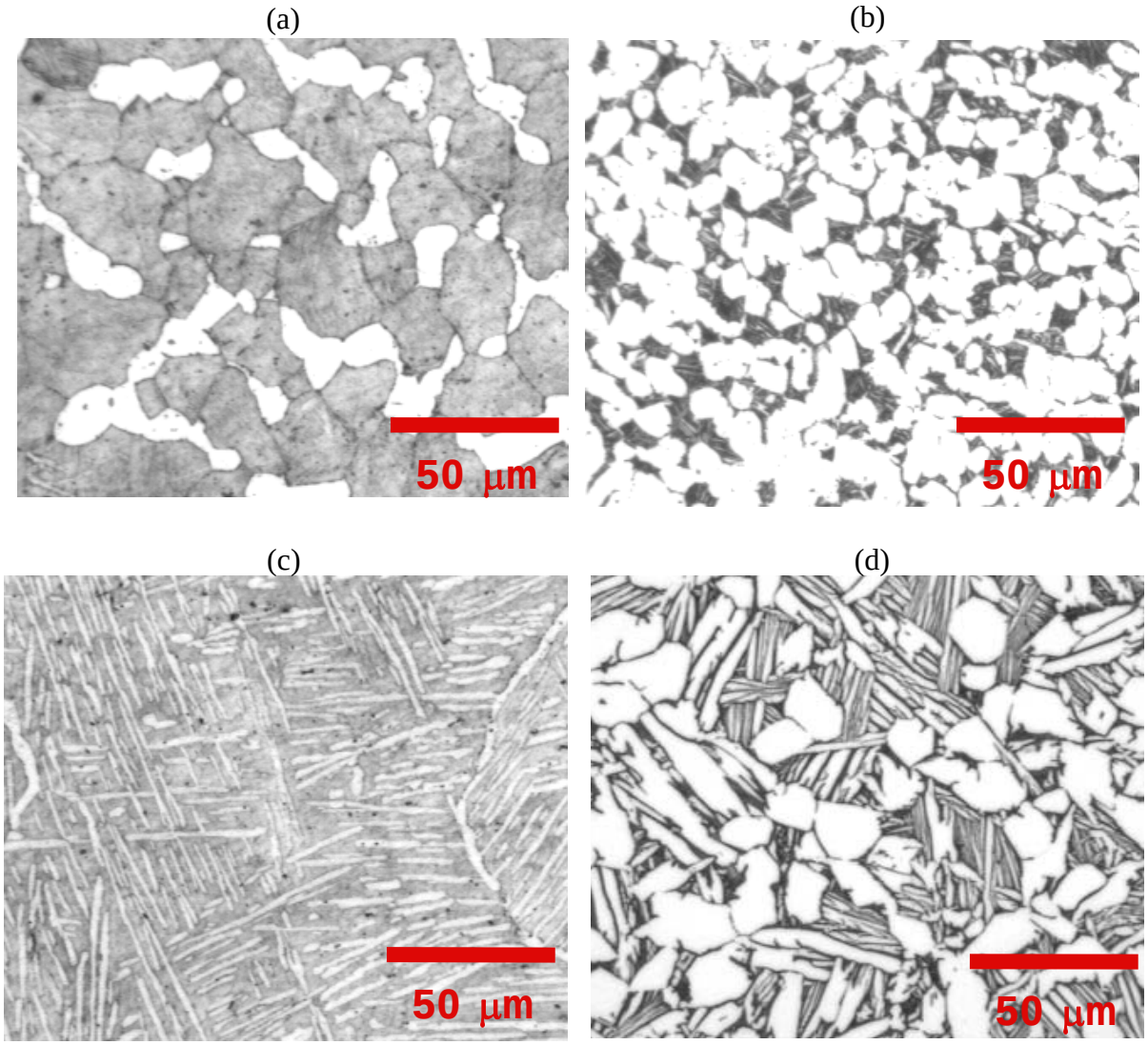

Figure 8. Optical Micrographs of the Forgings Tested in This Research (a) Forging 1, α/β-Forged; (b) Forging 2, α/β-Forged; (c) Forging 3, β-Forged; and (d) 1970s-1980s Vintage Material, α/β-Forged

2.2.1 Microtexture Analysis.

The microtexture of the three α/β-forged material was evaluated using the Electron Backscatter Diffraction (EBSD) techniques in an SEM. The orientation maps for the three α/β-forged alloys are presented in figure 9(a) through 9(c). Here, the points with the same color represent microstructural regions of similar crystallographic orientations. Forging 1 has minimal microtexture, whereas forging 2 and the vintage material have several large regions (size ~ 500 μm) that consist of grains with similar crystallographic orientations.

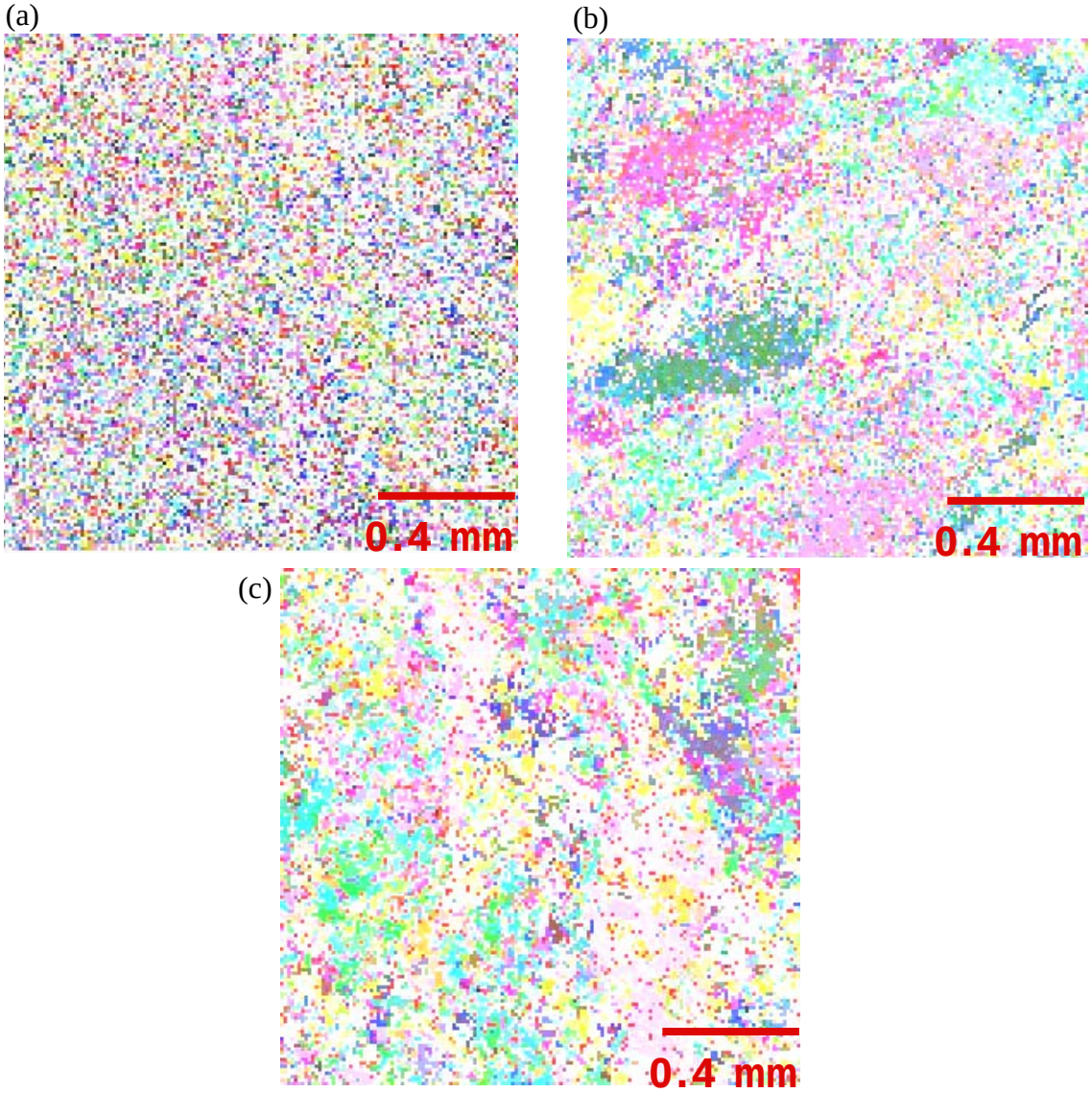

Figure 9. Analysis of Microtexture in the Three α/β-Forged Microstructures (a) Orientation Map of Forging 1, (b) Orientation Map of Forging 2, and (c) Orientation Map of 1980s Vintage Material

2.2.2 Normal Fatigue and Dwell-Fatigue Test Results.

The test conditions (load ratio, dwell time, and peak stress to yield strength ratio) for the three α/β-forged and one β-forged Ti-6242 alloy are shown in table 1 along with the corresponding plastic strain-to-failure, number of cycles to failure, and dwell life debit values. From the results summarized in table 1, it can be concluded that at a fixed peak stress to yield strength ratio of ~ 0.95, among the three Ladish pancakes investigated, pancake 2 (high microtexture, α/β-forged) material has the highest dwell-fatigue susceptibility and pancake 3 (β-forged) material has the lowest dwell-fatigue susceptibility. The comparison of results on Ladish pancake 2 material at two different peak stresses indicates that the dwell life debit is lowered as the peak stress is

reduced (table 1). The effect of peak stress on dwell life debit is consistent with the reports by Evans [6] and Kassner, et al. [7].

Table 1. Summary of Normal-Fatigue and Dwell-Fatigue Tests

Material	Load Ratio	σ_{max} / σ_{YS}	Dwell time (minutes)	Plastic Strain-to-Failure (ε^{pl}_f)	N_f (Cycles)	Dwell Life Debit
Ladish pancake 1 (low microtexture)	0	0.954	2	3.0%	8,803	6
			0	0.6%	51,235	
Ladish pancake 1 (low microtexture)	0	0.954	2	2.8%	11,946	4
			0	1.5%	47,906	
Ladish pancake 2 (high microtexture)	0	0.955	2	3.8%	1,303	18
			0	2%	22,991	
Ladish pancake 2 (high microtexture)	0	0.915	2	2.3%	3,074	15
			0	1.0%	45,843	
Ladish pancake 2 (high microtexture)	0	0.87	2	2.1%	13,763	
Ladish pancake 3 (β-forged)	0	0.957	2	3.2%	10,846	3
			0	0.5%	30,020	
Ladish pancake 3 (β-forged)	0	0.957	2	2.4%	12,927	2
			0	1.4%	30,374	
Retired impeller (α/β forged)	0	0.933	2	4%	2,492	11
			0	2.2%	27,755*	
Retired impeller (α/β forged)	0	0.933	2	3.3%	3,260	9
			0	2%	30,208	

*Specimen not shot-peened, rest all are shot-peened
Yield strength for the four microstructures were as follows: pancake 1: 1029 MPa; pancake 2: 950 MPa; pancake 3: 960 MPa; and retired-impeller: 930 MPa.

At a peak stress to yield strength ratio of ~ 0.93, the retired impeller material has a dwell life debit of ~10. Hence, at a lower peak stress of ~ 91% of yield strength, the dwell life debit will be reduced to a value less than 10. Based on these observations, it can be concluded that at a fixed peak stress to yield strength ratio of ~ 0.91, the Ladish pancake 2 material is more susceptible to dwell than the retired impeller material.

2.3 EARLY CRACK DETECTION.

The objectives of the early crack detection task are to (1) investigate crack initiation and small crack propagation under cold dwell and cyclic fatigue conditions, (2) develop methods for monitoring and localization of primary and secondary cracks, and (3) study growth rates of small dwell and cyclic fatigue cracks.

To understand the mechanism of cold dwell-fatigue (CDF) crack initiation and evolution, it is essential to detect just-initiated cracks and relate them to the surrounding microstructure. For this purpose, one needs experimental techniques that provide information on crack initiation, propagation and location. The difficulty is that the CDF cracks are initiated in the volume of the material, and thus cannot be observed by visual monitoring techniques.

First, the dwell-fatigue samples and mechanical testing methods are described. Next, the methods developed for small crack growth monitoring and localization are reported. Finally, the methodology for measurements of small dwell and cycling fatigue crack rates are discussed and compared with large cracks. Additional details are provided in appendix C.

2.3.1 Samples and Mechanical Testing.

The samples were prepared from Ti-6242 high microtexture α/β-forged material (pancake 2). The samples were machined by METCUT to flat fatigue samples 1.9 mm thick and 6 mm wide in the gauge length. The dwell and cycling fatigue tests were performed under stress control at maximum stress 126 ksi (869 MPa), R ratio 0. In most dwell-fatigue tests, the dwell time was 2 minutes at the maximum stress, and the frequency of the unloading-loading cycle was 1 Hz. Several dwell-fatigue tests were performed with hold for 30 minutes and at a single period dwell at the maximum stress until failure.

2.3.2 In Situ Dwell-Fatigue Crack Monitoring and Secondary Crack Localization.

For a better understanding of the dwell crack initiation mechanism, one needs to examine microstructural characteristics in the vicinity of just-initiated cracks and to determine crack initiation time and related accumulated strain. These may provide information on the mechanical and material conditions under which a dwell-fatigue crack can nucleate and propagate. In this task, necessary nondestructive characterization methods were developed, and related dwell-fatigue parameters and crack localization were obtained for the following microstructural characterization.

To monitor crack initiation and evolution, an in situ ultrasonic method was developed and implemented during the dwell and cycling fatigue and creep test. For this, a special real-time computer control data acquisition system was developed in-house. The method was combined with high resolution microradiographic imaging for precise secondary crack localization. As an example, figure 10 shows a radiographic match of the locations of two cracks as determined from ultrasonic monitoring of a dwell-fatigue test. The distance of a secondary crack determined from the image is 7.5 mm, which is very close to the distance (7.8 mm) determined from the ultrasonic signals. After the crack localization, the samples were further investigated near the crack tip by means of OIM and TEM. Similar experiments have been performed for cyclic

fatigue tests. The secondary cracks developed during the cyclic fatigue are much smaller than the dwell-fatigue cracks and exist near the fracture surface.

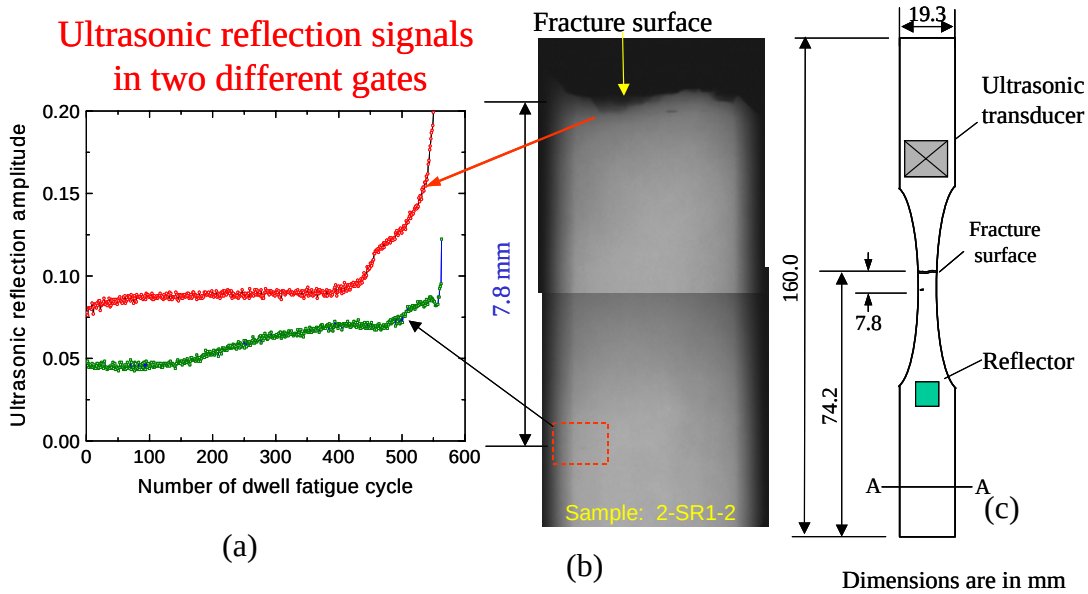

Figure 10. Radiographic Matching of the Locations of Two Cracks With Ultrasonic Monitoring (a) Peak Amplitudes of the Reflected Ultrasonic Signals From Initiated Cracks, (b) Obtained Positions of the Cracks Matched With Crack Sites Obtained From the Microradiographic Images, and (c) Sample Geometry of the Test Specimen

2.3.3 Crack Growth Rate Measurements, Interruptive Tests.

To determine the rates of small dwell and cyclic fatigue cracks, interruptive tests were performed. The samples were ultrasonically monitored during testing, and after the specified number of cycles, the tests were interrupted for microradiographic imaging. Figure 11 shows an example of the results of such a test for sample 2-SR2-3. To minimize the number of interruptions in the early stage of fatigue life, where no crack has yet initiated, the sample was continuously fatigued for the first 150 cycles. Then the test was interrupted after each 25 cycles until 400 cycles was reached. No crack indications were found at these number of cycles, and in the continuation of the test, it was interrupted after each 15 cycles until failure of the sample occurred at 663 cycles. The first crack was spotted both ultrasonically and by microradiography at 475 cycles. Nine more cracks were found during the following cycles. A summary of microradiographic images obtained for the prime crack of the sample 2-SR2-3 is shown in figure 11. The primary crack, which led to failure, appears at 550 cycles. The secondary cracks 2, 3, 4, and 6 were arrested after reaching a certain size, while cracks 1, 5, 7, 8, and 9 continued to grow until failure.

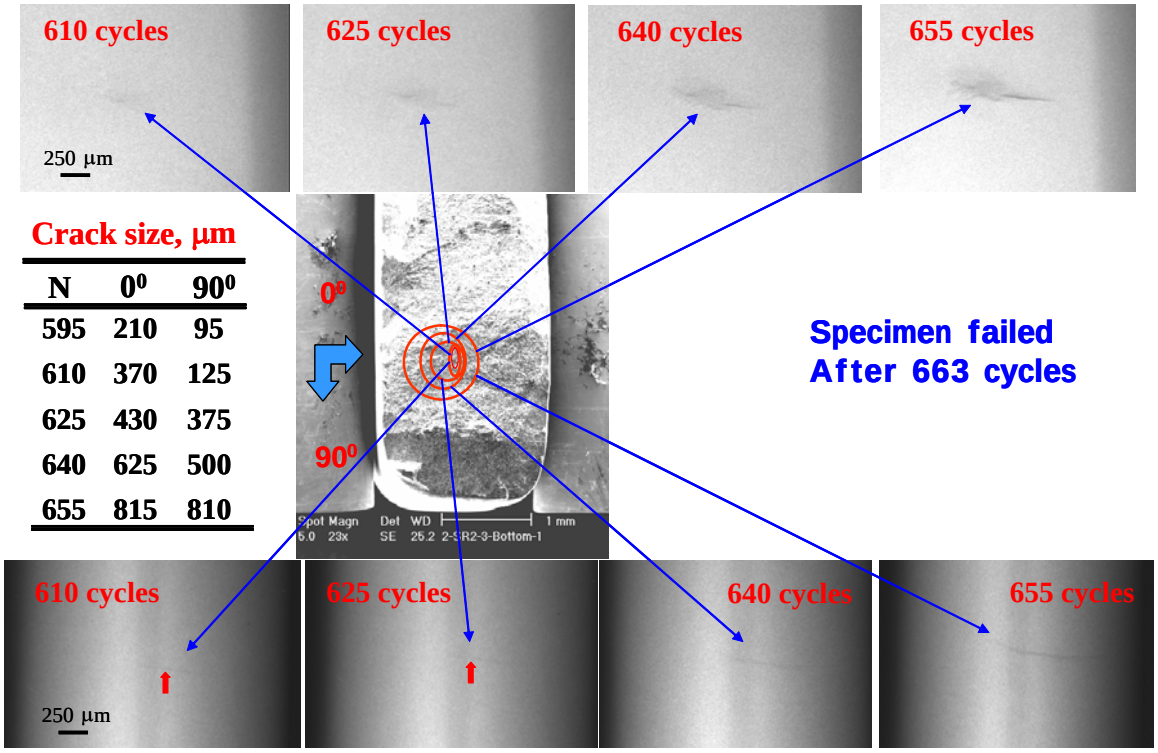

Figure 11. Microradiographic Images of the Primary Crack in the Sample 2-SR2-3

The top and bottom rows contain pictures taken from 0° and 90° angles, respectively. The table summarizes crack size versus number of cycles for both angles. The SEM image of the fractured surface relates crack areas at different stages of fatigue life (depicted with concentric circles) to the microradiographic images. In these experiments, the radiographic images obtained allow sizing of the cracks at different stages of the test and the ultrasonic monitoring data helps to obtain more precisely the initiation time. The accumulated strain was also measured, thus, the strain levels at crack initiation and sample failure are available.

The measurements shown in figure 11 were performed for several samples under dwell and fatigue conditions. The microradiographic crack sizing data were used to obtain small crack growth rates, which are shown in figure 12 by the solid points. The dwell-fatigue data are shown by solid squares and the cyclic fatigue by solid circles. The rates for small dwell-fatigue cracks are one to two orders of magnitude higher than those for small cyclic fatigue cracks.

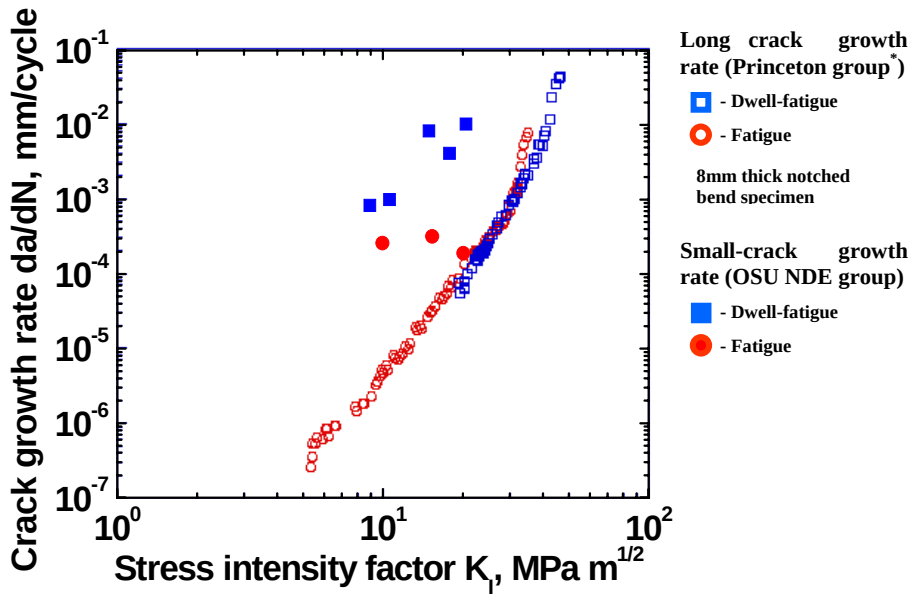

Taken from reference [8].

Figure 12. Comparison of Dwell-Fatigue (Squares) and Cyclic-Fatigue (Circles) Crack Growth Rates

In contrast to the small crack behavior, the rates obtained by Princeton's Soboyejo group for large dwell and cyclic fatigue cracks are identical [8]. The large crack growth rates are also shown in the figure (open squares and circles). Dwell-fatigue tests for large cracks were performed at the same stress level (869 MPa) as in the experiments for small cracks. However, for cyclic fatigue, a much larger range of stresses was used to obtain the larger range of crack growth rates (the lowest stress level was slightly above a threshold determined by such a level of stress-intensity factor that no crack initiation occurred for about 10^6 cycles). After reaching the threshold, different levels of constant load were applied to cover the full range of crack growth. The reason for the lower growth rate of large cyclic fatigue cracks is part of the cyclic fatigue data is below the rate for small fatigue cracks, which were obtained at high levels of stress. The rate of small-to-large cyclic fatigue crack evolution exhibits typical small and large crack behavior, if one considers the same stress level of the cyclic fatigue stress, while the rate for the small dwell-fatigue cracks is much higher.

2.3.4 Effect of Dwell Time on Sample Fatigue Life.

To investigate the effect of dwell time on fatigue life of Ti-6242 samples, dwell-fatigue tests were performed for different dwell (holding) times: 2 minutes, 30 minutes, and holding the sample at constant load to failure (creep test). The results show that the total dwell time is nearly constant, that is, $N*T_d$=constant, where (N) is the number of cycles to failure and (T_d) is the dwell time of a single cycle. Analysis of the results in the available literature for near-α IMI-829 alloy shows that they exhibit similar behavior. The data were obtained for near-α IMI-829 tested under maximum dwell load of 830 MPa and R=0.05 with 6.35-mm-diameter cylindrical samples

[9] and near-α IMI-834 tested under a maximum dwell load of 880 MPa and R=0.1 with 6-mm-diameter cylindrical samples [10]. It is, of course, expected that the total dwell-fatigue life depends on the sample microstructure, shape, and thickness due to different crack propagation time until failure.

2.4 SECONDARY CRACK CHARACTERIZATION.

Several orientation image maps have shown that secondary cracks arrest at or shortly into a softer-oriented microtextured region. To further characterize the secondary cracks and why they arrest, TEM foils were extracted from regions around the crack. Figure 13 shows the secondary crack used in this study and the corresponding OIM. The crack is lying on the basal plane in region 2 and has arrested in neighboring soft grains (i.e., where the basal plane is substantially inclined to the deformation axis), in regions 1 and 3, respectively. Using the FIB, TEM foils were extracted from regions ahead of each crack tip, in the wake of the crack, along the boarder of the soft and hard microtextured regions and far away from the crack. The results of this analysis indicate that

- The TEM foil extracted at the crack tip in region 1 (figure 14) shows many a-type dislocations, which is expected from Schmid factor considerations. However, there is also a high density of c+a-type dislocations. Due to the high CRSS for this slip system, and the unfavorable grain orientation, these were not expected. However, the <c+a> activity was probably produced from the triaxial stress state ahead of the crack tip.

- The TEM foil extracted at the crack tip in region 3 indicates a-type and once again c+a-type activity. The a-type dislocations are on basal planes and were likely induced by the triaxial stress state, since the Schmid factor for basal slip is very low. The minor misorientation between regions 2 and 3 is apparently sufficient to arrest the crack.

- The TEM foil extracted along the crack wake, just below the plane of the crack, shows a high density of both a-type and <c+a> type (figure 15). The latter are far larger in number than is observed further from the crack. These dislocations indicate that there is plasticity in the hard region and that the crack propagation is time-dependent.

These results indicate that there is substantial plasticity in the vicinity of these secondary cracks. In the bounding, softer-oriented grains, both a-type and <c+a> activity is generated. In the hard-oriented grain in which the crack lies, substantial plasticity parallel to the [0001] direction has occurred in the process of crack propagation. These results support the premise that propagation of very short cracks does not occur by a rapid, cleavage process. Additional details are provided in appendix D.

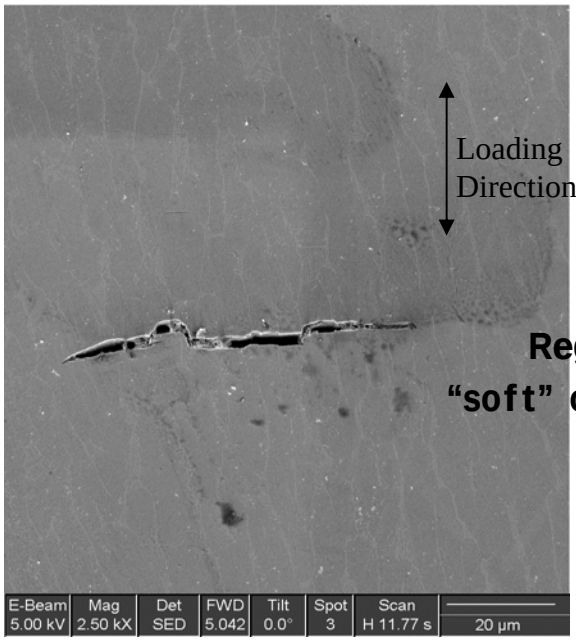

(a)

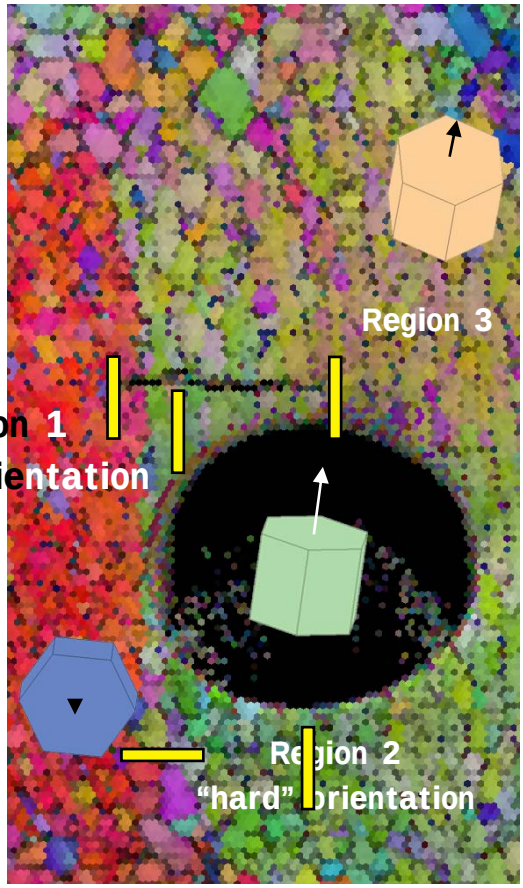

(b)

Figure 13. (a) An SEM Image of a Secondary Crack Lying on the Basal Plane and (b) the Corresponding OIM of the Same Crack, Indicating the Locations TEM Foils Were Extracted

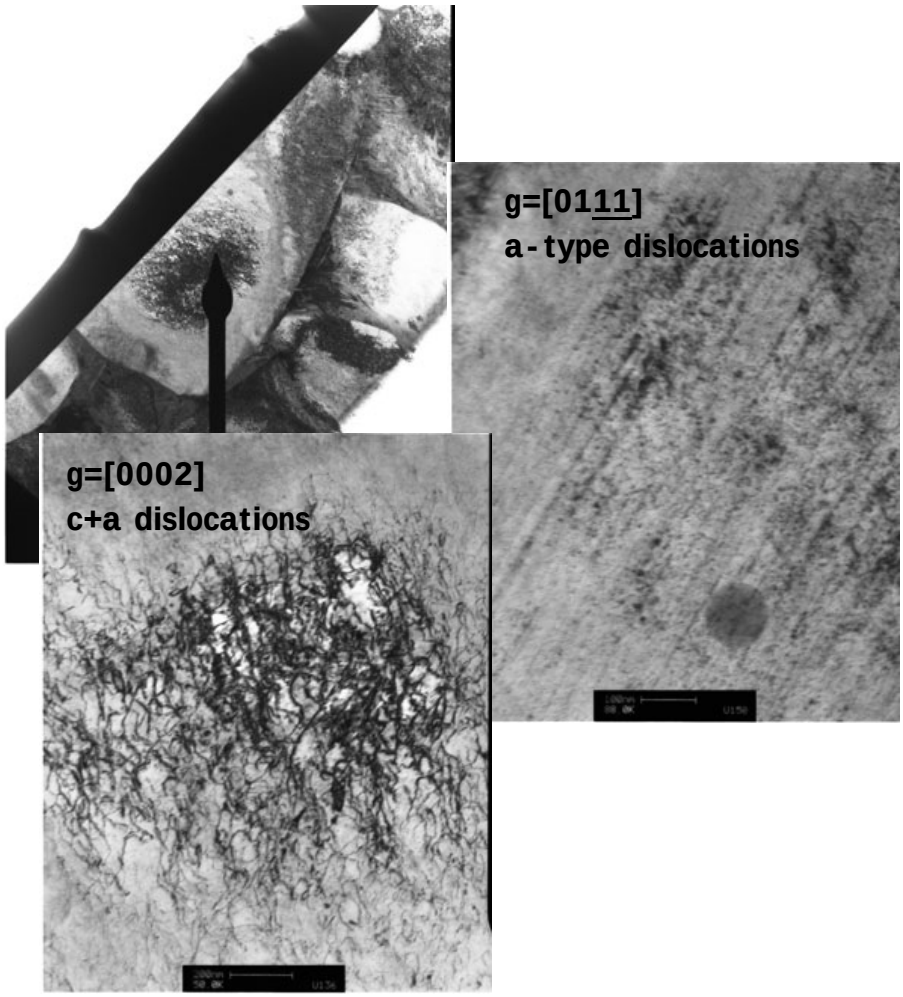

Figure 14. TEM Images Taken From the Crack Tip in Region 1, Showing Lots of a-Type and c+a-Type Activity

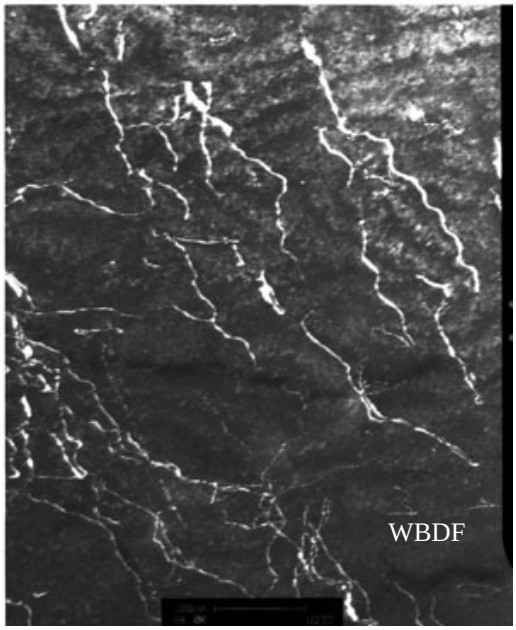

Figure 15. TEM Images Taken in Bright Field and Weak-Beam Dark Field From the Wake of the Crack

2.5 CONTRIBUTIONS OF NORMAL-FATIGUE AND STATIC-LOADING DEFORMATION/DAMAGE PROCESSES TO THE DWELL-FATIGUE FAILURE.

Although it was realized that both the creep and cyclic deformation/damage processes contribute to dwell-fatigue failure, the relative importance of these processes for the total damage has not been understood in a fundamental sense. To obtain an understanding of the relative contributions of the cyclic (repetitive) and static loading to the overall dwell-fatigue damage, the normal fatigue, dwell-fatigue, and static-loading tests were conducted at two different stress levels (see appendix E for details). These tests were done on pancake 2 alloy that had ~ 70 vol.% primary α and it also had a high level of microtexture.

2.5.1 Rupture Lives and Strain Accumulation.

The test conditions (dwell time and peak stress to yield strength ratio) are described in table 2 along with the corresponding plastic strain to failure, number of cycles to failure, and dwell life debit values. The comparison of results at two different peak stresses indicates that the dwell life debit is lowered as the peak stress is reduced (table 2). The effect of stress on dwell life debit is consistent with the reports by Kassner, et al. [7] and Evans [6]. Moreover, a higher plastic strain to failure was observed at a higher stress for both the normal fatigue and dwell-fatigue loading conditions (table 2).

Table 2. Summary of Normal-Fatigue and Dwell-Fatigue Tests

$\sigma_{max} / \sigma_{YS}$	Dwell Time (minutes)	ε^{pl}_f (Gage length ~ 18 mm)	N_f (Cycles)	Dwell Life Debit
0.955	2	3.8%	1303	18
	0	2%	22,991	
0.915	2	2.3%	3074	15
	0	1.0%	45,843	

The experimental results for the static-loading test condition are summarized in table 3. A comparison of the dwell and static-load tests at a fixed peak stress to yield strength ratio of ~ 0.95 shows that the statically loaded specimen fails in about twice the time and at similar plastic strain values as the dwell-fatigue-tested specimen (table 3). In other words, the dwell-fatigue specimen reaches the similar plastic strain as the statically loaded specimen in about half the time. It is also worthwhile to note that at a lower stress of ~91% of yield strength, the statically loaded sample did not fail even after about 7 times the time to failure for the corresponding dwell-fatigue specimen (table 3). Based on these observations, it can be concluded that as the applied peak stress is increased, the times to failure under dwell-fatigue and static-loading conditions approach each other, i.e., at high applied stresses, the contributions of the static damage processes to the overall dwell-fatigue failure become significant. On the other hand, at lower stresses, the cyclic damage processes are more important for dwell-fatigue fracture. This is evident from the fact that, as the applied peak stress is reduced, the number of cycles to failure under dwell-fatigue conditions approaches that under normal fatigue conditions,

i.e., the dwell life debit is reduced at lower stresses as discussed above (table 2). It is important to note that under the condition for which there is a larger dwell life debit (i.e., a higher peak stress condition), creep damage is the dominant process for dwell-fatigue failure.

Table 3. Comparison of Dwell-Fatigue and Static Load Tests

$\sigma max / \sigma YS$	Loading Condition	Time at Maximum Load, i.e., Rupture Life (hrs.)	ε^{pl}_{f} (Gage Length ~ 18 mm)
0.955	2-minute dwell	43.5	3.8%
0.955	Static load	84.8	3.6%
0.915	2-minute dwell	102.5	2.3%
0.915	Static load	673.9*	1.8%*

*Specimen did not fail.

2.5.2 Fractography and Failure Modes.

The fractographic observations on the failed specimens support the results obtained on the rupture lives under different test conditions. At the high peak stress, the crack initiation modes are similar under dwell-fatigue and static-loading test conditions, and these are quite different for the normal fatigue test condition (see appendix E). On the other hand, as the peak stress is reduced, the crack initiation mode under normal fatigue test condition starts to resemble that under dwell-fatigue condition, whereas the static load failure does not occur in a reasonably long period of time.

2.6 CRYSTALLOGRAPHIC ORIENTATION OF FRACTURE FACETS AT THE INITIATION SITE.

Facets have been observed on the fracture surface of near-α Ti alloys tested under normal fatigue, dwell-fatigue, and static-loading conditions [11-15]. To better understand the crack initiation mechanism, it is important to determine the crystallographic orientation of these fracture facets.

One of the common microstructural conditions in which Ti-6242 alloy is used in practice is the bimodal microstructure with a reasonably high volume fraction of primary α. Although the orientation of dwell-fatigue fracture facet for this microstructure was determined in an earlier study [16], there is very little work on the orientation determination of normal fatigue and static-loading fracture facets for this microstructure. The objective of this part of the current study was to determine the crystallographic orientation of the fracture facets obtained under three different test conditions (normal fatigue, dwell fatigue, and static loading) in Ti-6242 alloy that had a bimodal microstructure with a high volume fraction of primary α (pancake 2 material).

The normal fatigue, dwell-fatigue, and static-loading specimens examined in this investigation were taken from the work reported in appendix E. The normal fatigue test was carried out at ~ 91% of yield strength, the static-loading test was carried out at ~ 95% of yield strength, and the

dwell-fatigue tests were carried out at ~91% and ~95% of yield strength (see appendix E for details). As described in appendix E, the initiation site consisted of faceted features for each of the four specimens.

The crystallographic orientation of the fracture facets at the initiation site was determined using the quantitative tilt fractography and EBSD techniques in an SEM. The details of this methodology are described in appendix F. The results indicate that the normal fatigue (no dwell) fracture facets are oriented at ~ 5° or less with respect to the basal plane (figure 16); the dwell-fatigue fracture facets are oriented at ~ 10-15° with respect to the basal plane (figures 17 and 18), and the static-loading fracture facets are oriented at ~ 20° with respect to the basal plane (figure 19).

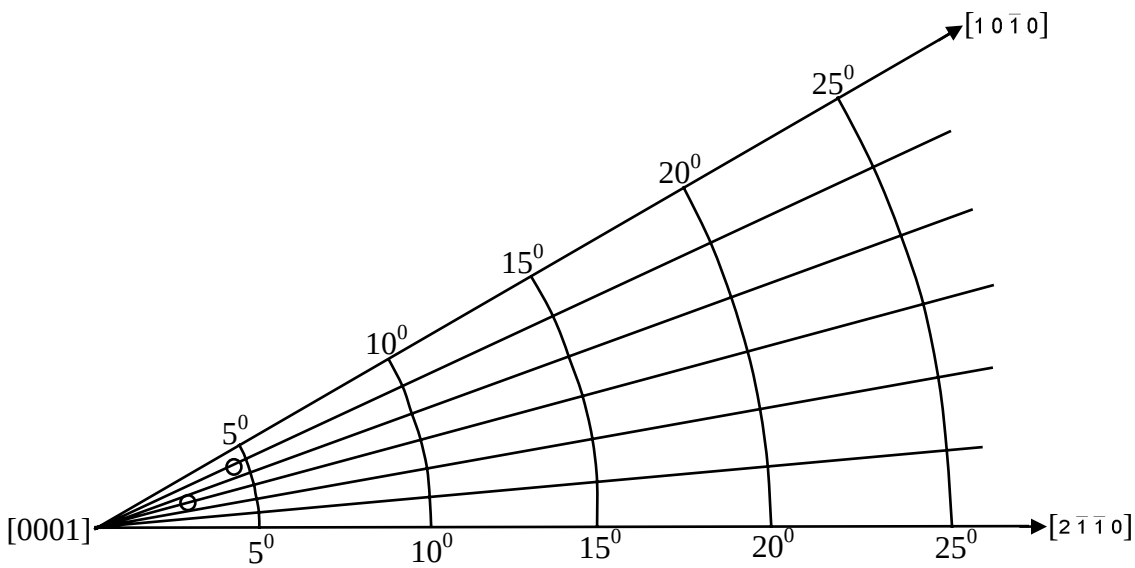

Figure 16. Crystallographic Orientation of Normal Fatigue Fracture Facet at the Initiation Site (Peak stress for normal fatigue test ~ 91% of yield strength (see appendix G for details).)

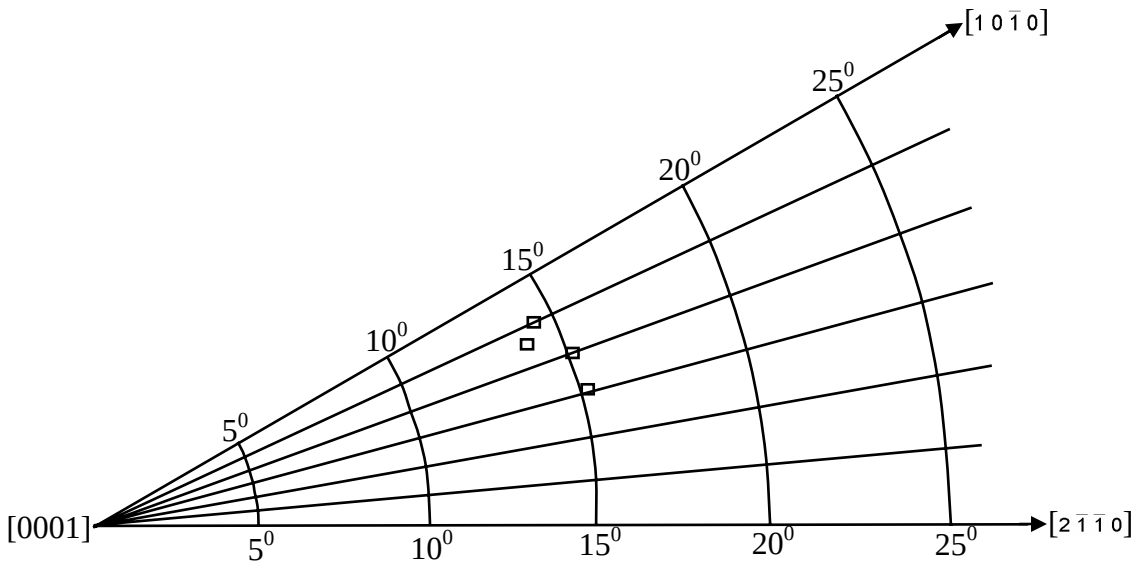

Figure 17. Crystallographic Orientation of Dwell-Fatigue Fracture Facet at the Initiation Site (Peak stress for dwell-fatigue test ~ 91% of yield strength (see appendix G for details).)

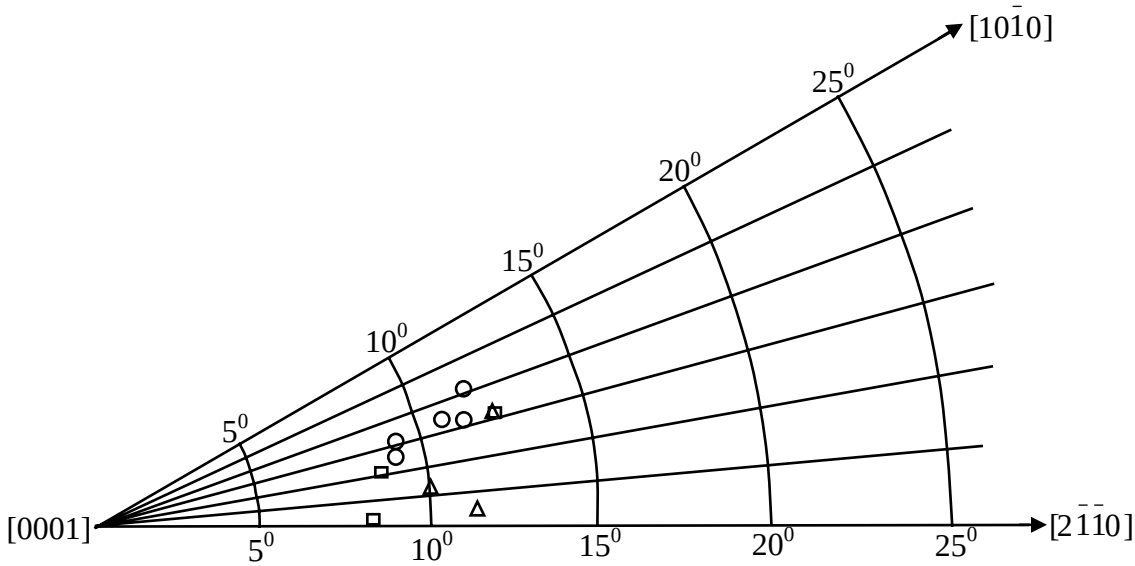

Figure 18. Crystallographic Orientation of Three Different Dwell-Fatigue Fracture Facets at the Initiation Site (Peak stress for dwell-fatigue test ~ 95% of yield strength (see appendix F for details).)

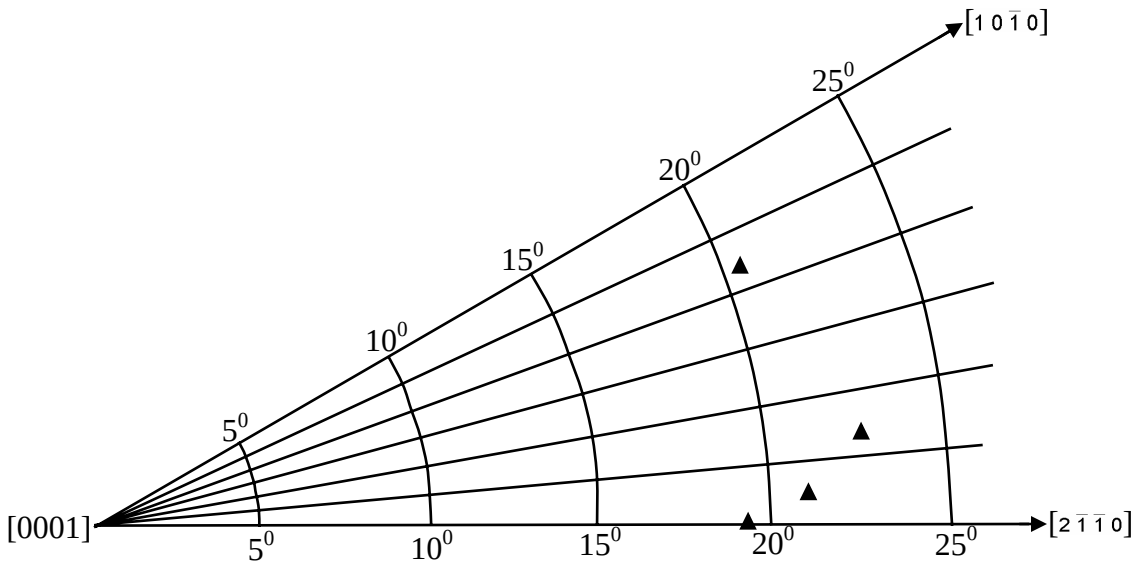

Figure 19. Crystallographic Orientation of Static-Loading Fracture Facet at the Initiation Site (Peak stress for static-loading test ~ 95% of yield strength (see appendix G for details).)

Therefore, of the three loading conditions (normal fatigue, dwell fatigue, and static loading), the deviation from the basal plane is the smallest for the normal fatigue fracture facets and it is the largest for the static-loading fracture facets. These results are described in more detail in appendix G.

2.7 CRYSTALLOGRAPHIC ORIENTATION OF THE REGIONS BELOW THE DWELL-FATIGUE FRACTURE SURFACE.

A faceted crack initiation site is typically observed on the fracture surface of Ti-6242 alloy that has been tested under dwell-fatigue loading conditions. In this part of the research, the orientation images of almost entire specimen cross section were obtained at different depths below the fracture surface. The aim was to obtain an idea about the crystallographic orientation and the size of the microtextured region that is associated with the faceted initiation site. This work was done on pancake 2 material (see appendix B).

The dwell-fatigue specimen had a rectangular cross-section with a gage section width and thickness of 6.48 mm and 1.93 mm, respectively. The length of the reduced section was 12.7 mm. The 2-minute dwell test was carried out at a peak stress of 869 MPa and a load-ratio of 0 (see appendix C).

The dwell-fatigue specimen failed in 447 cycles, whereas the normal fatigue life for this specimen geometry is 24,000 cycles. Thus, a 54 times reduction in life resulted because of the 2-minute hold at the peak stress. The dwell-fatigue crack initiation site is faceted (see appendix H), which is consistent with results obtained on other specimens machined from the same

pancake forging [15]. The value of life reduction varies from specimen to specimen, but is always large enough for this microstructure to be a concern.

To determine the crystallographic orientation of the grains at and around the dwell-fatigue crack initiation site, the polishing was done directly onto the fracture surface with the plane of polish being perpendicular to the loading axis. Serial sectioning and EBSD techniques were used to obtain the orientation images at different depths below the fracture surface.

The faceted initiation site on the fracture surface is circumscribed by a dotted curve in figure 20, and it is clear that the faceted region is more than 1 mm long.

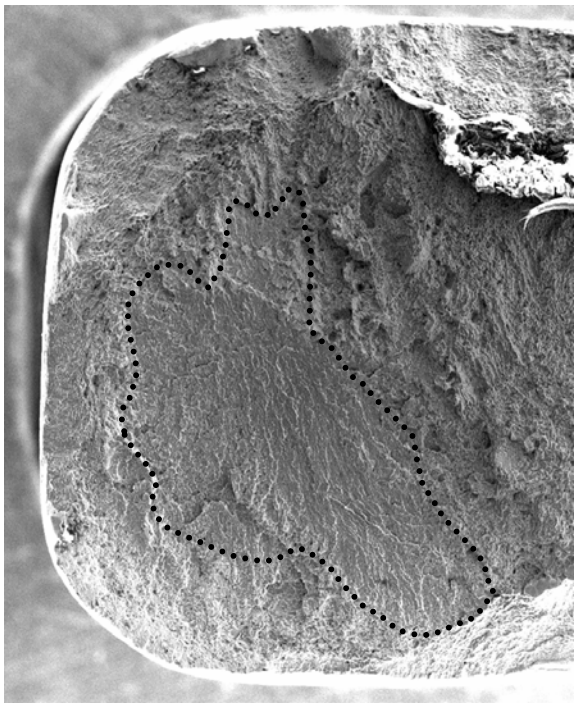

1 mm

Figure 20. Dwell-Fatigue Fracture Surface With the Faceted Initiation Site Circumscribed by a Dotted Curve

Figure 21 shows the orientation images of the entire polished surface at five different depths below the reference plane. The colors in the orientation images are based on the angle between the surface normal (i.e., the loading axis during dwell-fatigue test) and basal plane normal. For 15° increments in this angle, the color changes. For example, when this angle is in the 0°-15° range, the color at that point is red, when it is in the 15°-30° range, the color is pink and so on, per the key shown in the bottom of figure 21. The dotted curve in the left portion of figure 21(a) was copied from figure 20, and it circumscribes the region just below the faceted initiation site (see figure 20). It is clear from figure 21 that this red/pink microtextured region continues through the fifth serial sectioning step (~ 200 μm below the fracture surface) and probably deeper. It is also evident that the size of this red/pink region, in the left portion of the orientation

images (figures 21(a) through 21(e)), is reduced at greater depths below the fracture surface. In other words, the crack initiation (and probably, small crack growth) that leads to the specimen failure, occurs where the red/pink region is larger in size.

There is another red/pink microtextured region in the right portion of the orientation images (figures 21(a) through 21(e)). Its size increases at greater depths below the fracture surface. However, its size, even at the largest depth sectioned in the current work (figure 21(e)), is smaller than the size of the red/pink region just below the faceted initiation site (left portion of figure 21(a)). This observation reinforces the view that the crack initiation and small crack growth, which eventually leads to specimen failure, occurs in the larger red/pink region. In this context, it is important to note that the small crack growth is strongly dependent on the crystallographic orientation of the grains at the crack tip. The results suggest that the growth of small cracks is arrested when the crack tip approaches a region where the basal plane normal is inclined at a large angle with respect to the loading axis. On the other hand, the small cracks continue to grow (presumably at a much larger rate than large cracks) when they are still in the region where the basal plane normal makes a relatively small angle with respect to the loading axis (i.e., the red/pink region in figure 21). In such a scenario, the crack initiated in the large red/pink region can become the primary crack, eventually causing the specimen failure, which is consistent with the results of this part of the research.

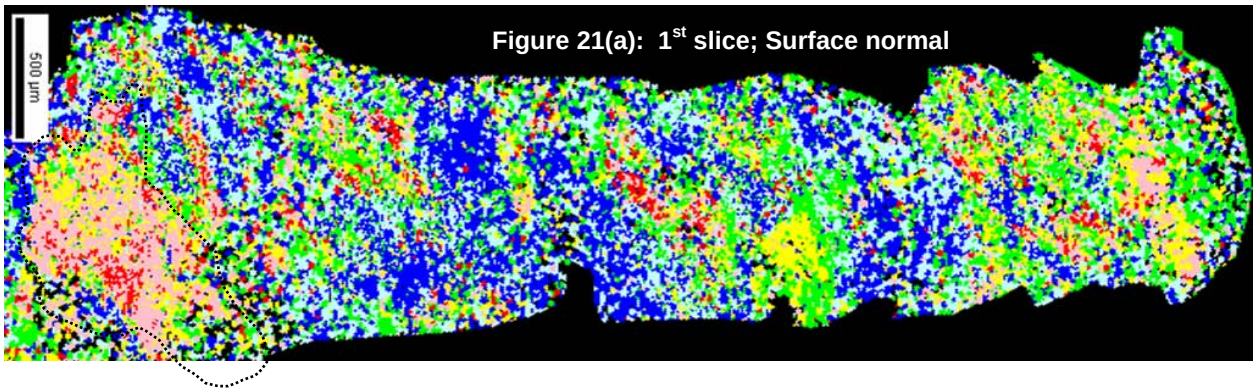

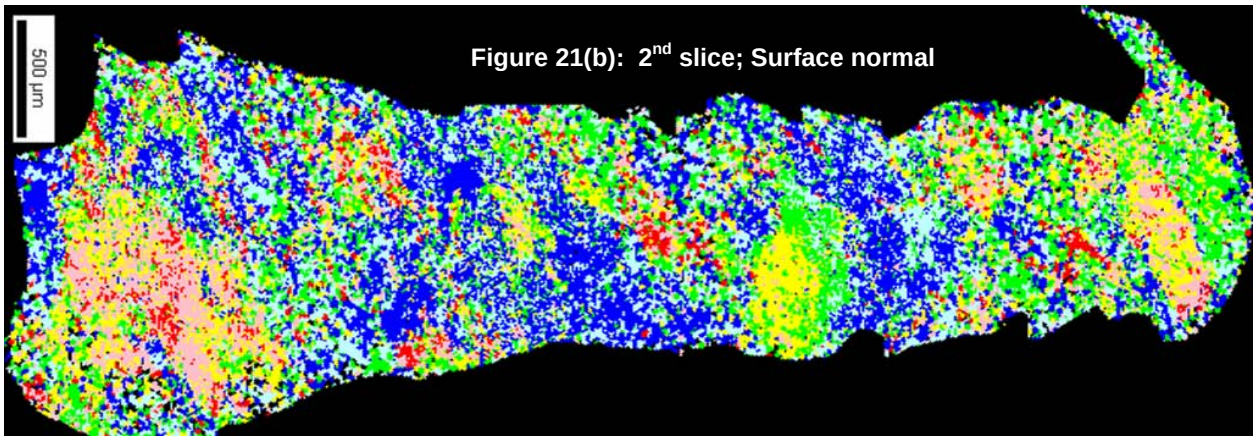

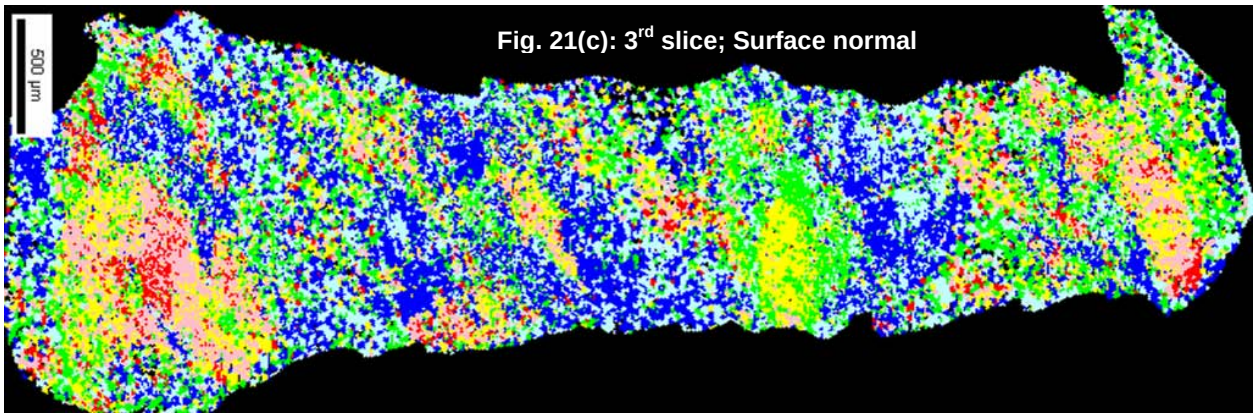

Figure 21. Orientations Images for the Entire Polished Surface at Five Different Depths Below the Reference Plane (a) After First Serial Sectioning Step (44 µM Below the Reference Plane); (b) After Second Serial Sectioning Step (83 µM Below the Reference Plane); (c) After Third Serial Sectioning Step (115 µM Below The Reference Plane); (d) After Fourth Serial Sectioning Step (155 µM Below the Reference Plane); and (E) After Fifth Serial Sectioning Step (187 µM Below the Reference Plane)

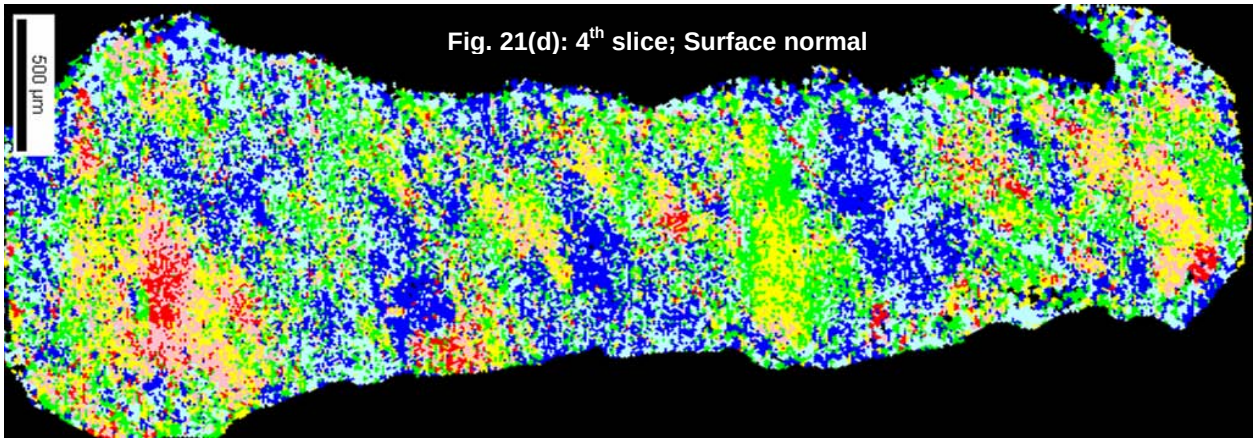

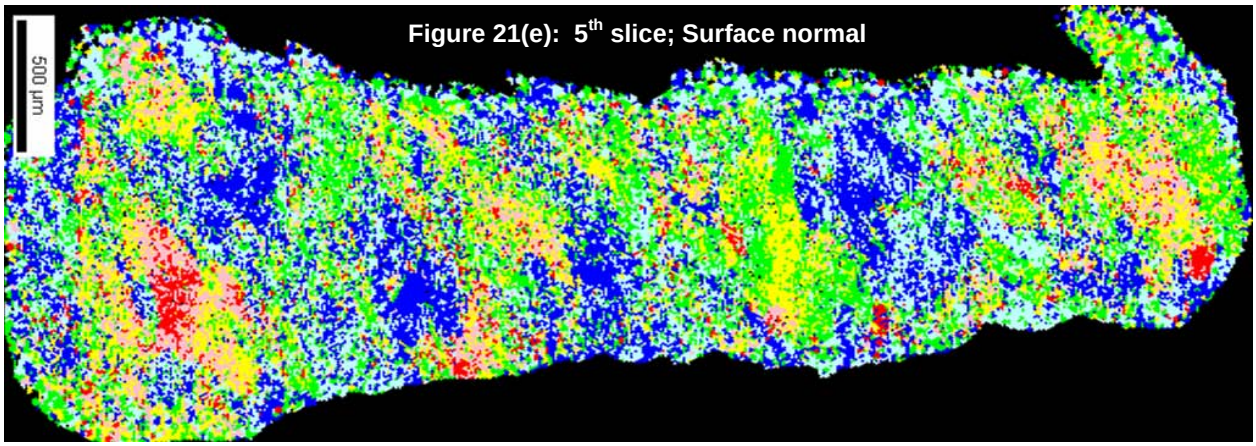

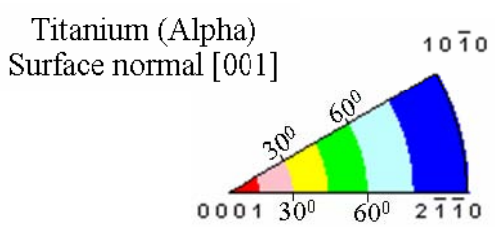

Figure 21. Orientations Images for the Entire Polished Surface at Five Different Depths Below the Reference Plane (a) After First Serial Sectioning Step (44 µM Below the Reference Plane); (b) After Second Serial Sectioning Step (83 µM Below the Reference Plane); (c) After Third Serial Sectioning Step (115 µM Below The Reference Plane); (d) After Fourth Serial Sectioning Step (155 µM Below the Reference Plane); and (E) After Fifth Serial Sectioning Step (187 µM Below the Reference Plane)

2.8 INFLUENCE OF HYDROGEN CONTENT.

One of the primary factors for dwell-fatigue susceptibility is thought to be related to the hydrogen present in these alloys. Hydrogen has the potential for affecting several important aspects of material behavior (e.g., deformation characteristics, tendency to form brittle hydrides, etc.), which in turn can change its propensity for dwell-fatigue failure. The near-α Ti alloys are so named because they contain α (hcp) as the major phase. The α phase is known to have very different elastic [17] and plastic [2] behavior in different crystallographic orientations. Furthermore, the deformation behavior of the two constituent phases, α (hcp) and β (bcc), are quite different. Both of these factors can cause stress redistributions under an applied stress, although the elastic and plastic anisotropy of the α phase will have a larger effect. This will result in regions of high hydrostatic (tensile) stress. Hydrogen is known to segregate to regions of high hydrostatic (tensile) stress, where the hydrogen concentration can attain values much higher than the nominal concentration.

Several researchers have studied the effects of hydrogen content on the dwell-fatigue response [6, 9, 13, and 18-20]. Most of the prior work has focused on one particular near-α Ti alloy, namely IMI 685 [6, 9, 13, and 18-20]. In the current study, the effects of hydrogen content on the dwell-fatigue response of a different near-α Ti alloy, Ti-6Al-2Sn-4Zr-2Mo, was examined. One common microstructural condition in which this alloy is used in practice is a bimodal microstructure consisting of 0.4-0.7 volume fraction of primary α (the balance being an α+β transformation product). However, very little work has been done in examining the correlation between hydrogen content and dwell-fatigue behavior in this microstructural condition. Therefore, in this investigation, we have selected Ti-6242 alloy with the bimodal microstructure (pancake 2 material) to study the effects of hydrogen content on its dwell-fatigue behavior.

The normal fatigue and dwell-fatigue test results, at ~ 95% of yield strength, are summarized in tables 4 and 5, respectively. Figure 22 shows the variation of normal fatigue and dwell-fatigue lives with hydrogen content. The dwell-fatigue lives are significantly lower than the normal fatigue lives. The normal fatigue life is a weak function of hydrogen content and it is slightly lower for hydrogen contents ≥ 100 ppm. On the other hand, the dwell-fatigue life is higher for higher hydrogen contents, especially for hydrogen contents ≥ 150 ppm. The trend curves drawn through the normal fatigue and dwell-fatigue lives appear to merge at hydrogen contents larger than 250 ppm. However, more data points at high hydrogen contents are needed for making this statement with confidence.

Table 4. Normal Fatigue Response at the Peak Stress ~ 95% of Yield Strength for Different Hydrogen Contents

Hydrogen Content (ppm by weight)	N_f (cycles)	Plastic Strain-to Failure, ϵplf (gage length ~ 18 mm)
7[a]	18,350	2.1%
49[a]	22,991	2%
100[b]	13,110	1.5%
110[a]	15,550	1.2%
127[b]	15,347	1.6%

[a] Air-cooled
[b] Furnace-cooled (see appendix I for details of these two conditions)

Table 5. Dwell-Fatigue (Hold Time = 2 Minutes) Response at the Peak Stress ~ 95% of Yield Strengh for Different Hydrogen Contents

Hydrogen Content (ppm by weight)	N_f (cycles)	Plastic Strain-to-Failure,εplf (gage length ~ 18 mm)
10[a]	1498	9.1%
49[a]	1303	3.8%
59[b]	1176	6.1%
150[a]	3773	5.6%
204[b]	3402	11.7%
230[a]	6849	5%

[a] Air-cooled
[b] Furnace-cooled (see appendix I for details of these two conditions)

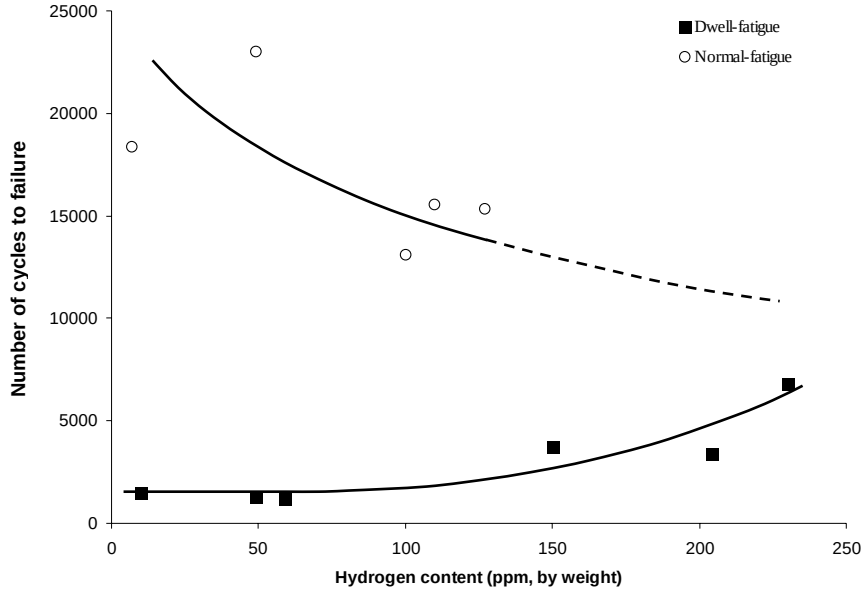

Figure 22. Variation in Fatigue Life With Hydrogen Content for Normal Fatigue and Dwell-Fatigue Test Conditions

The results on normal fatigue life as a function of hydrogen content (table 4 and figure 22) are, by and large, consistent with the results of prior studies on IMI 685 with colony microstructure [6 and 19-21]. On the other hand, in the prior studies, the dwell-fatigue life was found to be either a weak function of hydrogen content [6 and 18-20] or significantly lower for higher hydrogen content [9, 13, and 21]. In none of the prior reports reviewed, is there an instance where the dwell-fatigue life for a higher hydrogen alloy was found to be longer [6, 9, 13, and 18-20] by a factor of as high as 3 to 5, as has been observed in the current study (table 5 and figure 21). One possible reason for this apparent discrepancy could be a difference in the microstructural conditions: all the reviewed investigations [6, 9, 13, and 18-20] have been conducted on IMI 685 with colony microstructure, whereas the current study was conducted on Ti-6242 alloy with bimodal microstructure. One important distinction between the two microstructures is the relative continuity of the α and β phases. The colony microstructure typically consists of a continuous β phase matrix in which each α lath is surrounded by β phase and, thus, is disconnected from other α laths. On the other hand, the bimodal microstructure with ~ 70 vol. % primary α, which was examined in the current study, consists of a continuous α phase matrix and the β phase is discontinuous (see figure 1 of appendix I). The difference in the microstructure can have important implications for hydrogen-induced embrittlement because hydrogen has a larger solubility and mobility in the β phase than in the α phase. Therefore, it is easier for hydrogen to segregate to the regions of high tensile hydrostatic stresses in the continuous β matrix microstructure than in the continuous α matrix microstructure.

It is also of interest to note that the room temperature diffusion coefficient of hydrogen in Ti alloys can be two orders of magnitude higher for the interconnected β phase microstructure than for the discontinuous β phase microstructure [21]. Therefore, the estimated diffusion distance

for a continuous β matrix microstructure is about 10 times larger than for a continuous α matrix microstructure. Therefore, hydrogen diffusion to the regions of high (tensile) hydrostatic stresses can occur from a material volume that is roughly 1000 times larger in the continuous α matrix microstructure than in the continuous α matrix microstructure at the same time from the start of the test. This can lead to an increase in the local hydrogen concentration that is up to ~1000 times (the exact factor will also depend on thermodynamic feasibility) higher for the continuous β matrix microstructure than for the continuous α matrix microstructure for the same bulk hydrogen content. Hence, a colony microstructure (which has interconnected β phase) could be made more susceptible to dwell-fatigue failures with an increase in hydrogen content, as reported by Evans and Bache [20], Hack and Leverant [9], and Bache, et al. [13]. On the other hand, an increase in the bulk hydrogen content of a bimodal microstructure with discontinuous β phase is not likely to have such a significant detrimental effect on its dwell-fatigue susceptibility, which is by and large consistent with the results of the current study. Nonetheless, the reasons for a higher dwell-fatigue life with an increase in hydrogen content observed in the current study for the discontinuous β phase (bimodal) microstructure are currently not clear.

The crystallographic orientations of the dwell-fatigue fracture facets are essentially the same for as-received and hydrogen-charged alloys (see figures 4 through 6 of appendix F and figures 11 and 12 of appendix I): the facets are inclined at ~ 10°-15° with respect to the basal plane. Hence, the longer dwell-fatigue lives observed for the hydrogen-charged alloys (table 5 and figure 22) cannot be explained on the basis of the orientation of the fracture facets at the initiation site.

2.9 LONG CRACK GROWTH RATES.

The normal fatigue and dwell-fatigue crack (long and through-thickness) growth rates were experimentally measured using single-edge-notched bend specimens, which is described in detail in appendix J. The normal fatigue and dwell-fatigue crack growth rates are compared for the pancake 1, pancake 2, and pancake 3 materials in figures 23, 24, and 25, respectively. The results indicate that the long crack growth rates are comparable for the normal fatigue and dwell-fatigue test conditions (figure 23 through 25) for all three Ladish pancake materials. Therefore, a shorter dwell-fatigue life when compared with the normal fatigue life (appendix B) observed for the smooth specimens cannot be explained on the basis of any differences in the long crack growth rates under the two test conditions.

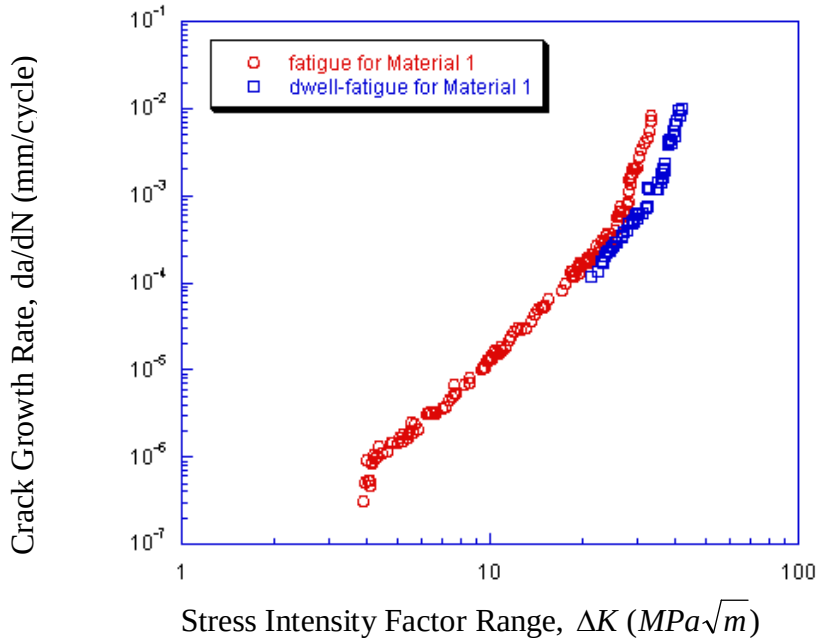

Figure 23. Comparison of Normal Fatigue and Dwell-Fatigue Crack Growth Rate Data for Pancake 1 Material

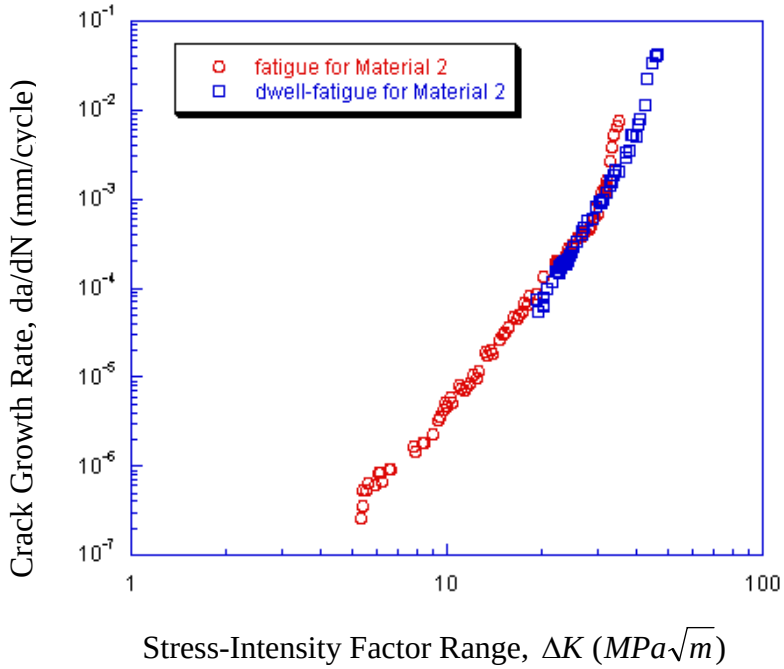

Figure 24. Comparison of Normal Fatigue and Dwell-Fatigue Crack Growth Rate Data for Pancake 2 Material

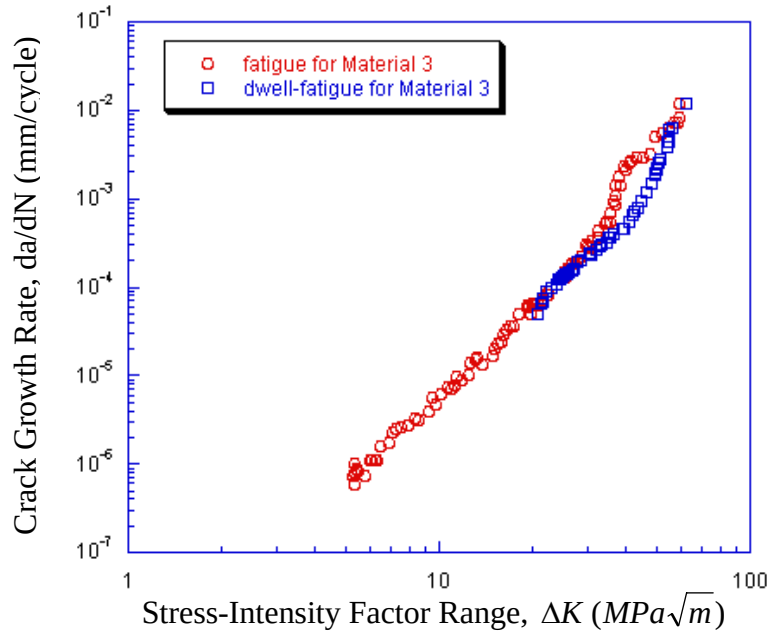

Figure 25. Comparison of Normal Fatigue and Dwell-Fatigue Crack Growth Rate Data for Pancake 3 Material

2.10 COMPUTATIONAL MODELING OF Ti-6242.

The aim of this research was to simulate the behavior of alloy Ti-6Al-2Sn-4Zr-2Mo (Ti-6242) using a crystal plasticity model. The parameters in the model were calibrated using the experiments for single colony results. The model was then used to simulate the behavior the polycrystal alloy containing both primary α and β phases and the results compared to experiments. Since the explicit modeling of all the features of Ti-6242 could prove to be computationally expensive, an equivalent model was developed and used in all the simulations.

The microstructure of Ti-6242 consists of regions of transformed β in a matrix of equiaxed primary α grains, as shown in figure 26. The amount of transformed β observed in the final microstructure depends on the temperature at which the hot working takes place, with higher temperatures leading to higher volume fraction of β phase.

The transformed β regions consist of α/β (hcp/bcc) colonies with a Burger's orientation relationship between the two phases. A crystal plasticity model is used to simulate the behavior of the hcp and bcc phases and an equivalent model developed to model the β phase.

A summary of the experimental results available for Ti-6242 is presented in section 2.10.1, followed by a description of the computational models, including the development of the equivalent model for the β phase, used in the simulation. Also described are the steps taken to calibrate the model using the experiments, so as to obtain the various crystal plasticity parameters. This is followed by polycrystal simulations and comparison with the experiments. The technique used to obtain a statistically equivalent orientation and misorientation distribution

with the experiment will also be discussed. Additional details are provided in appendices K and L.

2.10.1 Summary of Experiments.

Single colony Ti-6242 crystals were grown and mechanical-tested in tensile and compression directions. The orientations considered while performing the above tests were the ones that produced maximum slip in a_1, a_2, and a_3 basal and prismatic directions in tension and a_1, a_2, and a_3 basal directions in compression. The stress-strain data obtained from these tests were used to calibrate the crystal plasticity parameters as discussed in appendix L. Constant strain rate tension, compression, compression creep, and compression-tension tests were carried out on polycrystalline samples comprising of 70% primary α phase and 30% β phase.

2.10.2 Computational Modeling of Ti-6242.

2.10.2.1 Explicit Modeling of the Transformed β Region.

As shown in figure 26, the transformed β region has a lamellar microstructure consisting of hcp (α) and bcc (β) lathes. Hence, a finite element model having spatially separated α and β lamellae, with the α region being hcp with 30 slip systems and the β region being bcc with 48 slip systems was created. The Burger's relationship between the two phases is given by $(101)_\beta \parallel (0001)_\alpha [111]_\beta \parallel [2110]_\alpha$.

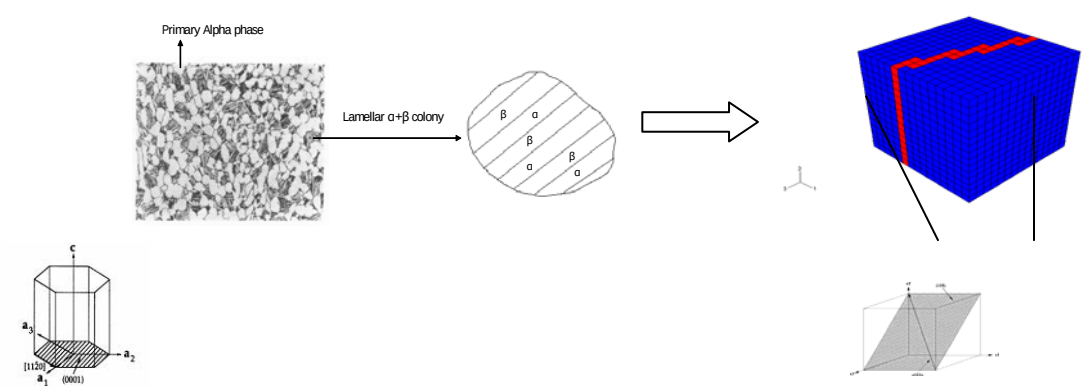

Equivalent Model: $\sigma^{equiv} = vf^{bcc} \times \sigma^{bcc} + vf^{hcp} \times \sigma^{hcp}$

Figure 26. Microstructure of Ti-6242 After Forging in the α+β Regime (The microstructure consists of transformed β (dark phase) colonies in a matrix of equiaxed primary α grains (light phase). The β phase can be modeled using an explicit mesh, which can then be represented by an equivalent model.)

The volume fraction of the α and β phases in the above model was adjusted to be 0.88 and 0.12 respectively. Minimum constraint boundary conditions, just enough to prevent rigid-body motions, were applied to the model. The parameters used for the hcp phase are taken to be slightly perturbed from the ones calibrated previously for Ti-6Al. The model is then used to calibrate the parameters for the bcc phase using a genetic algorithm (GA), which minimizes the difference between the experimental single colony Ti-6242 results and the simulation curves for constant strain rate tension and compression tests. A typical calibration is shown in figure 27.

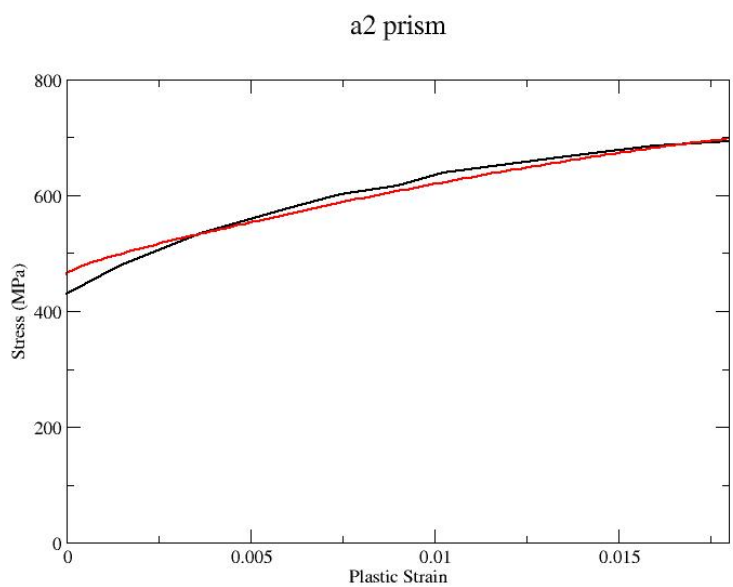

Figure 27. Calibration of bcc Parameters Single Colony Ti-6242 Samples

2.10.2.2 Equivalent Model for Ti-6242.

The explicit model described in the previous section is computationally expensive, and hence, a simpler model, which is capable of representing the essential features of Ti-6242 behavior, was developed for use in polycrystalline simulations. The β phase region is homogenized and an equivalent region, which contains both hcp and bcc slip systems at the same point, is considered. The two phases (at the same point) are subject to the macroscopic strain that is present at that point. As a result, the morphology of the β region can be represented using a single element, as depicted in figure 26. The stress response of the two phases are computed separately using a crystal plasticity model. The final macroscopic stress response at the point is computed as a weighted average of hcp and the bcc responses based on their volume fractions as shown below.

$$\sigma_{ij}^{equivalent} = vf^{hcp} \times \sigma_{ij}^{hcp} + vf^{bcc} \times \sigma_{ij}^{bcc}$$

In the above equation, σ_{ij}^{hcp} and σ_{ij}^{bcc} are the stress responses of the hcp and bcc systems respectively, vf^{hcp} and vf^{bcc} are the volume fractions of the hcp and bcc phases and $\sigma_{ij}^{equivalent}$ is the macroscopic stress at the point. In this model, the volume fractions are taken to be 0.88 and 0.12 for the α and β phases respectively. The model accommodates for the tension-compression asymmetry observed, with the crystal plasticity properties associated with a slip system chosen based on the sign of the hydrostatic stress. The bcc parameters are taken to be the same as those calibrated in the previous section and the hcp parameters are calibrated using GA. The experimental results available are a_1, a_2, and a_3 basals in tension and compression and a_1, a_2, and a_3 prismatics in tension. For the basal systems, there are two sets of parameters, one each for tension and compression. For the other slip systems, both the tension and compression directions are considered to have the same properties.

The equivalent model and the explicit model were also compared by observing the accumulated slip on various slip systems on both models. They were found to be in agreement with each other. This indicates that the equivalent model can be considered to be an adequate representation of the Ti-6242 colony behavior.

2.10.3 Polycrystal Simulations.

2.10.3.1 Material Properties Used.

The polycrystalline material used here consists of 70% primary α and 30% transformed β regions. Each element of the finite element model is considered to be a single grain. The transformed β regions are modeled using the equivalent model described in section 2.10.2.2.

The slip system hardness (strength) of the primary and secondary α phases are taken to be higher than the single colony ones, due to the presence of Hall Petch effects in the polycrystalline material, as a result of the much reduced size of the primary and secondary α phases in the polycrystals.

2.10.3.2 Orientations Distribution.

A large number of orientations in the form of Euler angles were obtained from the experiments. These were mapped onto the finite element mesh (which, in general, have much fewer elements/grains than the experiment) using an orientation distribution function, so that both the experimental microstructure and the model are statistically equivalent to each other. The experimental and simulation pole figures used in the simulation are shown in figure 28.

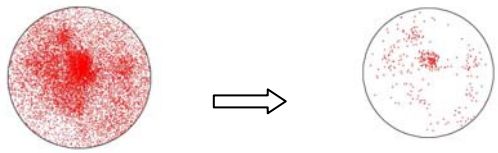

Figure 28. Experimental and Simulation Pole Figures Used in Polycrystalline Simulations

2.10.3.3 Misorientation Distribution.

Misorientation refers to the amount of misalignment between two neighboring grains, and the misorientation angle refers to the smallest angle required to transform one orientation to the other. An iterative process is used here for the model to match the misorientation distribution with the experiment. First, the orientation distribution is matched with the experiment, and the texture for the model is obtained. After matching the texture, the grains can be moved around, without disturbing the pole figure, to statistically match the experimental misorientation distribution. Initially, the average misorientation of the elements with their neighbors is calculated. Then the elements which produced the worst match with the experimental misorientation diagram is moved around while keeping the ones that best match the experimental misorientation at their current location. This process is iterated until a morphology, which matches with the experiment, is obtained (figure 29).

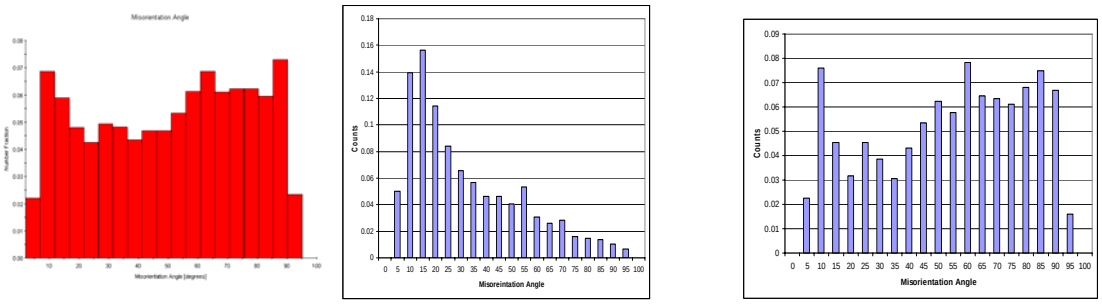

(a) (b) (c)

Figure 29. Matching the Misorientation Distribution (a) Experimental Misorientation Distribution, (b) Initial Misorientation Distribution for the Mesh, and (c) Final Misorientation Distribution for the Mesh

2.10.4 Polycrystalline Simulations.

Simulations are carried out using the model described for constant strain rate tension and compression and creep for a 343-element finite element mesh. The orientation distribution used for the simulation is shown in figure 30. The results and comparison with experiments are shown in figure 31. Good agreement is observed between the experiment and the simulation results.

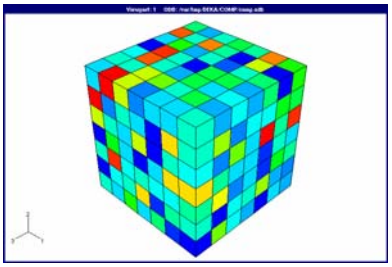

Figure 30. Orientation Distribution Used in the Polycrystalline Simulation Model

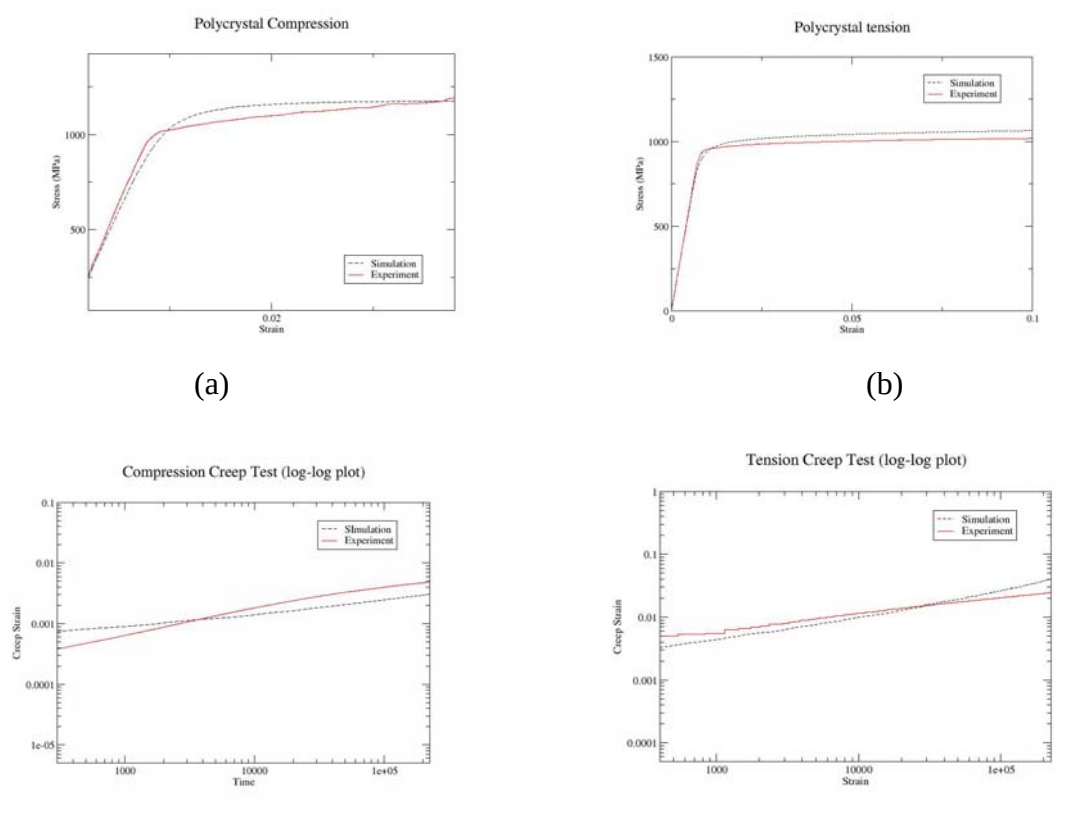

Figure 31. (a) Constant Strain Tension, (b) Constant Strain Compression, (c) Compression Creep Test, and (d) Tension Creep Test

3. CONCLUSIONS.

The project encompassed a multipronged comprehensive effort to understand the cause of dwell fatigue in Ti-6242 being used in engine components. The major observations and results that were obtained from experiments, involving microscopy and mechanical testing, are being incorporated in a computational model that is expected to have predictive capabilities. The entire undertaking was quite challenging due to the complex nature of the microstructure, deformation, and damage mechanisms governing the dwell-fatigue phenomenon of this material.

However, these details are crucial if a clear understanding of crack initiation, and the intrinsic and extrinsic factors controlling initiation, are to be developed. Significant progress has been made towards these objectives, which are summarized below.

An ambitious program was carried out to measure the time-dependent flow characteristics of the principal elements in the Ti-6242 microstructure. The results of compression testing of Ti-6wt% single-phase single crystals in three different orientations indicated that the [0001] orientation is over three times stronger than the prism and basal a-type slip systems. A similar anisotropy was assumed in the crystal plasticity model for Ti-6242. Single colony crystals of Ti-6242 were also grown and tested under constant strain rate conditions for seven distinct orientations to probe the plastic anisotropy for this important microstructural constituent. A large anisotropy in the critical resolved shear stress was observed for the three distinct basal orientations, while a smaller anisotropy was observed for the prism systems. The strength of the [0001] orientation was 40% larger than the weakest a-type orientation. A detailed transmission electron microscopy (TEM) investigation was performed on single colony specimens oriented for basal slip and deformed in compression. The results showed a remarkably different process of slip transmission for the three slip systems activated, which reflect the different orientation relationships between the slip directions in the alpha and beta phases. These results provided significant, new insight into the plastic anisotropy of these colony crystals. It was also observed that strengths in compression were significantly smaller than those in tension. Finally, a dramatic room temperature recovery of strain hardening was observed in one of the basal single colony crystals, indicating that large dislocation pileups in the alpha phase may induce generation of new dislocation sources, even when in the unloaded state. This recovery phenomenon is unusual at low homologous temperature and may have important implications for the development of local stress and strain distributions during alternating loading conditions. This effect was also confirmed in single phase Ti-6Al and two-phase Ti-6242 polycrystals.

Small-scale compression testing was conducted through a combination of Focused Ion Beam machining and nanoindentor testing (with a flattened tip) to measure the flow properties of major elements of the actual polycrystalline microstructure in situ. The feasibility of this approach was demonstrated, and it was shown that the anisotropy of single colony crystals was reproduced even at a small sample size (approaching 5 μm). However, a significant strengthening was discovered at small sample size over that measured in bulk. The source of this strengthening was not understood, but a TEM investigation was initiated to shed light on this effect.

Among the four microstructures of Ti-6242 alloy investigated in this program, the dwell-fatigue susceptibility (at a fixed peak stress to yield strength ratio) can be ranked from the most severe to the least severe as Ladish pancake 2 (α/β forged, ~ 70 vol. % primary α, high microtexture), retired impeller material (α/β forged, ~ 40 vol. % primary α, high microtexture), Ladish pancake 1 (α/β forged, ~ 25 vol. % primary α, low microtexture), and Ladish pancake 3 (β forged).

To characterize dwell-fatigue crack initiation and small crack growth, a large number of dwell-fatigue, cyclic fatigue, and creep experiments were performed on Ti-6242 alloy flat samples (microstructure 2). To monitor crack initiation and small crack evolution, an in situ ultrasonic crack monitoring system was developed. Secondary cracks were detected and localized by

ultrasonic and microradiographic methods for further characterization of the microstructures in the crack vicinity.

Small dwell-fatigue and cyclic fatigue crack growth rates were obtained from interruption experiments in which crack initiation and evolution were monitored by ultrasonic method and crack sizing, at different stages of fatigue, were determined by the microradiographic method. It was found that the rates for small dwell-fatigue cracks are one to two orders of magnitude higher than those for small cyclic fatigue cracks. This small crack growth behavior is greatly different from that of long cracks which exhibit identical rates for dwell and cyclic fatigue. The rate of small-to-large cyclic fatigue crack evolution exhibits typical small/large crack behavior if one considers the same stress level of the cyclic fatigue stress.

The effect of dwell time on fatigue life of Ti-6242 was investigated (dwell times 2 minutes, 30 minutes and creep experiment). It was found that for tested flat samples (microstructure 2), the total dwell time to failure was nearly constant for all experiments.

The experimental results obtained in this investigation indicate that at high stresses, the dwell-fatigue failure was caused primarily by static deformation/damage processes. On the other hand, at low stresses, the relative contributions of the cyclic (repetitive) processes to the overall dwell-fatigue failure became more dominant. This finding was supported by both the mechanical test results (i.e., the rupture lives at different stresses for the three different test conditions) and fracture mode studies conducted in a scanning electron microscope.

The plane of the fracture facets at the initiation site obtained for the normal fatigue test condition (peak stress ~ 91% of yield strength) was oriented at ~ 5° or less from the basal plane. The facets at the initiation site obtained for the dwell-fatigue test condition (peak stress ~ 91% and ~ 95% of yield strength) were oriented at ~ 10°-15° from the basal plane. On the other hand, the facets at the initiation site obtained for the static-loading test condition (applied stress ~ 95% of yield strength) were oriented at ~ 20° with respect to the basal plane. Therefore, of the three loading conditions (normal fatigue, dwell fatigue, and static loading), the deviation from the basal plane was the smallest for the normal fatigue fracture facets and largest for the static-loading fracture facets.

To determine the crystallographic orientation of the grains at and around the dwell-fatigue crack initiation site, polishing was done directly onto the fracture surface with the plane of polish being perpendicular to the loading axis. Serial sectioning and Electron Backscatter Diffraction techniques were used to obtain the orientation images at different depths below the fracture surface. The results indicate that the largest near-basal-oriented microtextured region in the sampled volume of material corresponds to the faceted initiation site on the fracture surface. This could be due to the possible arrest of small crack growth for the case when the size of the near-basal oriented microtextured region is relatively small.

The effects of hydrogen content on the normal fatigue and dwell-fatigue response were examined for the Ti-6242 alloy that contained ~ 70 vol. % primary α. This microstructure consisted of a continuous α-phase matrix. The results indicated that the normal fatigue life was a weak function of hydrogen content, and it was slightly lower for hydrogen contents $\geq$ 100 ppm. On

the other hand, the dwell-fatigue life was higher for higher hydrogen contents, especially for hydrogen contents ≥ 150 ppm. The crystallographic orientation of dwell-fatigue fracture facets was similar for both the as-received and hydrogen-charged alloys: the facets were inclined at ~ 10°-15° with respect to the basal plane. In some of the prior studies, the dwell-fatigue life was observed to be significantly lower at higher hydrogen contents. The apparent disagreement of this observation with the results reported in the current study can be understood on the basis of the differences in hydrogen diffusion kinetics for the different microstructures examined in the various studies.

The long crack growth rates are comparable for the normal fatigue and dwell-fatigue test conditions. Therefore, a shorter dwell-fatigue life, when compared with the normal fatigue life observed for the smooth specimens, cannot be explained on the basis of any differences in the long crack growth rates under the two test conditions.

Important results and observations made from the experimental work in this research were incorporated in a computational model for modeling the behavior of Ti-6242. The model integrates crystal plasticity constitutive relations with a finite deformation finite element code (ABAQUS and MARC) using the user-defined windows UMAT. A systematic approach to calibrating crystal plasticity parameters for the different constituents of Ti-6242 microstructure was adopted. The tasks included calibrating primary α slip parameters from the results of single phase Ti-6Al mechanical tests. This was followed by a validation study using the results of polycrystalline Ti-6Al testing. In this endeavor, a method for assigning equivalent orientation distributions to the finite element model was developed. The model was then used to extract crystal plasticity parameters for the β laths (bcc) in the transformed β microregions. The results of a the finite element model (FEM) model, consisting of explicitly defined hcp and bcc laths with the Burger's orientation relationship between them, were compared with single colony experimental results for this purpose. An important outcome of this model is the creation of an effective transformed β constitutive model with volume-averaged contributions from both of α and β phases. Tension-compression asymmetry was accommodated in each slip system through calibration of directional properties. An FEM model of the polycrystalline microstructure, consisting of primary α and transformed β phases was then set up with equivalent orientation and misorientation distribution functions (ODF and MODF). Simulations for constant strain rate tests in tension and compression as well as creep were conducted and compared with experimental results. With sufficient validation accomplished, the model was nearly ready for making microstructural observations with respect to characteristic variables that can cause crack initiation in the microstructure. The details that have gone into the model are novel and will have a strong impact on its predictive capabilities in fatigue failure.

4. REFERENCES.

1. Savage, M.F., Ph.D Thesis, Department of Materials Science and Engineering, The Ohio State University, Columbus, OH, 2000.

2. Williams, J.C., Baggerly, R.G., and Paton, N.E., *Metallurgical and Materials Transactions*, Vol. 33A, 2002, pp. 837-850.

3. Savage, M.F., Neeraj, T., and Mills, M., *Metall. and Mater. Trans*, 33A, (3), 2002, pp. 891.

4. Brandes, M. and Mills, M., *Materials Science and Engineering A*, 2004, pp. 570.

5. Ferreira, P.J., Robertson, I.M., and Birnbaum H.K., "Hydrogen Effects on the Interaction Between Dislocations," *Acta Materialia*, 1998, 46(5).

6. Evans, W.J., *Journal of Materials Science Letters*, Vol. 6, 1987, pp. 571-574.

7. Kassner, M.E., Kosaka, Y., and Hall, J.A., *Metallurgical and Materials Transactions*, Vol. 30A, September 1999, pp. 2383-2389.

8. Shen, W., Soboyejo, W.O., and Soboyejo, A.B.O., *Mechanics of Materials*, Vol. 36, 2004, pp. 117-140.

9. Hack, J.E. and Leverant, G.R., *Metallurgical Transactions*, Vol. 13A, 1982, pp. 1729-1738.

10. Bache and Evans, *Int. J. Fatigue*, 1997.

11. Davidson, D.L. and Eylon, D., *Metallurgical Materials Transactions*, Vol. 11A, 1980, pp. 837-843.

12. Bache, M.R., Davies, H.M., and Evans, W.J., *Titanium '95: Science and Technology*, 1995, pp. 1347-1354.

13. Bache, M.R., Evans, W.J., and Davies, H.M., *Journal of Materials Science*, Vol. 32, 1997, pp. 3435-3442.

14. Woodfield, A.P., Gorman, M.D., Corderman, R.R., Sutliff, J.A., and Yamrom, B., *Titanium '95: Science and Technology*, 1995, pp. 1116-1124.

15. Sinha, V., Mills, M.J., and Williams, J.C., *Metallurgical and Materials Transactions*, Vol. 35A, 2004, pp. 3141-3148.

16. Woodfield A.P. and Sutliff, J.A., *Microscopy and Microanalysis*, Vol. 3, Supplement 2, 1997, pp. 571-572.

17. Cho, J.R., Dye, D., Conlon, K.T., Daymond, M.R., and Reed, R.C., *Acta Materialia*, Vol. 50, 2002, pp. 4847-4864.

18. Neal, D.F., Proceedings of the Sixth World Conference on Titanium, France, 1988, pp. 175-180.

19. Evans, W.J. and Bache, M.R., *International Journal of Fatigue*, Vol. 16, No. 7, 1997, pp. 443-452.

20. Evans, W.J. and Bache, M.R., *Scripta Metallurgica et Materialia*, Vol. 32, No. 7, 1995, pp. 1019-1024.

21. Fishgoit, A.V., Kolachev, B.A., and Danilkin, V.A., *Izvestiya Vysshikh Uchebnykh Zavedenii*, Tsvetnaya Metallurgiya, Vol. 2, 1986, pp. 93-97.

APPENDIX A—CONSTITUTIVE DATA

A.1 INTRODUCTION.

A.1.1 COMPRESSION TESTING OF Ti-6Al SINGLE CRYSTALS.

The first step in developing the crystal plasticity model for deformation in titanium (Ti) alloys was the modeling of single phase α (hcp) Ti-6wt%Al. The α phase is the principal constituent in near-α alloys such as Ti-6242. In addition, the polycrystalline creep response for Ti-6wt%Al was previously determined by Neeraj [A-1]. This initial calibration of the crystal plasticity model then required the flow response of Ti-6wt%Al for basal, prism, and [0001] orientations. Once calibrated, the model was then applied to the case of polycrystalline Ti-6wt%Al. This validation of the model also required information regarding the texture of the polycrystalline Ti-6wt%Al alloy. This latter information was garnered from Orientation Imaging Microscopy (OIM) of the polycrystalline material.

A.1.2 ANISOTROPY IN THE ROOM TEMPERATURE DEFORMATION OF α/β COLONIES IN Ti-6242.

Since the α(hcp)/β(bcc) colony structure is one of the principal microstructural constituents in commercial Ti alloys, it is of critical importance to characterize the constitutive behavior of the colonies as a function of operative slip system. This information can then be incorporated into the crystal plasticity modeling for creep and load-shedding. To characterize the deformation response of single α/β colony crystals, microtensile, microcompression, and compression testing was utilized. In addition, detailed transmission electron microscopy (TEM) analysis was performed on the compression samples to develop physical insight into the source of the observed anisotropy as a function of operative slip system.

A.2 METHODS.

A.2.1 COMPRESSION TESTING OF Ti-6Al SINGLE CRYSTALS.

The Ti-6wt% Al alloy (Ti-6Al), a single phase α (hcp) Ti alloy that was used for the majority of the study was obtained from Duriron Company, Dayton, Ohio, as 12.7-mm-diameter cast rods. These samples have an average grain/variant size of approximately 500 μm. The nominal composition of the as-received material provided by Duriron is listed in table A-1.

Table A-1. Composition of Ti-6Al and Ti-6242Si in Weight Percent Used for the Single Crystal Studies

Material	Al	Mo	Sn	Zr	Si	Fe	O	N	C	Ti
Ti-6Al	6.28	-	-	-	-	0.014	0.042	0.002	0.008	balance
Ti-6242Si	6.01	1.96	1.96	4.01	0.10	-	0.131	0.012	-	
(±)	0.005	0.0035	0.0035	0.005	0.005	0.003	0.008	0.003	0.003	

Single crystals of Ti-6wt%Al were grown using a vertical float zone technique in a Crystalox furnace at Wright Patterson Air Force Base, Dayton, OH. Crystal growth of 12-mm-diameter rods were performed in an inert Argon (Ar) atmosphere to reduce contamination. A molten zone (approximately 12 mm high) was created in the rods using inductive radio frequency (RF) heating and was then translated at a rate of about 20 mm per hour. Several single crystal regions were successfully obtained on the order of 5-7 mm long.

The single crystal regions were oriented for mechanical testing in a three-axis goniometer using standard Laue back-reflection x-ray techniques to identify the crystallographic orientation of the α phase. Samples were oriented for single slip basal and prism orientations, as well as in the [0001] orientation. Note that in this latter orientation, there is no resolved shear stress for a-type dislocations, and therefore, <c+a> slip will necessarily be activated. The single crystal samples, with dimensions of 3.5- by 3.5- by 10-mm parallelpipeds, were extracted from the oriented single crystals using a Struers diamond saw. All surfaces were polished to 0.3-μm alumina on a vibratory polishing system in 1- and 0.25-μm alumina slurries to provide a suitable final surface finish to facilitate slip line analysis after mechanical testing. Constant strain rate testing was performed using an Instron testing machine equipped with a high-strength compression cage at a strain rate of 10^{-4} s^{-1}.

A.2.2 ANISOTROPY IN THE ROOM TEMPERATURE DEFORMATION OF COLONIES IN Ti -6242.

Single α/β colonies of Ti-6Al-2Sn-4Zr-2Mo-0.2Si were grown using a vertical float zone technique in a Crystalox furnace at Wright Patterson Air Force Base, Dayton, OH. Crystal growth of 15-mm-diameter rods were performed in an inert Ar atmosphere to reduce contamination. A molten zone (approximately 12 mm high) was created in the rods using inductive RF heating and was translated at a rate of 2.16 mm per hour. Successfully grown colonies ranged in size from 5 to 25 mm. Detailed elemental analysis of the single colony material is provided in table A-1.

Large colonies were oriented for mechanical testing in a three-axis goniometer using standard Laue back-reflection x-ray techniques to identify the crystallographic orientation of the α phase. Scanning Electron Microscopy (SEM) observations were made in a Philips XL30 SEM using backscattered electrons to determine the relative alignment of the broad face of the α/β interface, allowing for the unambiguous identification of the three **a**-type $\{11\underline{2}0\}$ slip directions. Figure A-1 shows the experimentally determined [A-2 and A-3] near-Burger's orientation relationship (OR) between the α and β phases in Ti-6242, and the relative misorientations of the possible Burger's vectors in both the α and β phases. The observed OR has the effect of creating three unique hcp **a**-type slip vectors in the colony structure as shown in figure A-1. Along with the 0.7° misorientation between $\mathbf{a_1}$ and $\mathbf{b_1}$, a misorientation of 11.1° was observed between the $\mathbf{a_2}$ and $\mathbf{b_2}$ directions. The third **a**-type slip direction in the α phase ($\mathbf{a_3}$) does not have a closely aligned $<111>_\beta$ direction in the colony structure. In figure A-1, the green vectors represent the residual Burger's vectors that remain in the α/β interface to conserve the displacements after the dislocation has passed. Full details of this orientation relationship, single colony morphology and the anisotropy in single colony slip behavior are given elsewhere [A-2 through A-5]. Samples for creep testing in compression were oriented to maximize the resolved

shear stress (0.5) on either the $\mathbf{a_2}$ or $\mathbf{a_3}$ Burger's vector on the basal plane. Details of these orientations are provided in reference A-4. The single colony compression samples were 3.5- by 3.5- by 10-mm parallelpipeds with all surfaces polished to 0.3 μm alumina on a vibratory polishing system in 1- and 0.25-μm alumina slurries to provide a suitable final surface finish to facilitate slip line analysis after mechanical testing.

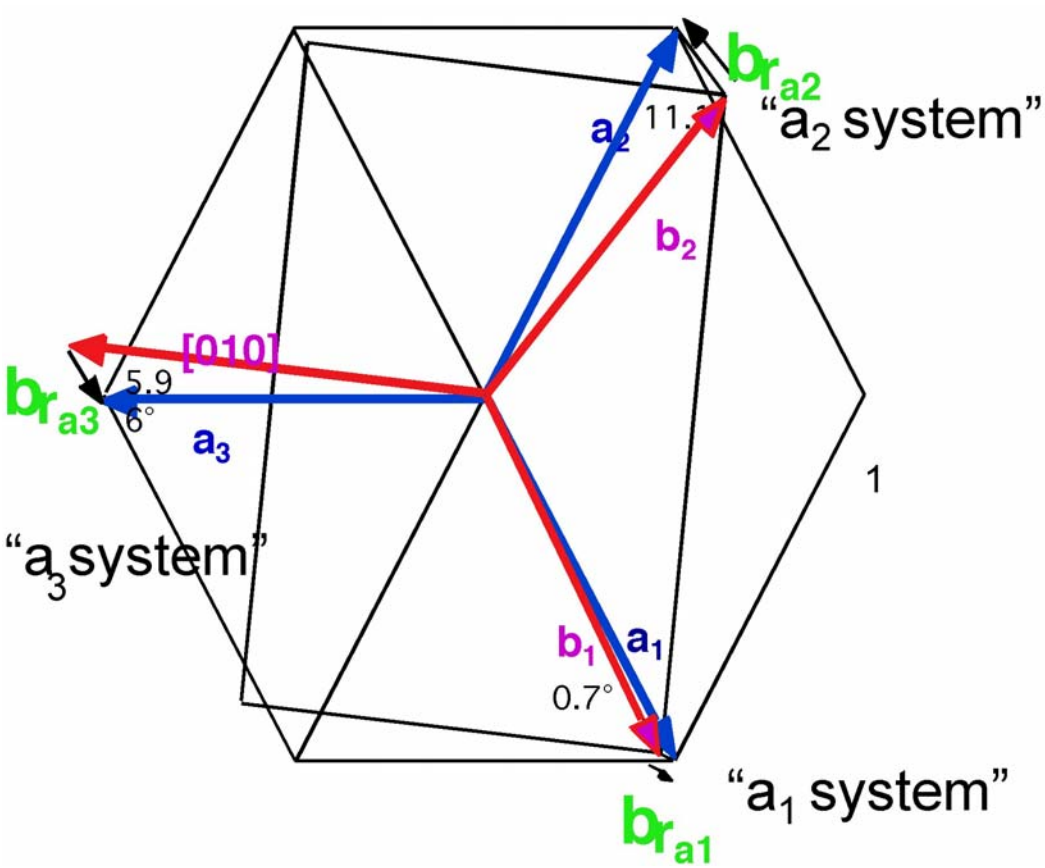

Figure A-1. Relationship Between A-Type Slip Vectors in the α Phase and 1/2<111> (Indicated as "B") Dislocations in β Phase for the Observed Near-Burger's Orientation Relationship Between the Phases

The compression and microtensile samples were each oriented to maximize the resolved shear stress on one of the three unique **a**-type slip directions on the basal plane. Crystallographic orientation was performed using Laue back-reflection x-ray techniques to identify the crystallographic orientation of the α phase. SEM observations were made in a Philips™ XL30 Field Emission SEM to determine the relative alignment of the broad face of the α/β interface, allowing for the unambiguous identification of the three **a**-type slip directions. The orientations used in this study (henceforth designated as $\mathbf{a_1}$, $\mathbf{a_2}$, and $\mathbf{a_3}$) are identical to those presented by Savage, et al. [A-2] for the microtensile testing of the basal slip orientations. Each compression sample was oriented with the basal plane at 45º to the tensile axis, and one of the faces of the compression sample was parallel to the prism plane containing the **a**-type slip direction to be activated. This results in a zero-resolved shear stress for the motion of the primary Burger's

vector on its corresponding prism slip plane. A Schmid factor of 0.5 is present for the primary **a**-type slip Burger's vector on the basal plane. Table A-2 lists the Schmid factors for each orientation for the three **a**-type <2110> slip directions (**a_1**, **a_2**, or **a_3**) on basal, prismatic, and first-order pyramidal planes plane. The Schmid factors for <111> slip on {101} and {112} planes in the β phase for each orientation are presented in table A-3.

Table A-2. Schmid Factors for a-Type Slip on Basal, Prism, and First-Order Pyramidal Planes in the α (hcp) Phase for the Three Orientations Used in This Study (The tensile axis is parallel to the plane normal given for each orientation.)

	Slip System	**a_1 Basal** (2~1~13)	**a_2 Basal** (~12~13)	**a_3 Basal** (~1~123)
Basal	**a/3**[~2110](0001)	**0.50**	0.25	0.25
	a/3[~12~10](0001)	0.25	**0.50**	0.25
	a/3[~1~120](0001)	0.25	0.25	**0.50**
Prism	**a/3**[~2110](01~10)	0.00	0.23	0.23
	a/3[~12~10](10~10)	0.23	0.00	0.23
	a/3[~1~120](~1100)	0.23	0.23	0.00
Pyramidal	**a/3**[~2110](0~111)	0.24	0.32	0.32
	a/3[~2110](0~11~1)	0.24	0.08	0.08
	a/3[~12~10](10~11)	0.32	0.24	0.32
	a/3[~12~10](~1011)	0.08	0.24	0.08
	a/3[~1~120](1~101)	0.32	0.32	0.24
	a/3[~1~120](1~10~1)	0.08	0.08	0.24

All the constant strain rate tests on the single colony crystals were performed in an Instron test frame at a constant rate of 1×10^{-4} to a final plastic strain of nominally 4%. A linear variable displacement transducer (LVDT) coupled to the compression platens via a rigid rod and tube assembly provided displacement data and strain rate control feedback to ensure an accurate and constant strain rate. All single colony creep tests were performed at room temperature at an applied stress of 640 MPa, which corresponded to 78% and 84% of the 0.2% offset yield strength for the **a_2** and **a_3** basal slip orientations. Constant strain rate testing of the **a_1**, **a_2**, and **a_3** basal and prism slip orientations are detailed in references A-2 and A-4. Due to the limited supply of single colony material, creep testing in compression was not performed for the **a_1** basal orientation. Strain during creep testing was measured directly from the sample surface using epoxy-mounted strain gages. Using appropriate noise filtering, the strain resolution of these strain gages at a 5-V excitation level was approximately 5 microstrain. Rapid acquisition rates (10 points per second) of strain and load data were employed during loading and unloading of creep tests to allow for the extraction of stress-strain curves to gage the elastic response of the material. Loading and unloading experiments were performed using a hydraulic elevator system to ensure smooth loading and unloading of the sample. Values of Young's modulus were measured to ensure the proper functioning of the strain gage system and ensure proper loading and unloading. During creep deformation in compression, 5-μm teflon films were placed between the single colony sample and platens of the compression cage to ensure good lubrication between the two faces. Constant strain rate compression testing was performed at room temperature using a screw-driven mechanical test frame equipped with a compression cage.

Table A-3. Schmid Factors For A/2<111>-Type Slip On {110} And {111} Planes In The β (Bcc) Phase For The Three Orientations Used In This Study (The Tensile Axis Is Parallel To The Plane Normal Given For Each Orientation.)

	Slip System	a_1 **Basal** (2~1~13)	a_2 **Basal** (~12~13)	a_3 **Basal** (~1~123)
b_1	[11~1](101)	**0.5**	0.25	0.25
	[11~1](011)	0.25	0.07	0.07
	[11~1](~110)	0.25	0.32	0.32
	[11~1](112)	0.43	0.10	0.10
	[11~1] (~121)	0	0.23	0.23
	[11~1](~21~1)	0.43	0.33	0.33
b_2	[~111](101)	0.17	**0.5**	0.32
	[~111](110)	0.23	0.33	0.05
	[~111](01~1)	0.06	0.16	0.06
	[~111](211)	0.23	0.47	0.41
	[~111](~1~21)	0.17	0.10	0.26
	[~111](~11~2)	0.06	0.37	0.15
b_3	[111](~110)	0.28	0.32	0.13
	[111](01~1)	0.20	0.08	0.12
	[111](~101)	0.48	0.25	0.01
	[111](~211)	0.43	0.32	0.08
	[111](~12~1)	0.04	0.25	0.14
	[111](~1~12)	0.40	0.10	0.06
b_4	[1~11](011)	0.11	0.15	0.20
	[1~11](110)	0.30	0.34	0.13
	[1~11](~101)	0.19	0.48	0.07
	[1~11](~112)	0.03	0.37	0.15
	[1~11](121)	0.24	0.11	0.19
	[1~11](~2~11)	0.28	0.48	0.04

For microtension, a thin (<500 micron) slice was then cut from the rod using a SiC abrasive saw, polished down to 1200 grit on both sides, and subsequently mounted to an aluminum block using Dynaloy 325, a silver paste conductive epoxy. Dogbone-shaped microsamples were cut out using a Chevalier ED203 sinking plunge electrical discharge machine (EDM) with a superfinishing controller. The superfinishing controller regulates the power being induced on the working part, thereby reducing the recast layer left behind by the cutting procedure. Settings for the machine can be found in reference A-6. The electrodes were made of high-density fine-grained graphite, manufactured by Micro Machining Inc. in Baltimore, MD. The EDM process must be allowed to cut not only through the sample, but through the epoxy and into the substrate to avoid trapezoidal cross sections, which create bending while testing. A micrograph of a microsample and a schematic showing how it is aligned for maximizing a Schmid factor are shown in figure A-2 [A-7]. The sample gage length is 1700 μm, with a width of 300 μm, and a typical thickness of 300 μm.

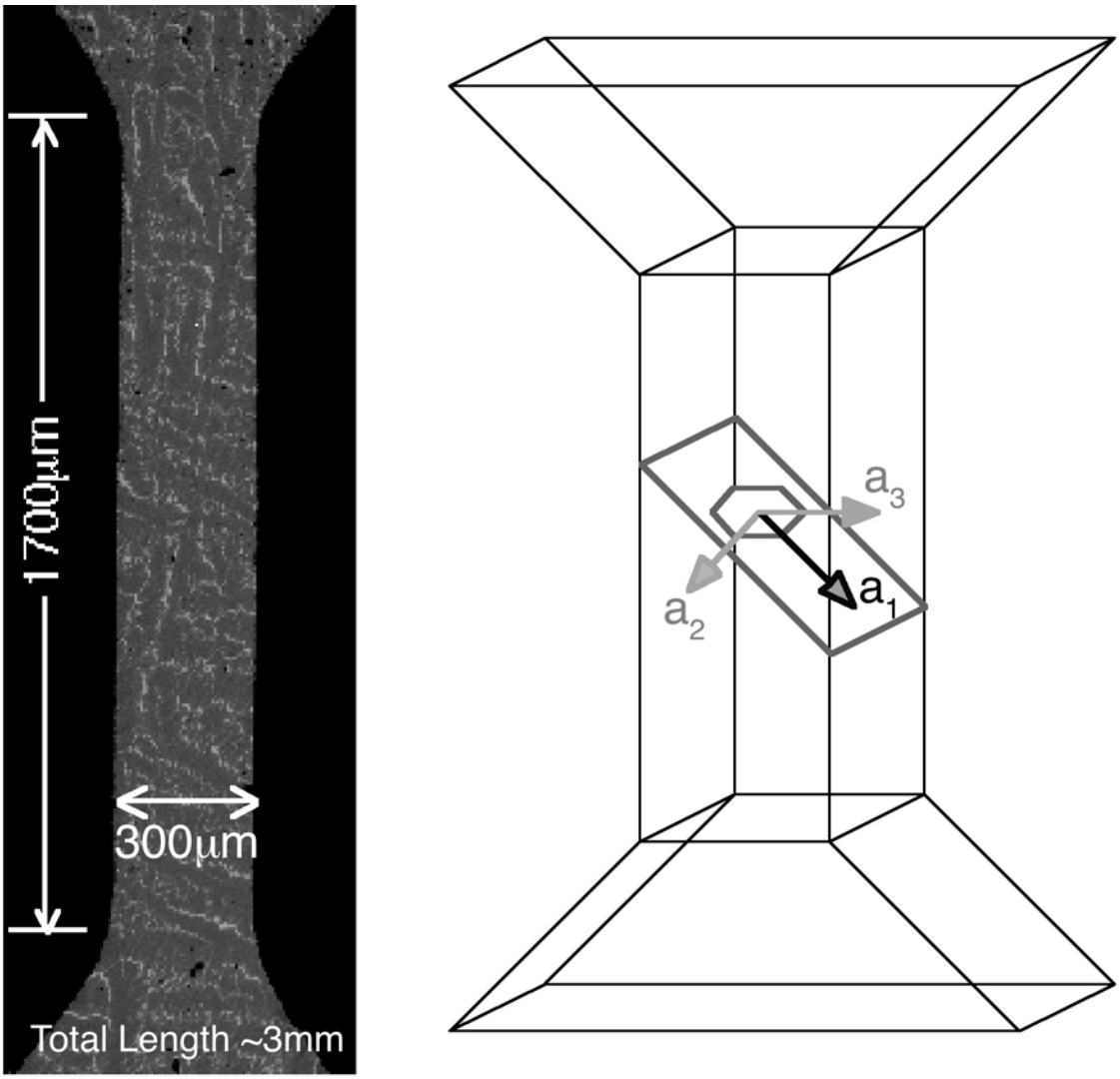

(a) (b)

Figure A-2. (a) Backscattered SEM Micrograph Showing the Gage Section of a Microtensile Sample Oriented for a_1 Basal Slip, and (b) Schematic of the Microtensile Sample Showing the Orientation of the Primary Slip System: **a**/3[2-1-10](0-110) [A-2]

Once the sample was set free using Dynaloy solvent, it was mounted onto a tripod polisher to do the fine polishing. Diamond lapping films of 3, 1, 0.5, and 0.1 microns were used in successive steps to produce a mirror-like finish and maintain parallel faces. Any defects on the gage can affect the laser interferometry strain measurement.

Because of the size of the sample, typical strain gages cannot be used. Instead, an optical technique that measures strain directly in the gage section was used; a method developed by W.N. Sharpe of The Johns Hopkins University [A-8]. The Interferometric Strain/Displacement Gage (ISDG) system requires that two reflective markers be placed on the pristine parallel faces to act as gage markers, as illustrated in figure A-3. These markers were either microindents or platinum lines. The lines were deposited using the Ga+ ion liquid source of the FEI Dual Beam

235 Focused Ion Beam (FIB) at the Campus Electron Optics Facility at The Ohio State University. Two lines 50 microns long, 2 microns wide, and 0.55 micron high were spaced approximately 250 microns apart. It is important that the lines have rounded ends and be placed precisely.

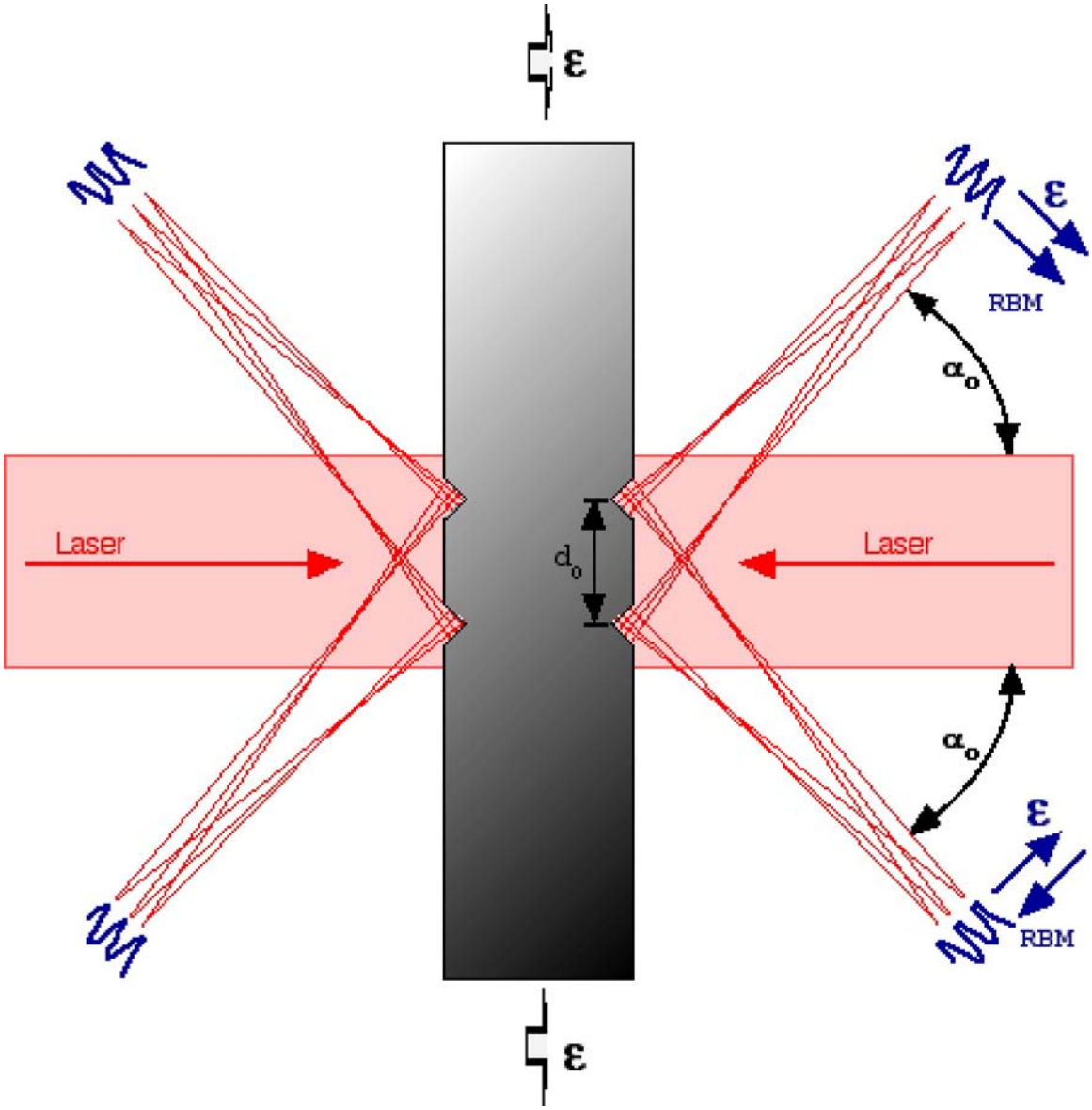

Figure A-3. Schematic Showing the Generation of Frige Patterns Through Illumnation of Microindents Spaced 300 μm apart by a Laser Source. (This fringe generation is analagous to Young's two slit experiment. The displacement of the resulting fringe patterns due to an applied tensile strain is shown, as well as the displacement due to rigid body motion (RBM). The fringe displacement is related to the engineering strain through equation A-3 [A-2].)

Microsample testing has been a successful way of measuring strain for a variety of sample types and has been used on Ti-6242Si single colony specimens for **a**-type slip [A-7]. The major thrust of this work was to create a microsample tensile tester for The Ohio State University to be used, at least initially, for room temperature creep tests on Ti-6242Si and Ti-6Al, although it has been proven to work on other systems, including Gamma TiAl [A-6], steel weldments [A-9], MEMS-related LIGA Ni [A-10 and A-11], and nanocrystalline material [A-12].

The dead load creep unit at Ohio State is shown in figures A-4(a) and A-4(b), and the load frame is shown in figure A-5. The load frame sits atop a Technical Manufacturing Corporation 63-533 vibration isolation table that takes 35 psi of compressed air from tanks. The air bearing works off the same air source of 35 psi and provides a near frictionless loading path and ensures that there is no shear from multiaxial loading. Load is measured using a Sensotec load cell transducer, model 31/1430-05. The load cell has a range of 0-50 lb and was calibrated by hanging weights on the dead load creep frame.

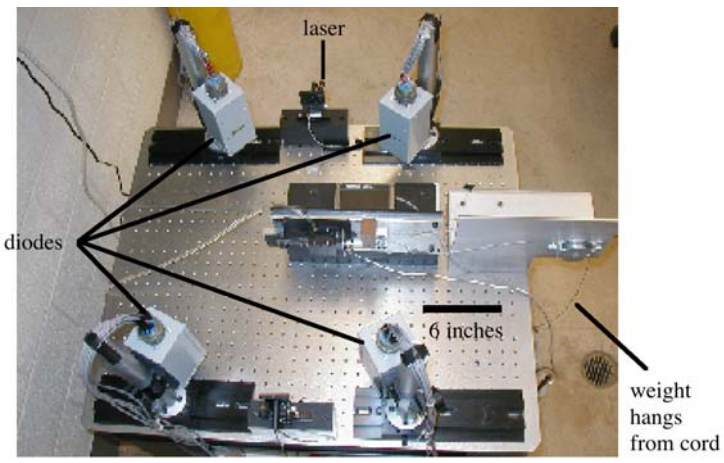

(a)

(b)

Figure A-4. Microsample Dead Load Tensile Creep Tester at the Ohio State University

The strain measurement is obtained by using interference patterns resulting from beams of light hitting the markers on the sample faces. Sharpe has demonstrated that, for two parallel markers placed perpendicular to the direction of strain measure, the motion of the resultant interference fringe pattern is proportional to the displacement of the markers [A-8]. The optics is analogous to Young's two slit experiment in reflection instead of transmission [A-13]. When a coherent beam of light is directed toward the markers, the reflected light causes the formation of an interference pattern envelope [A-8], a schematic of which is shown in figure A-3. The location of the interference pattern is directly proportional to the distance between the two reflecting markers:

$$m\lambda = d \sin \theta \tag{A-1}$$

λ is the wavelength of the laser being used, θ is the angle between the incident laser and the location the interference pattern is observed, d is the spacing between the markers, and m is the order of the fringe. Therefore, the change in marker spacing (δd) as the sample is being strained is proportional to the fringe pattern shift

$$d = \delta m\lambda/\sin \theta \tag{A-2}$$

The fringe patterns displace as the sample is being strained as a result of the material response and rigid-body motion. The following equation relates the displacement of fringes and sample strain with two phase shifts, eliminating rigid-body motion:

$$(\delta m):\varepsilon = (\delta m_1\lambda/2d_0\sin \alpha_1) - (\delta m_2\lambda/2d_0\sin \alpha_2) \tag{A-3}$$

In the equation, λ is the wavelength of the laser, d_0 is the initial marker spacing (effective gage length), dm1 and dm2 are the fringe displacements and α_1 and α_2 are the angles between the incident laser and the diffracted beams [8].

On the Ohio State system, two platinum lines on each sample, facing 250 microns apart, are illuminated with 670-nm wavelength radiation (Power Technology, Inc. PM08 G2 lasers with LDCU5 5-volt power supply) creating fringe interference patterns. Fringe displacement was captured using Hamamatsu S394-512Q MOS linear image sensors with C7885 driver circuits.

This data is processed using a LabVIEW data acquisition system. Sharpe processed the data by tracking the minimum of the fringe pattern as the test proceeded, but Zupan improved on the signal processing by tracking the entire fringe pattern using a Fourier transform. Fringe pattern analysis and application of Fourier transform to the ISDG data can be found in references A-6 and A-11.

A backup strain measurement system was also incorporated into the load frame. A Macro Sensors CD 375-050 LVDT with an Omega LDX-3A signal conditioner was attached to the load frame, as shown in figure A-5, to measure the crosshead displacement. The resolution is not as good as the ISDG because it measures strain outside the gage section. However, the LVDT provides reliable and stable data.

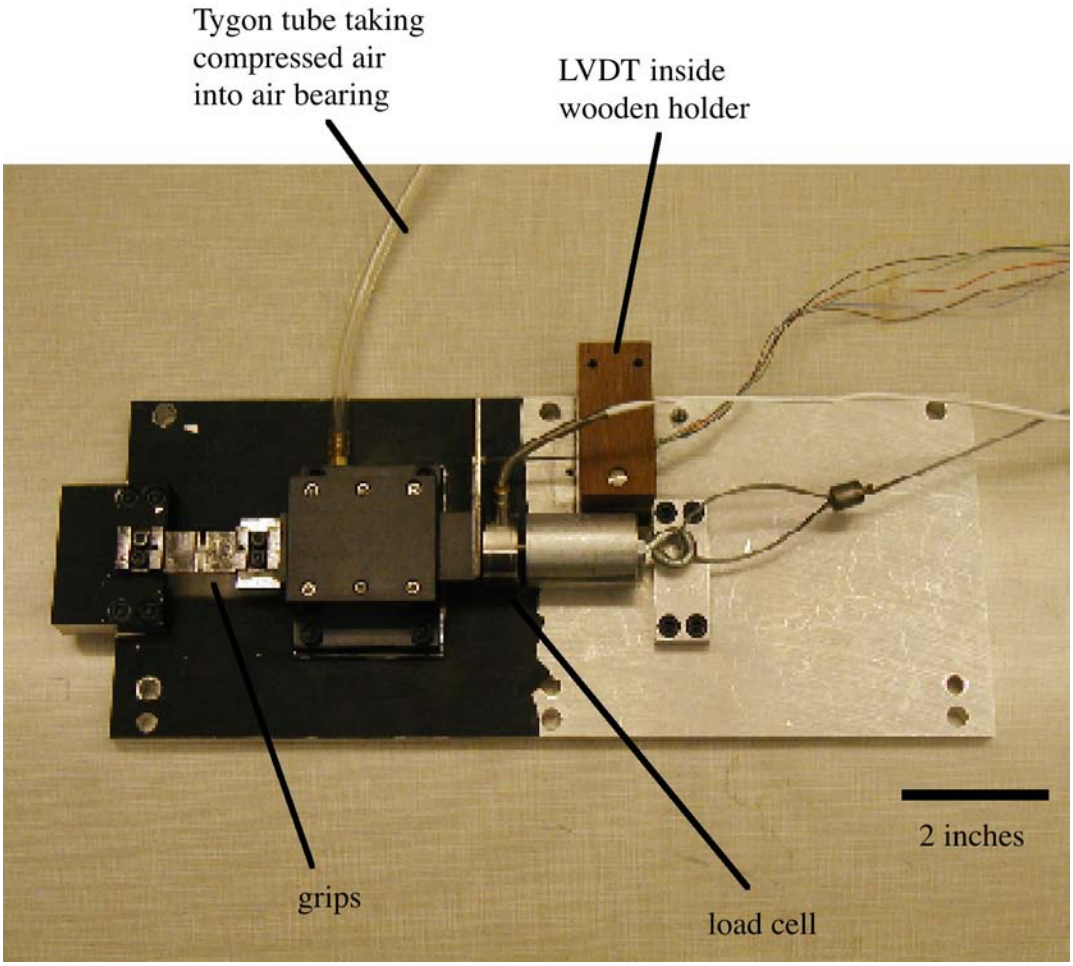

Figure A-5. Load Frame of The Creep Tester at the Ohio State University (One half of it is painted black to reduce reflections.)

TEM was done on a single colony Ti-6242Si a_2 basal tension microsample. First, one of the tails of the microsample was cut off using a 0.010-inch SiC blade on a Struers Accutom-50. The sample was then mounted with Crystalbond to a Pyrex stub with the sliced end facing down on a South Bay Model 590 Tripod Polisher. The end was polished down to 1200 grit, and then diamond lapping film was used in successive steps to 0.1 micron. The sample was taken off using acetone and remounted using Crystalbond to polish one of the side faces down to 1 micron using the Tripod Polisher.

The sample was taken off again using acetone. The Polisher was planarized with just the Pyrex stub on 600 grit. The back legs of the Tripod Polisher were advanced approximately two turns (i.e., about 1.146 degrees). With the unpolished face up, the sample was attached 0.5 mm from the edge of the stub with a cyanoacrylate super glue and sat overnight.

The second face was polished down to 1 micron, creating a wedge shape approximately 10 microns on the thin side. The stub was placed in acetone with a piece of filter paper below it. The sample was mounted to a copper grid with M Bond 610 (See figure A-6) and cured for about

2 hours on a hot plate at 100°C. The sample was later put in a small vice in the FIB, and material was milled away to create an H-bar shape along the wedge (see figures A-6 and A-7). This area is electron transparent and can be used for TEM. Multiple H-bars can be milled from the same microsample.

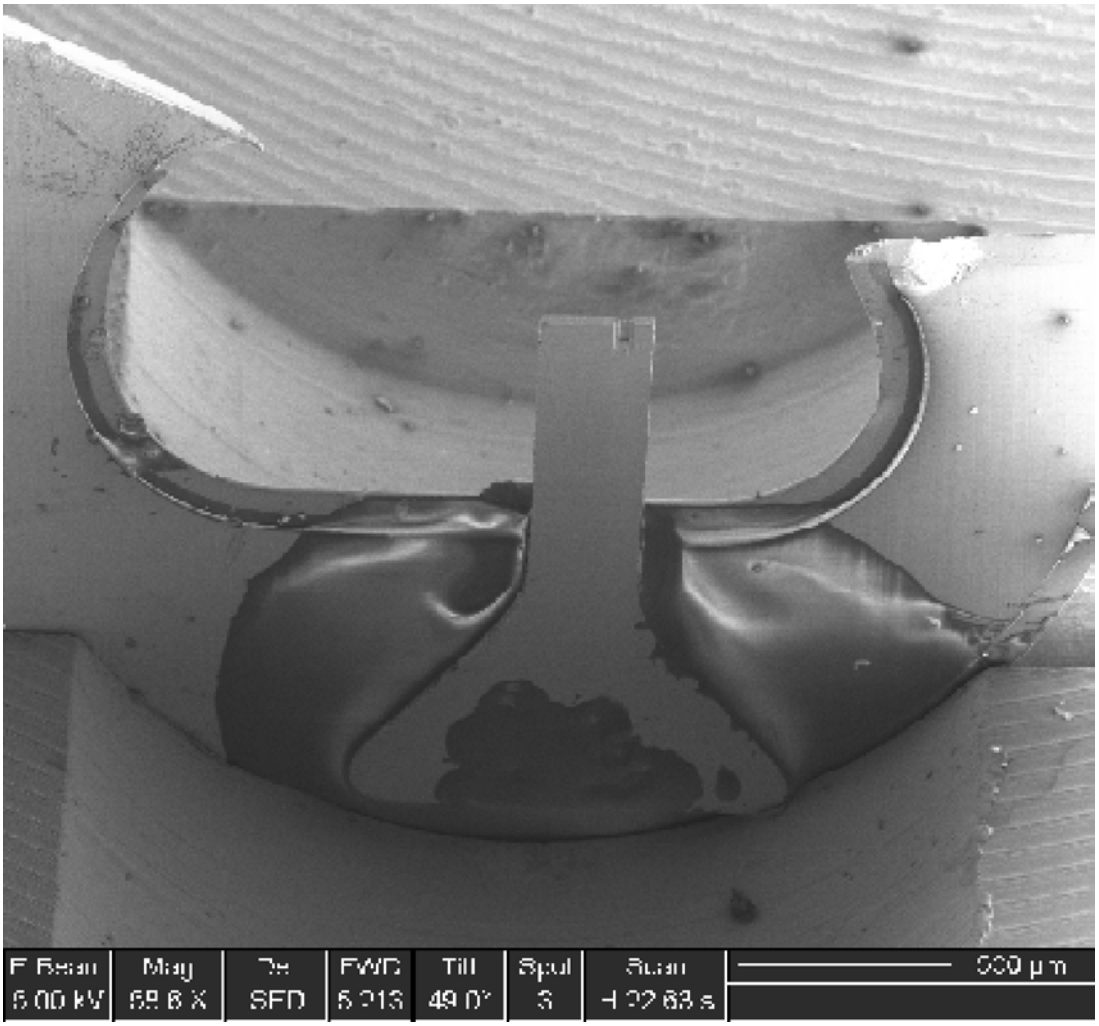

Figure A-6. Microsample Mounted With M Bond 610 to Copper Grid

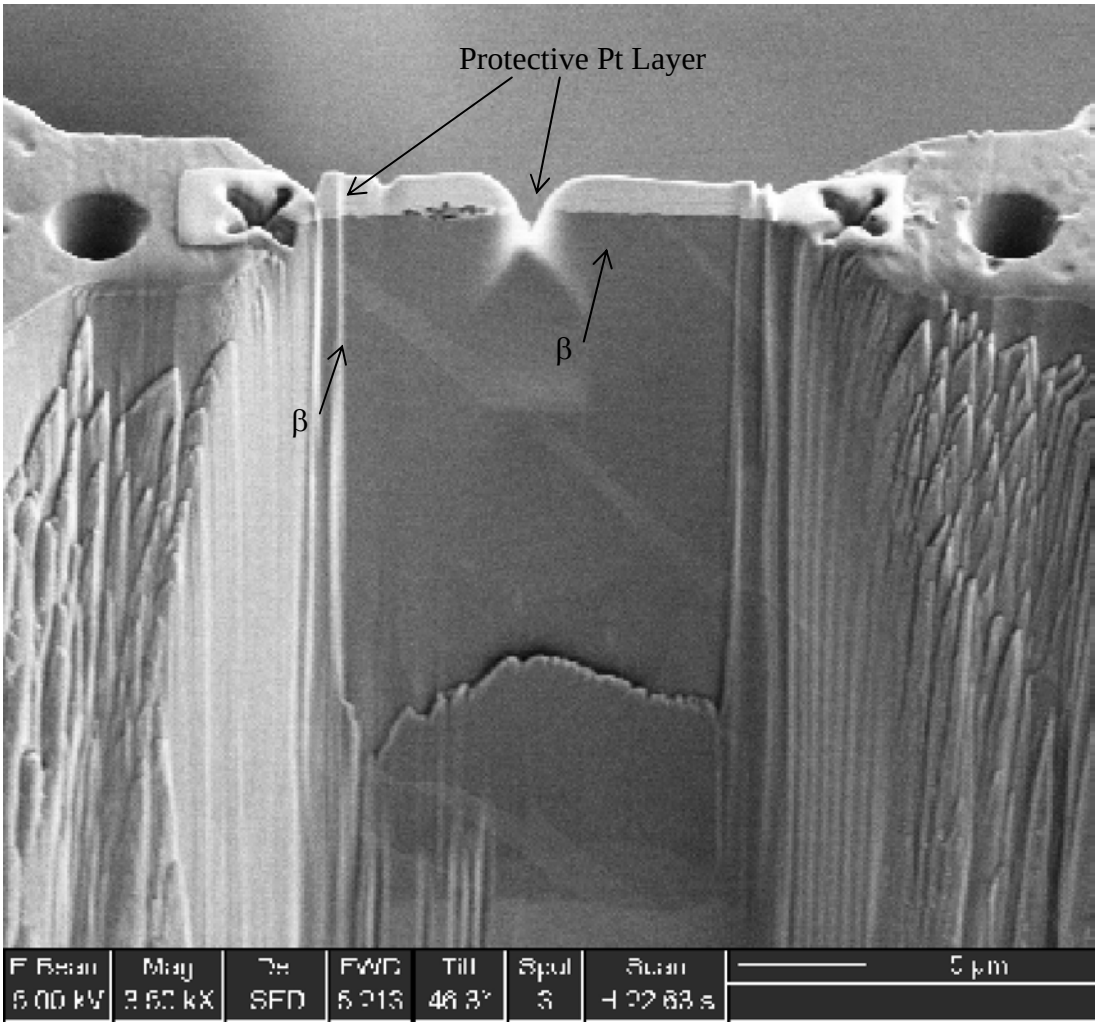

Figure A-7. Electron Transparent Region of the Microsample After the FIB Milling Process

The TEM samples made from the compression samples were carefully prepared in nonaqueous solutions to avoid the formation of hydrides in the thin foils. Thin (350-µm) sections from the compression samples were extracted using a low-speed saw equipped with an SiC wafering blade. Three-mm discs were prepared using an SiC abrasive oil-based slurry drill. The TEM samples were prepared parallel to the basal glide plane of the compression specimens, allowing a large field of view of the dislocations on their glide plane. This view also facilitates the observation of dislocation interactions with the β laths. The 3-mm discs were then double-sided dimpled to 15 µm thick, using a diamond slurry with a final abrasive particle size of 0.25 µm. Final thinning to electron transparency was performed using ion milling at 6 kV and 1 mA total current. Sector control was employed during the ion milling process to avoid preferential sputtering of the β phase. This was accomplished by automatically switching off the ion guns within ±30º of the α/β interface direction.

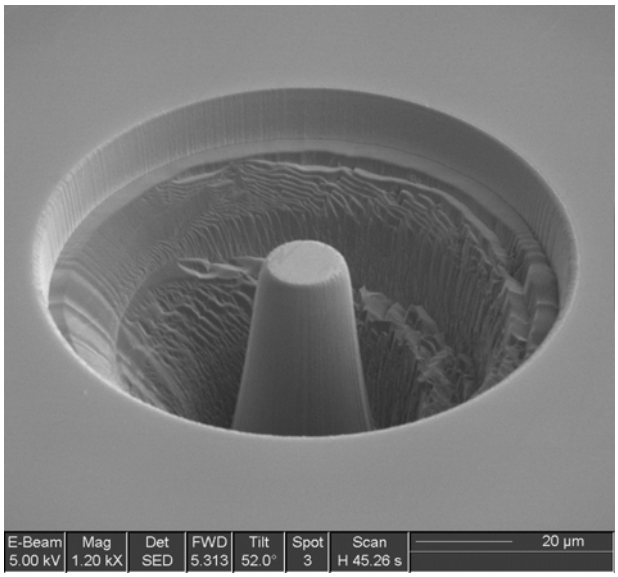

(a)

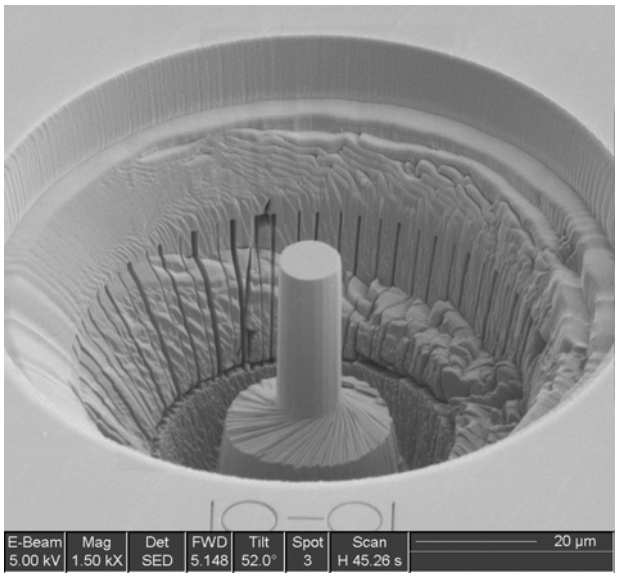

(b)

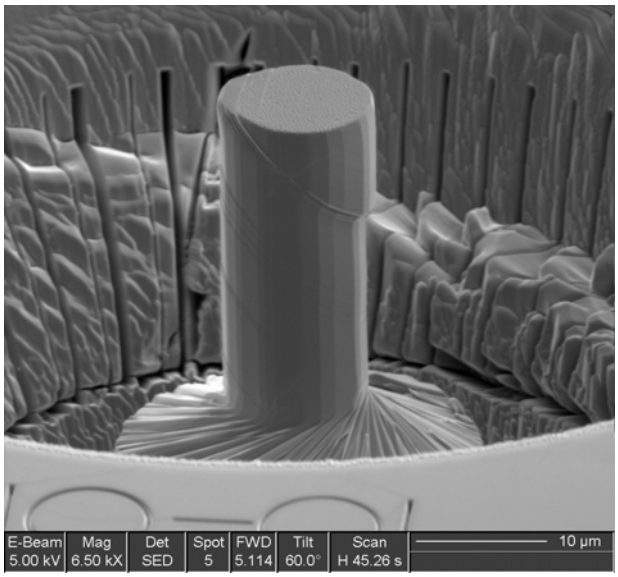

(c)

Figure A-8. (a) Secondary Electron Image Showing the Taper on the Pillar After Milling Perpendicular to the Sample Surface; (b) SE Image of the Sample Pillar After the Lathing Process; and (c) SE Image of the Same Pillar After the Compression Test, Slip Traces are Visible Throughout the Gauge Length of the Specimen

A.2.3 MICROCOMPRESSION OF Ti-6242 (TENSION/COMPRESSION ASYMMETRY).

In an effort to study the tension/compression asymmetry that exists in these alloys, micron-sized compression samples were fabricated onto the grip ends of the microtensile samples, allowing the study of the same material chemistry and the same loading direction of the microtensile samples. The orientations studied were a_2 basal, a_3 basal, a_1 prism, a_2 prism, and a_3 prism. These micron-sized compression samples were machined into the surface of the sample, using an FIB, by preferentially removing material, (as shown in figure A-8). This was done in two steps, outlined in reference A-14. First, the stage was tilted to 52° and ion milling is performed perpendicular to the sample surface. However, the tailing off of the ions leaves a tapered pillar without a constant cross section. Therefore, a lathing process was required to establish a constant cross section. Second, the stage was backtilted to -10°, such that the ion beam was close to parallel with the sample surface. Vertical cutting boxes were placed on one side of the pillar and material was removed to eliminate the taper. The stage was rotated -5° and this process was repeated, lathing the pillar to a constant cross section, until the stage was rotated a full 360°. The final sample diameter was 12 μm, and the aspect ratios vary between 2.5:1 and 3:1. The samples were uniaxially compressed using an MTS Nano Indenter XP outfitted with a flat diamond indenter tip. The compression tests were performed under constant displacement rate loading conditions. In all tests, the desired strain rate was 10^{-4} mm/mm.

A.2.4 MICROCOMPRESSION OF Ti-6242 (SIZE EFFECTS).

From the results of the tests in section A.2.3, it became apparent that there was inherent size effects associated with the deformation process at this size scale. For this to be a viable technique to acquire data, these size effects must be understood. Therefore, a single colony was oriented for maximum shear stress along the a1 direction $[2\underline{11}0]$ on the basal plane (0001) using Electron Backscatter Diffraction on a FEI XL-30 ESEM. To minimize the strengthening from the β phase as well as to simplify defect evolution and hardening mechanisms, this single slip orientation was chosen for this study. The sample was subsequently mechanically parallel-polished using an Allied High Tech MultiPrep System to 0.05 μm using colloidal silica.

Micron-sized compression samples were machined into the surface of the sample using an FEI dual beam FIB. Two different types of specimens were fabricated, cylindrical (described in section A.2.3) and orthorhombic. The cylindrical samples ranged between 1 to 22 microns in diameter. The orthorhombic samples consisted of 2 tetragonal samples (10 by 10 mm) and four samples with cross-section dimensions of ~15 by ~7.5 mm. The aspect ratios for all samples varied between 2:1 and 3:1. The orthorhombic samples were fabricated such that the Burger's vector was parallel to a given broad face, see figure A-9.

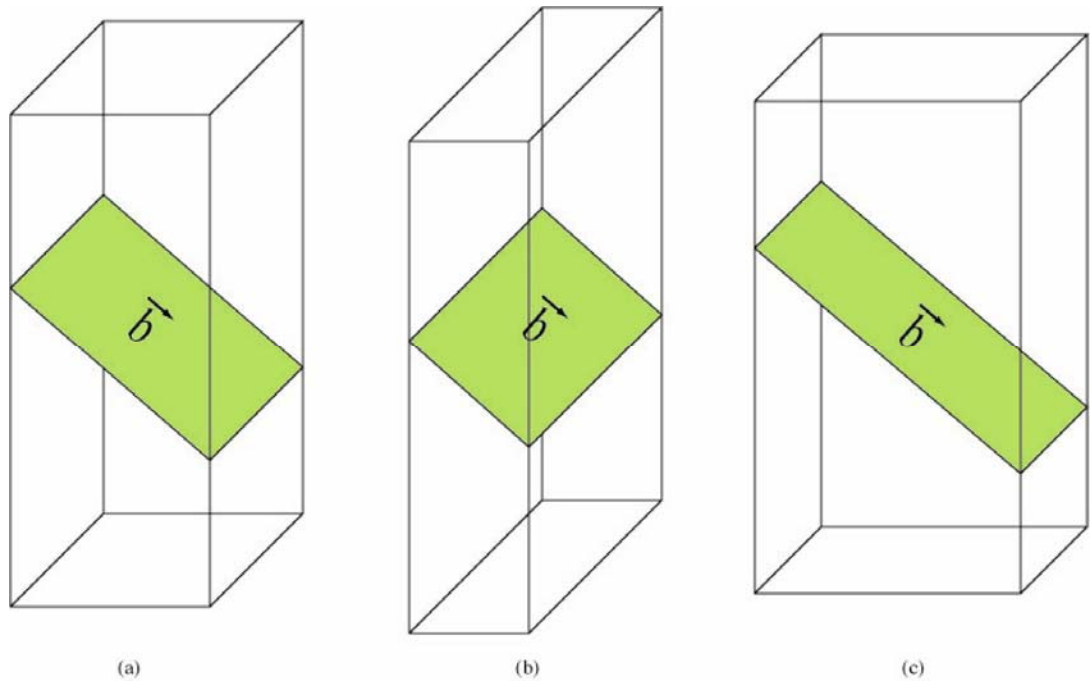

Figure A-9. Orientation of the Orthorhombic Samples With Burger's Vector Orientation Shown (a) Tetragonal Sample (10 by 10 mm), (b) Long Screw Component, and (c) Short Screw Component

The samples were uniaxially compressed using an MTS Nano Indenter XP outfitted with at flat diamond indenter tip. To ensure proper sample alignment with the indenter tip, a goniometer stage was used to make fine adjustments. The compression tests were performed under constant displacement rate loading conditions. In all tests, the desired strain rate was 10^{-4} mm/mm. TEM samples were extracted from the samples using an OmniProbe, an in situ plucking device.

A.3 RESULTS AND DISCUSSION.

A.3.1 COMPRESSION TESTING OF Ti-6Al SINGLE CRYSTALS.

The results of the constant strain rate tests are shown in figure A-10. The yield and flow strengths for the prism and basal orientations are very similar, while the [0001] orientation has a much larger yield strength. Slip line analysis using SEM confirmed that single basal and prism slip systems were dominant for these two crystal orientations, while for the [0001] orientation, multiple <c+a> slip occurs on several first-order pyramidal planes. This information was used to calibrate the crystal plasticity model, as described in appendix K.

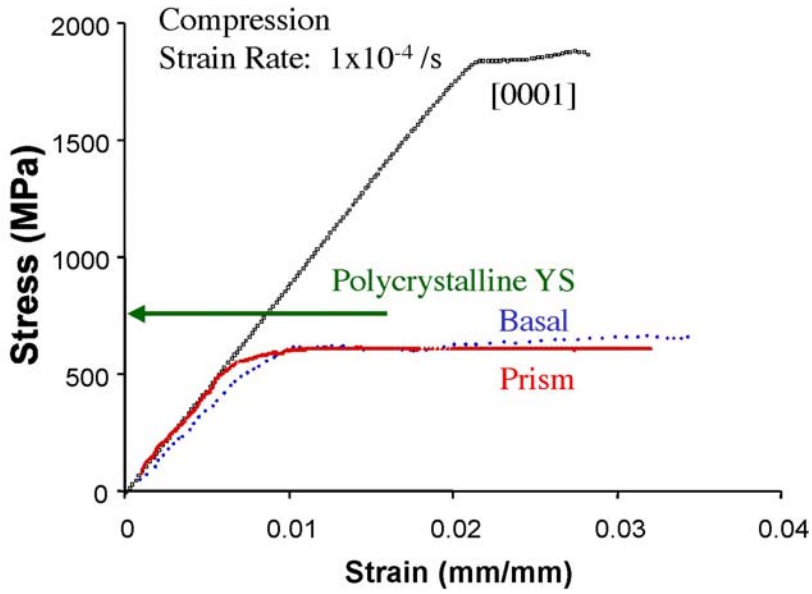

Figure A-10. Compression Stress-Strain Curves of the Various Orientations for Ti-6Al Single Crystals

A.3.2 [0001] MICROTENSILE TESTING OF PREVIOUSLY DEFORMED Ti-6wt%Al SINGLE CRYSTALS PREDEFORMED FOR BASAL SLIP.

Microsamples were cutout (See figure A-11) of a previously deformed single crystal Ti-6Al basal-oriented compression sample (stress-strain curve shown in figure A-10). One sample contains a large slip band across the gage section while the other was cutout in between intense slip bands. The microsamples were cutout using an EDM, and constant strain rate (1×10^{-4}) tests were performed at Wright Laboratories.

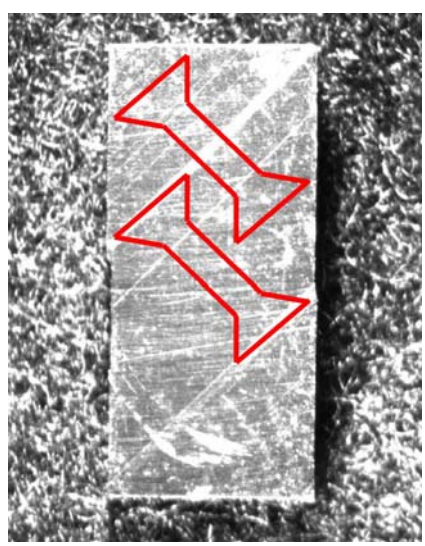

Figure A-11. Microsamples Cutout of the Single Crystal Ti-6Al Basal-Oriented Compression Sample (roughly 3 by 3 by 8 mm)

These experiments were done to determine cleavage strengths for the [0001] orientation, and the influence of prior deformation on these strengths. In binary Ti-Al alloys, there is a slip transition from homogeneous to planar slip due to short range ordering with increasing aluminum contents above 4 wt.%. The large dislocation densities present may create preferential paths for crack propagation. In addition, Neeraj, et al. [A-15 and A16] found weak fringes (basal, prism, and pyramidal planes) containing<a>-type slip bands using TEM in samples subjected to creep and constant strain rate conditions using several heat treatments. These fringes indicate residual displacements, leading to fringing in the slip bands. Once again, this structural defect may also create a favorable crack path.

The results of the tests run on the microsamples with and without a large slip band across the gage section shown in figure A-12 revealed similar yield strengths (in both cases, about half that of the compression c-oriented yield strength). A relatively lower yield strength in tension versus compression, consistent with the literature was noted [A-17 and A-18]. However, figure A-13 shows an SEM backscattered electron micrograph of the sample cutout in between the slip bands deformed almost exclusively in the grips. Figure A-14 shows a secondary electron image of the sample with the large slip band in the middle showing slip lines consistent with pyramidal slip. Based on these tests, it was concluded there is no dramatic effect of prior basal deformation on the cleavage strength of the a-grains when under loading along [0001].

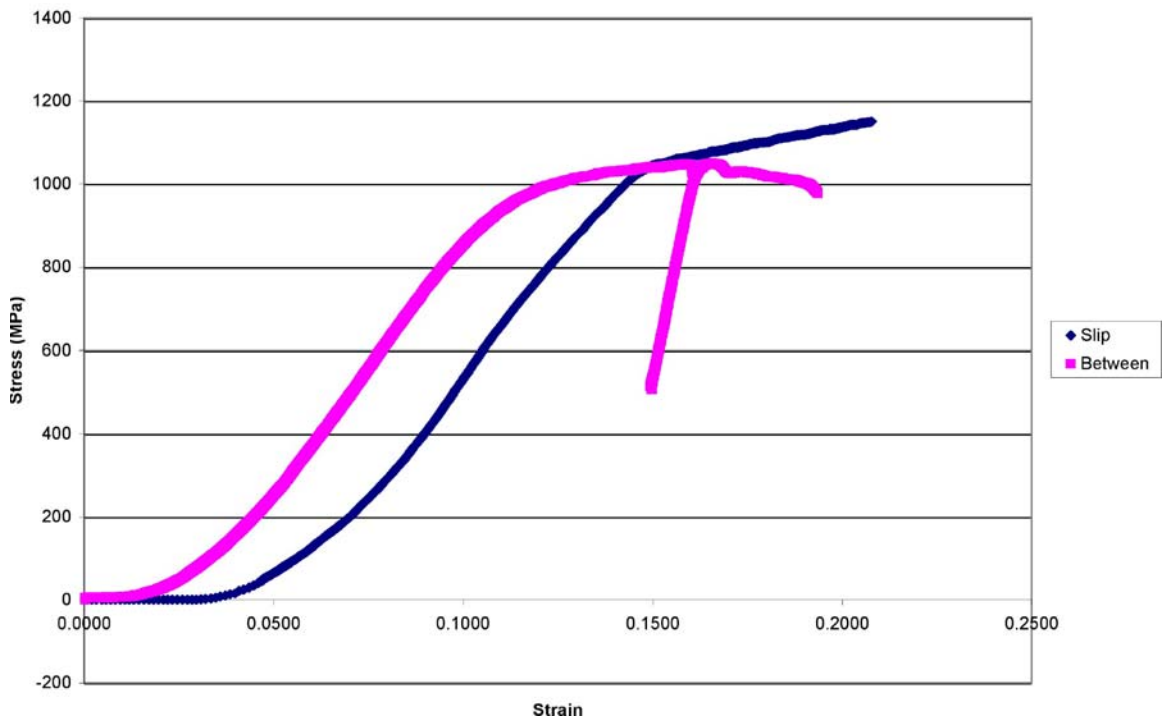

Figure A-12. Stress-Strain Curves for the Predeformed C-Oriented Ti-6Al MicroSample Tensile Tests From the Bulk Basal-Oriented Compression Sample (The slip curve refers to the sample with the large slip band in the middle of the gage section, and the between sample designates the one cut in between bands.)

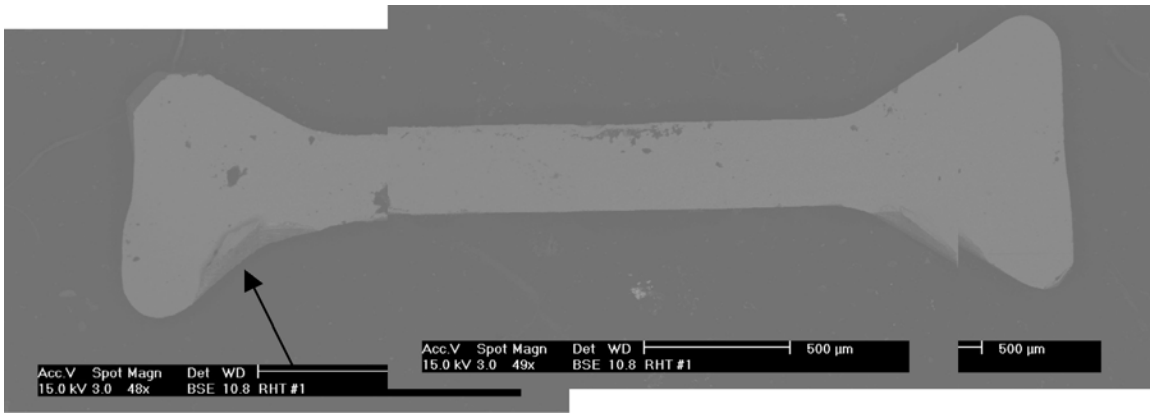

Figure A-13. Backscattered Electron Image of Between Sample Showing Large Deformation in the Grip

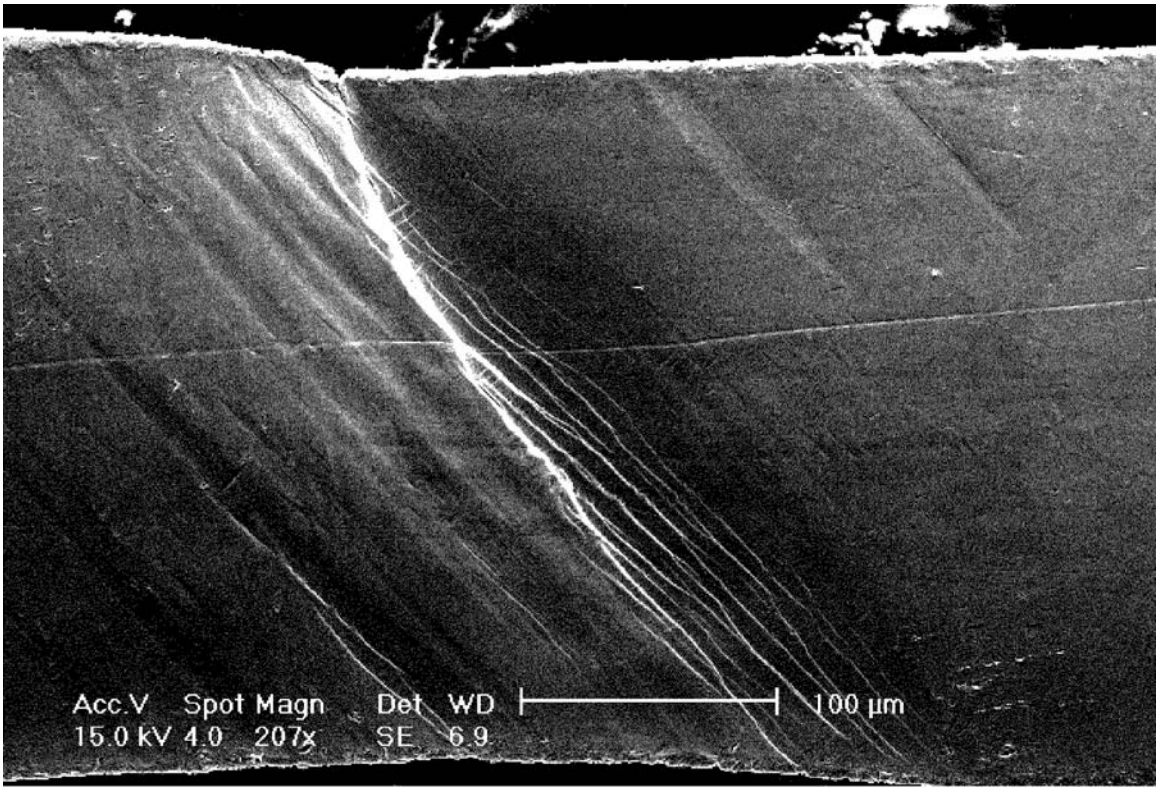

Figure A-14. Secondary Electron Image of the Ti-6Al Slip Sample Showing Failure at Approximately a 45 Degree Angle

A.3.3 ANISOTROPY IN THE ROOM TEMPERATURE DEFORMATION OF α/β COLONIES IN Ti-6242.

Prior to presenting the results of the single colony tests, it is important to discuss the crystallography associated with the α/β colony structure in more detail. The observed near-Burger's orientation relationship (OR) in α/β Ti alloys has the effect of creating three unique hcp **a**-type slip vectors in the colony structure [A-4 and A-5] as shown in figure A-1. The Burger's OR states:

$$(101)_\beta \parallel (0001)_\alpha, [1\bar{1}\bar{1}]_\beta \parallel [2\bar{1}\bar{1}0]_\alpha$$

This crystallographic relationship brings one of the hcp <2$\underline{11}$0> close- packed directions into coincidence with the bcc <1$\underline{11}$> slip direction. A deviation from the Burger's OR exists in single α/β colonies of Ti-6242, with a 0.7° misorientation between $\mathbf{a_1}$ and $\mathbf{b_1}$, and a misorientation of 11.1° between the $\mathbf{a_2}$ and $\mathbf{b_2}$ directions [A-2 to A-5 and A-19]. The third **a**-type slip direction in the α-phase ($\mathbf{a_3}$) does not have a closely aligned $<111>_\beta$ direction in the colony structure. These three slip directions were always observed to be aligned at the same angle to the broad face of the β lath structure, as predicted using the invariant line construction [A-3 and A-20]. The angle between the $\mathbf{a_1}$ slip vector and the broad face (the face that is parallel to the invariant line) is always observed to be a shallow angle close to 15°. Similarly, the $\mathbf{a_2}$ and $\mathbf{a_3}$ directions typically form angles of 75° and 45°. The appropriate prism slip plane for each **a**-type <2$\underline{11}$0> slip direction is indicated, while all three **a**-type directions share a common basal slip plane.

A.3.4 RESULTS FOR SINGLE COLONY MICROTENSILE TESTS.

Figure A-15 summarizes the results for the microtensile tests on Ti-6242 single colony crystals. In all cases, the imposed strain rate is 1×10^{-4} s^{-1}. Significant anisotropy was observed in the critical resolved shear stress (CRSS) values, depending on the a-type slip vector that is active, and between basal and prism systems. The CRSS values are small for a1 slip on both basal and prism planes, with the latter having the smallest value tested (250 MPa). The a_2 basal system has a significantly larger CRSS value compared to the other a-type systems. Quite unexpectedly, the a_3 basal system has a relatively small CRSS value. Insight into this remarkable result is provided later with the TEM observations on the single colony compression samples in section A.3.5. The anisotropy is, in general, less pronounced for the prism slip systems. The [0001] orientation has a significantly larger CRSS value compared to all of the a-type slip systems, consistent with the fact that <c+a> slip must be activated in this orientation. Thus, the CRSS for the [0001] orientation is between 17% and 40% larger than for a-type slip systems.

A limited number of creep tests were performed on microtensile samples. The results of two such tests are shown in figure A-16. Even at very low stress levels, significantly below the CRSS values reported above, measurable and substantial time-dependent creep is observed. Additional creep tests on the various orientations and as a function of stress level are required to fully map out this behavior.

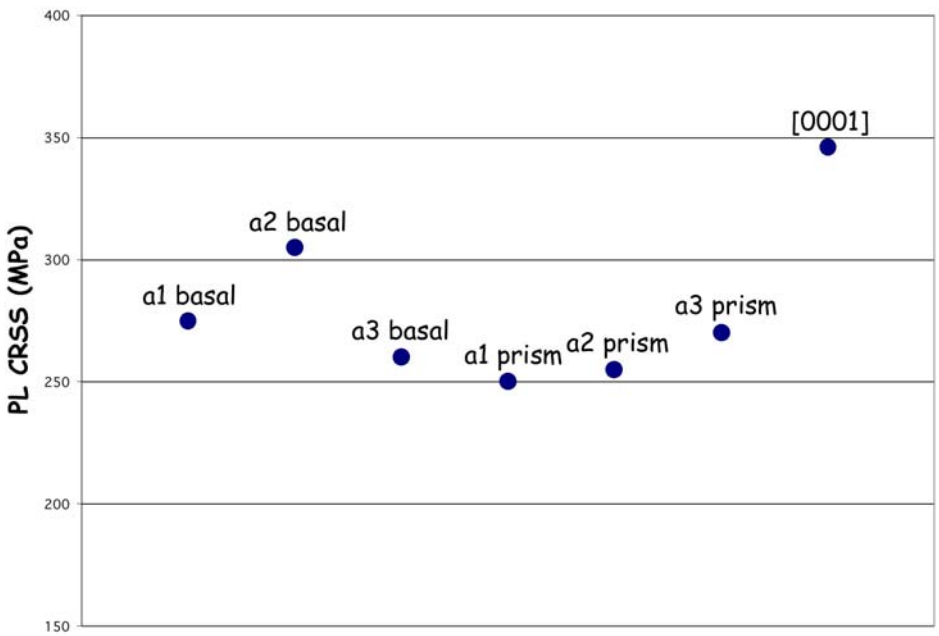

Figure A-15. CRSS Values Based on Proportional Limits for the Ti-6242 Single Colony Crystals Deformed at a Strain Rate of 10^{-4} s^{-1} (The CRSS value for the [0001] orientation is calculated for the first-order pyramidal plane)

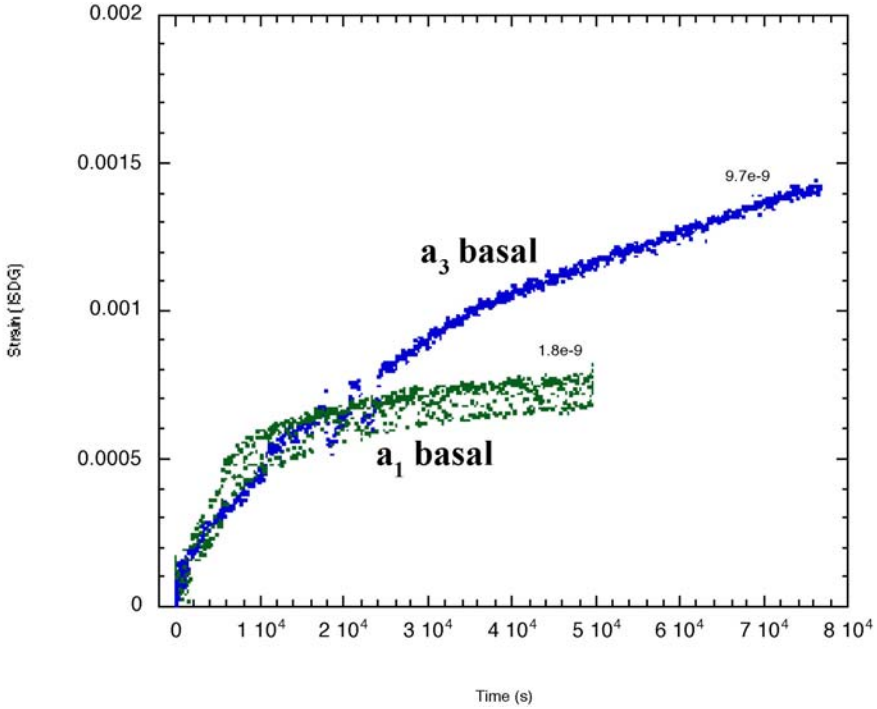

Figure A-16. Microtensile Creep Tests for Two Basal Orientations Showing Significant Creep Strain Accumulation Even at Very Low Axial-Applied Stresses of 380 MPa, Which is Only About 40% of the Polycrystalline Yield Strength of This Material (~ 950 MPa)

A.3.5 RESULTS FOR SINGLE COLONY COMPRESSION TESTS RESULTS AND SUBSTRUCTURE ANALYSIS.

Figure A-17 summarizes the observed anisotropy in CRSS (as determined from the proportional limit) for Ti-6242 single colonies in compression and compares these results with those just described for the microtensile Ti-6242 single colony tests [A-2 and A-4]—all work performed under this FAA program. Included for comparison are compression results for Ti-5Al-2.5Sn single colonies tested in compression under a previous Air Force Office Of Scientific Research (AFOSR) program [A-5]. The 0.2% offset yield strengths of 670 MPa, 824 MPa, and 765 MPa were measured for the $\mathbf{a_1}$, $\mathbf{a_2}$, and $\mathbf{a_3}$ basal slip orientations for Ti-6242, respectively. The corresponding values for CRSS are 330 MPa, 405 MPa, and 375 MPa.

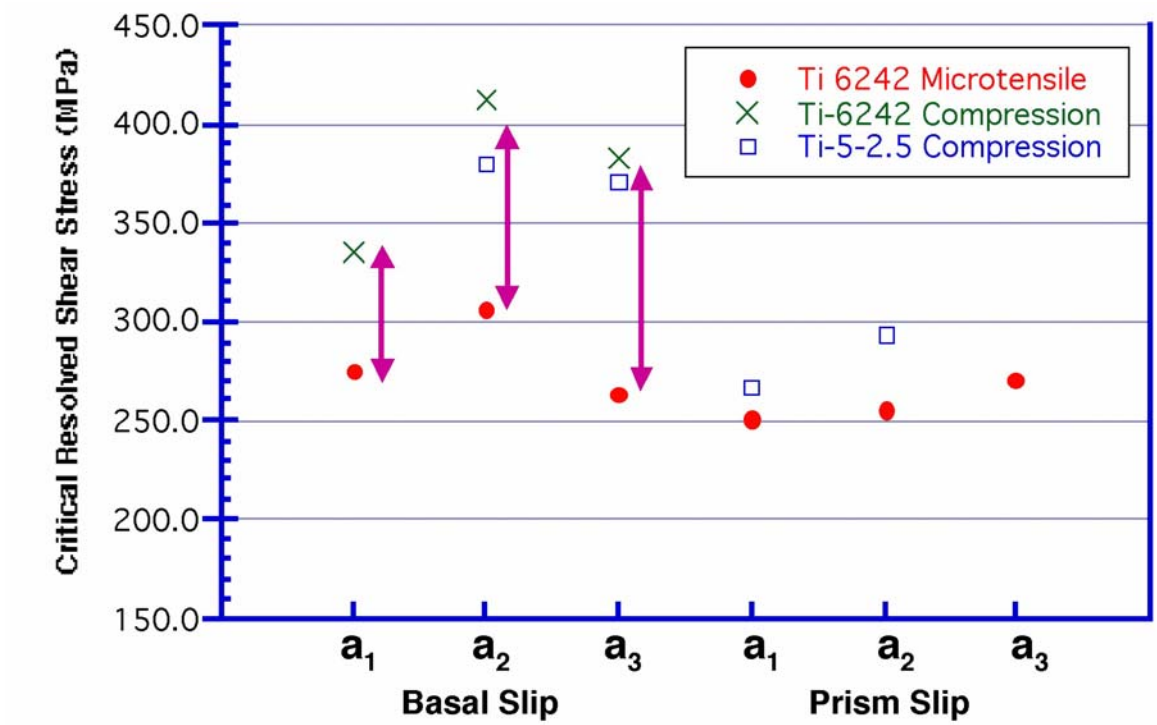

Figure A-17. Summary of the CRSS Values (as Determined From the Proportional Limit) for Microtension and Bulk Compression Tests

SEM was performed on compression sample surfaces after deformation to investigate the slip line morphology. For $\mathbf{a_1}$ basal slip, intense, widely spaced slip lines are observed on the side face of the samples (i.e., the face containing the slip vector), with large shear offsets observed at the α/β interfaces and at fiducial scratches in the α phase. Large shear offsets are observed every 40-70 μm. Packets of more closely spaced planar bands are also observed, each with somewhat smaller offsets. Intense wavy slip lines are observed on the exit face of the samples, indicating frequent cross slip of screw character dislocations. Taken together, these views indicate that screw dislocations remain relatively straight and in planar arrays, even though cross slip is frequent during their motion. A dramatically different slip line morphology was observed for single α/β colony compression samples oriented for $\mathbf{a_2}$ and $\mathbf{a_3}$ basal slip. No slip lines were

apparent on the sample surfaces of the prism faces containing the $\mathbf{a_2}$ or $\mathbf{a_3}$ slip directions. This may be due to an insufficiently smooth surface finish achieved on these faces before testing. However, the slip line morphology on the exit face of the $\mathbf{a_2}$ compression sample (an identical slip line morphology was observed on the exit face of the $\mathbf{a_3}$ basal compression sample) shows finely distributed, relatively straight slip lines. The average spacing of these slip lines is nominally 7 μm. Slip lines are frequently observed to be continuous through the broad faces of the β laths, indicating that shearing of the β laths by screw character dislocations is occurring. In comparison to the $\mathbf{a_1}$ basal case, significantly less overall cross slip by screw dislocations appears to have taken place for the $\mathbf{a_2}$ and $\mathbf{a_3}$ basal orientations, in comparison to that for $\mathbf{a_1}$ basal slip, as indicated by the more linear nature of the slip lines on the exit face.

TEM investigations of the dislocation mechanisms active during deformation of single α/β colonies oriented for basal slip were performed to provide insight into the observed anisotropy in constant strain rate behavior and to elucidate the role of the α/β interface. A detailed discussion of these results is provided in reference A-4.

Figure A-18 shows a bright-field TEM micrograph taken with **g**=[2$\underline{11}$2] near the [$\underline{2}$113] zone axis. An array of long screw character $\mathbf{a_1}$ (**b**=**a**/3[2$\underline{11}$0] dislocations are observed neighboring a β lath. This microstructure is consistent with the observation of a significantly lower mobility for screw character **a**-type dislocations compared to the mixed or edge character. Additional diffraction conditions confirm that only $\mathbf{a_1}$ dislocation content was present at the α/β interfaces, as well as within the bulk of the α phase.

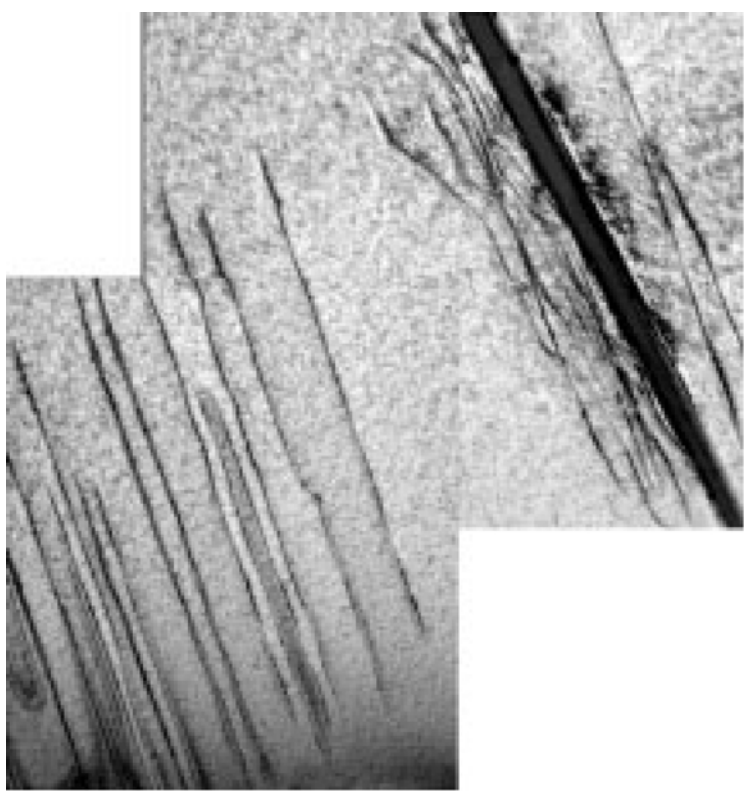

Figure A-18. Bright-Field TEM Micrograph Taken With **g**=[2$\underline{11}$2] Near the [$\underline{2}$113] Zone Axis

A relatively homogeneous distribution of screw character $\mathbf{a_2}$ ($\mathbf{a}$/3[1$\underline{2}$10]) dislocation arrays was observed, as shown in figure A-19(a) (taken with $\mathbf{g}$ = [$\underline{1}$100] near the [0001] zone axis). This distribution indicates very closely spaced dislocation arrays within the α laths, with overlapping of the arrays observed in the thin foil. The dislocations are often found in narrow loop-like configurations, elongated along screw orientation. A one-to-one correspondence of dislocations across the β laths exists. No pileups have been observed in the α-phase at the α/β interface. Figure A-19(b) is a bright-field image from the same region taken with $\mathbf{g}$ = [$\underline{1}$010] near the [0001] zone axis, showing the $\mathbf{g}\cdot\mathbf{b}$=0 imaging condition for the $\mathbf{a_2}$ dislocations. Significant non-$\mathbf{a_2}$ dislocation content is present within the α phase on both sides of the α/β interface. These residual matrix dislocations are believed to form as a result of the dislocation content accumulated at the α/β interface during persistent shearing of the β laths. The term residual matrix dislocations was adopted since they are observed exclusively where β lath shearing has occurred, and hence it is postulated that they have formed as a direct result of this process. The residual dislocations in the upper portion of figure A-19(b) have been confirmed using standard $\mathbf{g}\cdot\mathbf{b}$ analysis to be $\mathbf{a_3}$ dislocations ($\mathbf{b}$=$\mathbf{a}$/3[$\underline{11}$20]). Conversely, the residual dislocations in the lower portion of the montage are $\mathbf{a_1}$ dislocations ($\mathbf{b}$=$\mathbf{a}$/3[2$\underline{11}$0]). Additional study of dislocations in the b phase indicate that in thicker laths, pileups of $\mathbf{b_2}$ dislocations on both the primary $(101)_\beta$ slip plane and $(211)_\beta$cross slip plane are observed. Closely spaced edge character dislocation pileups are visible in the β lath, with less frequent observations of the screw character segments, which comprise the remainder of the dislocation loops in the β lath. Detailed $\mathbf{g}\cdot\mathbf{b}$ analysis indicated the presence of primarily $\mathbf{b_2}$ dislocations within the β phase, although some $\mathbf{b_1}$ dislocation content has been observed. The intense $\mathbf{b_2}$ dislocation pileups are observed at the exit face within the β laths, primarily on the $(211)_\beta$ cross slip planes, which are inclined with respect to the foil normal. Due to the OR between the phases, the $(211)_\beta$ plane does not have a crystallographically well-aligned slip plane in the α phase for slip transmission, which explains the observed dislocation pileups at the exit α/β interface.

In the $\mathbf{a_3}$ basal slip case, a distinct dislocation substructure is found. Figure A-20(a) shows a TEM micrograph where an $\mathbf{a_3}$ dislocation transmission through a β lath has commenced. This image was taken with $\mathbf{g}$ = [-2110], near the basal zone axis. An extended $\mathbf{a_3}$ ($\mathbf{b}$=$\mathbf{a}$/3[11$\underline{2}$0]) dislocation pileup is observed in the α phase at the entrance side of the b lath (as indicated by the curvature of the dislocations). A series of imaging conditions within the β phase were also obtained to identify the nature of the dislocations active within the β laths upon slip transmission. A network of dislocations can be observed forming in the β phase upon slip transmission through the α/β interface, as shown in figure A-20(b) using a β reflection. This analysis indicates that not all of the dislocation contrast observed is consistent with <111> dislocation content, with many dislocations near the entrance interface consistent with $\mathbf{b}$=$\mathbf{a}$[010] dislocations. These edge character $\mathbf{a}$[010] dislocations appear to have a one-to-one correspondence with the $\mathbf{a_3}$ dislocations within the α phase. Within the β phase, these [010] dislocations terminate at nodes that form a dislocation network, including significant $\mathbf{b_1}$ ($\mathbf{b}$=$\mathbf{a}$/2[11$\underline{1}$]) dislocation content, confirmed through $\mathbf{g}\cdot\mathbf{b}$ analysis. Thus, the mating slip vector for the a_3 dislocations appears to be $\mathbf{a}$[010] dislocation in the β phase. This is a surprising result since the $\mathbf{a}$[010] slip vector is not usually observed in bcc metals.

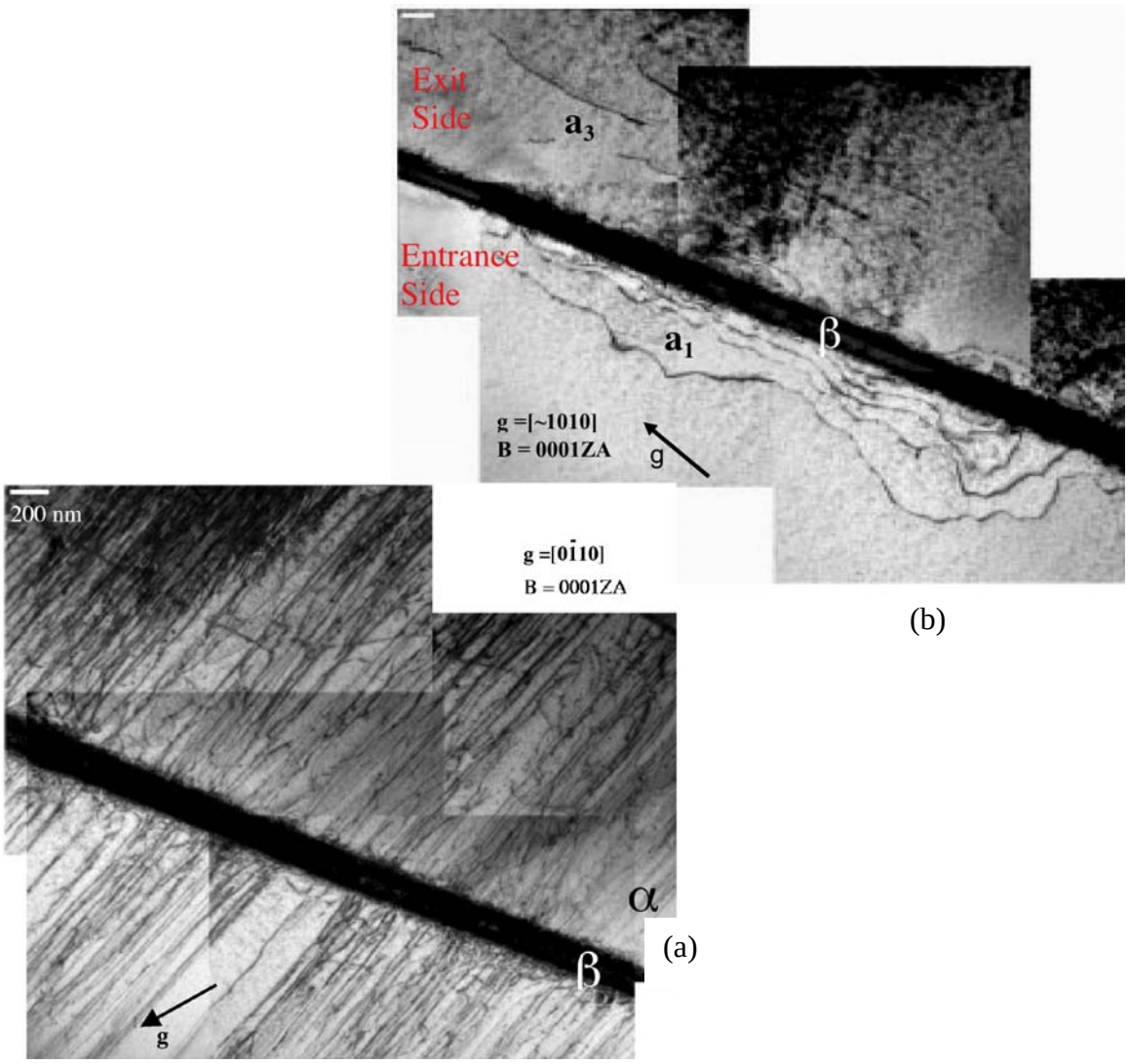

Figure A-19. Slip Transmission for the a_2 Basal Orientation (a) Bright-Field Image Using G[0-110] Showing Relatively Homogeneous Distribution of a_2 Dislocations and (b) a Bright-Field Image Using G[-1010] of Same Region For Which a_2 Dislocations Are Invisible and a_1 and a_3 Residual Matrix Dislocations Can Be Seen That Resulted From the Slip Transmission Process

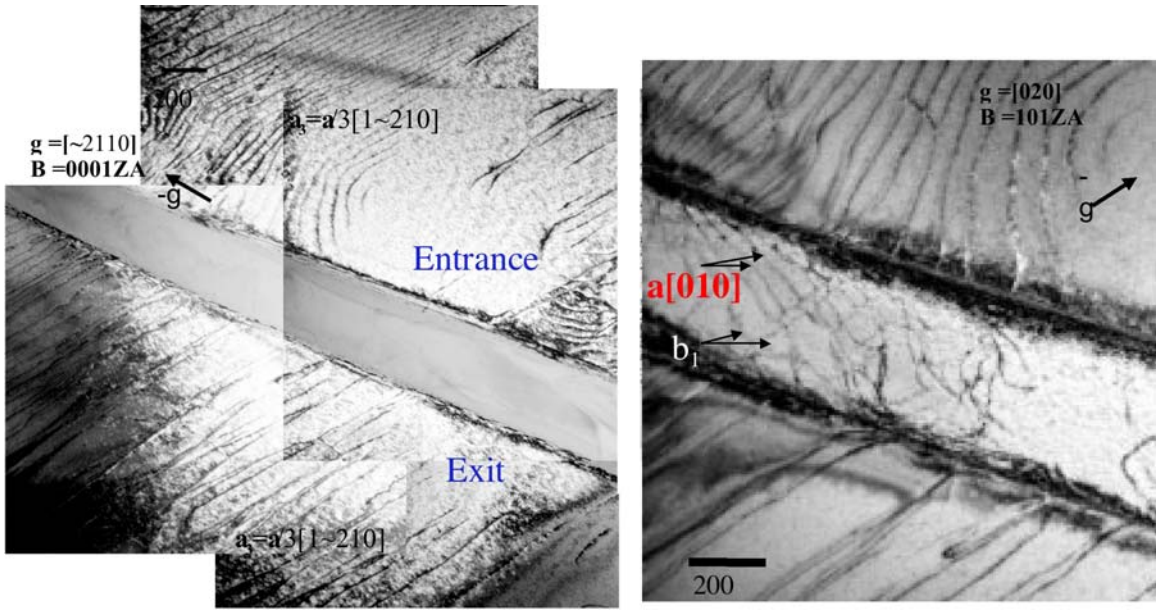

(a) (b)

Figure A-20. Slip Transmission for the a_3-Basal Case (a) Bright-Field TEM Image Taken With g[2110] Showing a_3 Dislocation Pileups at the Entrance Interface of the β Lath and (b) Bright-Field Image Using a g[020] β Reflection Showing the Presence of a[010] Dislocations Near the Entrance Interface of the β Lath and b_1 Dislocations Further Into the Lath

A.3.6 DISCUSSION OF RELATIVE INTERFACIAL BARRIERS FOR THE THREE BASAL ORIENTATIONS.

Hall-Petch hardening mechanisms within single α/β colonies have been discounted for the case of prism slip in Ti alloys [A-2 and A-5]. It was observed that the slip length in the α phase for screw dislocations is approximately 35 μm for all three a-type dislocations, while the slip length for the edge segments varies from 10 μm (for $\mathbf{a_2}$) to approximately 40 μm (for $\mathbf{a_1}$). These length scales were observed to be considerably larger than the length scales of the dislocation pileups in Ti-5-2.5 [A-5]. In the present case of basal slip, all three systems have similar slip lengths relative to the broad faces. While the line orientations vary for all three, in all cases, they are of mixed character. Thus, the difference in CRSS for the three orientations is not likely to be a result of varying slip length in the α phase.

For $\mathbf{a_1}$ basal slip, the small CRSS value can be associated with the relatively small magnitude of the residual matrix dislocation created with each shearing event. The small strain-hardening exponent exhibited by this orientation can be explained by the effective path available for annihilation of the interfacial residual dislocation content that must buildup in the course of numerous shearing events. It should be noted that, in principle, this same annihilation path is available for the $\mathbf{a_2}$ and $\mathbf{a_3}$ basal cases (since the primary slip planes in the α and β phases are the same in all cases). However, for these latter two orientations, slip does not, in fact, remain planar in the β phase, hindering the effectiveness of this annihilation path.

The moderately large CRSS for $\mathbf{a_3}$ basal slip may be rationalized by the combined effect of (1) the formation of large residual dislocation content at the entrance and exit α/β interfaces of the β laths and (2) the relatively large (presumed) CRSS for motion of the **a**[010] dislocations within the β phase. The larger strain-hardening exponent can be related to cross slip of $\mathbf{b_1}$ and $\mathbf{b_2}$ dislocations (after decomposition of the **a**[010] has occurred), which will tend to drive dislocations off the primary (101) slip plane. The consequent development of a three-dimensional dislocation network structure will result in large forest interactions within the β phase. More rapid accumulation of strain energy at the exit α/β interface may also be expected since the formation of residual matrix dislocations, which might relieve this interfacial strain energy, will be much more difficult due to the more diffuse distribution of $\mathbf{b_1}$ and $\mathbf{b_2}$ dislocations at the exit interface.

The observed CRSS for $\mathbf{a_2}$ basal slip is larger still (by about 7% relative to the $\mathbf{a_3}$ basal case). This indicates that the highest energy barrier in the $\mathbf{a_2}$ basal slip transmission process is less efficiently overcome than for slip transmission in the $\mathbf{a_3}$ basal case. It should be mentioned that the magnitude of the residual dislocation for this case is the largest of all three orientations. Thus, it is tempting to correlate the large CRSS for $\mathbf{a_2}$ basal slip with the large residual Burger's vector that must be created at the exit face of the α/β interface. However, the slip transmission process in this case is quite complex, particularly in wider β laths. The systematic cross slip of $\mathbf{b_2}$ dislocations onto {112} planes, for which no mating slip plane in the β phase is available, appears to significantly inhibit the exit of the dislocations from the β lath, and probably contributes to both the relatively large CRSS and strain-hardening exponent for $\mathbf{a_2}$ basal slip.

For both the $\mathbf{a_2}$ and $\mathbf{a_3}$ basal cases, the barrier to slip transmission is sufficiently large that dislocation pileups are developed. However, the location of these pile-ups is different for these the two orientations. In the $\mathbf{a_3}$ case, the primary barrier is created by the entrance interface, and extended pileups in the α phase are common. In the $\mathbf{a_2}$ case, the slip transfer reaction at the entrance interface is energetically favorable, and entry into the β lath is easy. However, the opposite is true upon exiting the β lath. Hence, pileups are formed within the β lath. The relatively thin β laths limits the potential concentration of stress due to dislocation pileups. Additionally, the strong short range order effects that promote planar slip in the α phase [A-21] are absent in the β phase. Therefore, the effective stress concentration at the tip of the pileups in the $\mathbf{a_2}$ basal case are expected to be considerably smaller than that for the $\mathbf{a_3}$ basal case. Consequently, a larger applied stress is required for slip transmission and general yielding to occur for $\mathbf{a_2}$ basal slip.

A.3.7 OBSERVATIONS OF RAPID ROOM TEMPERATURE RECOVERY IN SINGLE COLONY CRYSTALS.

Creep testing on oriented single α/β colonies of Ti-6242Si has provided dramatic insight into a phenomenon that was previously unknown to occur in Ti alloys prior to the present work, which was the recovery of strain hardening at room temperature [A-19]. The TEM results to date indicate that very similar slip transmission processes under creep conditions are very similar to those described above under constant strain rate conditions. Figure A-21 shows an example of the slip transmission event for the a_3 basal creep sample, with a corresponding schematic illustration of the dislocation configurations. Figure A-22a shows the strain-time curve for this creep sample. This test was performed at a stress level of 640 MPa corresponding to 84% of the observed 0.2% offset yield strength. An exhaustive primary creep behavior was observed during the initial portion of the creep test, indicative of rapid strain hardening. The sample was crept for 50 hours until the strain rate exhausted to a final rate of 1.24×10^{-9} s^{-1}, at a creep strain of 0.05%. For this initial loading portion, a power law regime was observed, with values of A and a measured to be 1.74×10^{-5} and 0.28, respectively. The sample was subsequently unloaded for 24 hours. The strain on the unloaded compression sample was monitored as a function of time using a strain gage fixed to the sample. A small but detectable amount of forward flow of the order of 40 microstrain was measured while in this unloaded state. Upon reloading, a creep rate of 1.4×10^{-7} s^{-1} was observed. This corresponds to over a two order of magnitude increase in creep rate upon reloading. The extrapolated power law primary creep behavior of the initial loading portion of the test is shown in figure A-22a to demonstrate the large effect of the unloading and reloading sequence on the accumulated creep strain. A second 24-hour unload was performed on the same compression sample after the creep strain rate had exhausted to 2.8×10^{-9} s^{-1}. A remarkably similar two order of magnitude increase in creep rate (to 3.3×10^{-7} s^{-1}) was again observed upon reloading.

A similar test of the recovery for a Ti-6242 single α/β colony sample oriented for $\mathbf{a_2}$ basal creep was also performed, as shown in figure A-22b. This test was performed at a stress level of 640 MPa, corresponding to 78% of the 0.2% offset yield strength. An exhaustive primary creep behavior was observed during the initial portion of the creep test. After the $\mathbf{a_2}$ basal slip creep test creep strain rate had exhausted to 4.4×10^{-9} s^{-1}, the sample was unloaded for 24 hours, as indicated in figure A-22b. Minimal forward flow was exhibited by the compression sample during the 24-hour unload. Upon reloading, the sample then resumed power law (exhaustive) creep behavior at a rate of 1.70×10^{-8} s^{-1}. A second unloading for 24 hours was performed when the sample reached a creep rate of 2.85×10^{-9} s^{-1}, as shown in figure A-22b. A similar strain response was observed during the second unloading, with a forward flow of less than 20 microstrain while the sample was unloaded. Upon reloading, the sample resumed power law creep behavior at a rate of 1.87×10^{-9} s^{-1}. Neither of the 24-hour unloads appear to have had any significant effect on the creep rate or accumulated creep strain observed for the $\mathbf{a_2}$ basal orientation compression sample.

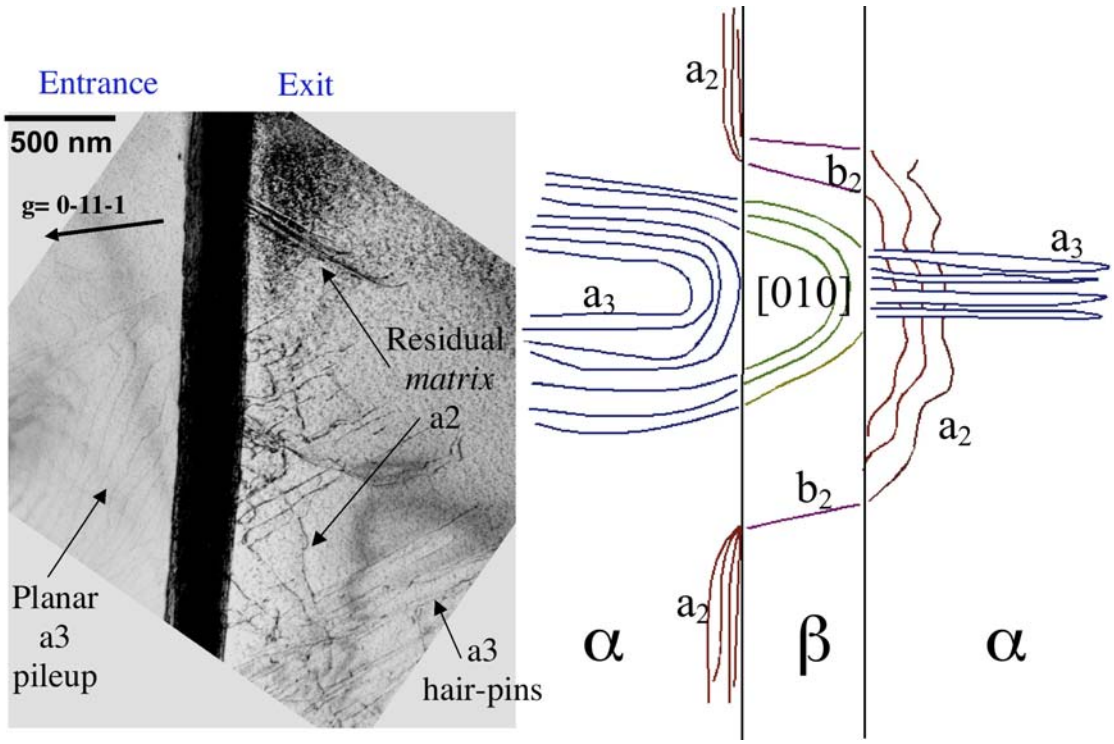

(a) (b)

Figure A-21. Slip Transmission Process Observed After Compression Creep of the a_3 Orientation (a) Bright-Field TEM Image Using g[0-11-1] and (b) Schematic of the Dislocation Configurations During Transmission. Structures are very Similar to Those Observed After Constant Strain Rate Testing

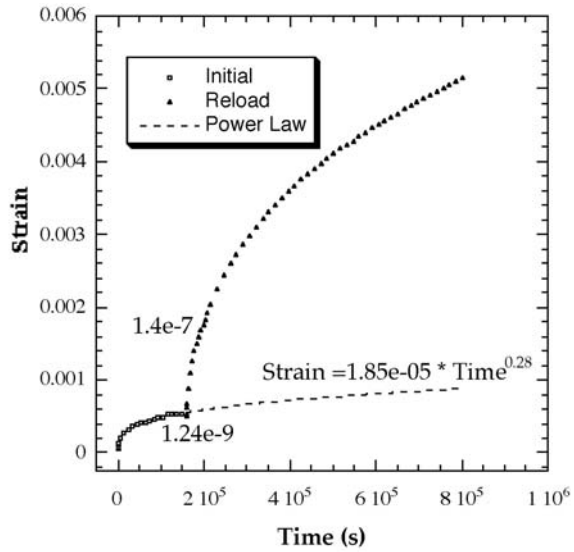

Figure A-22a. Strain Versus Time Plot From a Room Temperature Creep Test of a Single Colony Ti-6242 Compression Sample Oriented to Maximize the Resolved Shear Stress on the a_3 Basal Slip System (A 24-hour unload was performed during this test with over a 2 order of magnitude increase in creep rate observed upon reloading. The increase in creep strain compared to the predicted power law behavior is indicated.)

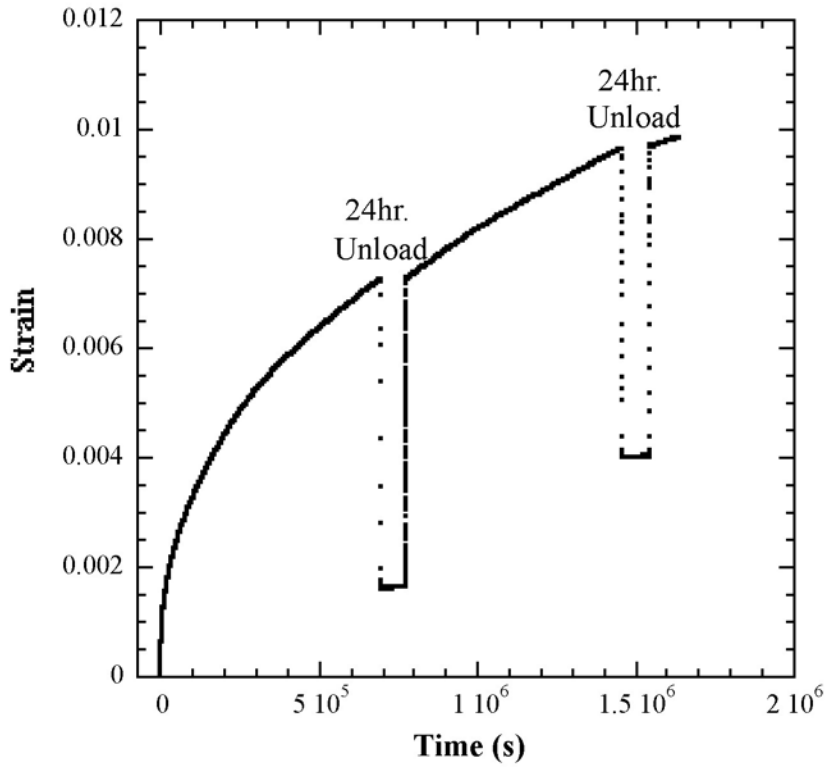

Figure A-22b. Strain Versus Time Plot From a Room Temperature Creep Test of a Single Colony Ti-6242 Compression Sample Oriented to Maximize the Resolved Shear Stress on the a_2 Basal Slip System. (Two 24-hour unloads were performed during this test and no acceleration of creep rate was observed upon reloading.)

To gain insight into the deformation mechanisms resulting in the dramatically different creep recovery behavior observed for the $\mathbf{a_2}$ and $\mathbf{a_3}$ basal slip orientations, refer to the TEM observations described above. Recall that for the $\mathbf{a_3}$ basal slip orientation (figures A-20 to A-21), large planar arrays of approximately 20 $\mathbf{a_3}$ (A-11 to A-20) dislocations is observed in the α phase, piled up at the entrance α/β interface. Long line lengths of edge-character dislocations are observed in the pileup parallel to the broad face of the β lath, with long line lengths of screw character $\mathbf{a_3}$ dislocations nearly perpendicular to the α/β interface. Large stress concentrations at the α/β interface are apparently required for slip transmission into the β phase. These intense, planar dislocation pileups within the α phase provide a source for likely relaxation and recovery during unloading. These extended pileups in the α phase are absent for the $\mathbf{a_2}$ basal slip-orientated sample (see figure A-19).

It was, therefore, postulated that large pileups of **a**-type dislocations exist in the α phase stimulates the activation of fresh dislocation sources, even when the sample is under no macroscopically applied stress. The precise mechanism by which relaxation of these pileups leads to the activation of new sources in the α phase is yet be elucidated. It is likewise possible that these large local stress concentrations may also cause preferential diffusion of hydrogen to these regions. The theories of hydrogen-induced plasticity postulated by Birnbaum, et al. [A-22]

would then suggest that enhanced, localized plasticity in these regions may be promoted by the locally elevated hydrogen levels. The more complete understanding of the role of hydrogen in this process would require testing of colony crystal in hydrogen charged versus uncharged conditions. It should also be emphasized that room temperature recovery was also observed in polycrystalline samples of Ti-6wt%Al and Ti-6242 as part of an AFOSR-funded program. The time scales over which measurable recovery is observed are much longer than that seen in the present case for the a_3 basal single colony crystal. However, in this latter case, the recovery effect may be dramatically accelerated and enhanced due to the fact that every β lath present in the single colony crystal is acting as a significant dislocation barrier such that pileups are present at all of these interfaces. Therefore, a significant volume of the sample is being acted upon by large local stresses in the unloaded state, giving rise to the more dramatic and rapid recovery effect.

It is believed that these preliminary recovery results have important implications for the development of local stress and strain distributions during alternating loading conditions. In particular, the effect of length of time in the unloaded state has not been explored in detail previously, and yet could have significant effect on local recovery processes as a function of individual grain or colony orientation. While not part of the present FAA program, it is believed that this previously unknown phenomenon of room temperature recovery in Ti alloys deserves additional study to fully characterize the magnitude and kinetics of the process.

A.3.8 RESULTS FOR SINGLE COLONY MICROCOMPRESSION TESTS (TENSION/ COMPRESSION ASYMMETRY).

A typical stress-strain curve for a microcompression test is shown in figure A-23. Initially, there is some take-up from the load frame due to the high compliance of the system. The elastic region is linear, although a little soft for this alloy. This is due to misalignment between the indenter head and the sample. This was resolved with the use of a goniometer to make fine adjustments.

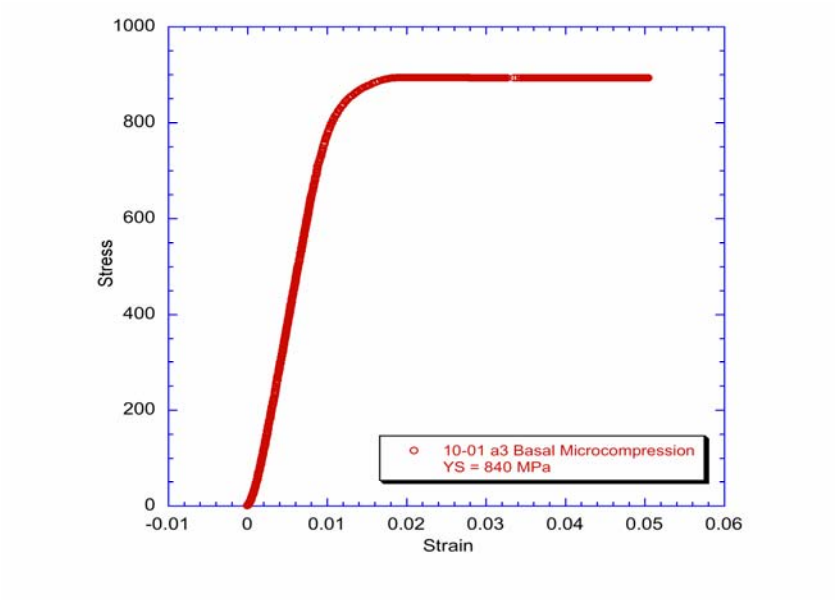

Figure A-23. A Typical Stress-Strain Curve for a Microcompression Test (This is from a 12-µm diameter a_3 basal sample.)

Figure A-24 shows a plot of CRSS versus slip system for the microtensile, bulk compression, and microcompression samples. Although there are differences in the CRSS values, it is apparent that there is a consistent trend between the different systems, once again illustrating the anisotropy that exists between these systems. The microcompression tests lie between those of the bulk specimens and the microtensile samples. Since these values do not match those of the bulk samples, there must be a size effect associated with testing at this size scale. If this size effect varied linearly, then the values would increase in the order of microcompression, microtensile, and then bulk compression. However, this is not the case; therefore, confirming that there is a tension/compression asymmetry that exists in this material. To place a quantitative value on the tension/compression asymmetry, these size effects must be understood.

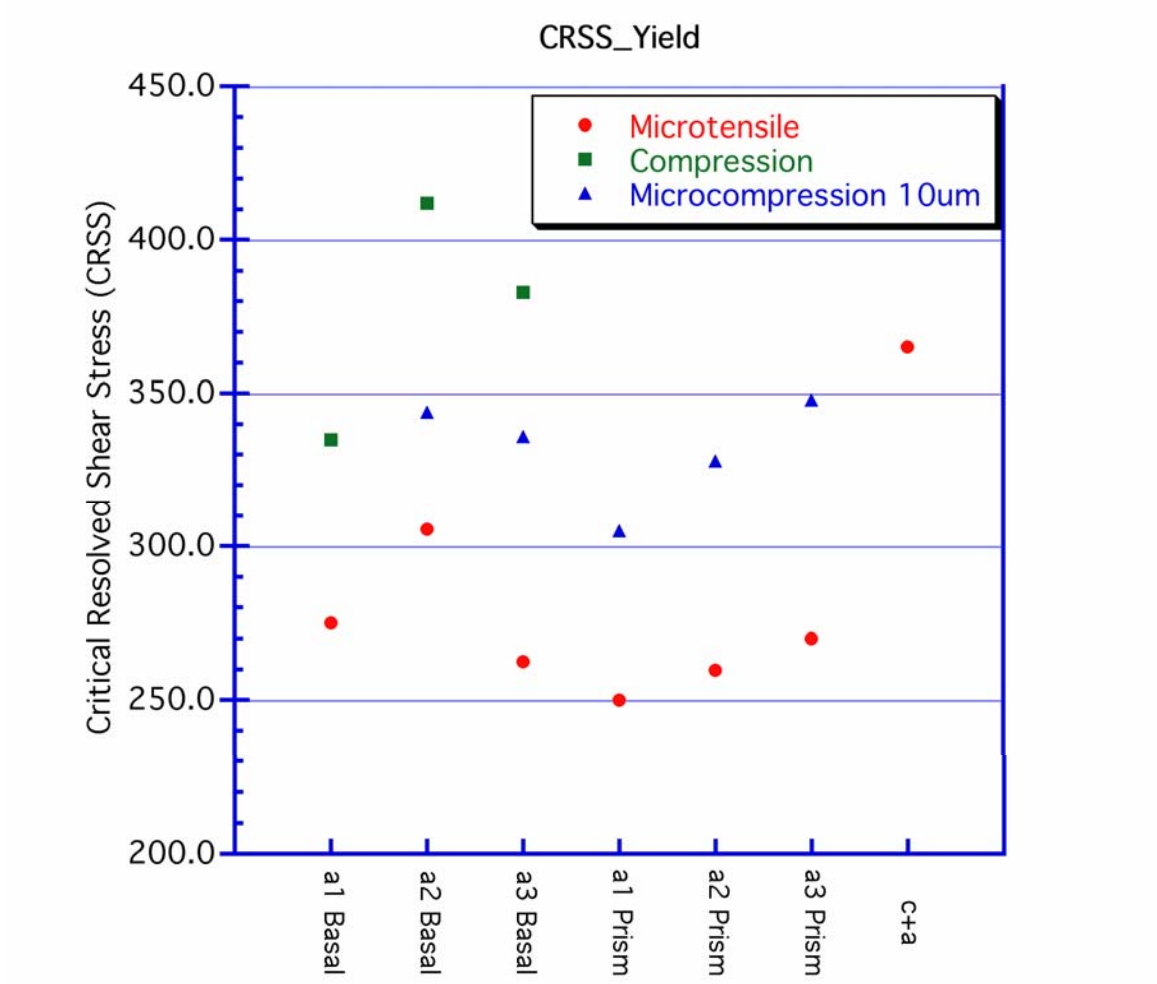

Figure A-24. Plot of CRSS Versus Slip System for the Microtensile, Bulk Compression, and Microcompression Samples

A.3.9 RESULTS FOR SINGLE COLONY MICROCOMPRESSION TESTS (SIZE EFFECTS).

Figure A-25 shows a plot of stress versus sample size showing both yield stress and proportional limit. It is apparent from the yield stress data that there is no Hall-Petch type behavior as the diameter of the sample is reduced. In fact, the proportional limit data suggests that the reverse is true. This is contrary to the observations made by Uchic, et al. [A-23] in pure nickel (Ni) and Ni_3Al, showing a strong size dependence as the sample size is decreased. A possible explanation for this unexpected result is discussed below, and supported by TEM evidence.

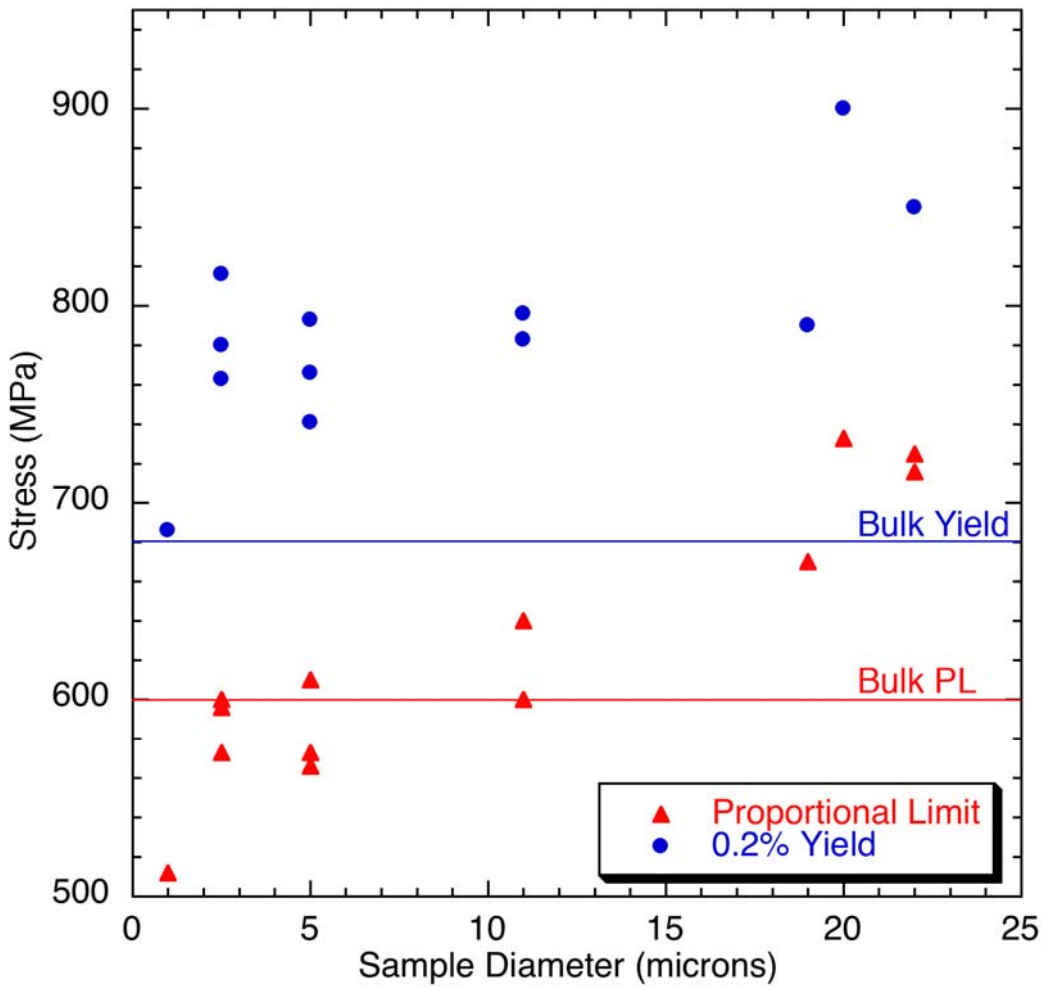

Figure A-25. Plot of Stress Versus Sample Size Showing Both Yield Stress and Proportional Limit (The horizontal lines indicate the properties measured on bulk samples.)

The inverse Hall-Petch effect may be due to the way that Ti deforms in the microplasticity regime, wherein the mobility of the screw dislocation is much less than that of the edge. The a-type screw dislocations have a nonplanar core that is dissociated onto both the prism and basal planes [A-24]. The edges run out very quickly leaving behind long screw segments. The motion of these screws is driven by atomic-scale jumps forming kink pairs along the length of the screw. As these screws move, they can cross slip easily due to the nature of the nonplanar core. This causes small jogs to form along the line length that act as pinning points. One would expect that as this line length is increased, indicated by the diameter of the sample, the stresses needed to move the dislocation would also increase. It is for this reason that the study of different geometries was performed. The goal of this study was to change the sample orientation with respect to the Burger's vector; the screw line length can be varied without changing the volume of material tested.

Figure A-26 shows a plot of yield strength for three different sample shapes: tetragonal, short screw length, and long screw length. The tetragonal samples were tested to establish a control,

by which the length of the sides are equal to that of a 10-μm-diameter sample. Comparing the results from figures A-25 and A-26, it is apparent that there is good agreement between these two tests. From the data presented in figure A-26 is can also be seen that there is a strong influence on the length of the screw dislocations and the mechanical behavior. The proportional limit and 0.2% yield stress are ~100 MPa stronger for the longer screws compared to the short screws. To confirm whether or not this is due to the formation of jogs, TEM studies where performed, as described in section A.3.10. However, the nature of the screw dislocations cannot explain the fact that the 0.2% yield stress is displaced by 100 MPa compared to the bulk specimens. Larger samples will be tested in the near future to determine if these yield stresses will drop to reach those of the bulk specimens.

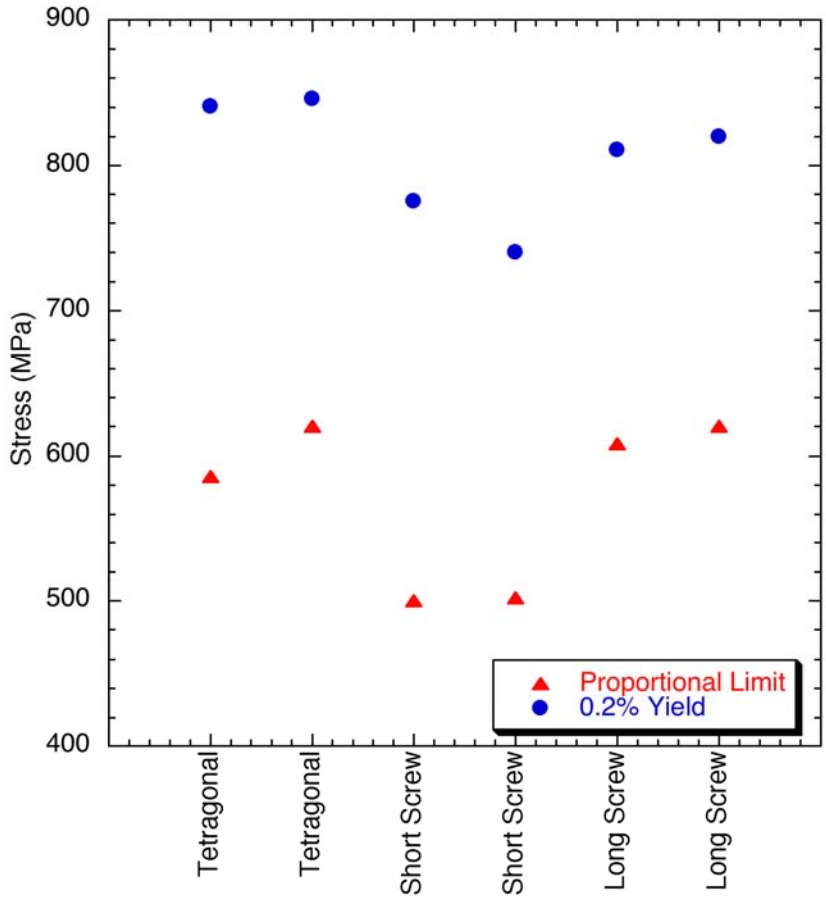

Figure A-26. Plot of Stress Versus Sample Shape, Illustrating the Effect of Screw Line Length on the Deformation Behavior at This Size Scale

A.3.10 TEM RESULTS.

Using the OmniProbe, TEM samples were extracted from two 5-micron pillars. Figure A-27 is a montage of TEM images taken of a TEM foil such that the Burger's vector is out of the plane of the foil, allowing the view of long arrays of a/3[2$\underline{11}$0] screw dislocations. These arrays traverse the entire length of the sample and appear to be influenced little by the presence of the β lath. This is consistent with studies performed by M. Savage [A-7] for the a1 basal colony orientation.

Figure A-27. Montage of Bright-Field TEM Images Taken From a 5-Micron Pillar Burger's vector is out of the plane G=(1$\underline{1}$01) B=[$\underline{2}$113])

Figure A-28 is a montage of TEM images taken from a TEM foil such that the Burger's vector is in the plane of the foil. In this sample, the bulk of the deformation took place near the surface of the material, indicated by the large presence of a/3[2$\underline{11}$0] type dislocations. It is not apparent

why some samples only deform near the top surface, but during these tests, several samples only showed slip traces in this region. The rounding on the top surface is an artifact from the TEM extraction process and was not present during testing.

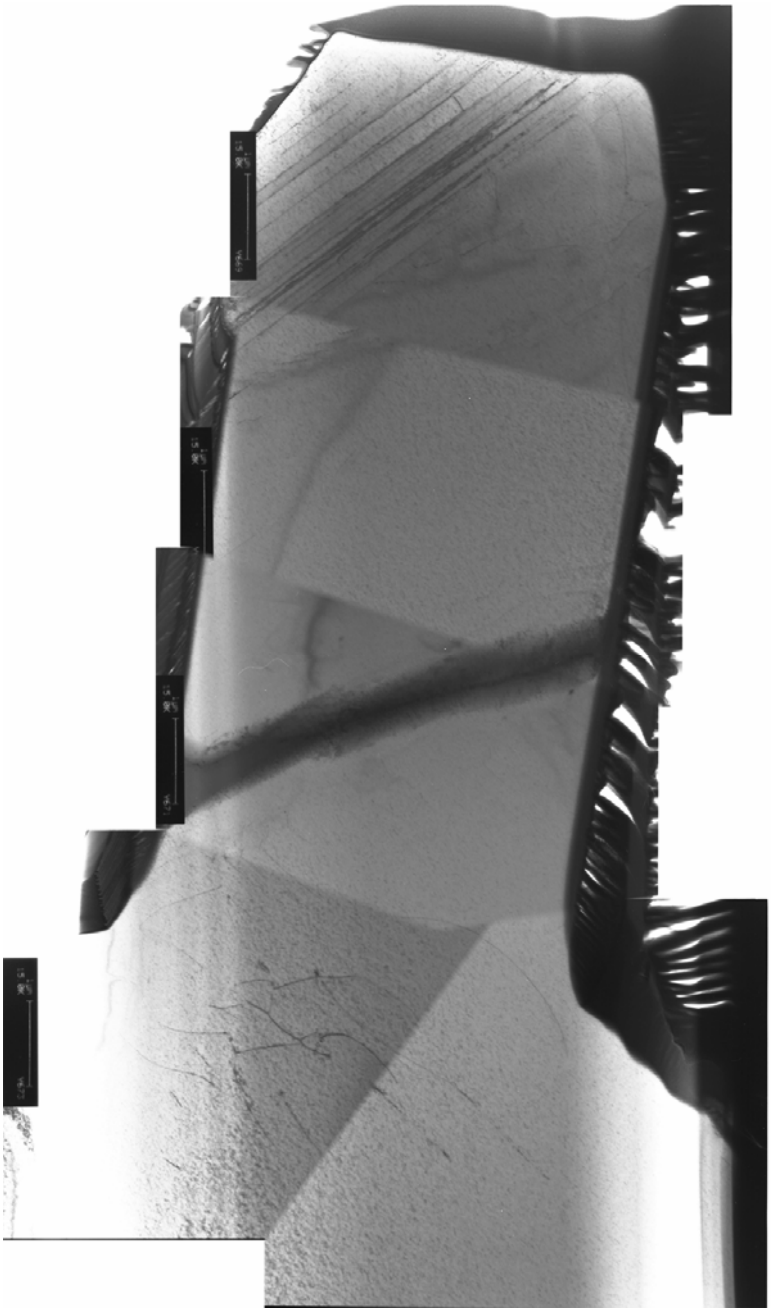

Figure A-28. Montage of Bright-Field TEM Images Taken From a 5-Micron Pillar (Burger's vector is in the plane G={1$\underline{2}$1$\underline{2}$} B=[0002])

The last TEM foil extracted is from the slip plane of one of the tetragonal samples. A montage of Bright-Field (BF) scanning transmission electron microcopy (STEM) (BFSTEM) images is shown in figure A-29. The low mobility of the screws is clearly evident by the very long line

length, which spans the entire slip plane. At higher magnification, the jogs are clearly visible. Although the majority of the jogs are very small, in some areas they become fairly large, see figure A-30. It is these jogs that contribute to the strengthening of the pillars as the sample diameter is increased.

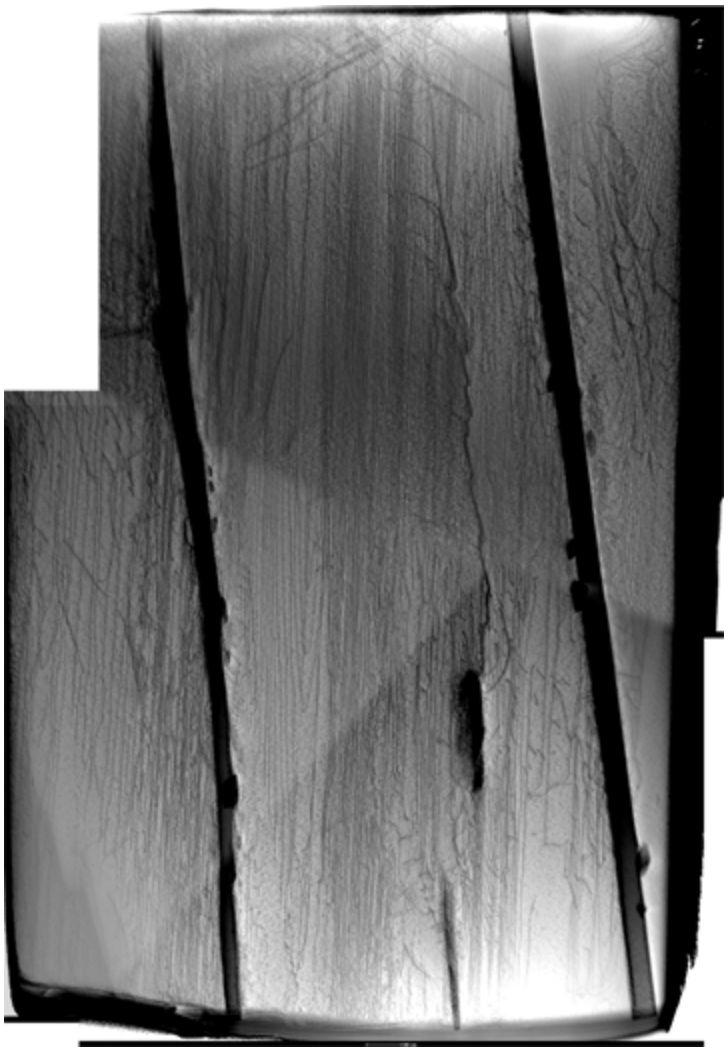

Figure A-29. Montage of BFSTEM Images From the Slip Plane of a Tetragonal Sample (The screw line length can traverse the entire sample length.)

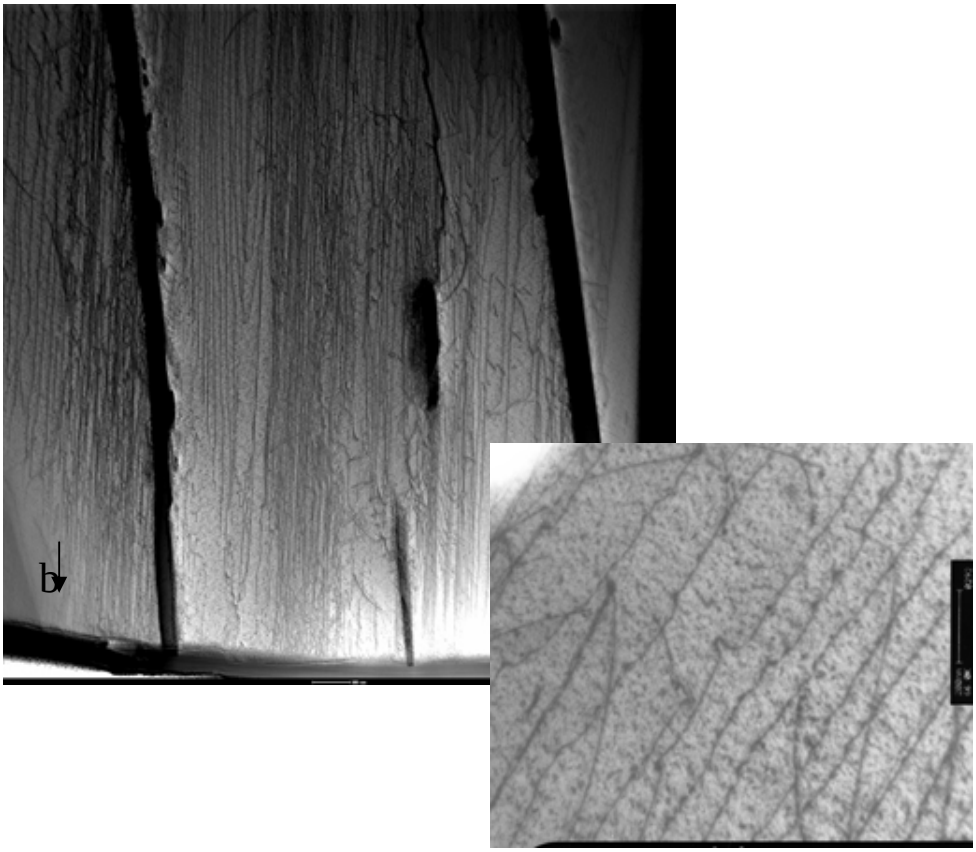

Figure A-30. TEM Images Showing the Jogs Present in the Sample

A.4 CONCLUSIONS.

Compression testing of Ti-6wt% single-phase, single crystals in three different orientations was performed to provide data to calibrate the crystal plasticity model for the hcp α phase. The results indicate that the [0001] orientation is over three times stronger than the prism and basal a-type slip systems.

Single colony crystals of Ti-6242 were grown and tested under constant strain rate conditions for seven distinct orientations to probe the plastic anisotropy for this important microstructural constituent. A large anisotropy in the critical resolved shear stress was observed for the three distinct basal orientations, while a smaller anisotropy was observed for the prism systems. The [0001] orientation is 40% larger than for the weakest a-type orientation.

A detailed transmission electron microscopy investigation was performed on single colony specimens oriented for basal slip and deformed in compression. The results showed a remarkably different process of slip transmission for the three slip systems activated, which reflect the different orientation relationship between the slip directions in the α and β phases. These results provide significant, new insight into the plastic anisotropy of these colony crystals.

Small-scale compression testing revealed a size effect associated with deformation behavior in the a1 basal orientation. This size effect has an inverse Hall-Petch behavior associated with it, contrasting the results observed by others in different materials. This appears to be influenced by the formation of jogs along the screw line length.

A dramatic room temperature recovery of strain hardening was observed in one of the basal single colony crystals, indicating that large dislocation pileups in the α phase may induce generation of new dislocation sources, even in the unloaded state. This recovery phenomenon is unusual at low homologous temperature and may have important implications for the development of local stress and strain distributions during alternating loading conditions.

A.5 REFERENCES.

A-1. Neeraj, T., Ph.D Thesis, Department of Materials Science and Engineering, The Ohio State University, Columbus, OH, 2000.

A-2. Savage, M.F., Tatalovich, J., Zupan, M., Hemker, K.J., and Mills, M.J., *Mater. Sci. Eng.* A, **319**, 2001, p. 398.

A-3. Mills, M.J. Hou, D.H. Suri S., and Viswanathan, G.B in "Boundaries and Interfaces in Materials," TMS Publications, Warrendale, PA, 1998, p. 295.

A-4. M.F. Savage, Ph.D Thesis, Department of Materials Science and Engineering, The Ohio State University, Columbus, OH, 2000.

A-5. Suri, S., Viswanathan, G.B., Neeraj, T., Hou, D.H., and Mills, M.J., *Acta Mater*, Vol. 47, 1999, p. 1019.

A-6. Zupan, M., Ph.D Thesis, Department of Mechanical Engineering, 2000, The Johns Hopkins University, Baltimore, MD.

A-7. Savage, M.F., Ph.D Thesis, Department of Materials Science and Engineering. 2000, The Ohio State University, Columbus, OH.

A-8. Sharpe Jr., W.N., *An Interferometric Strain/Displacement Measurement System*, Langley Research Center, NASA, Hampton, VA, 1989, p. 67.

A-9. Yuan, B. and Sharpe, W.N., *Journal of Testing and Evaluation*, **25**, 5, 1997, pp. 485-490.

A-10. Sharpe Jr., W.N. and McAleavey, A., *Symposium on Materials and Device Characterization in Micromachining*, SPIE, **3512**, pp. 130-7, 1998.

A-11. Zupan, M. and Hemker, K.J., *Experimental Mechanics*, 2002, **42**.

A-12. Legros, M., Hemker, K.J., LaVan, D.A., Sharpe, Jr., W.N., Rittner, M.N., and Weertman, J.R., *Nanophase and Nanocomposite Materials II*, MRS, 1996, p. 273.

A-13. Young, M., *Optics and Lasers*, Springer-Verlag, New York, NY, 1993.

A-14. Uchic, M.D., Dimiduck, D.M., Florando, J.N., and Nix, W.D., *Mat. Res. Soc. Symp. Proc*., 2003, p. 753.

A-15. Neeraj, T., D.-H. Hou, Daehn, G.S., and Mills, M.J., *Acta Mater.*, **48**, 2000, p. 1225.

A-16. Neeraj, T. and M.J. Mills, *Phil. Mag. A*, 82A, 2002, p. 779.

A-17. Paton, N.E., Baggerly, R.G., and Williams, J.C., *Rockwell*, 1976.

A-18. Williams, J.C., Baggerly, R.G., and Paton, N.E., *Met.Trans. A*, **33A**, 2002, p. 837.

A-19. Savage, M.F., Neeraj, T., and Mills, M., *Metall. and Mater. Trans A*, **33,** 2002, p. 891.

A-20. Dahmen, U., 1982, *Acta Metall.*, **30**, p. 63.

A-21. Neeraj, T. and Mills, M.J., *Mater. Sci. Eng.* A, **319**, 2001, p. 415.

A-22. Ferreira, P.J., Robertson, I.M., and Birnbaum, H.K., "Hydrogen Effects on the Interaction Between Dislocations," *Acta Materialia*, 1998, 46(5).

A-23. Uchic, M.D., Dimiduck, D.M., Florando, J.N., and Nix, W.D., *Science*, 2004, p. 305.

A-24. Neeraj, T., Savage, M.F., Tatalovich, J., Kovarik, L., Hayes, R.W., and Mills, M.J., *Phil. Mag*, 85, 2005, p. 279.

APPENDIX B—INFLUENCE OF MICROSTRUCTURE ON DWELL-FATIGUE SUSCEPTIBILITY OF Ti-6242 ALLOY

B.1 INTRODUCTION.

In the current program, four different microstructural conditions of Ti-6242 alloy were examined: three of these are α/β forged and the fourth one is β-forged. Two of the α/β-forged Ti-6242 alloys were supplied by Ladish Co. and the third α/β forged alloy was taken out of the field-returned (retired) impellers. The β-forged material was again supplied by Ladish Co. The thermomechanical processing (TMP) parameters for the three (two α/β forged and one β-forged) Ladish pancakes represent the current or prior industrial forging practice for aircraft engine compressor components. To facilitate the comparison and integration of the various activities within this program, the same three Ladish pancakes were studied in the various parts of the program, i.e., crack initiation, crack propagation, in situ crack detection, etc.

The basic microstructural characterization for the four different forgings was conducted by optical microscopy and the microtexture of the three α/β-forged material was evaluated using the Electron Backscatter Diffraction (EBSD) techniques in a scanning electron microscope (SEM). The dwell life debit was evaluated for the different microstructural conditions.

B.2 METHODS.

B.2.1 THERMOMECHANICAL PROCESSING AND OPTICAL MICROSCOPY.

The Ti-6Al-2Sn-4Zr-2Mo-0.1Si alloy that was used in this study was supplied by Ladish Co., Cudahy, WI. This alloy was supplied in the form of three pancake forgings. The three forgings have undergone three different TMP routes, as described in detail in figure B-1. The billet for pancake 1 was α/β forged to a very high strain (~ 89%) to cause recrystallization and randomization of the aligned α (colony) structure of the starting material, thereby producing a randomly oriented primary α grains in the microstructure. This was subsequently solution heat-treated at T_β - 20°C to obtain a low volume fraction (~ 20-25%) of primary α (figure B-2(a)) and oil quenched to suppress the regrowth of primary α grains during cooling. The resulting microstructure consisted of globular α grains and lamellar-transformed β regions. All these steps are representative of current industrial practice and are thought to reduce the dwell-fatigue susceptibility of this class of alloys. The billet for pancake 2 was also α/β forged, however, along the TMP route representative of earlier industrial practice. This was forged to a relatively lower strain level (~58%) and subsequently solution heat-treated at T_β - 56°C to obtain a higher volume fraction (~ 65-70%) of primary α (figure B-2(b)). It was then air cooled to obtain a microstructure consisting of primary α grains and transformed β regions. The TMP parameters for pancake forging 3 (figure B-1(c)) are consistent with current β-processing practice used by aero engine companies. The resulting microstructure (figure B-2(c)) is used mostly because of the better creep resistance at high temperatures.

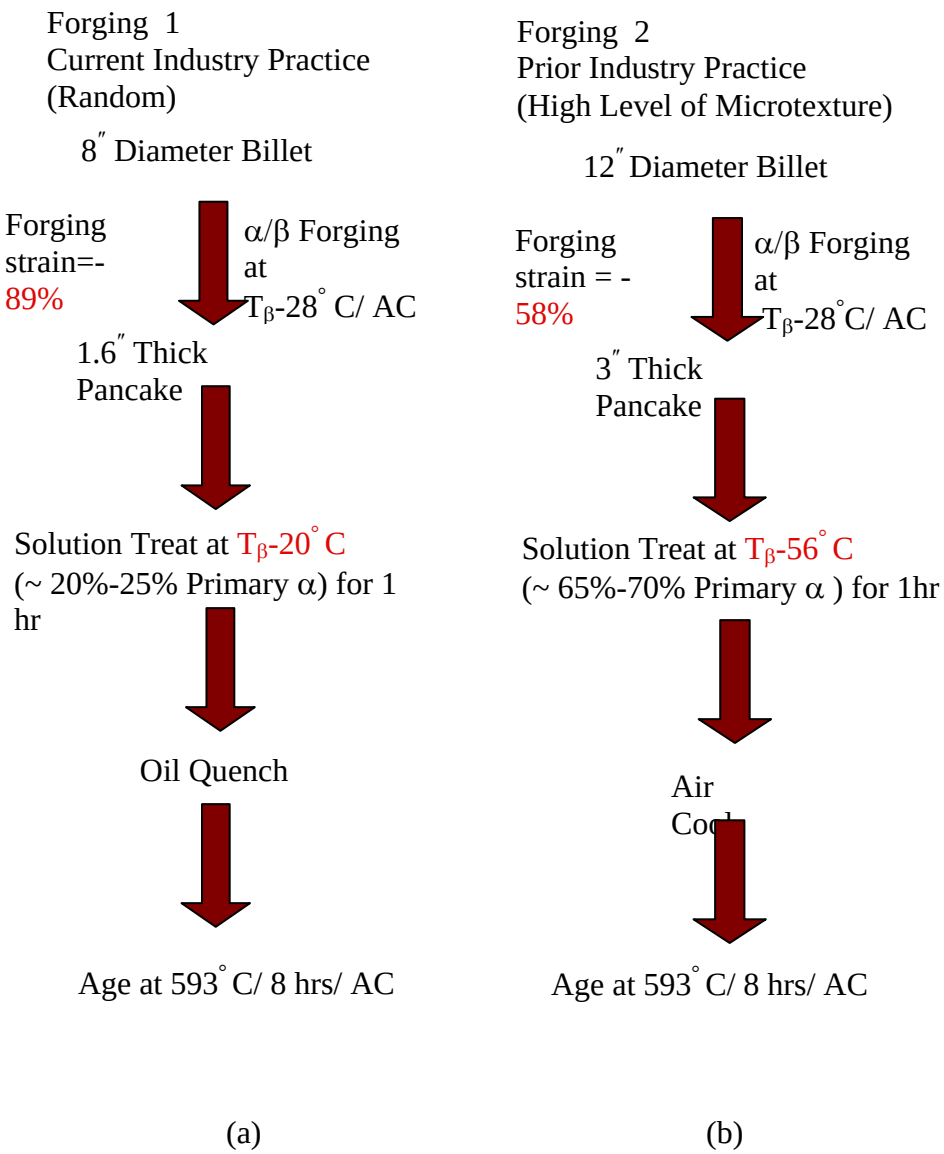

Figure B-1. Thermomechanical Processing Routes (a) Ladish Pancake Forging 1, (b) Ladish Pancake Forging 2, (c) Ladish Pancake Forging 3, and (d) Retired Impeller Material

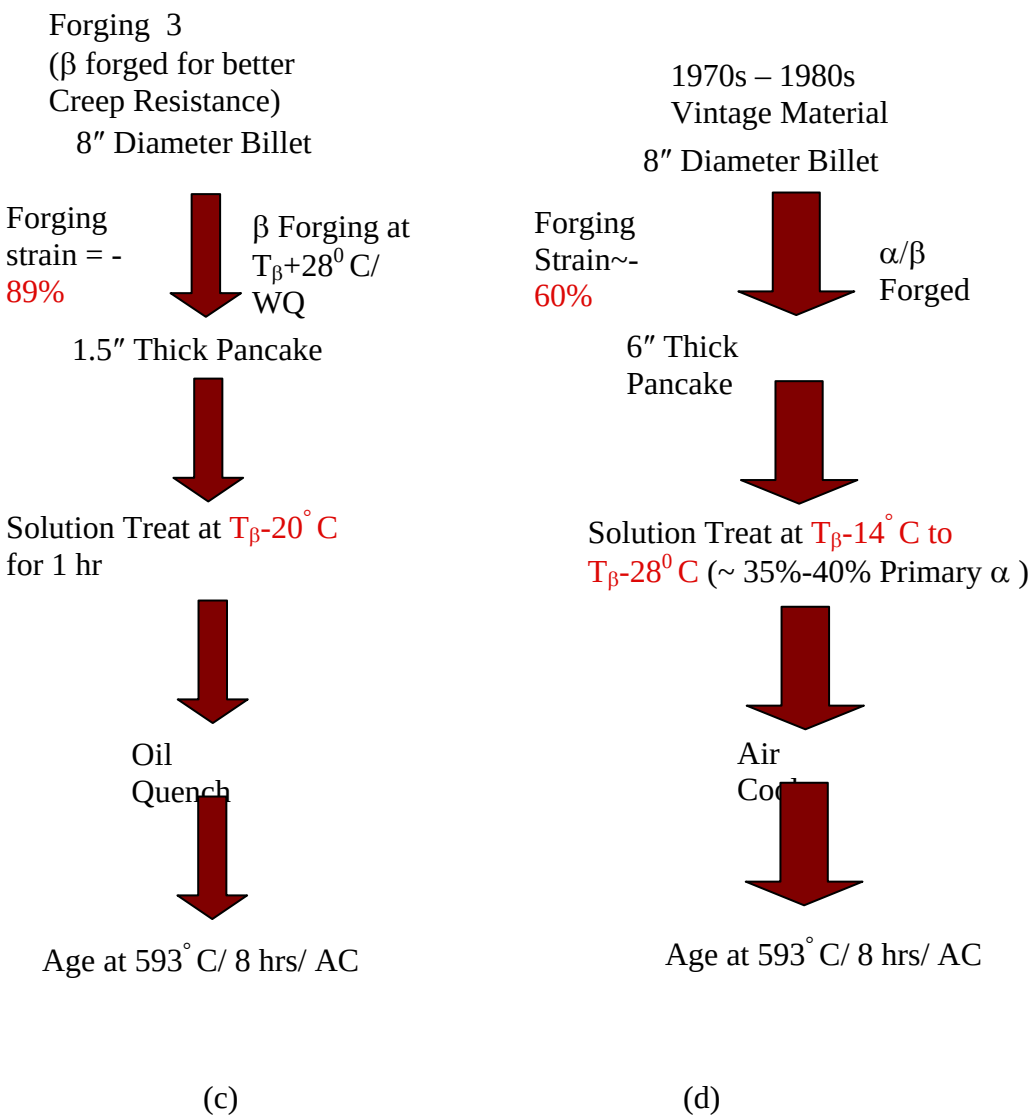

Figure B-1. Thermomechanical Processing Routes (a) Ladish Pancake Forging 1, (b) Ladish Pancake Forging 2, (c) Ladish Pancake Forging 3, and (d) Retired Impeller Material (Continued)

In addition to the three pancake forgings supplied by Ladish Co., specimen blanks from a few field-returned (retired) impellers were also electrical-discharge machined for an evaluation of their dwell-fatigue susceptibility. These vintage materials were processed in the 1970s-1980s. The approximate TMP parameters for the vintage materials examined in this study are described in figure B-1(d). This material, also Ti-6Al-2Sn-4Zr-2Mo alloy, has a bimodal microstructure as shown in figure B-2(d).

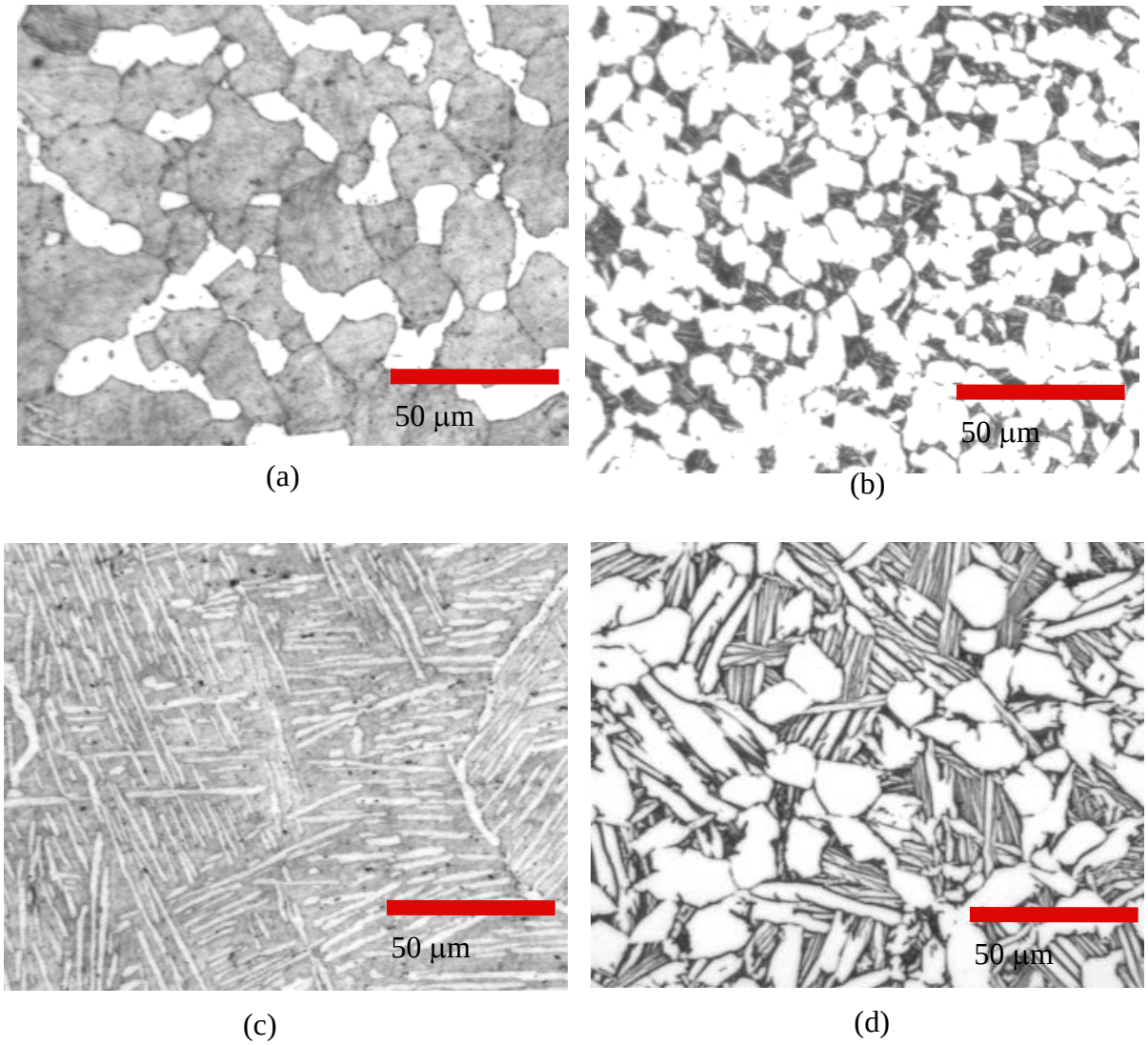

Figure B-2. Optical Micrographs of the Forgings Tested in This Research (a) Forging 1, α/β Forged; (b) Forging 2, α/β Forged; (c) Forging 3, β Forged; and (d) 1970s-1980s Vintage Material, α/β Forged

For the purpose of optical microscopy, small samples were cut from each of the three Ladish forgings and also from the retired impeller material. The samples were metallographically ground using silicon carbide grinding paper and then polished to a 0.06-μm finish using colloidal silica. Thereafter, the polished samples were etched in Kroll's reagent for about 30 seconds to reveal the microstructure when viewed under an optical microscope (figure B-2).

B.2.2 ELECTRON BACKSCATTER DIFFRACTION EXPERIMENTS.

Since the level of microtexture is a key variable in the dwell-fatigue susceptibility of α/β forged near-α titanium alloys; the level of microtexture in the three α/β-forged pancakes (forging 1,

forging 2, and vintage material) was determined using the EBSD techniques. Small rectangular coupons were taken from forging 1, forging 2, and vintage material.

The rectangular coupons from the three α/β-forged pancakes were mounted using conductive mounting powder. The mounted specimens were first ground with the silicon carbide grinding paper and then polished to a 0.06-μm finish in a vibratory polisher using colloidal silica. The specimens were subsequently cleaned ultrasonically in distilled water, dried, and baked in an oven (temperature ~ 70°C) before being loaded in the SEM specimen chamber.

The optimum conditions to obtain a good quality electron backscattered diffraction pattern (EBSP) for this material were found to be 70° tilt and 20 kV accelerating voltage. The background signal was collected by averaging 128 frames, and the subtraction of this background from raw pattern was found to give a high quality EBSP. The computer software (Supplier: HKL Technology, Burnt Hills, NY, USA) looks for a match of the measured and calculated interplanar angles for a phase under investigation to index the EBSP from any grain. These interplanar angles are a function of c/a ratio in hcp structures. Consequently, the c and a lattice parameters for the α phase (hcp) in Ti-6242 alloy were determined from a standard x-ray diffraction (θ–2θ) run. The lattice parameters were determined to be, a_α = 0.293 nm and c_α = 0.468 nm. The lattice parameter for the β phase (bcc) was determined to be, a_β = 0.324 nm. These lattice parameters were input into the crystal files of the computer package, which the software uses to calculate the various interplanar angles and compares those with the observed interplanar angles in the actual (experimental) EBSPs searching for a best fit.

To obtain an idea about the area occupied by similarly oriented α grains, a relatively large area (1.5 by 1.5 mm) compared with the apparent size of microstructural features (figure B-2) was analyzed for each specimen. For analyzing such a large area, the stage scan mode was found to be more appropriate than the beam scan mode. The step size was selected to be 10 μm for all three specimens, which is on the order of the primary α grain size (figure B-2).

B.2.3 MECHANICAL TESTING AND SEM FRACTOGRAPHIC STUDIES.

To obtain basic mechanical properties data for the three Ladish forging materials, tensile tests were conducted on these materials in laboratory air at room temperature using a closed-loop servo-hydraulic test frame. The specimens for the tensile tests have a circular cross section with a gage section diameter of 6.35 mm (0.25″), the length of reduced section = 31.75 mm (1.25″) and they have a threaded grip section of diameter = 9.52 mm (0.375″). The other dimensions of these tensile specimens are selected in accordance with ASTM E 8 specifications. The loading direction (i.e., the longitudinal axis of the specimen) for all the tensile specimens was along the circumferential (tangential) direction of the pancakes from which they were machined out. The tensile tests were conducted under displacement control at an actuator speed corresponding to a strain rate of ~ $1 \times 10^{-4}\ S^{-1}$.

Both the normal fatigue and dwell-fatigue experiments were also carried out in laboratory air at room temperature using a closed-loop servo-hydraulic test frame. The specimens for these tests have a circular cross section with a gage section diameter of 5.08 mm (0.2″) and the length of reduced section = 19.05 mm (0.75″). The other dimensions of the specimens are selected in

accordance with ASTM E 466 specifications. After machining, the specimens were shot-peened as per the following conditions: intensity: 005 A; shot type: Spherical Conditioned Cut Wire (SCCW) -14; and coverage: 200%. The gage section of a limited number of specimens was not shot-peened. Even for these specimens, the threaded grip-section was shot-peened to avoid any failure that may be caused due to fretting-fatigue in this region. Just as in the case of the tensile specimens, the loading direction (i.e., the longitudinal axis of the specimen) for all the fatigue specimens was along the circumferential (tangential) direction of the pancakes from which they were machined. A schematic of the normal fatigue and dwell-fatigue cycles are shown in figure B-3. Both types of tests are conducted under load control. The rate of loading and unloading is the same in both cases. The only difference is that the load is held for 2 minutes at the maximum value in each dwell-fatigue cycle. The time of loading and unloading between the minimum and maximum loads in a cycle was kept fixed at 1 second each for both the normal fatigue and dwell-fatigue cycles. A load ratio of 0 was used in all the tests. The loading and test conditions (load ratio, dwell time, and temperature) are chosen to correspond to the takeoff transients of a typical flight with which the dwell-fatigue life debit is thought to be associated. The strain accumulation was monitored as a function of time using an extensometer that had a gage length of 12.7 mm (0.5″). In addition, two ink marks (~ 18 mm apart) were made on the reduced section of the fatigue specimens. The reported values of plastic strain-to-failure (ε^{pl}_{f}) were calculated from the measurements of the distance between these two marks, before and after the test, using an optical microscope at a magnification of 50 times. After the test, the two broken parts of a specimen were aligned carefully and the gap between them along the longitudinal axis was subtracted from the measured distance between the marks to obtain the correct distance for the broken specimens. The topography of the fracture surfaces of the failed specimens was examined in an SEM using a secondary electron detector.

.

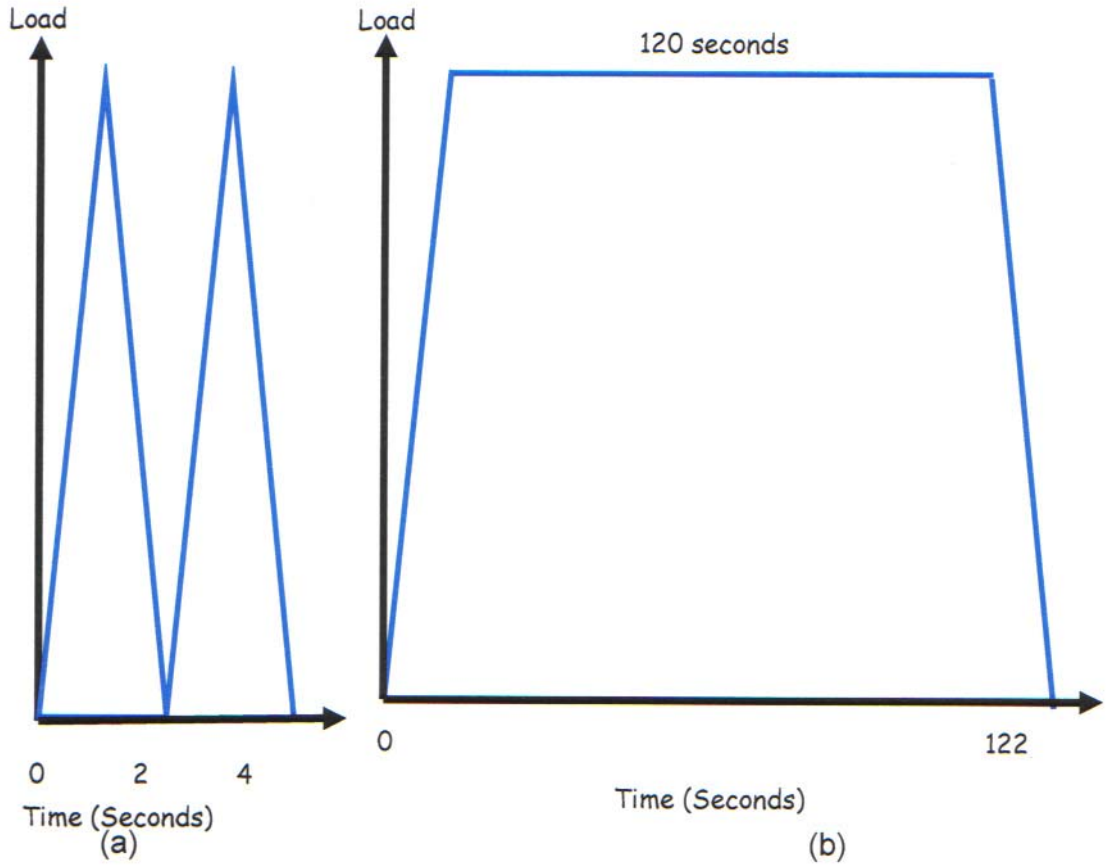

Figure B-3. Schematic of Loading Cycles (a) Normal Fatigue (30 cycles per minute) and (b) Dwell-Fatigue Cycle With a 2-Minute Dwell at the Maximum Load

B.3 RESULTS AND DISCUSSION.

B.3.1 MICROTEXTURE ANALYSIS.

The orientation maps for the three α/β-forged alloys are presented in figure B-4(a) through B-4(c). Here, the points with the same color represent microstructural regions of similar crystallographic orientations. Forging 1 has minimal microtexture, whereas forging 2 and the vintage material have several large regions (size ~ 500 μm) that consist of grains with similar crystallographic orientations.

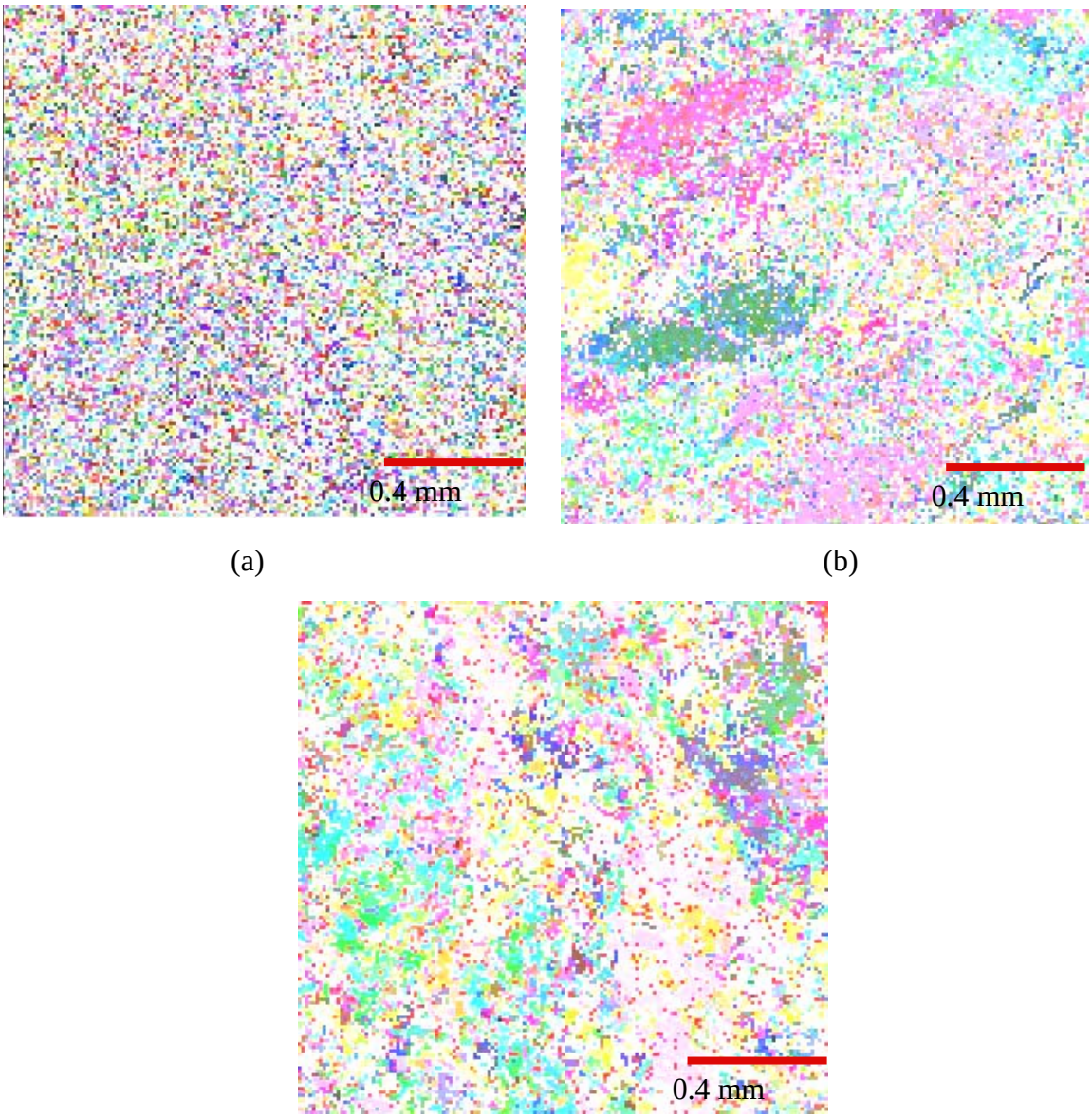

Figure B-4. Analysis of Microtexture in the Three α/β-Forged Microstructures (a) Orientation Map of Forging 1, (b) Orientation Map of Forging 2, and (c) Orientation Map of 1980s Vintage Material

B.3.2 BASIC TENSILE PROPERTIES.

The basic tensile properties of the three Ladish forgings are shown in table B-1. The values of these properties correspond to the portion of the pancakes from where the fatigue specimens have been machined out. It is evident from table B-1 that of the two α/β-forged pancakes, pancake 1 has a higher 0.2% offset yield strength (YS) and a higher ultimate tensile strength (UTS) than pancake 2 (high microtexture, high primary α volume fraction material). This difference may be attributable to a lower volume fraction of primary α (because of a higher

solution treatment temperature) and finer transformed β regions (because of the faster cooling rate after solution treatment) in pancake 1. The elongation to failure values for the two α/β-forged pancakes are similar and ~ 17%. In contrast, Ladish pancake 3, which was β forged, has the YS and UTS values in between those for pancakes 1 and 2. The elongation to failure for this pancake (~10%) is lower than for pancakes 1 and 2 (~17%). Figure B-5 shows the stress-strain plots for the three Ladish pancakes.

Table B-1. Basic Mechanical Properties of the Three Ladish Pancakes

Mechanical Property	Forging 1 (α/β forged) Low Microtexture	Forging 2 (α/β forged) High Microtexture	Forging 3 (β-forged)
0.2% offset Yield Strength (MPa)	1029	950	960
Ultimate Tensile Strength (MPa)	1149	1017	1075
Elongation to failure	16.9%	17.6%	9.8%
Elastic Modulus (GPa)	122	124	120

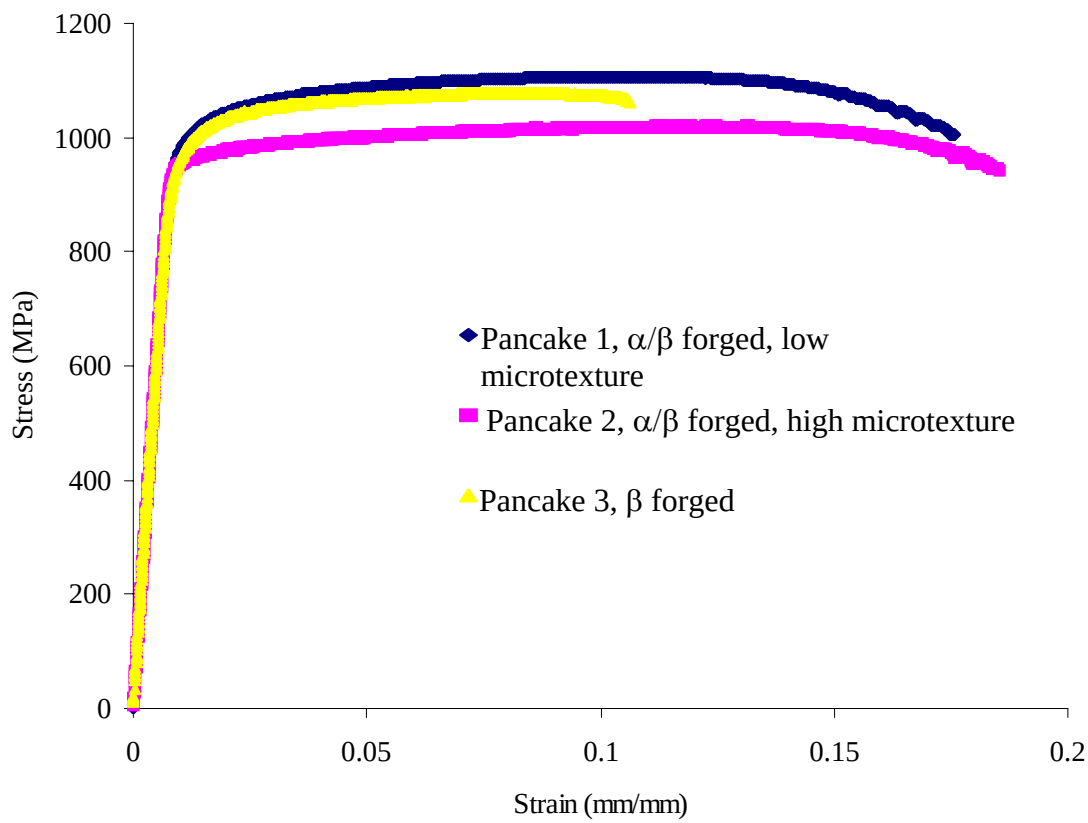

Figure B-5. Stress-Strain Curves for the Three Ladish Pancake Forgings

The room temperature YS for retired impeller material is approximately 930 MPa.

B.3.3 NORMAL FATIGUE AND DWELL-FATIGUE TEST RESULTS.

The test conditions (load ratio, dwell time, and peak stress-to-yield strength ratio) for the three α/β forged and one β forged Ti-6242 alloy are shown in table B-2 along with the corresponding plastic strain-to-failure, number of cycles to failure, and dwell life debit values. From the results summarized in table B-2, it can be concluded that at a fixed peak stress-to-yield strength ratio of ~ 0.95, among the three Ladish pancakes investigated, pancake 2 (high microtexture, α/β forged) material has the highest dwell-fatigue susceptibility, and pancake 3 (β forged) material has the lowest dwell-fatigue susceptibility. The comparison of results on Ladish pancake 2 material at two different peak stresses indicates that the dwell life debit is lowered as the peak stress is reduced (table B-2). This effect of peak stress on dwell life debit is consistent with the reports by Evans [B-1] and Kassner, et al. [B-2].

Table B-2. Summary of Fatigue and Dwell-Fatigue Tests

Material	Load Ratio	σ_{max} / σ_{YS}	Dwell Time (minutes)	Plastic Strain-to-Failure (ε^{pl}_f)	N_f (Cycles)	Dwell Life Debit
Ladish pancake 1 (low microtexture)	0	0.954	2	3.0%	8,803	6
			0	0.6%	51,235	
Ladish pancake 1 (low microtexture)	0	0.954	2	2.8%	11,946	4
			0	1.5%	47,906	
Ladish pancake 2 (high microtexture)	0	0.955	2	3.8%	1,303	18
			0	2%	22,991	
Ladish pancake 2 (high microtexture)	0	0.915	2	2.3%	3,074	15
			0	1.0%	45,843	
Ladish pancake 2 (high microtexture)	0	0.87	2	2.1%	13,763	
Ladish pancake 3 (β-forged)	0	0.957	2	3.2%	10,846	3
			0	0.5%	30,020	
Ladish pancake 3 (β-forged)	0	0.957	2	2.4%	12,927	2
			0	1.4%	30,374	
Retired impeller (α/β forged)	0	0.933	2	4%	2,492	11
			0	2.2%	27,755*	
Retired impeller (α/β forged)	0	0.933	2	3.3%	3,260	9
			0	2%	30,208	

*Specimen not shot-peened, the rest are all shot-peened.

At a peak stress-to-yield strength ratio of ~ 0.93, the retired impeller material has a dwell life debit of ~10. Hence, at a lower peak stress of ~ 91% of YS, the dwell life debit will be reduced to a value less than 10. Based on these observations, it can be concluded that at a fixed peak stress-to-yield strength ratio of ~ 0.91, the Ladish pancake 2 material is more susceptible to dwell than the retired impeller material. The results on the α/β-forged Ti-6242 alloy indicate that microtexture is a key variable in dwell-fatigue susceptibility of this class of materials. These results are in agreement with the work of Woodfield, et al. [B-3].

When tested at a peak stress ~ 93% of YS, the retired impeller material has a normal fatigue life of 30,208 in the shot-peened condition and 27,755 without shot-peening (table B-2). Since the two lives are quite similar, it can be concluded that the specimen fabrication process introduces some residual compressive stresses on the specimen surface akin to the shot-peening of the specimen surface.

The accumulated plastic strain as a function of time is shown in figure B-6. From this figure, it is clear that the plastic strain accumulation for the dwell-fatigue condition is larger than that for the no-dwell condition at all times. Moreover, the dwell-fatigue specimen fails in a considerably longer total clock time than the no-dwell specimen, even though the number of cycles to failure for the dwell-fatigue specimen is 11 times shorter than for the corresponding no-dwell specimen (table B-2).

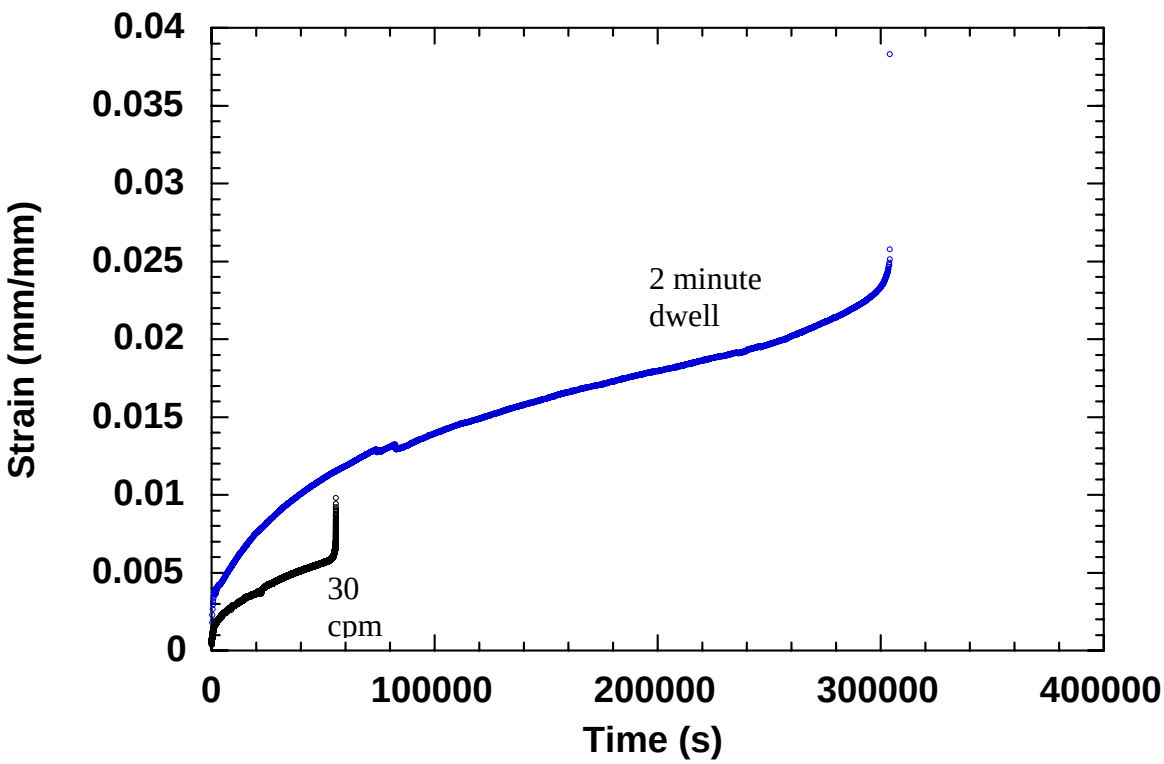

Figure B-6. Strain Accumulation During Fatigue and Dwell-Fatigue Tests for Retired Impeller Ti-6242 Alloy (Applied peak stress = 126 ksi (~ 93% of YS))

B.3.4 FRACTOGRAPHY AND FAILURE MODES.

The salient features on the fracture surfaces for the microstructure with large dwell life debit are depicted in the SEM images of figures B-7 through B-11. The initiation site for the normal fatigue (no-dwell) test for the retired impeller material specimen is internal (figure B-7). This is as expected since this specimen was shot peened and had some residual surface compressive stresses before the test. The fracture features are faceted at the initiation site (figure B-7) and consist of striations at some distance away from the initiation site (figure B-8). These striations typically correspond to the Paris Law regime of stable crack propagation under cyclic loading conditions for this class of alloys. The size of the faceted initiation site is ~ 700 - 750 μm for this material and test condition (figure B-7). The initiation site for the corresponding 2-minute dwell test specimen also consists of faceted features (figure B-9). This specimen was also shot peened and the initiation site is internal.

The size of the faceted initiation site is ~ 1.5 - 2 mm (figure B-9), which is about 2 to 3 times larger than for the corresponding no-dwell test (figure B-7). Again, for the dwell-fatigue test, striations are observed at some distance away from the initiation site (figure B-10), which correspond to the Paris Law regime of the stable crack propagation under cyclic loading conditions. For another retired impeller material specimen with a short dwell life (N_f = 2492 cycles), the crack initiation site is again faceted (figure B-11). The noteworthy feature of this initiation site is that it is quite shiny and very large (~ 3-4 mm long). This suggests that a very short dwell life is associated with a very large (~ 1.5-4 mm long) faceted initiation site.

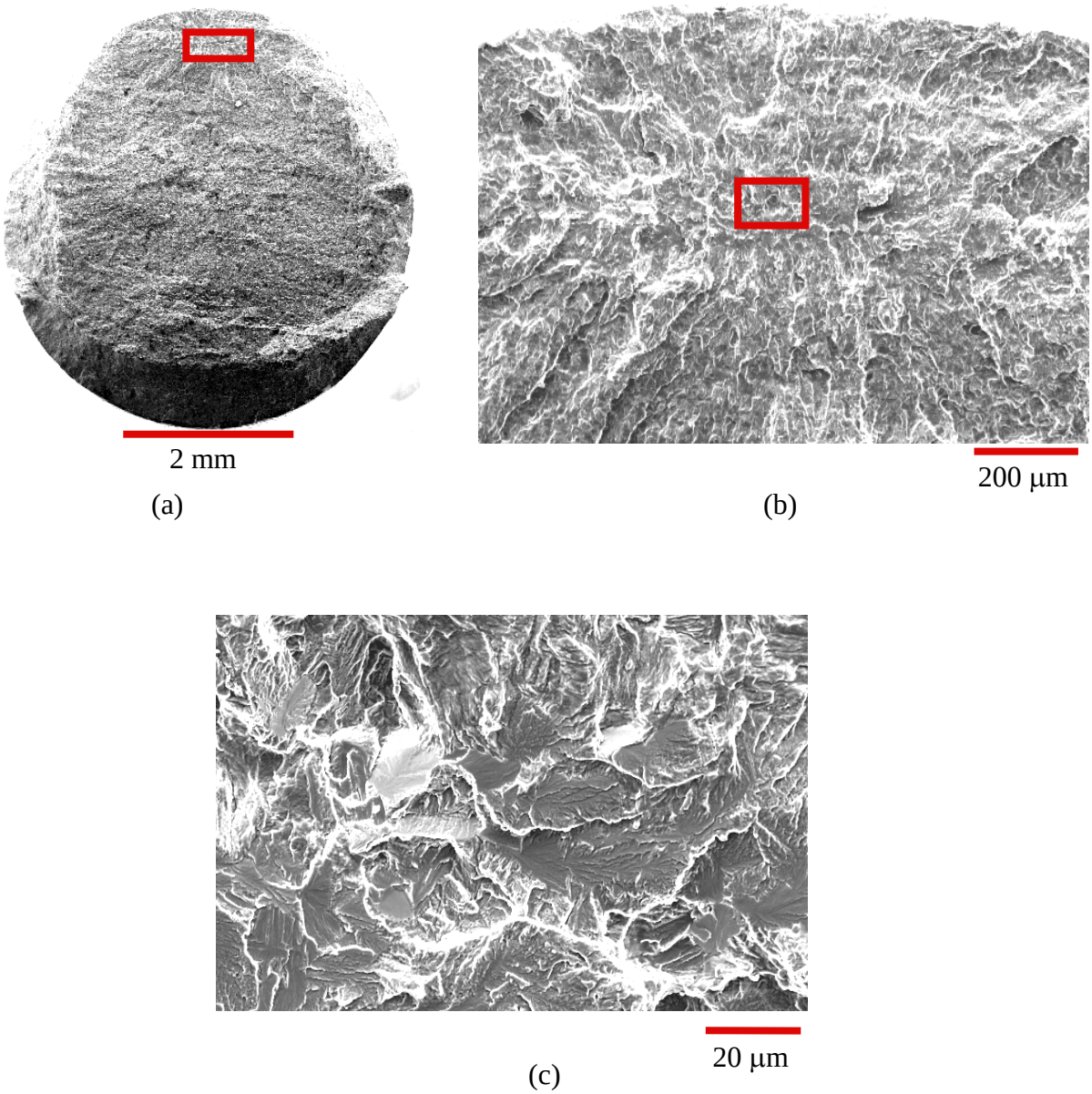

Figure B-7. Fractography of Fatigue (No-Dwell)-Tested Retired Impeller Material Specimen (Test Conditions: R = 0, and Maximum Stress = 126 Ksi. N_f = 30,208 Cycles (a) Low Magnification Image, (b) Higher Magnification Image of the Rectangular Region Shown in (a), and (c) Still Higher Magnification Image of the Rectangular Region Shown in (b). Closer Views of the Crack Initiation Site Are Shown in (b) and (c).)

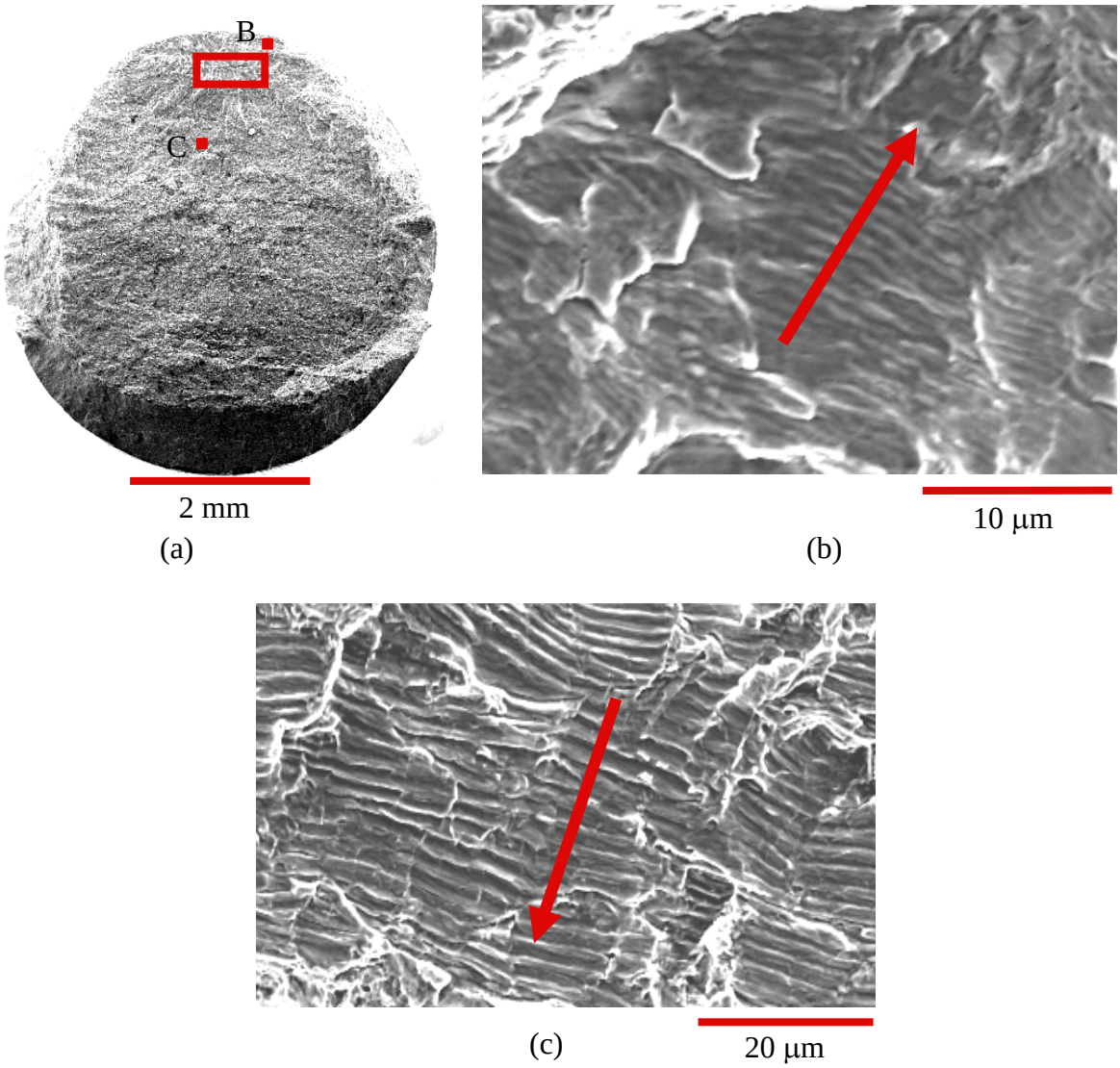

Figure B-8. Fractography of Fatigue (No-Dwell)-Tested Retired Impeller Material Specimen (Test Conditions: R = 0, and Maximum Stress = 126 Ksi. N_f = 30,208 Cycles. (a) Low Magnification Image, (b) Higher Magnification Image of the Solid Square Region Indicated as B in (a), and (c) Higher Magnification Image of the Solid Square Region Indicated as C in (a). The Arrow Indicates the Crack Growth Direction in (b) and (c).)

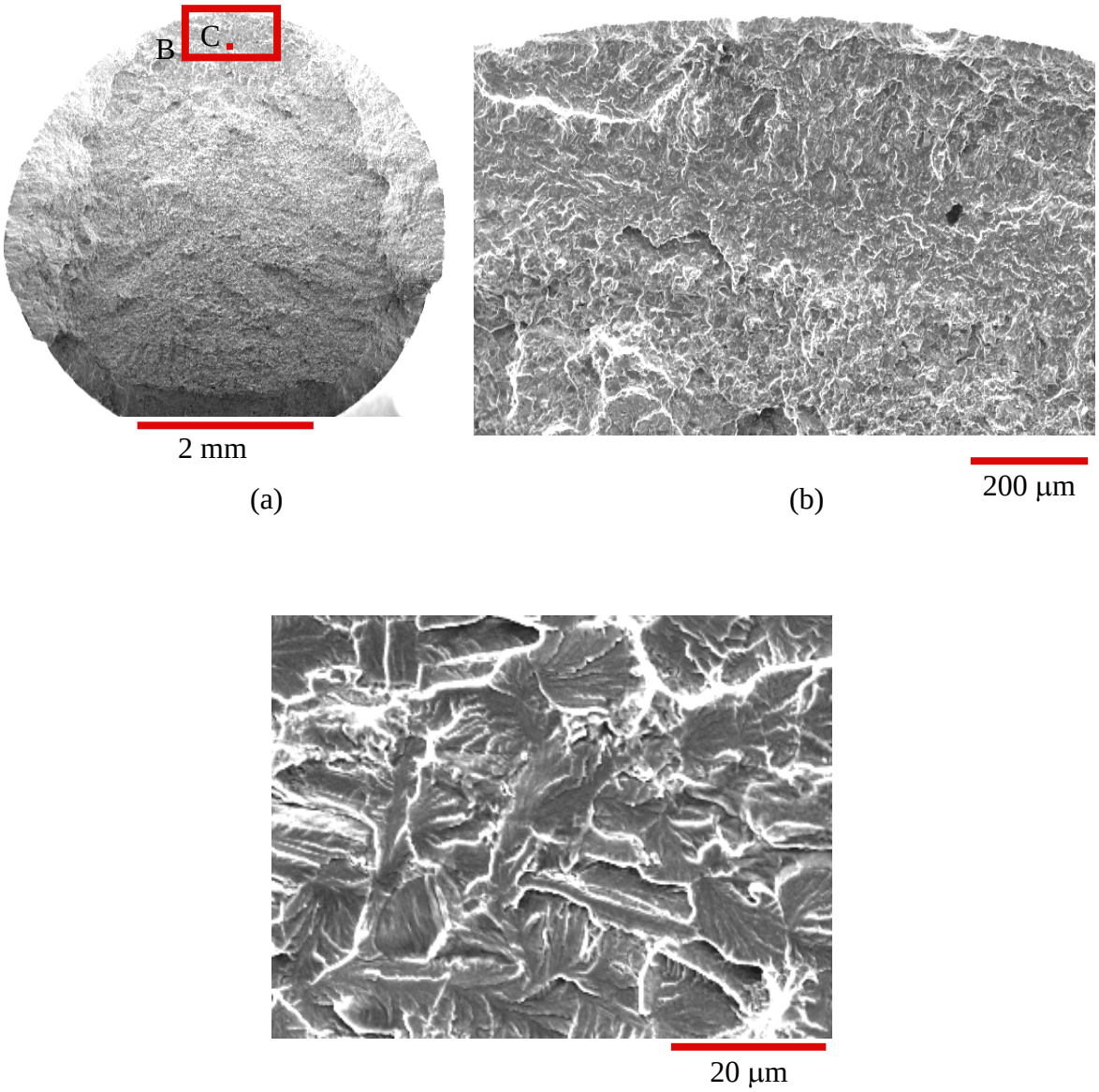

Figure B-9. Fractography of Dwell-Fatigue-Tested Retired Impeller Material Specimen (Test Conditions: R = 0, Dwell Time = 2 Minutes, and Maximum Stress = 126 ksi. N_f = 3260 Cycles (a) Low Magnification Image, (b) Higher Magnification Image of the Open Rectangular Region Indicated as B in (a), and (c) Still Higher Magnification Image of the Solid Square Region Indicated as C in (a). Closer Views of the Crack Initiation Site are Shown in (b) and (c).)

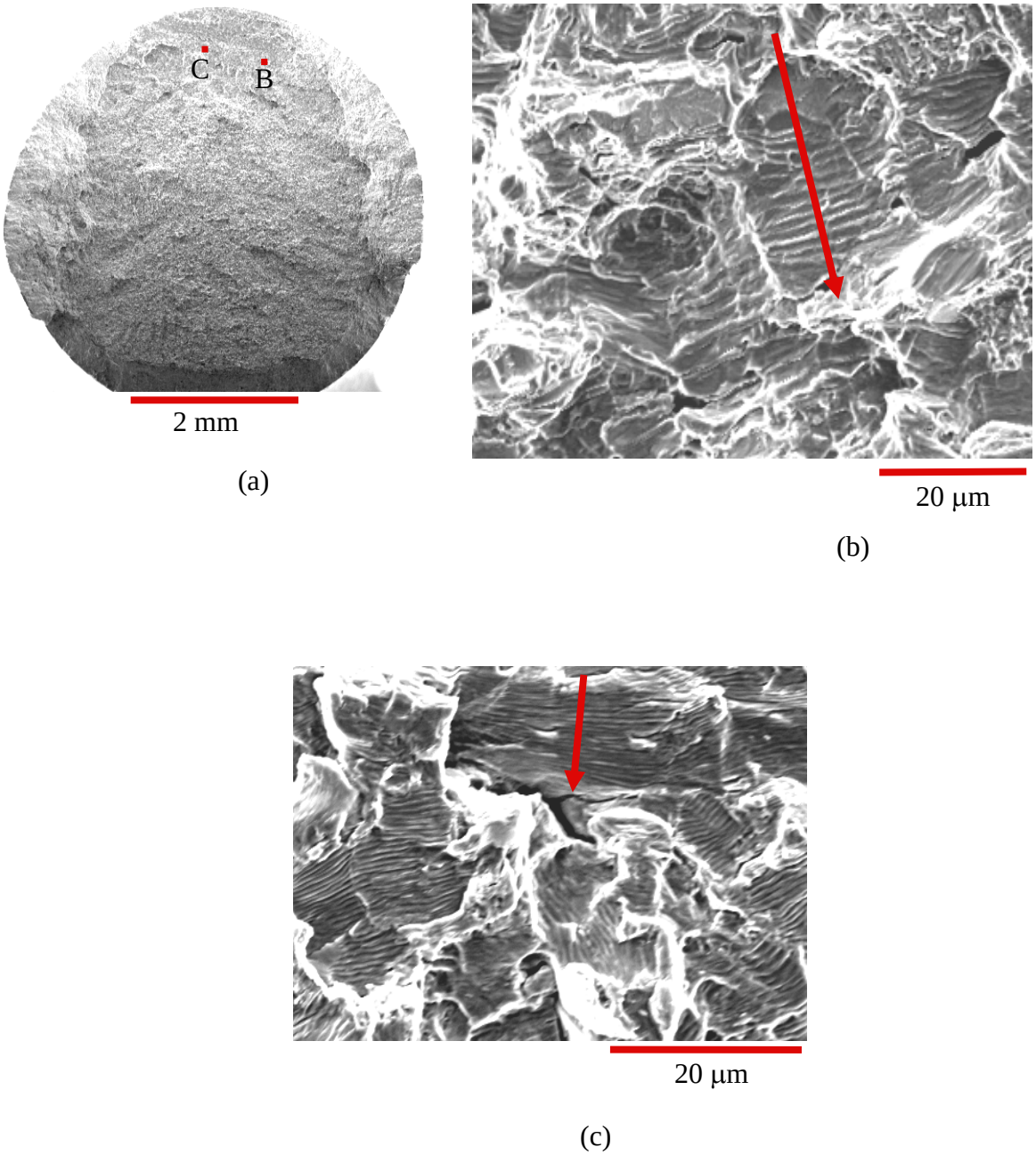

Figure B-10. Fractography of Dwell-Fatigue-Tested Retired Impeller Material Specimen (Test conditions: R = 0, dwell time = 2 minutes, and maximum stress = 126 ksi. N_f = 3260 cycles (a) Low magnification image, (b) higher magnification image of the solid square region indicated as B in (a), and (c) higher magnification image of the solid square region indicated as C in (a). The arrow indicates the crack growth direction in (b) and (c).)

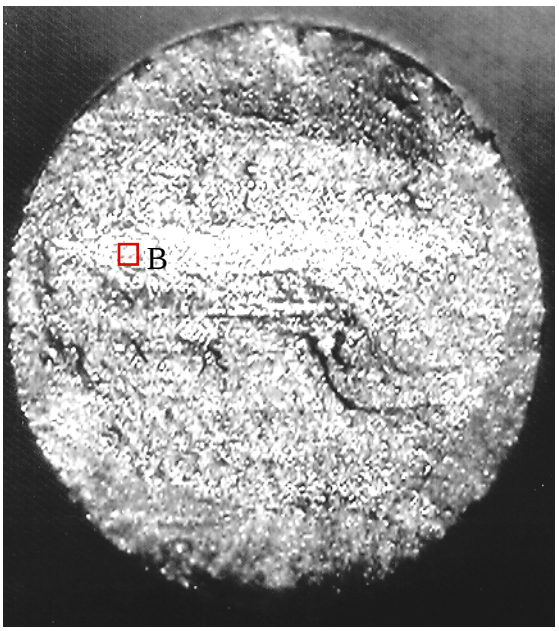

5.08 mm

(a)

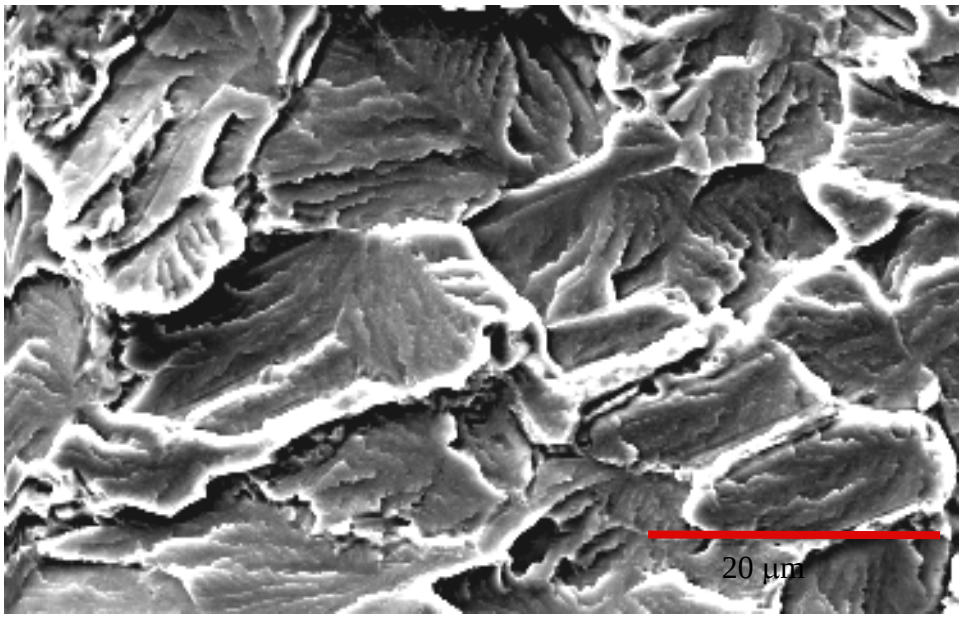

(b)

Figure B-11. Fractography of Dwell-Fatigue-Tested Retired Impeller Material Specimen (Test conditions: R = 0, dwell time = 2 minutes, and maximum stress = 126 ksi. N_f = 2492 cycles (a) Low magnification image, and (b) higher magnification image of the open square region indicated as B in (a). A closer view of the crack initiation site, which was quite shiny and very large (~ 3-4 mm long) for this particular specimen is shown in (b).)

B.4 CONCLUSION.

Among the four microstructures of Ti-6242 allowy investigated in this program, the dwell-fatigue susceptibility (at a fixed peak stress-to-yield strength ratio) can be ranked from the most severe to the least severe as Ladish pancake 2 (α/β forged, ~ 70 vol. % primary α, high microtexture), retired impeller material (α/β, ~ 40 vol. % primary α, high microtexture), Ladish pancake 1 (α/β forged, ~ 25 vol. % primary α, low microtexture) and then, Ladish pancake 3 (β forged).

B.5 REFERENCES.

B-1. Evans, W.J., *Journal of Materials Science Letters*, Vol. 6, 1987, pp. 571-574.

B-2. Kassner, M.E., Kosaka, Y., and Hall, J.A., *Metallurgical and Materials Transactions*, Vol. 30A, September 1999, pp. 2383-2389.

B-3. Woodfield, A.P., Gorman, M.D., Corderman, R.R., Sutliff, J.A., and Yamrom, B., *Titanium '95: Science and Technology*, 1995, pp. 1116-1124.

APPENDIX C—EARLY CRACK DETECTION

C.1 INTRODUCTION.

C.1.1 OBJECTIVES.

The objectives of the early crack detection task were (1) to investigate crack initiation and small crack propagation under cold dwell and cyclic fatigue conditions, (2) to develop methods for monitoring and localization of primary and secondary cracks, and (3) to study growth rates of small dwell and cyclic fatigue cracks.

C.1.2 BACKGROUND.

To understand the mechanism of cold dwell-fatigue (CDF) crack initiation and evolution, it is essential to detect just-initiated cracks and relate them to the surrounding microstructure. For this purpose, one needs experimental techniques that provide information on crack initiation, propagation, and location. The difficulty is that CDF cracks are initiated in the volume of the material, and thus cannot be observed by visual monitoring techniques.

C.1.3 SCOPE.

To address the program objectives, in situ surface acoustic wave techniques were developed and implemented for real-time monitoring of crack initiation and evolution during cold dwell-fatigue, cyclic fatigue, and creep tests. From the ultrasonic signals obtained during the tests, the cracks developed in the samples were localized and crack initiation time and growth history were assessed. For localization of the dwell-fatigue cracks, a new ultrasonic immersion scanning method and an experimental system, which is called vertical C-scan, was developed. From scanned images together with microradiographic images and ultrasonic data from insitu measurements, the locations, orientations, and sizes of the cracks can be determined. Application of these three techniques overcomes the technical limitations of each of the methods and serves as a useful tool for monitoring, localization, and sizing of fatigue cracks. The samples with localized cracks are further used for near-crack-tip microstructure characterization, which may reveal the dwell crack initiation mechanism.

This appendix will (1) describe the dwell-fatigue samples and mechanical testing methods, (2) report the methods developed for small crack growth monitoring and localization, and (3) discuss the methodology for measurements of small dwell and cycling fatigue crack rates and compare them to large cracks.

C.2 METHODS: MECHANICAL TESTING AND EXPERIMENTAL METHODOLOGY FOR EARLY SMALL CRACK DETECTION AND CHARACTERIZATION.

C.2.1 SAMPLES.

The samples were prepared from Ti-6242 high microtexture α/β-forged material (pancake 2). The samples were machined by METCUT to be flat fatigue samples 2 mm thick and 6 mm wide in the gage length, as shown in figure C-1 (top). The sample geometry shown in figure C-1 was later modified to increase the length for easier placement of ultrasonic monitoring transducers (figure C-1, bottom). Those samples have the same cross-section and gage length.

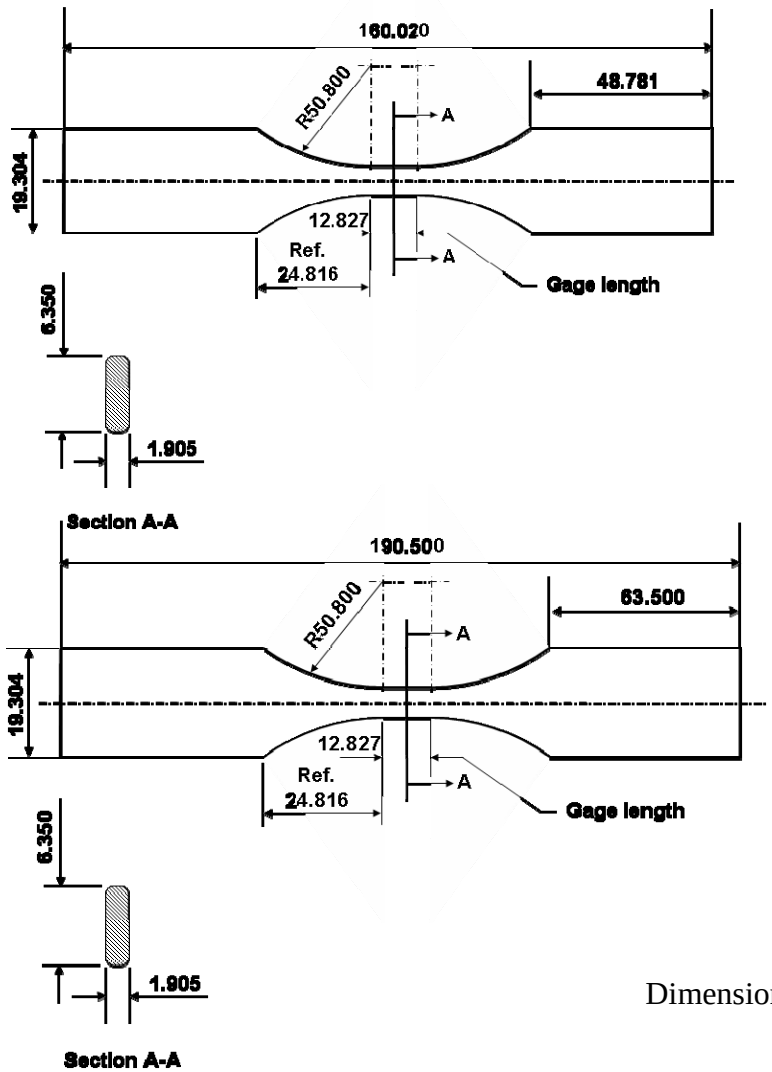

Dimensions in mm

Figure C-1. Ti-6242 Flat Fatigue Sample for Initial Experiments (Top) and for Later Experiments (Bottom) (The later sample is longer but has the same gage length.)

C.2.2 MECHANICAL TESTING.

C.2.2.1 Dwell-Fatigue, Fatigue, and Static Hold Test.

The tests were performed under dwell-fatigue conditions with a 2-minute hold at the maximum stress and under cycling fatigue (no-dwell) conditions. A creep test (static holding at maximum stress) was also performed. The maximum stress was 126 ksi (869 MPa. and 95% of yield stress), and the R ratio was 0. During the dwell test, the frequency of the unloading and loading cycle was 1 Hz, and the tests were performed under stress control. The load patterns and ultrasonic data monitoring described in section C.2.4 are shown in figure C-2.

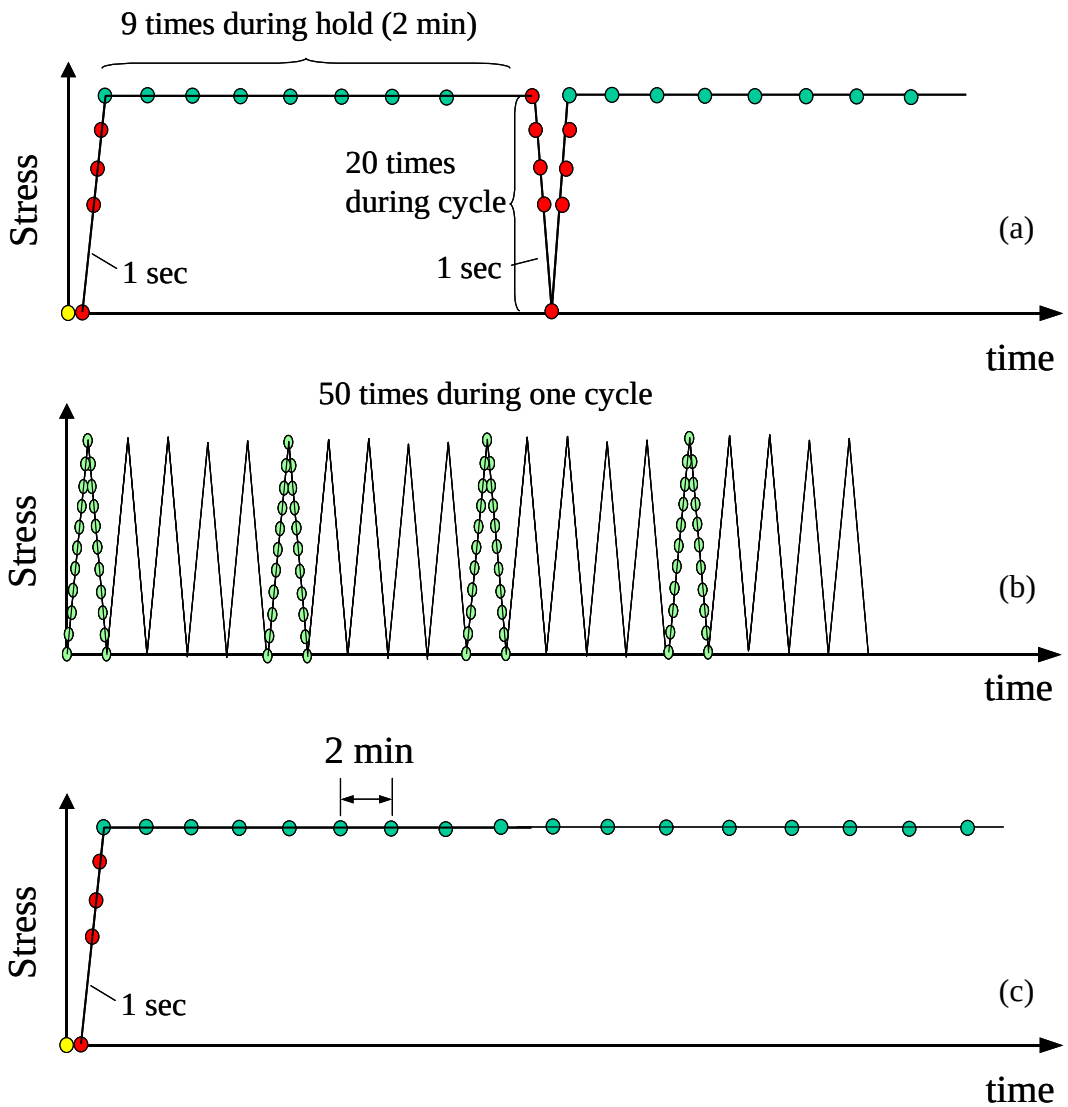

Figure C-2. Load Patterns and Data Acquisition for (a) Dwell-Fatigue Test, (b) Cyclic Fatigue Test, and (c) Creep Test

To determine the growth rate of small cracks, interrupted fatigue experiments were also performed on two samples (2-SR2-1 and 2-SR2-3) under dwell-fatigue conditions and on three samples (2-SR2-4, 2-SR2-5, and 2-SR2-B1) under normal fatigue (no-dwell) conditions.

The results of all mechanical tests for flat Ti-6242 samples with high microstructure (microstructure 2) are summarized in table C-1. Different types of tests were performed to investigate mechanical behavior under different loading conditions.

C.2.2.2 Tensile Tests on Flat Samples.

To have a reference for the strain level responsible for crack initiation in dwell-fatigue testing, strain and crack monitoring measurements were performed during the tensile tests. The tensile tests were performed in displacement control mode with equivalent strain rate 1×10^{-4} per second. The tensile properties obtained for the samples are presented in table C-2. Two samples were tested with identical results; the strain at failure was 12% and 13% respectively. The results are in good agreement with those obtained by the group of Professor Soboyejo at Princeton (figure C-3) for 3-mm-thick and 6-mm-wide flat specimens for three different microstructures (table C-2 right column). The results for the flat sample are also in good agreement with those for round samples performed at The Ohio State University (OSU). It was concluded that the tensile properties of the OSU flat Ti-6242 fatigue sample are the same as those for other sample geometries used by the team.

The in situ surface acoustic wave reflection measurements performed during the tensile tests show no indication of secondary crack initiation and growth. This was confirmed by microradiographic testing of the tensile samples after failure. The microradiographs (figure C-4) showed no visible cracks. The large variation of gray level in the radiographic image corresponds to thickness variation due to high deformation. This result implies that crack initiation in an experiment holding at constant load is a time-dependent phenomenon and does not depend solely on total strain accumulation.

Table C-1. Summary of Mechanical Test Results for Flat Samples

Sample ID	Test Type	Sample Life	No. of Secondary Cracks	Accumulated Strain at Full Load
Noninterruptive Tests				
2-SR1-B2	Tensile	-	0	0.12
2-SR1-C5	Tensile	-	0	0.13
2-SR1-3	Cyclic fatigue	12,095 cycles	2	
2-SR1-1	2-min. dwell-fatigue	352 cycles	5	
2-SR1-2	2-min. dwell-fatigue	563 cycles	5	
2-SR1-B1	2-min. dwell-fatigue with modulation	599 cycles	5	
2-SR1-B5	2-min. dwell-fatigue with modulation	569 cycles	8	
2-SR1-C1	2-min. dwell-fatigue with modulation	309 cycles	6	0.021
2-SR1-C3	2-min. dwell-fatigue with modulation	449 cycles	16	0.029
2-SR1-5	30-min. dwell-fatigue	22 cycles	4	
2-SR1-4	Creep	744 min	6	0.019
2-SR1-B3	Creep	678 min	7	0.022
Interruptive Tests				
2-SR2-1	2-min. dwell-fatigue with modulation	447 cycles	0	0.016
2-SR2-3	2-min. dwell-fatigue with modulation	663 cycles	9	0.033
2-SR2-4	Cyclic fatigue with modulation	24,000 cycles	0	
2-SR2-5	Cyclic fatigue with modulation	16,000 cycles	0	0.012
2-SR2-B1	Cyclic fatigue with modulation	21,250 cycles	0	

Table C-2. Results of Tensile Test for Flat Fatigue Sample

Property	OSU-Rokhlin	Princeton-Soboyejo*
Young's modulus (Gpa)	117	119 ±5
Ultimate tensile strength (MPa)	970	996 ±17
0.2% offset yield stress (MPa)	914	920 ±0
Strain at failure	0.13	0.21

* Princeton sample is 3 mm thick and 6 mm wide.

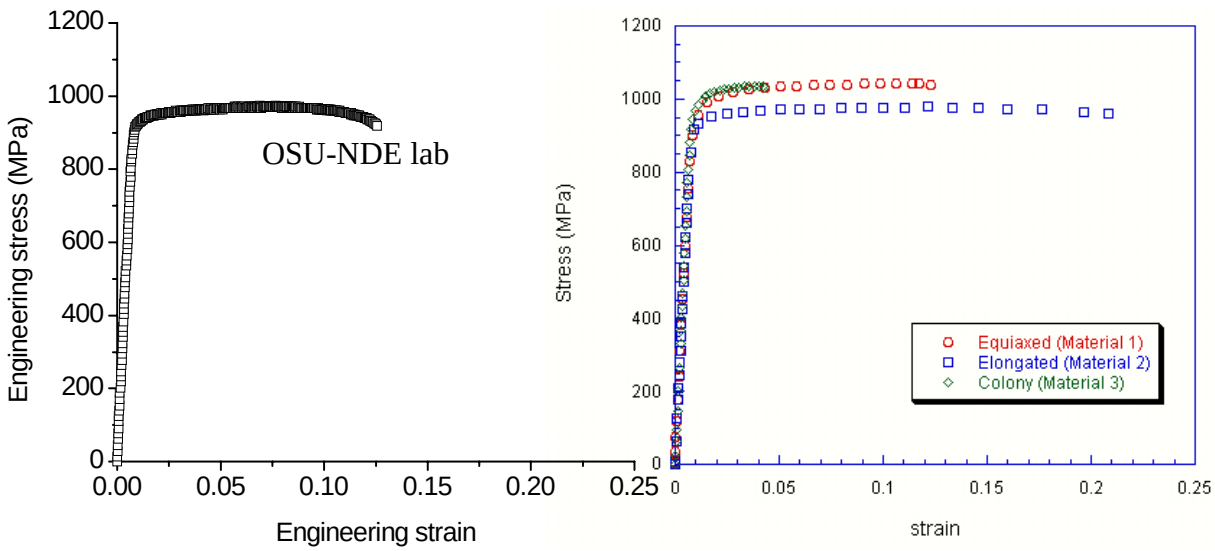

(a) (b)

Figure C-3. Stress-Strain Curves for Tensile Test (a) Data Obtained at OSU for 2-mm-Thick Flat Sample With High Microstructure and (b) Results Obtained by Princeton Group for 3-mm-Thick Flat Samples With Three Different Microstructures (Data in (a) should be compared with open squares (material 2) in (b).)

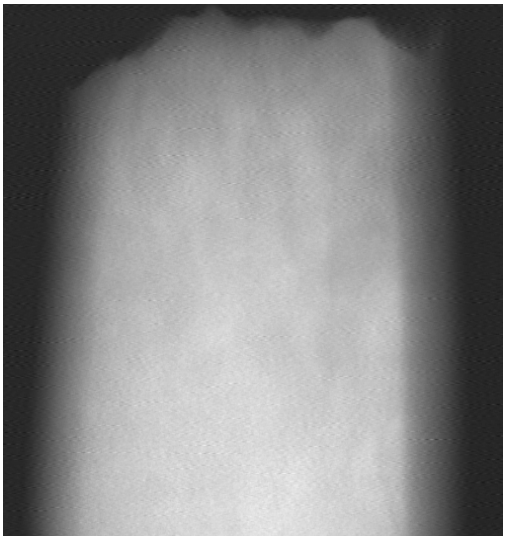

6 mm

Figure C-4. Microradiograph of 2-SR1-B2 Sample Which Failed During Tensile Test (Total strain to failure was 12%. No indication of secondary crack was found in the radiographs.)

C.2.3 NOVEL EXPERIMENTAL TECHNOLOGIES FOR SMALL CRACK MONITORING, LOCALIZATION, AND SIZING.

C.2.3.1 In Situ Surface Acoustic Wave Technique.

To monitor the initiation and propagation of the dwell-fatigue cracks, an experimental technique was developed employing ultrasonic surface waves (more precisely, S_0 and A_0 Lamb waves, which are asymptotically close to a surface wave at these frequencies and sample thicknesses). For fatigue ultrasonic measurements during a dwell-fatigue test, the transducer assembly is mounted using a small clamp on the sample undergoing the fatigue test so that the ultrasonic reflection signals are collected. The longitudinal wave transducer with center frequency of 5 MHz is used with a specially designed polystyrene wedge to generate the surface wave in the Ti-6242 alloy sample, as shown in figure C-5. A surface wave reflector was designed and mounted on the opposite side of the sample. This was done to have a reference signal throughout the fatigue test, which will help in interpretation and processing of the signals acquired.

The development of software moduli for fatigue control and of the experimental system for ultrasonic data acquisition was completed. The software controls a 12-bit, 125-MHz digitizing computer board to acquire and process acoustic wave reflection signals at different levels of fatigue load. The data acquisition and the ultrasonic pulser/receiver are triggered by a counter that is controlled by the computer, allowing the system to be triggered at predetermined loads and time intervals. The control and data acquisition system is shown schematically in figure C-6.

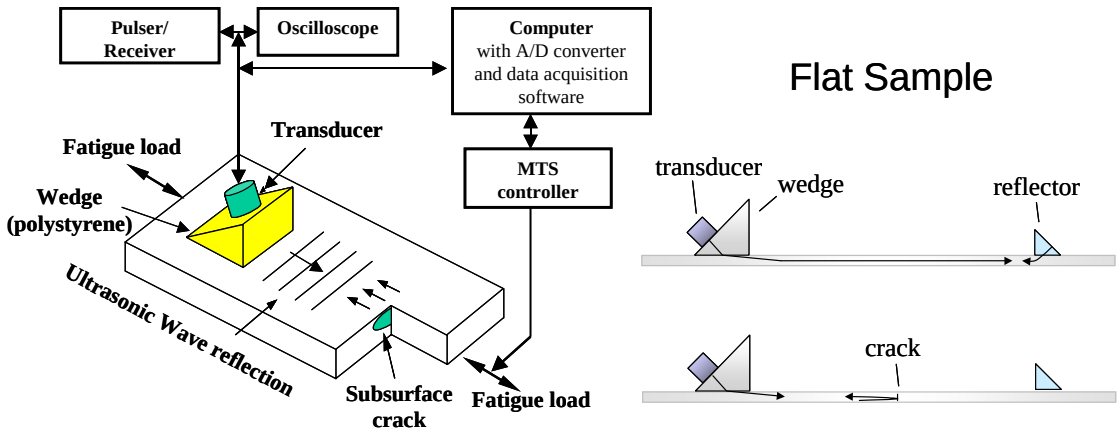

Figure C-5. Schematics of In Situ Ultrasonic Experiment

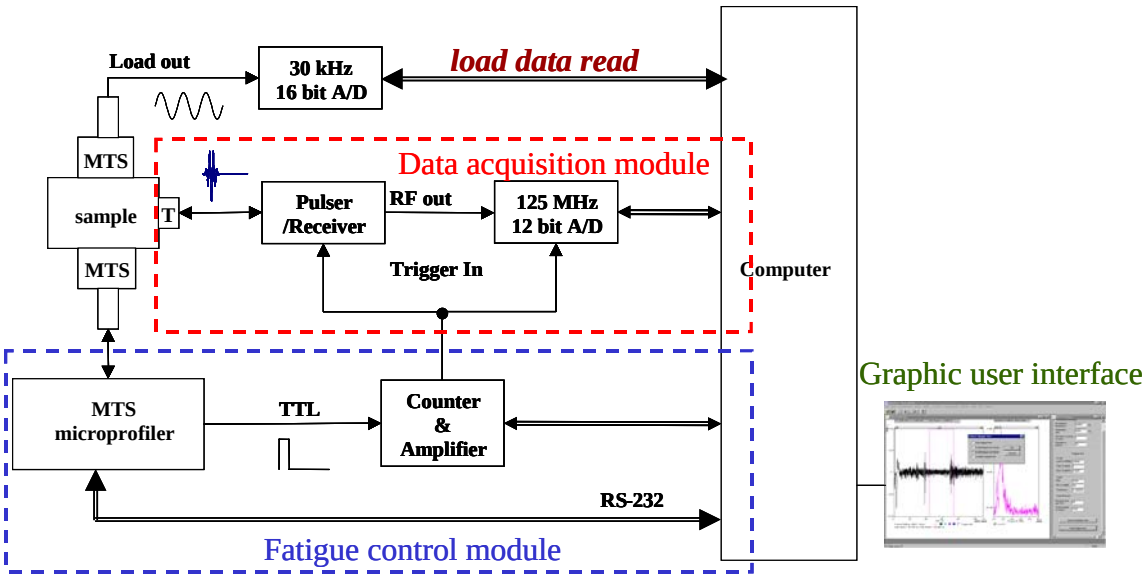

Figure C-6. Real-Time Data Acquisition System for In Situ Ultrasonic Experiment During Fatigue Test

The system allows almost continuous ultrasonic monitoring of the sample during fatigue. The acquisition period is limited by the repetition rate of the ultrasonic system, which is selected to allow decay of the ultrasonic events in the sample. This technique monitors crack initiation and propagation by obtaining ultrasonic signals at different levels of load continuously during fatigue tests.

C.2.3.2 Ultrasonic Angle Beam Vertical Scanning System.

Photographs of the ultrasonic angle beam scan system are shown in figure C-7. The system is composed of two ultrasonic focus transducers, transducer holder assembly, motor-driven X-Y scan table, motor drivers, immersion tank, ultrasonic pulser/receiver, sample, mechanical alignment device, and control computer. The center frequencies of the transducers are 25 and 20 MHz for the transmitter and receiver, respectively. The focal length of the transducers is 2 inches. The diameter of the transmitter is 0.25 inch and the receiver is 0.5 inch. The sample cross-section scans are performed at different locations along the sample producing a vertical set of the scans, known as VC-scan. The sample is mounted on a mechanical alignment device. The diameter of the beam is 1 mm. The step size of the scanning is 0.1 mm.

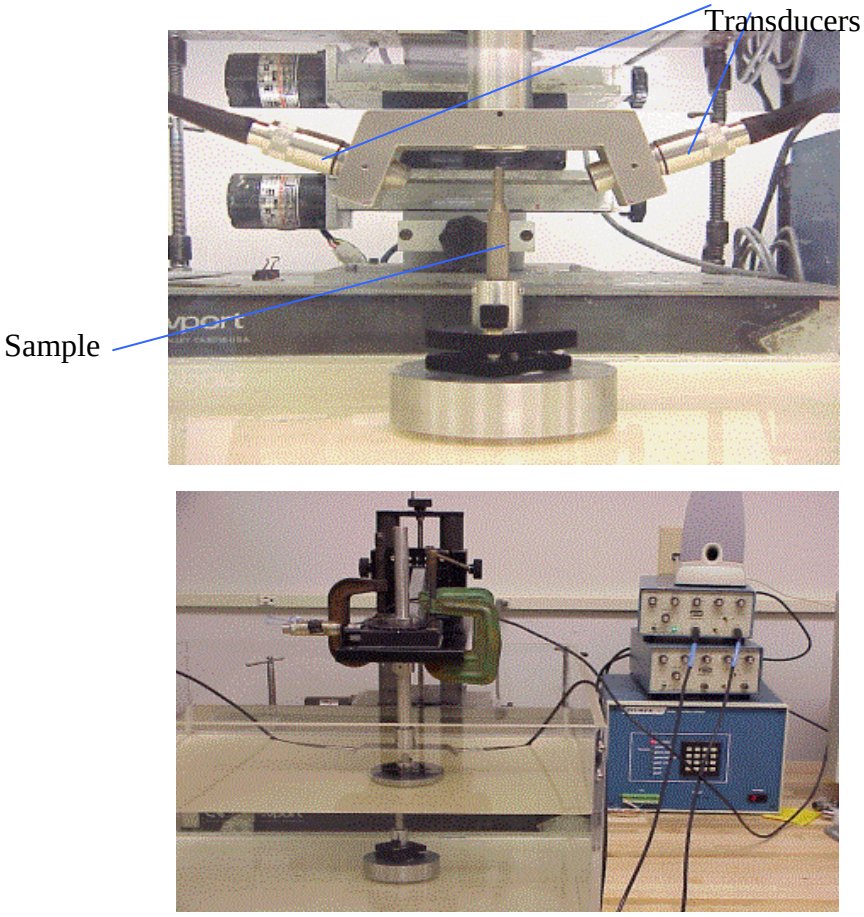

Figure C-7. Ultrasonic Vertical Scanning System

C.2.2.3 Microradiographic System.

In addition to the in situ ultrasonic monitoring and the ultrasonic immersion VC-scanning modes, microradiographs of the failed samples in the dwell and cyclic fatigue and in the creep tests were performed to localize cracks whose indications were found by ultrasonic means. A 225-kV x-ray unit with a 5-µm focal size is used as an x-ray source. A precise positioning system with three

linear (with 2-micron resolution) and one rotating (with 0.01° resolution) computer-controlled axis was used to control the position of the sample. One high-resolution linear axis was used for translation of the image intensifier. In addition, an X-Y manipulator was used for positioning the x-ray source. An image intensifier integrated with a charge coupled device camera was used for real-time radiography and also for alignment of the sample prior to film microradiography.

C. 2.4. IN SITU MONITORING METHODS.

C.2.4.1 In Situ Crack Monitoring During Dwell and Cyclic Fatigue and Creep Tests.

In situ ultrasonic monitoring was implemented during the dwell-fatigue test. Using the real-time computer control data acquisition system, the ultrasonic reflection signals from the initiated cracks were acquired continuously during the whole fatigue test period, as shown in figure C-2. The ultrasonic signals were acquired 9 times during the dwell period and 20 times during the unloading and loading period (figure C-2(a)). The signals may be acquired much more often; the number of acquisitions was limited to reduce the amount of stored experimental data. During the cyclic fatigue test, data acquisition was performed every 2000 cycles. At each event of data acquisition, 50 signals were obtained per cycle (figure C-2(b)).

To address the effect of creep on dwell time and number of dwell cycles, a single period dwell experiment was performed (figure C-2(c)). The maximum stress level was the same as in the dwell-fatigue tests: 126 ksi (869 MPa). The ultrasonic signals were obtained at minute intervals. A dwell (creep) test was performed with in situ ultrasonic, acoustic emission, and strain gauge monitoring.

C.2.4.2 In Situ Modulation Method for Early Crack Detection.

In addition to the surface acoustic wave technique described above, ultrasonic modulation technique, suited for early detection of dwell-fatigue cracks, was developed. This was needed since a small, just-initiated fatigue crack does not produce a strong ultrasonic reflection and is masked by ultrasonic grain scattering noise and, thus, cannot be detected. The ultrasonic modulation technique was applied to improve the signal-to-noise ratio.

The modulation technique is potentially promising for material diagnostics and damage detection in complex media since it has been established that imperfect interfaces associated with damage generate nonlinearity anomalously higher than in bulk solids. The method is based on the modulation of an ultrasonic wave on an imperfect interface or a crack by an external dynamic load with a frequency lower than the probing ultrasonic wave. This produces crack closure modulation, enhancing the detectability of the crack.

This technique is implemented using the same experimental setup and software that was developed for the surface acoustic wave (SAW) reflection experiments. A small amplitude, 10-Hz vibration load was applied to the sample under measurement and ultrasonic reflection signals were recorded during a number of modulation cycles. The small modulation stress will negligibly affect grain scattering since modulation stress does not change the grain boundary conditions. However, the reflection of ultrasonic pulses changes due to the modulation of the crack closure conditions. The crack reflection is changed synchronously by the external

modulation loading. Therefore, by extracting and analyzing the change of harmonic amplitude corresponding to the modulation frequency, one can determine crack initiation earlier than by surface acoustic measurements under static load.

Different mechanisms may be responsible for the nonlinear parametric modulation of acoustic waves interacting with a crack depending on the total stress acting on the crack. The total stress results from an external load action (including static and/or dynamic modulation loads) and the intrinsic crack closure stresses due to crack tip plasticity. For example, when the modulation stress is much higher than the intrinsic closure stress, crack clapping occurs and produces nonlinear modulation. When the modulation stress and the crack closure stress are comparable, the crack opens and closes with the modulation load[1]. In this case, the change of open crack segment length is the mechanism responsible for the modulation.

In the experiments, the amplitude of the modulation load was 80 lb and the frequency was 10 Hz. The modulation load was applied for 5-10 seconds (50-100 cycles) at three different levels of dwell-fatigue load, maximum and minimum loads and one in the middle, as shown in figure C-8. The modulation measurements were done during every dwell cycle. The acquired pulses were demodulated by low-pass filtering and cross-correlated with the modulation load for signal-to-noise ratio improvement. Considering the amplitude and the duration of the modulation load, the modulation would not influence the dwell-fatigue behavior of the material (it has in fact been observed that the life of the samples in the dwell-fatigue test with modulation was on the average the same as without modulation).

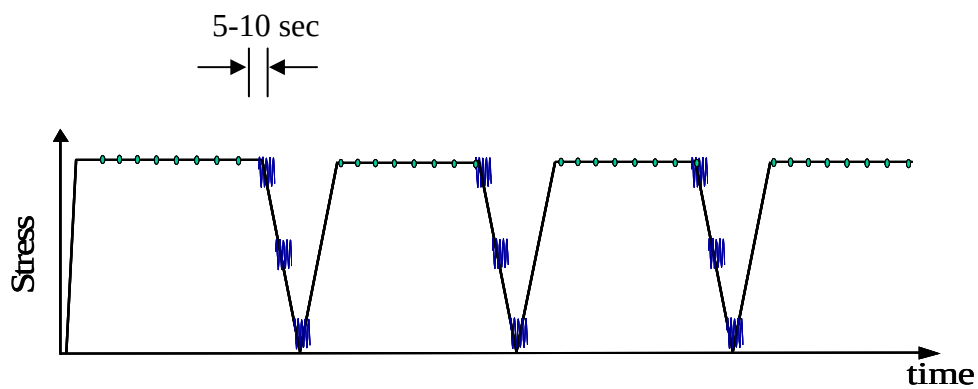

Figure C-8. Load Patterns and Data Acquisition for Dwell-Fatigue Test With Modulation Load (Modulation period is indicated on the loading pattern as a 5-to-10 sec long burst.)[1]

C.2.5 INTERRUPTIVE COLD DWELL-FATIGUE AND CYCLIC FATIGUE TESTS MICRORADIOGRAPHIC CRACK SIZING.

To determine the growth rate of small cracks, interrupted fatigue experiments were performed under dwell-fatigue conditions and cyclic fatigue (no-dwell) conditions. The interrupted fatigue experiments were performed with the same parameters as continuous ones. In addition to in situ ultrasonic monitoring, radiographic imaging was used for crack sizing and rate of growth

[1] Kim, Yakovlev, and Rokhlin, 2003

determination. The latter was accomplished by periodically stopping the fatigue tests after a predetermined number of cycles followed by microradiography of the samples. At each stop, both 0° and 90° microradiographic pictures were taken (figure C-9). Following the test, all radiographic images were analyzed for crack indication and size determination.

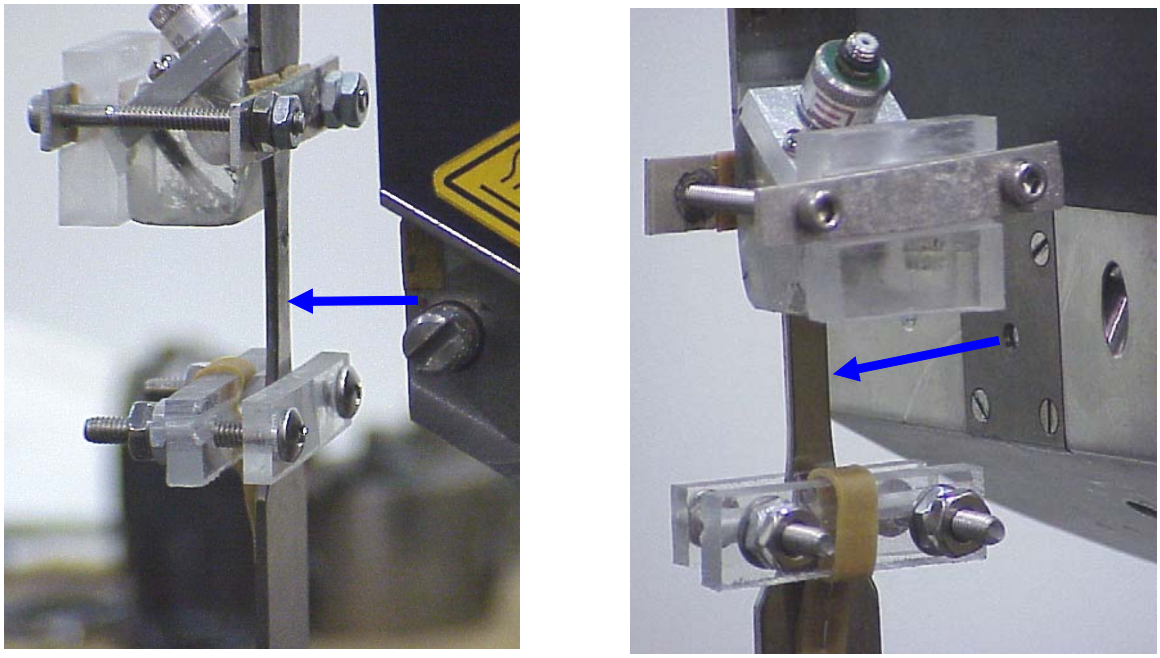

0°-shot 90°-shot

Figure C-9. Microradiographic Exposure of the Sample of Fatigue at 0° and 90°

Figure C-10 shows the setup for the microradiography of a titanium specimen, where the relative positions of the x-ray source, the sample, and the image plane are given. To get a sufficient projection magnification of 16 times (relative to the central plane of the sample), the sample is placed relatively close to the x-ray tube target (1.5 inches).

To size the crack from the microradiographic image, it is important to correctly determine the right projection magnification for the cross-sectional position of the crack. This is depicted in figure C-11(a), where 0-degree exposure is considered. The X-ray beams hit the two sides of the sample at different oblique angles (*h* is the sample thickness).

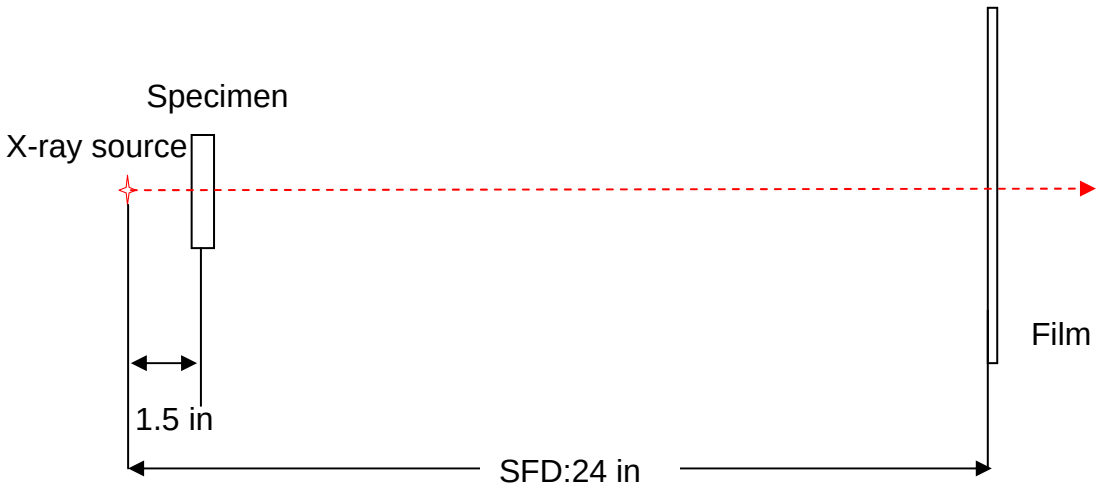

Figure C-10. Setup for Microradiography of Titanium Specimen (Source-to-film distance and sample position are selected to get radiographic image magnification 16 times.)

Due to the finite thickness of the sample, the projection magnifications for the two surfaces of the sample are different, and therefore, the images of the two opposite faces of the sample (the face close to the target and the one towards the film) show up on the radiograph with different sizes, and the actual size of the sample corresponds to the middle plane and is indicated in the radiographic image figure C-11(b). It is important to account for this effect for crack localization (determining their actual distances from the sample edges) and crack sizing.

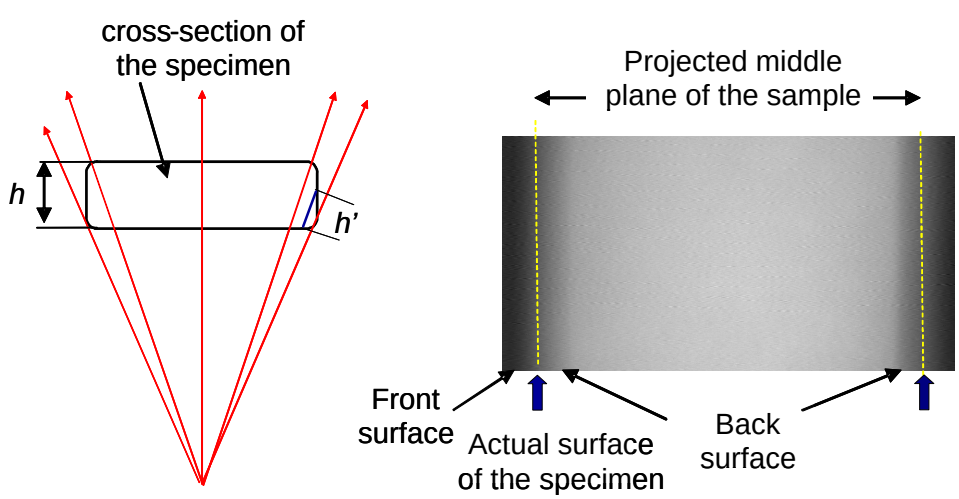

(a) (b)

Figure C-11. (a) Effect of Sample Thickness (*h*) on Image Magnification Due to Oblique Incidence of X-ray Beams at 0° Exposure and (b) Radiographic Image Showing the Actual Edge of the Sample on the Radiograph for Crack

The above effect is much stronger at 90° exposure of a flat fatigue sample. The projection magnification 16 times, which is set for all images, corresponds to the middle plane of the sample (figure C-12). In this case, the projection magnification for the front surface of the sample, which is closer to the x-ray tube target, is 18.9 times and for the opposite side of the sample (film side), it is 13.8 times. At any plane of the sample between these two surfaces the magnification is between 13.8 times and 18.9 times. Accounting for this effect is extremely important for correct crack sizing. For example, figure C-12(b) illustrates that a crack with a given position is magnified in the image 15.7 times. The correction for an exact projection magnification in the 90° exposures is applied during the measurement.

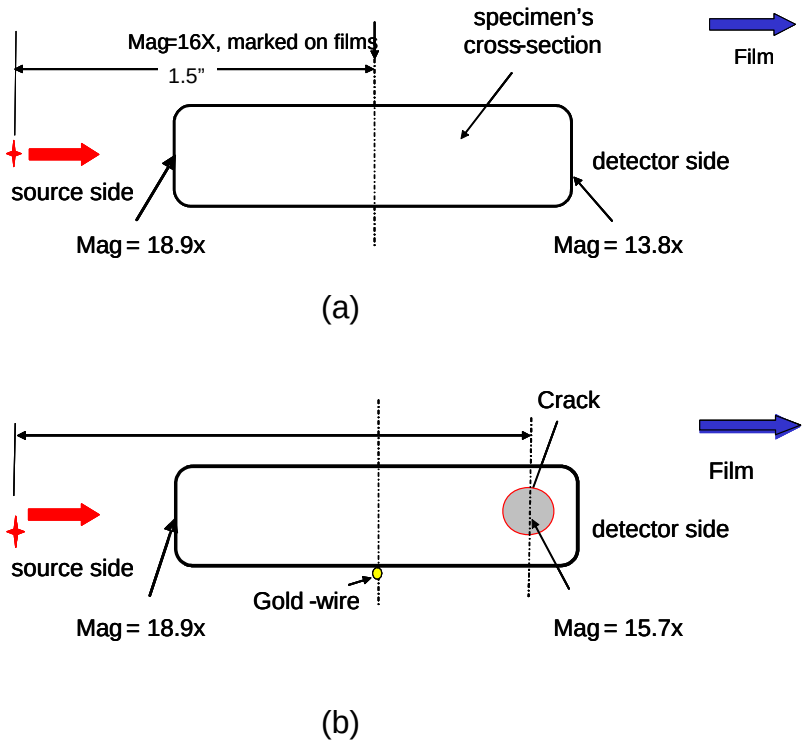

Figure C-12. (a) The Exact Projection Magnification for Each Side of the Sample at 90° Exposure and (b) Example of a Crack at Projection Magnification Equal to 15.7 Times

Figure C-13 shows typical examples of microradiographs of the sample with secondary cracks. The images are taken at 0° and 90°. Figure C-14 shows how, from 0° and 90° images, the correct location of the crack in the sample cross section is determined.

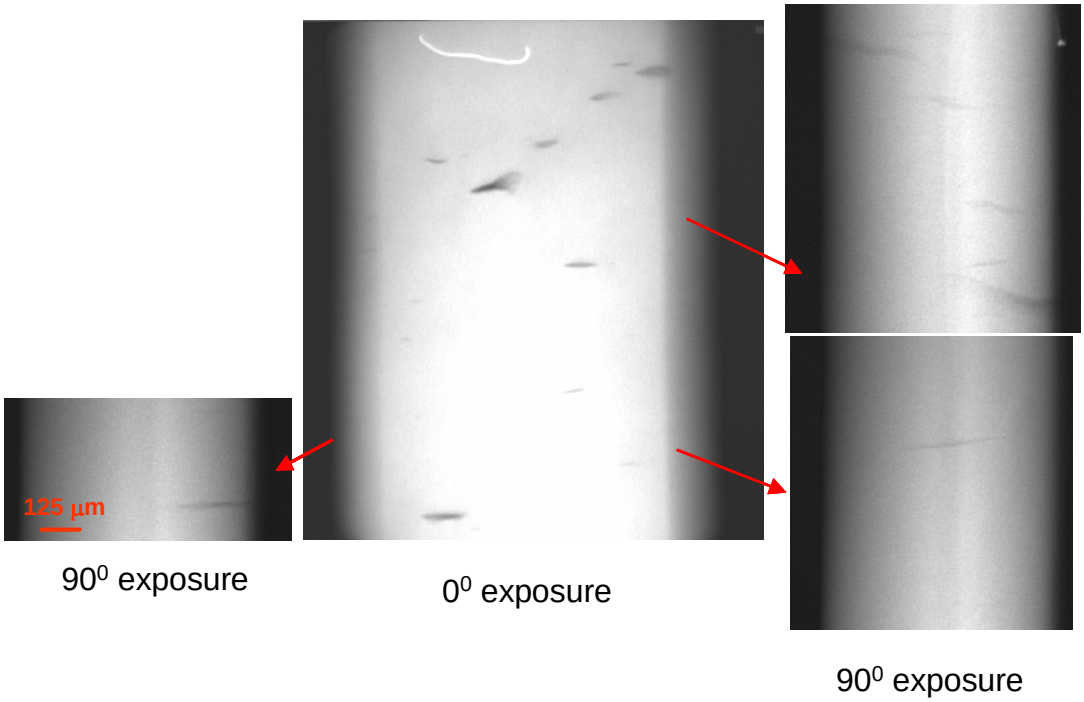

Figure C-13. Example of Secondary Cracks at 0° and 90° Exposures

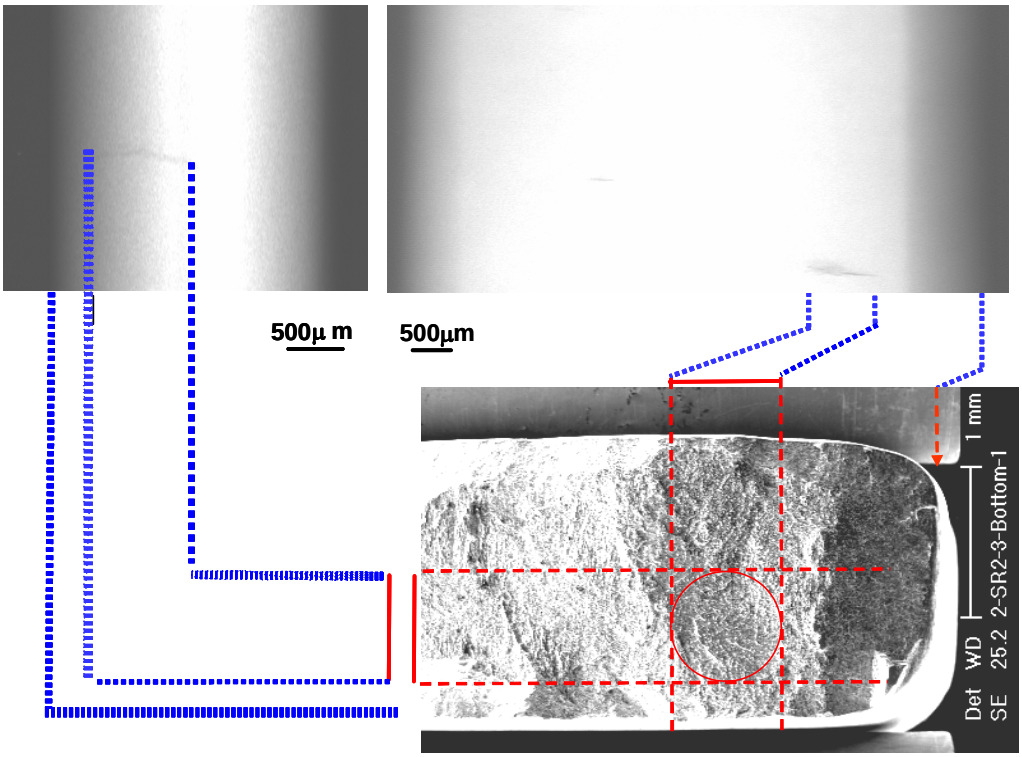

Figure C-14. Localizing the Primary Crack by Using Microradiographs From Two Perpendicular Exposures and Comparison With the Fractograph

C.3 RESULTS AND DISCUSSION.

C.3.1 CRACK DETECTION, LOCALIZATION, AND SIZING IN FATIGUE, DWELL-FATIGUE AND CREEP TESTS.

C.3.1.1 Ultrasonic Monitoring of Crack Initiation.

The dwell-fatigue lives of the flat samples tested were 352 and 563 cycles and the cyclic fatigue life was 12,095 cycles. Note that the low cycle fatigue life is 20-30 times higher than the dwell-fatigue life. This is consistent with the results of similar tests on cylindrical samples that were also machined from high microtexture Ladish forging 2. Figure C-15 shows several ultrasonic signal recordings during dwell time at different numbers of dwell-fatigue cycles. Changes can be seen in the signal amplitudes in the ultrasonic recordings that correspond to different locations in the sample, which implies multiple crack initiation and growth. Also, a drastic change occurs during the final stage of fatigue life. Figure C-16 shows the changes of the reflection amplitudes in different time gates. From the time delays of the gates, it was found that gate 1 corresponds to a major crack that led to sample failure (location of the fracture surface), and the signals in all the other gates are from locations behind the fracture surface. For example, the time delay of gate 4 is 4.8 μ sec, which corresponds to 7.5 mm from the fracture surface. It should be noted that from figure C-15 the crack growth history could be inferred. For example, the signal in gate 1 shows crack initiation at around 400 cycles since, until this number of cycles, the ultrasonic reflection does not show appreciable change. Likewise, the signal in gate 4 shows that the crack initiated at 200 cycles, which is much earlier than the major crack initiated, and for some reason, it became retarded at about 400 cycles while the major crack initiated and continued to grow to failure. The retarded crack became active again and continued its growth before sample failure. Using this technique, some information can be obtained on the initiation times for different cracks in the sample.

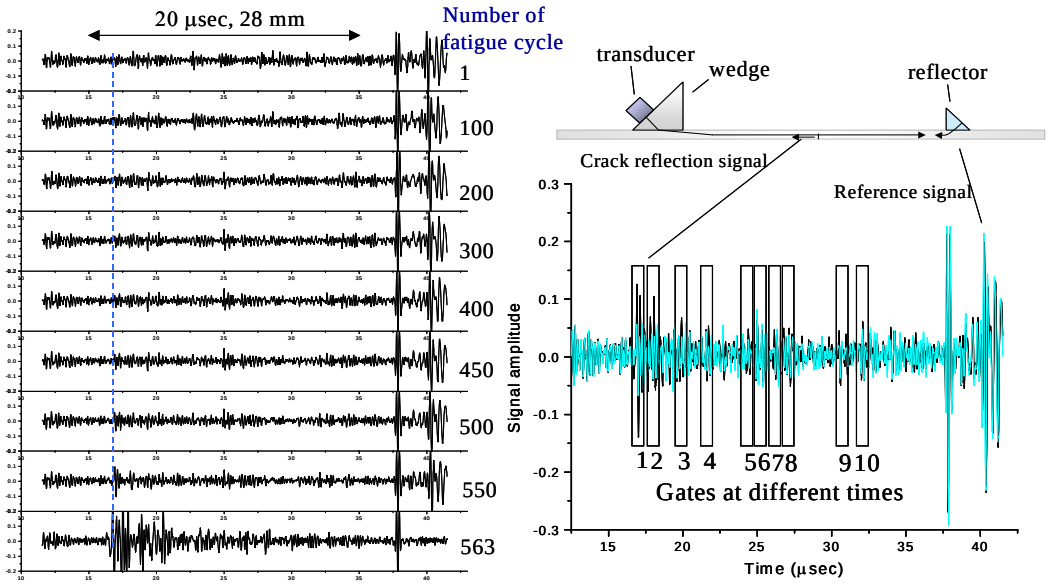

(a) (b)

Figure C-15. Ultrasonic Signals Acquired From the Flat Fatigue Sample During Dwell-Fatigue Test (dwell time = 2 minutes) (a) Signals at Different Numbers of Dwell-Fatigue Cycles and (b) Gates and Their Corresponding Locations in the Sample (Flat Ti-6242 Sample: 2-SR1-2)

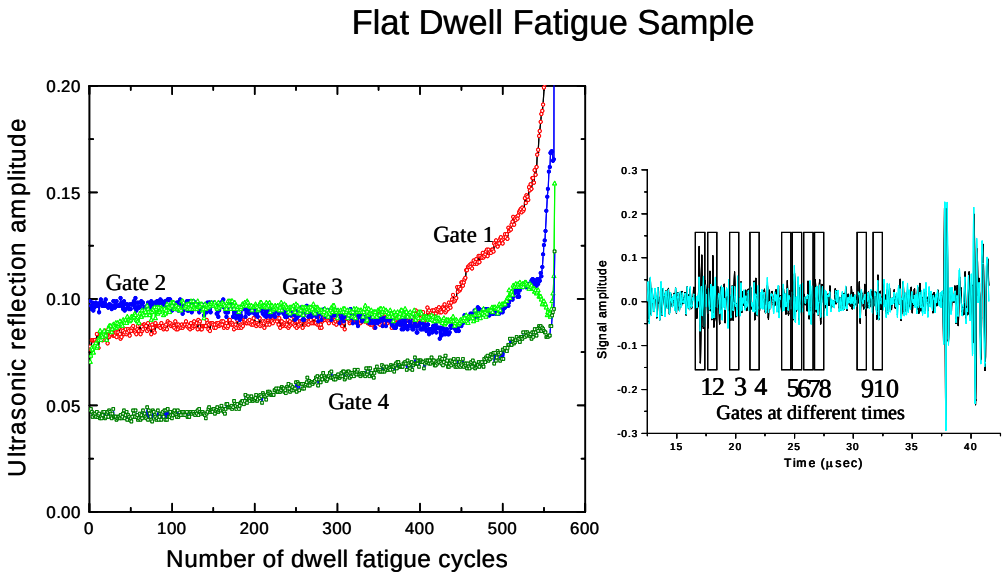

Figure C-16. Changes of Ultrasonic Signals in Different Time Gates (Flat Ti-6242 sample: 2-SR1-2)

Figure C-17 shows the change of ultrasonic reflection from the major crack during the holding (dwell) time at different numbers of cycles. It is noted that although the change of the ultrasonic signal during each holding (dwell) period is small, except for the last one, the amplitude at different numbers of cycles changes significantly. Figure C-18 shows the changes of ultrasonic signals during the unloading and loading period at different numbers of cycles; the amplitude change during the unloading and loading period is very small, which indicates that the crack is open all the time. This may be due to a large strain accumulated during the dwell period.

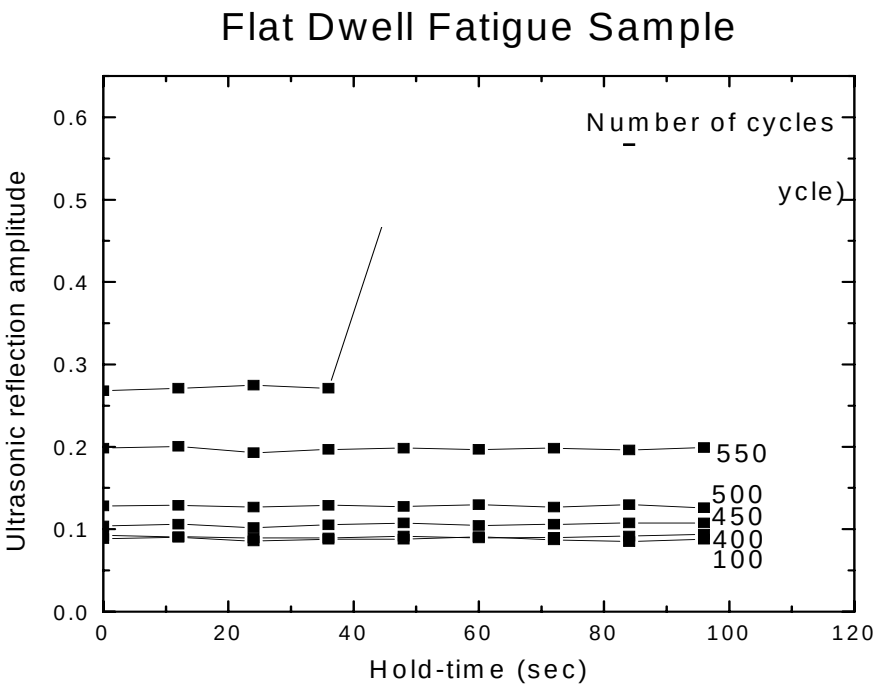

Figure C-17. Changes of Ultrasonic Signal Amplitude During Holding (Dwell) Time at Different Numbers of Cycles (Flat Ti-6242 sample: 2-SR1-2)

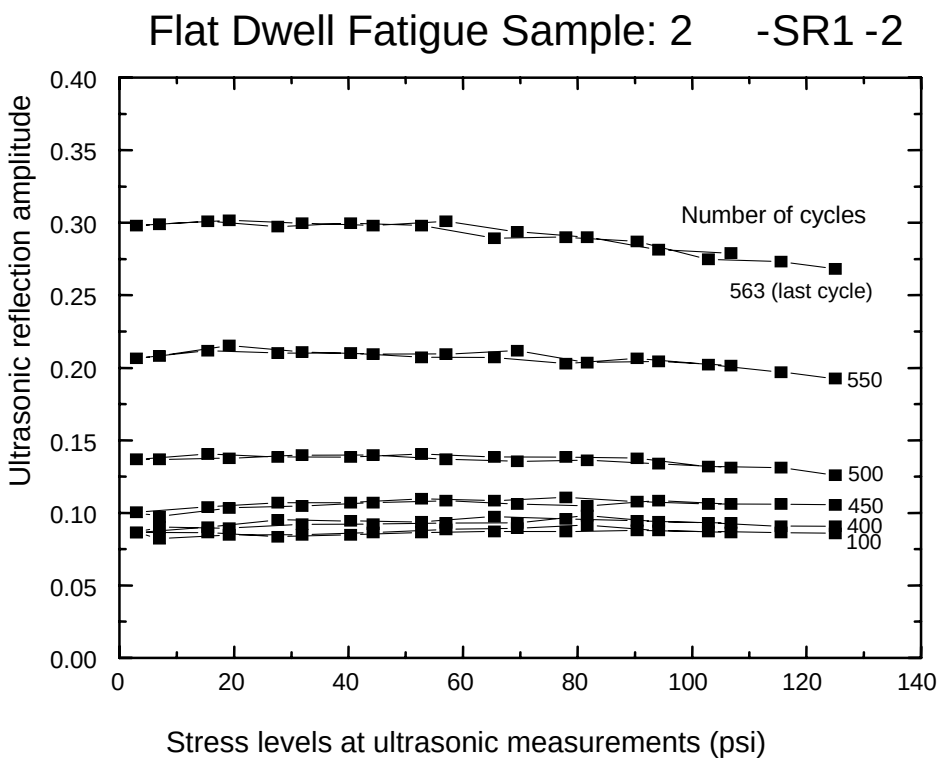

Figure C-18. Changes of Ultrasonic Signal Amplitudes During Loading and Unloading Cycle at Different Numbers of Cycles (Flat Ti-6242 sample: 2-SR1-2)

C.3.1.2 Microradiography and Ultrasonic-Microradiographic Dwell-Fatigue Crack Localization.

Figure C-19 shows a microradiographic image of dwell-fatigue sample 2-SR1-2. Besides the major crack on the failure surface, several cracks are found either near to or away from the fracture surface, which is consistent with the ultrasonic results. The crack locations in the sample cross section are also identified using the 90° shot. The observed cracks are aligned in the plane perpendicular to the loading direction.

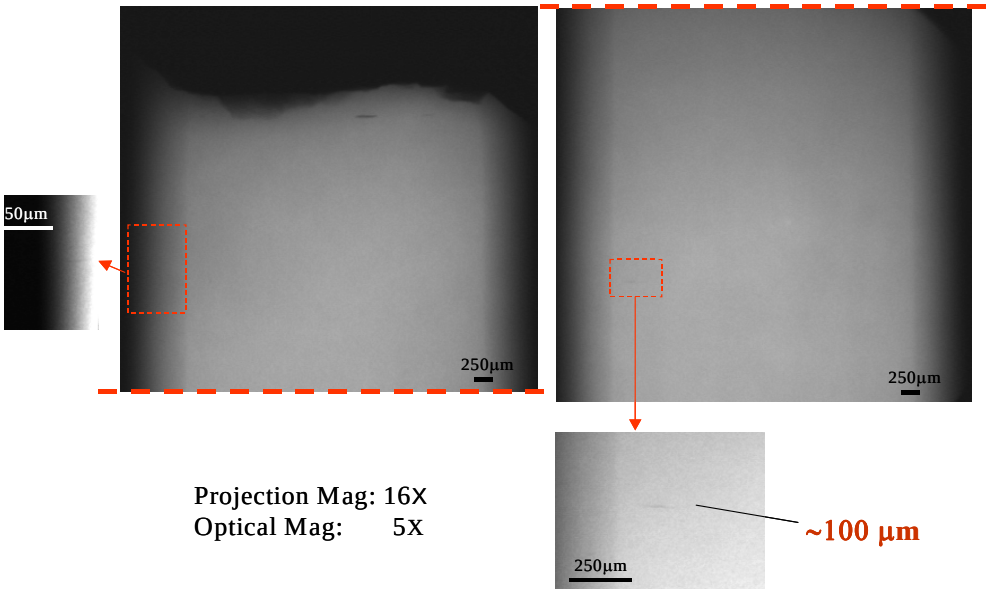

(a) 0° shot

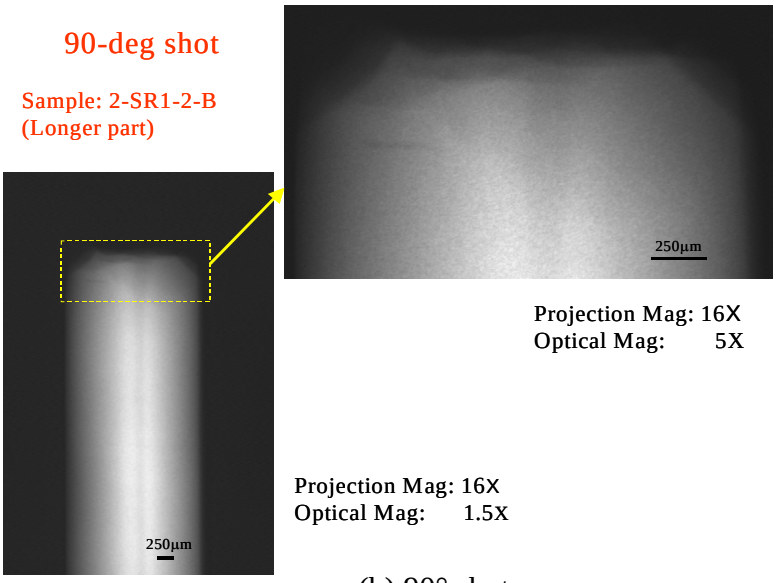

(b) 90° shot

Figure C-19. Microradiographic Images of Dwell-Fatigue Sample 2-SR1-2 That Failed at 563 Cycles (a) 0° Shot and (b) 90° Shot

For this sample, a careful comparison of actual crack locations with ultrasonic crack locations was performed. Figure C-20 shows a radiographic match of the locations of two cracks, as determined from the ultrasonic monitoring. The distance of a secondary crack determined from the image is 7.5 mm, which is very close to the distance (7.8 mm) determined from the ultrasonic signals. Figure C-21 shows microradiographic images for dwell-fatigue sample 2-SR1-1. Similarly to sample 2-SR1-2, there are several secondary cracks at different locations from the fracture surface. After the crack localization, these two samples were further investigated near the crack tip by means of Orientation Image Maps and transmission electron microscopy. Figure C-.22 shows a microradiographic image for sample 2-SR1-3 that failed during the cyclic fatigue test. Note that the secondary cracks are much smaller than the dwell-fatigue cracks and exist near the fracture surface.

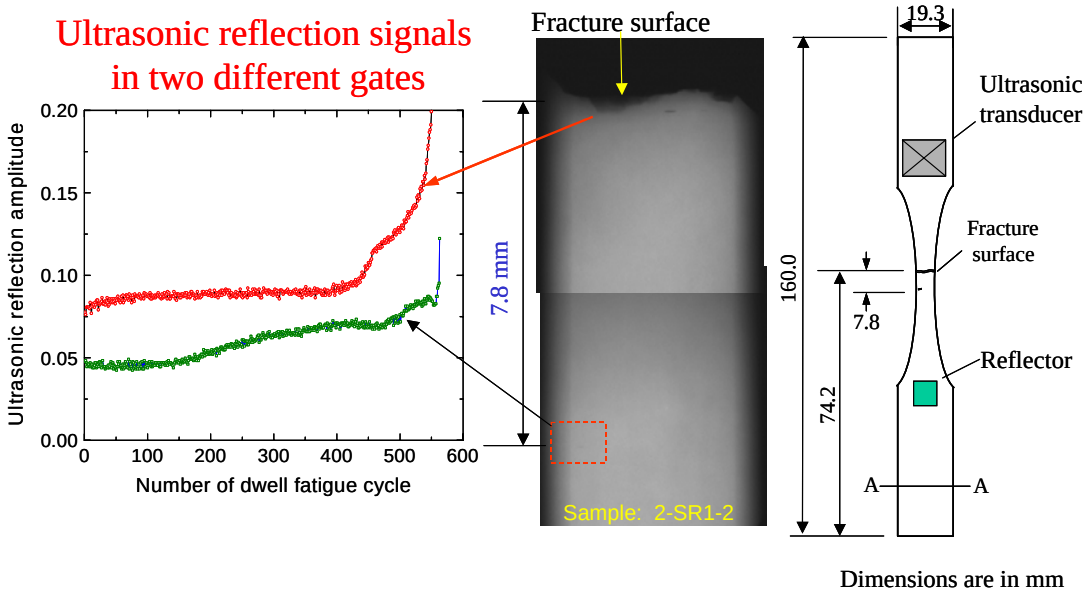

Figure C-20. Matching of Crack Indications in Ultrasonic Signals and Microradiographic Image of Dwell-Fatigue Sample 2-SR1-2 That Failed at 563 Cycles

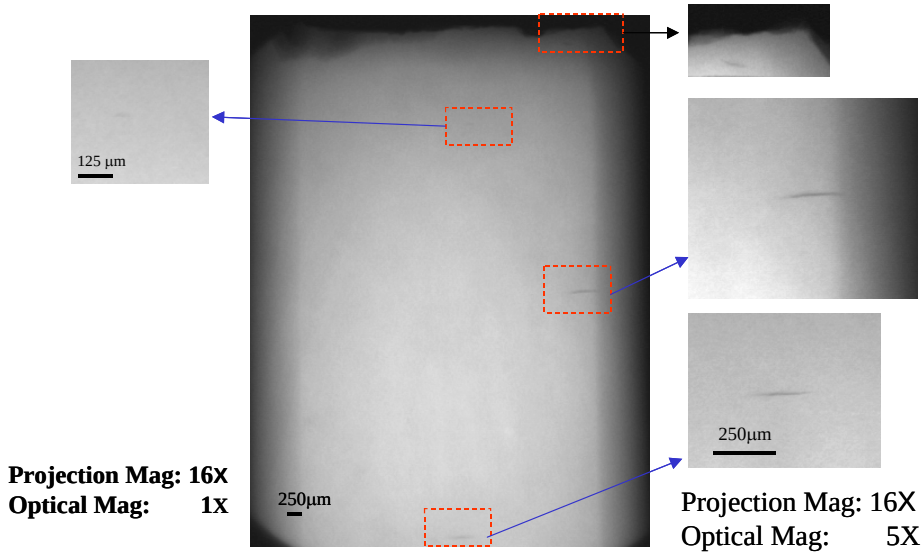

(a) 0° shot

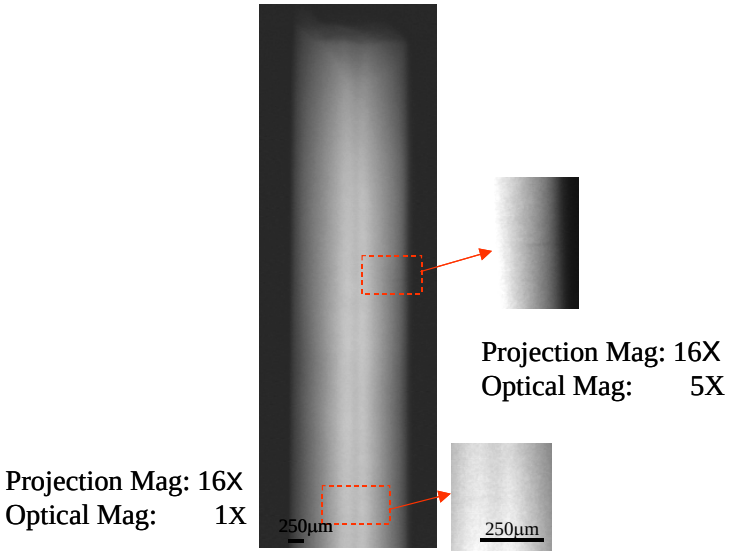

(b) 90° shot

Figure C-21. Microradiographic Images of Dwell-Fatigue Sample 2-SR1-1 That Failed at 352 Cycles (a) 0° Shot and (b) 90° Shot

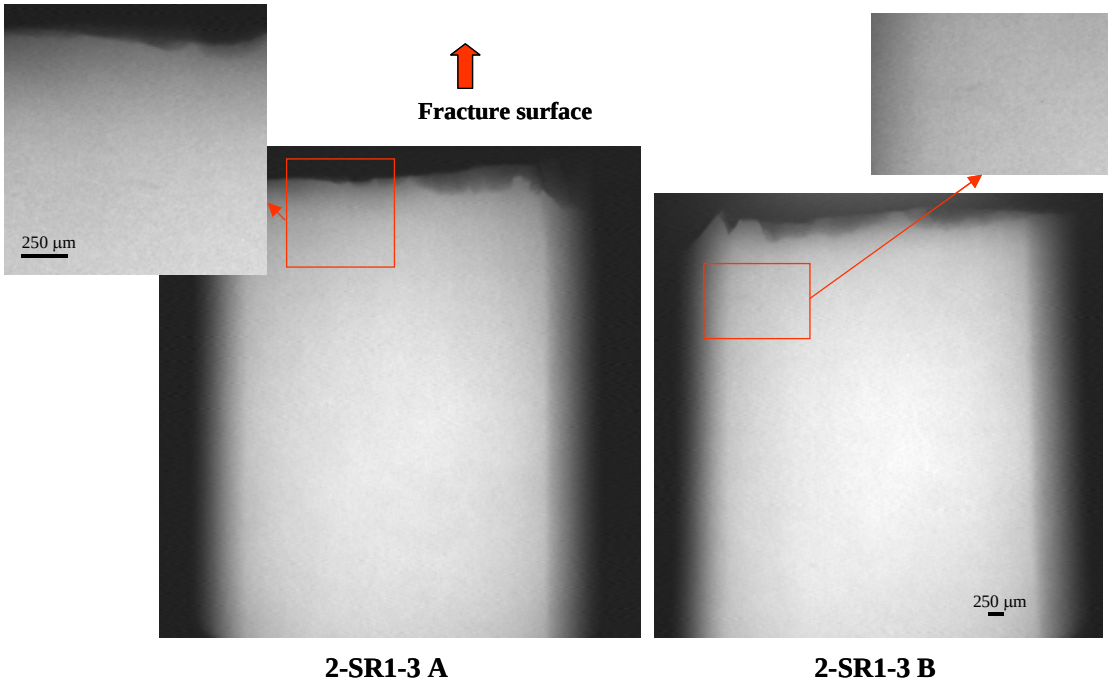

Figure C-22. Microradiographic Images of Fatigue Sample 2-SR1-3 That Failed During Cyclic Fatigue Test After 12,095 Cycles

C.3.1.3 Ultrasonic VC-Scan.

C.3.1.3.1 Flat Dwell and Cyclic Fatigue Samples.

The images of ultrasonic VC-scans for two rectangular flat samples are shown in figures C-23 and C-24. As an example, the results are given for two samples: 2-SR1-1, which failed during dwell-fatigue test after 352 cycles, and 2-SR1-3, which failed during cyclic fatigue test after 12,095 cycles. Figure C-23, compares the images from the ultrasonic VC-scans and microradiography. The VC-scan image of the crack about 3 mm below the fracture surface cannot be obtained since the corner effect in the sample prevents beam refraction. Images were obtained for three dwell-fatigue cracks, as shown in figure C-23, one of which the microradiography image does not show. This may be because the crack is inclined to the surface and the microradiography cannot detect it. Figure C-24 also compares the ultrasonic VC-scan image to the microradiography.

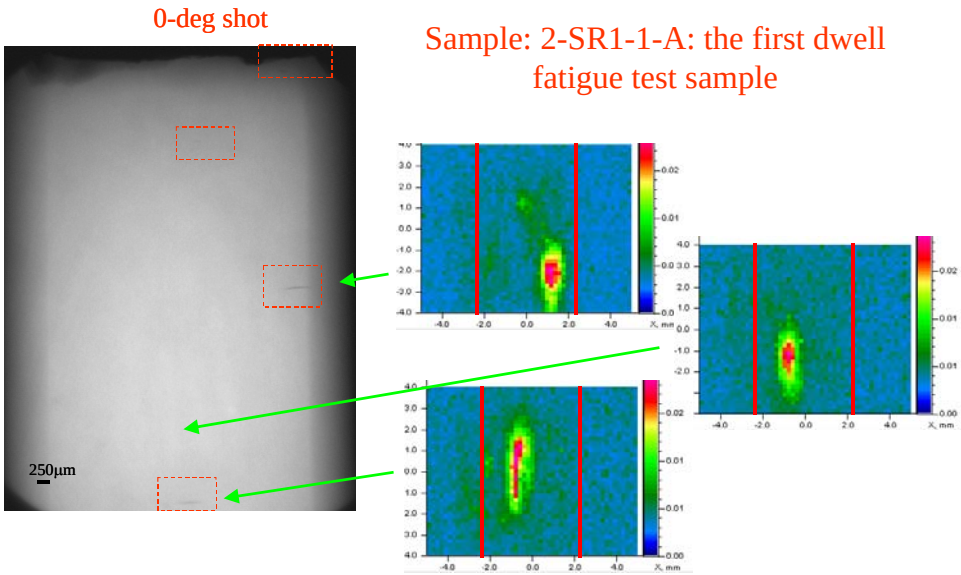

Figure C-23. Comparison of Ultrasonic Angle Beam VC-Scanning Images With Microradiographic Image for Flat Dwell-Fatigue Sample (The microradiographic image does not show one of the indications in the second ultrasonic image.)

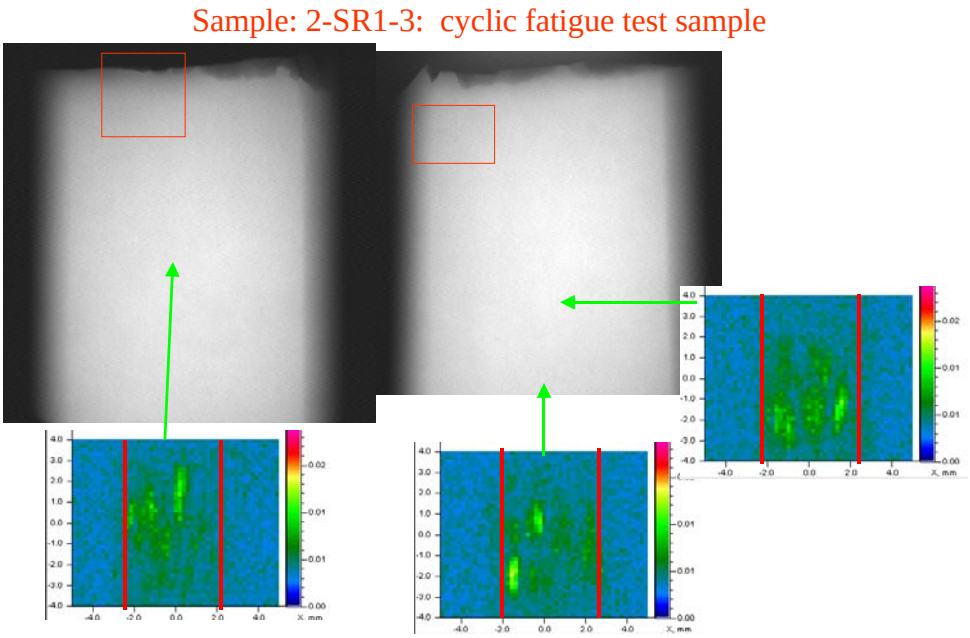

Figure C-24. Comparison of Ultrasonic Angle Beam VC-Scanning Images With Microradiographic Image for Cyclic Fatigue Sample (The microradiographic image does not show the indications in the ultrasonic images.)

C.3.1.3.2 Cylindrical Dwell-Fatigue Samples.

Figure C-25 shows two images taken from a round sample (ID-87-A1). This particular sample was also machined from a high microtexture Ti-6242 forging. The sample was shot peened and failed at 1,654 cycles during a dwell test with a 2-minute dwell time, a maximum load of 126 ksi, and an R ratio of 0. At z = 5.98 mm from the top of the sample, no indication of the flaw is seen in the image. The sample boundary, which is seen due to ultrasonic scattering on the shot-peened surface and also obtained from the calibration test, is marked in the image. The dark area in the central part of the image is thought to be grain noise. The grain noise may be important if it is correlated with dwell crack initiation. At the height z = 6.82 mm the image shows a clear indication of an internal crack.

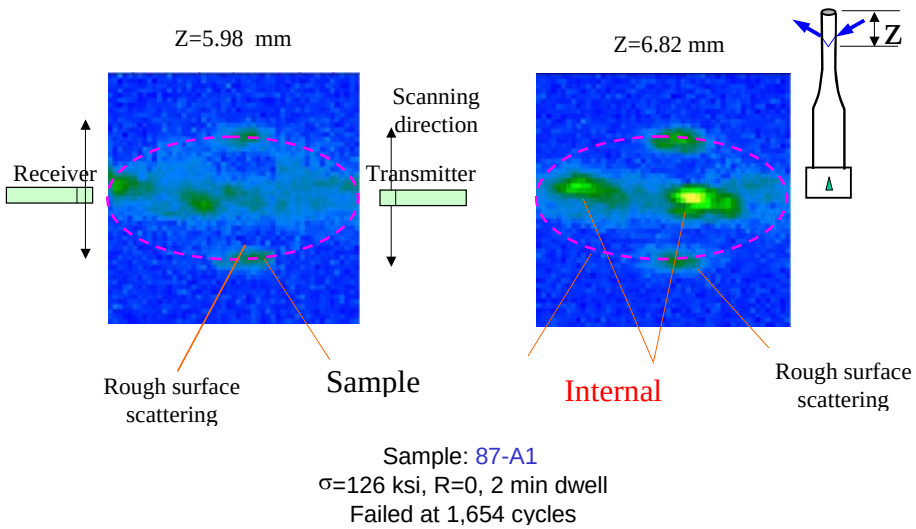

Figure C-25. Ultrasonic Angle Beam Scan Images at Different Heights for the Round Sample With Shot Peening

Figure C-26 shows an ultrasonic scan image for a round sample (ID-1504-1C) without shot peening. The sample failed at 17,877 cycles during a dwell test with a 1-minute dwell time, a maximum load 120 ksi, and an R ratio of 0. At distance z = 3.94 mm from the fracture surface, no indication of the flaw is seen in the image. Since this sample has a smooth surface, there is no surface scattering; so it is difficult to identify the sample boundary compared to the shot-peened sample. Similarly to the previous sample, grain noise appears in the image. At distance z = 7.01 mm from the top, the image shows indications. The depth of the crack from the surface is determined to be 1.7 mm.

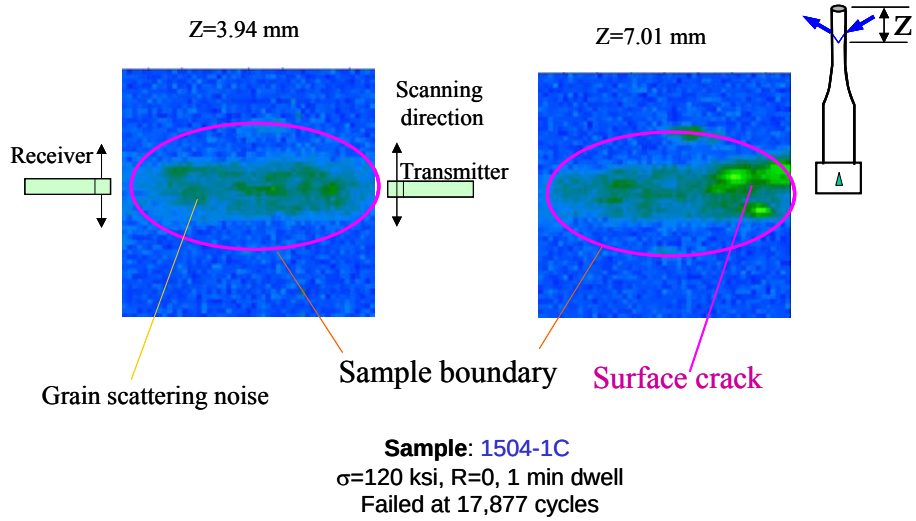

Figure C-26. Ultrasonic Angle Beam Scan Images at Different Heights for the Round Sample Without Shot Peening

The comparison of the ultrasonic image for this sample with microradiography is shown in figure C-27. The distance of the crack from the fracture surface determined from the microradiography image is 7.2 mm, which is very close to that determined by the ultrasonic scan image. The depth from microradiography is 1.5 mm, which is close to that determined from the ultrasonic image.

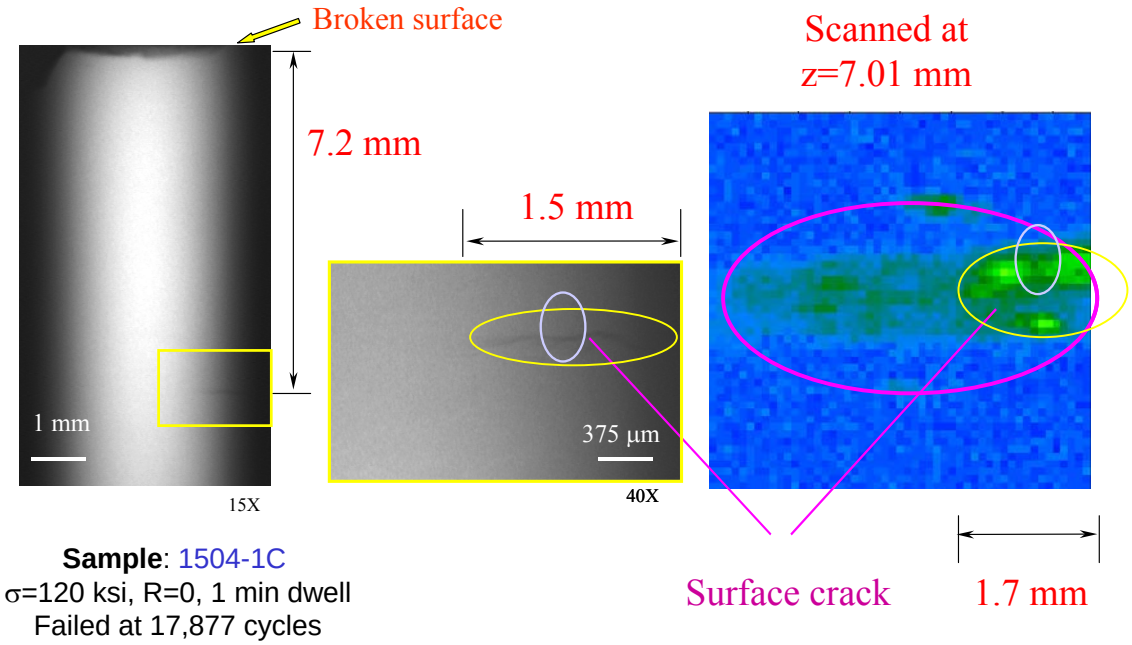

Figure C-27. Comparison of Ultrasonic Angle Beam Scan Image With Microradiographic Image for Round Sample

C.3.1.4 Early Crack Detection by Ultrasonic Modulation Method.

Two dwell-fatigue tests were performed on samples 2-SR1-C3 and 2-SR1-C1 with ultrasonic modulation monitoring. Figure C-28 shows the changes of ultrasonic reflection amplitude with dwell-fatigue time (C-28(a)) and the amplitude of the modulated ultrasonic signal (C-28(b)) from the primary crack for sample 2-SR1-C3. The amplitude of the reflected ultrasonic signal grows with the number of cycles until 200 cycles where the ultrasonic signal decreases due to growth of secondary cracks appearing below the primary crack (closer to the transducer). The behavior of the reflected signal depends on whether the other cracks shield the ultrasonic reflection from the crack of interest. As shown in figure C-28(a), particularly for this crack, it is difficult to determine the crack initiation time from the ultrasonic reflection signals measured under constant load level. The ultrasonic modulation signal (figure C-28(b)) clearly shows a peak in the very early fatigue stage. This may be regarded to be the crack initiation time, as marked in the figure. According to this indication, the primary crack initiation in this sample occurs at 25 cycles. Figure C-28(c) shows the strain curves measured for this sample at maximum and minimum levels of dwell-fatigue load. The total accumulated strain was 0.029 (2.9%), and the accumulated strain at the crack initiation time was determined to be 0.0059 (0.59%). It is also observed that during the steady crack propagation from 150 cycles to 350 cycles, the amplitude of the modulation signal is much smaller than at other times. This is because the crack is sufficiently open due to strain accumulation, and modulation-induced crack-surface interaction is reduced. This was already illustrated by the independence of ultrasonic reflection signals on the level of fatigue load shown in figure C-18. During the final unstable crack growth, the modulation signal also grows due to crack tip modulation and fluctuates greatly until sample failure.

Figure C-29 shows the modulation results for the secondary crack in the same sample. The amplitudes of the ultrasonic reflection modulation signals from a secondary crack (crack 4) are shown versus number of cycles (see figure C-30 for the microradiographs of the sample). In the initial stage of fatigue before 100 cycles, the ultrasonic reflection signal is below the noise (C-30(a)), however, the modulation signal (C-30(b)) shows significant changes during this period. This activity may be related to the crack initiation and small crack propagation (the validity of this hypothesis will require further study). Figure C-30 shows microradiographs of two mating pieces of the failed sample together with a table summarizing the crack sizes and locations determined from the microradiographs. The microradiographs show 16 secondary cracks, which is the largest number observed in the 10 samples for dwell-fatigue and creep tests.

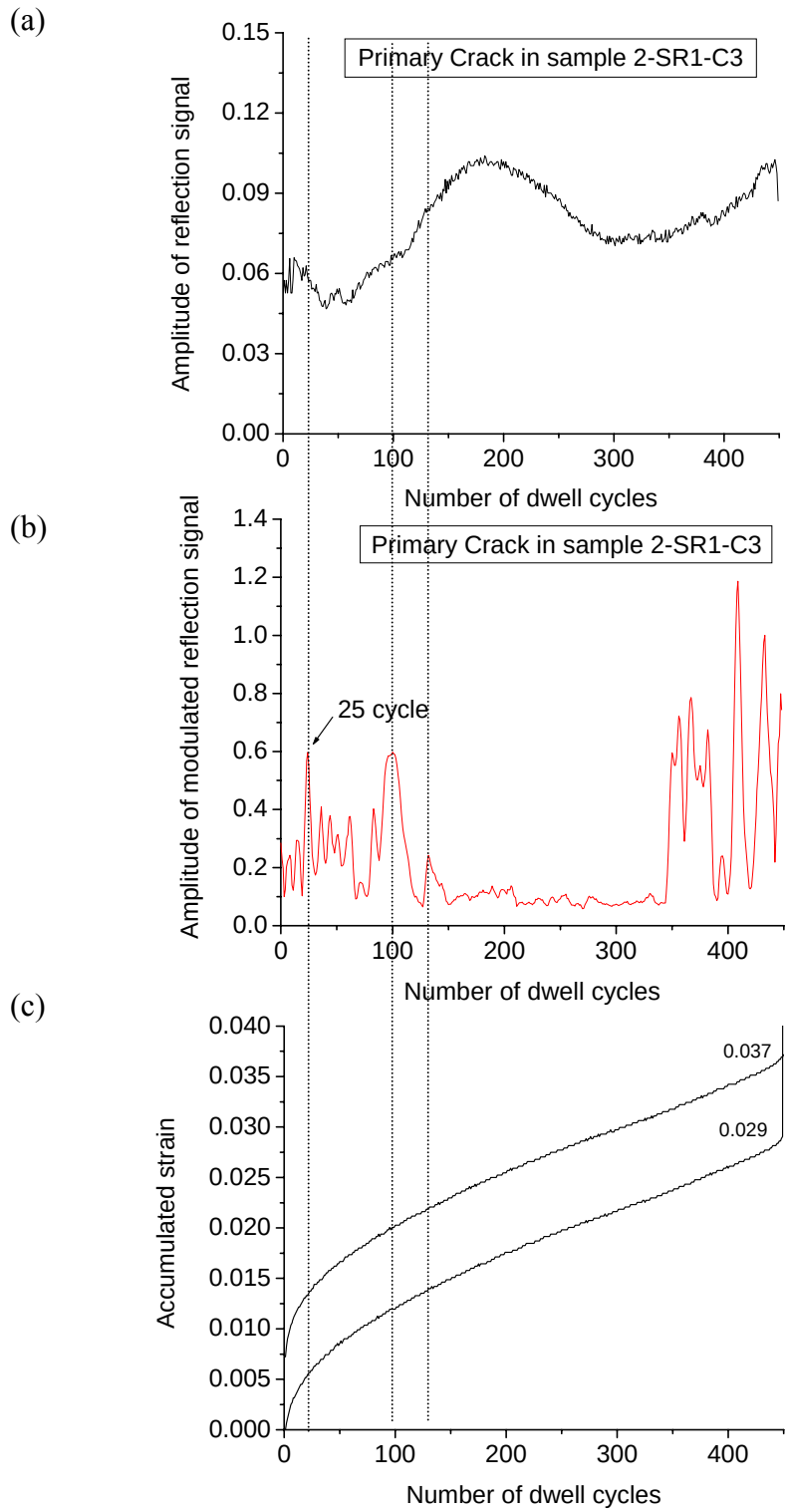

Figure C-28. Ultrasonic Reflection Amplitudes From the Primary Crack and Strains Versus Number of Dwell-Fatigue Cycles for Sample 2-SR1-C3 (a) Amplitude of Reflection Ultrasonic Signal, (b) Amplitude of Modulated Reflection Ultrasonic Signal, and (c) Strain Measured at Maximum and Minimum Loads

(a)

(b)

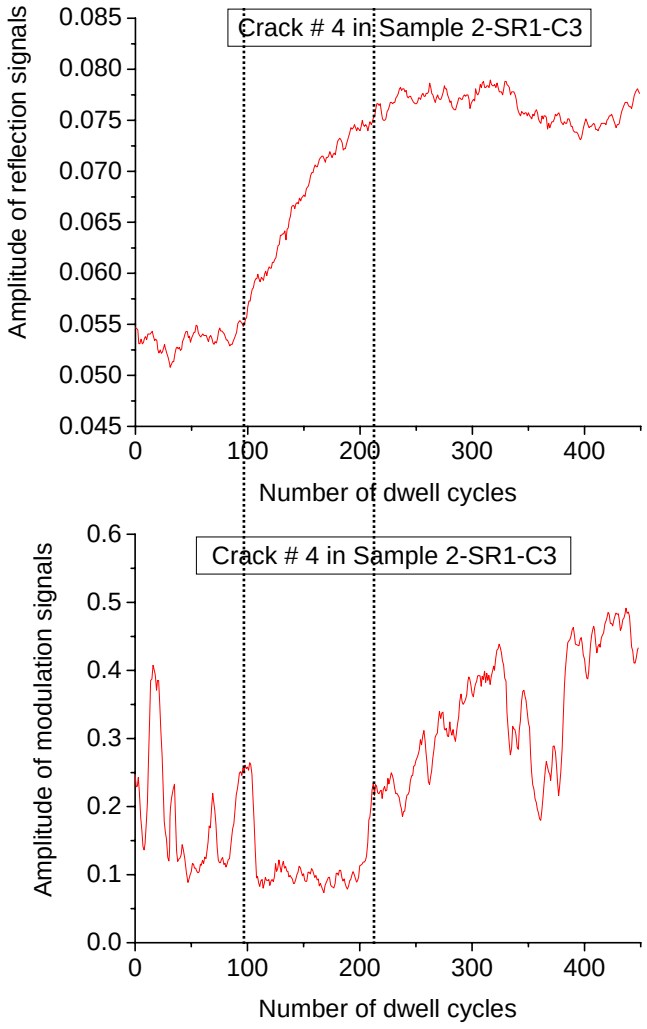

Figure C-29. Ultrasonic Reflection Amplitudes From Secondary Crack 4 Versus Number of Dwell-Fatigue Cycles for Sample 2-SR1-C3 (a) Amplitude of Reflection Ultrasonic Signal and (b) Amplitude of Modulated Reflection Ultrasonic Signal

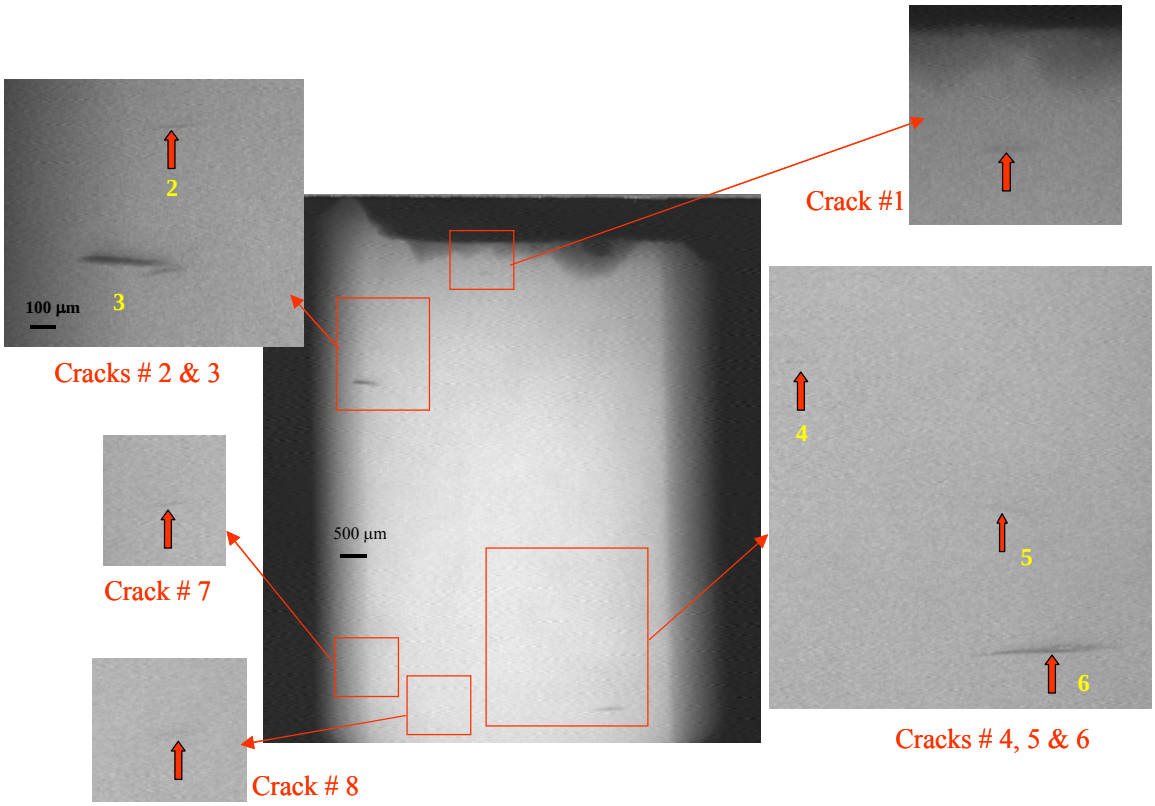

Crack #	Length, mm	Distance to the broken surface, mm	Distance to the nearest edge, mm
1	0.2	0.47	2.3
2	0.16	1.6	0.9
3	5.0	2.12	0.62
4	0.16	5.75	2.7
5	0.18	6.37	1.8
6	0.62	6.87	1.56
7	0.18	7.5	2.3
8	0.13	7.2	1.0

(a)

Figure C-30. Microradiographs of Sample 2-SR1-C3 (a) Part of the Broken Sample on Which the Transducer was Mounted and (b) Opposite Part of the Broken Sample

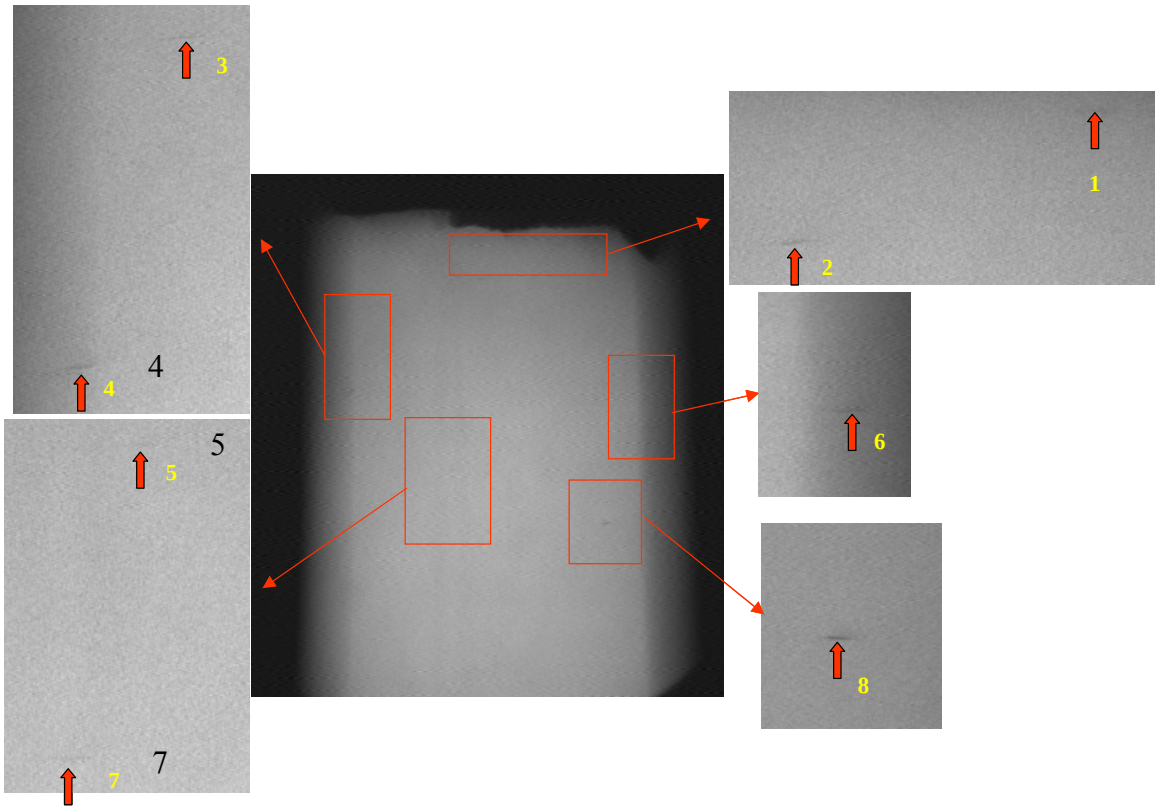

Crack #	Length, mm	Distance to the broken surface, mm	Distance to the nearest edge, mm
1	0.13	0.25	1.8
2	0.16	0.8	2.6
3	0.18	1.4	1.0
4	0.16	2.75	0.68
5	0.06	2.5	2.5
6	0.19	3.1	0.62
7	0.19	3.75	2.25
8	0.13	4.6	1.4

(b)

Figure C-30. Microradiographs of Sample 2-SR1-C3 (a) Part of the Broken Sample on Which the Transducer was Mounted and (b) Opposite Part of the Broken Sample (Continued)

Figure C-31(a) shows the change of the reflection signal amplitude from secondary crack 1 (see figure C-32 for the microradiographs of the sample) in the second sample (2-SR1-C1). From this figure, the crack initiation is determined to be at 45 cycles. Figure C-31(b) shows the corresponding modulation signal. The result of modulation shows slightly earlier crack initiation time at about 40 cycles, marked in the figure. Based on the modulation results, the accumulated strain at the crack initiation determined from the strain curve figure C-31(c) is 0.47%, while the static ultrasonic measurement is 0.51%, which is a little higher. As in the previous sample (2-SR1-C3), the modulation amplitude is smaller while the crack grows steadily. Figure C-32 shows microradiographs of two mating pieces of the failed sample together with sizes and locations determined from the microradiographs. The microradiographs show six secondary cracks.

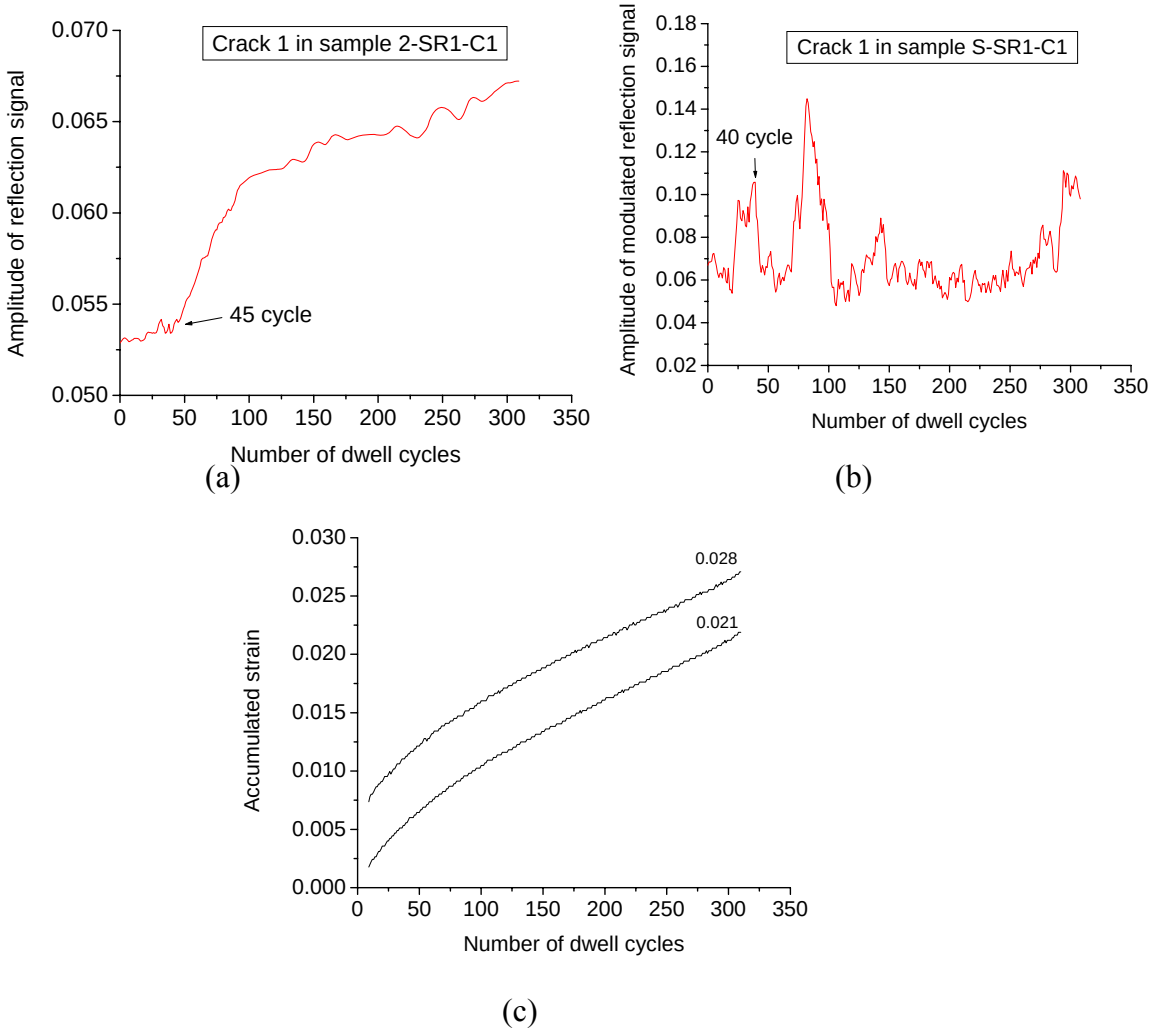

Figure C-31. Ultrasonic Reflection Amplitudes From Secondary Crack 1 and Strains Versus Number of Dwell-Fatigue Cycles for Sample 2-SR1-C1 (a) Amplitude of Reflection Ultrasonic Signal, (b) Amplitude of Modulated Reflection Ultrasonic Signals, and (c) Strain Measured at Maximum and Minimum Loads

From the examples shown above, the modulation technique shows promise for early detection of crack initiation. However, it should be noted that the ultrasonic modulation as well as the ultrasonic reflection measurements are affected by other cracks that may interfere and shield the ultrasonic reflection from a crack of interest. A calibration study is planned that will quantitatively relate the ultrasonic signature to the initiated crack size.

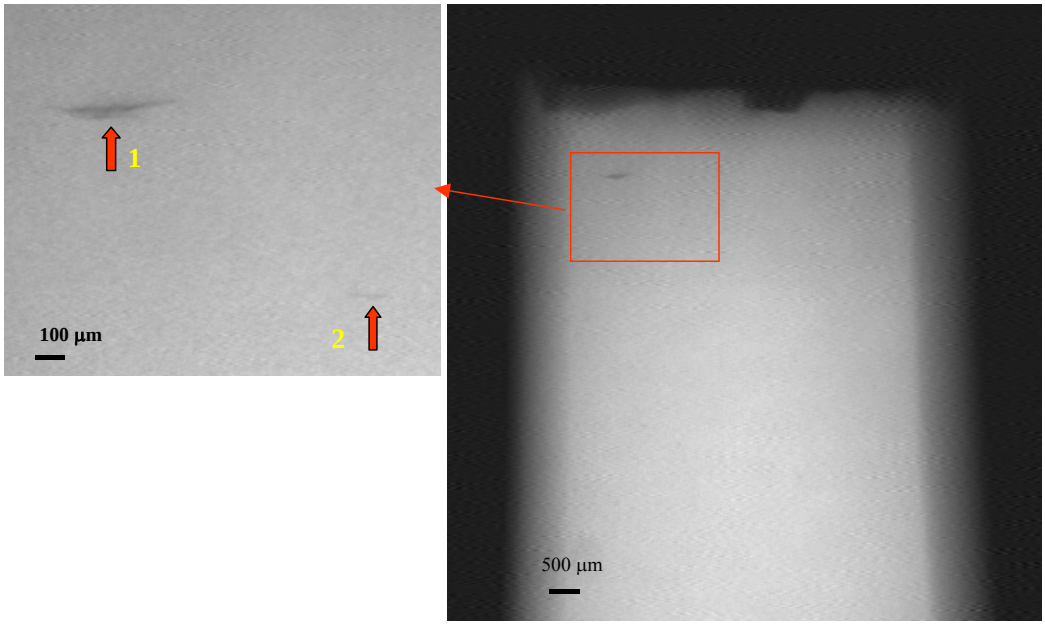

Crack #	Length, mm	Distance to the broken surface, mm
1	0.44	1.2
2	0.13	1.7

Figure C-32. Microradiographs of Sample 2-SR1-C3 (a) the Transducer was Mounted on This Part and (b) Other Broken Part of the Sample

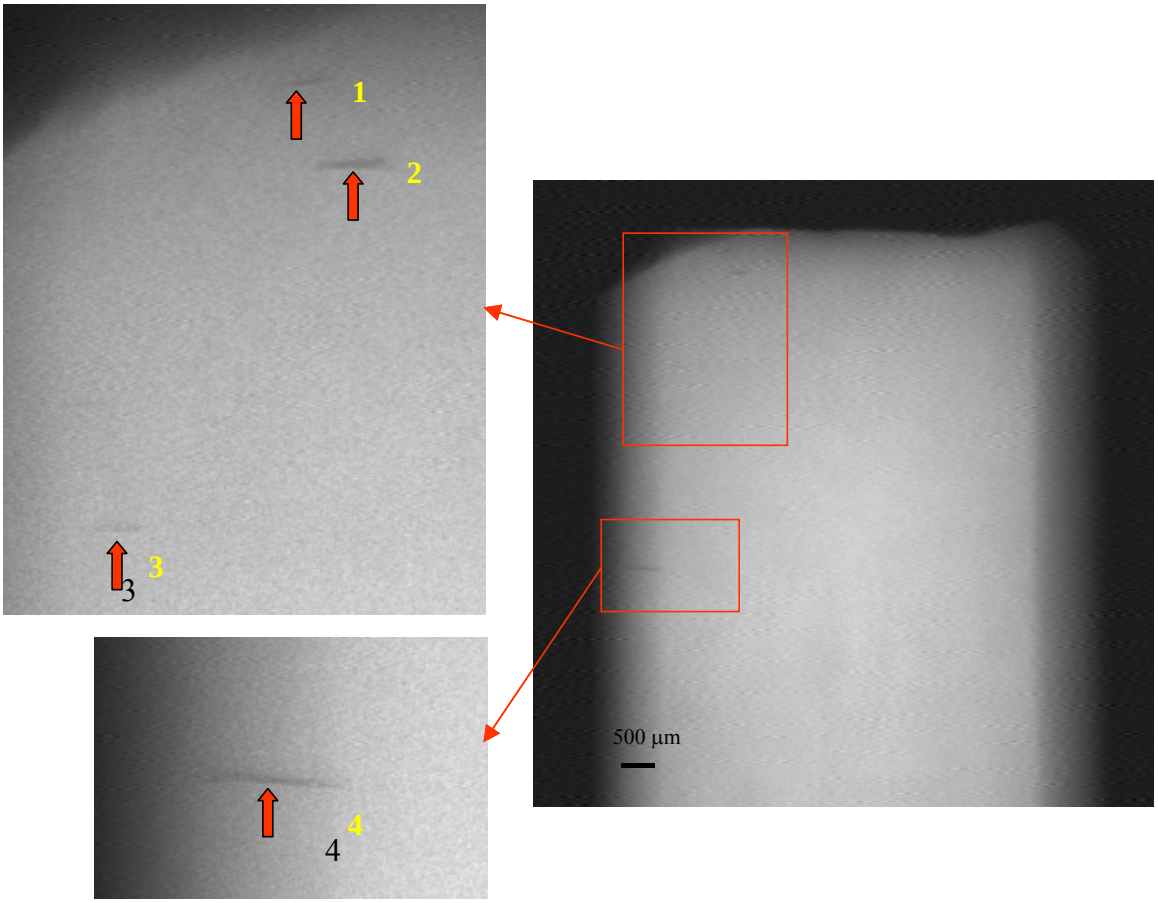

Crack #	Length, mm	Distance to the broken surface, mm
1	0.19	0.25
2	0.16	1.18
3	0.13	1.6
4	0.5	4.0

Figure C-32. Microradiographs of Sample 2-SR1-C3 (a) the Transducer was Mounted on This Part and (b) Other Broken Part of the Sample (Continued)

C.3.1.5 Crack Detection and Characterization in Creep Specimen.

C.3.1.5.1 Monitoring Of Crack Initiation.

The creep time to failure was 744 minutes. This is equivalent to 372 dwell-fatigue cycles with a 2-minute hold period in the cycle. Figure C-33 shows the applied load that was recorded during the creep test, indicating a small reduction of the load in the beginning. Therefore, the actual load applied to the sample was slightly lower than the set load. Figure C-34 shows the recorded strain history in linear and in log-log scales. The total accumulated strain was 0.019. This value is very close to the accumulated strain (0.022) measured during the dwell-fatigue test of round specimen that was machined from the same high microtexture Ladish pancake.

Figure C-35 shows the change of the ultrasonic signal amplitudes in different gates recorded during the creep test. It was found from the time delay that the signal in gate J corresponds to a major crack that led to the sample failure. The signal in gate H is from the crack located nearly 3 mm closer to the transducer from the fracture surface and the signals in gates K and N are from the cracks located 1.5 and 6 mm from the fracture surface. It is seen from this figure that the major crack was initiated at 450 minutes.

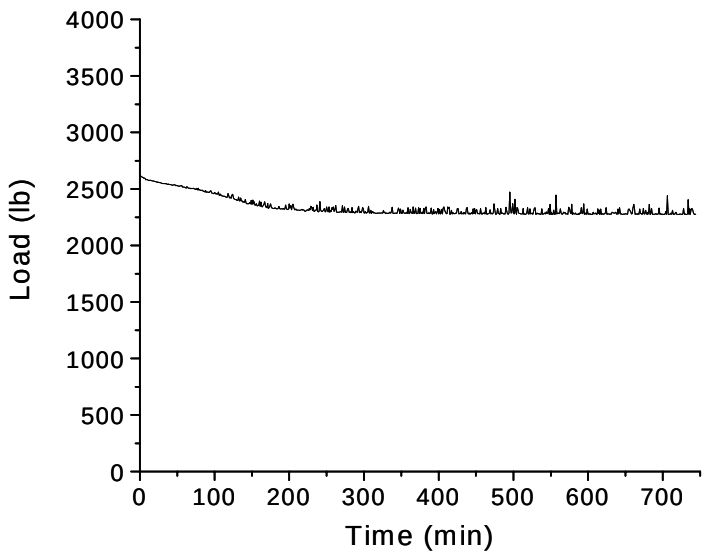

Figure C-33. Applied Load Recorded During the Creep Test for Flat Fatigue Sample 2-SR1-4

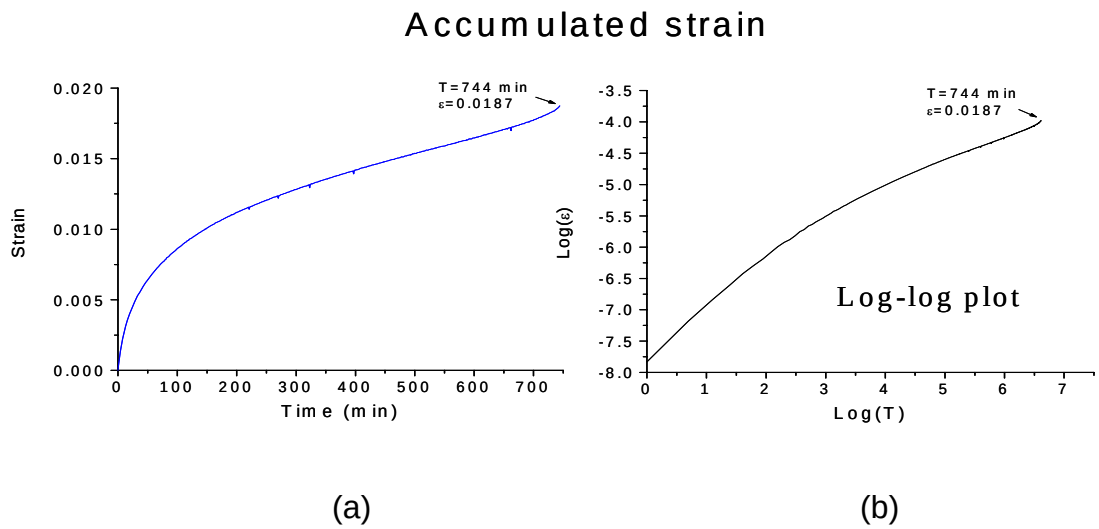

Figure C-34. Accumulated Strain During the Creep Test for Flat Fatigue Sample 2-SR1-4 (a) Linear Scale and (b) Log-Log Scale

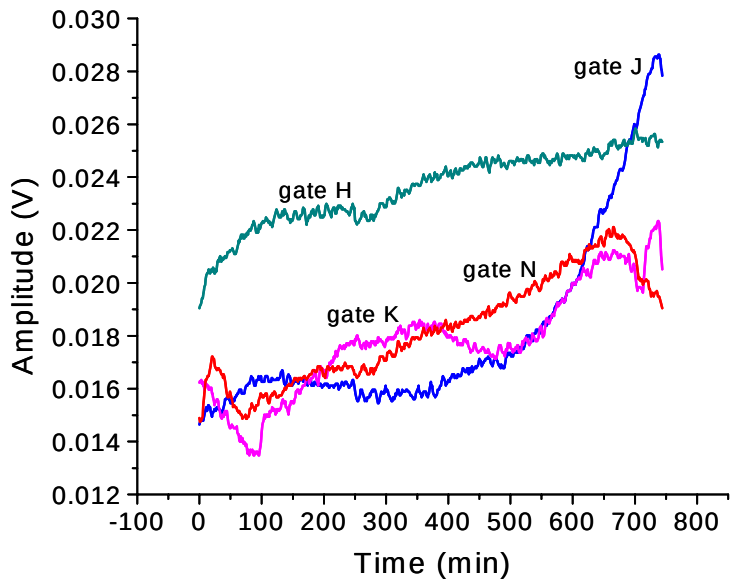

Figure C-35. Changes of Reflected Ultrasonic Wave Signal Amplitudes in Different Time Gates During Creep Test for Flat Fatigue Sample 2-SR1-4

C.3.1.5.2 Microradiographic and Ultrasonic Crack Localization in Creep Tests.

In figure C-36, the microradiographic images of the creep samples show clearly identifiable large secondary cracks. The orientations of the secondary cracks, which are visible as dark lines, are perpendicular to the sample surface; some of them are inclined to the load direction. As seen in the dotted boxes in Figure C-36(b), the image also shows several wider, darker areas, which may correspond to cracks inclined to the surface.

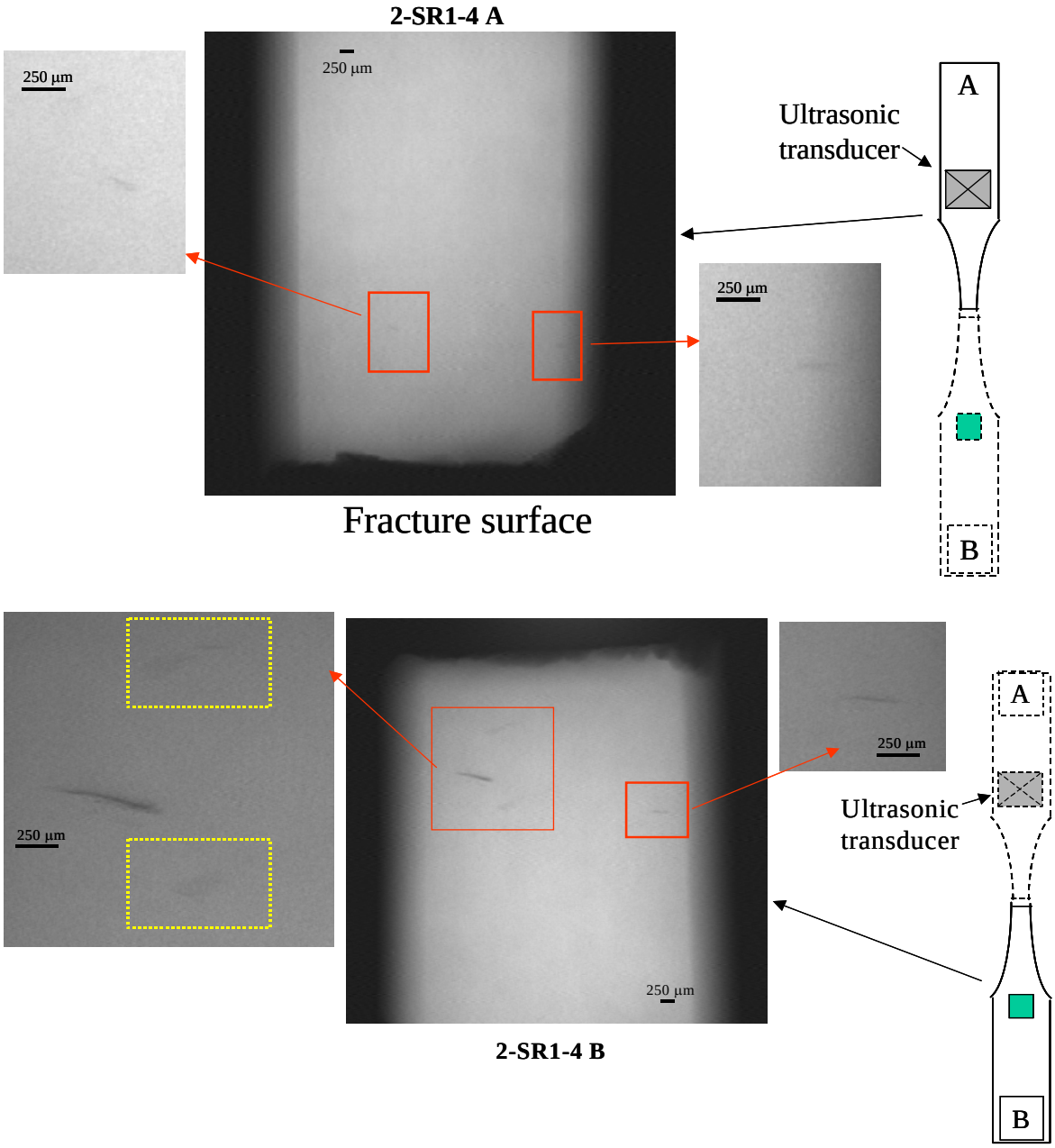

Figure C-36. Microradiographic Images of Flat Sample 2-SR1-4 (Failed during creep test.)

In figure C-37, the ultrasonic surface wave crack monitoring curves, ultrasonic VC-scans and microradiographic images are compared for the creep sample. The locations of the secondary cracks identified from the ultrasonic signals are 3 mm from the fracture surface in the upper part of the sample and 1.5 and 6 mm from the fracture surface in the lower part of the sample. All these locations, except the 6-mm location in the second sample, are visible at the corresponding locations in the microradiographic image. They match quite well.

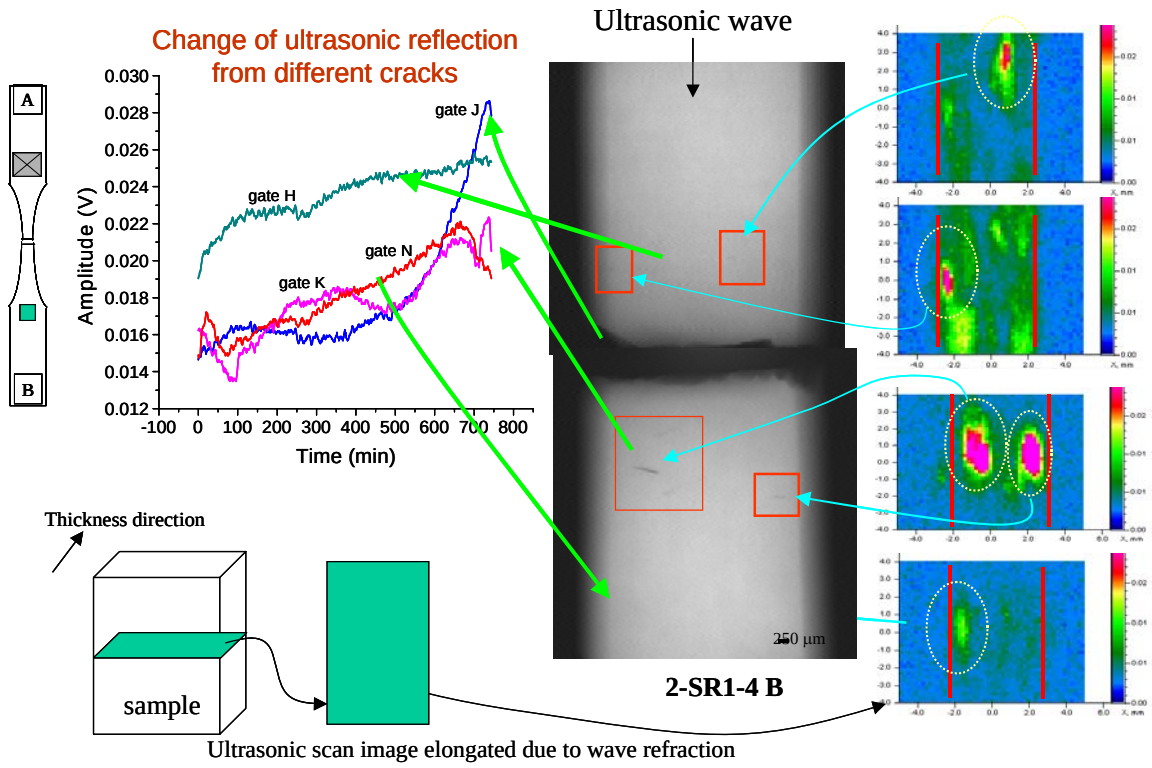

Figure C-37. Comparison and Matching of Crack Indications From Ultrasonic Monitoring, Ultrasonic V-Scan, and Microradiographic Images (2-SR1-4 flat sample; failed during creep test at 744 minutes.)

C.3.2 MEASUREMENT OF SMALL CRACK GROWTH RATE. DWELL FATIGUE AND CYCLIC FATIGUE INTERRUPTIVE TESTS.

C.3.2.1 Cold Dwell-Fatigue Interruptive Tests.

To determine rates of small dwell and cyclic fatigue cracks, interruptive tests were performed. The samples were ultrasonically monitored during testing, and after the specified number of cycles, the tests were interrupted for microradiographic imaging. Two samples (2-SR2-1 and 2-SR2-3) were used for interrupted dwell-fatigue tests. The test can be represented as a set of periodically repeating segments (figure C-38). During the dwell part, the samples were subjected to 126 ksi (869 MPa; 0.95 of the yield stress) load for 2 minutes, followed by unloading to a very small nonzero load to avoid compression. The stress ratio was zero.

Ultrasonic data were collected 10 times within the dwell part of each segment. Modulation measurements were implemented during the unloading and loading parts of the test in the way described above.

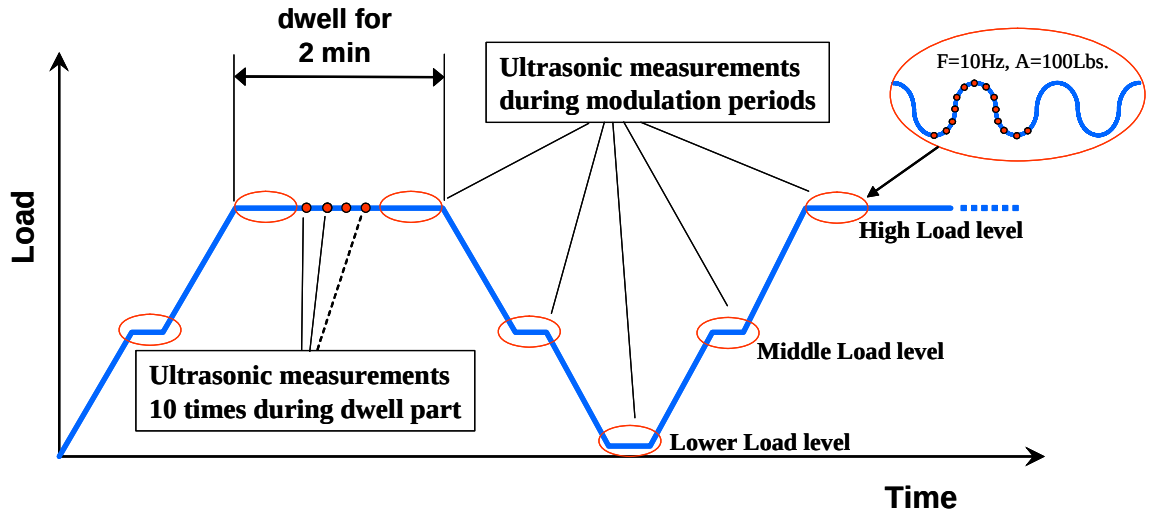

Figure C-38. Load Pattern and Data Acquisition for Interrupted Dwell-Fatigue Tests

C.3.2.1.1 Results for Sample 2-SR2-1.

Sample 2-SR2-1 was fatigued for 50 cycles with no interruptions and then interrupted after each 25 cycles to perform microradiography. The sample failed after 447 cycles.

Figure C-39 summarizes the ultrasonic data obtained for this sample. The data were acquired at the full load (dwell part). The top graph depicts normalized crack reflection amplitude versus number of cycles, while the bottom graph shows normalized reflection from a reflector wedge mounted at the opposite edge of the sample. Therefore, ultrasonic measurements provide both pulse-echo (the crack) and double through transmission (the reflector wedge) information. Crack initiation can be identified by sudden and continuous increase in the crack reflection signal or decay in the reflector signal. The dashed red line indicates crack initiation at about 380 cycles. Both figures demonstrate sudden change in signal level in the first part of the test (between 0 and 100 cycles), which does not correspond to crack initiation and can be attributed to surface roughening of the sample.

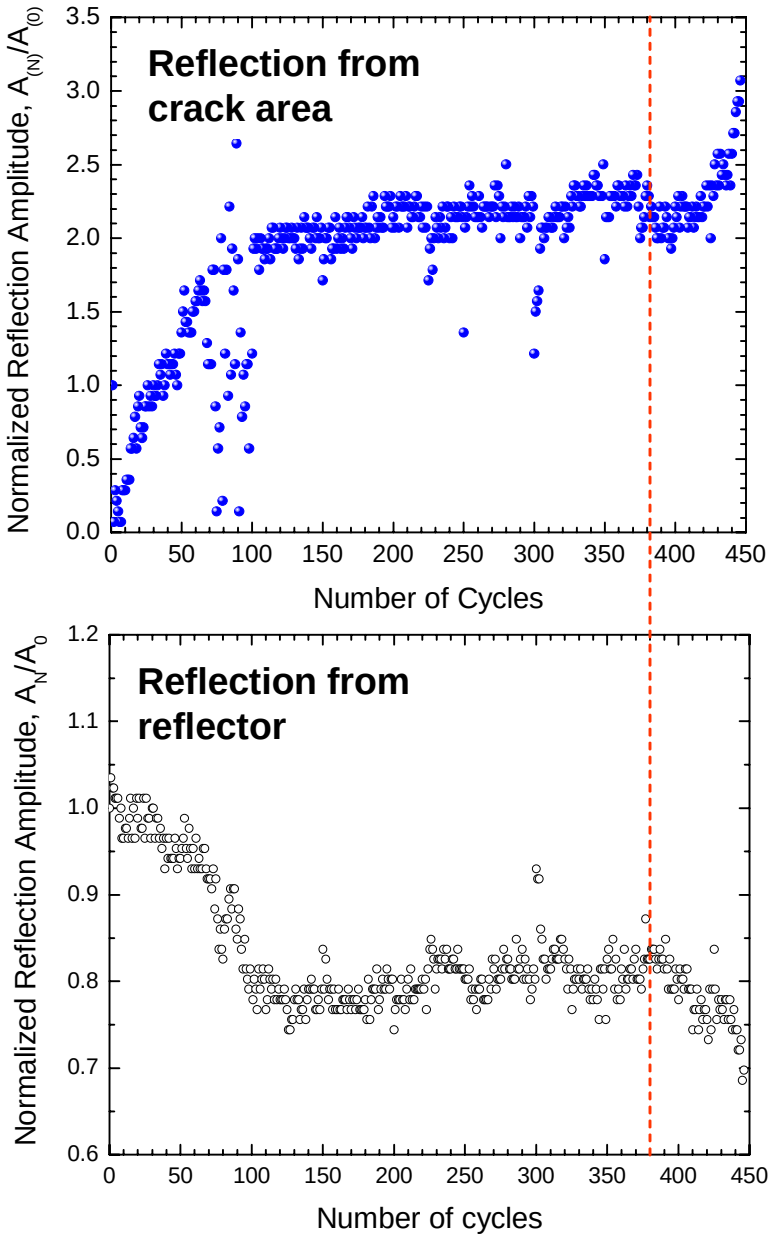

Figure C-39. Change in Ultrasonic Signal Amplitude During Interrupted Dwell-Fatigue Test of Sample 2-SR2-1

Figures C-40 and C-41 present microradiographic images for sample 2-SR2-1. No crack can be found at 400 cycles (figure C-40). The next x-ray shot reveals a big fatigue crack visible from both 0° and 90° directions (figure C-41). The scanning electron microscope (SEM) image of a fractured surface with a crack region encircled is shown in Figure C-42. The location of the region corresponds to that determined from ultrasonic and microradiographic measurements.

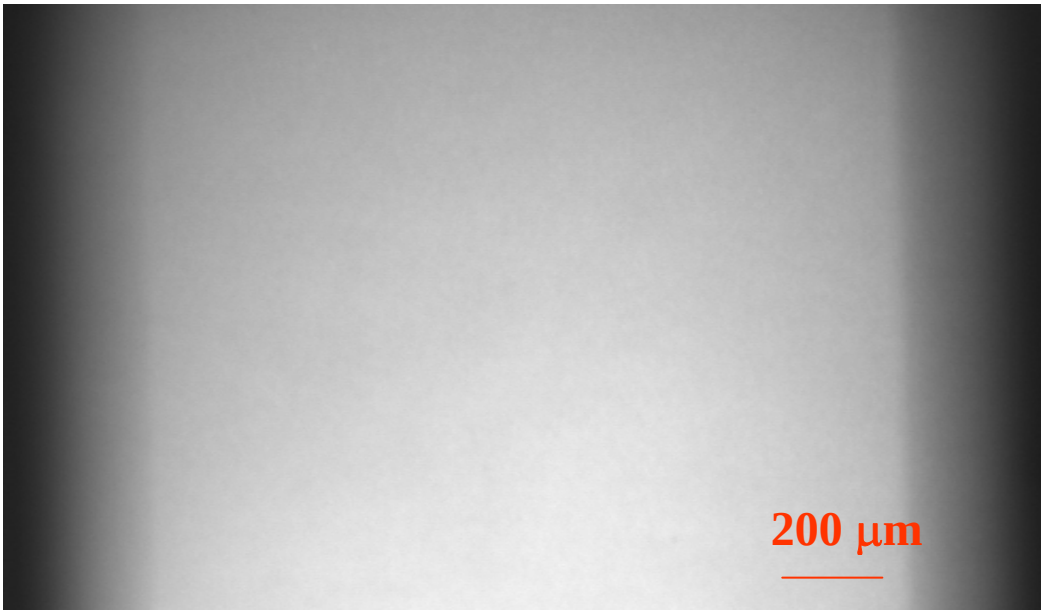

Figure C-40. Microradiographic Image of Dwell-Fatigue Sample 2-SR2-1 at 400 Cycles, Crack Area, 0° Shot (No microcracks are observed. The sample failed after 447 cycles.)

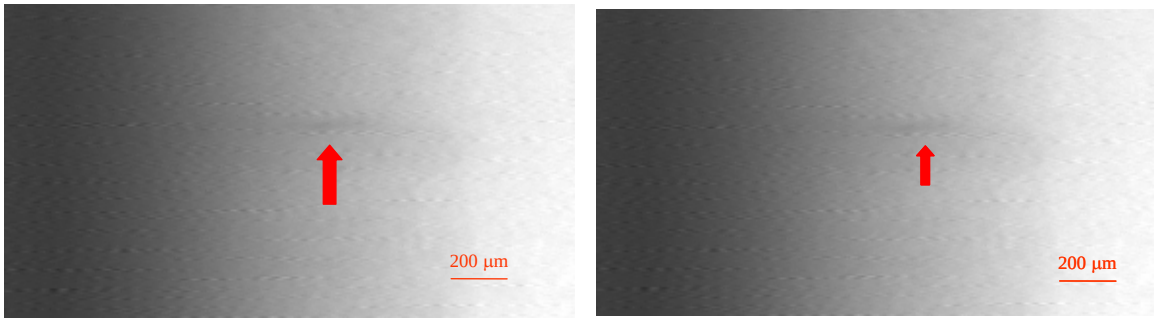

(a) (b)

Figure C-41. Microradiographic Image of Dwell-Fatigue Sample 2-SR2-1 at 425 Cycles, Crack Area (a) 0° Shot and (b) 90° Shot (The microcrack is indicated by the arrow. The sample failed after 447 cycles.)

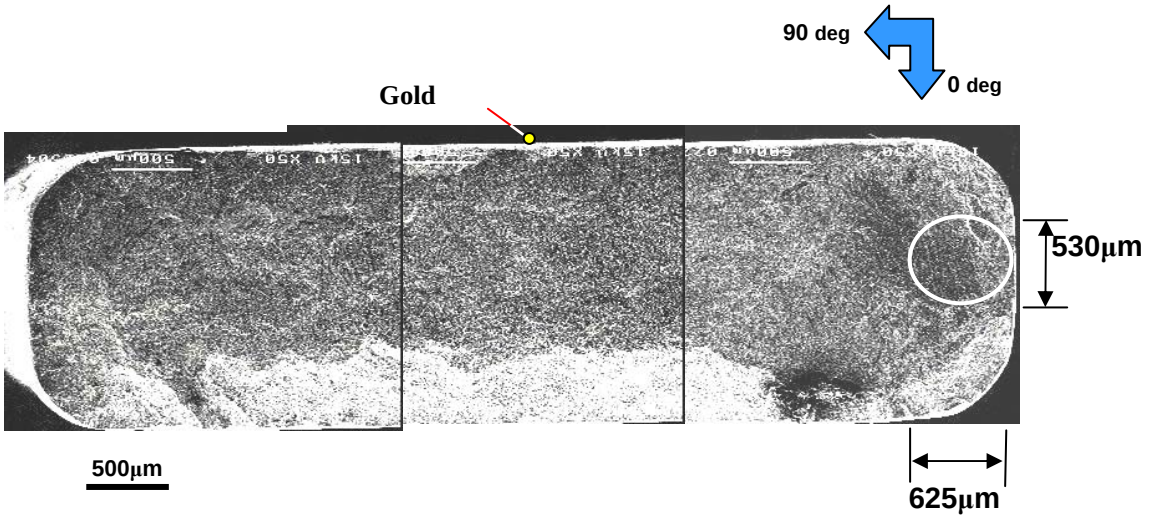

Figure C-42. An SEM Image of the Fractured Surface of Dwell-Fatigue Sample 2-SR2-1 With Encircled Crack Region

In summary, for this sample, ultrasonic measurements indicated crack initiation at about 380 cycles, whereas microradiography revealed a 625- to 530-µm crack only at 425 cycles and no crack at 400 cycles. Thus, the ultrasonic monitoring method provides much earlier indication of small crack initiation than by microradiography. The rate of small crack growth cannot be determined for this sample since only one microradiographic image was available to size the crack.

C.3.2.1.2 Results For Sample 2-SR2-3.

To minimize the number of interruptions in the early stage of fatigue life, the number of test interruptions was limited in the first stage of the test where no crack initiation was expected. Thus, sample 2-SR2-3 was continuously fatigued for the first 150 cycles. Then the test was interrupted after each 25 cycles until 400 cycles was reached. No crack indication was observed at 400 cycles, and the test was continued with interruptions after each 15 cycles until the sample failure at 663 cycles.

The first crack initiated was observed at 475 cycles (both ultrasonically and from microradiographic images). Nine more cracks were discovered during the following cycles. Figure C-43 summarizes the crack formation sequence and location for all the cracks found in the sample. The primary crack, which led to the failure, was observed first at 550 cycles. The secondary cracks 2, 3, 4, and 6 were arrested after reaching a certain size, while cracks 1, 5, 7, 8, and 9 continued to grow until the failure.

Number of cycles	2c (micrometers) 1	2	3	4	5 Primary	6	7	8	9	10
460	No cracks imaged									
475	120									
490	160	300								
505	160	320								
520	190	470								
535	190	560	90	60						
550	190	560	155	60	90					
565	190	560	155	60	90	90				
580	250	630	155	125	95	90				
595	250	700	190	125	210	140				
610	250	750	190	125	370	140				
625	280	750	190	125	430	140	125			
640	310	750	220	125	625	140	310	60		
655	345	750	220	125	815	140	370	125	60	
663	500	750	220	125	Failure	140	470	160	160	160

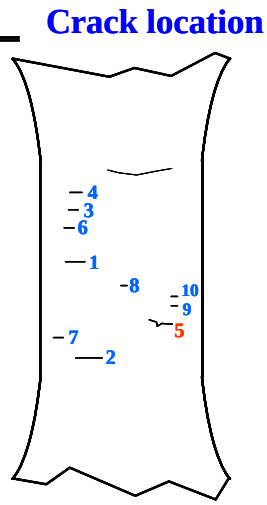

Figure C-43. Crack Formation Sequence and Size for Sample 2-SR2-3 (Failed after 663 cycles.)

A summary of microradiographic images obtained for the prime crack of sample 2-SR2-3 is presented in figure C-44. The top and bottom rows contain images taken from 0° and 90° angles, respectively. The table summarizes crack size versus number of cycles for both angles. The SEM image of the fractured surface relates crack areas at different stages of fatigue life (depicted with concentric circles) to the microradiographic images.

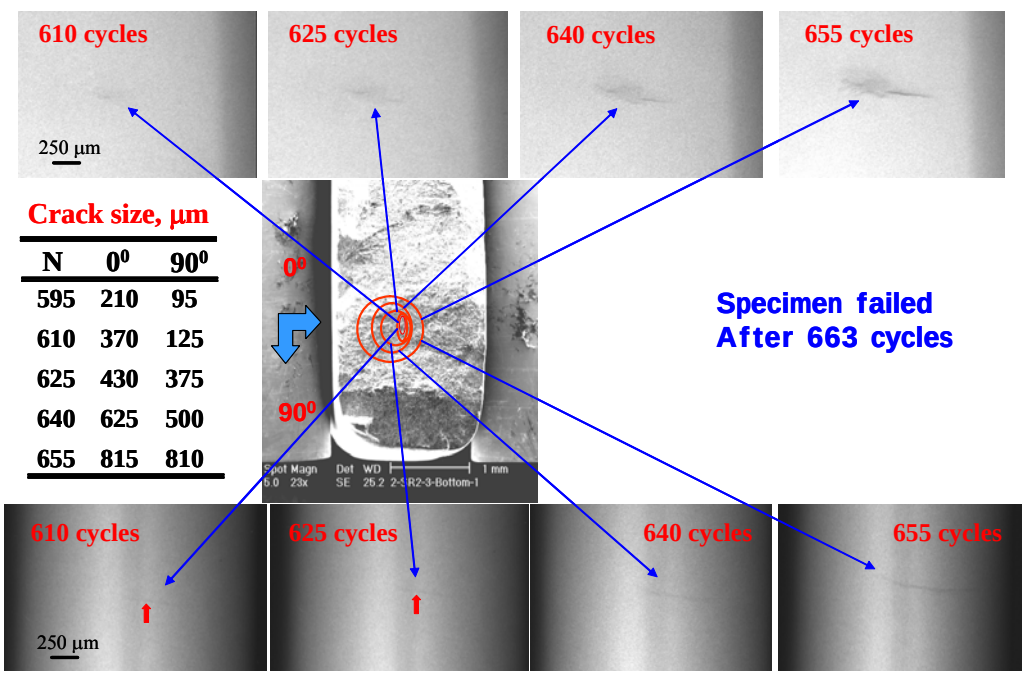

Figure C-44. Microradiographic Images of the Primary Crack in Sample 2-SR2-3

Figure C-45 shows, in more detailed, how microradiographic images can be overlapped with the fractured surface of the sample.

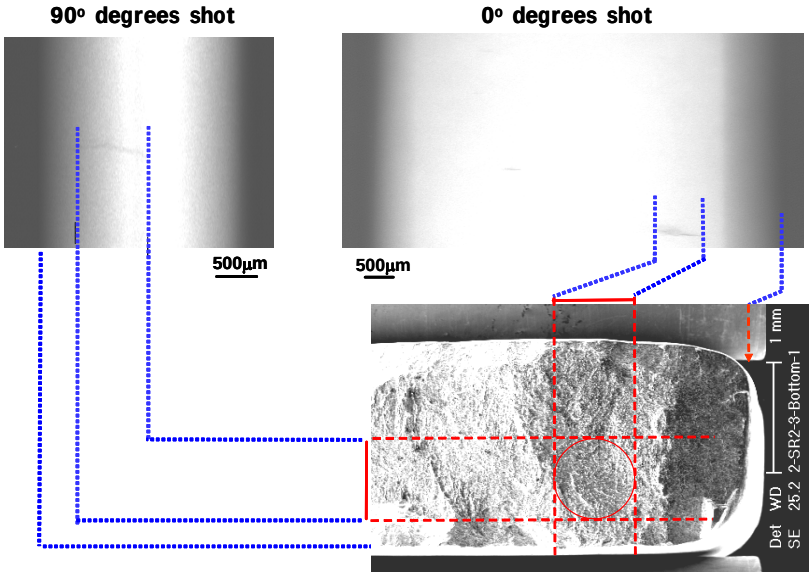

Figure C-45. Crack Overlay on SEM Fracture Surface Image at 655 Cycles (Sample 2-SR2-3)

Ultrasonic data of crack initiation monitoring for sample 2-SR2-3 are presented in figure C-46 (only the results for ultrasonic signals taken at maximum dwell load are shown). The top and bottom figures represent normalized crack and reflector reflections, respectively. The dashed line indicates crack initiation at about 475 cycles. Small vertical lines below the ultrasonic data in the top figure indicate test interruptions for microradiographic imaging. As one can see, the figure shows catastrophic crack growth during the last loading cycle. Several jumps in ultrasonic reflection amplitude prior to the crack formation correspond to the change in ultrasonic transducer contact conditions that occurred during the test (transducer was removed from the sample and couplant reapplied to ensure a better acoustic contact).

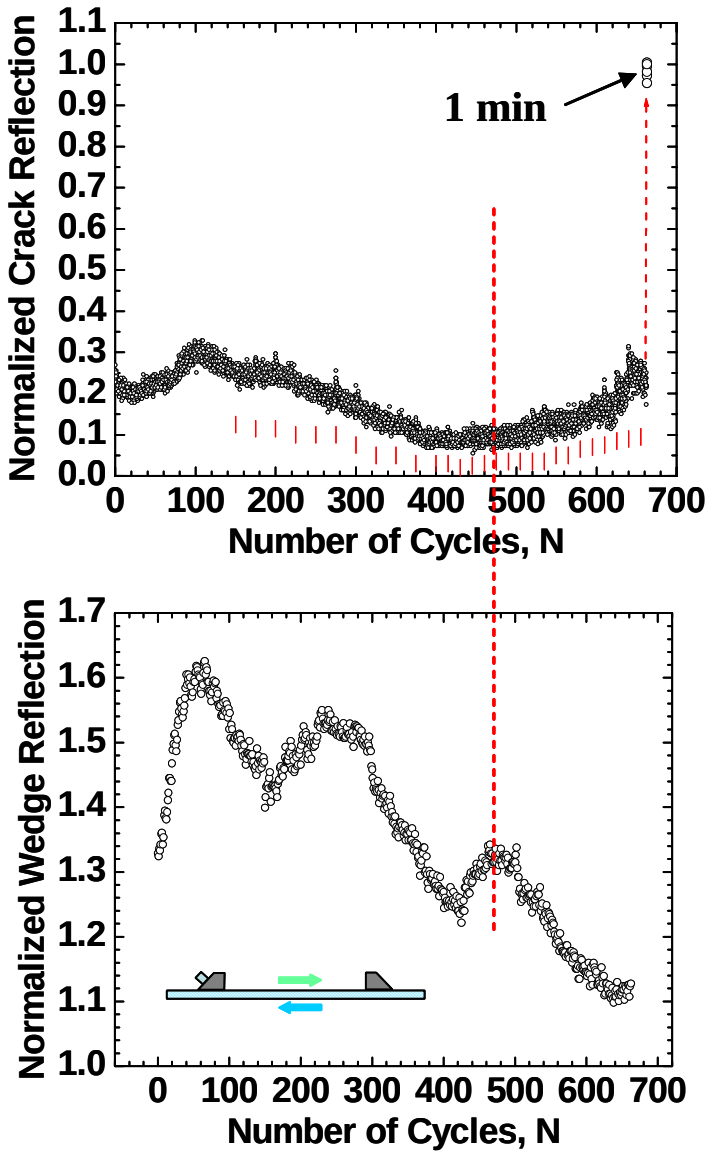

Figure C-46. Change in Ultrasonic Signal Amplitude During Interrupted Dwell-Fatigue Test of the Sample 2-SR2-3

Figure C-47 shows cumulative strain measured for each fatigue at three different load levels: maximum load, intermediate (half of the full load), and minimum load. Due to the interruptive nature of the experiment, the tensitometer had to be removed and then put back on the sample each time the experiment was stopped, causing the strain to zero out. This problem was solved by adjusting the strain level at the beginning of each new cycle to the end of the previous cycle. As one can see, the strain noticeably changes its slope at about 600 cycles, providing an additional sign of crack presence inside the sample. Finally, figures C-48 and C-49 represent crack size versus number of cycles and crack growth rate versus crack size for the prime crack.

The crack sizes were obtained from the microradiographic images at 0° and 90° exposure. The prime crack size versus number of cycles measured is shown in figure C-48.

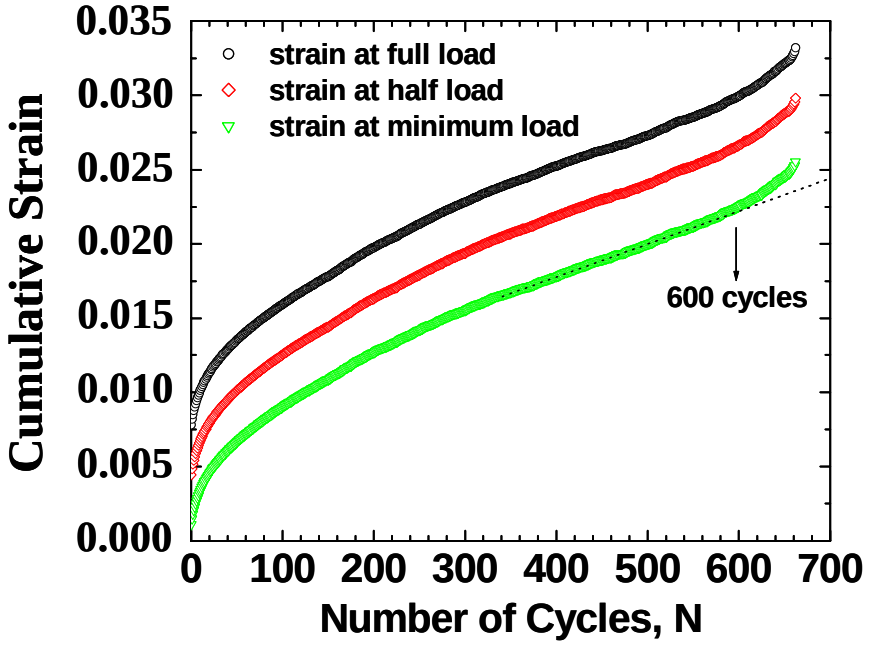

Figure C-47. Cumulative Strain Versus Number of Cycles for Sample 2-SR2-3 (The strain was measured at three different load levels: full load (top curve), half of the full load (middle curve), and minimum load (bottom curve).)

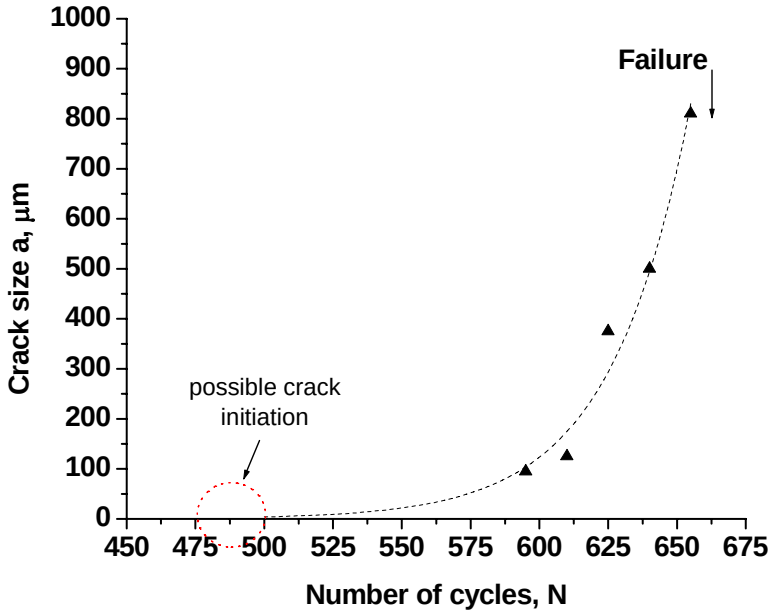

Figure C-48. Crack Size Versus Number of Cycles for the Prime Crack in Sample 2-SR2-3

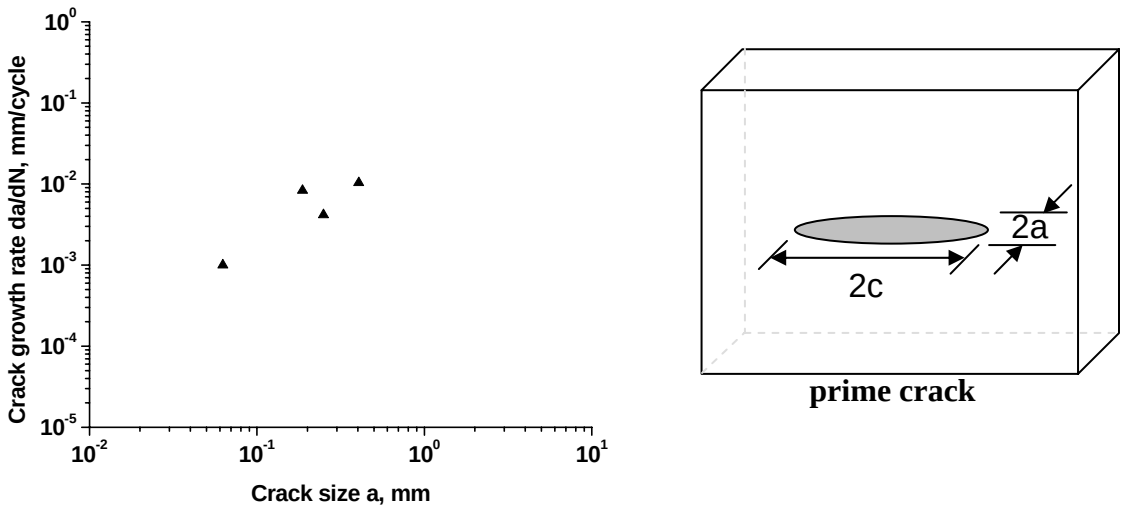

Figure C-49. Crack Growth Rate Versus Crack Size for the Prime Crack in Sample 2-SR2-3 (The sketch on the right side shows the crack geometry.)

As can be seen from figure C-48, the prime crack demonstrates significant growth from approximately 600 cycles (corresponds to the change of slope in strain data, figure C-47). The growth rate for this crack (figure C-49) increases linearly and is within the range of 10^{-3}-10^{-2} mm/cycle during all stages of crack evolution. The sketch on the right side of the figure C-49 shows the crack geometry (2c—crack size from 0°, and 2a—crack size from 90°). In the beginning, the crack is elliptical and its shape becomes a circle with increase in size prior to failure (see table in Figure C-44).

C.3.2.2 Fatigue Interruptive Tests.

Three samples (2-SR2-4, 2-SR2-5, and 2-SR2-B1) were tested to measure small crack growth rates at cycling fatigue conditions. As for dwell-fatigue tests, the maximum load was 126 ksi (0.95 of the yield stress); the stress ratio was close to 0. One load segment with indicated ultrasonic monitoring events is shown in figure C-50. Ultrasonic measurements were performed after each 250 fatigue cycles. At each data acquisition interval, 32 ultrasonic signals were acquired during one sinusoidal cycle (quasi-static measurements) to obtain reflection amplitudes at different load levels; then immediately after the quasi-static measurements, modulation measurements were performed at three load levels (maximum load, half of maximum load, and minimum load).

It was only possible to measure the crack rate for sample 2-SR2-4, because an insufficient number of microradiographic images was collected for the other samples. Therefore, the experimental results are given for this sample only.

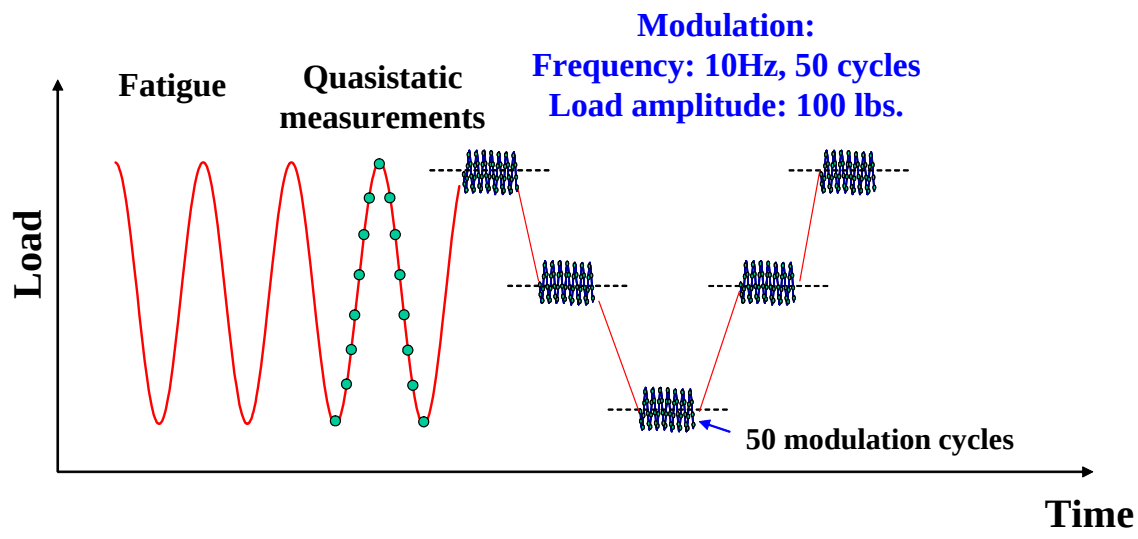

Figure C-50. Load Pattern and Ultrasonic Data Acquisition Sequence for Interrupted Fatigue Tests

C.3.2.2.1 Results for Sample 2-SR2-4.

The fatigue test for sample 2-SR2-4 was interrupted first at 6,000 cycles, then every 1,000 cycles until 14,000 cycles, and then every 500 cycles until the failure at 24,000 cycles. The microcrack was first detected ultrasonically at about 19,000 cycles, and it was observed in the microradiographic image as about a 100-micron crack at 22,000 cycles. The crack growth evolution is shown in figure C-51 as a sequence of microradiographic images.

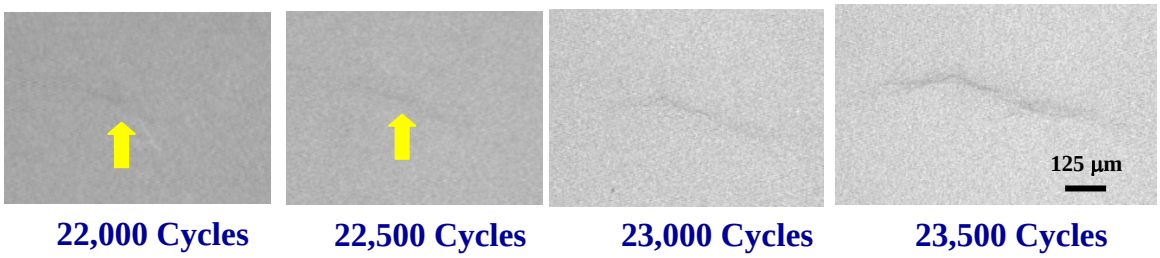

Figure C-51. Microradiographic Images Showing Evolution of Fatigue Crack in the Sample 2-SR2-4

The ultrasonic data for the test are summarized in figures C-52 and C-53. Quasi-static ultrasonic measurements (figure C-52) indicate crack initiation at about 19,000 cycles. One can see an ultrasonic reflectivity minimum between 22,000 and 23,000 cycles, which may be attributed to wave interference at this crack size. This is followed by catastrophic crack growth during the last 1000 cycles. The signals were acquired during the quasi-static part of the measurements at different loads (maximum, middle, and minimum). The top and bottom rows represent normalized crack and reflector reflections, respectively. The left column depicts data obtained

during the loading part of the cycle, whereas the right column shows data measured during unloading. The left column dashed lines indicate crack initiation from ultrasonic data at about 19,000 cycles. For the comparison, the right column dashed lines correspond to crack detection from microradiographic images. Little difference can be seen in reflection amplitudes at different load levels and between loading and unloading parts of the cycle. Modulation measurements are shown in figure C-53. Strong modulation is shown for the minimum fatigue load in ranging from 20,000 cycles to failure (top row of the figure, crack modulation index). It occurs due to crack presence at this stage of fatigue: a small load is required to open the crack and cause modulation. Higher loads keep the crack fully open under modulation force, thus eliminating modulation of the reflected signal. Significant modulation is also observed at around 10,000 cycles (the modulated reflection signature is localized to the vicinity of the same crack). This modulation possibly indicates some damage initiation; the modulation occurs only at the maximum load. Because the damage at this stage is very small and has low compliance, a maximum fatigue load is required to cause ultrasonic modulation of the reflected pulse (recall the maximum fatigue stress is 0.95 of the yield stress).

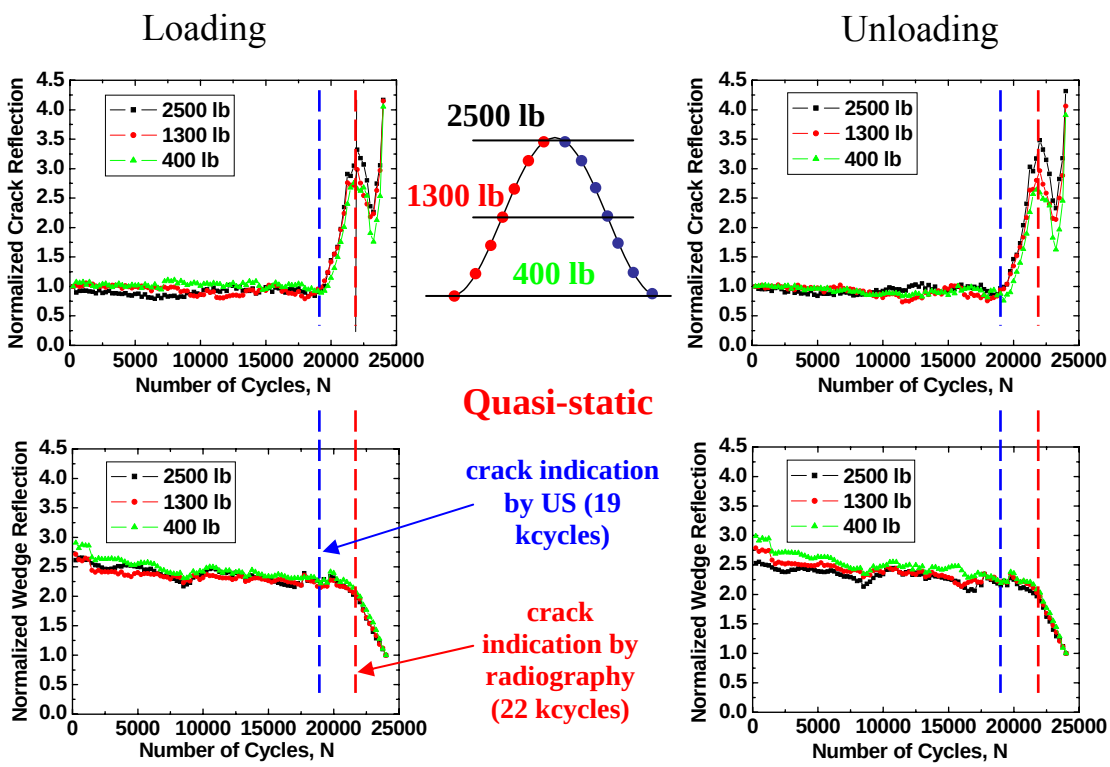

Figure C-52. Change in Ultrasonic Signal Amplitude During Interrupted Fatigue Test of Sample 2-SR2-4

Absence of useful modulation results from the reflector (bottom row in the figure C-53) can be explained by wave attenuation due to the large distance traveled by the signal. The signals were acquired during the modulation part of the measurements at different loads (maximum, middle, and minimum). The top and bottom rows represent normalized crack and reflector modulation

index, respectively. The left column depicts data obtained during loading, whereas the right shows data measured during unloading.

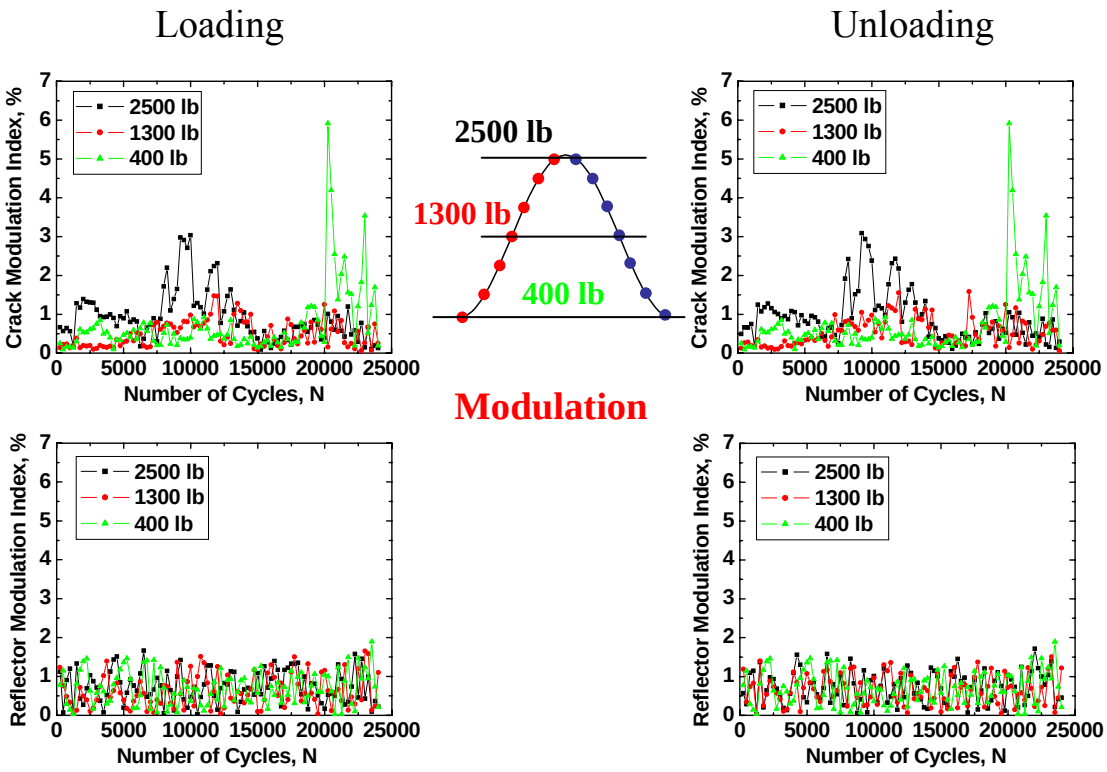

Figure C-53. Change in Ultrasonic Modulation Index During Interrupted Fatigue Test of the Sample 2-SR2-4

The size of the fatigue crack was determined from radiographic images. Only 0° exposure produces as indication of a microcrack in the images. The crack is too closed to be detected at a 90° x-ray exposure. The results of radiographic crack size measurements are presented in figure C-54 (crack size versus number of cycles) and figure C-55 (crack growth rate versus crack size). As one can see from the figures, the crack grows during the last 4000 cycles with virtually constant rate, which lies between 0.2 and 0.3 μm/cycle.

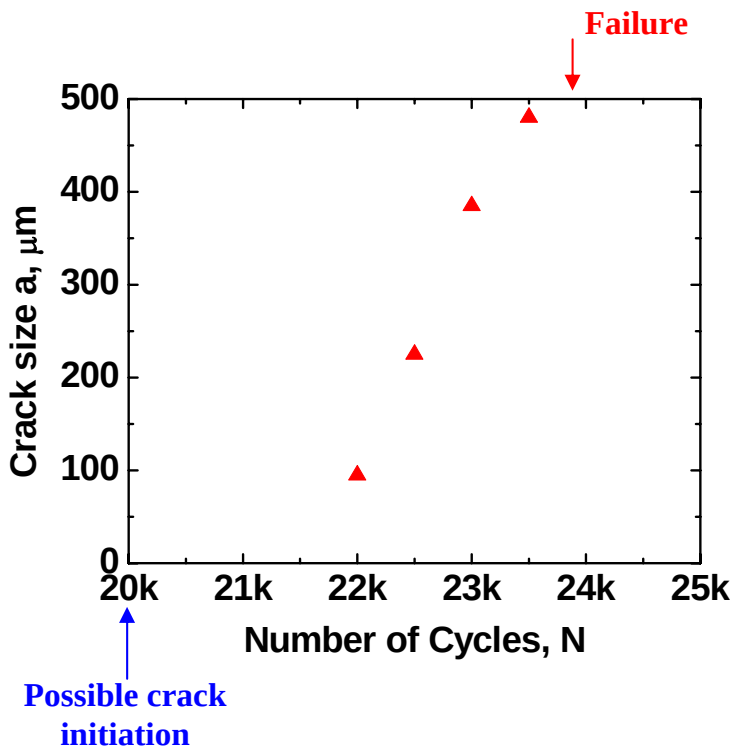

Figure C-54. Crack Size Versus Number of Cycles for the Fatigue Crack in Sample 2-SR2-4

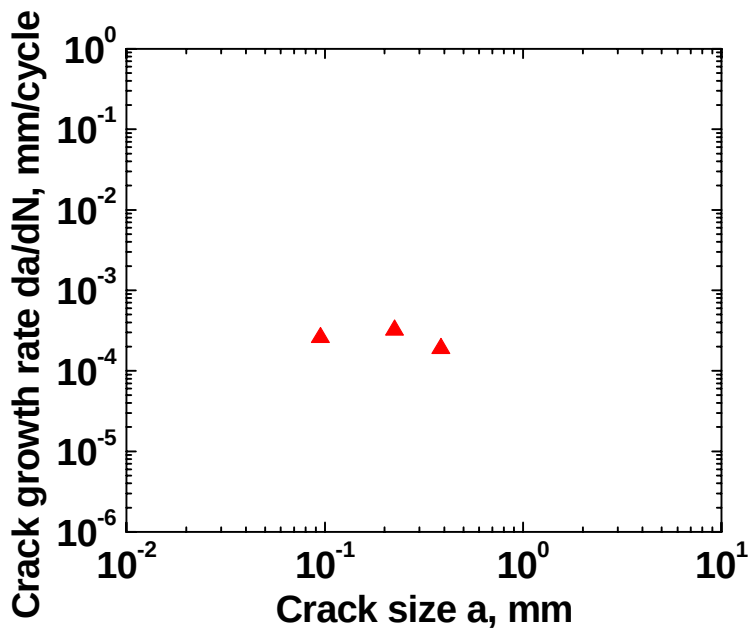

Figure C-55. Crack Growth Rate Versus Crack Size for the Fatigue Crack in Sample 2-SR2-4

C.3.3 CRACK GROWTH RATE.

The measurements described in section C.3.2 were performed for several samples under dwell and fatigue conditions. The microradiographic crack sizing data were used to obtain small crack growth rates, as shown in figure C-56 by the solid points. The dwell-fatigue data are shown by solid squares and cyclic fatigue by solid circles. The rates for small dwell-fatigue cracks are one to two orders of magnitude higher than those for small cyclic fatigue cracks.

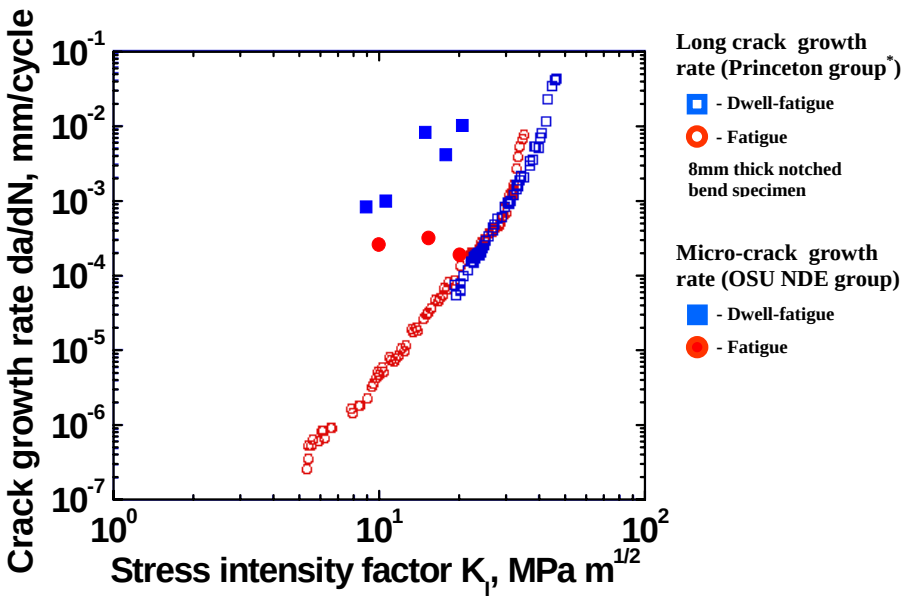

*** - W. Shen, W.O. Soboyejo, A.B.O. Soboyejo: Mechanics of Materials, Vol 36, 2004, pp. 117-140.**

Figure C-56. Comparison of Crack Growth Rate for Microcracks in Ti-6240 Alloy With Large Cracks

In contrast to the small crack behavior, the rates obtained by the Princeton's Soboyejo group for large dwell and cyclic fatigue cracks are identical[2]. The large crack growth rates are also shown in the figure (open squares and circles). Dwell-fatigue tests for large cracks were performed at the same stress level (869 MPa) as in OSU experiments for small cracks. However, for cyclic fatigue, a much larger range of stresses was used to obtain the larger range of crack growth rates (the lowest stress level was slightly above a threshold determined by such a level of stress-intensity factor that no crack initiation occurred for about 10^6 cycles). After reaching the threshold, different levels of constant load were applied to cover the full range of crack growth. The reason for the lower rate growth of large cyclic fatigue cracks was because part of the cyclic fatigue data was below the rate for small fatigue cracks that were obtained at high levels of stress. The rate of small-to-large cyclic fatigue crack evolution exhibits typical small and large crack behavior if one considers the same stress level of the cyclic fatigue stress, while the rate for the small dwell-fatigue cracks is much higher.

[2] Shen, W.O. Soboyejo, A.B.O. Soboyejo: W. Mechanics of Materials, Vol. 36, 2004, pp. 117-140.

C.3.4 EFFECT OF DWELL TIME ON SAMPLE FATIGUE LIFE.

To investigate the effect of dwell time on fatigue life of Ti-6242 samples, dwell-fatigue tests were performed on flat samples for different dwell (holding) times: 2 minutes, 30 minutes and holding the sample at constant load to failure (creep test). Figure C-57 shows the number of cycles to failure (N) versus dwell time of a single cycle (T_d) in log-log scale. The estimated crack initiation times determined from the ultrasonic reflection and modulation measurements for the same samples are also shown (solid triangles).

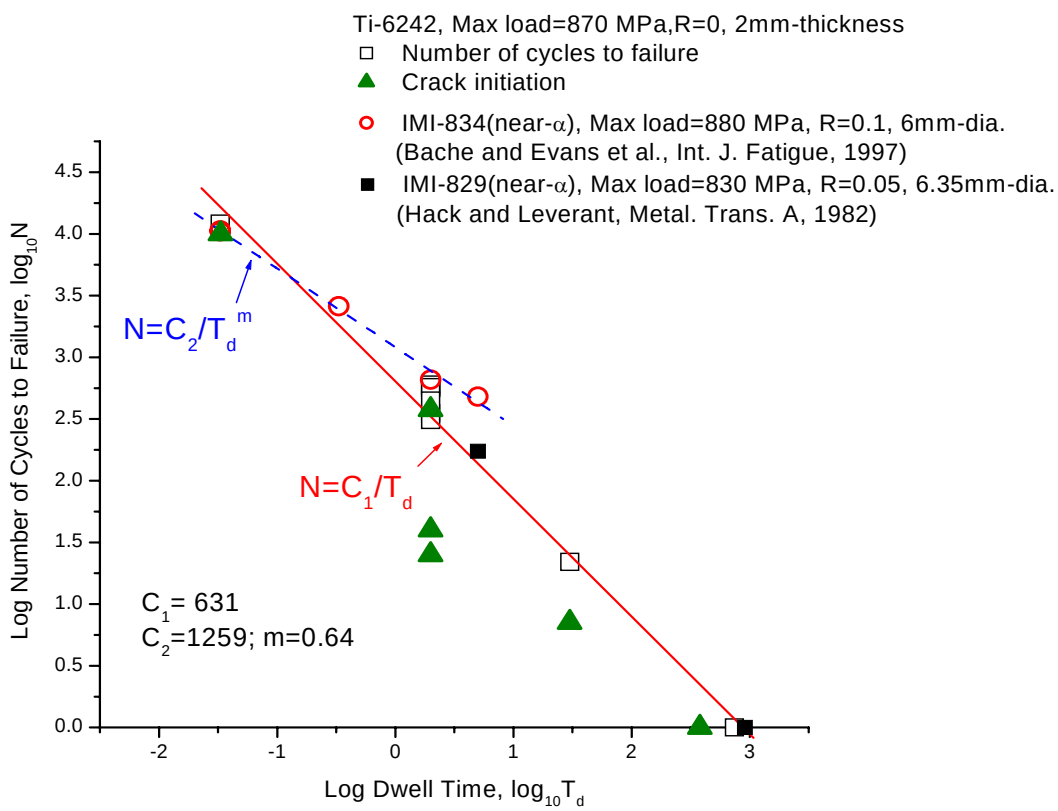

Figure C-57. The Effect of Dwell Time on Sample Fatigue Life (Log of number of fatigue cycles to failure is plotted versus log of dwell time.)

The results show that the total dwell time is nearly constant, that is, $N*T_d$=constant, where (N) is the number of cycles to failure and (T_d) is the dwell time of a single cycle. Analysis of the results in the available literature for near-α IMI-829 alloy shows that they exhibit similar behavior. The results for near-αIMI-829 tested under maximum dwell load 830 MPa and R=0.05 with 6.35-mm-diameter cylindrical samples[3]. and near-α IMI-834 tested under maximum dwell load 880 MPa and R=0.1 with 6-mm-diameter cylindrical samples[4] are shown in the figure together with OSU data.

[3] Hack and Leverant, Metal. Trans. A, 1982
[4] Bache and Evans Int. J. Fatigue, 1997

It is, of course, expected that the total dwell-fatigue life depends on the sample microstructure, shape, and thickness. The mechanical tests described above were performed on 1.9-mm-thick, 6.35-mm-wide flat samples with microstructure 2. In these samples, the size of the faceted areas is comparable to the sample thickness, and as a result, (see figure C-44), the small dwell-fatigue crack grows rapidly to half of the sample thickness and after that the sample catastrophically failed at several additional cycles. For this microstructure and sample thickness, the failure is associated with small crack growth in the faceted area at maximum holding load. Therefore, the failure mechanism is essentially the same for dwell-fatigue and creep tests, thus the total life time is nearly the same for dwell-fatigue and creep samples. For larger samples, the result will be different. After a small crack initiated in the dwell-fatigue test grows larger than the faceted area, the crack propagation mechanism changes to that of fatigue (the growth rate for large dwell fatigue and fatigue cracks is the same, see figure C- 56). However, the small crack initiated in creep test may be arrested outside the faceted area or will continue to grow by the creep mechanism, which is much slower. Therefore, the life of the larger sample at creep test may be longer than at dwell-fatigue test.

C.4 SUMMARY.

To characterize dwell-fatigue crack initiation and small crack growth, a large number of dwell-fatigue, cyclic fatigue, and creep experiments were performed on a titanium (Ti-6242) alloy flat samples (microstructure 2). To monitor crack initiation and small crack growth an in situ ultrasonic crack monitoring system were developed. Secondary cracks were detected and located using ultrasonic and microradiographic methods to further characterize of the microstructures in the vicinity of the cracks.

Dwell-fatigue and cyclic fatigue crack growth rates for small cracks were obtained from interruption experiments in which crack initiation and growth were monitored by an ultrasonic method. Cracks, at different stages of fatigue, were sized by a microradiographic method. It was found that the rates for small dwell-fatigue cracks were one to two orders of magnitude higher than those for small cyclic fatigue cracks. This small crack growth behavior is greatly different from that of long cracks which exhibit identical rates for dwell and cyclic fatigue. The rate of small-to-large cyclic fatigue crack growth exhibits typical small-to-large crack behavior if one considers the same stress level of the cyclic fatigue stress for both small and large.

The effect of dwell time on fatigue life of Ti-6242 was investigated for dwell times of 2 minutes, 30 minutes, and in a creep experiment). It was found that for the flat samples tested (1.9 mm thick, microstructure 2) the total dwell time to failure was nearly constant for all experiments.

APPENDIX D—SECONDARY CRACK CHARACTERIZATION

Understanding and predicting failure due to dwell fatigue has been very difficult because of the nature of cracks, which initiate below the surface and appear to be closely related to the local, intrinsic microstructural features [D-1-D-8]. The possibility of obtaining two-dimensional, let alone three-dimensional (3D), microstructural information about crack initiation regions under dwell-fatigue conditions was an extremely tedious task involving successive mechanical polishing steps. Polishing and serial sectioning techniques are presently being developed using a dual-beam focused ion beam (FIB) to expose crack initiation regions and allow for 3D characterization of the crack geometry relative to the existing microstructure and local microtexture of the crack region. Techniques are also being developed to use FIB to also create transmission electron microscopy (TEM) foils from potentially interesting areas around the crack regions to study deformation processes. Orientation Imaging Microscopy (OIM) analysis has revealed that fatigue cracks generated during dwell testing are invariably aligned parallel to basal planes, even when the basal plane is not oriented precisely normal to the stress axis. Cracks span microtextured regions of similar basal-plane alignment. The bounding regions, which may be either the locations of crack initiation or arrest, typically have large misorientation relative to the cracked regions and can be oriented favorably for both basal or prism slip. These results support the hypothesis that cracking is caused by the time-dependent load-shedding from favorably oriented to unfavorably oriented regions. However, the possible crystallographic scenarios for which cracking occurs appear to be larger in number than previously suspected. In order to further characterize the secondary cracks and why they arrest, TEM foils were extracted from regions surrounding a secondary crack using FIB.

D.1 METHODS.

A secondary crack was located by x-ray and acoustic emission data and subsequently polished to the surface of the sample using standard metallographic polishing procedures. The final polish was 0.05-μm colloidal silica. OIM was performed using Electron Backscatter Diffraction on an FEI XL-30 ESEM. Site-specific TEM samples were extracted using an FEI dual-beam FIB (FEI DB-235) outfitted with an OmniProbe, an in situ plucking device. This procedure involves preferentially removing material away from the location of interest, soldering the OmniProbe onto the TEM foil, attaching the foil to a TEM grid, and cutting away the OmniProbe. This is depicted in figure D-1. TEM foils were extracted from regions ahead of each crack tip, in the wake of the crack, along the boarder of the soft and hard microtextured regions and far away from the crack, refer to figure D-2. TEM samples were studied using an FEI CM 200 operating at 200kV with an LaB_6 source.

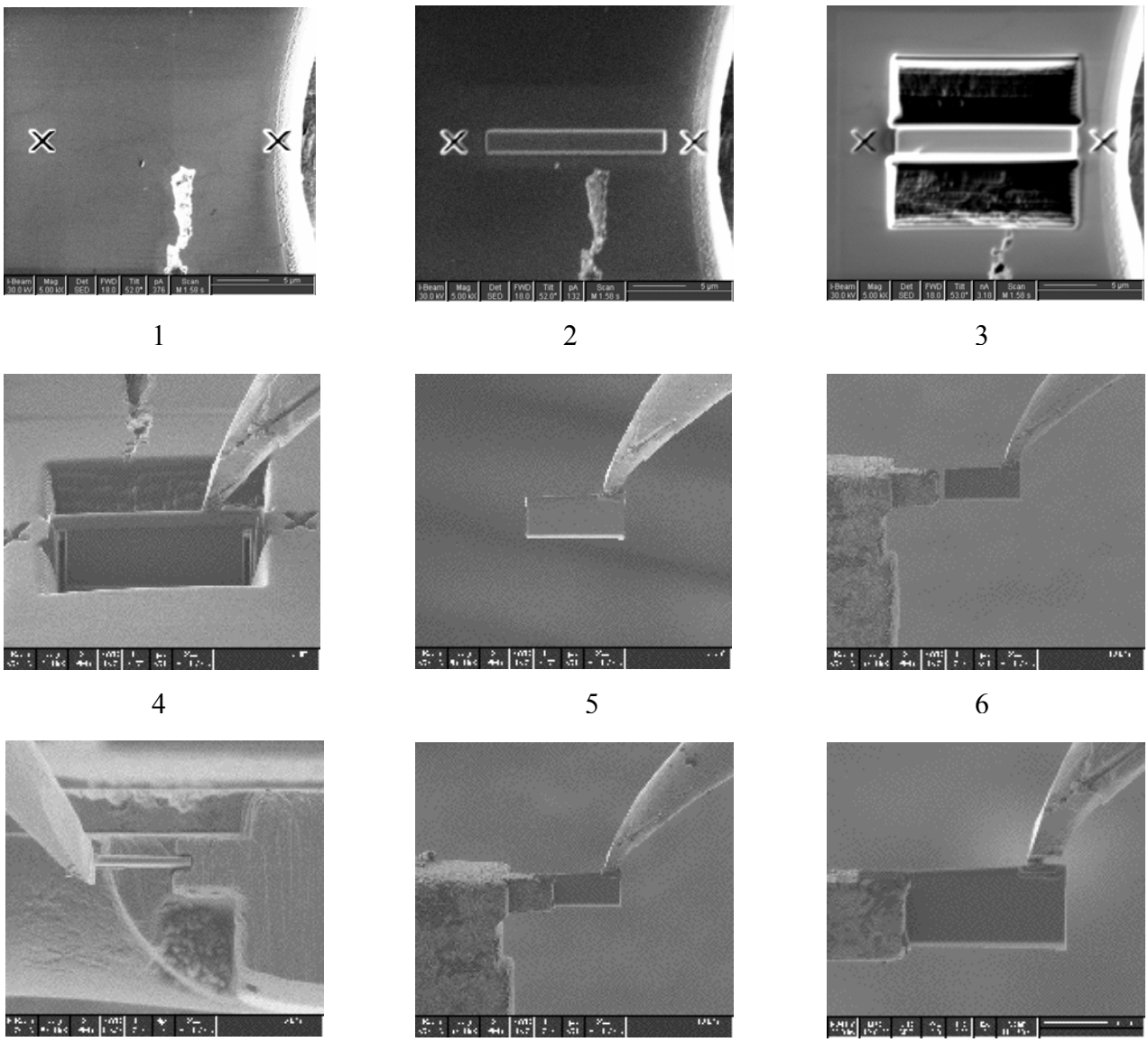

Figure D-1. Steps Involved in Extracting a TEM Foil (1) Image Recognition Marks in Front of Crack Tip, (2) Protective Platinum Cap, (3) Remove Material Around Foil, (4) Thin and Attach OmniProbe Using Platinum, (5) Foil Attached to OmniProbe, (6) Lining Up the Foil With the TEM Grid, (7) Foil Lined Up and in Contact With the Grid, (8) Soldering the Foil Onto the Grid Using Platinum, and (9) Cutting Away the OmniProbe

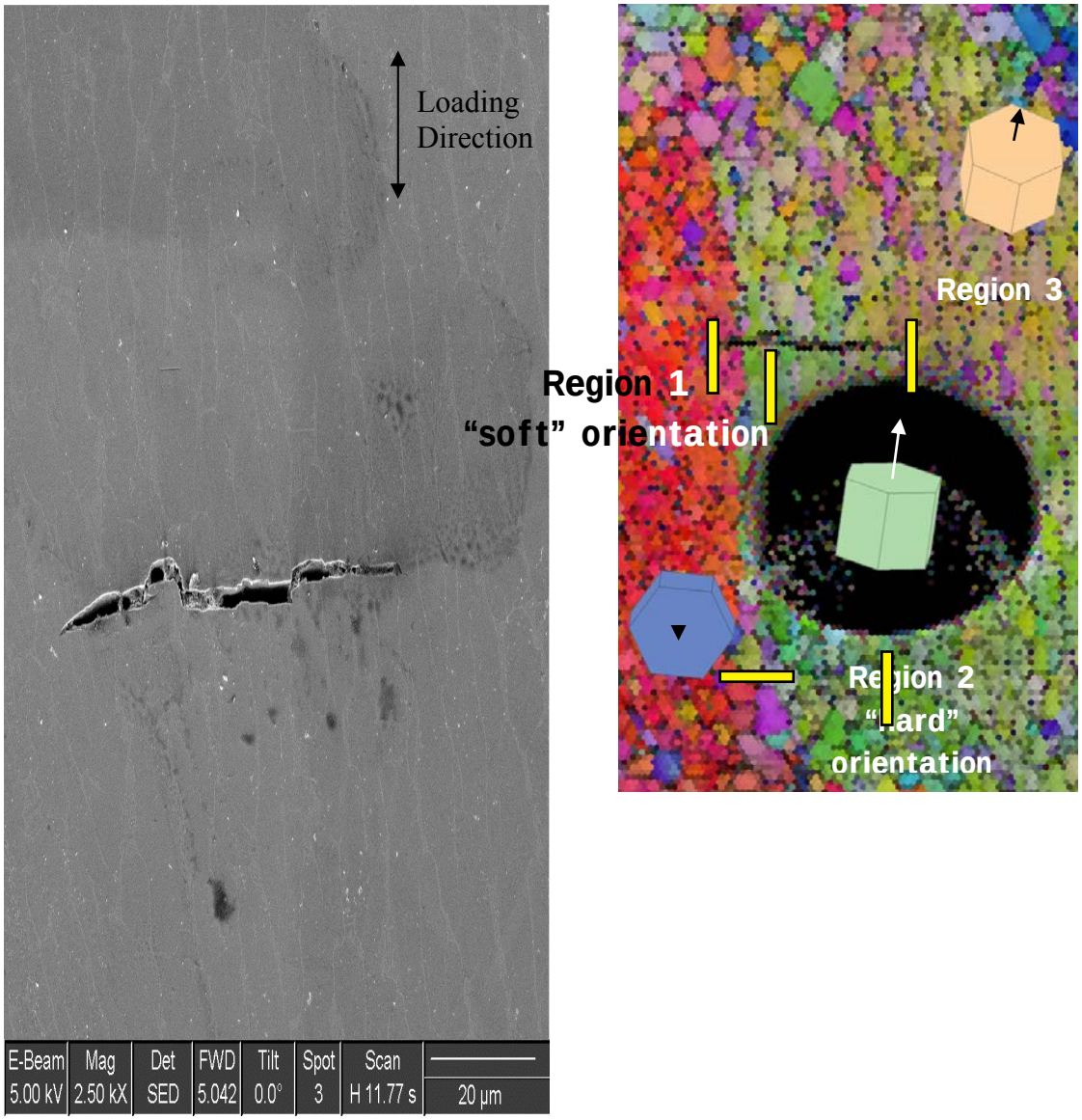

Figure D-2. SEM Image of a Secondary Crack Lying on the Basal Plane
(The corresponding OIM of the same crack, indicating the locations TEM foils were extracted.)

D.2 RESULTS.

D.2.1 ORIENTATION IMAGING MICROSCOPY OF SECONDARY CRACK REGIONS.

With knowledge of secondary crack locations from the x-ray microradiography, secondary crack regions have been successfully revealed using the grinding polishing techniques. The techniques for using the FIB to reveal the crack regions have not been fully developed. Sample geometry, amount of material to mill per sectioning step, and OIM capabilities in the FIB are just some of the issues that are currently being addressed in ongoing work. Once these issues and others are

addressed, it is believed that the FIB will allow for new 3D characterization techniques that will expand knowledge of the microstructural and crystallographic relation to crack initiation under dwell conditions.

Several secondary SEM images and corresponding OIM maps of the secondary crack regions that have been studied are shown in figures D-3 through D-5. In the initial microradiographic examination of the crack region (specimen: 2-SR1-2B) shown in figure D-3(a), only one crack was detected. As shown in figure D-3(a) though, there are at least two cracks present. This was also the case in another dwell-fatigue-tested specimen (specimen: 2-SR1-1A) in which other crack(s) (figure D-5) were discovered during examination of a crack region (figure D-4) detected by microradiography. In the three crack regions examined, cracks appear to have initiated and grown in the α phase only. The cracks also appear to be perpendicular and angled approximately 40°-50° with respect to the loading direction. The OIM maps in figures D-3 through D-5 display different colors for different orientations with respect to the [0001] pole of each grain. Each OIM was created using a background scan of 128 frames with a 16-frame average and a time delay of 600 ms between scans.

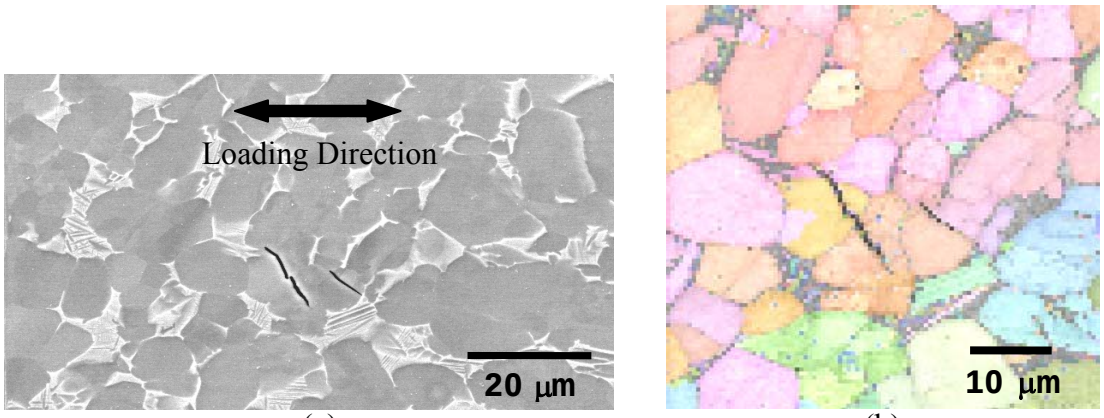

(a) (b)

Figure D-3. (a) Secondary SEM Image of Secondary Crack Region in Cold Dwell-Fatigued Ti-6242 Specimen 2-SR1-2B Showing at Least Two Cracks and (b) Corresponding OIM of Secondary Crack Region

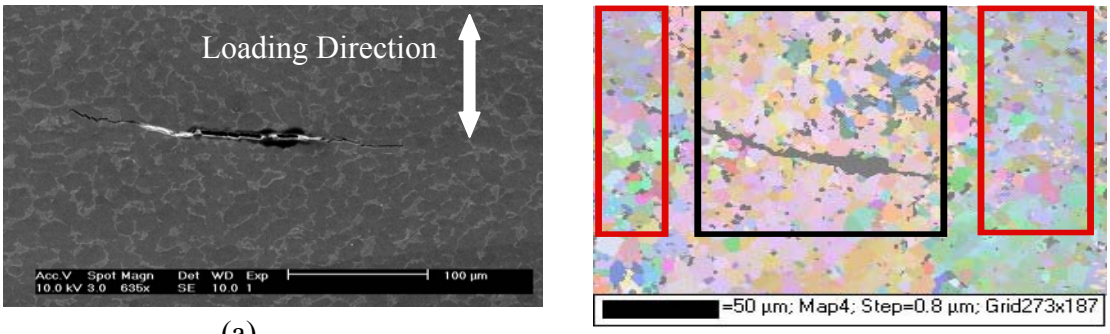

(a) (b)

Figure D-4. (a) Secondary SEM Image of Secondary Crack Region in Cold Dwell-Fatigued Ti-6242 Specimen 2-SR1-1A and (b) Corresponding OIM of Secondary Crack Region

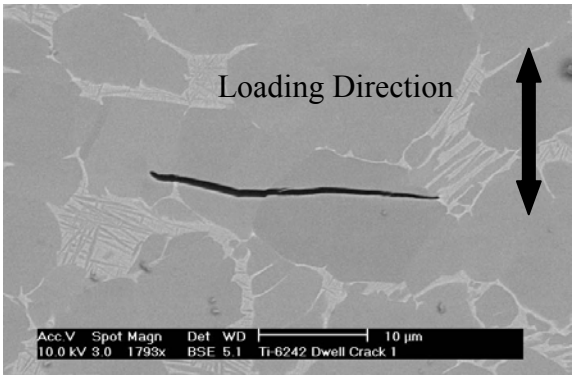

(a)

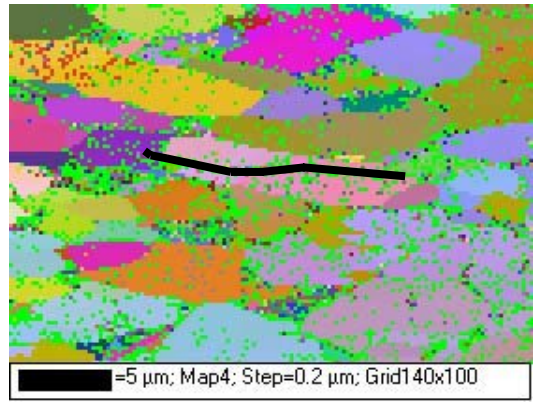

(b)

Figure D-5. (a) Secondary SEM Image of Secondary Crack Region in Cold Dwell-Fatigued Ti-6242 Specimen 2-SR1-1A and (b) Corresponding OIM of Secondary Crack Region (Each color represents a different orientation with respect to the [0001] pole.)

Pole figures for all the grains located near all the cracks were created from the OIM information obtained. Figure D-6 shows the OIM map from figure D-3(a) with corresponding pole figures. The pole figures show that the lengths of the cracks are oriented perpendicular to the [0001] pole as previously suggested in published literature [D-1-D-10]. The pole figures of the other two crack regions examined (figures D-7 and D-8) show similar results. A comparison of the pole figures obtained for grains directly across the crack on the left in figure D-6 shows that the [0001] poles for each grain are at the same orientation, but with a rotation present about this pole. The rotation was found to be approximately 20° about the [0001] pole when the $\{10\underline{1}0\}$ pole figures were compared. This, however, was not present in the other two crack regions examined.

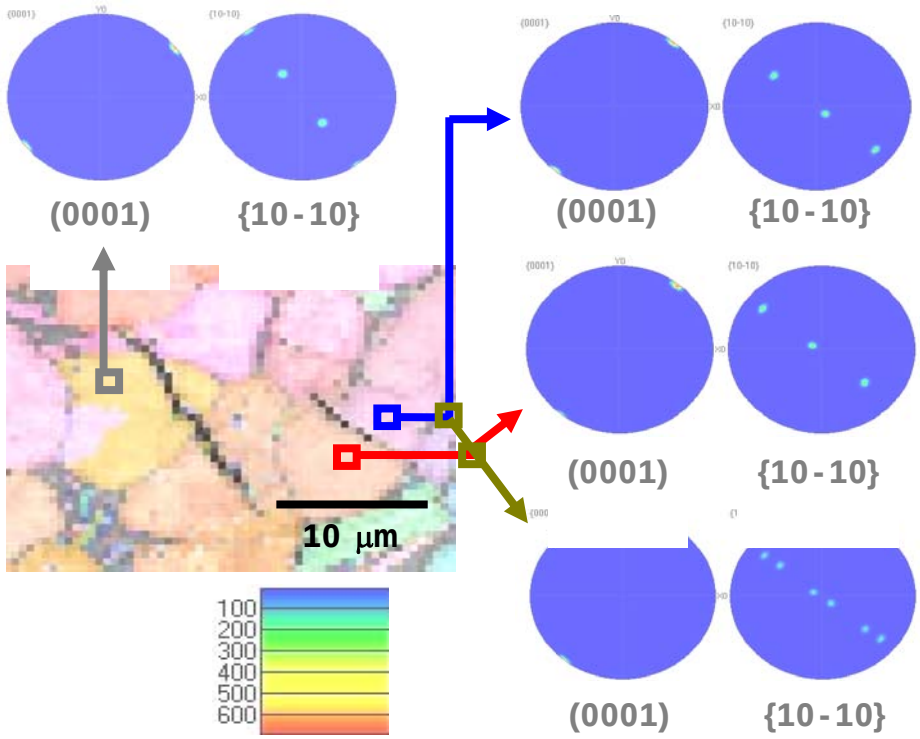

Figure D-6. Pole Figures for Specified Areas Near Two Secondary Cracks of Cold Dwell-Fatigued Ti-6242 Sample (OIM Map of Figure D-3(a)) (All three areas examined here show that the [0001] pole is perpendicular to the length of the crack. The pole figures for the crack on the right of the OIM map shows that the grains across the crack are similarly oriented, but with an approximate 20° rotation along the [0001] pole.)

The OIM map in figure D-4(b) shows distinct regions of similarly oriented grains as marked by the red and black rectangles. The crack appears to be completely in the black rectangle and bounded by the red rectangles on both sides. The pole figures of these regions shows that the red rectangles are oriented such that the basal planes of the grains are parallel to the tensile direction, while the basal planes of the grains in the region marked by the black rectangle seemed to be angled approximately 30° from normal to the tensile direction. Similar results are shown for the other crack examined in this specimen (figures D-5 and D-8). This crack is bounded by grains that are oriented such that the basal planes of the grains are parallel to the tensile direction, while the basal planes of the grains that contain the crack seem to be angled approximately 5°-15° from normal to the tensile direction. This is not consistent with previously published literature in which the grains containing the crack had basal planes oriented normal to the tensile direction with the grains ahead and behind the crack having basal planes oriented 45° to the tensile direction [D-1, D-2, and D-4-D-7].

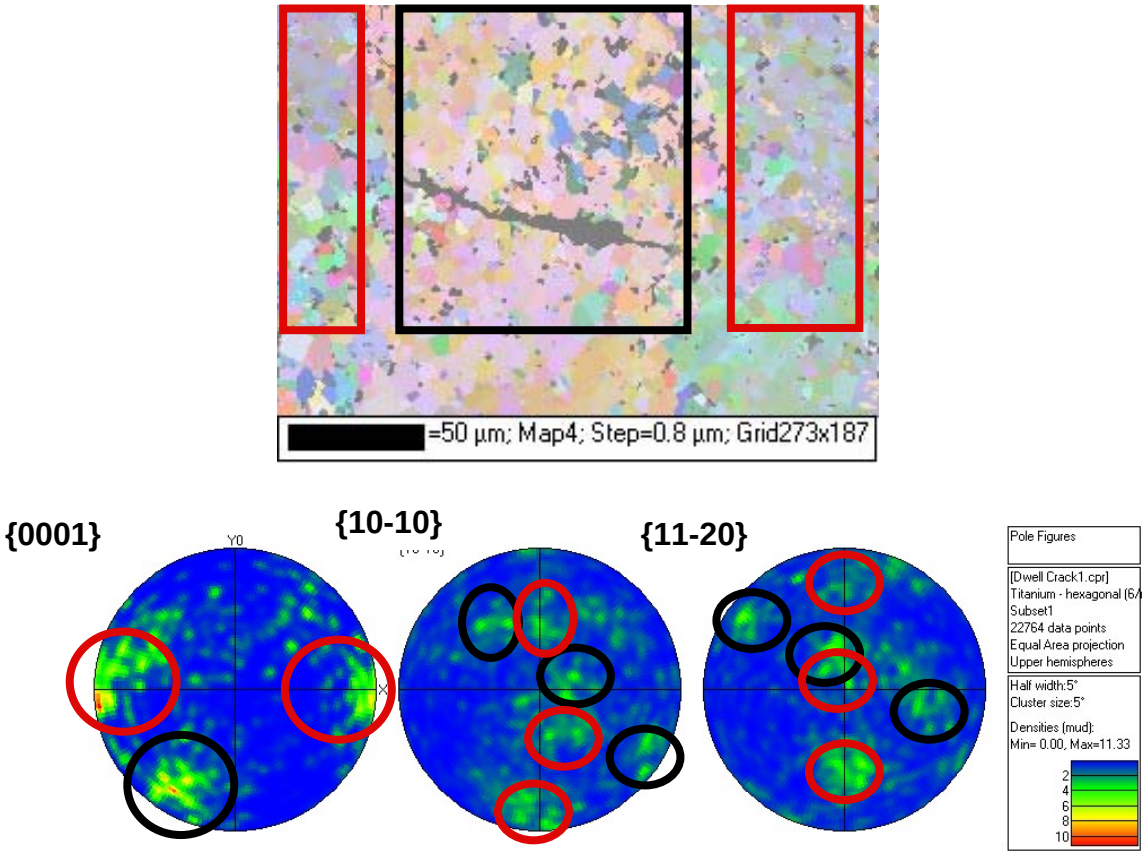

Figure D-7. Pole Figures of Regions of a Secondary Crack (figure D-4) of Cold Dwell-Fatigued Ti-6242 Specimen 2-SR1-1A (Regions defined by red rectangles in the OIM map correspond to the red circles in pole figures. Regions defined by a black rectangle in the OIM map corresponds to the black circles in pole figures. The regions of grains defined by red have basal planes oriented parallel to the tensile direction. The region of grains defined by black has basal planes oriented 30° from normal to the tensile direction with the basal planes parallel to the length of the crack.)

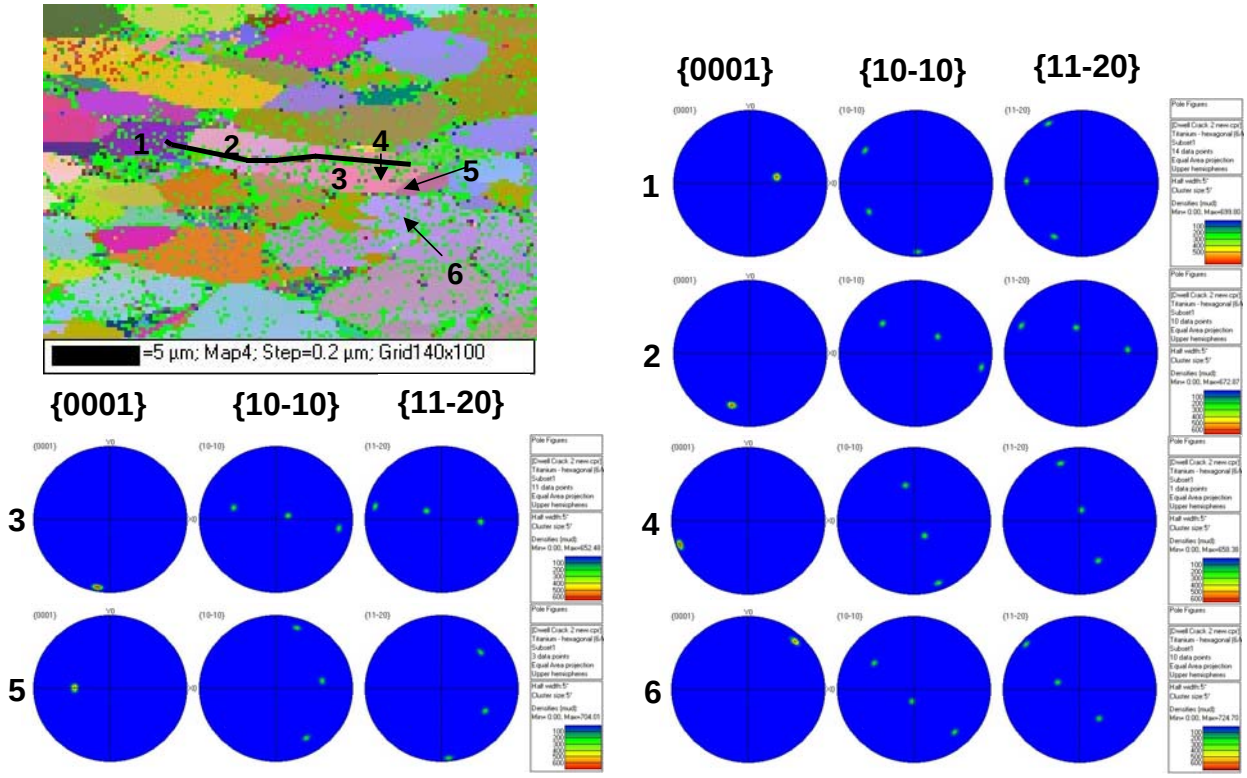

Figure D-8. Pole Figures of a Secondary Crack (figure D-5) of Cold Dwell-Fatigued Ti-6242 Specimen 2-SR1-1A (The pole figures of each grain numbered correspond to the grains numbered in the OIM. The grains (1 and 5) ahead and behind the crack have basal planes oriented parallel to the tensile direction. The grains containing the crack (2 and 3) have basal planes oriented 5°-15° from normal to the tensile direction with the basal planes parallel to the length of the crack.)

Slip on the basal planes oriented 45° to the tensile direction is preferred (based on Schmidt factors), and it is stated by Evans, et al. [4 and 5] and Woodfield, et al. [6 and 7] that dislocations pileup at the grain boundaries and stress off-loading from the grains with basal planes oriented 45° to the tensile direction (favorably oriented for slip) to grains with basal planes oriented normal to the tensile direction (unfavorably oriented for slip) occurs. In all previous reports, only slip on the basal planes is discussed. In the case of the two crack regions shown in figures D-4 and D-5, the basal planes of the grains ahead and behind the cracks are not preferably oriented for basal slip. They are, however, preferably oriented for prism slip, as shown in figures D-9 and D-10. These figures show the Schmidt factors calculated for all the different types of slip in α titanium. Based on these results, it is believed that slip, not only on basal planes but also on prism planes, can create the dwell-fatigue cracks that are being examined. In the case of prism planes, dislocations would pileup at the grain boundaries and stress off-loading from the grains with prism planes favorably oriented for slip (as shown in figures D-9 and D-10) to grains with prism planes unfavorably oriented for slip.

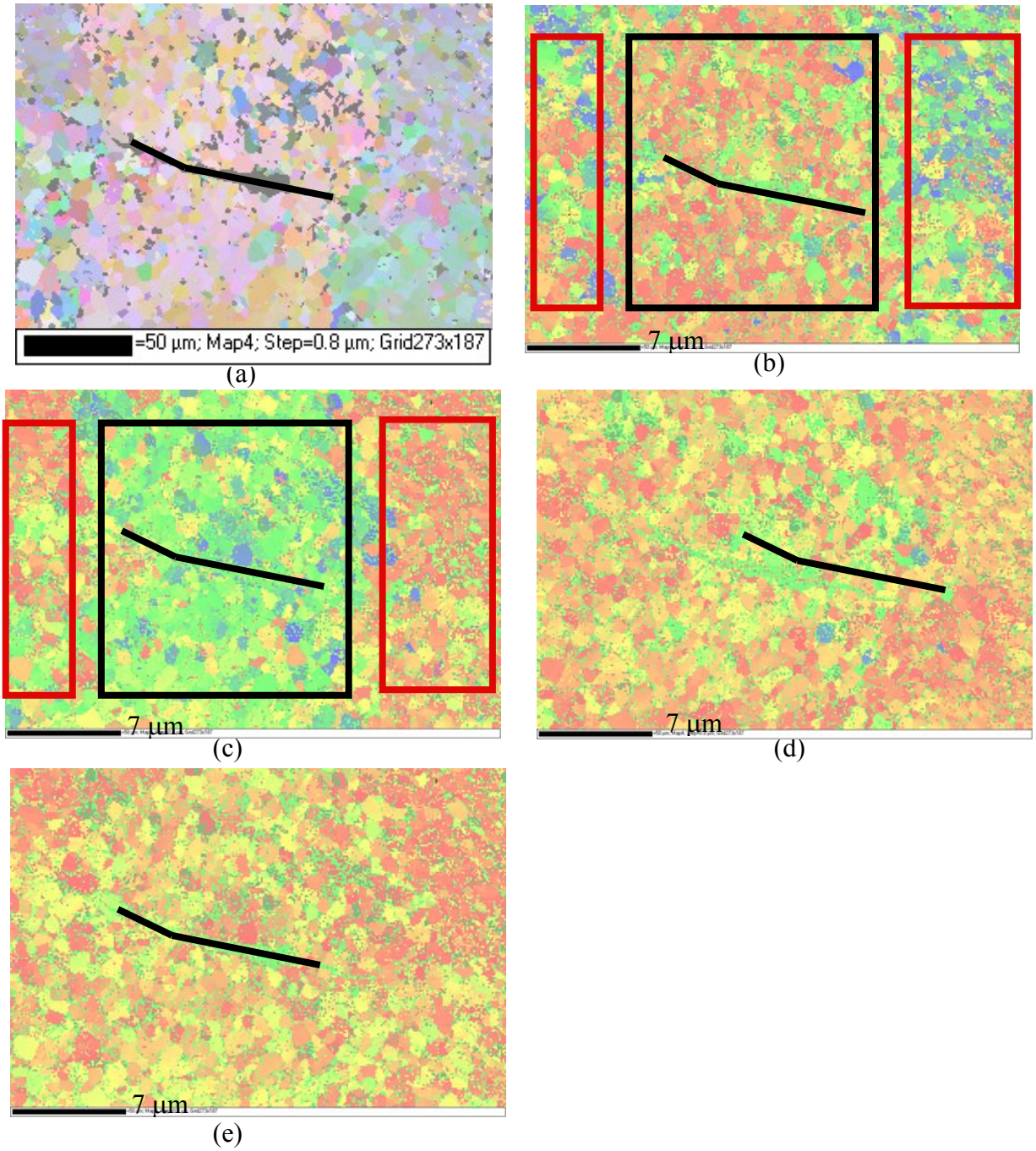

Figure D-9. Schmidt Factor Calculations of Various Slip Systems in α Titanium for Secondary Crack Region Shown in Figures D-4 and D-7 (a) OIM, (b) Basal Slip, (c) Prism Slip, (d) Pyramidal Slip, and (e) <**c**+**a**>-Type Slip

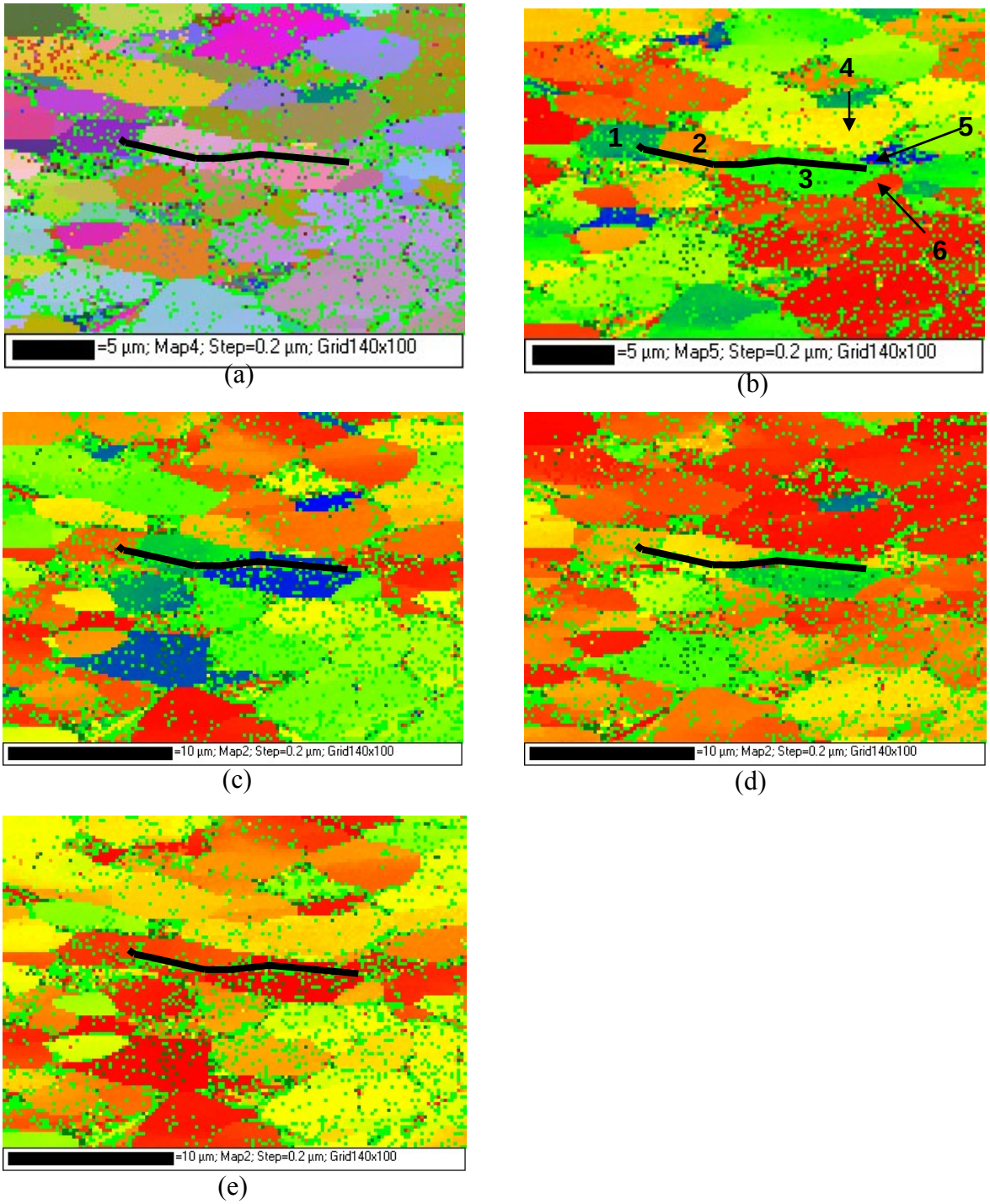

Figure D-10. Schmidt Factor Calculations of Various Slip Systems in α Titanium for Secondary Crack Region Shown in Figures D-5 and D-8 (a) OIM, (b) Basal Slip, (c) Prism Slip, (d) Pyramidal Slip, and (e) <**c+a**>-Type Slip

D.2.2 THREE-DIMENSIONAL CHARACTERIZATION AND TEM FOIL PREPARATION OF SECONDARY CRACK REGIONS USING FIB.

The initial thought of using FIB was to create TEM foils of potentially interesting areas around the crack regions to study deformation processes. This is a new area of use for a FIB since it has only recently been used to create TEM foils from bulk metallic samples [D-9 and D-10]. In fact, FIB has been used for years to study semiconductors, but only recently for studying metals in general.

As the first crack region of interest in figure D-3 was initially having material milled away, the microstructure and new cracks that were revealed brought the idea of the possibility for 3D characterization, as discussed in section D.2.1. The new cracks, revealed from initial FIBing, were unable to be characterized because of their location and sample geometry. A crack region from a different dwell fatigue-tested specimen (specimen: 2-SR1-1A) was created such that the crack could be examined. A movie was created using the SEM images obtained. The preliminary results seem to be promising but more work needs to be completed including implementing OIM into the serial sectioning/movie process.

The original intentions of creating TEM foils was also successfully completed. Figures D-11(a), (b), (c), and (d) show some of the steps that were taken to create two TEM foils. Figures D-11(a) and (b) are from the work done on the crack on the left in figure D-3(a), while D-11(c) and (d) are from work done on the crack on the right of figure D-3(a). Initially, platinum was laid over the specific area of interest to protect it from ion damage. The platinum did not initially fill into the crack, but by the end of the foil creation process the crack appeared to be filled. This is thought not to introduce any new deformation because the stresses induced would not be large enough. Trenches were then created on both sides of the area of interest (figure D-11(a)) and material was milled away at different rates to create a fine polish on the two newly created surfaces (figure D-11(c)) and the desired thickness for TEM analysis (less than 0.3 μm). The material along the bottom and on one side of the area of interest was then milled away (figures D-11(b) and (c)) in that order to ensure that there were not any significant stresses on the material that cause it to break or introduce new deformation. The material on the other side was then milled away and the newly created TEM foils were lifted and plucked using an electrostatic probe.

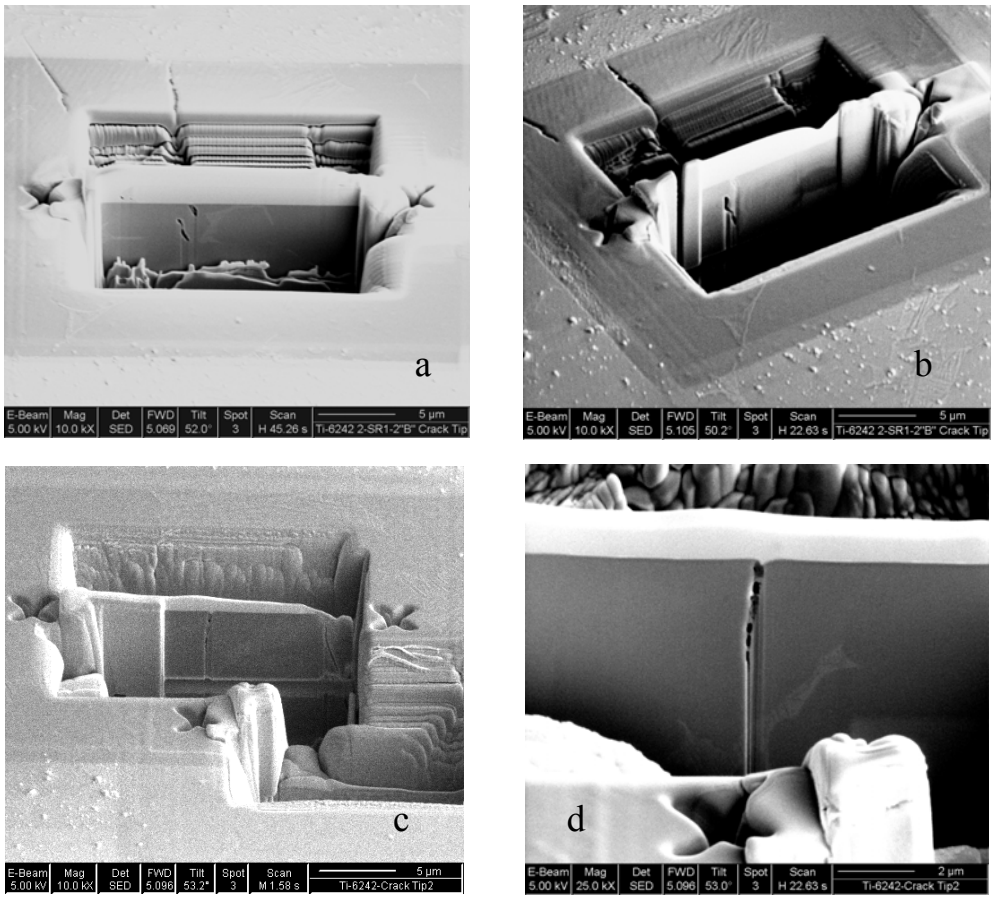

Figure D-11. Scanning Electron Microscope Images of TEM Foil Preparation of the Two Cracks Shown in Figure D-3 Using an FIB

Although using the FIB to create TEM foils of potential areas of interest was successfully completed, there are still some concerns that are being addressed. The TEM foils made so far have been thin enough for TEM analysis, but extraction of one sample was unsuccessful. The crack(s) in the TEM foils are weak links, and as such, the foils can break along them easier, particularly for very thin foils. The breaking of the foil along the crack(s) is not thought to introduce new deformation because the stresses induced would not be large enough. Another concern currently being addressed is the imaging capability of the TEM foils obtained. As stated before, this is a new technique, and as such, the elimination of ion damage to the TEM foils is a concern. As will be seen in section D.2.3, the TEM images are good to study the deformation processes from dwell conditions, but they could be significantly better. The elimination of the ion damage would ensure that no significant information is unrevealed.

D.2.3 TEM OF SECONDARY CRACK REGIONS.

Two TEM foils were successfully created using FIB, but only one was studied. An overall view of the TEM foil of the crack on the left in figure D-6 is shown in figures D-12(a) and (b). As previously mentioned, the entire foil was unable to be plucked. The side of the crack that was obtained was good enough to study the deformation introduced under dwell conditions. In figure D-12(b), the yellow numbers show the five different grains near the crack surface that are separated by low angle grain boundaries. It can be seen that there are at least five different grains separated by low-angle grain boundaries. The misorientations of the grains, with respect to each other, is still being studied. The diffraction patterns of each grain were studied to ensure that each of the five grains were still α phase. The two white lines show the transformed β region (figure D-5(d)). Since in this case the crack surface was 90° to the polished surface, the crack surface is perpendicular to the [0001] pole.

The initial thought, after looking at figure D-11(d) and D-12(b), was that this was a deep crack. A closer look at both images reveals that this deep crack could be at least two cracks that were separated before the FIBing process. This would agree with some of the TEM results obtained. The two possible crack regions are depicted by a red and blue oval in figure D-11(d). Measurements of these two possible crack regions using SEM/FIB and TEM images along with further examination of the region using the TEM is needed before it can be confidently stated that there were two crack regions and not one. However, it is felt that the following results will support the theory of a two-crack region.

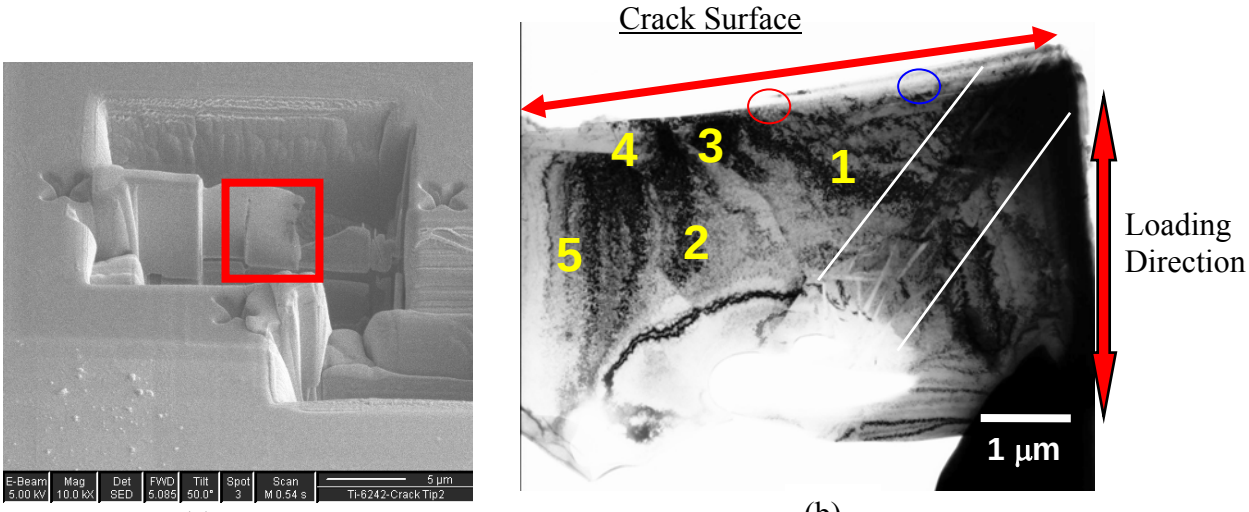

(a) (b)

Figure D-12. (a) SEM Image of the Original TEM Foil of the Crack on the Left in Figure D-3(a) (The Red Box Depicts the Part of the Foil That was Plucked, the Foil Broke Along the Crack (figure D-5(c) and (d).) (b) Bright Field TEM Image the Entire Foil Obtained as Shown in (a)

One of the possible two cracks begins or ends at the grain boundary between grains 1 and 3 as is shown by a red oval in figure D-12(b). The deformation observed in this region was unique compared to what was observed in the other grains. Numerous amounts of **<c+a>**-type screw dislocations were observed throughout all five grains. Figure D-13 shows some representative **<c+a>**-type screw dislocations observed in the region shown by the blue oval in figure D-12(b). These dislocations were determined to be either <11$\underline{2}$3> or <11$\underline{2}\underline{3}$> slip. In the region near the possible crack tip between grains 1 and 3 (shown by red oval in figure D-12(b)), arrays of **<a>**-type screw dislocations were observed. Figures D-14(a) and (b) show some representative arrays of these dislocations. These dislocations were determined to be [11$\underline{2}$0] type on (0001). These results are similar to those published by White, et al. [D-8].

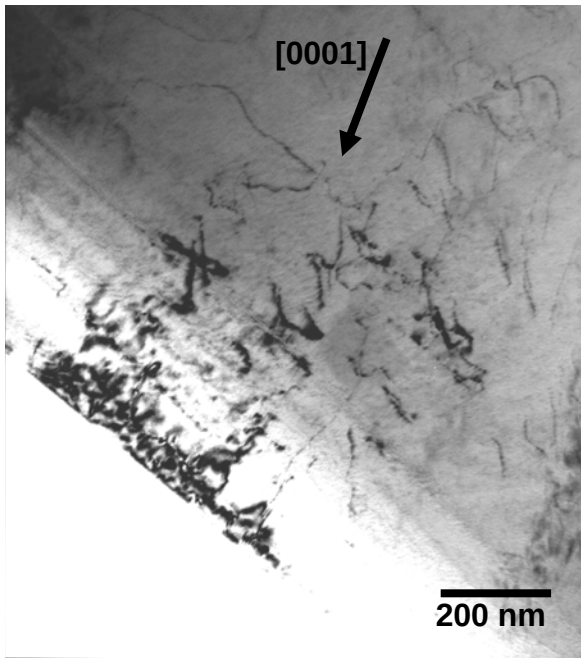

Figure D-13. Bright Field TEM Image of Representative **<c+a>**-Type Dislocations

During the examination of the TEM foils, bands or lines were discovered along the crack surface near where the dislocation analysis was completed. Theses bands or lines have not been fully examined, but preliminary results show the possibility of this feature being associated with hydrides. Further TEM analysis is needed to be sure and care must be taken to ensure that if it is hydrogen, it was present during dwell fatigue testing and not a sample preparation artifact.

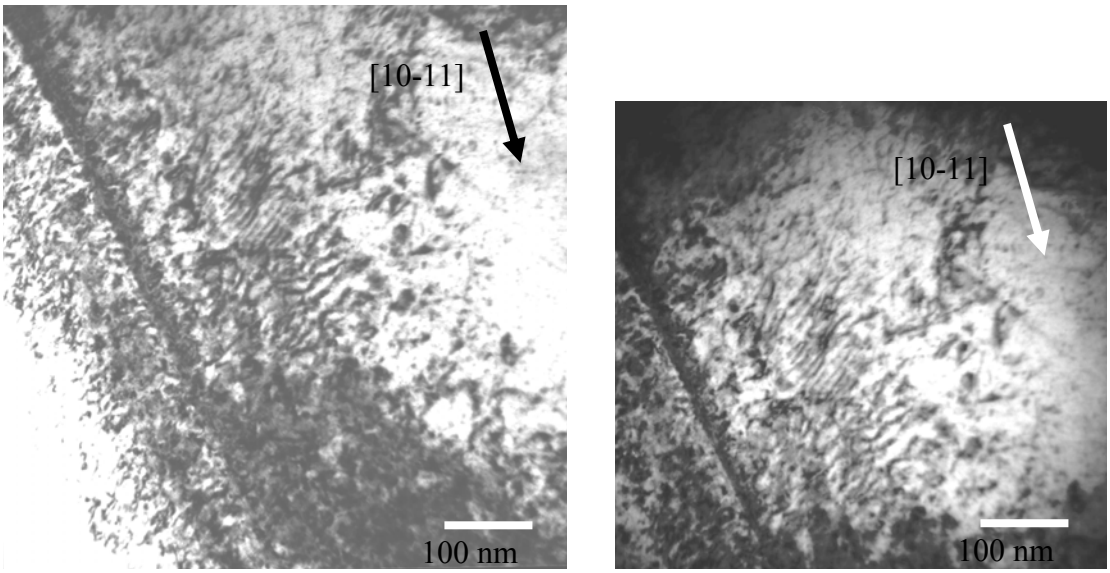

Figure D-14. Bright Field TEM Images of a-Type Dislocations

Figure D-2 shows the secondary crack used in this study and the corresponding OIM. The crack is lying on the basal plane in region 2 and has arrested in neighboring soft grains, regions 1 and 3 respectively. To determine the propensity for slip to occur on certain planes, a Schmid factor plot was constructed for the four dominate slip systems, as shown in figure D-15.

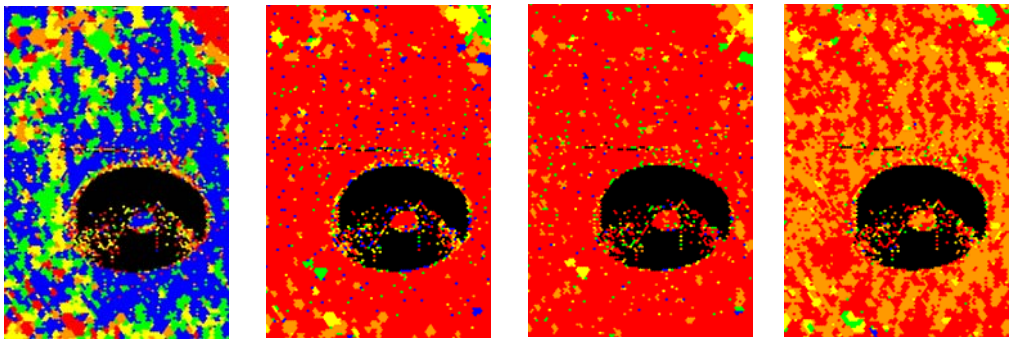

Basal Slip a-type | Prism Slip a-type | Pyramidal a-type | Pyramidal c+a-type

Gray Scale Map Type: <none>
Color Coded Map Type: Schmid Factor

Min	Max	Total Fraction	Partition Fraction
1.84539e-005	0.100015	0.420	0.420
0.100015	0.200011	0.192	0.192
0.200011	0.300007	0.112	0.112
0.300007	0.400003	0.077	0.077
0.400003	0.499999	0.077	0.077

Boundaries: <none>

Gray Scale Map Type: <none>
Color Coded Map Type: Schmid Factor

Min	Max	Total Fraction	Partition Fraction
0.000257036	0.100205	0.028	0.028
0.100205	0.200153	0.020	0.020
0.200153	0.300101	0.031	0.031
0.300101	0.400049	0.069	0.069
0.400049	0.499997	0.729	0.729

Boundaries: <none>

Gray Scale Map Type: <none>
Color Coded Map Type: Schmid Factor

Min	Max	Total Fraction	Partition Fraction
0.0104514	0.108356	0.007	0.007
0.108356	0.206261	0.018	0.018
0.206261	0.304166	0.018	0.018
0.304166	0.402071	0.056	0.056
0.402071	0.499976	0.778	0.778

Boundaries: <none>

Gray Scale Map Type: <none>
Color Coded Map Type: Schmid Factor

Min	Max	Total Fraction	Partition Fraction
0.28456	0.32764	0.001	0.001
0.32764	0.37072	0.016	0.016
0.37072	0.4138	0.039	0.039
0.4138	0.456881	0.386	0.386
0.456881	0.499961	0.434	0.434

Boundaries: <none>

Figure D-15. Corresponding Schmid Factors for Grains Surrounding the Secondary Crack

D.2.4 HARD/SOFT BOUNDARY.

The first TEM foil extracted was along the boundary of regions 1 and 2. As shown in figure D-16, in the soft region, there is an a-type slip on one prism plane, and in the hard region, there is a slip occurring on two prism planes. However, in the hard region, there is limited c+a activity, indicating that limited load-shedding has occurred during the dwell fatigue.

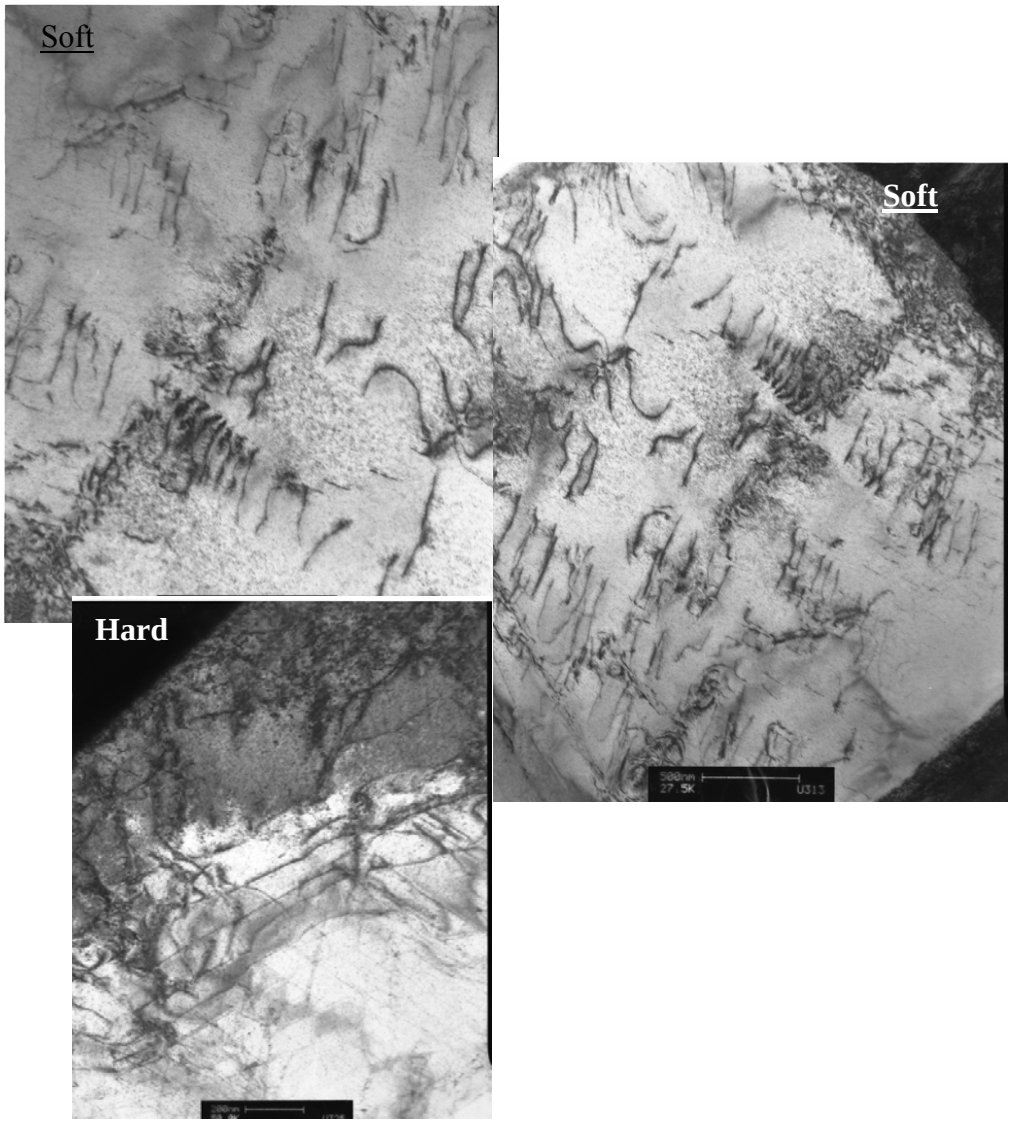

Figure D-16. Transmission Electron Microscope Images Taken From the Boundary Between the Soft and Hard Microtextured Regions

D.2.5 CRACK TIP REGION 1.

As shown in figure D-17, the TEM foil extracted at the crack tip, in region 1, shows many a-type dislocations, which is expected from the Schmid factor plot. However, there is also a high density of c+a type dislocations. Due to the high critical resolved shear stress, these were not expected, but were probably produced from the large, triaxial stress state ahead of the crack tip.

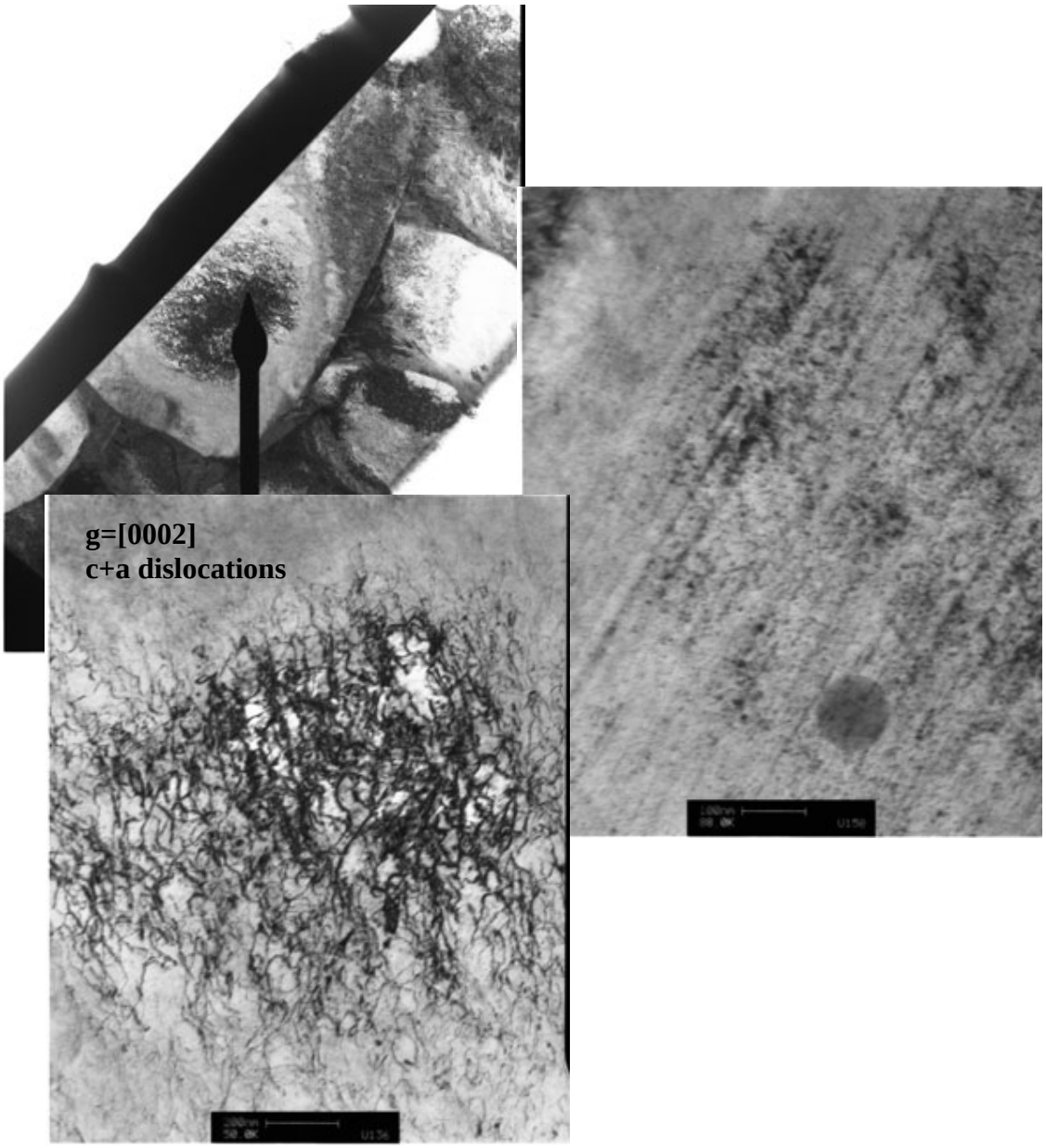

Figure D-17. Transmission electron Microscope Images Taken From the Crack tip in Region 1

D.2.6 CRACK TIP REGION 3.

The TEM foil extracted at the crack tip, in region 3, indicates a-type and c+a-type activity (see figure D-18). The a-type dislocations are on basal planes and likely induced by the triaxial stress state since the Schmid factor for basal slip is very low. The minor misorientation between regions 2 and 3 appears to have been enough to arrest the crack.

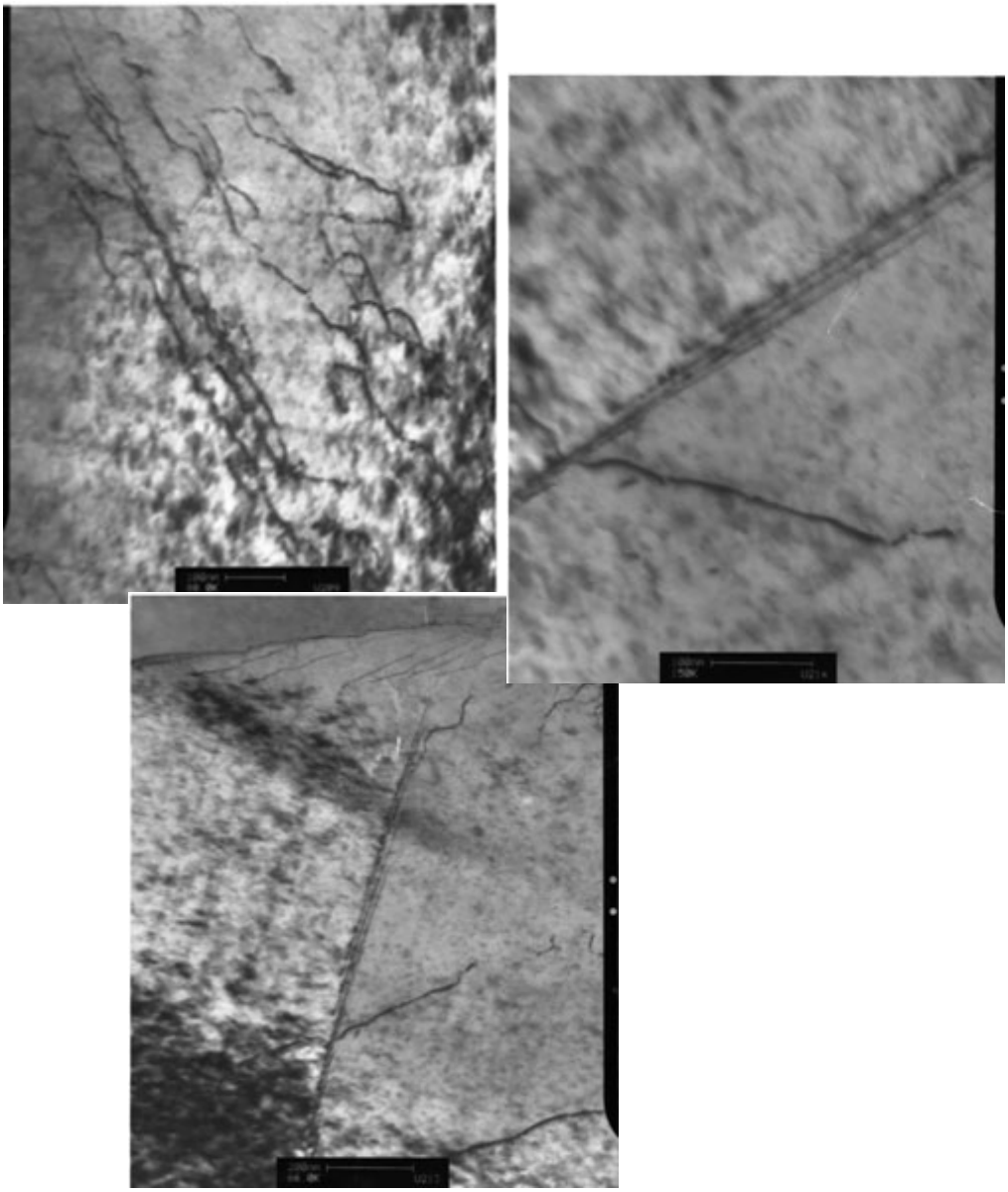

Figure D-18. Transmission Electron Microscope Images Taken From Near the Crack Tip in Region 3, Showing a-Type and c+a-Activity

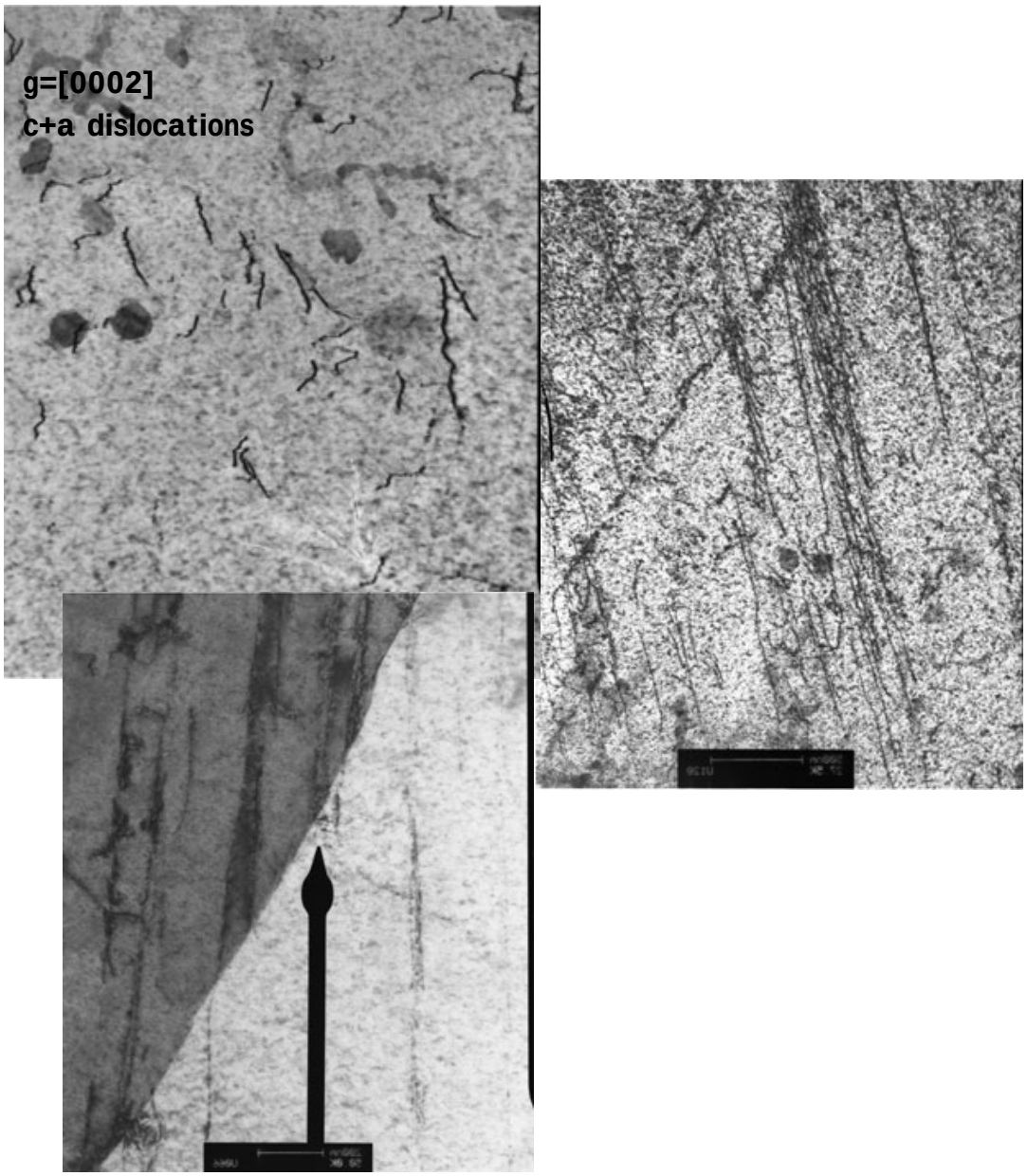

Figure D-19. Transmission Electron Microscope Images Taken From Region 2 Far Away From the Crack, With Minimal c+a Activity

D.2.7 FAR-FIELD REGION 2.

The TEM foil extracted far away from the crack, but still in region 2, shows very few c+a-type dislocations and several a-type dislocations lying on prism planes (see figure D-19). This supports the claim that the c+a dislocations are induced by the stress triaxiality of the crack tip.

D.2.8 CRACK WAKE REGION 2.

The TEM foil extracted along the crack wake shows a high density of <c+a> dislocations. Images taken in bright field and weak-beam dark field are shown in figure D-20. The density of <c+a> dislocations is much larger than observed far field from the crack in region 2 (figure

D-19), indicating that the crack has induced significant local plasticity along the [0001] direction. Such displacements would be induced by a mode I crack in this region.

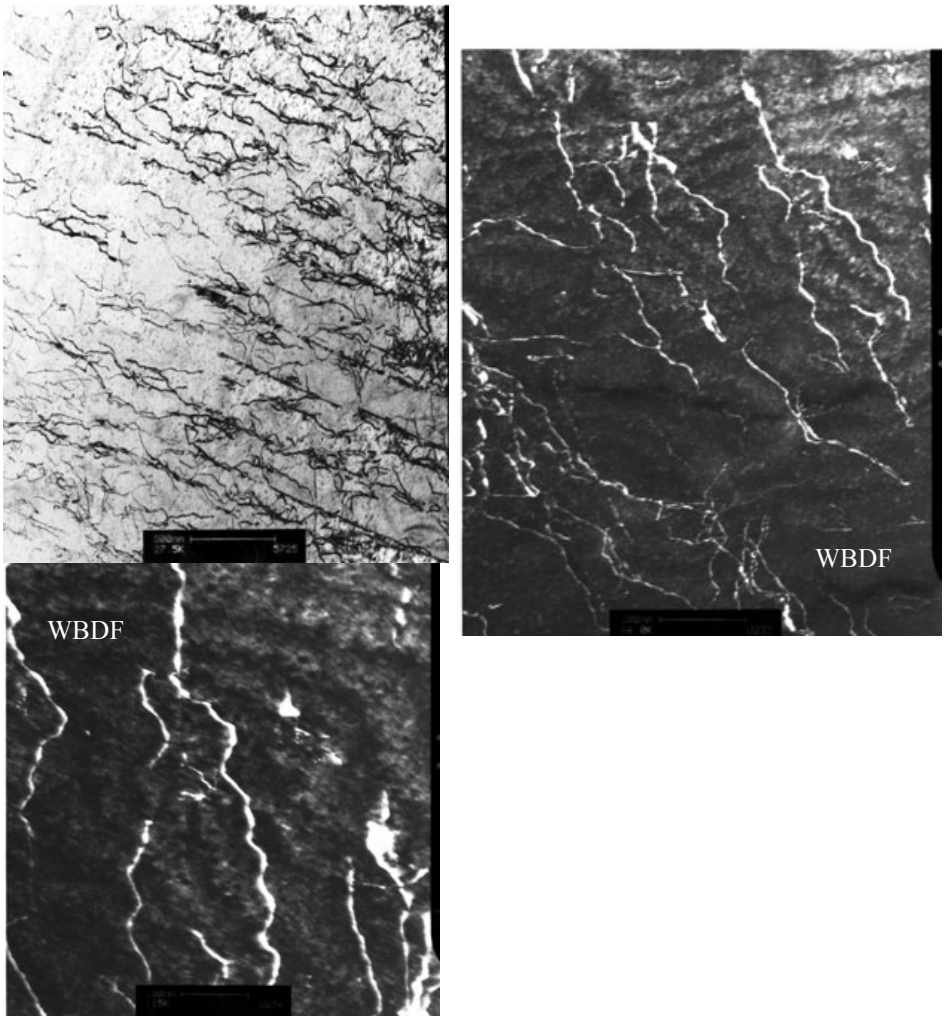

Figure D-20. Transmission Electron Microscope Images Taken in Bright Field and Weak-Beam Dark Field From the wake of the Crack (These disclocations indicate that there is significant plasticity along the [0001] direction in the hard region during crack propagation.)

D.3 REFERENCES.

D-1 Bache, M.R., Cope, M., Davies, H.M., Evans, W.J., and Harrison, G. *Int. J. Fatigue* 1997, 19 Suppl. 1, 1st International Conference on Fatigue Damage in Structural Materials, 1996:S83.

D-2 Evans, W.J. and Bache, M.R., *Titanium '95 Science and Technology*; Proceedings of the 8thWorld Conference, Publisher: Inst. of Materials, 1995:1339.

D-3 Winstone, M.R., Titanium Science and Technology, Proceedings of the 6th World Conference. 1988:169.

D-4 Evans, W.J. and Bache, M.R., *Int. J. Fatigue* 1994, 16(7):443.

D-5 Evans, W.J. and Gostelow, C.R., *Metall. Trans.* A 1979, 10A(12):1837.

D-6 Woodfield, A.P., Gorman, M.D., Corderman, R.R., Sutliff, J.A., and Yamrom, B., Titanium '95 Science and Technology, Proceedings of the 8th World Conference. Publisher: Inst. of Materials. 1995:1116.

D-7 Woodfield, A.P., Gorman, M.D., Sutliff, J.A., Corderman, R.R., "Fatigue Behavior of Titanium Alloys", Proceedings of an International Symposium held at the TMS Fall Meeting '98. 1999:111.

D-8 White, J., Loretto, M.H., Smallman, R.E., and Winstone, M.R., Titanium Science and Technology, 5th International Conference on Titanium, 1984.

D-9 Ishitani, T., Tsuboi, H., Yaguchi, T., and Koike, H., *Journal of Electron Microscopy*, October 1994.

D-10 Yaguchi, T., Matsumoto, H., Ishitani, T., and Urao, R., *Microscopy and Microanalysis*, May-June 2001.

Appendix E

Understanding the Contributions of Normal-fatigue and Static-loading to the Dwell-fatigue in a Near-alpha Titanium Alloy*

V. Sinha, M.J. Mills, and J.C. Williams

Department of Materials Science and Engineering, The Ohio State University,
2041 College Road, Columbus, OH 43210

Abstract

This paper presents the results of a recent study of the response of an α/β forged Ti-6Al-2Sn-4Zr-2Mo alloy during static, normal-fatigue and dwell-fatigue loading. The plastic strain accumulation under different loading conditions is reported. The failure modes and associated fractographic features under static, normal-fatigue and dwell-fatigue loading conditions are also discussed. These results are used to obtain a better understanding of the relative contributions of the cyclic and creep processes to the overall damage under dwell-fatigue conditions.

1 INTRODUCTION:

The alloy Ti-6242 is widely used in the higher temperature portion of the compressor rotor of aircraft engines. In work conducted in several laboratories around the world, a significant debit in the fatigue capability (reduced lifetimes) of this class (near-α) of titanium alloys has been found when comparing results obtained from continuous cycling and holding at maximum load (dwell fatigue) conditions. Because the magnitude of the life debit decreases with increasing temperature, the phenomenon has been called "cold dwell fatigue". Although it has been realized that both the creep and cyclic deformation/ damage processes contribute to failure under dwell-fatigue loading conditions, the relative importance of these processes for the total damage has not been understood in a fundamental sense. The objective of this study was to obtain an understanding of the relative contributions of the cyclic (repetitive) and static loading to the overall damage under dwell-fatigue loading conditions.

In the open literature, there are earlier reports about the correlation between the times to failure under static-loading and dwell-fatigue test conditions for different alloys and test conditions. For IMI 829 with a colony microstructure, the results of White et. al. [1] indicate that at 89 % of the 0.2 % proof stress, the creep specimen did not break even at ~ 8 times the equivalent time to failure for the corresponding dwell specimen. Hack and Leverant [2] have observed similar times to failure under dwell-fatigue and static-loading conditions at 95 % of 0.2 % offset yield strength for IMI 685 with a colony microstructure. Evans and Gostelow [3] have also reported similar times to failure (i.e. rupture lives) for constant load (creep) and dwell-fatigue specimens tested at ~ 95 % to 101 % of 0.1 % proof stress for a colony microstructure IMI 685 alloy. Furthermore, the results of Kassner, et. al. [4] indicate that for a Ti-6242 alloy (bimodal microstructure with a

* This paper is published in Metallurgical and Materials Transactions (vol. 35A, pp. 3141-3148, 2004).

primary α volume ~ 33 %) some creep specimens have a shorter rupture life (by a factor of 4 or more) than the corresponding dwell-fatigue specimens at ~ 113 % of 0.2 % yield strength. In this paper, we have attempted to evaluate the correlation between the static-load and dwell-fatigue rupture lives as a function of stress. This information is then used in an effort to help understand the data in the literature.

This study was carried out on Ti-6242 alloy in the α/β forged condition. The mechanical tests were conducted at two different stress levels. The variation in relative contributions of cyclic and creep processes to the overall dwell-fatigue damage as a function of stress was evaluated in some detail. The strain accumulations under normal-fatigue, dwell-fatigue and static loading conditions have been measured. These data are important for understanding any possible relationship between plastic deformation and dwell fatigue failures. The failure modes and associated fractographic features under normal-fatigue, dwell-fatigue and static-loading conditions have also been examined in detail.

2. MATERIAL AND MICROSTRUCTURE:

The Ti-6Al-2Sn-4Zr-2Mo (+ Si) alloy that was used in this study was provided in the form of a pancake forging by Ladish Co., Cudahy, WI. The composition of the heat of the alloy is shown in Table I, along with the oxygen and hydrogen contents of the as-received pancake forging. The alloy was thermo-mechanically processed (TMP) at Ladish Co. as follows: the billet was α/β forged at T_β - 28 0C to a strain level of ~58%, solution heat treated at T_β - 56 0C, and then air cooled. This was followed by aging at 593 0C for 8 hours and then air cooling to room temperature. Oxygen and hydrogen contents of the as-received Ladish pancake forging were determined at Luvak Inc. (Boylston, MA) by inert gas fusion (ASTM E1019) and vacuum hot extraction (ASTM E146) methods, respectively. The oxygen and hydrogen contents were determined to be 1440 ppm and 35 ppm (both by weight), respectively. Although there is a negligible difference in the oxygen content of the starting ingot and the fabricated forging, the hydrogen contents are quite different for the two (see Table I). This may be due to the possibility of hydrogen pick-up during the ingot-to-billet conversion, forging and/or heat treatment steps of the pancake fabrication. The concentrations of other major alloying elements in the as-received forging are expected to be essentially the same as in the starting ingot (Table I).

TABLE I: CHEMICAL COMPOSITION OF Ti-6242 ALLOY

Element	Based on the ingot analysis provided by Ladish Co. (weight %)	Based on the analysis of pancake forging, i.e. as-received alloy (weight %)
Al	6.18	
Zr	3.98	
Sn	1.94	
Mo	2.00	
Fe	0.02	
O	0.141 (1410 ppm)	0.144 (1440 ppm)
Cu	<0.01	
Mn	<0.01	
Si	0.09	
C	0.01 (100 ppm)	
N	0.0024 (24 ppm)	
H	0.0005 (5 ppm)	0.0035 (35 PPM)
Cr	<0.003	
Ni	0.004	
Y	<0.0005	
B	<0.001	
Others each	<0.10	
Others total	<0.30	
Ti	Balance	

Calculated β-transus = 1004 ^{0}C

Samples from the pancake forging were metallographically ground using silicon carbide grinding paper and then polished to a 0.06 μm finish using colloidal silica. The polished samples were etched in Kroll's reagent for about 30 seconds to reveal the microstructure when viewed under an optical microscope. The samples for scanning electron microscopy (SEM) were not etched after being polished. The alloy examined in this study had a bimodal microstructure, consisting of primary α grains and transformed β regions (Fig. 1). The light phase is α (h.c.p.) and the dark phase is β (b.c.c.) in the optical micrograph (Fig. 1a), whereas the contrast is reversed for the α and β phases in the SEM micrographs (Fig. 1b and 1c) that were taken using a backscattered electron (BSE) detector. It is clear from the SEM images (Fig. 1b and 1c) that the transformed β regions consist of α-laths (dark phase) in a β-matrix (light phase). The amount of primary α in the alloy was estimated to be ~ 65 – 70 vol. %. The degree of micro-texture in the as-received alloy was determined using the electron backscatter diffraction (EBSD) techniques in an SEM. This technique has been described in detail elsewhere [5]. The specimen for orientation imaging scan was prepared in the same manner as for the SEM observations. The step-size for the automated scan was 10 μm, which is on the order of the primary α grain size (Fig. 1).

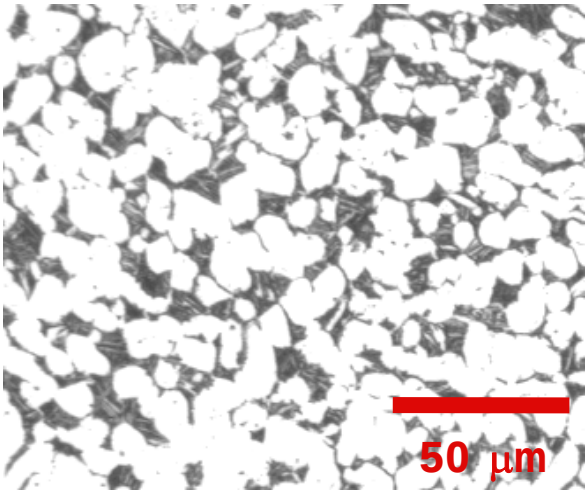

Figure 1 (a)

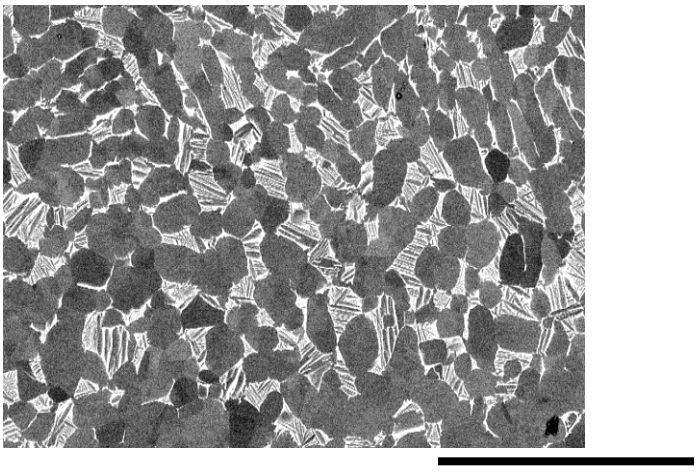

(B)

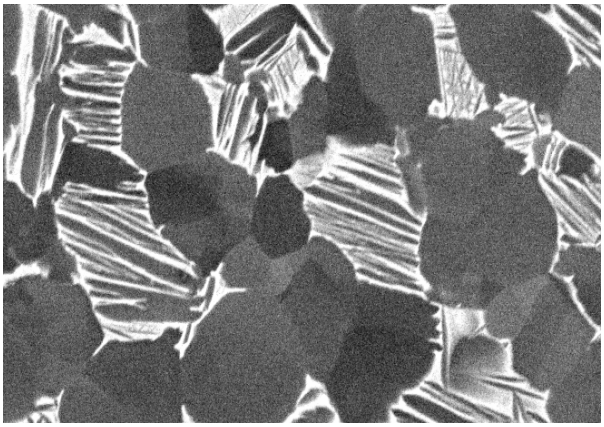

(c)

Figure 1 Microstructure of the as-received α/β forged Ti-6242 alloy. (a) Optical Micrograph, (b) Scanning electron Microscope (SEM) Image, and (c) SEM Image at a Higher Magnification.

The resulting orientation image is color-coded with points of same crystallographic orientation being represented by the same color. The color-coded orientation image has been converted to a grayscale image (Fig. 2a), where the gray level at any point represents the crystallographic orientation at that point as per the scheme shown in Fig. 2b. According to Fig. 2b, when the surface normal at a given point on the specimen surface is parallel to the $(10\bar{1}0)_\alpha$ pole for that point it will be denoted by a darker shade in the orientation image than for the case when it is parallel to the $(2\bar{1}\bar{1}0)_\alpha$ pole. From Fig. 2a, it is clear that there are large regions in the as-received alloy with essentially the same crystallographic orientation. In other words, this material has a high level of micro-texture, which has been shown to correspond to a large dwell life debit in this alloy system [6]. The basal-plane pole figure for the same specimen is shown in Fig. 3, which was determined using the conventional X-ray diffraction techniques with a Cu K_α radiation (λ = 1.5418 Å). From Fig. 3 it is clear that the basal poles are primarily located along the circumference of the pole figure. Thus, a majority of the basal poles are perpendicular to the forging axis, which is located at the center of the pole figure. Williams and Starke, Jr. have reported a similar texture for Ti-6Al-4V alloy after α/β forging near the β-transus under the conditions of axisymmetric flow [7].

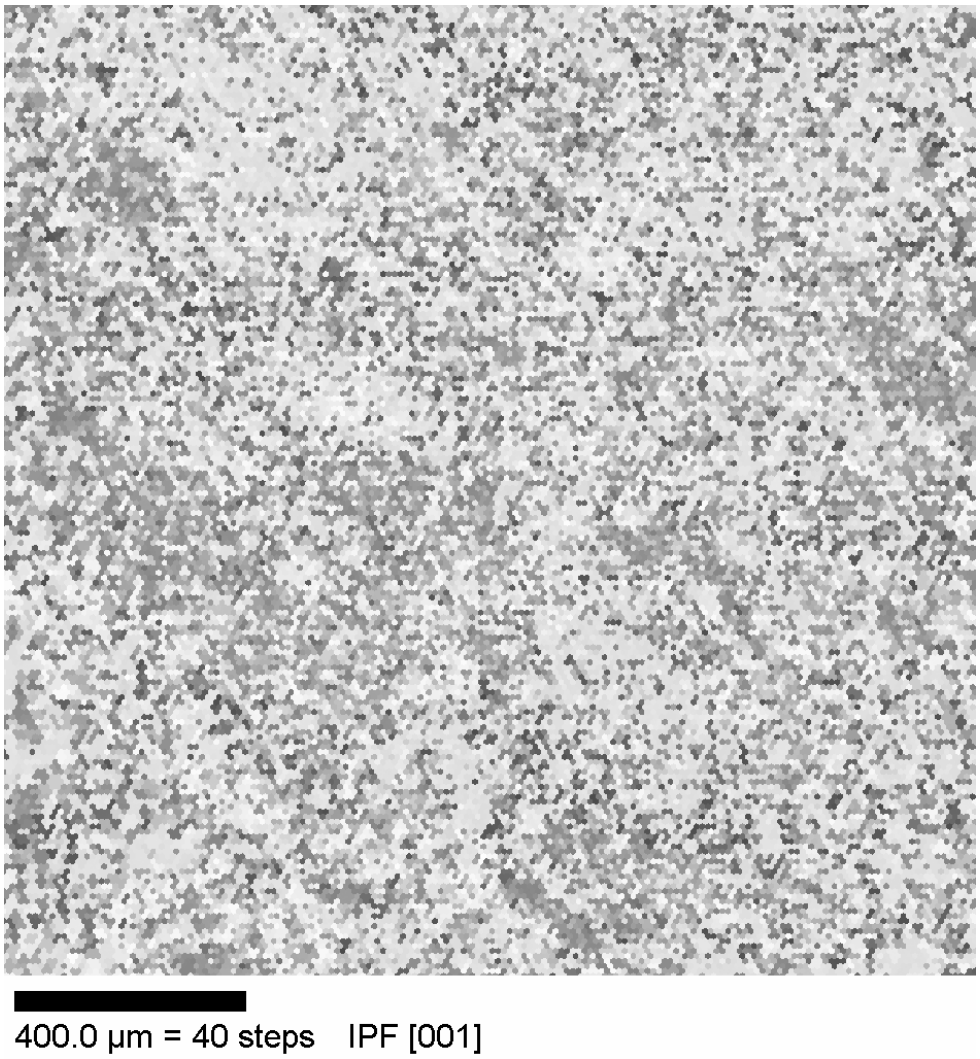

(a)

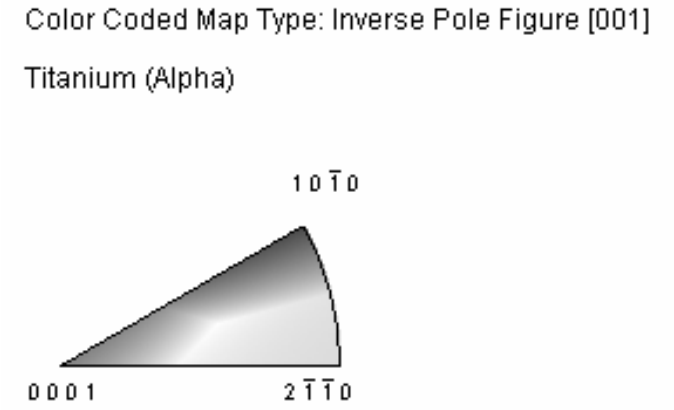

(b)

Figure 2: (a) Orientation map of the as-received α/β forged Ti-6242 alloy, and (b) legend for orientation map (a).

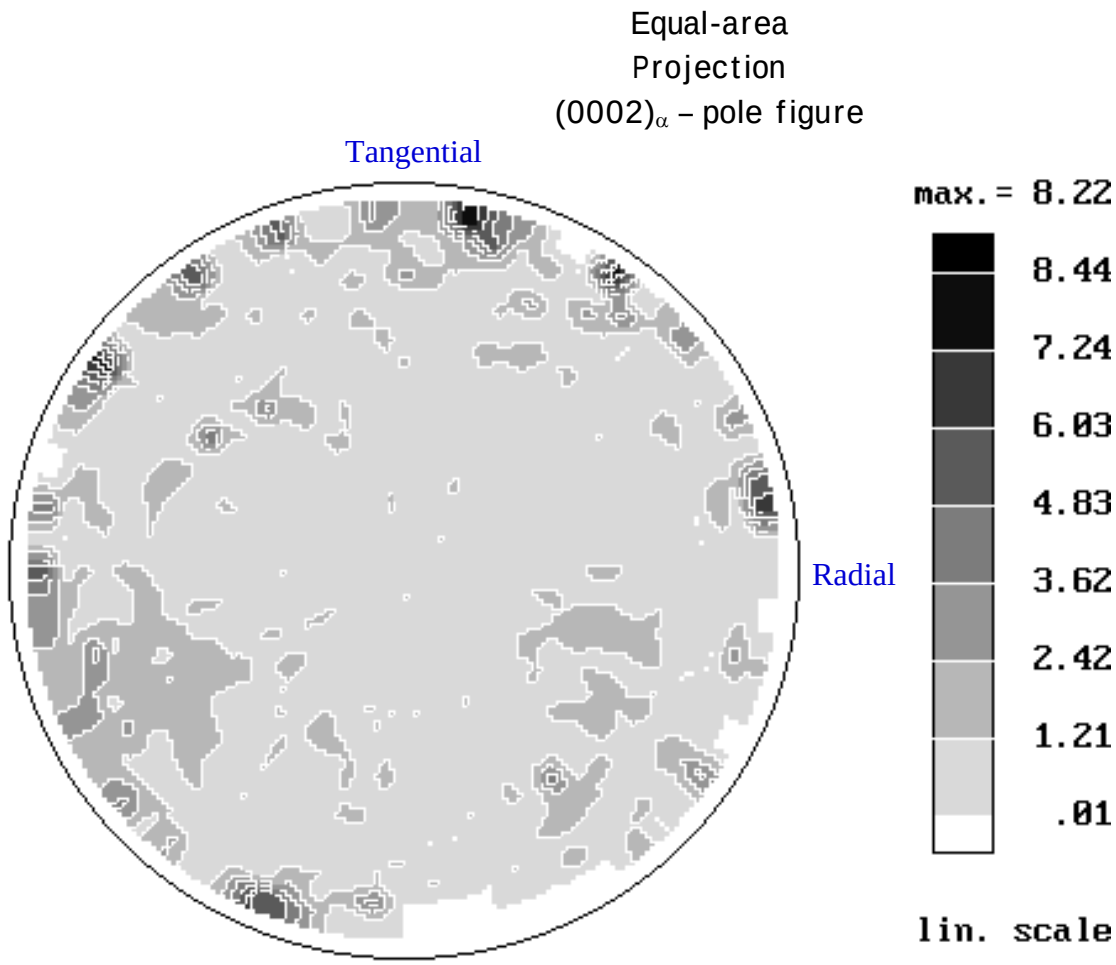

Figure 3: Basal-plane pole figure for the as-received α/β forged Ti-6242 alloy obtained by the X-ray diffraction techniques.

3. EXPERIMENTAL PROCEDURES:

In order to obtain basic mechanical properties data for the as-received alloy, the tensile specimens were machined from the pancake forging such that their axes (i.e. loading direction) were along its circumferential (tangential) direction. The tensile tests were conducted in lab air, at room temperature using a closed-loop servo-hydraulic test-frame. The specimens for the tensile tests had a uniform circular cross-section with a gage section diameter of 6.35 mm (0.25”), the length of reduced section = 31.75 mm (1.25”) and they had a threaded grip section of diameter = 9.52 mm (0.375”). The other dimensions of these tensile specimens were selected in accordance with ASTM E8 specifications. The tensile tests were conducted under displacement control at an actuator speed corresponding to a strain rate of ~ 1 X 10-4 S-1. The basic tensile properties of the supplied alloy were as follows: 0.2 % offset yield strength = 950 MPa, ultimate tensile strength = 1017 MPa, and elongation = 17.6 %.

The specimens for normal-fatigue and dwell-fatigue tests had a uniform circular cross-section with a gage section diameter of 5.08 mm (0.2”), the length of reduced section = 19.05 mm (0.75”) and they had a threaded grip section of diameter = 15.88 mm (0.625”). The other dimensions of the specimens were selected in accordance with ASTM E466 specifications. After machining, the specimens were shot-peened as per the following conditions: intensity: 005 A; shot-type: S1-10 CW14; and coverage: 200%. Both the normal-fatigue and dwell-fatigue experiments were carried out at room temperature in air under load-control using a closed-loop servo-hydraulic test-frame. The time of loading/unloading between the minimum and maximum loads in a cycle was kept fixed at 1 second each for both the normal-fatigue and dwell-fatigue cycles. A load-ratio of 0 was used in all the tests. The only difference between the normal-fatigue and dwell-fatigue tests was that the load was held for 2 minutes at the maximum value in each dwell-fatigue cycle. The schematic representations of the normal-fatigue and dwell-fatigue cycles are shown in Fig. 4. In actual operation, the stress on the rotor of an aircraft engine is applied immediately during take-off while the rotor is still well below the maximum operating temperature. Furthermore, Neal has reported a significantly larger dwell-life debit at lower temperatures, when tests were carried out at temperatures in the range of 20 to 200 ^{0}C [8]. Therefore, we have elected to do isothermal tests at room temperature to create a worst-case situation, and this selection of test temperature is related to the actual operating conditions in a jet engine. The loading and test conditions (load ratio, dwell-time and temperature) were chosen to assess the effect of the take-off transients of a typical flight with which the dwell-fatigue life debit is thought to be associated. For the static-load tests, the specimen geometry and the shot-peening conditions were the same as for normal-fatigue and dwell-fatigue tests. The static load tests were conducted in a dead-load creep frame and the strain accumulation was monitored as a function of time using an extensometer. For all three test conditions, the specimens were machined from the pancake such that their axes (i.e. loading direction) were along its circumferential (tangential) direction. The failure modes of the tested (fractured) specimens were examined in an SEM with the help of a secondary electron detector.

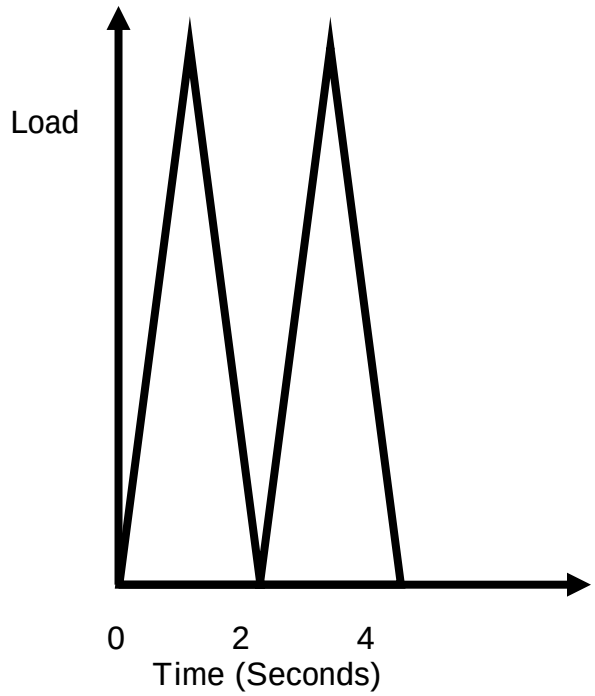

(a)

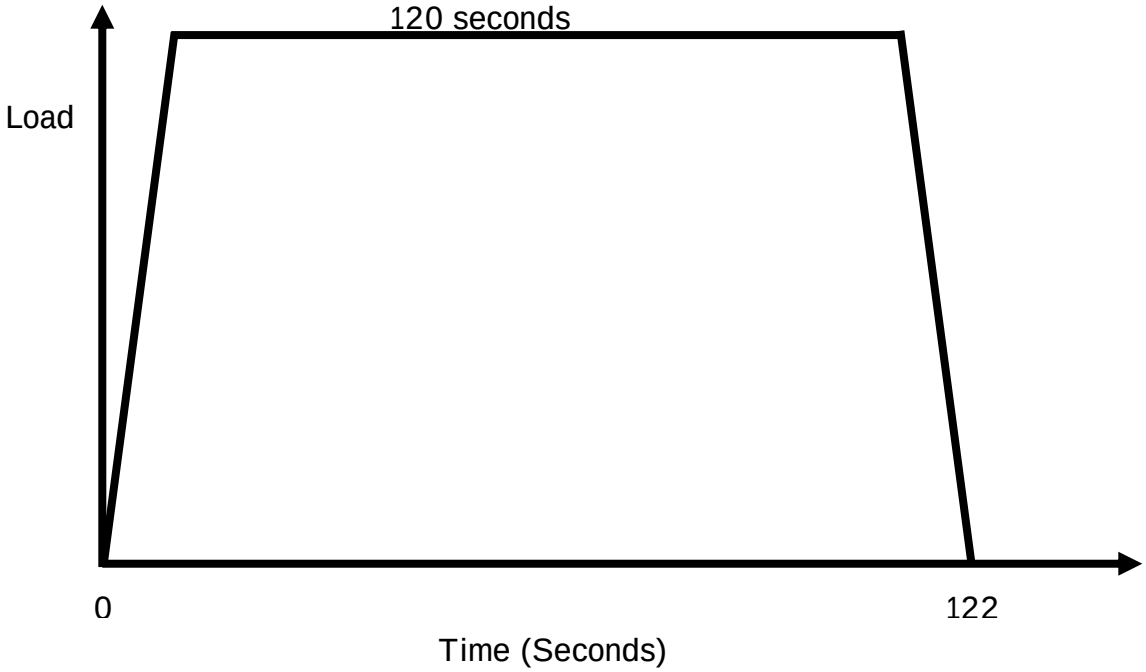

(b)

Figure 4: Schematic of loading cycles. (a) Normal-fatigue (30 cycles per minute), and (b) dwell-fatigue cycle with 2 minute dwell at the maximum load.

4. RESULTS AND DISCUSSION:

4.1 RUPTURE LIVES AND STRAIN ACCUMULATION:

The test conditions (dwell-time and peak stress to yield strength ratio) for the Ti-6242 alloy are described in Table II along with the corresponding plastic strain to failure, number of cycles to failure and dwell life debit values. The comparison of results at two different peak stresses indicates that the dwell life debit is lowered as the peak stress is reduced (Table II). This effect of stress on dwell life debit is consistent with the reports by Kassner, et. al. [4] and Evans [9]. Moreover, a higher plastic strain to failure was observed at a higher stress for both the normal-fatigue and dwell-fatigue loading conditions (Table II).

TABLE II: SUMMARY OF FATIGUE AND DWELL-FATIGUE TESTS

σ_{max} / σ_{YS}	Dwell time, minutes	ε^{pl}_f (Gage length ~ 18 mm)	N_f (Cycles)	Dwell life debit
0.955	2	3.8%	1303	18
	0	2%	22,991	
0.915	2	2.3%	3074	15
	0	1.0%	45,843	

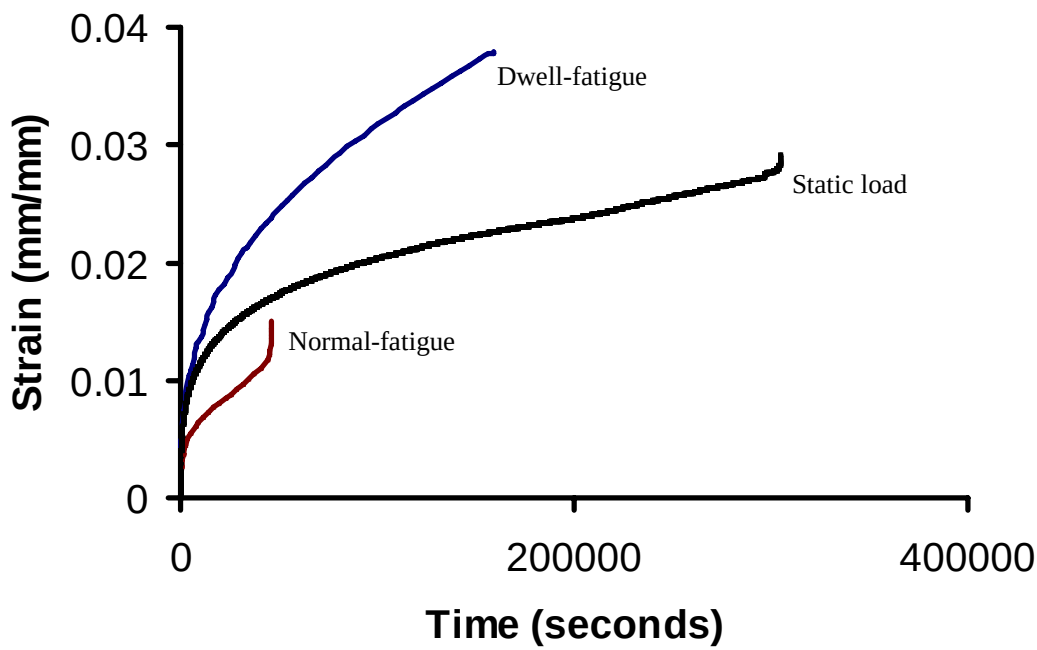

Figure 5: Strain accumulation during normal-fatigue (30 cpm), 2-minute dwell-fatigue and static load tests for α/β forged Ti-6Al-2Sn-4Zr-2Mo alloy. Applied peak stress ~ 95 % of YS.

The experimental results for static loading test condition are summarized in Table III. A comparison of the dwell and static-load tests at a fixed peak stress to yield strength ratio of ~

0.95 shows that the statically loaded specimen fails in about twice the time and at similar plastic strain values as the dwell-fatigue tested specimen (Table III). Fig. 5 shows the accumulated plastic strain as a function of time for normal-fatigue, dwell-fatigue and static-load tests at the same peak stress of ~ 95% of yield strength. With respect to Fig. 5, it should be noted that the gage length for strain measurement for static-load test was ~ 18 mm, whereas that for dwell-fatigue (and normal-fatigue) test was ~12.7 mm. Even after taking this factor into account, it is clear that plastic strain accumulates more rapidly during a dwell-fatigue test than a static-loading test. The specimens tested under these two conditions show similar plastic strains for the same gage length of ~18 mm (Table III) at different times. *i.e.* the dwell-fatigue specimen reaches the similar plastic strain as the statically loaded specimen in about half the time. White et. al. [1] have reported a similar trend for strain accumulation under 2-minute dwell fatigue, creep and normal-fatigue loading conditions for an IMI 829 alloy with colony microstructure. On the other hand, Hack and Leverant [2] have reported similar strain to failure values and strain accumulation rates for 5-minute dwell fatigue and static-load tests of an IMI 685 alloy with colony microstructure. The exact explanation for this apparent discrepancy is unclear. However, the role of different dwell times (2-minute in reference [1] and the current study, *versus* 5-minute in reference [2]), alloy composition and/or microstructure cannot be ruled out. It is also worthwhile to note that at a lower stress of ~91% of yield strength, the statically loaded sample did not fail even after about 7 times the time to failure for the corresponding dwell-fatigue specimen (Table III). Based on these observations, it can be concluded that as the applied peak stress is increased, the times to failure under dwell-fatigue and static-loading conditions approach each other, i.e. at high applied stresses, the contributions of the static damage processes to the overall dwell-fatigue failure become significant. On the other hand, at lower stresses, the cyclic damage processes are more important for dwell-fatigue fracture. This is evident from the fact that as the applied peak stress is reduced, the number of cycles to failure under dwell-fatigue conditions approaches that under normal-fatigue conditions, i.e. the dwell life debit is reduced at lower stresses as discussed above (Table II). It is important to note that under the condition for which there is a larger dwell life debit (i.e. a higher peak stress condition), creep damage is the dominant process for dwell-fatigue failure.

TABLE III: COMPARISON OF DWELL-FATIGUE AND STATIC LOAD TESTS

$\sigma_{max} / \sigma_{YS}$	Loading condition	Time at Maximum Load, i.e. Rupture Life (hrs.)	ε^{pl}_{f} (Gage length ~ 18 mm)
0.955	2 minute-dwell	43.5	3.8%
0.955	Static Load	84.8	3.6%
0.915	2 minute-dwell	102.5	2.3%
0.915	Static Load	673.9*	1.8%*

*Specimen did not fail

4.2 Fractography and failure modes:

The failure modes for the different test and loading conditions are depicted in Fig. 6 – 10. The fracture initiation site is sub-surface for all the conditions investigated in this study (Fig. (6-10) a). This is not surprising, considering the fact that the specimens were shot-peened. At the high stress of ~ 95% of yield strength, the dwell-fatigue crack initiation site is essentially faceted with little evidence of ductility (Fig. 6b). At this stress, the same fracture mode is observed for the static-loading test condition (Fig. 7b). In fact, the fracture facets for static-load condition appear sharper than those for dwell-fatigue condition (Fig. 6b and 7b). This is likely due to crack-closure at R = 0 and resultant rubbing of the mating fracture surfaces (which can lead to debris formation) during the unloading portion of dwell-fatigue cycles. The underlying microstructure is also evident on the brittle fracture surfaces (Fig. 6b and 7b). On the other hand, the normal-fatigue crack initiation site obtained at ~ 95% of yield strength shows evidence of cyclic growth with a higher degree of local plasticity than is seen during dwell testing (Fig. 8b).

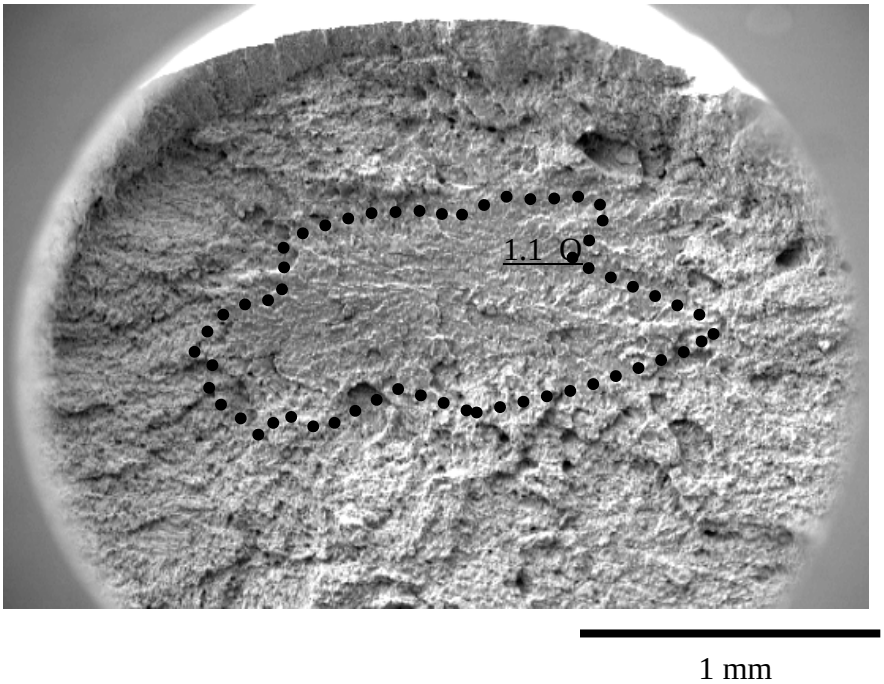

Figure 6 (a)

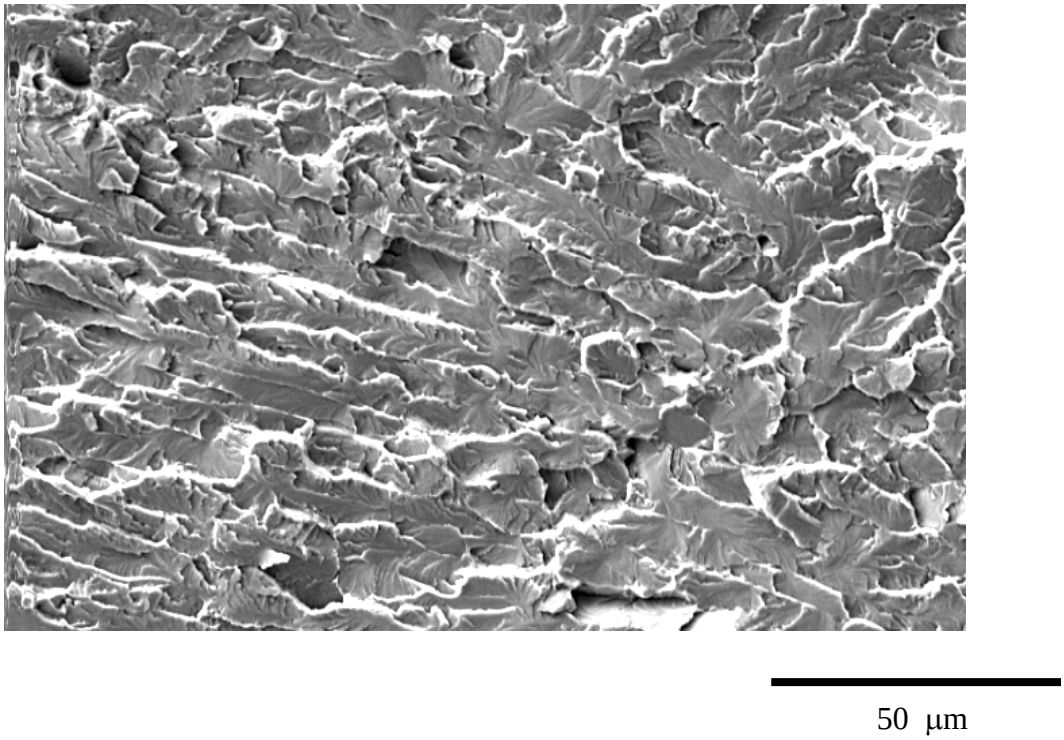

(b)

Figure 6: SEM images of the fracture surface for dwell-fatigue test condition. Applied peak stress ~ 95 % of YS. (a) Low magnification image with the faceted initiation site circumscribed by dotted curve; and (b) higher magnification image of a region, characteristic of the initiation site, that has been labeled ‘O’ in figure (a).

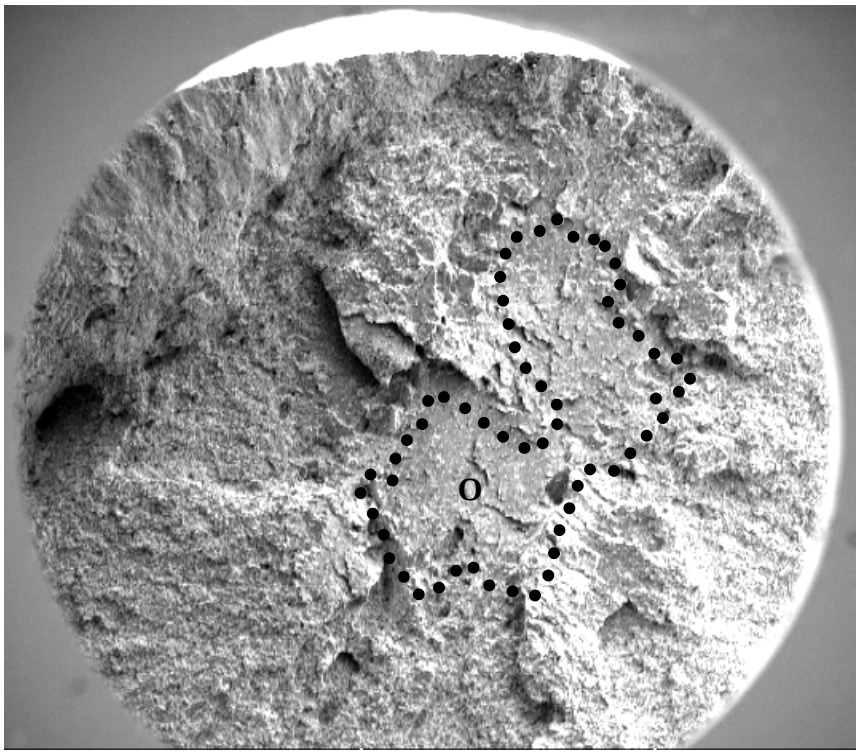

Figure 7 (a) 1 mm

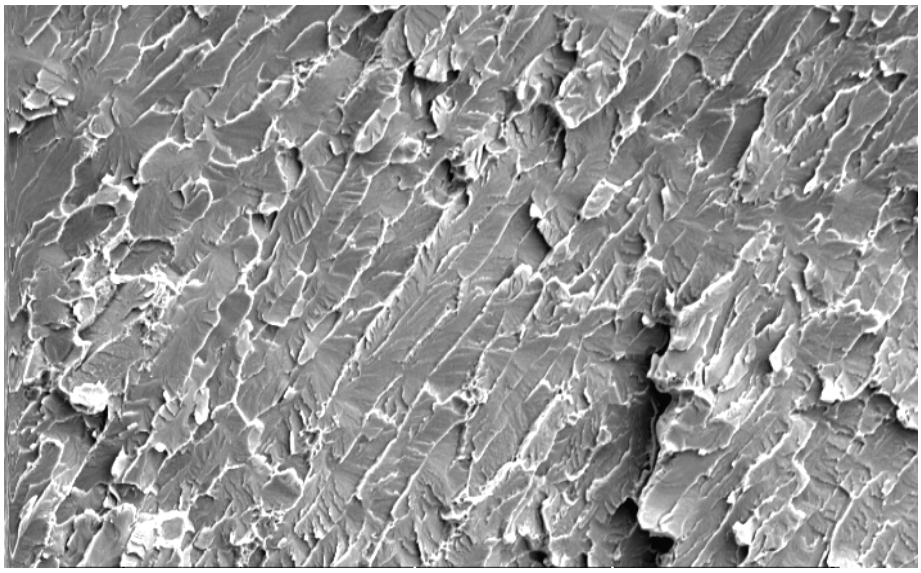

(b) 50 μm

Figure 7: SEM images of the fracture surface for static loading test condition. Applied peak stress ~ 95 % of YS. (a) Low magnification image with the faceted initiation site circumscribed by dotted curve; and (b) higher magnification image of a region, characteristic of the initiation site, that has been labeled ‘O’ in figure (a).

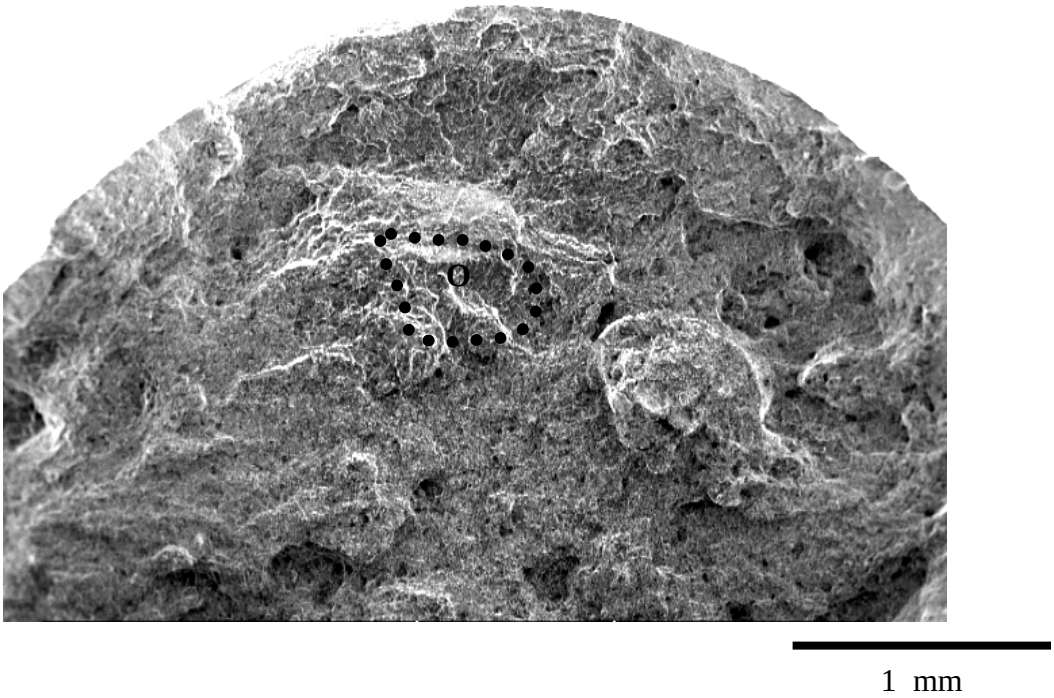

Figure 8 (a)

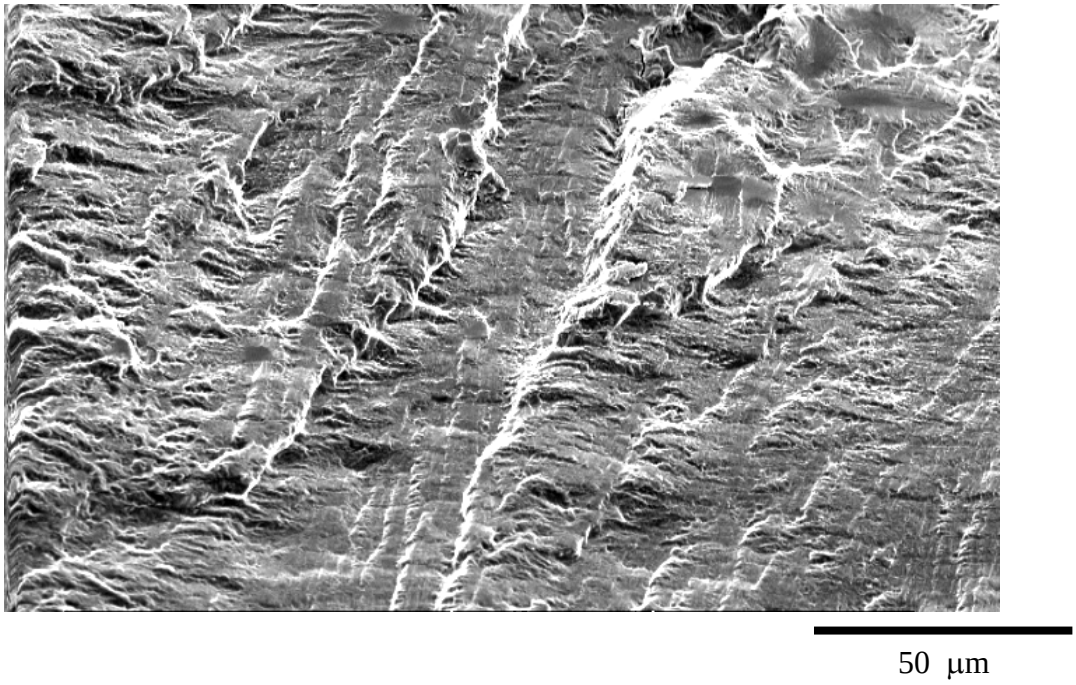

(b)

Figure 8: SEM images of the fracture surface for normal-fatigue test condition. Applied peak stress ~ 95 % of YS. (a) Low magnification image with the initiation site circumscribed by dotted curve; and (b) higher magnification image of a region, characteristic of the initiation site, that has been labeled ‘O’ in figure (a).

At a lower peak stress (~ 91% of yield strength), the dwell-fatigue crack initiation mode is again faceted (Fig. 9b), akin to the failure mode observed at the higher stress. At this low stress (~ 91% of yield strength), the normal-fatigue fracture topography in the vicinity of the crack initiation site also consists of faceted features (Fig. 10b), typical of low ΔK crack propagation in titanium alloys [10]. This is consistent with the fact that during the normal-fatigue test a lower applied peak stress corresponds to a lower ΔK-value at the same crack size, and this translates into a larger area undergoing faceted crack growth at a lower peak stress. It is also noteworthy that the size of this faceted region is smaller for the normal-fatigue test condition (Fig. 10b) when compared with that for the dwell-fatigue test condition (Fig. 9). A comparison of Fig. 9b and Fig. 10b shows that the dwell-fatigue crack initiation site consists of facets at different elevations that are joined by small, sharp steps. The presence of such small steps is not as prevalent for normal-fatigue condition (Fig. 10b).

Shen, et. al. have reported on the long crack growth of Ti-6242 alloy under the normal-fatigue and dwell-fatigue test conditions [11]. They find no significant differences in the fracture topography between these two test conditions. They do report, however, the well-known transition from faceted growth to striation growth with increasing ΔK. In the present work, the applied peak stresses are quite high (~ 91% and ~ 95% of yield strength). Consequently, the transition from faceted growth to striation growth occurs very quickly.

These fractographic observations support the results obtained on the rupture lives under different test conditions in this study. At the high peak stress, the crack initiation modes are similar under dwell-fatigue and static-loading test conditions, and these are quite different for the normal-fatigue test condition. On the other hand, as the peak stress is reduced, the crack initiation mode under normal-fatigue test condition starts to resemble that under dwell-fatigue condition, whereas the static-load failure does not occur in a reasonably long period of time.

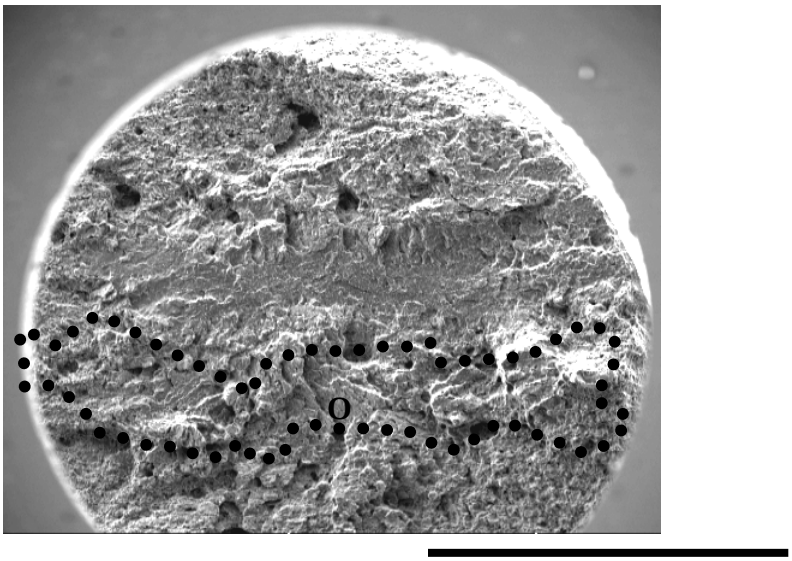

Figure 9 (a) 1 mm

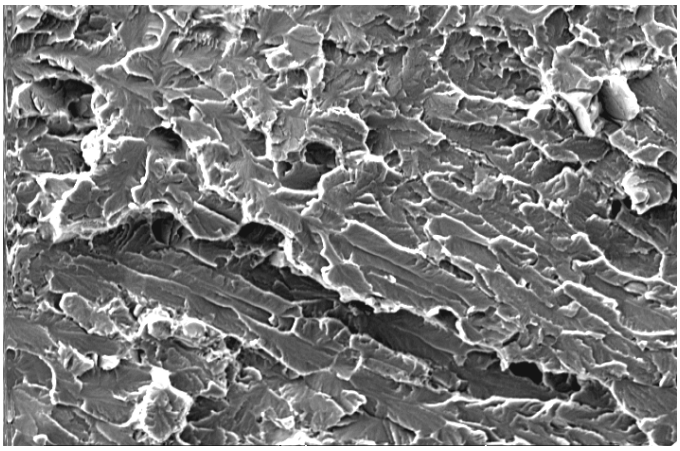

(b) 50 μm

Figure 9: SEM images of the fracture surface for dwell-fatigue test condition. Applied peak stress ~ 91 % of YS. (a) Low magnification image with the faceted initiation site circumscribed by dotted curve; and (b) higher magnification image of a region, characteristic of the initiation site, that has been labeled ‘O’ in figure (a).

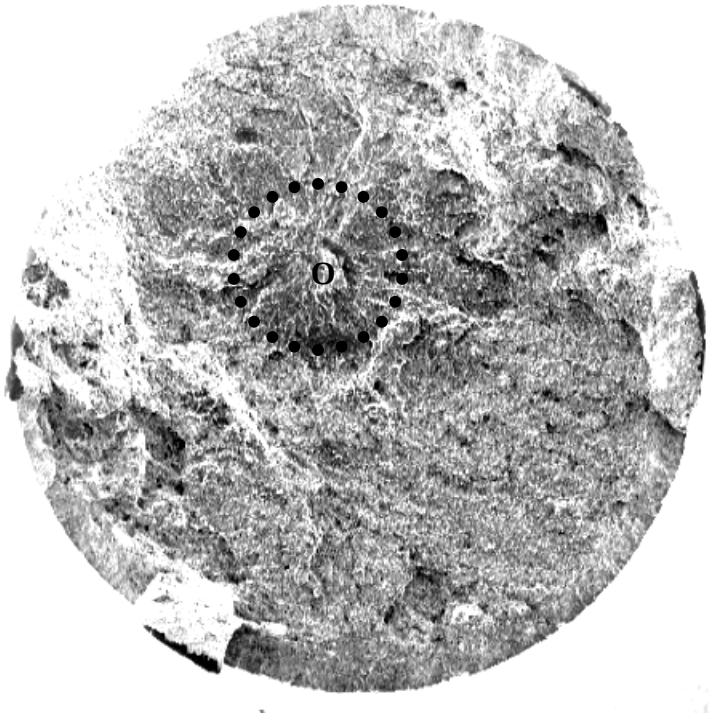

2 mm

Figure 10 (a)

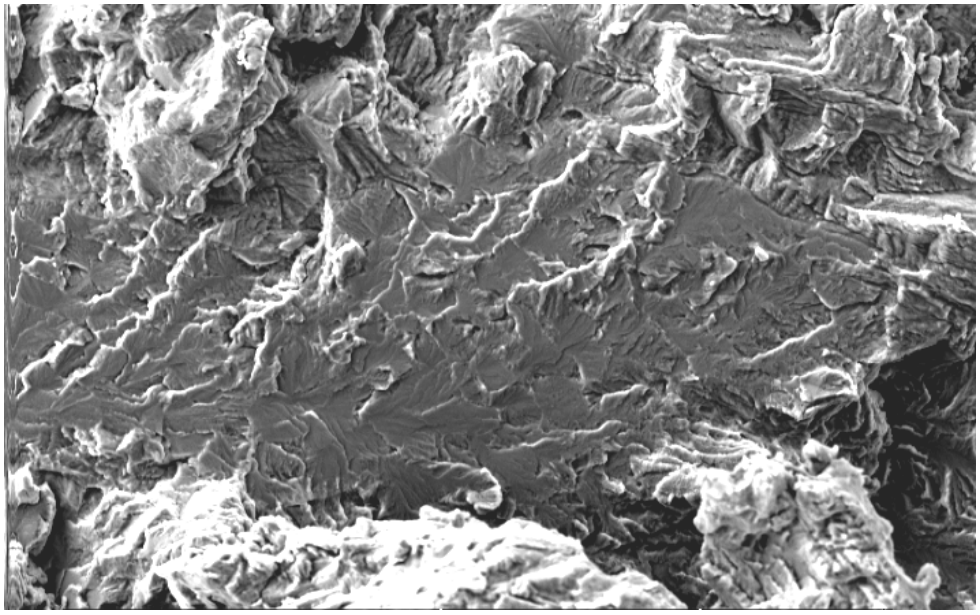

(b)

50 μm

Figure 10: SEM images of the fracture surface for normal-fatigue test condition. Applied peak stress ~ 91 % of YS. (a) Low magnification image with the initiation site circumscribed by a dotted circle; and (b) higher magnification image of a region, characteristic of the initiation site, that has been labeled ‘O’ in figure (a).

5. SUMMARY AND CONCLUSIONS:

The experimental results obtained in this investigation indicate that at high stresses, the dwell-fatigue failure is caused primarily by static deformation/ damage processes. On the other hand, at low stresses, the relative contributions of the cyclic (repetitive) processes to the overall dwell-fatigue failure become more dominant. This finding is supported by both the mechanical test results (i.e. the rupture lives at different stresses for the three different test conditions) and fracture mode studies conducted in an SEM.

As has been discussed in this paper, White et. al. have observed shorter rupture life under dwell-fatigue condition than that under static-loading condition [1]. On the other hand, other groups of investigators have reported similar rupture lives for dwell-fatigue and static-loading conditions [2,3]. Moreover, Kassner et. al. [4] have reported shorter rupture lives for static-loading condition than for dwell-fatigue condition. Based on our observations in the current investigation, we propose that the relative rupture lives for the dwell-fatigue and static-loading conditions depend strongly on the applied peak stress. As the applied peak stress is increased, the rupture lives under the two test conditions approach each other. In contrast, at low applied peak stress, the numbers of cycles to failure under normal-fatigue and dwell-fatigue conditions approach each other. This indicates the dominance of the cyclic (repetitive) damage processes for the dwell-fatigue failure in the low stress regime. It appears that there is a perceptible transition from the cyclic-damage control mode to the static-damage control mode with a relatively modest increase (4 % of the yield strength) in the applied peak stress. It is quite likely that this transition stress is dependent on the alloy composition, microstructure and/ or hold time used for the dwell-fatigue tests. However, in all likelihood, for a given system (i.e. alloy composition, microstructure and dwell-time), a transition in the operating mode for dwell-fatigue failure will occur akin to the observations in the current investigation, albeit at different applied peak stresses.

6. REFERENCES:

1. J. White, M.H. Loretto and R.E. Smallman, Titanium Science and Technology, Proceedings of the fifth International Conference on Titanium, vol. 4, pp. 2297-2304, 1984.

2. J.E. Hack and G.R. Leverant, Metallurgical Transactions, Vol. 13A, pp. 1729-1738, 1982.

3. W.J. Evans and C.R. Gostelow, Metallurgical Transactions, Vol. 10A, pp. 1837-1846, 1979.

4. M.E. Kassner, Y. Kosaka and J.A. Hall, Metallurgical and Materials Transactions, vol. 30A, pp. 2383-2389, September 1999.

5. S.I. Wright, Electron Backscatter Diffraction in Materials Science, A.J. Schwartz, M. Kumar, and B.L. Adams (editors), Kluwer Academic/ Plenum Publishers, New York, N.Y., pp. 51-64, 2000.

6. A.P. Woodfield, M.D. Gorman, R.R. Corderman, J.A. Sutliff and B. Yamrom, Titanium ’95: Science and Technology, pp. 1116-1124, 1995.

7. J.C. Williams and E.A. Starke, Jr., Deformation, Processing, and Structure, G.F. Krauss (editor), ASM, Metals Park, OH, pp. 279-354, 1984.

8. D.F. Neal, Proceedings of the Sixth World Conference on Titanium, France, pp. 175-180, 1988.

9. W.J. Evans, Journal of Materials Science Letters, vol. 6, pp. 571-574, 1987.

10. N.E. Paton, J.C. Williams, J.C. Chesnutt and A.W. Thompson, AGARD Conference Proceedings No. 185, Specialists Meeting on Alloy Design for Fatigue and Fracture Resistance, pp. (4-1) – (4-14), 1976.

11. W. Shen, W.O. Soboyejo and A.B.O. Soboyejo, Mechanics of Materials, vol. 36, pp. 117-140, 2004.

Appendix F

Determination of Crystallographic Orientation of Dwell-fatigue Fracture Facets in Ti-6242 Alloy*

V. Sinha, M.J. Mills, and J.C. Williams

Department of Materials Science and Engineering, The Ohio State University,
Columbus, OH 43210, USA

Abstract

A technique to determine the crystallographic orientation of the fracture facets has been described. The physical orientation of the facet plane is determined in a scanning electron microscope (SEM) using a quantitative tilt fractography technique. The crystallographic orientation of the grain, which contains a particular fracture facet, is determined using the electron backscattered diffraction (EBSD) technique in an SEM. These two pieces of information were combined to obtain the orientation of the fracture facet normal. This technique was used for the characterization of dwell-fatigue fracture facets in Ti-6242 alloy. Our results indicate that these facets are not exactly aligned with the basal plane, but are inclined at ~ 10^0 to it.

Keywords: Crystallographic orientation, Tilt fractography, Fracture facets, Dwell-fatigue, Titanium alloy

* This paper has been submitted to "Journal of Materials Science".

1. INTRODUCTION:

Faceted initiation site has been observed on the fracture surface of various near-α titanium alloys that were tested under different loading conditions [1-5]. Davidson and Eylon [1] have determined the crystallographic orientation of facets using the electron channeling technique in a scanning electron microscope (SEM). In this technique, the SEM stage rotate and tilt controls were adjusted to bring the plane of the facet perpendicular to the electron optic axis. Furthermore, obtaining electron channeling patterns directly from the fracture facets was difficult and the facets were electropolished before being characterized using this technique [1].

The advances in the electron backscattered diffraction (EBSD) technique over the past decade have made it possible to obtain the EBSD patterns directly from the fracture facet. Bache, et al. [3] were able to obtain EBSD patterns from fracture facets after lightly etching them. However, it is not clear from their work [3] if and how they accounted for the physical orientation of the facets (i.e. the physical orientation of the facets with respect to the loading axis/ longitudinal axis of the specimen).

Themelis, et al. [6] have described a quantitative tilt fractography technique for the determination of the physical orientation of the facet plane. This technique, in essence, involves the analyses of the fractographs obtained in an SEM at two different tilt angles.

In the present work, a technique for the determination of crystallographic orientation of fracture facets in Ti-6242 alloy has been described. The physical orientation of the facet plane was determined using a modified version of the technique of Themelis, et al. [6]. The EBSD patterns were obtained directly from the fracture facets in an SEM and they were indexed in order to determine the crystallographic orientation of the grains through which the facets had been produced. The crystallographic orientations of the fracture facets are presented as inverse pole figures in which both pieces of information (crystallographic orientation of the grain determined by EBSD analysis and physical orientation of the facet plane determined by quantitative tilt fractography), obtained in an SEM, are combined.

2. EXPERIMENTAL PROCEDURES:

2.1 Material and Specimen:

The Ti-6Al-2Sn-4Zr-2Mo (+ Si) alloy that was used in this study was provided in the form of a pancake forging by Ladish Co., Cudahy, WI. The as-received alloy had a bimodal microstructure, consisting of primary α grains and transformed β regions (Fig. 1). A more detailed description of microstructure, macro-texture and micro-texture of the as-received alloy is presented elsewhere [5]. This material had a high level of micro-texture that has been shown to correspond to a large dwell life debit in this alloy system [4].

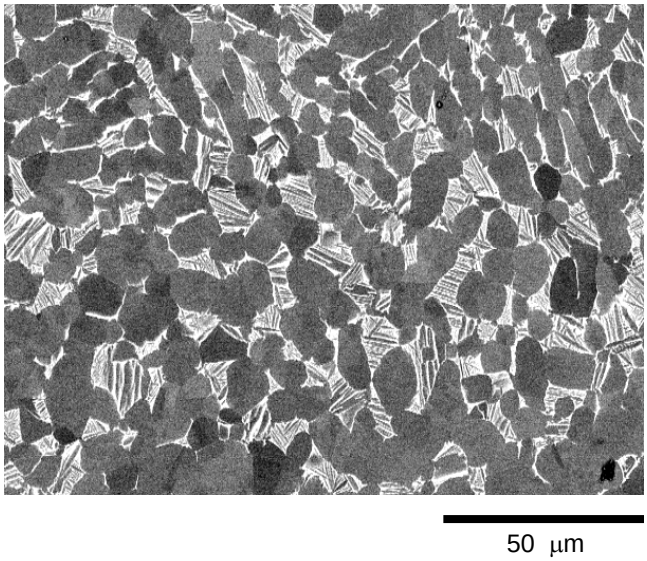

Fig. 1: SEM micrograph of the as-received α/β forged Ti-6242 alloy, acquired using a backscattered electron detector.

The dwell-fatigue specimen examined in this investigation is taken from a previously reported work [5]. The peak stress during dwell-fatigue testing of this specimen was ~ 95 % of yield strength (see ref. [5] for details). As has been described in ref. [5], the initiation site consisted of faceted features for this test condition. The fractured dwell-fatigue specimen was cleaned in an ultrasonic cleaner with acetone and then, with methanol. Thereafter, the specimen was baked overnight in an oven kept at ~ 70 ^{0}C before being characterized in an SEM.

2.2 SEM Examination:

The SEM used in the current study is a Philips XL-30 ESEM instrument that has a field emission gun (FEG) as the electron source. The crystallographic orientation of the grains, which contained dwell-fatigue fracture facets, was determined using the Electron Back Scattered Diffraction (EBSD) technique in the SEM. The details of this technique have been described elsewhere [7]. A critical step in applying this technique for the analysis of the fracture facets is the collection of background signal, which is typically collected at a low magnification on the sample being characterized for the case of polished specimens. Due to the unevenness of the fracture surface, a good background signal was difficult to obtain directly from the faceted fracture region. Therefore, the background signal was collected from a polished polycrystalline Ti-6242 specimen at a low magnification (200 X) under the operating conditions (i.e. accelerating voltage, spot size, working distance and stage tilt) that were subsequently used for the EBSD data collection on the fracture facets. The background subtraction improved the quality of the EBSD patterns obtained from the fracture facets. The operating conditions for EBSD experiments were as follows: accelerating voltage = 20 KV, working distance = 21 mm and SEM stage tilt = 70^0. Increasing the number of frames to be averaged for the facet characterization also helped improve the quality of EBSD patterns. The bands in the EBSD patterns so obtained were

detected manually and the patterns indexed using the computer software (supplier: TSL, Draper, UT) to determine crystallographic orientation for several locations on a particular dwell-fatigue fracture facet. In order to appropriately indicate the crystallographic orientation of the facet using an inverse pole figure, the determination of the physical orientation of the fracture facet was necessary, which will be described next.

The physical orientation of the dwell-fatigue fracture facets was determined using a quantitative tilt fractography technique in the SEM. This technique involves obtaining SEM images of the facets at two different tilt angles. The coordinates of three non-collinear fracture features on any one facet are measured on the SEM images at the two tilt angles. Thereafter, the coordinates of any fracture feature 'A', in the SEM stage axes system, are calculated using the relations (see ref. [6] for derivation):

$$X^A = (x_1^A.\sin\theta_2 - x_2^A.\sin\theta_1)/ \sin(\theta_2 - \theta_1) \qquad \text{……. 1(a)}$$

$$Y^A = y_1^A = y_2^A = (y_1^A + y_2^A)/ 2 \qquad \text{……. 1(b)}$$

$$Z^A = (-x_1^A.\cos\theta_2 + x_2^A.\cos\theta_1)/ \sin(\theta_2 - \theta_1) \qquad \text{……. 1(c)}$$

where (x_1^A, y_1^A) and (x_2^A, y_2^A) are the coordinates of a particular feature 'A' at tilt angles θ_1 and θ_2, respectively. X^A, Y^A, and Z^A denote the coordinates of point 'A' in the SEM stage axes system (X, Y, and Z). X-direction of the SEM stage axes system points to the top of the SEM images, Y-direction to the left of the SEM images and Z-direction is anti-parallel to the electron beam direction. The fractured specimens were loaded in the SEM specimen chamber such that their longitudinal direction (i.e. the loading axis during the dwell-fatigue testing) is aligned with the Z-direction of the SEM stage axes system.

Equations (1) are used to calculate the coordinates (X^B, Y^B, Z^B) and (X^C, Y^C, Z^C) in the SEM stage axes system of two additional fracture features 'B' and 'C', respectively. The vector connecting point 'A' to point 'B' is given by:

$$\overrightarrow{AB} = (X^B - X^A)\,\mathbf{i} + (Y^B - Y^A)\,\mathbf{j} + (Z^B - Z^A)\,\mathbf{k} \qquad \text{……. (2)}$$

where **i**, **j** and **k** are the unit vectors along X, Y and Z (SEM stage axes system), respectively. Similarly, the vector connecting point 'B' to point 'C' is given by:

$$\overrightarrow{BC} = (X^C - X^B)\,\mathbf{i} + (Y^C - Y^B)\,\mathbf{j} + (Z^C - Z^B)\,\mathbf{k} \qquad \text{……. (3)}$$

The cross product of these two vectors, $\overrightarrow{AB}$ and $\overrightarrow{BC}$, gives the vector representing the facet plane normal ($\vec{n}$):

$$\vec{n} = \begin{vmatrix} \mathbf{i} & \mathbf{j} & \mathbf{k} \\ (X^B - X^A) & (Y^B - Y^A) & (Z^B - Z^A) \\ (X^C - X^B) & (Y^C - Y^B) & (Z^C - Z^B) \end{vmatrix} \quad \text{..... (4a)}$$

i.e. $\vec{n} = \{(Y^B - Y^A).(Z^C - Z^B) - (Z^B - Z^A).(Y^C - Y^B)\}\ \mathbf{i} - \{(X^B - X^A).(Z^C - Z^B) - (Z^B - Z^A).(X^C - X^B)\}\ \mathbf{j} + \{(X^B - X^A).(Y^C - Y^B) - (Y^B - Y^A).(X^C - X^B)\}\ \mathbf{k}$ ..... (4b)

The angle between the loading axis (Z) and the facet plane normal is calculated using the formula:

$$\alpha = \cos^{-1}\left(\frac{\vec{n}.\mathbf{k}}{|\vec{n}|}\right) \quad \text{..... (5)}$$

This quantitative tilt fractography technique was first applied on a polished smooth specimen under the operating conditions used for imaging of the fracture surfaces. The analysis gave the angle between the Z-axis and the normal to the plane of polish as less than 1^0 and therefore, this technique is believed to be very reliable. Thereafter, this technique was applied on the dwell-fatigue fracture facets and the results are discussed in section 3.

The quantitative tilt fractography and the EBSD experiments were completed on a particular facet in one SEM session. Care was taken not to rotate the SEM stage in order to keep the orientation of the fracture facet same for the two sets of experiments (quantitative tilt fractography and EBSD). Based on the EBSD analyses results, the inverse pole figure was plotted for the direction that represents the fracture facet normal (equation (4)). This inverse pole figure describes the crystallographic orientation of the dwell-fatigue fracture facet being characterized. The inverse pole figures for fracture facets are presented in section 3.

3. RESULTS AND DISCUSSION:

In order to obtain an idea about the orientation of the large faceted area with respect to the loading axis, the quantitative tilt fractography experiments were conducted on the faceted region shown in Fig. 2. As described in section 2, the SEM fractographs of the same area were obtained

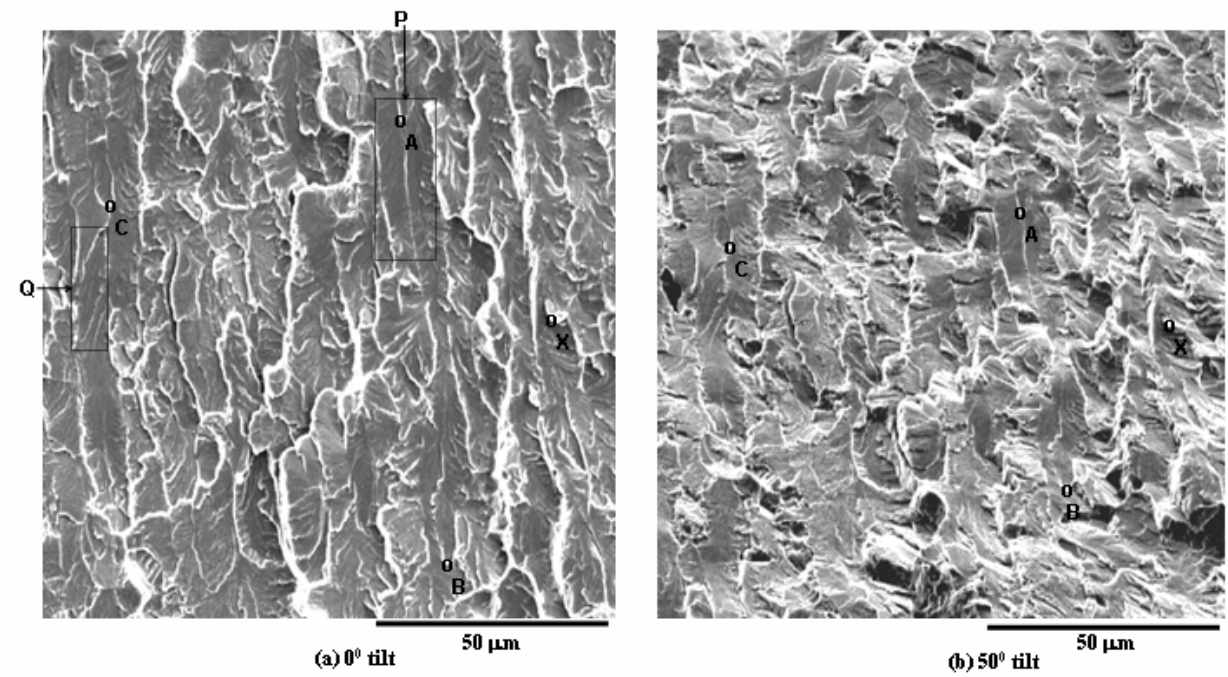

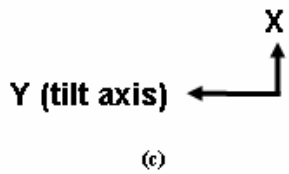

(c)

Fig. 2: SEM images of the faceted region at two different tilt angles. (a) 0^0 tilt, and (b) 50^0 tilt. Four recognizable features are labeled 'X', 'A', 'B' and 'C' in the SEM images. The points labeled 'X', 'A', 'B' and 'C' refer to the same features in (a) as in (b). The facets, complementary to 'P' and 'Q' indicated in fig. (a), on the other fracture surface of the same specimen are shown at a higher magnification in Fig. 4 (a) and 5 (a), respectively. (c) Schematic representation of the orientation of SEM stage axes system with respect to the SEM images. X-axis points to the top of SEM image, Y-axis to the left and Z-axis is coming out of the plane of paper. The origin of the SEM stage axes system is effectively at point labeled 'X' in SEM images, for the purposes of quantitative tilt fractography analyses. The orientation of the SEM stage axes system with respect to the SEM images remains same in Fig. 3 – 5.

at two tilt angles, 0^0 and 50^0 (Fig. 2). A recognizable feature on the fractographs was chosen as origin, labeled as 'X' in Fig. 2 (a) and (b). It should be noted that the fracture features labeled 'X' in Fig. 2 (a) and in Fig. 2 (b) are one and the same. Three additional recognizable features on the fractographs were identified and are labeled 'A', 'B' and 'C' in Fig. 2 (a) and (b). Similar to the case of the feature labeled 'X', the features labeled 'A', 'B' and 'C' in Fig. 2 (a) correspond to 'A', 'B' and 'C', respectively in Fig. 2 (b). The x and y coordinates of the points 'A', 'B' and 'C', with respect to the origin 'X', were measured at both the tilt angles 0^0 and 50^0 (Fig. 2 (a) and (b)). Since tilt axis is along the Y-direction, the x coordinates of the points 'A', 'B' and 'C' change with a change in the tilt angle whereas the y coordinates remain essentially unchanged. From the (x,y) coordinates of the points 'A', 'B' and 'C' at the two tilt angles, their X, Y and Z coordinates were determined, using the relations (1), in the SEM stage axes system with the origin at point labeled 'X' in Fig. 2 (a) and (b). Thereafter, the vectors connecting point 'A' to 'B', and point 'B' to 'C' at 0^0 tilt are calculated using relations (2) and (3). The vector representing the facet (defined by points 'A', 'B' and 'C') normal, at 0^0 tilt, is $\mathbf{i} - 2.4\,\mathbf{j} + 35.19\,\mathbf{k}$, as calculated using relation (4). The angle between the loading axis and the facet plane normal is $\sim 4^0$, as determined using equation (5). From this result one might conclude that the dwell-fatigue fracture facets are approximately normal to the loading axis. However, it should be noted that the analysis presented above is for a region that contains several facets. More specifically, all the facets between points 'A' and 'B', and points 'B' and 'C' (Fig. 2) are included in the calculations. If we were to focus our attention on one particular facet, we might obtain somewhat different result, as will be discussed next.

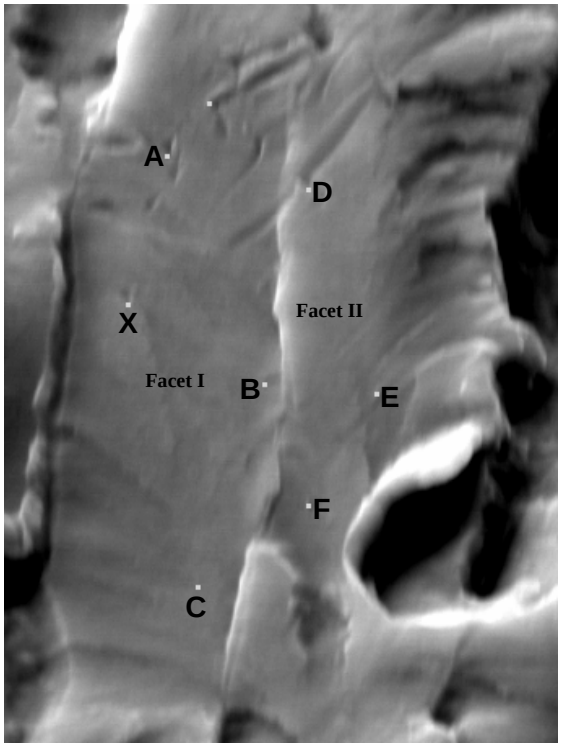

(a) 50^0 tilt

5 μm

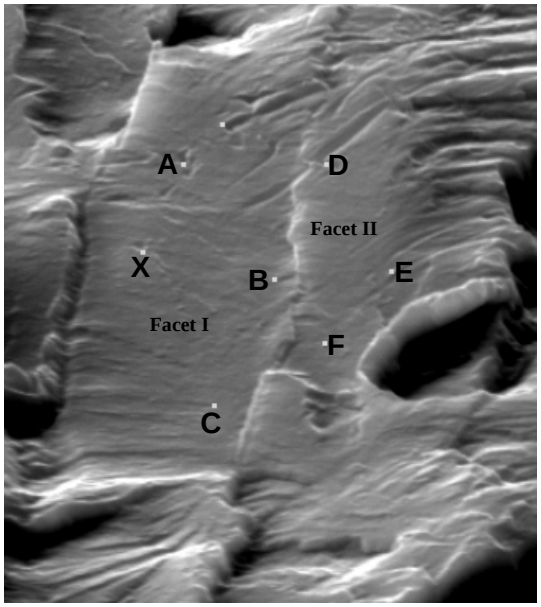

5 μm

(b) 70^0 tilt

Fig. 3: SEM images of the dwell-fatigue fracture facets at two different tilt angles. (a) 50^0 tilt, and (b) 70^0 tilt. Seven recognizable features are labeled 'X', 'A', 'B', 'C', 'D', 'E' and 'F' in the SEM images. The point labeled 'X' refers to the same feature in (a) as in (b). Similarly, the points labeled 'A', 'B' 'C', 'D', 'E' and 'F' refer to the same features in (a) and (b).

The quantitative tilt fractography analyses were done on individual facets as per the procedures described above. The only difference was that the SEM images were acquired at a much higher magnification than in Fig. 2. An example of the analyses conducted separately on the two adjacent dwell-fatigue facets is presented in Fig. 3. As before, an origin 'X' was identified at both the tilt angles. Moreover, three additional points ('A', 'B' and 'C') on facet I and three points ('D', 'E' and 'F') on facet II were identified. From the measurements of the coordinates of these six points at the two tilt angles, the vector representing the facet normal was determined for both the facets. The angle between the loading axis and facet normal is 18^0 for facet I and 15^0 for facet II. Therefore, the individual facets are oriented at $72^0 – 75^0$ to the loading axis even though the region encompassing several facets is approximately normal to the loading axis.

The quantitative tilt fractography analysis was conducted on one additional dwell-fatigue fracture facet and the results are summarized in Table I. From Table I it is clear that the individual facet normal is oriented at $12^0 – 18^0$ with respect to the loading axis.

Table I: Summary of quantitative tilt fractography results

Reference figure	Vector representing the facet normal ($\bar{n}$)	Angle between facet normal ($\bar{n}$) and loading axis
Fig. 2	**i** – 2.40 **j** +35.19 **k**	4^0
Fig. 3 & 4 (facet I)	- **i** + 6.63 **j** +20.02 **k**	18^0
Fig. 3 & 4 (facet II)	- **i** + 6.12 **j** +23.62 **k**	15^0
Fig. 5 (a)	- **i** + 2.60 **j** +12.89 **k**	12^0

The crystallographic orientation of the facets I and II in Fig. 4 (a) are shown in the inverse pole figures (Fig. 4 (b) and (c)). The EBSD analyses were done at five locations on facet I and three locations on facet II, as indicated in Fig. 4 (a). It should be mentioned that a small image drift (~ 1 μm) in the + X-direction (the direction of X-axis with respect to the SEM images is shown in Fig. 2 (c)) was noticed during the time needed (~ 10 minutes) for manual detection of the bands and computer software-aided indexing of multiple EBSD patterns. Nonetheless, it was ensured that all the points for which the EBSD analyses were conducted corresponded to the facet under consideration. The inverse pole figures (Fig. 4 (b) and (c)), based on the EBSD analyses at multiple locations on facets I and II, indicate a good reproducibility in the overall methodology used to determine the crystallographic orientation of individual facets. It is also clear from Fig. 4 (b) and (c) that the dwell-fatigue fracture facets are not exactly aligned with the basal plane, but are inclined at ~ 10^0 to it. It is important to note that if one were to assume that the fracture facets are approximately normal to the loading axis based on the analysis presented in Fig. 2 and were to plot an inverse pole figure for the case of facet normal being aligned with the loading axis, it would result in an inaccurate representation of the crystallographic orientation of the facet. Fig. 4 (d) is such an inverse pole figure for facet I of Fig. 4 (a), where the facet normal has been assumed to be along the loading axis. A comparison of Fig. 4 (b) and (d) indicates the degree of error that can be caused by such an assumption. Therefore, it is important to apply the quantitative tilt fractography technique to determine the orientation of the individual facets, as we have described above. Another dwell-fatigue fracture facet is shown in Fig. 5 (a) and its crystallographic orientation is depicted in Fig. 5 (b). Similar to the facets I and II in Fig. 4 (a), the facet shown in Fig. 5 (a) is inclined at ~ 10^0 to the basal plane.

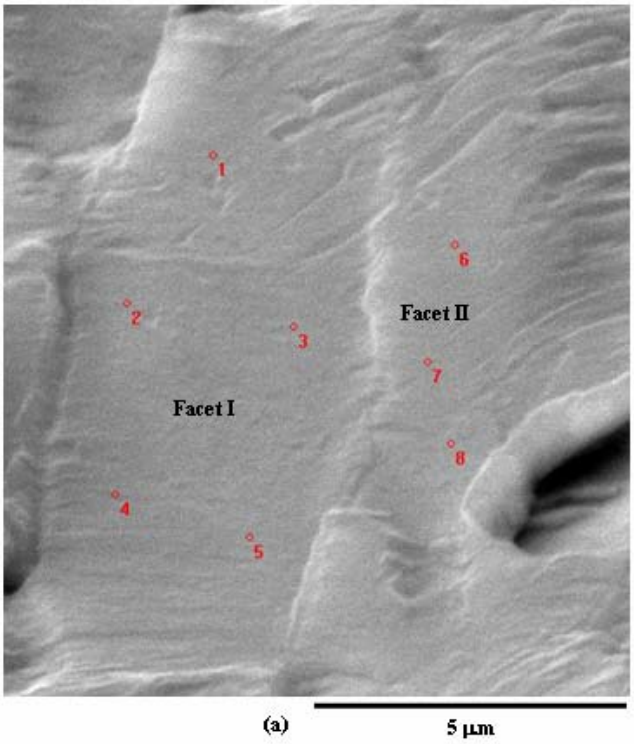

Fig. 4: Crystallographic orientation determination of individual dwell-fatigue fracture facets. (a) SEM image at 70^0 tilt of two adjacent facets I and II showing the locations of five points on facet I and three points on facet II from where the EBSD patterns were obtained and subsequently indexed to determine the crystallographic orientation of the grains through which these two facets had been produced. (b) Inverse pole figure showing the orientation of facet I normal based on the EBSD analyses on five locations shown in (a) and the physical orientation of the facet (facet normal, $\bar{n} = -\mathbf{i} + 6.63\,\mathbf{j} + 20.02\,\mathbf{k}$), as determined by the quantitative tilt fractography technique (see Fig. 3 and Table I). (c) Inverse pole figure showing the orientation of facet II normal based on the EBSD analyses on three locations shown in (a) and the physical orientation of the facet (facet normal, $\bar{n} = -\mathbf{i} + 6.12\,\mathbf{j} + 23.62\,\mathbf{k}$), as determined by the quantitative tilt fractography technique (see Fig. 3 and Table I). (d) Inverse pole figure showing the orientation of facet I normal based on the EBSD analyses on five locations shown in (a) and assuming the facet to be normal to the loading axis, i.e. $\bar{n} = \mathbf{k}$ (see text for details).

Crystallographic orientation determination of individual dwell-fatigue fracture points. (a) SEM image at 70 tilt of two adjacent facets I and II showing the locations of five points on facet I and three points on facet II from where the EBSD patterns were obtained and subsequently indexed to determine the crystallographic orientation of the grains through which these two facets had been produced.

Therefore, the dwell-fatigue fracture facets are not exactly aligned with the basal plane, but are inclined at ~ 10^0 to it. Davidson and Eylon have reported similar facet orientation for IMI 685 dwell specimens [1]. Blackburn and Williams [8] have also determined the crystallographic orientation of facets in Ti-8Al alloy using back-reflection X-ray techniques and our results on dwell-fatigue fracture facets are consistent with their results.

For the three dwell-fatigue facets characterized in the current study, the orientations of the facet normal and the loading axis are shown in Fig. 6 (a) and (b), respectively. The inclination of facet normal with respect to the basal plane normal lies in the range of $8^0 – 12^0$ with an average of ~ 10^0 (Fig. 6 (a)). On the other hand, the inclination of loading axis with respect to the basal plane normal lies in the range of $14^0 – 20^0$ with an average of ~ 17^0 (Fig. 6 (b)).

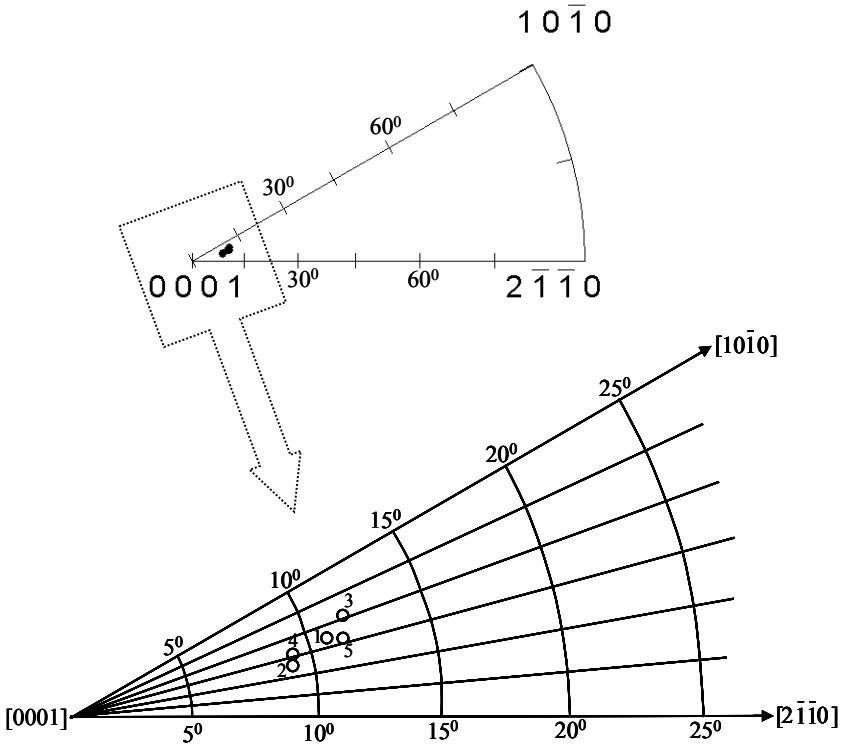
1 0 $\bar{1}$ 0
60⁰
30⁰
0 0 0 1
30⁰
60⁰
2 $\bar{1}$ $\bar{1}$ 0
[10$\bar{1}$0]
25⁰
20⁰
15⁰
10⁰
5⁰
3
4
1
5
2
[0001]
5⁰
10⁰
15⁰
20⁰
25⁰
[2$\bar{1}\bar{1}$0]

Fig. 4 (b)

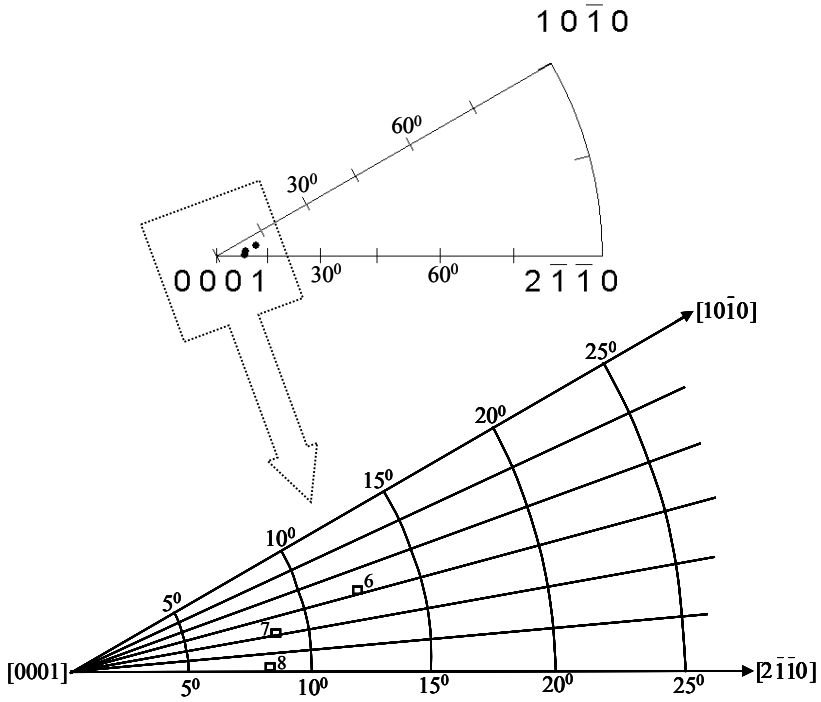
1 0 $\bar{1}$ 0
60⁰
30⁰
0 0 0 1
30⁰
60⁰
2 $\bar{1}$ $\bar{1}$ 0
[10$\bar{1}$0]
25⁰
20⁰
15⁰
10⁰
5⁰
6
7
8
[0001]
5⁰
10⁰
15⁰
20⁰
25⁰
[2$\bar{1}\bar{1}$0]

Fig. 4 (c)

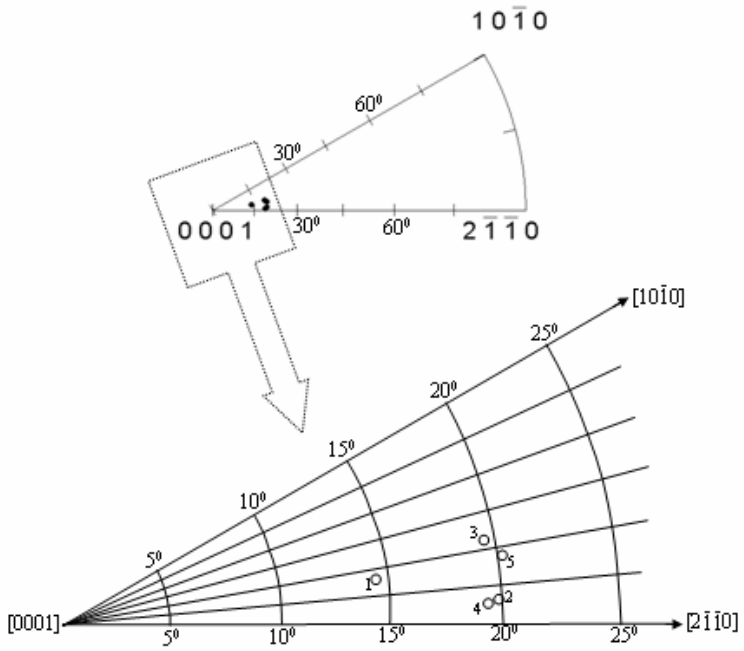
10$\bar{1}$0
60°
30°
0001
30°
60°
2$\bar{1}\bar{1}$0
[10$\bar{1}$0]
25°
20°
15°
10°
5°
3
5
1
4
2
[0001]
5°
10°
15°
20°
25°
[2$\bar{1}\bar{1}$0]

Fig. 4 (d)

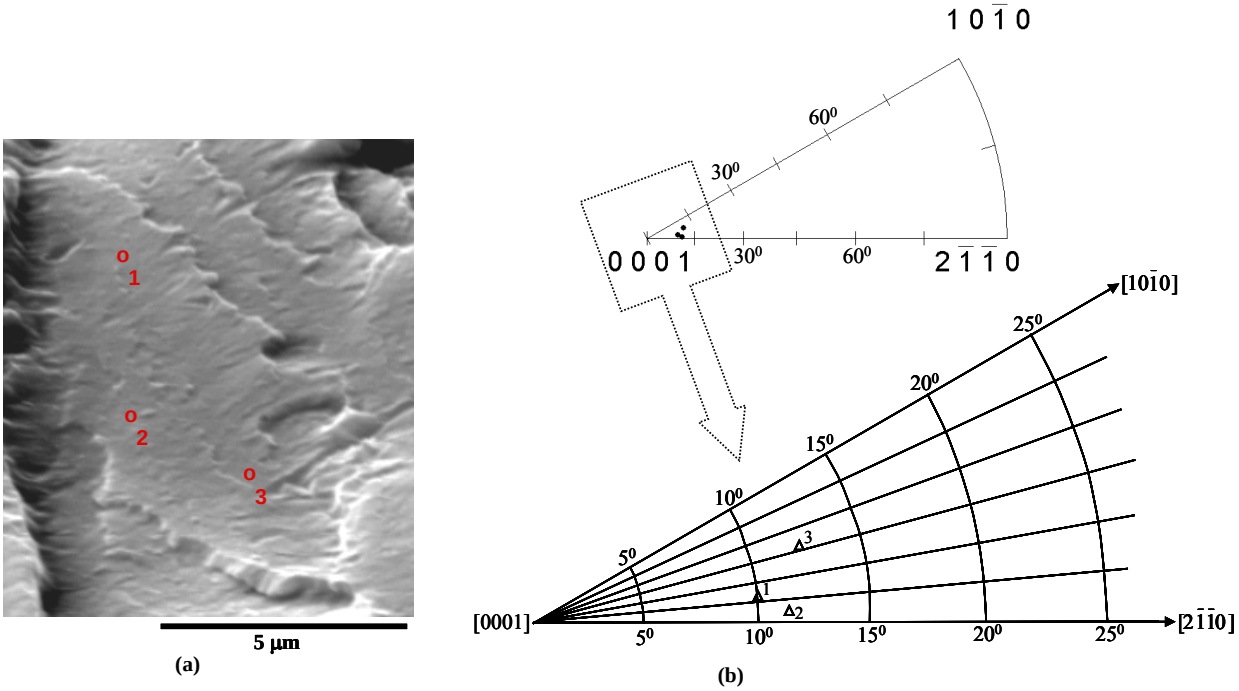

Fig. 5: Crystallographic orientation determination of another dwell-fatigue fracture facet. (a) SEM image at 70^0 tilt of a facet showing the locations of three points on the facet from where the EBSD patterns were obtained and subsequently indexed to determine the crystallographic orientation of the grain through which this facet had been produced. (b) Inverse pole figure showing the orientation of the facet normal based on the EBSD analyses on three locations shown in (a) and the physical orientation of the facet (facet normal, $\underline{n}$= - **i** + 2.60 **j** +12.89 **k**), as determined by the quantitative tilt fractography technique (see Table I).

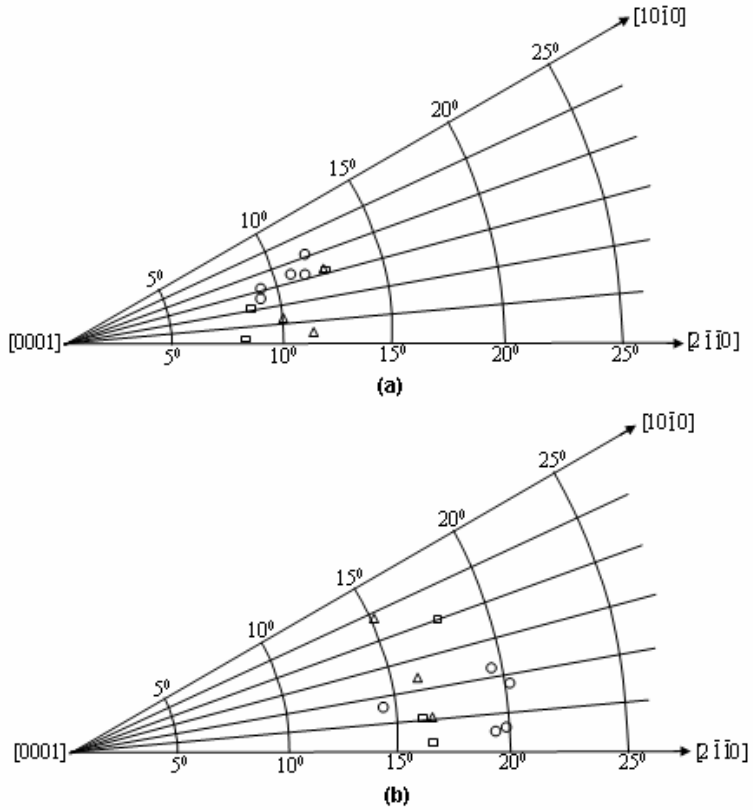

Fig. 6: Inverse pole figures showing the orientation of (a) facet normal, and (b) loading axis for the facets shown in Fig. 4 (a) and 5 (a). ○: Facet I of Fig. 4 (a); □: Facet II of Fig. 4 (a); and △: Facet shown in Fig. 5 (a).

An example of the EBSD pattern obtained from a dwell-fatigue fracture facet in the current study is shown in Fig. 7(a). Part of the phosphor screen in our laboratory is damaged and this keeps part of the pattern (labeled 'A' in Fig. 7(a)) from being detected. Furthermore, there is another dark region (labeled 'B' in Fig. 7(a)) which is caused due to the fact that the facet plane is not perpendicular to the electron beam at 0^0 tilt (as is the case for the specimens polished specifically for EBSD analysis). The result of the indexing of the pattern shown in Fig. 7(a), using the technique outlined in the current paper, is shown in Fig. 7(b). It is clear that in spite of part of the EBSD pattern missing, the indexing yields an unambiguous (Fig. 7(b)) and reproducible (see Fig. 4 and 5) crystallographic orientation.

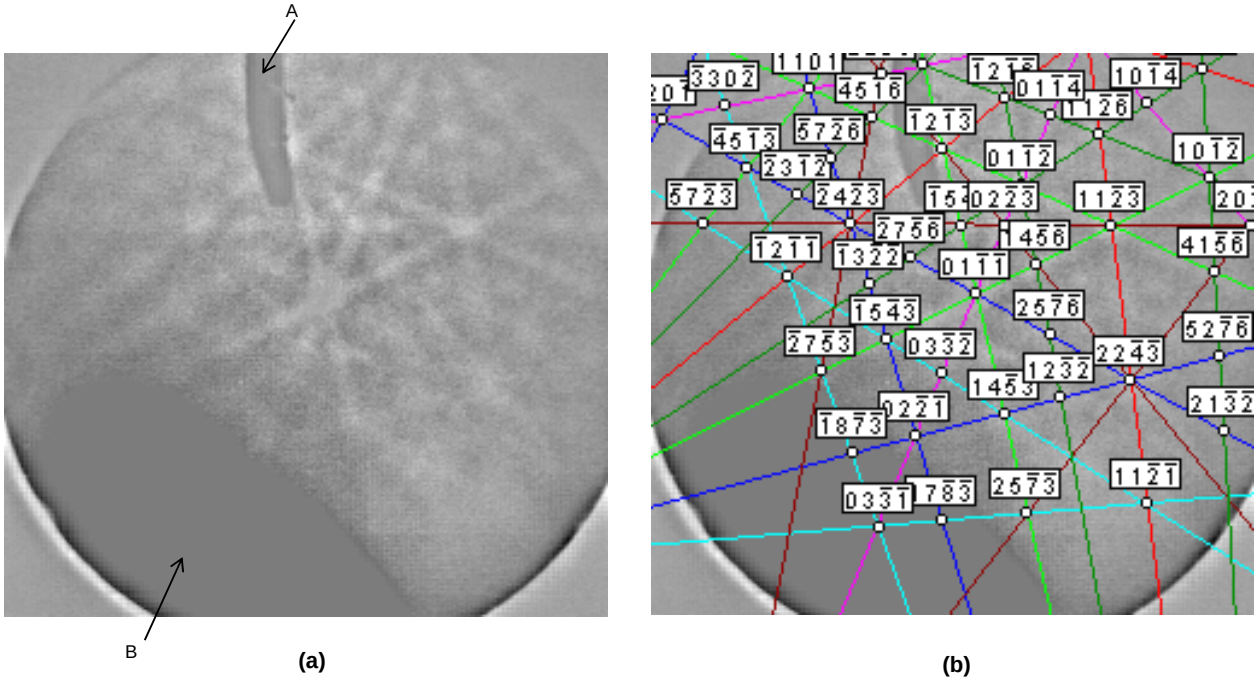

Fig. 7: (a) An example of the EBSD pattern obtained from the facet I shown in Fig. 4, and (b) Indexing of the pattern shown in (a). Parts of the pattern is not detected: the region labeled 'A' in Fig. (a) is due to the damage in this small part of the phosphor screen, whereas the region labeled 'B' is due to the fact that the fracture facet is not exactly normal to the electron beam prior to tilting for the EBSD experiments. Even with part of the pattern missing, the indexing yields an unambiguous, correct and reproducible result.

It is important to note that the typical spot size for the electron channeling technique is ~ 50 μm [1], whereas it is much less than 1 μm for the EBSD-based technique described in the present paper. Therefore, significantly smaller facets can be characterized using the latter technique. Furthermore, the facets were electropolished for characterization by electron channeling technique in the work of Davidson and Eylon [1]. In the current study, the EBSD patterns were obtained directly from the fracture facet and the electropolishing of facets was not needed. Thus, the alloys with finer microstructural features are amenable to the characterization by the technique presented in the current paper, because electropolishing causes a loss of finite thickness of material. Moreover, the technique proposed in the current paper is simpler to apply because it does not require electropolishing of the fracture facets.

4. SUMMARY AND CONCLUSIONS:

In this paper, a technique to determine the crystallographic orientation of the fracture facets has been described. The physical orientation of the facet plane was determined by the quantitative tilt fractography technique in an SEM. The crystallographic orientation of the grain, through which the fracture facet had been produced, was determined by EBSD analysis, also in an SEM. These two pieces of information were combined to obtain the crystallographic orientation of the fracture facets.

In the technique proposed in this paper, electropolishing of the fracture facets is not needed and the EBSD patterns are obtained directly from the facets. Thus, this technique is simpler and more straightforward than the electron channeling technique proposed by Davidson and Eylon [1]. The spot size for the EBSD analysis is much less than 1 μm, whereas it is typically ~ 50 μm for the electron channeling technique [1]. Therefore, an alloy with finer microstructural features and smaller fracture facets can be characterized using the technique described in the current paper.

Though Bache, et al. have obtained the EBSD patterns directly from the fracture facets after a light etch, the determination of the physical orientation of the fracture facets has not been discussed explicitly in their work [3]. As we have discussed in the current paper, the determination of the physical orientation of the fracture facets is essential for an appropriate determination of their crystallographic orientation, unless the specimen is oriented to make the facet plane perpendicular to the electron beam (as Davidson and Eylon [1] have done in their work) prior to tilting for the EBSD experiments. We have described a technique to determine the physical orientation of the fracture facets, which is based on the work of Themelis, et al. [6].

We have used the technique described in the current paper to determine the crystallographic orientation of several dwell-fatigue fracture facets in Ti-6242 alloy. Our results indicate that these facets are inclined at ~ 10^0 to the basal plane.

REFERENCES:

1. D.L. Davidson and D. Eylon, Metallurgical Transactions, vol. 11A, pp. 837-843, 1980.

2. M.R. Bache, H.M. Davies, and W.J. Evans, Titanium ’95: Science and Technology, pp. 1347-1354, 1995.

3. M.R. Bache, W.J. Evans, and H.M. Davies, Journal of Materials Science, vol. 32, pp. 3435-3442, 1997.

4. A.P. Woodfield, M.D. Gorman, R.R. Corderman, J.A. Sutliff and B. Yamrom, Titanium ’95: Science and Technology, pp. 1116-1124, 1995.

5. V. Sinha, M.J. Mills, and J.C. Williams, Metallurgical and Materials Transactions, vol. 35A, pp. 3141-3148, 2004.

6. G. Themelis, S. Chikwembani and J. Weertman, Materials Characterization, vol. 24, pp. 27-40, 1990.

7. S.I. Wright, Electron Backscatter Diffraction in Materials Science, A.J. Schwartz, M. Kumar, and B.L. Adams (editors), Kluwer Academic/ Plenum Publishers, New York, N.Y., pp. 51-64, 2000.

8. M. J. Blackburn and J. C. Williams, "Metallurgical Aspects of the Stress Corrosion Cracking of Titanium Alloys,” Proc. Conf. on the Fundamental Aspects of Stress Corrosion Cracking, N.A.C.E., 1969, p 620.

Appendix G

Crystallography of Fracture Facets in a Near-alpha Titanium Alloy

V. Sinha, M.J. Mills, and J.C. Williams

Department of Materials Science and Engineering, The Ohio State University,
2041 College Road, Columbus, OH 43210

Abstract

A faceted initiation site is observed in Ti-6242 alloy for both the cyclic and static-loading test conditions. Tilt fractography has been used to obtain the angle between the facet normal and the loading axis. The crystallographic orientation of the facets has been determined using the electron backscattered diffraction (EBSD) technique in conjunction with the tilt fractography in a scanning electron microscope. The results indicate that the normal-fatigue (no-dwell) fracture facets are oriented at ~ 5^0 with respect to the basal plane; the dwell-fatigue fracture facets are oriented at ~ 10^0-15^0 with respect to the basal plane and the static-loading fracture facets are oriented at ~ 20^0 with respect to the basal plane.

Facets have been observed on the fracture surface of near-α titanium alloys tested under normal-fatigue, dwell-fatigue and static-loading conditions [1-5]. In order to better understand the crack initiation mechanism, it is important to determine the crystallographic orientation of these fracture facets.

Davidson and Eylon [1] determined the orientations of fracture facets obtained under normal-fatigue (no-dwell) and dwell-fatigue conditions in a colony microstructure IMI 685. The facets, near the fracture origin, had a pure-basal orientation for the normal-fatigue test condition; whereas they had a near-basal orientation (7^0 – 15^0 away from the basal plane) for the dwell-fatigue test condition [1]. Bache, et al. [2, 3] have also observed a near-basal orientation for the initiation site fracture facets in colony microstructure IMI 685 and also in bimodal microstructure IMI 834. Woodfield and Sutliff [6] have reported that the dwell-fatigue fracture facet is of pure-basal or near-basal orientation for an α/β forged and heat-treated Ti-6242 alloy. In another study, the dwell-fatigue fracture facets are observed to be oriented at ~ 10^0 with respect to the basal plane in an α/β forged and heat-treated Ti-6242 alloy [7]. It is interesting to note that similar facets have been reported as the result of aqueous stress corrosion cracking [8].

One of the common microstructural conditions in which Ti-6242 alloy is used in practice is the bimodal microstructure with a reasonably high volume fraction of primary α. Though the orientation of dwell-fatigue fracture facet for this microstructure has been determined in earlier studies [6, 7], there is very little work on the orientation determination of normal-fatigue and static-loading fracture facets for this microstructure. The objective of the current study was to determine the crystallographic orientation of the normal-fatigue and static-loading fracture facets in Ti-6242 alloy that had a bimodal microstructure with a high volume fraction of primary α. The results of this study can lead to an improved understanding of the crack initiation mechanism under different loading conditions.

The normal-fatigue, dwell-fatigue and static-loading specimens examined in this investigation are taken from a previously reported work [5]. The normal-fatigue and dwell-fatigue tests had been carried out at ~ 91 % of yield strength; whereas the static-loading test had been carried out at ~ 95 % of yield strength (see ref. [5] for details). As has been described in ref. [5], the initiation site consisted of faceted features for each of the three specimens (i.e. the normal-fatigue and dwell-fatigue specimens that had been tested at ~ 91 % of yield strength and the static-loading specimen that had been tested at ~ 95 % of yield strength). The characterization results on the dwell-fatigue fracture facets that were produced at ~ 95 % of yield strength have been reported elsewhere [7].

The crystallographic orientation of the fracture facets was determined using the quantitative tilt fractography and electron backscattered diffraction (EBSD) techniques in a scanning electron microscope (SEM). The details of this methodology have been described elsewhere [7]. The quantitative tilt fractography also provides the orientation of the facets with respect to the loading axis.

The faceted initiation site obtained for the normal-fatigue test condition (peak stress ~ 91 % of yield strength) is depicted in Fig. 1. The crystallographic orientation of two adjacent facets

(labeled ‘I’ and ‘II’ in Fig. 1) was determined. Facet ‘I’ is oriented less than 5^0 away from the basal plane (Fig. 2), whereas facet ‘II’ is oriented at ~ 5^0 with respect to the basal plane (Fig. 3).

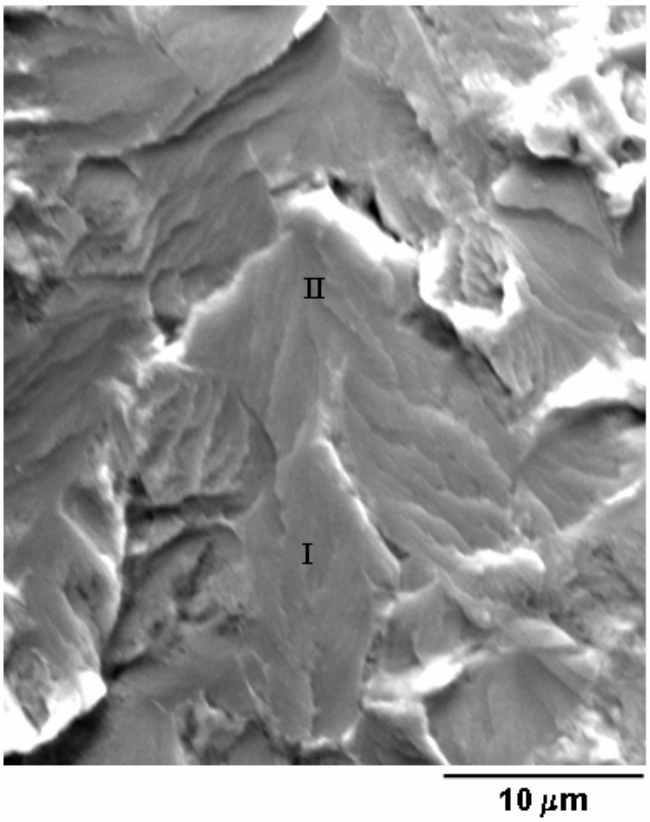

Fig. 1: Faceted initiation site for the normal-fatigue test condition. The crystallographic orientation of the facets labeled ‘I’ and ‘II’ has been determined.

The faceted initiation site obtained for the dwell-fatigue test condition (peak stress ~ 91 % of yield strength) is depicted in Fig. 4. The crystallographic orientation of two facets, labeled ‘I’ and ‘II’ in Fig. 4, was determined. Facets ‘I’ and ‘II’ are oriented at ~ 12^0 and ~ 15^0, respectively with respect to the basal plane (Fig. 5 and 6). For the same alloy, the dwell-fatigue fracture facets, which were produced at ~ 95 % of yield strength, are observed to be oriented at ~ 10^0 with respect to the basal plane [7].

The faceted initiation site obtained for the static-loading test condition (applied stress ~ 95 % of yield strength) is shown in Fig. 7. The facets, labeled ‘I’ and ‘II’ in Fig. 7, are oriented at ~ 20^0 with respect to the basal plane (Fig. 8 and 9).

Therefore, of the three loading conditions (normal-fatigue, dwell-fatigue and static-loading), the deviation from the basal plane is the smallest for the normal-fatigue fracture facets and it is the largest for the static-loading fracture facets (Fig. 10 (a)).

The orientation of the loading axis is also shown in the stereographic projections for the fracture facets obtained under three loading conditions: normal-fatigue, dwell-fatigue and static-loading

(Fig. 10 (b)). It is clear from this figure that the deviation of loading axis from the basal plane normal is the smallest for the normal-fatigue fracture facets and it is the largest for the static-loading fracture facets.

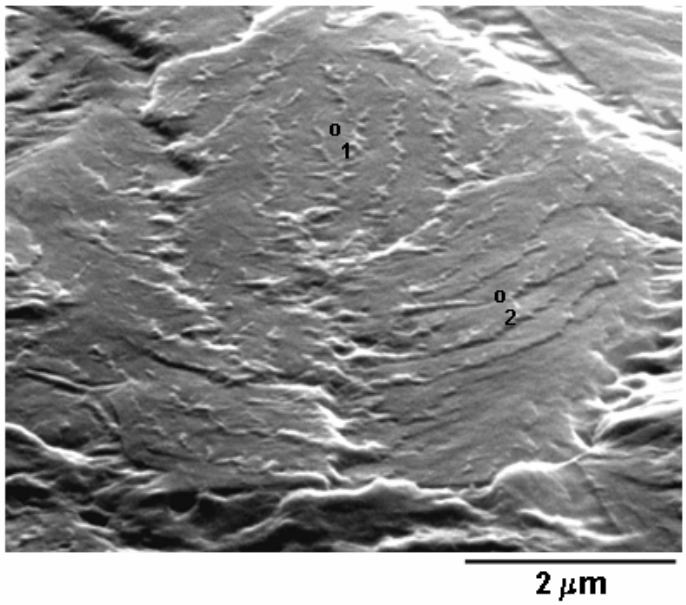

(a)

Fig. 2: Crystallographic orientation determination of normal-fatigue fracture facet that has been labeled 'I' in Fig. 1. (a) SEM image of the facet at 70^0 tilt showing the locations of two points from where the EBSD patterns were obtained and subsequently indexed to determine the crystallographic orientation of the facet. (b) Inverse pole figure showing the crystallographic orientation of facet based on the EBSD analyses on two locations shown in (a) and the spatial orientation of the facet (facet normal, $\mathbf{n} = \mathbf{i} + 1.28\,\mathbf{j} + 26.33\,\mathbf{k}$), as determined by the quantitative tilt fractography technique (see Table I).

From the quantitative tilt fractography experiments conducted in this work, it is also possible to obtain the angle between facet normal and the loading axis. The results for the two normal-fatigue, two dwell-fatigue and two static-loading fracture facets are summarized in Table I. The normal to the normal-fatigue facets shown in Fig. 2 and 3 are oriented with respect to the loading axis at 4^0 and 3^0, respectively (Table I). Moreover, the normal to the dwell-fatigue facets shown in Fig. 5 and 6 are oriented to the loading axis at 6^0 and 12^0, respectively (Table I). On the other hand, the normal to the static-loading facets shown in Fig. 8 and 9 are oriented with respect to the loading axis at 19^0 and 24^0, respectively (Table I). For the same alloy, the normal to the dwell-fatigue facets, which were produced at ~ 95 % of yield strength, are oriented with respect to the loading axis at angles in the range of $12^0 – 18^0$ [7]. Therefore, the deviation from the loading axis is the smallest for the normal-fatigue facet normal and it is the largest for the static-loading facet normal.

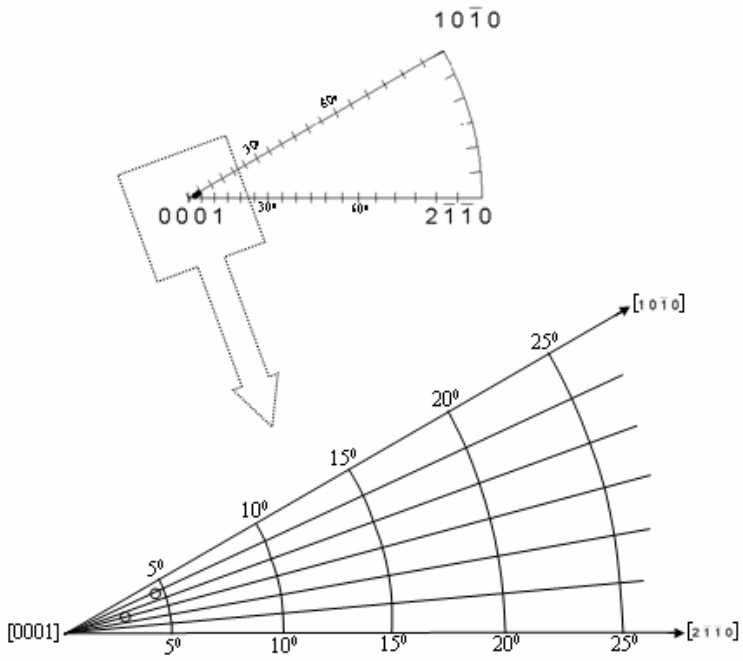

Fig. 2 (b)

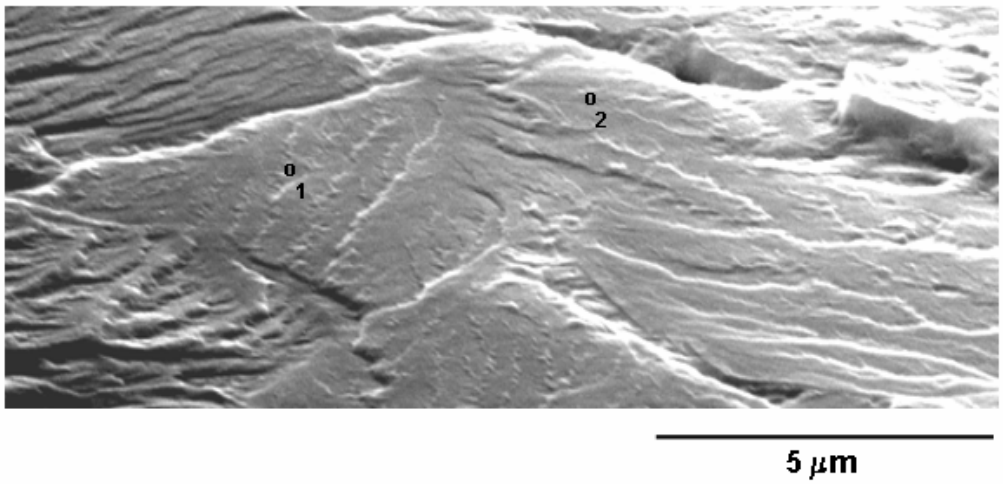

(a)

Fig. 3: Crystallographic orientation determination of normal-fatigue fracture facet that has been labeled 'II' in Fig. 1. (a) SEM image of the facet at 70⁰ tilt showing the locations of two points from where the EBSD patterns were obtained and subsequently indexed to determine the crystallographic orientation of the facet. (b) Inverse pole figure showing the crystallographic orientation of facet based on the EBSD analyses on two locations shown in (a) and the spatial orientation of the facet (facet normal, $\mathbf{n} = \mathbf{i} + 0.46\,\mathbf{j} + 21.83\,\mathbf{k}$), as determined by the quantitative tilt fractography technique (see Table I).

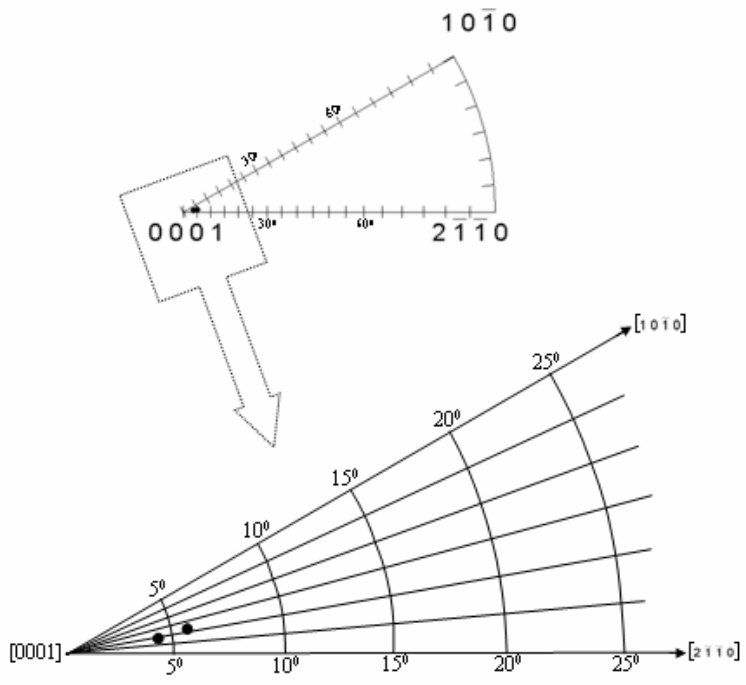

Fig. 3(b)

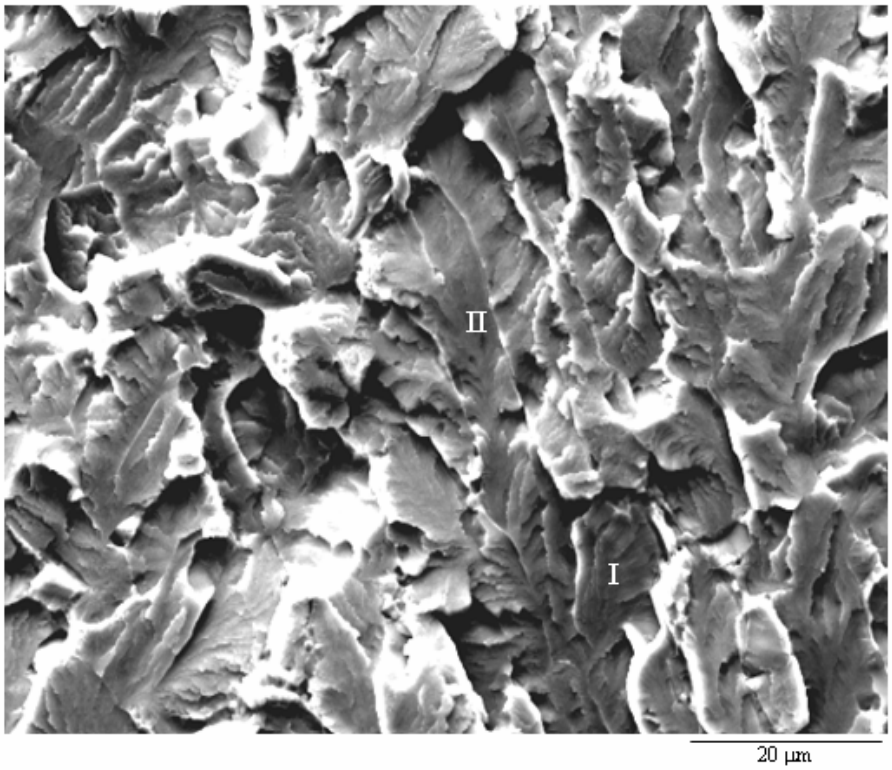

Fig. 4: Faceted initiation site for the dwell-fatigue test condition. The crystallographic orientation of the facets labeled 'I' and 'II' has been determined.

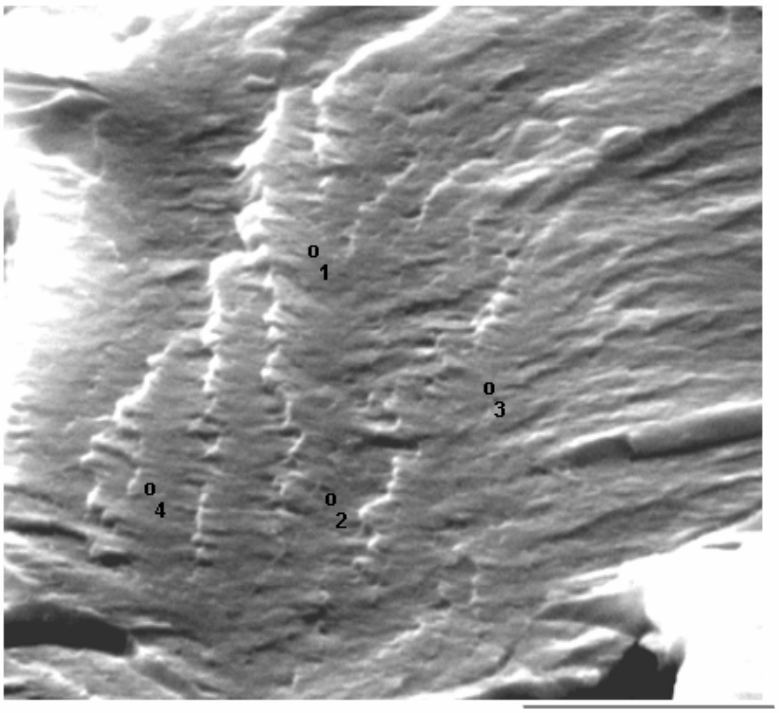

(a)

Fig. 5: Crystallographic orientation determination of dwell-fatigue fracture facet that has been labeled 'I' in Fig. 4. (a) SEM image of the facet at 70° tilt showing the locations of four points from where the EBSD patterns were obtained and subsequently indexed to determine the crystallographic orientation of the facet. (b) Inverse pole figure showing the crystallographic orientation of facet based on the EBSD analyses on four locations shown in (a) and the spatial orientation of the facet (facet normal, $\mathbf{n} = -\mathbf{i} - 0.31\,\mathbf{j} + 10.42\,\mathbf{k}$), as determined by the quantitative tilt fractography technique (see Table I).

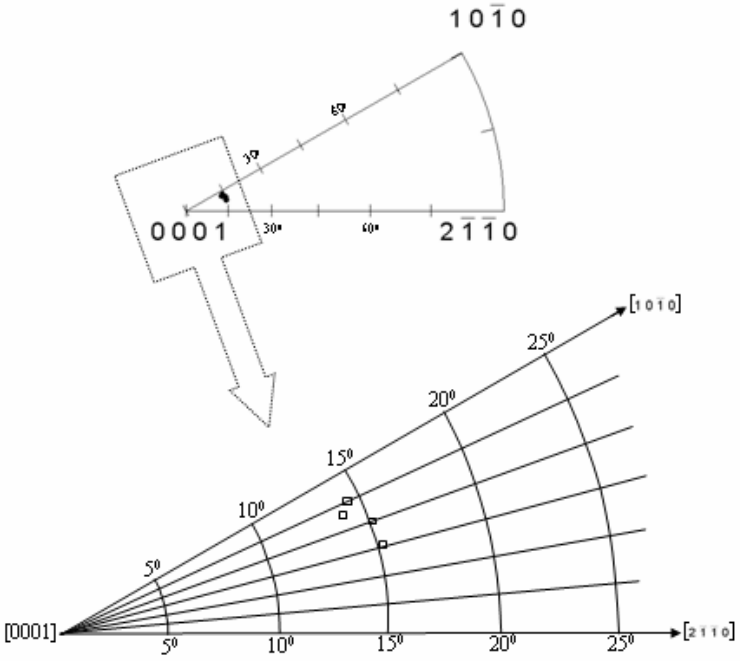

Fig. 5 (b)

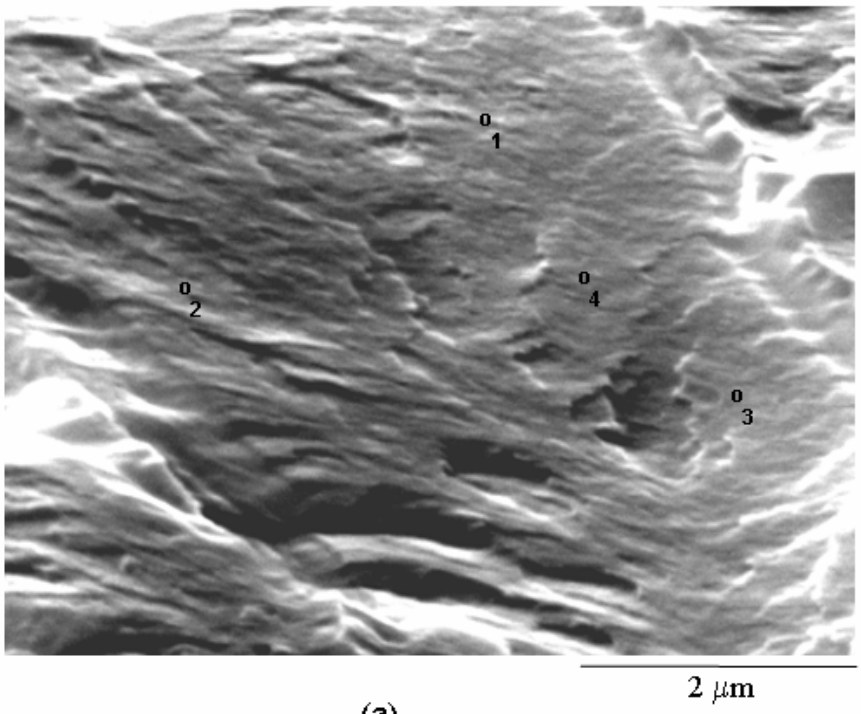

(a)

Fig. 6: Crystallographic orientation determination of dwell-fatigue fracture facet that has been labeled 'II' in Fig. 4. (a) SEM image of the facet at 70° tilt showing the locations of four points from where the EBSD patterns were obtained and subsequently indexed to determine the crystallographic orientation of the facet. (b) Inverse pole figure showing the crystallographic orientation of facet based on the EBSD analyses on four locations shown in (a) and the spatial orientation of the facet (facet normal, $\mathbf{n} = \mathbf{i} - 4.38\,\mathbf{j} + 21.11\,\mathbf{k}$), as determined by the quantitative tilt fractography technique (see Table I).

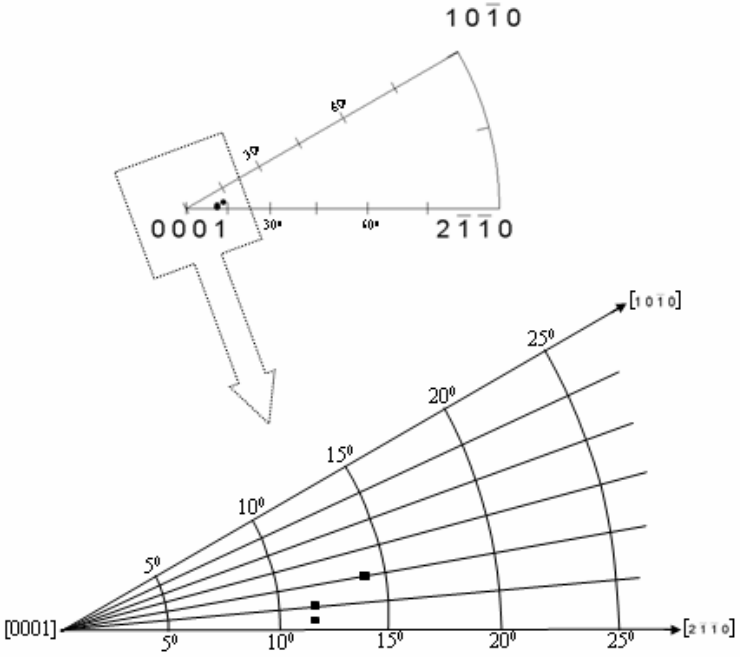

Fig. 6(b)

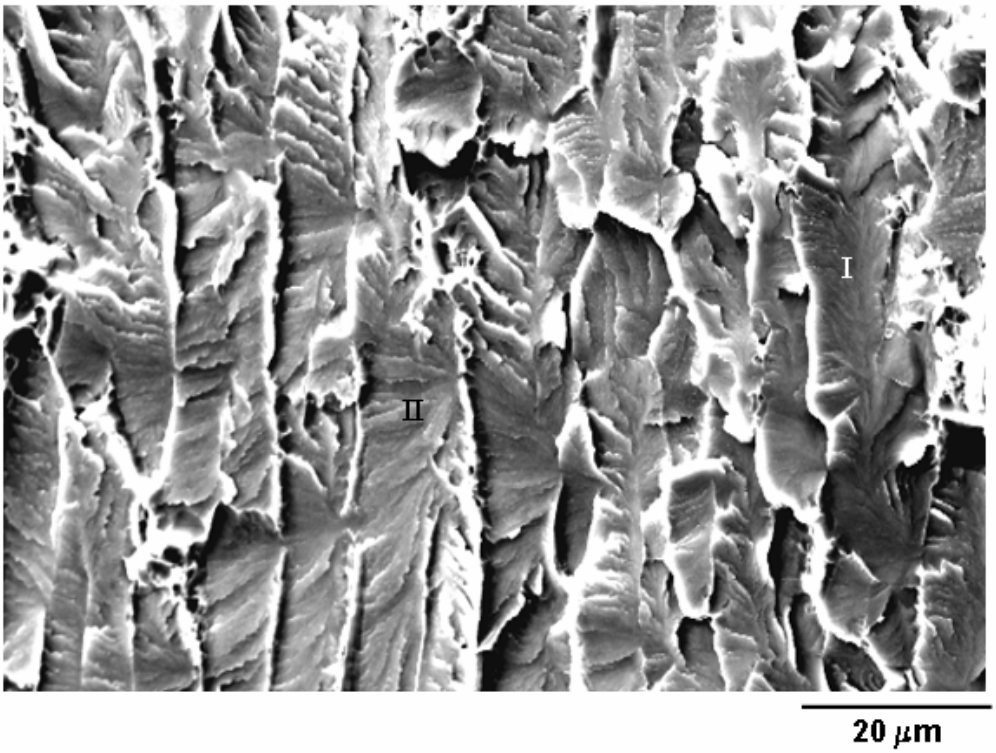

Fig. 7: Faceted initiation site for the static-loading test condition. The crystallographic orientation of the facets labeled 'I' and 'II' has been determined.

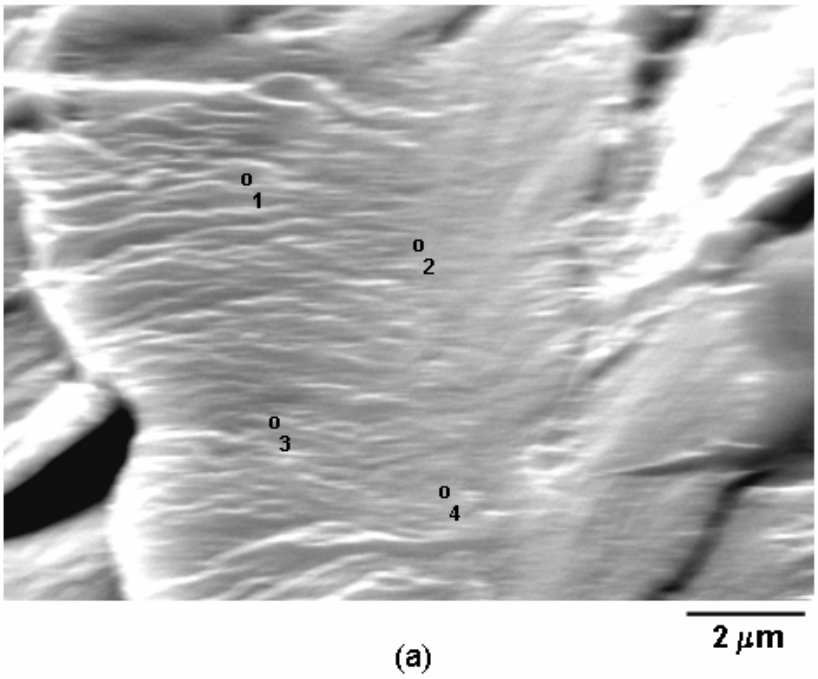

Fig. 8: Crystallographic orientation determination of static-loading fracture facet that has been labeled 'I' in Fig. 7. (a) SEM image of the facet at 70^0 tilt showing the locations of four points from where the EBSD patterns were obtained and subsequently indexed to determine the crystallographic orientation of the facet. (b) Inverse pole figure showing the crystallographic orientation of facet based on the EBSD analyses on four locations shown in (a) and the spatial orientation of the facet (facet normal, $\mathbf{n} = -\mathbf{i} + 2.56\,\mathbf{j} + 7.79\,\mathbf{k}$), as determined by the quantitative tilt fractography technique (see Table I).

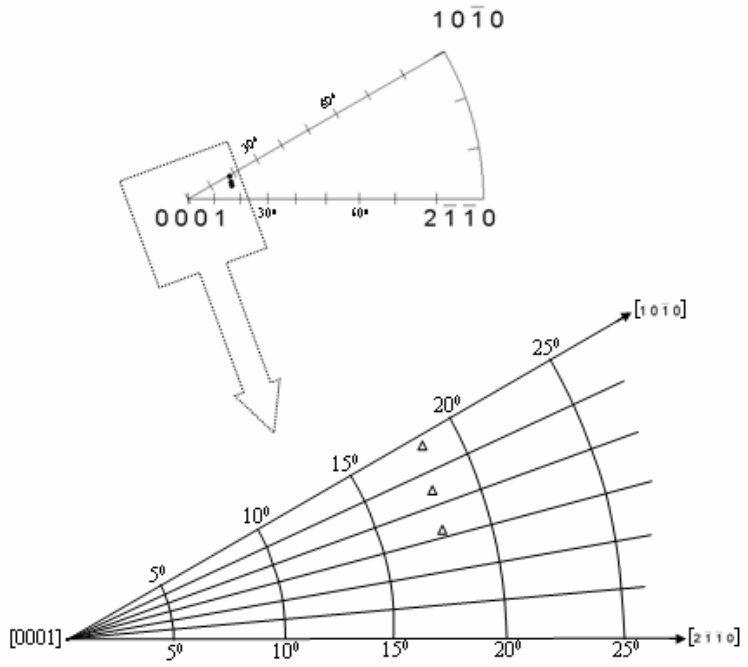

Fig. 8(b)

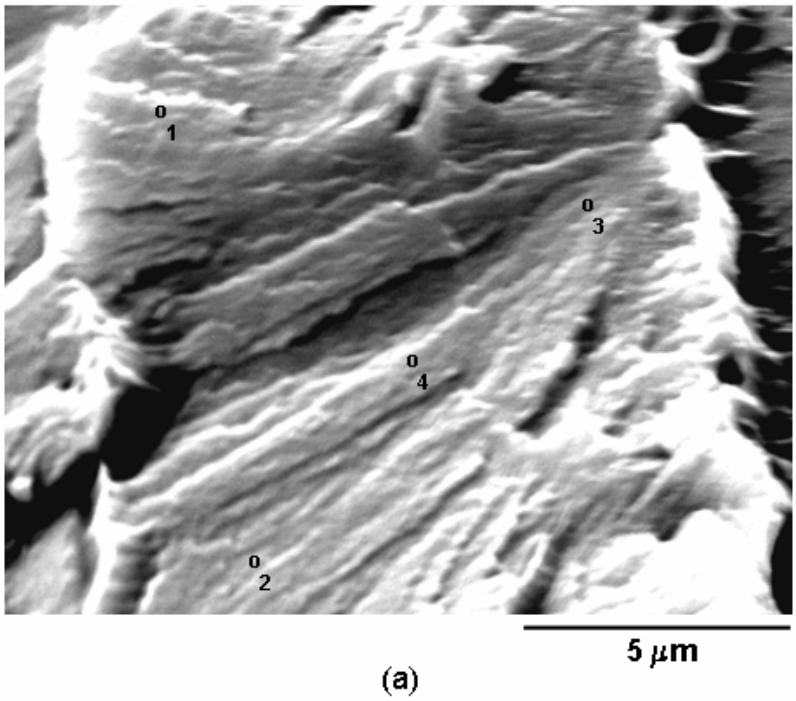

(a)

Fig. 9: Crystallographic orientation determination of static-loading fracture facet that has been labeled 'II' in Fig. 7. (a) SEM image of the facet at 70⁰ tilt showing the locations of four points from where the EBSD patterns were obtained and subsequently indexed to determine the crystallographic orientation of the facet. (b) Inverse pole figure showing the crystallographic orientation of facet based on the EBSD analyses on four locations shown in (a) and the spatial orientation of the facet (facet normal, $\mathbf{n} = -\mathbf{i} + 1.93\,\mathbf{j} + 4.79\,\mathbf{k}$), as determined by the quantitative tilt fractography technique (see Table I).

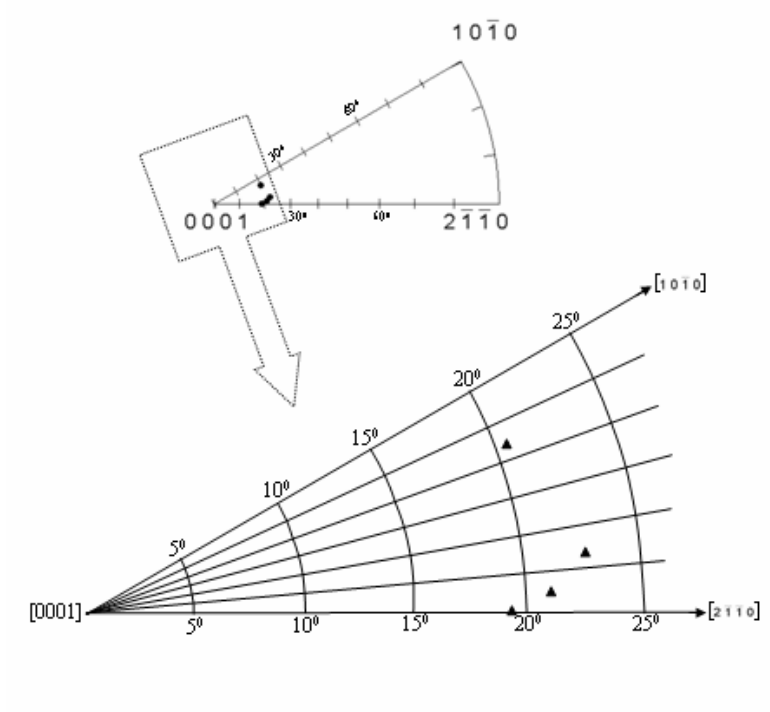

Fig. 9(b)

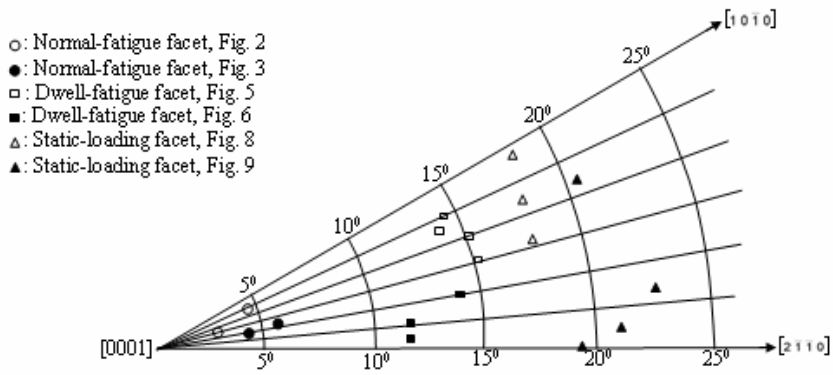

(a)

Fig. 10: Inverse pole figures showing the orientation of (a) facet normal, and (b) loading axis for the facets shown in Fig. 2 - 9.

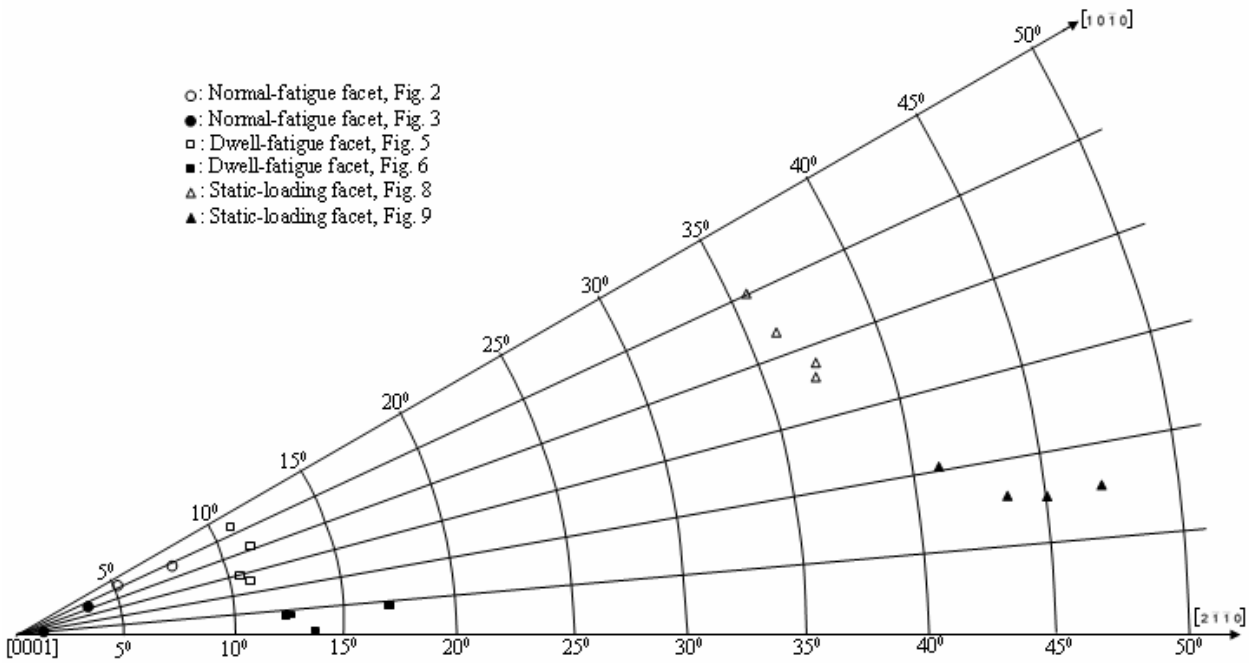

Fig. 10 (b)

Table I: Summary of quantitative tilt fractography results

Test condition	Reference figure	Vector representing the facet normal (**n**)	Angle between facet normal (**n**) and loading axis
Normal-fatigue (peak stress ~ 91 % of yield strength)	Fig. 2	**i** + 1.28 **j** + 26.33 **k**	4^0
Normal-fatigue (peak stress ~ 91 % of yield strength)	Fig. 3	**i** + 0.46 **j** + 21.83 **k**	3^0
Dwell-fatigue (peak stress ~ 91 % of yield strength)	Fig. 5	- **i** - 0.31 **j** + 10.42 **k**	6^0
Dwell-fatigue (peak stress ~ 91 % of yield strength)	Fig. 6	**i** - 4.38 **j** + 21.11 **k**	12^0
Static-loading (test stress ~ 95 % of yield strength)	Fig. 8	- **i** + 2.56 **j** + 7.79 **k**	19^0
Static-loading (test stress ~ 95 % of yield strength)	Fig. 9	- **i** + 1.93 **j** +4.79 **k**	24^0

REFERENCES

1. D.L. Davidson and D. Eylon, Metallurgical Transactions, vol. 11A, pp. 837-843, 1980.

2. M.R. Bache, H.M. Davies, and W.J. Evans, Titanium ’95: Science and Technology, pp. 1347-1354, 1995.

3. M.R. Bache, W.J. Evans, and H.M. Davies, Journal of Materials Science, vol. 32, pp. 3435-3442, 1997.

4. A.P. Woodfield, M.D. Gorman, R.R. Corderman, J.A. Sutliff and B. Yamrom, Titanium ’95: Science and Technology, pp. 1116-1124, 1995.

5. V. Sinha, M.J. Mills, and J.C. Williams, Metallurgical and Materials Transactions, vol. 35A, pp. 3141-3148, 2004.

6. A.P. Woodfield, and J.A. Sutliff, Microscopy and Microanalysis, vol. 3, Supplement 2, pp. 571-572, 1997.

7. V. Sinha, M.J. Mills, and J.C. Williams, “Determination of Crystallographic Orientation of Dwell-fatigue Fracture Facets in Ti-6242 Alloy”, Journal of Materials Science (submitted).

8. M. J. Blackburn and J. C. Williams, "Metallurgical Aspects of the Stress Corrosion Cracking of Titanium Alloys,” Proc. Conf. on the Fundamental Aspects of Stress Corrosion Cracking, N.A.C.E., 1969, p 620.

Appendix H

Observations on Crystallographic Orientations of the Regions below the Dwell-Fatigue Fracture Surface in Ti-6242 alloy

V. Sinha[1], J.E. Spowart[2], M.J. Mills[1], and J.C. Williams[1]

[1]Department of Materials Science and Engineering, The Ohio State University, Columbus, OH 43210, USA

[2]UES Incorporated, Dayton, OH 45433, USA

Abstract

A faceted crack initiation site is typically observed on the fracture surface of Ti-6242 alloy that has been tested under dwell-fatigue loading conditions. In this experimental study, the serial sectioning and electron backscattered diffraction (EBSD) techniques were used to obtain the orientation images of almost entire specimen cross section at different depths below the fracture surface. The orientation images are color-coded on the basis of the angle between the loading axis and basal plane normal, the Schmid factor for prism slip and the Schmid factor for basal slip. The aim was to obtain an idea about the crystallographic orientation and the size of the micro-textured region that is associated with the faceted initiation site.

1. INTRODUCTION:

The near-α titanium alloys, such as Ti-6242, are known to exhibit a significant reduction in fatigue life under dwell-fatigue conditions than under normal-fatigue (continuous cycling) test conditions [1-5]. Furthermore, the orientation of the facets comprising the dwell-fatigue crack initiation site has been observed to be near-basal [6-9]. A large faceted dwell-fatigue crack initiation site has been observed for Ti-6242 alloy with a high level of microtexture [2,5]. In the current study, a representative dwell-fatigue tested specimen of an α/β forged Ti-6242 alloy has been characterized. To determine the crystallographic orientation of the grains at and around the dwell-fatigue crack initiation site, the polishing was done directly onto the fracture surface with the plane of polish being perpendicular to the loading axis. Serial sectioning and electron backscattered diffraction (EBSD) techniques were used to obtain the orientation images at different depths below the fracture surface. These detailed characterization and analyses were carried out with an aim to determine the various aspects of the crystallographic orientation of the dominant (i.e. the one that leads to eventual specimen failure) faceted initiation site. These experiments also permitted an evaluation of the micro-textured region size-effects associated with the dominant crack initiation site.

2. MATERIAL AND SPECIMEN:

The Ti-6Al-2Sn-4Zr-2Mo (+ Si) alloy that was used in this study had a bimodal microstructure. A detailed description of the as-received alloy has been presented elsewhere [5]. The dwell-fatigue specimen had a rectangular cross-section with the gage section width and thickness of 6.48 mm and 1.93 mm, respectively. The length of reduced section was 12.7 mm. The dwell-fatigue test was carried out at room temperature in air under load-control at a peak stress of 869 MPa and a load-ratio of 0. The dwell-fatigue cycle consisted of loading to maximum load in 1 second, holding the load at maximum value for 2 minutes and unloading to zero load in 1 second.

The dwell-fatigue specimen failed in 447 cycles, whereas the normal-fatigue life for this specimen geometry is 24,000 cycles [10]. Thus a 54 X reduction in life resulted because of the 2 minute hold at the peak stress. The dwell-fatigue crack initiation site is faceted (Fig. 1), which is consistent with prior results obtained on other specimens machined from the same pancake forging [5]. The value of life reduction varies from specimen to specimen, but is always large enough for this microstructure to be a concern.

3. EXPERIMENTAL PROCEDURES:

In order to obtain an idea about the correspondence between the fracture surface features and the orientation images, the polishing was done directly onto the fracture surface. One of the two fractured parts of the dwell-fatigue specimen was mounted in a specimen holder in a way that the longitudinal axis of the specimen (i.e. the loading axis during the dwell-fatigue test) was normal to the intended plane of polish. The mounted specimen was loaded in the MultiPrep™ System (supplier: Allied High Tech Products, inc.; Rancho Dominguez, CA), which is a precise

semiautomatic polishing equipment. A reference plane for depth measurements was needed, which was not straightforward on the fracture surface with a rough topography. Therefore, the specimen was first ground on 1200 grit silicon carbide paper for a short period of time (~ 80 seconds with the MultiPrep™ System settings as follows: load = 100g, platen speed = 10 rpm and the specimen being held stationary) in order to render a part of the fracture surface flat. This plane of grinding was taken as the reference from which the subsequent depth measurements were done.

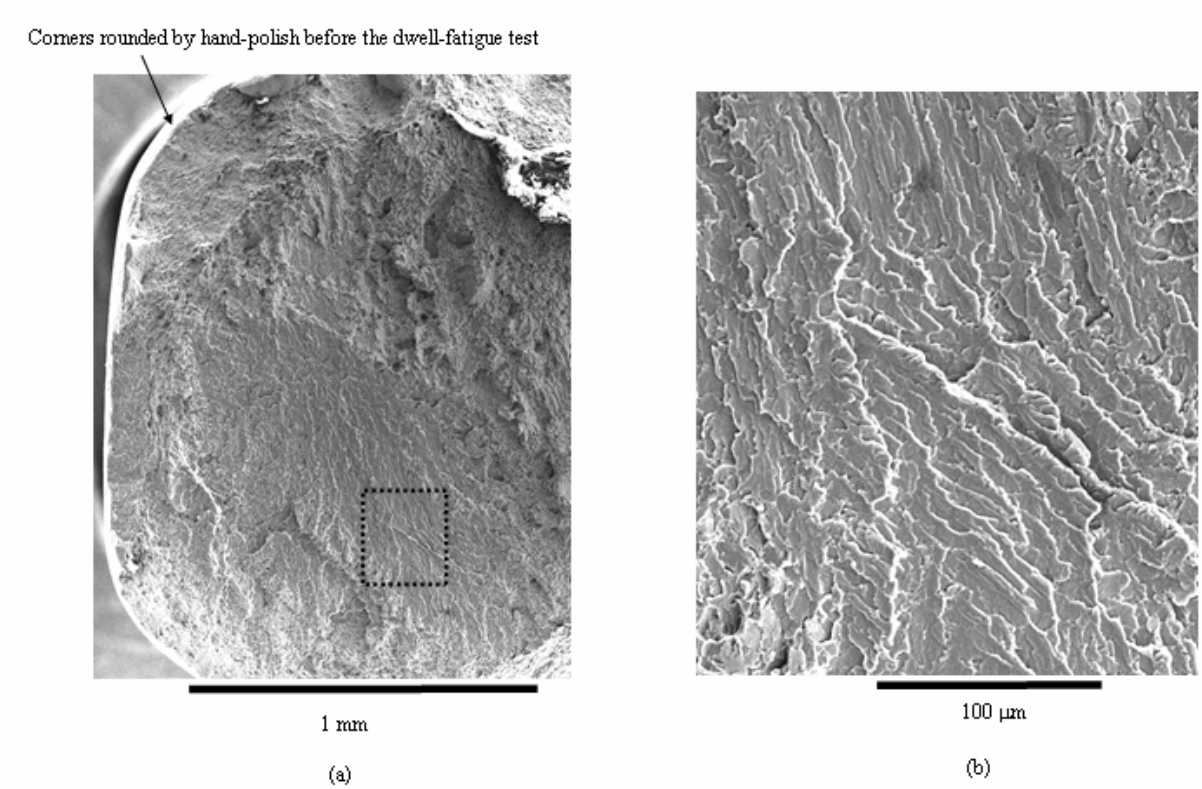

Figure 1: Dwell-fatigue failure modes observed for the as-received alloy. Scanning electron microscope (SEM) images obtained using a secondary electron detector. (a) Low magnification image showing the faceted initiation site; and (b) higher magnification image of a part of the faceted region that has been circumscribed by a dotted rectangle in figure (a).

After establishing the reference plane, the serial sectioning and OIM (Orientation Imaging Microscopy) scans were performed in order to obtain the orientation images at five different depths. The crystallographic orientation image of the entire polished surface was determined using the electron backscattered diffraction (EBSD) techniques in an SEM. The details of this technique have been described elsewhere [11]. The step size for the automated OIM scan was 10 μm and these experiments were conducted in the beam scan mode. Because of a large specimen width, a total of four OIM scans were needed to characterize the entire polished surface (i.e. approximately the complete specimen cross-section). The orientation data for the adjacent scan areas were merged using the TSL (Draper, UT) OIM analysis software to obtain a single, large orientation image that represented the entire polished surface at a particular depth.

Since the plane of fracture facets at the initiation site is nearly parallel to the basal plane, one set of orientation images were color-coded based on the inclination of the loading axis with respect to the basal plane normal. It was also of interest to obtain an idea about the feasibility of slip for the different regions including the faceted initiation site region. The slip is easiest along the <a> -direction on the basal and prism planes in the h.c.p. α-phase. Therefore, the orientation images were color-coded on two additional bases: (i) Schmid factor for prism slip and (ii) Schmid factor for basal slip.

4. RESULTS AND DISCUSSION:

The faceted initiation site on the fracture surface is circumscribed by a dotted curve in Fig. 2 and it is clear that the faceted region is more than 1 mm long. Figure 3 shows the orientation images of the entire polished surface at five different depths below the reference plane. In this figure, the color of a particular point is based on the angle that the basal plane normal at that point makes with the loading axis. The dotted curve in the left portion of Fig. 3 (a) circumscribes the region just below the faceted initiation site. It is clear from Fig. 3 that this "red/ pink" micro-textured region continues through the fifth serial sectioning step (~ 200 μm below the reference plane) and probably deeper. It is also evident that the size of this "red/ pink" region, in the left portion of orientation images (Fig. 3a – 3e), is reduced at greater depths below the fracture surface. In other words, the crack initiation (and probably, small crack growth) that leads to the specimen failure, occurs where the "red/ pink" region is larger in size.

There is another "red/ pink" micro-textured region in the right portion of orientation images (Fig. 3a – 3e). Its size increases at greater depths below the fracture surface. However, its size even at the largest depth sectioned in the current work (Fig. 3e) is smaller than the size of "red/ pink" region just below the faceted initiation site (left portion of Fig. 3a). This observation reinforces the view that the crack initiation and small crack growth, which eventually leads to specimen failure, occurs in larger "red/ pink" region. In this context, it is important to note that the small crack growth is strongly dependent on the crystallographic orientation of the grains at the crack-tip. Our results suggest that the growth of small cracks is arrested when the crack-tip approaches a region where the basal plane normal is inclined at a large angle with respect to the loading axis. On the other hand, the small cracks continue to grow (presumably at a much larger rate than large cracks) when they are still in the region where the basal plane normal makes a relatively small angle with respect to the loading axis (i.e. the "red/ pink" region in Fig. 3). In such a scenario, the crack initiated in the large "red/ pink" region can become the primary crack eventually causing the specimen failure, which is consistent with the results of this work.

The orientation images that are color-coded based on the Schmid factor for prism slip and basal slip are shown in Fig. 4 and 5, respectively. Figures 3 – 5 show the orientation images at five different depths below the reference plane and are obtained from the same set of crystallographic orientation data, only color-coded on different bases (as described above). From Fig. 4, it is clear that prism slip is unlikely to occur in the microtextured region associated with faceted initiation site, whereas Fig. 5 shows that basal slip is possible in this region.

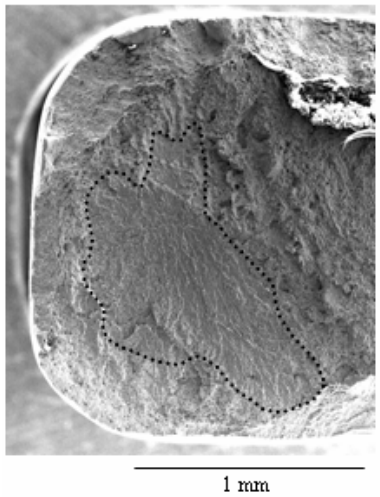

Figure 2: Dwell-fatigue fracture surface with the faceted initiation site circumscribed by a dotted curve.

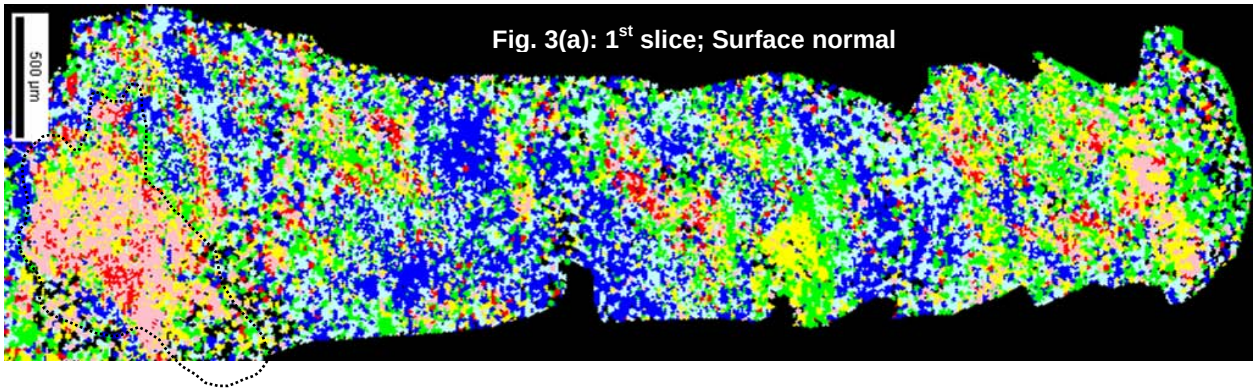

Fig. 3(a): 1st slice; Surface normal

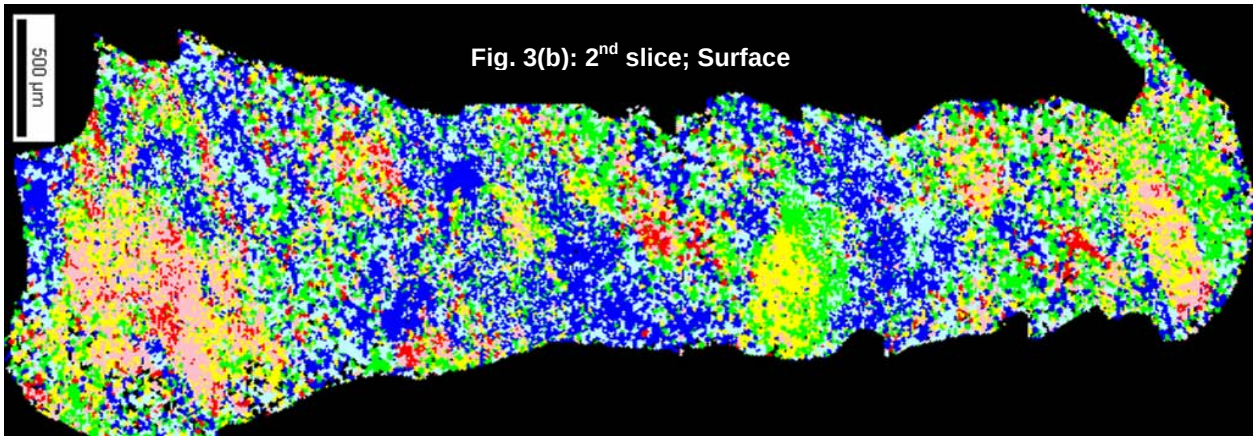

Fig. 3(b): 2nd slice; Surface

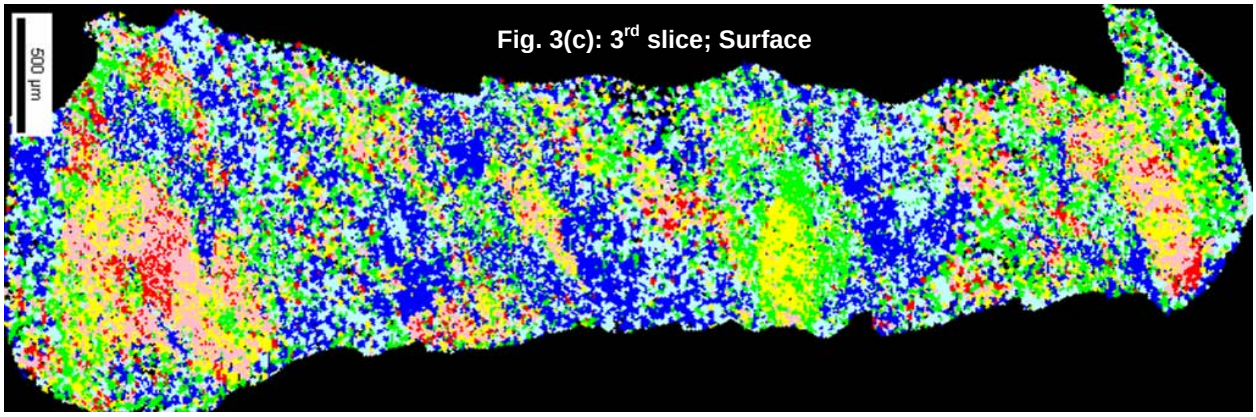

Fig. 3(c): 3rd slice; Surface

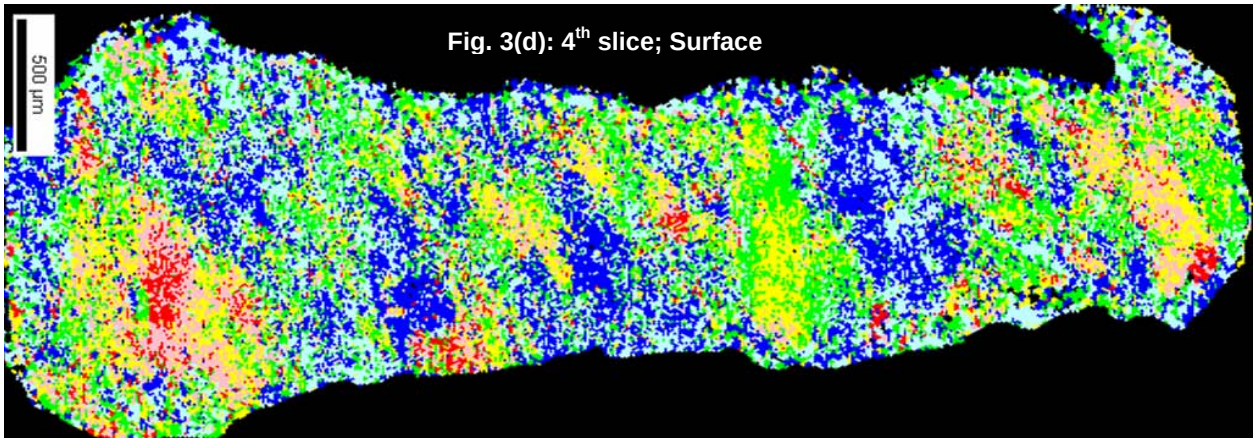

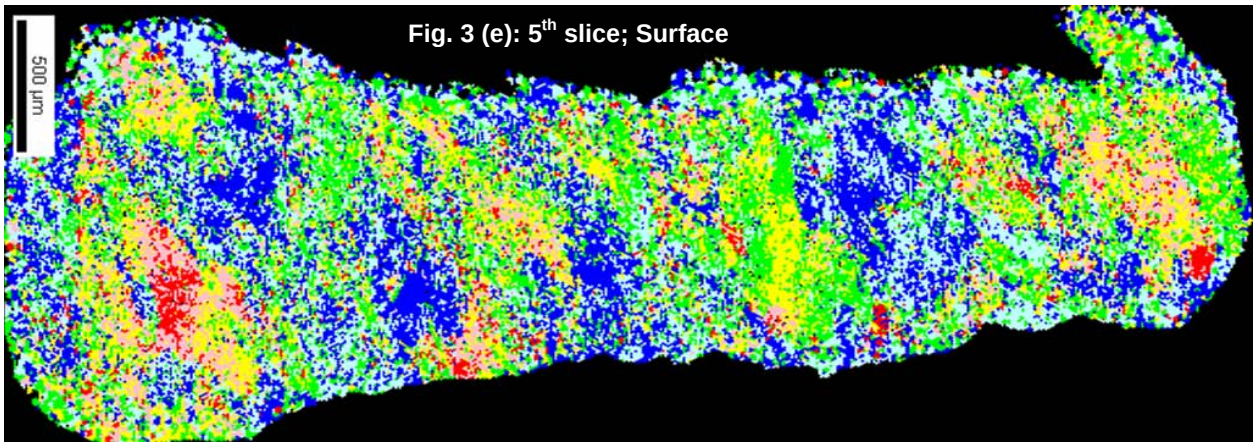

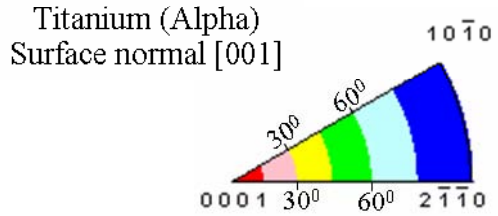

Figure 3: Orientations images for the entire polished surface at five different depths below the reference plane. (a) After first serial sectioning step (44 µm below the reference plane); (b) after second serial sectioning step (83 µm below the reference plane); (c) after third serial sectioning step (115 µm below the reference plane); (d) after fourth serial sectioning step (155 µm below the reference plane); and (e) after fifth serial sectioning step (187 µm below the reference plane). The colors in the orientation images are based on the angle between the surface normal (i.e. the loading axis during dwell-fatigue test) and basal plane normal. For 15^0 increments in this angle, the color changes. For example, when this angle is in the range $0^0 – 15^0$ the color at that point is red, when it is in the range $15^0 – 30^0$ the color is pink and so on as per the key shown in the bottom. The dotted curve in the left portion of figure (a) has been copied from figure 2 and it circumscribes the region just below the faceted initiation site (see figure 2).

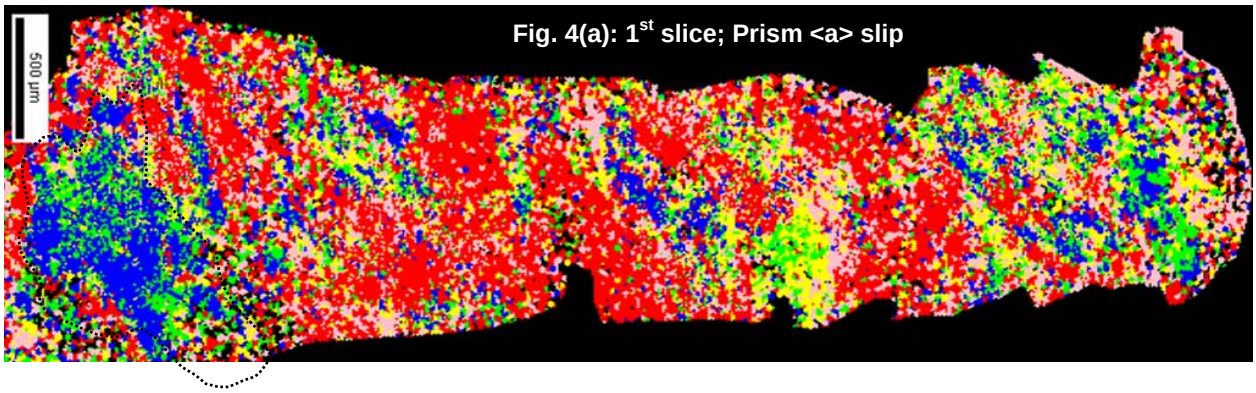

Fig. 4(a): 1st slice; Prism <a> slip

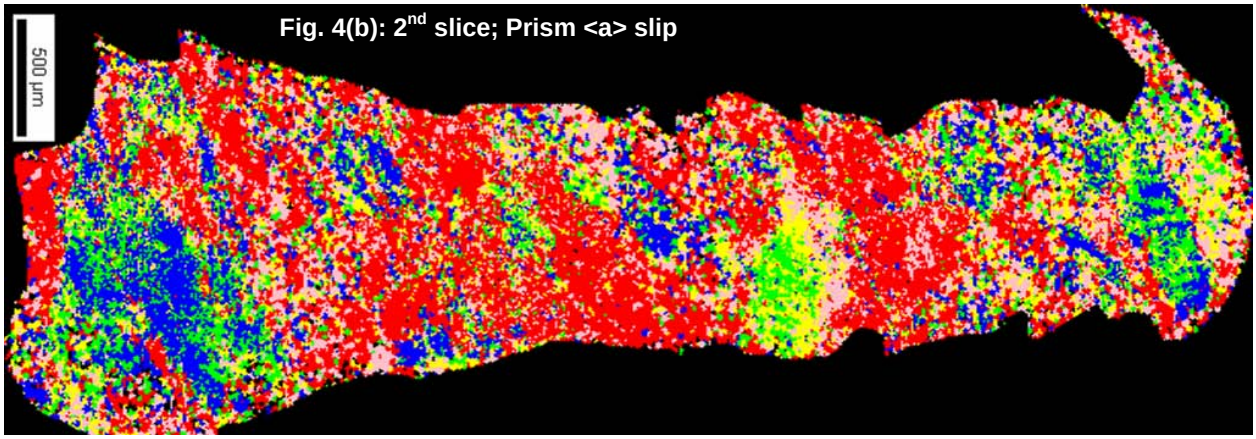

Fig. 4(b): 2nd slice; Prism <a> slip

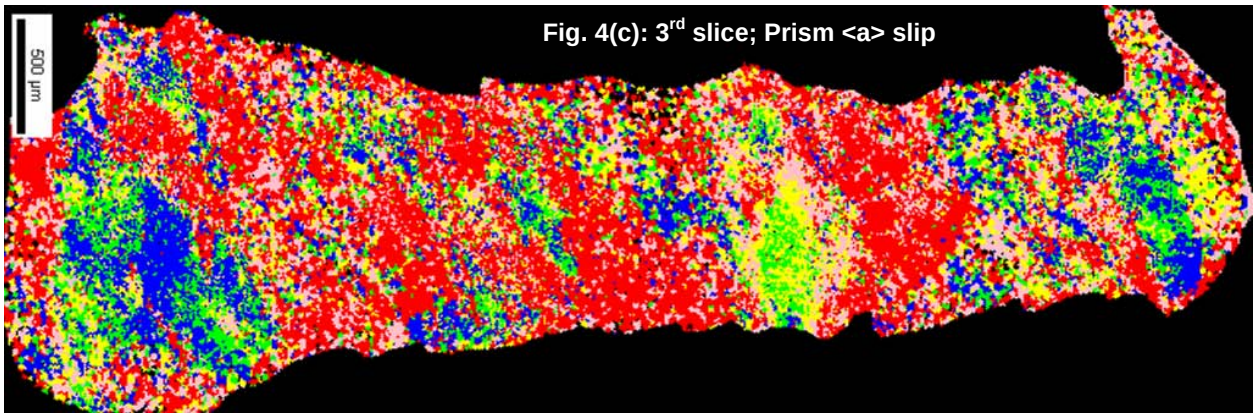

Fig. 4(c): 3rd slice; Prism <a> slip

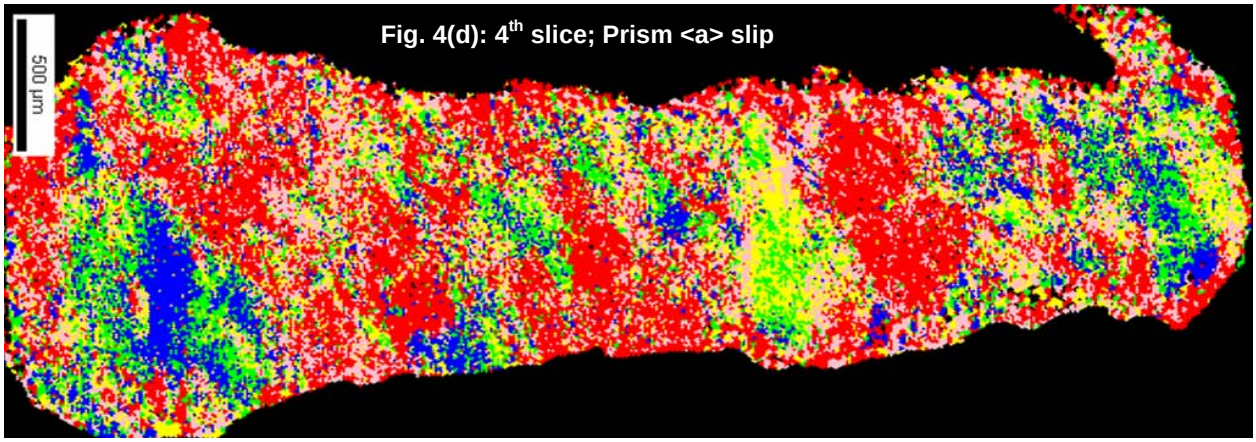

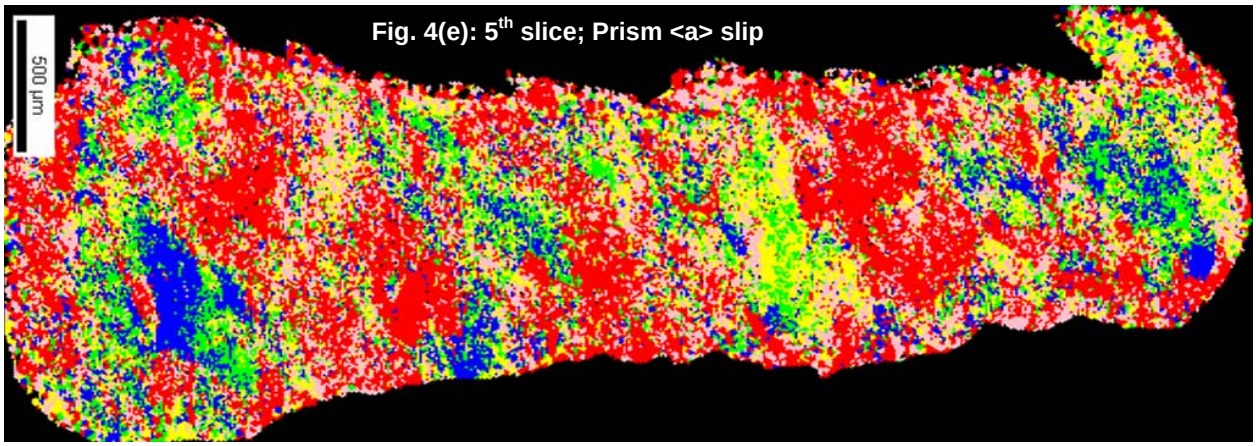

Schmid Factor	Resolved Shear Stress (MPa)
0 – 0.1	0 - 87
0.1 – 0.2	87 - 174
0.2 – 0.3	174 - 261
0.3 – 0.4	261 - 348
0.4 – 0.5	348 - 435

Figure 4: Orientations images for the entire polished surface at five different depths below the reference plane. (a) After first serial sectioning step (44 µm below the reference plane); (b) after second serial sectioning step (83 µm below the reference plane); (c) after third serial sectioning step (115 µm below the reference plane); (d) after fourth serial sectioning step (155 µm below the reference plane); and (e) after fifth serial sectioning step (187 µm below the reference plane). The colors in the orientation images are based on the Schmid factor for prism slip (along <a> -type direction). For increments in the value of Schmid factor by 0.1, the color changes. For example, when the Schmid factor for prism slip lies in the range 0 – 0.1 the color at that point is blue, when it is in the range 0.1 – 0.2 the color is green and so on as per the key shown in the bottom. The dotted curve in the left portion of figure (a) has been copied from figure 2 and it circumscribes the region just below the faceted initiation site (see figure 2).

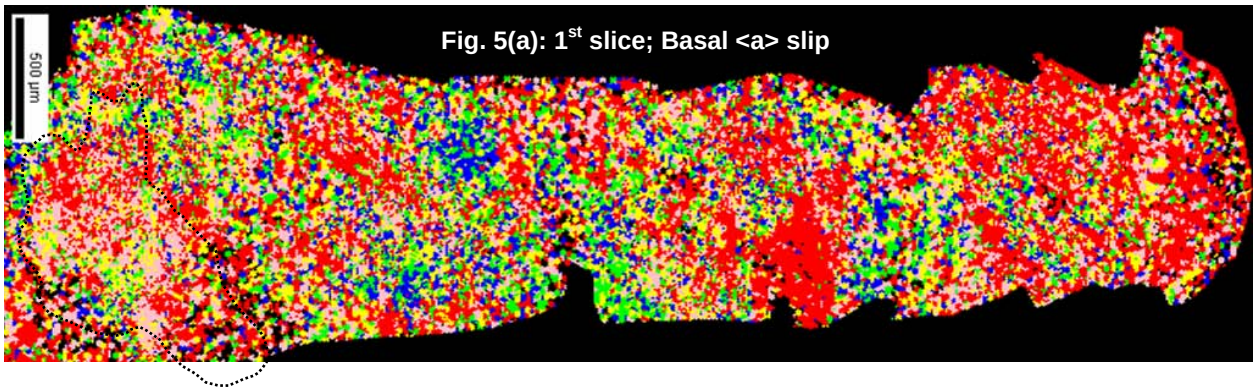

Fig. 5(a): 1st slice; Basal <a> slip

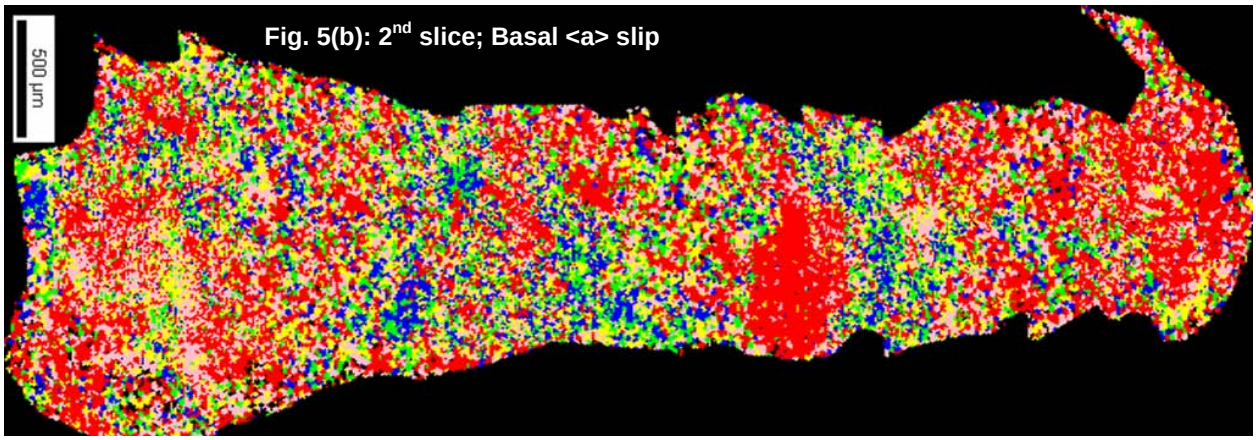

Fig. 5(b): 2nd slice; Basal <a> slip

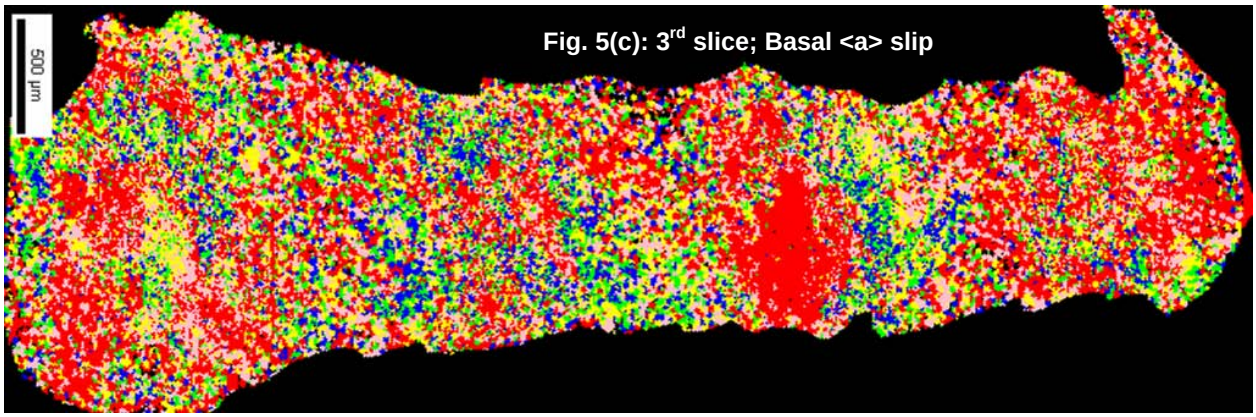

Fig. 5(c): 3rd slice; Basal <a> slip

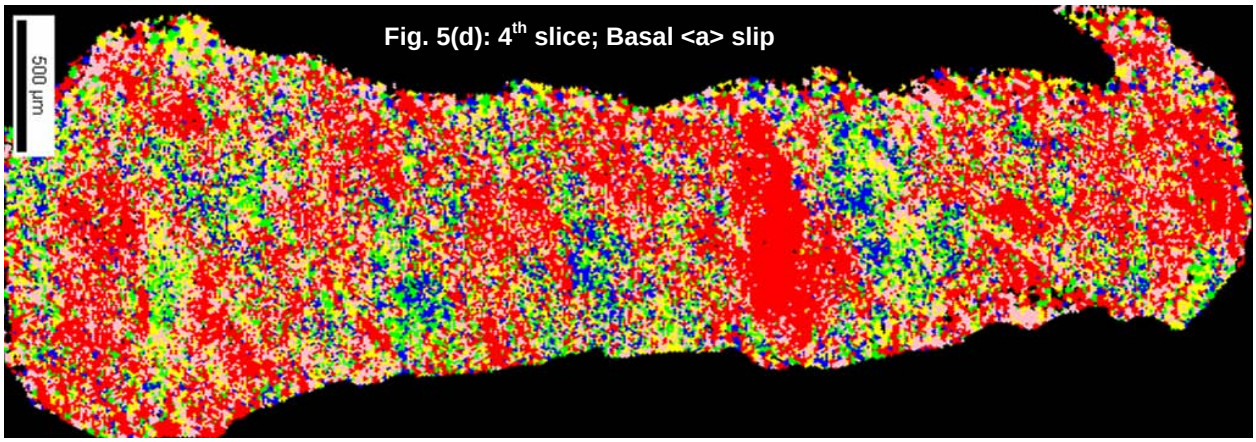

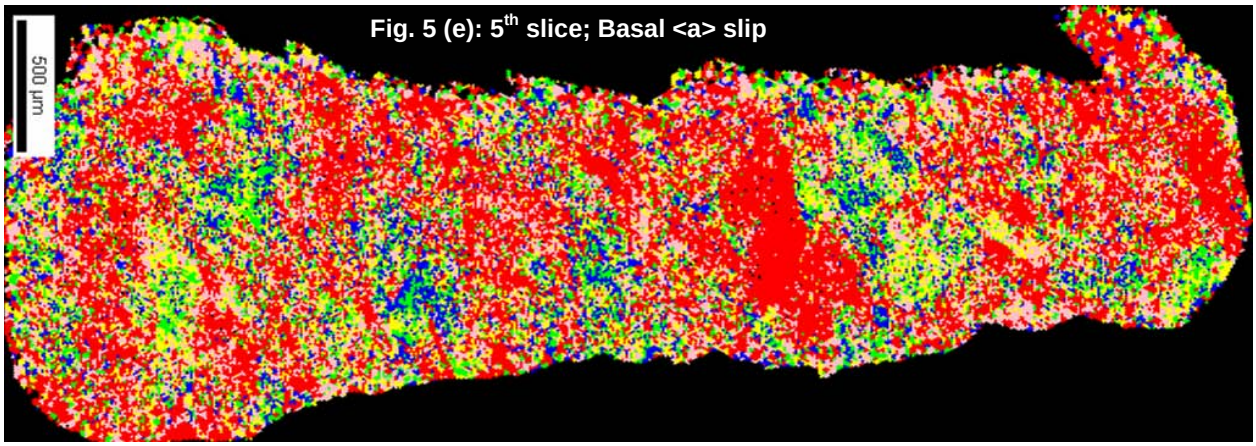

Schmid Factor	Resolved Shear Stress (MPa)
0 – 0.1	0 - 87
0.1 – 0.2	87 - 174
0.2 – 0.3	174 - 261
0.3 – 0.4	261 - 348
0.4 – 0.5	348 - 435

Figure 5: Orientations images for the entire polished surface at five different depths below the reference plane. (a) After first serial sectioning step (44 µm below the reference plane); (b) after second serial sectioning step (83 µm below the reference plane); (c) after third serial sectioning step (115 µm below the reference plane); (d) after fourth serial sectioning step (155 µm below the reference plane); and (e) after fifth serial sectioning step (187 µm below the reference plane). The colors in the orientation images are based on the Schmid factor for basal slip (along <a> -type direction). For increments in the value of Schmid factor by 0.1, the color changes. For example, when the Schmid factor for basal slip lies in the range 0 – 0.1 the color at that point is blue, when it is in the range 0.1 – 0.2 the color is green and so on as per the key shown in the bottom. The dotted curve in the left portion of figure (a) has been copied from figure 2 and it circumscribes the region just below the faceted initiation site (see figure 2).

4. CONCLUSION:

Our results indicate that the largest near-basal oriented micro-textured region in the sampled volume of material corresponds to the faceted initiation site on the fracture surface. This could be due to the possible arrest of small crack growth for the case when the size of the near-basal oriented micro-textured region is relatively small.

REFERENCES

1. W.J. Evans and C.R. Gostelow, Metallurgical Transactions, Vol. 10A, pp. 1837-1846, 1979.

2. A.P. Woodfield, M.D. Gorman, R.R. Corderman, J.A. Sutliff and B. Yamrom, Titanium '95: Science and Technology, pp. 1116-1124, 1995.

3. M.R. Bache, M. Cope, H. M. Davies, W.J. Evans, and G. Harrison, International Journal of Fatigue (1998), Volume Date 1997, 19(Suppl. 1, First International Conference on Fatigue Damage in Structural Materials, 1996), pp. S83-S88.

4. M.E. Kassner, Y. Kosaka and J.A. Hall, Metallurgical and Materials Transactions, vol. 30A, pp. 2383-2389, September 1999.

5. V. Sinha, M.J. Mills, and J.C. Williams, Metallurgical and Materials Transactions, vol. 35A, pp. 3141-3148, 2004.

6. M.R. Bache, W.J. Evans, and H.M. Davies, (1997). Journal of Materials Science, vol. 32, pp. 3435-3442.

7. M.R. Bache, H.M. Davies, and W.J. Evans, Titanium '95: Science and Technology, pp. 1347-1354, 1995.

8. A.P. Woodfield, and J.A. Sutliff, Microscopy and Microanalysis, vol. 3, Supplement 2, pp. 571-572, 1997.

9. V. Sinha, M.J. Mills, and J.C. Williams, "Determination of Crystallographic Orientation of Dwell-fatigue Fracture Facets in Ti-6242 Alloy", Journal of Materials Science (submitted).

10. S.I. Rokhlin, Jin-Yeon Kim, and Bahman Zoofan, unpublished research, The Ohio State university, 2004.

11. S.I. Wright, Electron Backscatter Diffraction in Materials Science, A.J. Schwartz, M. Kumar, and B.L. Adams (editors), Kluwer Academic/ Plenum Publishers, New York, N.Y., pp. 51-64, 2000.

Appendix I

Influence of Hydrogen Content on the Dwell Fatigue Behavior of Ti-6242 Alloy*

V. Sinha[1], R.B. Schwarz[2], M.J. Mills[1], and J.C. Williams[1]

[1]Department of Materials Science and Engineering, The Ohio State University, Columbus, OH 43210, USA

[2]Structure/Properties Relations Group, Los Alamos National Laboratory, Mail Stop G755, Los Alamos, NM 87545, USA

Abstract

In this experimental study, we have examined the influence of variations in the hydrogen content on the normal-fatigue and dwell-fatigue response of a near-α titanium alloy, Ti-6Al-2Sn-4Zr-2Mo (+Si). Dwell-fatigue refers to cyclic testing where the load is held at its maximum value for 2 minutes in each cycle. The strain accumulations under dwell-fatigue test conditions for the different hydrogen contents are presented. The fracture modes and associated fractographic features for the different test and material conditions are discussed. Quantitative tilt fractography analysis shows that the dwell-fatigue fracture facets are oriented at ~ 70^0 – 80^0 with respect to the loading axis. The normal to the dwell-fatigue fracture facets is oriented at ~ 10^0 – 15^0 with respect to the basal plane normal. The dwell-fatigue life has been observed to be higher for higher hydrogen contents. In some of the prior works, a significantly lower dwell-fatigue life has been reported for higher hydrogen contents. The discrepancy between some of the prior studies and the current study is explained on the basis of the differences in the microstructures (which are associated with different diffusion kinetics of hydrogen) examined in the various studies.

* This paper has been submitted to "Metallurgical and Materials Transactions A"

1. INTRODUCTION:

One of the common applications of near-α titanium alloys is in the higher temperature sections of compressors in aircraft engines. Though this class of alloys has superior creep properties at moderately high temperatures, it is also known to be susceptible to the dwell fatigue failures [1-4]. The life predictions based on the conventional normal-fatigue response for these alloys can be quite non-conservative, since the life under dwell-fatigue conditions (where the load is held constant at the maximum value for a finite period of time, typically 1-5 minutes, in each cycle) can be significantly shorter [1-4]. The dwell fatigue susceptibility is known to be more severe under high peak stress and low temperature test conditions [3-5]. These conditions are also representative of the take-off transients of a typical flight. Thus, the conditions under which the dwell-fatigue effect is more severe are commonly encountered in actual flights. Therefore, an understanding of the material variables responsible for dwell-fatigue susceptibility is quite crucial from a practical standpoint.

One of the primary factors for dwell-fatigue susceptibility is thought to be related with the hydrogen present in these alloys. Hydrogen has the potential for affecting several important aspects of material behavior (e.g. deformation characteristics, tendency to form brittle hydrides, etc.), which in turn can change its propensity for dwell-fatigue failure. The near-α titanium alloys are so named because they contain α (h.c.p.) as the major phase. The α-phase is known to have very different elastic [6] and plastic [7] behavior in the different crystallographic orientations. Furthermore, the deformation behavior of the two constituent phases, α (h.c.p.) and β (b.c.c.), are quite different. Both of these factors can cause stress redistributions under an applied stress, although the elastic and plastic anisotropy of the α-phase will have a larger effect. This will result in regions of high hydrostatic (tensile) stress. Hydrogen is known to segregate to regions of high hydrostatic (tensile) stress, where the hydrogen concentration can attain values much higher than the nominal concentration.

Several researchers have studied the effects of hydrogen content on the dwell-fatigue response [5, 8-12]. Most of the prior work has focused on one particular near-α titanium alloy, namely IMI 685 [5, 8-12]. Neal [5] has examined the influence of hydrogen content in the range from less than 10 ppm to 190 ppm (in this paper, all hydrogen contents are given in ppm, by weight) at the applied peak stresses from 700 to 900 MPa. His results do not indicate any significant detrimental effect of higher hydrogen content on either the dwell or no-dwell life. Moreover, in some instances, he has reported slightly longer lives for higher hydrogen contents under both the dwell and no-dwell test conditions.

Evans [8] has reported slightly longer life (by a factor of ~ 2) for IMI 685 alloy containing 50 ppm hydrogen than for the same alloy containing below 10 ppm hydrogen under both the dwell and normal-fatigue test conditions. Evans and Bache [9] have reported similar lives for 20 ppm and 60 ppm hydrogen IMI 685 alloys for both the dwell and no-dwell conditions. In another study on IMI 685 alloy, Evans and Bache [10] have reported a shorter (by a factor of ~ 7) dwell life for 60 ppm hydrogen alloy than for the 20 ppm alloy in some instances, whereas the normal-fatigue life is only marginally shorter (by a factor of ~ 2 or less) for the higher hydrogen (60 ppm) alloy.

In contrast, in another study on IMI 685, Hack and Leverant [11] have reported a significantly lower (a factor of ~ 30 reduction) dwell life for a 140 ppm hydrogen alloy than for a 40 ppm alloy. Furthermore, Bache, et al. [12] have observed a modest reduction in normal-fatigue life (a factor of ~ 4 reduction) and a significantly higher reduction in dwell-fatigue life (a factor of ~ 60 reduction) for a change in hydrogen content from 60 to 250 ppm.

The results of the prior studies, summarized above, suggest that there is some disagreement in the findings on the correlation between hydrogen content and dwell-fatigue susceptibility in a near-α titanium alloy. Therefore, this topic merits further investigation.

In this study, we have examined the effects of hydrogen content on the dwell fatigue response of a different near-α titanium alloy, Ti-6Al-2Sn-4Zr-2Mo. One common microstructural condition in which this alloy is used in practice is a bimodal microstructure consisting of 0.4 - 0.7 volume fraction of primary α (the balance being an $\alpha+\beta$ transformation product). However, very little work has been done in examining the correlation between hydrogen content and dwell fatigue behavior in this microstructural condition. Therefore, in this investigation, we have selected Ti-6242 alloy with the bimodal microstructure to study the effects of hydrogen content on its dwell-fatigue behavior. The normal-fatigue and dwell-fatigue tests were conducted at ~ 95 % of yield strength for different hydrogen contents. The fractographic features at the crack initiation site were examined for different test and material conditions. The crystallographic orientation of the dwell-fatigue fracture facets was determined for the different hydrogen contents.

2. EXPERIMENTAL PROCEDURES:

2.1 As-received alloy:

The Ti-6Al-2Sn-4Zr-2Mo (+ Si) alloy used in this study was provided in the form of a pancake forging (i.e. a round forging with a diameter of 470 mm and thickness of 77 mm) by Ladish Co., Cudahy, WI. The composition of the particular heat of the alloy is shown in Table I, along with the oxygen and hydrogen contents of the as-received pancake forging. The alloy was thermo-mechanically processed at Ladish Co. as follows: the billet was α/β forged at T_β - 28 ^{0}C to a strain of ~58%, solution heat treated at T_β - 56 ^{0}C, and then air cooled. This was followed by aging at 593 ^{0}C for 8 hours and then air cooling to room temperature. Oxygen and hydrogen contents of the as-received Ladish pancake forging were determined at Luvak Inc. (Boylston, MA) by inert gas fusion (ASTM E1019 for oxygen and ASTM E1447 for hydrogen) technique. The oxygen and hydrogen contents were determined to be 1440 and 49 weight ppm, respectively. Although there is a negligible difference in the oxygen content of the starting ingot and the fabricated forging, the hydrogen contents are quite different for the two (see Table I). This suggests that the alloy picked up additional hydrogen during the ingot-to-billet conversion, forging and/or heat treatment steps of the pancake fabrication. The concentrations of other major alloying elements in the as-received forging are expected to be essentially the same as in the starting ingot (Table I).

TABLE I: CHEMICAL COMPOSITION OF AS-RECEIVED Ti-6242 ALLOY.

Element	Based on the ingot analysis provided by Ladish Co. (weight %)	Based on the analysis by inert-gas fusion technique (weight %)
Al	6.18	
Zr	3.98	
Sn	1.94	
Mo	2.00	
Fe	0.02	
O	0.141 (1410 ppm)	0.144 (1440 ppm)
Cu	<0.01	
Mn	<0.01	
Si	0.09	
C	0.01 (100 ppm)	
N	0.0024 (24 ppm)	
H	0.0005 (5 ppm)	0.0049 (49 ppm)
Cr	<0.003	
Ni	0.004	
Y	<0.0005	
B	<0.001	
Others each	<0.10	
Others total	<0.30	
Ti	Balance	

Calculated β-transus = 1004 ^{0}C

Samples from the pancake forging were metallographically ground using silicon carbide grinding paper and then polished to a 0.06 μm finish on a vibratory polisher using colloidal silica. The polished specimens were observed in a scanning electron microscope (SEM) using a backscattered electron detector. The as-received alloy had a bimodal microstructure, consisting of primary α grains and transformed β regions (Fig. 1). A more detailed description of microstructure, macro-texture and micro-texture of the as-received alloy is presented elsewhere [13]. This material had a high level of micro-texture that has been shown to correspond to a large dwell life debit in this alloy system [2].

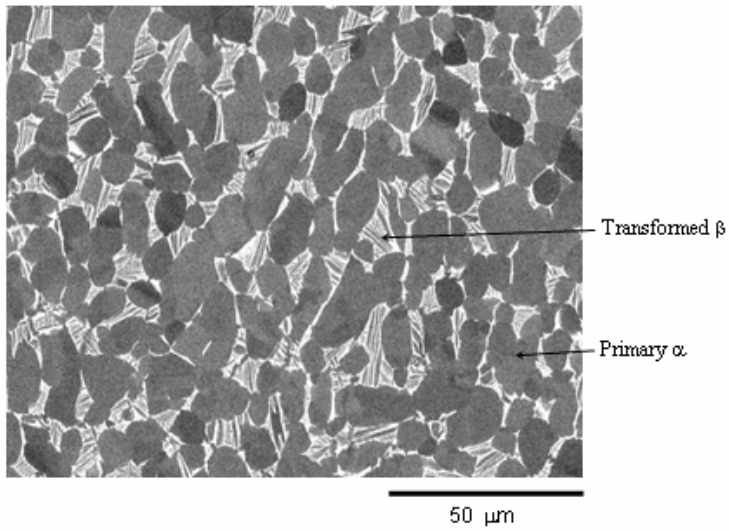

Fig. 1: SEM micrograph of the as-received α/β forged Ti-6242 alloy, acquired using a backscattered electron detector.

2.2 Hydrogen charging and degassing:

The specimen blanks for tensile and fatigue tests were hydrogen-charged, one at a time, in a Sieverts apparatus at a temperature of 550 - 600 ^{0}C. Electron diffraction patterns obtained by transmission electron microscopy gave a qualitative evidence of stronger α_2 superlattice reflections for the hydrogen-charged condition than for the as-received condition. This indicates a higher degree of short-range-order (SRO) and/ or volume fraction of α_2 precipitates in hydrogen-charged condition than in as-received condition. This may be caused by slow cooling from a temperature near 600 ^{0}C inside the Sieverts apparatus after the completion of hydrogen charging experiments. In order to eliminate this variable, some of the hydrogen-charged specimen blanks were again aged in air at 600 ^{0}C for 8 hours and then air cooled to room temperature. Those hydrogen-charged alloys that were given an additional aging and air-cooling treatment most likely have the same degree of SRO and/ or volume fraction of α_2 precipitates as in the as-received alloy. Thus, two kinds of hydrogen-charged alloys were tested in the current study: (a) alloys that were furnace cooled inside the silica tube in the Sieverts apparatus after being hydrogen-charged (these alloys will be referred to as “furnace-cooled” in the remainder of this paper), and (b) alloys that were re-aged at 600 ^{0}C for 8 hours and air-cooled after being

hydrogen-charged and furnace-cooled in the Sieverts apparatus (these will be referred to as "air cooled").

A few tensile and fatigue specimen blanks were degassed in a vacuum furnace under dynamic vacuum (chamber pressure ~ 3 X 10^{-6} torr) at 600 ^{0}C for 48 hours to reduce the hydrogen content of as-received alloy. The degassed specimen blanks were subsequently aged in air at 600 ^{0}C for 8 hours and then air-cooled, again with an aim to obtain the same degree of SRO and/ or volume fraction of α_2 precipitates as in the as-received alloy.

To summarize, in this study, the Ti-6242 alloy has been examined in four different material conditions: (a) as-received condition, (b) hydrogen-charged and furnace-cooled (FC) condition, (c) hydrogen-charged and air-cooled (AC) condition, and (d) degassed condition. Since the last heat treatment step for the as-received and the degassed alloys was air-cooling from a temperature near 600 ^{0}C, these alloys will also be referred to as "air-cooled" (AC) in this paper. The SEM examination of the alloy in four different conditions showed essentially no difference in the microstructure at the micron length scale (Fig. 1). The reported values of the hydrogen content for each of the specimens are based on the inert gas fusion (ASTM E1447) analyses conducted on the material taken from the grip section of the broken specimens.

2.3 Mechanical Testing:

Three types of mechanical tests were conducted in this study: tensile, normal-fatigue and dwell-fatigue tests. The specimen blanks had been cut from the pancake forging such that the longitudinal axes (i.e. loading direction) of the machined specimens for all three types of tests were along its circumferential (tangential) direction.

The tensile tests were conducted in lab air, at room temperature using a closed-loop servo-hydraulic test-frame. The specimens for the tensile tests had a uniform circular cross-section with a gage section diameter of 6.35 mm (0.25"), the length of reduced section = 31.75 mm (1.25") and they had a threaded grip section of diameter = 9.52 mm (0.375"). The other dimensions of these tensile specimens were selected in accordance with ASTM E8 specifications. The tensile tests were conducted under displacement control at an actuator speed corresponding to a strain rate of ~ 1 X 10^{-4} S^{-1}.

The specimens for normal-fatigue and dwell-fatigue tests had a uniform circular cross-section with a gage section diameter of 5.08 mm (0.2"), the length of reduced section = 19.05 mm (0.75") and they had a threaded grip section of diameter = 15.88 mm (0.625"). The other dimensions of the specimens were selected in accordance with ASTM E466 specifications. After machining, the specimens were shot-peened as per the following conditions: intensity: 005 A; shot-type: CW14; and coverage: 200%. Both the normal-fatigue and dwell-fatigue experiments were carried out at room temperature in air under load-control using a closed-loop servo-hydraulic test-frame. A load-ratio (R) of 0 was used in all the tests. The schematic representations of the normal-fatigue and dwell-fatigue cycles are shown in Fig. 2. The strain accumulation was monitored as a function of time using an extensometer that had a gage length of 12.7 mm (0.5"). In addition, two ink-marks (~ 18 mm apart) were made on the reduced

section of the fatigue specimens. The reported values of plastic strain-to-failure (ε^{pl}_f) were calculated from the measurements of the distance between these two marks, before and after the test, using an optical microscope at a magnification of 50 X. After the test, the two broken parts of a specimen were aligned carefully and the gap between them along the longitudinal axis was subtracted from the measured distance between the marks to obtain the correct distance for the broken specimens.

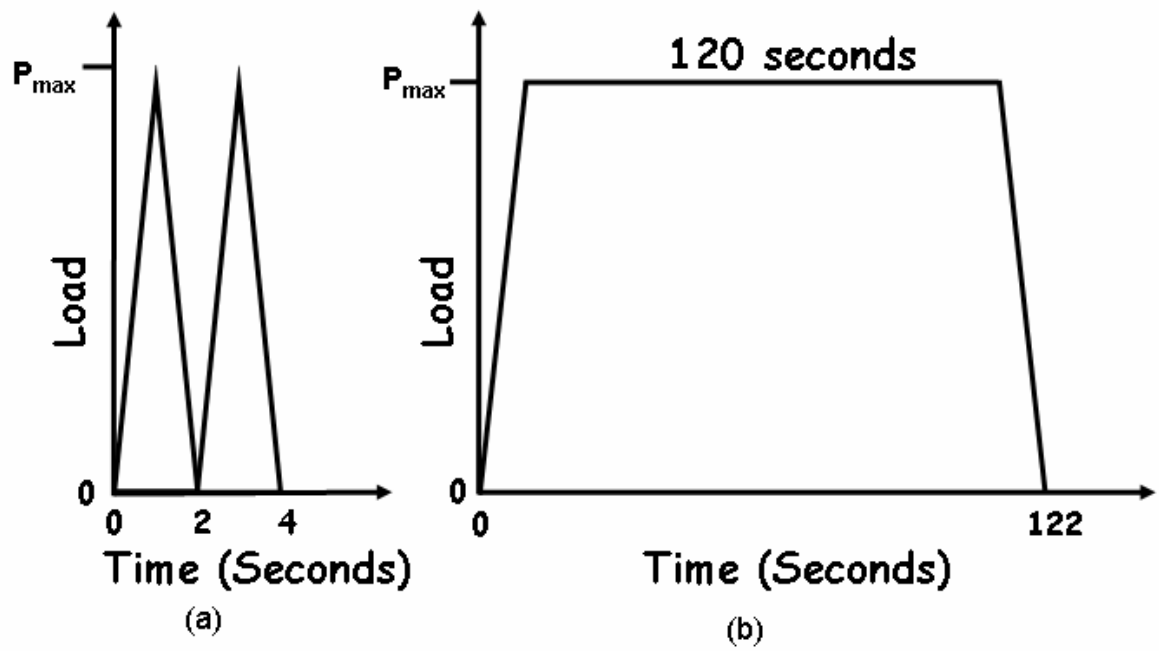

Fig. 2: Schematic of (a) normal-Fatigue, and (b) dwell-fatigue cycles.

2.4 SEM Examination:

The failure modes of the tested (fractured) normal-fatigue and dwell-fatigue specimens were examined in an SEM with the help of a secondary electron detector. The orientation of the dwell-fatigue fracture facets was determined using a quantitative tilt fractography technique in an SEM [14]. The crystallographic orientation of the grain, through which the fracture facet is produced, is determined by the electron backscattered diffraction (EBSD) technique in the SEM. These two pieces of information were combined to determine the crystallographic orientation of dwell-fatigue fracture facets. The details of this technique have been described in ref. [14].

3. RESULTS:

3.1 Tensile, normal-fatigue and dwell-fatigue test results:

The variation of 0.2 % offset yield strength (YS) with hydrogen content is shown in Fig. 3. YS is higher for higher hydrogen content, and it is also higher for the furnace-cooled condition than for the air-cooled condition (Fig. 3). To eliminate the possibility of the variations in YS affecting the normal-fatigue and dwell-fatigue test results, these tests were conducted at the peak stress of ~ 95 % of the actual YS for each specimen. The hydrogen content of the hydrogen-charged fatigue specimens was estimated based on the amount of hydrogen introduced in the Sieverts apparatus chamber for the specimen blank of known weight. Based on this estimate and knowing the material condition (i.e. furnace-cooled or air-cooled) for each fatigue specimen, the peak stress was calculated (from the trend-lines shown in Fig. 3) to be equal to ~ 95 % of YS. Thus, slightly higher peak stress was used for higher hydrogen content alloys. A still higher peak stress was used for the furnace-cooled alloys in order to get ~ 95 % of their YS since they have higher YS (Fig. 3). Although there was some mismatch between the Sieverts apparatus estimate and the actual hydrogen content (determined using inert gas fusion after the fatigue test); the peak stress was always within ± 1 % of 0.95 X YS for the hydrogen content and material condition (FC or AC) under consideration because the slope of YS vs. hydrogen content line is relatively small (Fig. 3). This small difference of up to ± 1 % from the target peak stress is likely to have negligible effects on the normal-fatigue and dwell-fatigue test results.

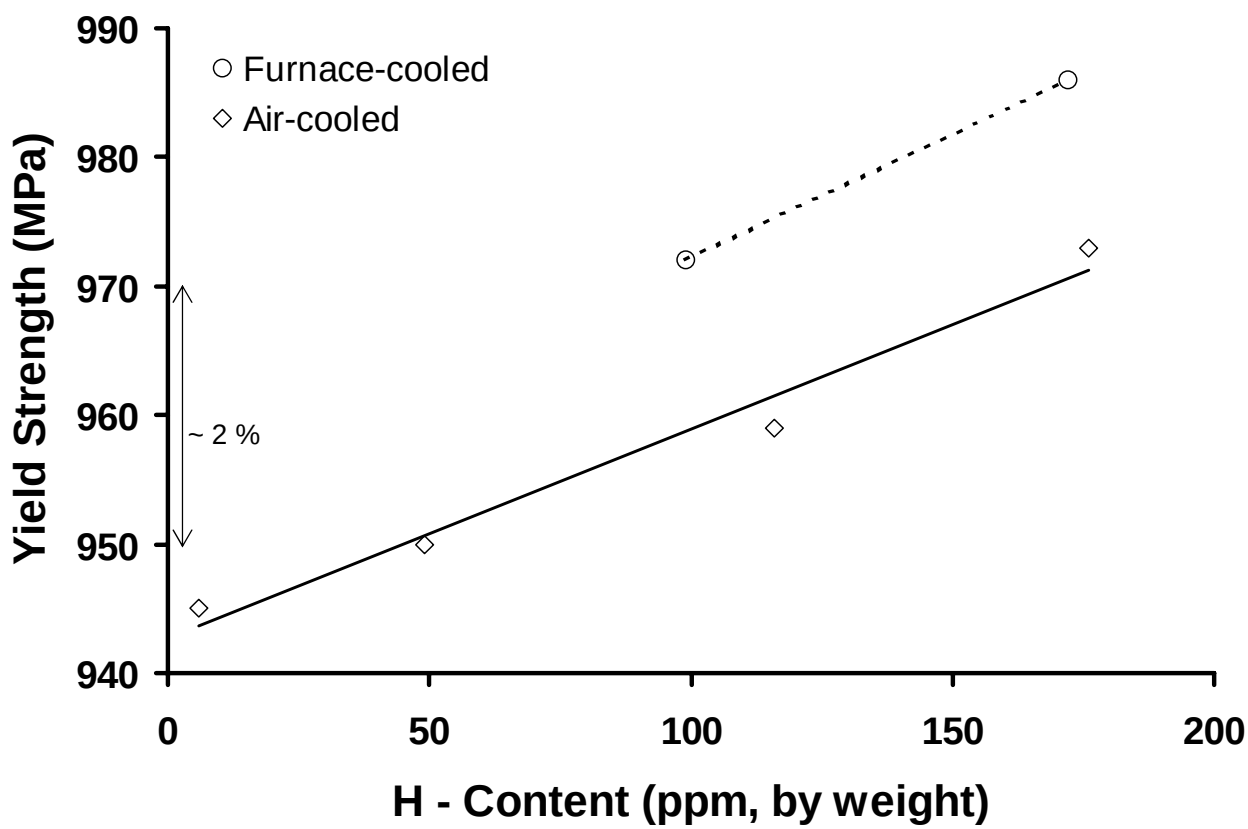

Fig. 3: Variation of 0.2 % offset yield strength with hydrogen content.

The normal-fatigue and dwell-fatigue test results are summarized in Table II and III, respectively. Fig. 4 shows the variation of normal-fatigue and dwell-fatigue lives with hydrogen content. The dwell-fatigue lives are significantly lower than the normal-fatigue lives. Furthermore, slow-cooling does not have a strong effect on either the normal-fatigue or dwell-fatigue life (Fig. 4). The trend-curves drawn through the normal-fatigue and dwell-fatigue lives appear to merge at hydrogen contents larger than 250 ppm. However, more data points at high hydrogen contents are needed for making this statement with confidence.

Table II: Normal-fatigue response at the peak stress ~ 95% of YS for different hydrogen contents

Hydrogen Content, ppm (by weight)	N_f(Cycles)	Plastic strain-to-failure, ε^{pl}_f (Gage length ~ 18 mm)
7[a]	18,350	2.1%
49[a]	22,991	2%
100[b]	13,110	1.5%
110[a]	15,550	1.2%
127[b]	15,347	1.6%

[a] Air-cooled, [b] Furnace-cooled

Table III: Dwell-fatigue (hold time = 2 minutes) response at the peak stress ~ 95% of YS for different hydrogen contents

Hydrogen Content, ppm (by weight)	N_f(Cycles)	Plastic strain-to-failure, ε^{pl}_f (Gage length ~ 18 mm)
10[a]	1498	9.1%
49[a]	1303	3.8%
59[b]	1176	6.1%
150[a]	3773	5.6%
204[b]	3402	11.7%
230[a]	6849[c]	5%

[a] Air-cooled, [b] Furnace-cooled
[c] There was a momentary (inadvertent) overload during one cycle after 6225 cycles. Subsequently, this specimen failed in an additional 624 cycles (total life = 6849 cycles) at a total strain of ~ 5%. Any effect of this momentary overload on total life is insignificant since the life was already much longer than any other specimen.

The plastic strain-to-failure is observed to be higher for the dwell-fatigue than for the normal-fatigue tests (Table II and III). Furthermore, the plastic strain-to-failure is a weak function of hydrogen content for normal-fatigue tests (Table II). On the other hand, a wider variation in plastic strain-to-failure with hydrogen content is observed for dwell-fatigue tests (Table III). Therefore, it is of interest to compare the plastic strain versus time plots for different hydrogen contents for dwell-fatigue test conditions, which will be described next.

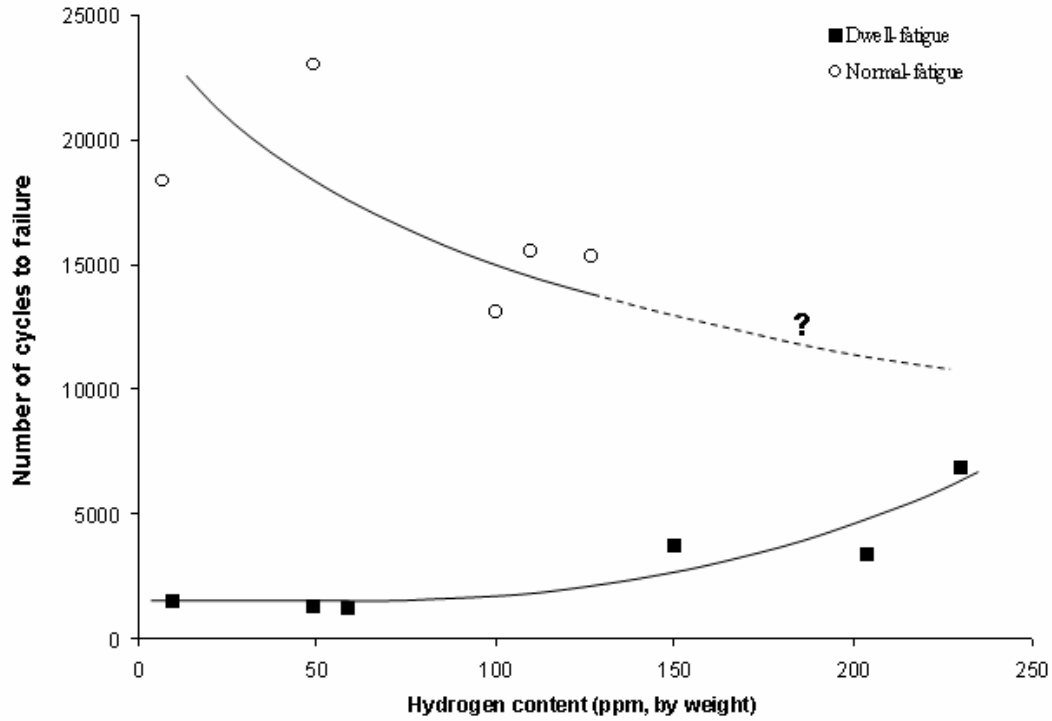

Fig. 4: Variation in fatigue life with hydrogen content for normal-fatigue and dwell-fatigue test conditions.

3.2 Plastic strain versus time plots:

The accumulated plastic axial strain versus time plots for different hydrogen contents under dwell-fatigue test conditions are shown in Fig. 5. The six curves presented in Fig. 5 can be divided into two groups: (a) Curves with high strain accumulation rates: 10, 59 (furnace-cooled) and 204 (furnace-cooled) ppm alloys; and (b) Curves with relatively low strain accumulation rates: 49, 150 and 230 ppm alloys. As has been mentioned earlier, of the six different hydrogen content alloys; 10, 49, 150 and 230 ppm hydrogen alloys have been aged at ~ 600 ^{0}C and then air cooled in their final heat treatment step, whereas the 59 and 204 ppm hydrogen alloys have been furnace cooled from a temperature near 600 ^{0}C. The alloys that were air-cooled from ~ 600 ^{0}C (i.e. 10, 49, 150 and 230 ppm hydrogen alloys) do show a definite trend with respect to their strain accumulation rates: the strain rate decreases with an increase in hydrogen content (Fig. 5). It is also noteworthy that the reduction in strain rate is rather significant for an increase in hydrogen content from 10 ppm to 49 ppm, when compared with that for an increase in hydrogen content from 49 to 150 or even 230 ppm. In contrast, the furnace-cooled (i.e. 59 and 204 ppm hydrogen) alloys have strain accumulation rates that lie between the rates for 10 and 49 ppm hydrogen (both air cooled from ~ 600 ^{0}C) alloys. Thus, the degree of SRO and/ or volume fraction of α_2 precipitates (which is influenced by the final cooling rate) does seem to affect the strain accumulation rate under the dwell-fatigue test conditions. It is also notable that the 204

ppm (furnace-cooled) alloy has accumulated a total of ~ 12 % plastic strain prior to failure. The reason for this unusually high plastic strain accumulation is currently unclear.

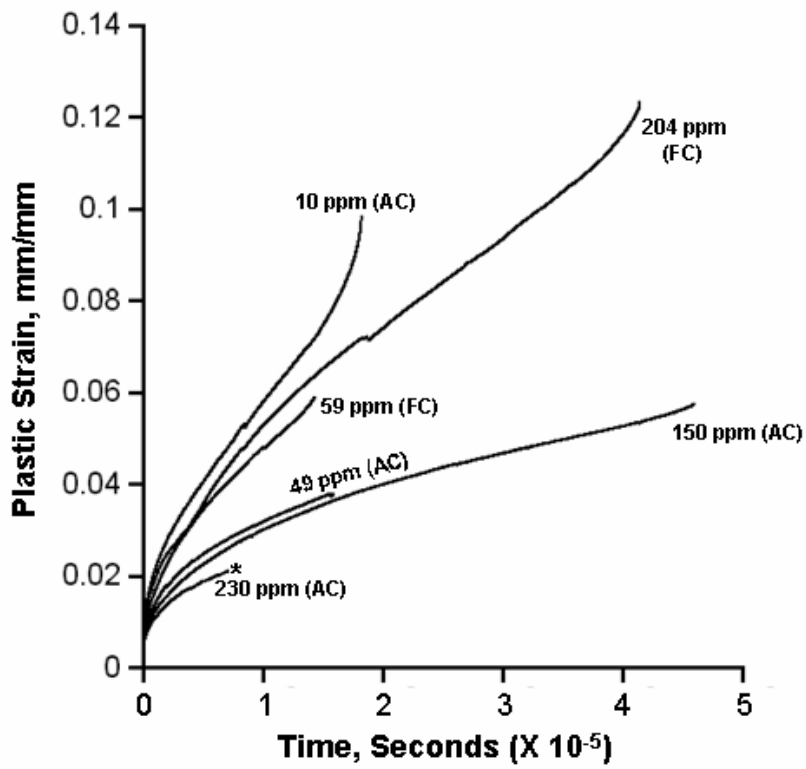

Fig. 5: Plastic strain accumulation under dwell-fatigue loading conditions for different hydrogen contents. For the 230 ppm hydrogen alloy, the strain values could not be acquired beyond the point indicated by an asterisk (*), due to the slippage of extensometer. AC: air-cooled from a temperature near 600 ^{0}C, and FC: furnace-cooled from a temperature near 600 ^{0}C.

3.3 Fractography and failure modes:

(a) Normal-fatigue specimens: The fracture initiation site consists primarily of facets for all the hydrogen contents examined in this study. The crack-initiation site has similar fractographic features in degassed (Fig. 6) and as-received (see ref. [13]) alloys. Furthermore, similar fractographic features at the initiation site are observed for 100, 110 and 127 (Fig. 7) ppm alloys. The crack initiation site in degassed (Fig. 6) and as-received alloys shows evidence of cyclic growth with a higher degree of local plasticity than is seen for hydrogen-charged (Fig. 7) alloys. In other words, the facets are less well-defined for degassed and as-received alloys when compared with those for hydrogen-charged alloys. It is also of interest to note that the normal-fatigue life is slightly higher for the degassed and as-received alloys than for the hydrogen-charged alloys (Table II and Fig. 4).

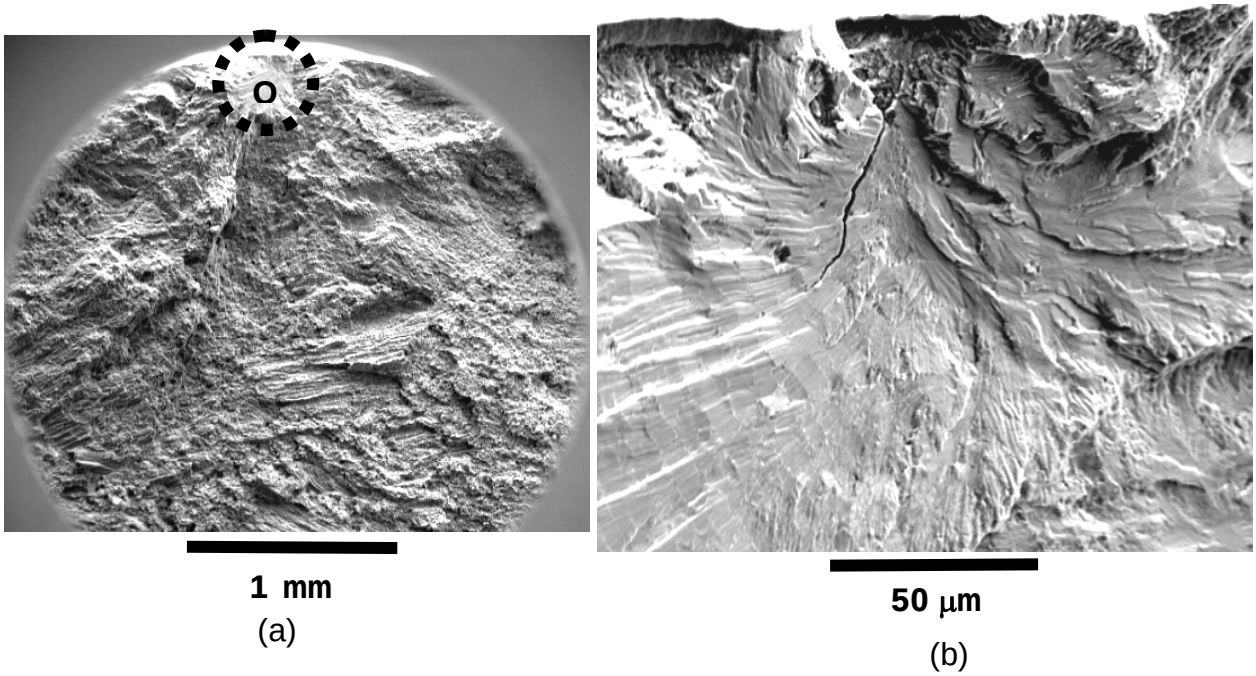

Fig. 6: Normal-fatigue failure modes observed for the 7 ppm hydrogen alloy. .(a) Low magnification image with the initiation site circumscribed by a dotted circle; and (b) higher magnification image of a region, characteristic of the initiation site, that has been labeled 'O' in figure (a).

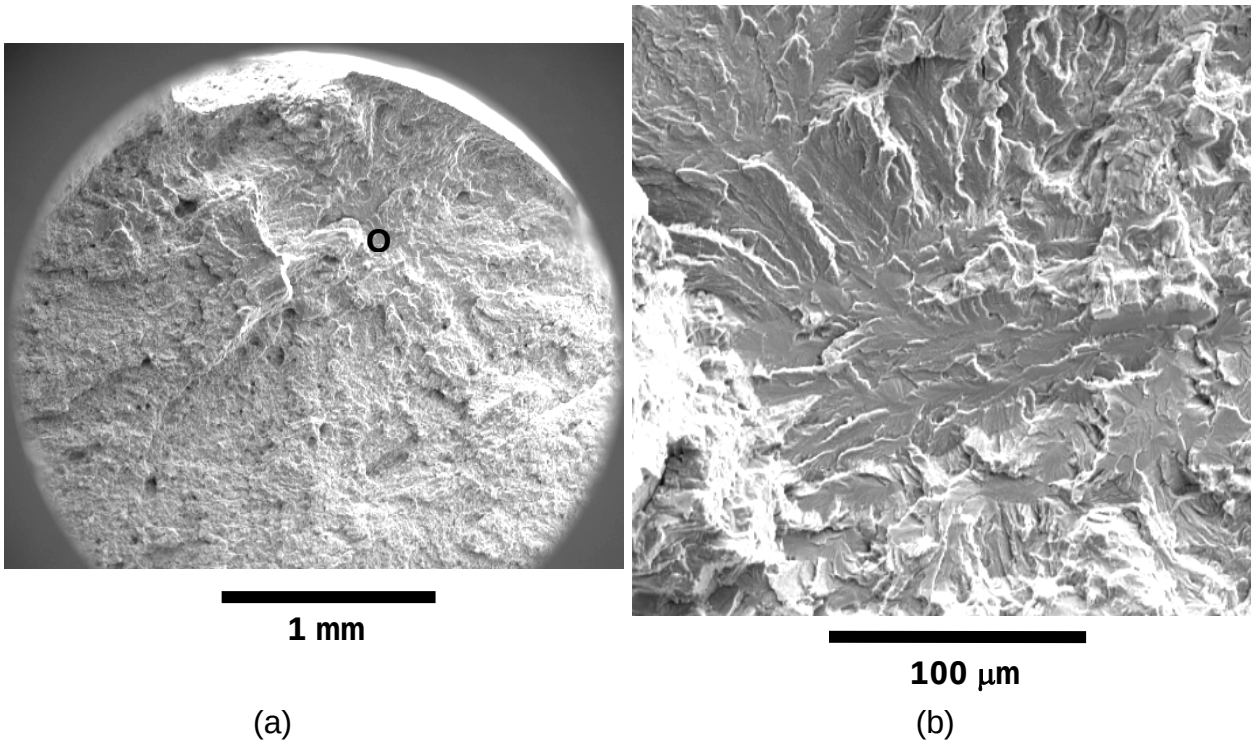

Fig. 7: Normal-fatigue failure modes observed for the 127 ppm hydrogen alloy. (a) Low magnification image with one of the initiation sites indicated as 'O'; and (b) higher magnification image of a region, characteristic of the internal faceted initiation site, that has been labeled 'O' in figure (a).

(b) Dwell-fatigue specimens: Similar to the normal-fatigue fracture initiation sites, the fracture initiation site for the dwell-fatigue test conditions consists primarily of facets for all the hydrogen contents examined in this study. It is worthwhile to note that the dwell-fatigue fracture facets are more well-defined than the normal-fatigue fracture facets for the degassed (compare Fig. 6 and 8) and the as-received (see ref. [13]) alloys. Similar fractographic features at the dwell-fatigue initiation site are observed for 10 (Fig. 8), 49, 59, 150, and 204 (Fig. 9) ppm alloys. Furthermore, the dwell-fatigue initiation sites for 10 - 204 ppm alloys are internal (sub-surface). The dwell-fatigue fracture surface for the 230 ppm alloy consists of one near-surface initiation site (Fig. 10). The size of the faceted region in the initiation site for the 230 ppm alloy is markedly lower than that observed at lower hydrogen contents (compare Fig. 10 with Fig. 8 and 9). It is also of interest to note that the dwell-fatigue life is much higher for the 230 ppm alloy than for the lower hydrogen content alloys (Table III and Fig. 4).

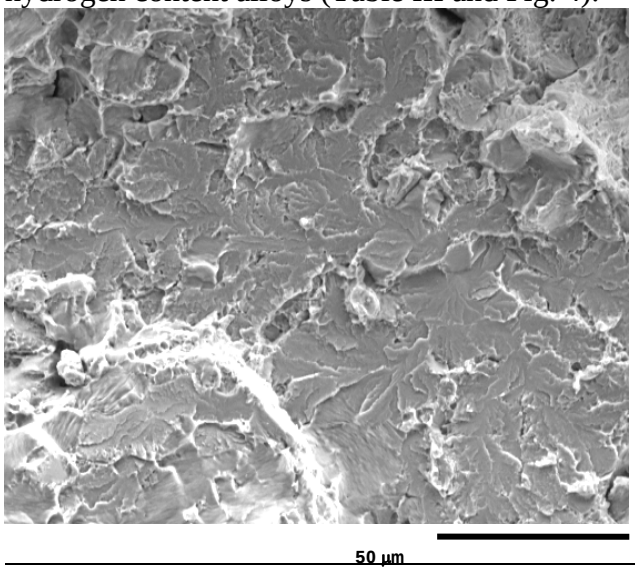

Fig. 8: Dwell-fatigue failure modes observed for the 10 ppm hydrogen alloy. SEM image of the internal, faceted initiation site.

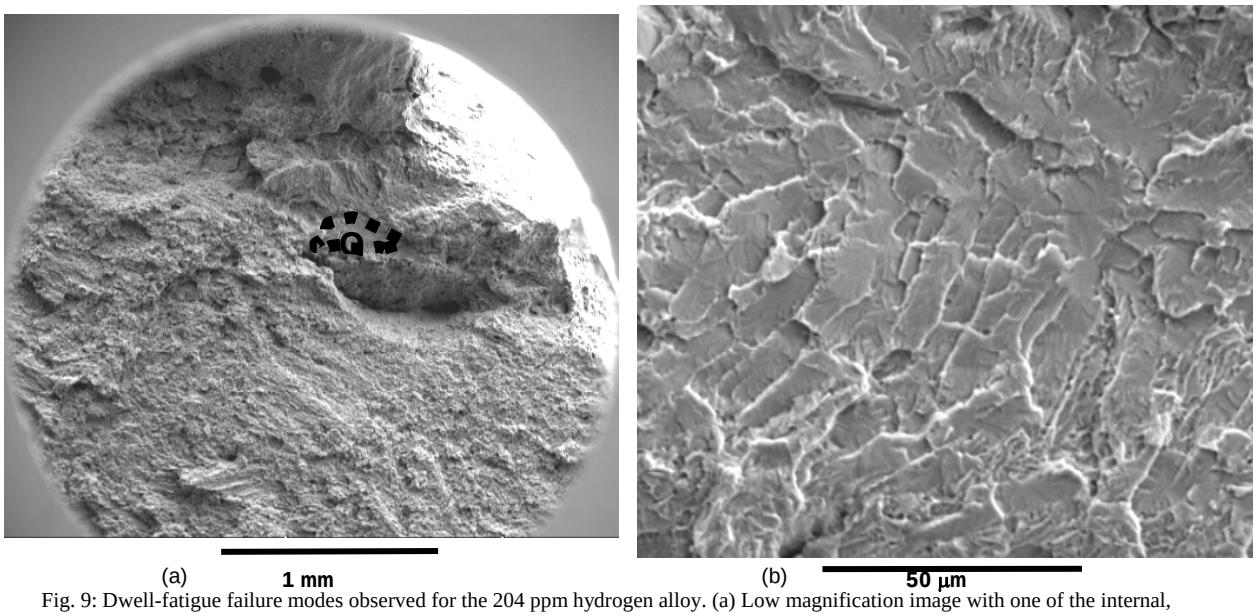

Fig. 9: Dwell-fatigue failure modes observed for the 204 ppm hydrogen alloy. (a) Low magnification image with one of the internal, faceted initiation sites circumscribed by dotted curve; and (b) higher magnification image of a region, characteristic of the faceted initiation site, that has been labeled 'O' in figure (a).

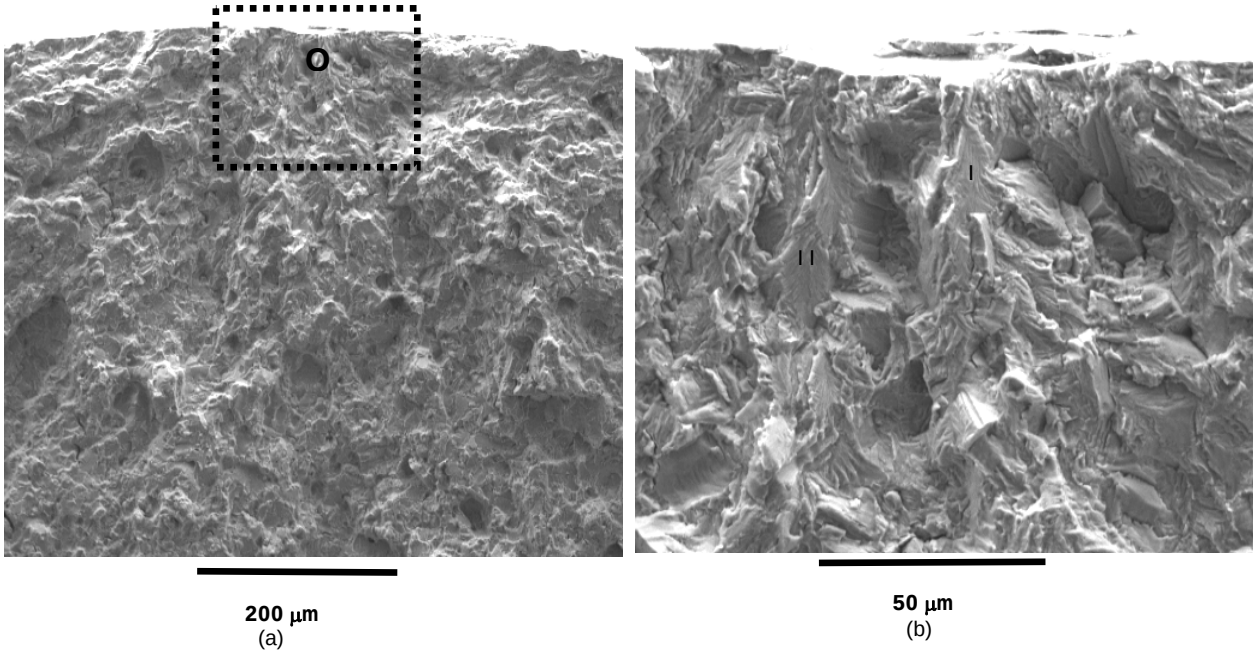

Fig. 10: Dwell-fatigue failure modes observed for the 230 ppm hydrogen alloy. (a) Low magnification image with the initiation site circumscribed by dotted lines; and (b) higher magnification image of the initiation site, that has been labeled 'O' in figure (a). 'I' and 'II' in figure (b) denote two facets with non-faceted region in between them.

3.4 Orientation of the dwell-fatigue fracture facets:

The orientation of the dwell-fatigue fracture facets at the crack initiation site in 204 and 230 ppm alloys was determined. The vectors denoting the normal to the facets shown in Fig. 11 (a) and 12 (a) are (- **i** - 2.58 **j** + 18.12 **k**) and (- **i** + 7.81 **j** + 21.24 **k**), respectively; where **i**, **j** and **k** are unit vectors along X, Y and Z – axes, respectively. X-axis points to the top in the SEM images, Y-axis (tilt axis) to the left in the SEM images and Z-axis is anti-parallel to the electron beam direction (Fig. 11 (b)). Z-axis is also parallel to the loading direction during the dwell-fatigue tests. Thus, the facet normal is oriented at 9^0 and 20^0 with respect to the loading axis for the facets shown in Fig. 11 (a) and 12 (a), respectively. Fig. 11 (c) shows that the fracture facet shown in Fig. 11 (a) is inclined at ~ 15^0 to the basal plane and Fig. 12 (b) shows that the fracture facet shown in Fig. 12 (a) is inclined at ~ 10^0 – 15^0 with respect to the basal plane.

In an earlier work [14], we reported that the dwell-fatigue fracture facets for the as-received alloy are inclined at ~ 10^0 with respect to the basal plane. Therefore, for both the as-received and hydrogen-charged alloys, the dwell-fatigue fracture facets are not exactly aligned with the basal plane, but are inclined at ~ 10^0 – 15^0 to it. These results agree with the earlier work of Blackburn and Williams [15], who used the back-reflection X-ray techniques to determine the crystallographic orientation of facets in Ti-8Al alloy.

Therefore, the crystallographic orientations of the dwell-fatigue fracture facets are essentially the same for as-received and hydrogen-charged alloys (Fig. 11 – 12, and ref. [14]). Hence, the longer dwell-fatigue lives observed for the hydrogen-charged alloys (Table III and Fig. 4) cannot be explained on the basis of the orientation of the fracture facets at the initiation site.

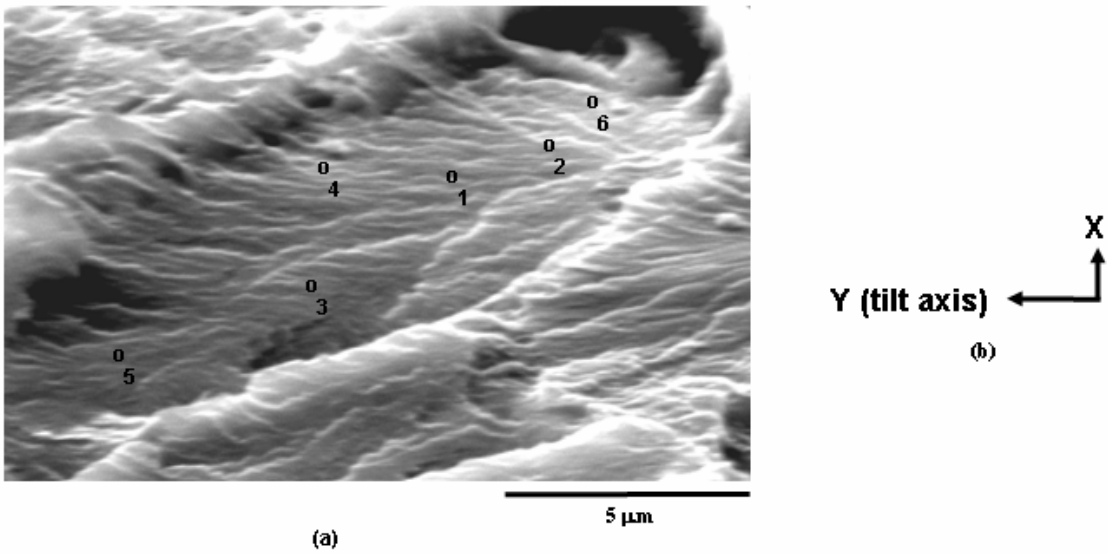

Fig. 11: Crystallographic orientation determination of individual dwell-fatigue fracture facet in the 204 ppm hydrogen (furnace-cooled) alloy. (a) SEM image at 70° tilt of a facet showing the locations of six points on the facet from where the EBSD patterns were obtained and subsequently indexed to determine the crystallographic orientation of the grain through which this facet had been produced. (b) Schematic representation of the orientation of SEM stage axes system with respect to the SEM images. X-axis points to the top of SEM image, Y-axis to the left and Z-axis is coming out of the plane of paper. (c) Inverse pole figure showing the orientation of the facet normal based on the EBSD analyses on six locations shown in (a) and the orientation of the facet (facet normal = - **i** - 2.58 **j** +18.12 **k**), as determined by the quantitative tilt fractography technique.

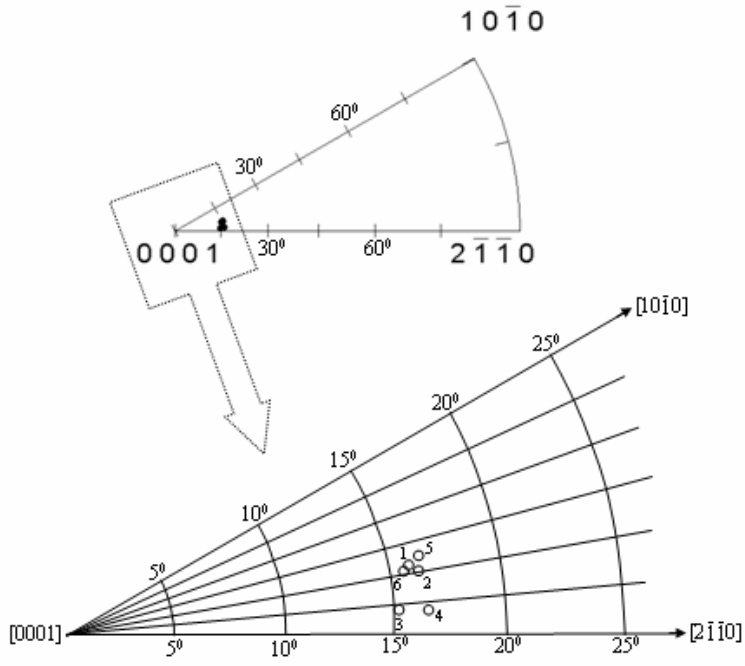
10$\bar{1}$0
60⁰
30⁰
0001
30⁰
60⁰
2$\bar{1}\bar{1}$0
[10$\bar{1}$0]
25⁰
20⁰
15⁰
10⁰
5⁰
1
5
6
2
3
4
[0001]
5⁰
10⁰
15⁰
20⁰
25⁰
[2$\bar{1}\bar{1}$0]

Fig. 11 (c)

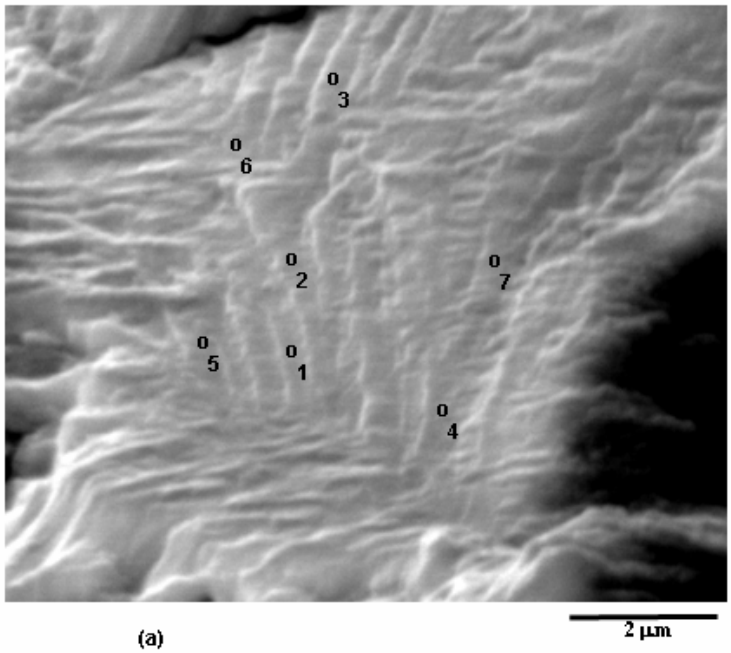

Fig. 12: Crystallographic orientation determination of individual dwell-fatigue fracture facet in the 230 ppm hydrogen (air-cooled) alloy. (a) SEM image at 70^0 tilt of a facet (that was labeled 'I' in Fig. 10) showing the locations of seven points on the facet from where the EBSD patterns were obtained and subsequently indexed to determine the crystallographic orientation of the grain through which this facet had been produced. (b) Inverse pole figure showing the orientation of the facet normal based on the EBSD analyses on seven locations shown in (a) and the orientation of the facet (facet normal = - **i** + 7.81 **j** +21.24 **k**), as determined by the quantitative tilt fractography technique.

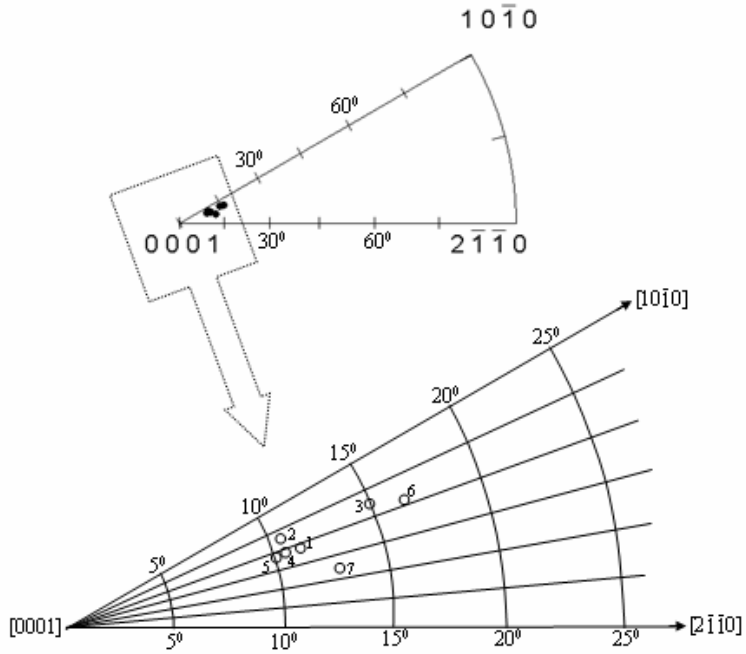

Fig. 12 (b)

4. DISCUSSION:

Our results on the variation of normal-fatigue and dwell-fatigue lives with hydrogen content at ~ 95 % of YS are summarized in Fig. 4. In the work by Neal [5] and Evans [8] on IMI 685, the applied peak stress has not been normalized by the actual strength for the different hydrogen content alloys. Therefore, some of the reported longer lives (both normal-fatigue and dwell-fatigue) for higher hydrogen content [5, 8] can, at least in part, be attributed to a higher strength for higher hydrogen content. Nonetheless, our results on normal-fatigue life as a function of hydrogen content (Table II and Fig. 4) are, by and large, consistent with the results of the prior studies on IMI 685 with colony microstructure [5, 8-10].

On the other hand, in the prior studies, the dwell-fatigue life has been found to be either a weak function of hydrogen content [5, 8-10] or significantly lower for higher hydrogen content [10-12]. It should be noted that in the study of Hack and Leverant [11] the applied peak stress has not been normalized by the strength for different hydrogen content alloys. However, if one were to normalize the applied peak stress by the strength, it would mean a higher peak stress for the higher hydrogen alloy and therefore, a much lower dwell-fatigue life. In none of the prior reports that we have reviewed, is there an instance where the dwell-fatigue life for a higher hydrogen alloy had been found to be longer [5, 8-12] by a factor of as high as 3 to 5, as has been observed

in the current study (Table III and Fig. 4). One possible reason for this apparent discrepancy could be a difference in the microstructural conditions: all the reviewed prior investigations [5, 8-12] have been conducted on IMI 685 with colony microstructure, whereas the current study has been conducted on the Ti-6242 alloy with bimodal microstructure. One important distinction between the two microstructures is the relative continuity of the α and β phases. The colony microstructure typically consists of a continuous β-phase matrix in which each α lath is surrounded by β-phase and thus, is disconnected from other α laths. On the other hand, the bimodal microstructure with ~ 70 vol. % primary α, which has been examined in the current study, consists of a continuous α-phase matrix and the β-phase is discontinuous (Fig. 1). This difference in the microstructure can have important implications for hydrogen induced embrittlement; because hydrogen has a larger solubility and mobility in the β-phase than in the α-phase, and therefore, it is easier for hydrogen to segregate to the regions of high tensile hydrostatic stresses in the continuous β-matrix microstructure than in the continuous α-matrix microstructure. In fact, for Ti-6Al-4V alloy (an α+β alloy) tested in gaseous hydrogen (pressure ~ 680 torr) environment, Nelson, et al. [16] have reported that under the same test conditions, the microstructures containing a continuous β-phase matrix are more severely embrittled than the one containing a continuous α-phase matrix. Furthermore, Nelson [17] has also examined the effects of the variations in the hydrogen pressure on embrittlement of Ti-6Al-4V alloy in two different microstructural conditions: one containing a continuous β-phase matrix and another containing a continuous α-phase matrix. His results indicate that the influence of variation in the hydrogen pressure on the embrittlement is greater for the continuous β-matrix microstructure than for the continuous α-matrix microstructure.

It is also of interest to note that the diffusion coefficient of hydrogen in VT6 (an alloy with the same nominal composition as the Ti-6Al-4V alloy) has been found to be quite sensitive to its microstructural condition [18]. The experimentally measured values of diffusion coefficient of hydrogen in VT6 at room temperature are equal to 6×10^{-11} $m^2 s^{-1}$ and 7×10^{-13} $m^2 s^{-1}$, for a β-annealed (lamellar) and an equiaxed microstructures, respectively [18]. Thus, for the same nominal alloy composition, the room temperature diffusion coefficient of hydrogen in Ti-alloys can be two orders of magnitude higher for the interconnected β-phase microstructure than for the discontinuous β-phase microstructure.

The distance that hydrogen atoms diffuse in time Δt is on the order of $2\sqrt{D\,\Delta t}$, where D is the diffusion coefficient. This expression enables us to obtain an order of magnitude estimate of the diffusion distance for different microstructures. Using the hold time of the dwell-fatigue tests (= 2 minutes) as the diffusion time Δt, and the values of diffusion coefficient of hydrogen in VT6 mentioned above, we estimate diffusion distances of 170 μm and 18 μm in one dwell-fatigue cycle for a continuous β-phase matrix microstructure and a continuous α-phase matrix microstructure, respectively. Thus, the estimated hydrogen diffusion distance during one dwell-fatigue cycle for the continuous α-matrix microstructure is on the order of the primary α grain size in the microstructure examined in the current study (Fig. 1). The estimated diffusion distance for a continuous β-matrix microstructure is about 10 times larger than for a continuous α-matrix microstructure. Therefore, hydrogen diffusion to the regions of high (tensile) hydrostatic stresses can occur from a material volume that is roughly 1000 times larger in the continuous β-matrix microstructure than in the continuous α-matrix microstructure at the same

time from the start of the test. This can lead to an increase in the local hydrogen concentration that is up to ~ 1000 times (the exact factor will also depend on thermodynamic feasibility) higher for the continuous β-matrix microstructure than for the continuous α-matrix microstructure for the same bulk hydrogen content. Hence, a colony microstructure (which has interconnected β–phase) could be made more susceptible to dwell-fatigue failures with an increase in hydrogen content, as has been reported by Evans and Bache [10], Hack and Leverant [11] and Bache, et al. [12]. On the other hand, an increase in the bulk hydrogen content of a bimodal microstructure with discontinuous β-phase is not likely to have such a significant detrimental effect on its dwell-fatigue susceptibility, which is by and large consistent with the results of the current study. Nonetheless, the reasons for a higher dwell-fatigue life with an increase in hydrogen content observed in the current study for the discontinuous β-phase (bimodal) microstructure are currently not clear.

5. SUMMARY AND CONCLUSIONS:

In this study, the normal-fatigue and dwell-fatigue experiments were conducted on Ti-6242 alloy in the bimodal microstructural condition (~ 70 vol. % primary α). This microstructure consisted of a continuous α-phase matrix. Our results indicate that the normal-fatigue life is a weak function of hydrogen content and it is slightly lower for hydrogen contents ≥ 100 ppm. On the other hand, the dwell-fatigue life is higher for higher hydrogen contents, especially for hydrogen contents ≥ 150 ppm. The plastic strain-to-failure is higher for dwell-fatigue than for normal-fatigue test conditions. The crack initiation site is essentially faceted for all the material and test conditions used in the current study. The crystallographic orientation of dwell-fatigue fracture facets is similar for both the as-received and hydrogen-charged alloys: the facets are inclined at ~ $10^0 – 15^0$ with respect to the basal plane. In some of the prior studies, the dwell-fatigue life has been observed to be significantly lower at higher hydrogen contents. The apparent disagreement of this observation with the results reported in the current study can be understood on the basis of the differences in hydrogen diffusion kinetics for the different microstructures examined in the various studies.

ACKNOWLEDGMENTS

This research was supported by the Federal Aviation Administration. The authors thank the Technical Monitor, Joseph Wilson, for his encouragement and support of this work. The donation of Ti-6242 pancake forging by Ladish Co. Foundation (Cudahy, WI) is also gratefully acknowledged. The authors also thank Dr. Fred Meisenkothen for help with the degassing experiments.

REFERENCES

1. W.J. Evans and C.R. Gostelow, Metallurgical Transactions, Vol. 10A, pp. 1837-1846, 1979.

2. A.P. Woodfield, M.D. Gorman, R.R. Corderman, J.A. Sutliff and B. Yamrom, Titanium '95: Science and Technology, pp. 1116-1124, 1995.

3. M.R. Bache, M. Cope, H. M. Davies, W.J. Evans, and G. Harrison, International Journal of Fatigue (1998), Volume Date 1997, 19(Suppl. 1, First International Conference on Fatigue Damage in Structural Materials, 1996), pp. S83-S88.

4. M.E. Kassner, Y. Kosaka and J.A. Hall, Metallurgical and Materials Transactions, vol. 30A, pp. 2383-2389, September 1999.

5. Neal, D.F. (1988). Proceedings of the Sixth World Conference on Titanium, France, pp. 175-180.

6. J.R. Cho, D. Dye, K.T. Conlon, M.R. Daymond, and R.C. Reed, Acta Materialia, vol. 50, pp. 4847-4864, 2002.

7. Williams, J.C., Baggerly, R.G., and Paton, N.E., Metallurgical and Materials Transactions, vol. 33A, pp. 837-850, 2002.

8. W.J. Evans, Journal of Materials Science Letters, vol. 6, pp. 571-574, 1987.

9. Evans, W.J. and Bache, M.R. (1994). International Journal of Fatigue, vol. 16, no. 7, pp. 443-452.

10. Evans, W.J. and Bache, M.R. (1995). Scripta Metallurgica et Materialia, vol. 32, no. 7, pp. 1019-1024.

11. J.E. Hack and G.R. Leverant, Metallurgical Transactions, Vol. 13A, pp. 1729-1738, 1982.

12. Bache, M.R., Evans, W.J. and Davies, H.M. (1997). Journal of Materials Science, vol. 32, pp. 3435-3442.

13. V. Sinha, M.J. Mills, and J.C. Williams, Metallurgical and Materials Transactions, vol. 35A, pp. 3141-3148, 2004.

14. V. Sinha, M.J. Mills, and J.C. Williams, "Determination of Crystallographic Orientation of Dwell-fatigue Fracture Facets in Ti-6242 Alloy", Journal of Materials Science (submitted).

15. M. J. Blackburn and J. C. Williams, "Metallurgical Aspects of the Stress Corrosion Cracking of Titanium Alloys," Proc. Conf. on the Fundamental Aspects of Stress Corrosion Cracking, N.A.C.E., 1969, p 620.

16. H.G. Nelson, D.P. Williams, and J.E. Stein, (1972). Metallurgical Transactions, vol. 3, February 1972, pp. 469-475.
17. H.G. Nelson, (1973). Metallurgical Transactions, vol. 4, January 1973, pp. 364-367.
18. A.V. Fishgoit, B.A. Kolachev, and V.A. Danilkin, Izvestiya Vysshikh Uchebnykh Zavedenii, Tsvetnaya Metallurgiya, vol. 2, 1986, pp. 93-97.

Appendix J

Effects of Microstructure on Normal-Fatigue and Dwell-Fatigue Crack Growth in Ti-6242

W.O. Soboyejo*, E. Akpan†*, W. Shen[x] , C. Mercer* and F. MacBagonluri[+]

[+]Department of Materials Engineering, Dayton University, Dayton, OH

[x]Princeton Materials Institute, and Department of Civil and Environmental Engineering, Princeton University, Princeton, NJ

*Princeton Materials Institute and Department of Mechanical and Aerospace Engineering, Princeton University, Princeton, NJ

† Department of Mechanical Engineering, Drexel University, Philadelphia, PA

Introduction

Mechanistic studies of fatigue crack nucleation have shown that surface or sub-surface crack nucleation are likely to occur in α/β titanium alloys under normal fatigue and dwell fatigue loading conditions [1, 2]. In many cases, surface or sub-surface nucleation occurs from inclusions such as hard α phase, rogue particles or interfaces/grain boundaries [3]. Fatigue crack nucleation may also occur by a Stroh mechanism [2, 4-6], i.e. due to dislocation pile-up, and the onset of sub-surface cleavage on favorably-oriented grains (Figure 1)[6].

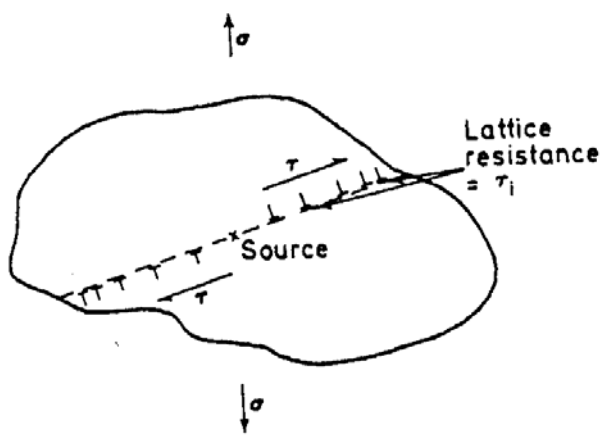

Figure 1 – Schematic Illustration of the Nucleation of Cleavage Fracture from Dislocation Pile-up at Grain Boundaries (Taken from Ref. 6)

However, although the occurrence of surface or sub-surface fatigue crack nucleation in α/β titanium alloys is well documented [2,3,7-10], the crack shape evolution and crack growth mechanisms associated with subsequent crack growth are less well understood. There have also been no prior reports of sub-surface fatigue crack growth rates in α/β titanium alloys. The absence of such crack profile and growth rate data has limited our ability to predict the early stages of fatigue crack growth in α/β titanium alloys. Since the early stages of crack growth can

represent significant fractions of the total failure life of a structure [9], there is a need for improved understanding of the basic mechanisms of fatigue in this regime.

This appendix presents the results of an experimental investigation of normal fatigue and dwell fatigue in smooth hourglass specimens of Ti-6242 in three microstructural conditions provided by Ladish Co. (described in appendix B). Sub-surface fatigue crack nucleation is shown to occur in these microstructures, during cycling to 80% of the uniaxial yield stress at a stress ratio of 0.1. The subsequent crack growth and crack shape profiles are then tracked using beachmarking techniques [8, 11, 12]. The underlying crack growth rates and crack growth mechanisms are evaluated before presenting possible fracture mechanics approaches for the modeling of fatigue crack growth. The implications of the results are then discussed for the life prediction and non-destructive inspection of aeroengine structures and components fabricated from Ti-6242.

Experimental Methods

(a) Materials

The three microstructures of Ti-6242, examined in this part of the work, were donated by Ladish Co. and are described in detail in appendix B.

(b) Normal Fatigue

Two types of fatigue experiments were performed in this study. The first involved long crack growth studies on single edge notched bend (SENB) specimens, while the second involved studies of fatigue crack nucleation and growth on smooth hourglass type specimens (Figure 2). All the fatigue experiments were conducted at room-temperature in a servo-hydraulic testing machine that was operated at a cyclic frequency of 10 Hz. Beachmarking sequences (Figures 3a and 3b) were used to track the evolution of crack shapes.

The first set of experiments were carried out to establish beachmarking procedures, whilst obtaining long crack growth rate data at a stress ratio, $R = K_{min}/K_{max}$, of 0.1. The experiments were carried out on single edge notched bend (SENB) specimens with notches/cracks in the R-T orientation. After fatigue pre-cracking under cyclic compression [10], beachmarking was effected by increasing the K_{min}, while keeping the K_{max} constant (Figure 3a) [8,11-13]. The effective stress ratio, R, was thus increased from 0.1 to 0.5 during beachmarking (Figure 3a). Approximately 0.5 mm of crack growth was allowed during beachmarking, while ~ 1 mm of growth was allowed during regular growth at a stress ratio, R, of 0.1. Crack growth in the SENB tests was monitored using notch mouth compliance techniques [14]. The tests were continued until specimen fracture occurred. The fracture surfaces of the specimens were then examined using low magnification optical and scanning electron microscopy (SEM).

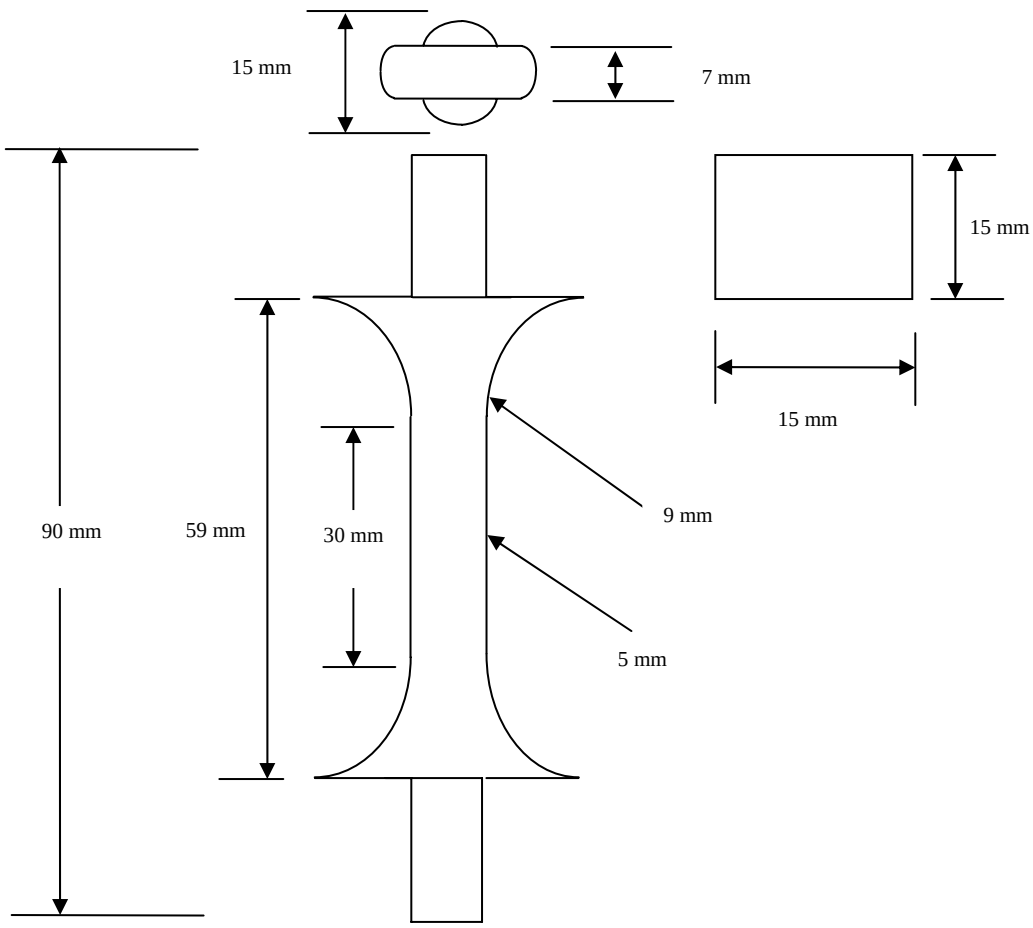

Figure 2 – Dimensions of Smooth Hourglass Specimen

The second type of experiment involved the stress-life testing of smooth hourglass specimen (Figure 2). The specimens were deformed under load control by cycling between 0.08 and 0.8 of the cyclic yield stresses for the three microstructures (Table 1). The initial tests involved continuous cycling to failure. These were used to establish the number of cycles to failure, N_f, for the three microstructures. Subsequent incremental fatigue tests were then conducted by loading for 5% of N_f at a stress ratio of 0.1, and 10% of N_f at a stress ratio of 0.5 (keeping σ_{max} constant in each of the loading blocks)[8,11-13](Figure 3a). In this way, beachmarks were introduced onto the fracture surfaces of the smooth hourglass specimens. These beachmarks tracked the onset of surface or sub-surface crack nucleation and growth, and the evolution of subsequent crack profiles. Hence, the evolution of crack shape was monitored (from the onset of crack nucleation) until the catastrophic failure occurred. After specimen failure, the beachmarks and the fracture modes were analyzed using low magnification optical and scanning electron microscopy (SEM). The crack nucleation sites were also identified using SEM and energy dispersive x-ray spectroscopy.

Microstructure	Type of Test	Microstructural Unit Size/μm	Distance Nucleation from Surface (h/μm)	$\frac{h}{d}$
Equiaxed (1)	Fatigue	22	80	3.6
Elongated (2)	Fatigue	17	25	1.5
Colony (3)	Fatigue	77	140	1.8

Table 1 – Positions of Fatigue Crack Nucleation Sites: Effects of Microstructure

(a)

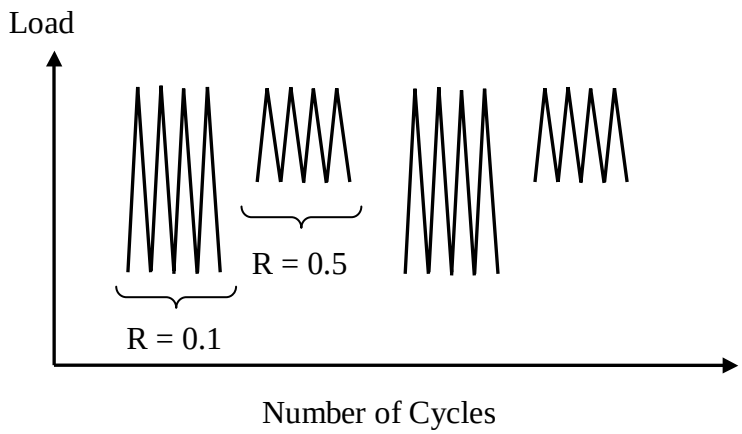

(b)

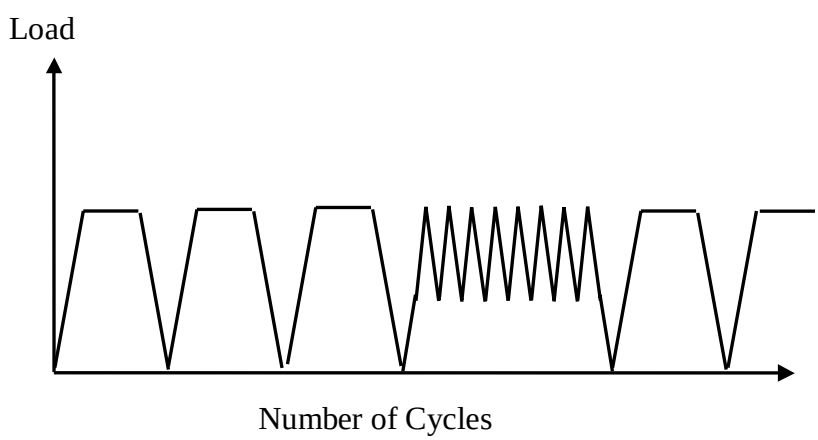

Figure 3 – Schematic of Beachmarking Load Profiles (a) Normal Fatigue Waveform, (b) Dwell Fatigue Waveform

(c) Dwell Fatigue

As in the case of the normal fatigue experiments, two types of dwell fatigue experiments were performed. The first involved measurements of dwell crack growth rates in through-thickness crack specimens, while the second set of experiments examined the mechanisms of sub-surface and surface crack growth under dwell fatigue loading conditions. The studies of dwell fatigue crack growth were carried out at room-temperature in a computer-controlled servo-hydraulic testing machine. These involved a ramp at a constant rate to a peak stress in 1/6 of a second, a one minute dwell, and a ramp down to minimum load in 1/6 of a second. Due to the relatively slow cyclic frequency, each dwell fatigue test took about one month to complete.

The first set of dwell crack growth experiments were performed of single edge notched bend experiments (SENB) with rectangular cross-sections (6.3 mm x 12.7 mm) and lengths of ~52 mm. The initial notch-to-width ratios were ~0.25. The SENB specimens were pre-cracked under dwell loading conditions at a stress intensity factor of ~ 18-20 MPa$\sqrt{m}$. This was used to introduce pre-cracks that were ~ 0.5 mm long. After pre-cracking, the dwell crack growth experiments were continued under increasing stress intensity factor ranges, ΔK, until specimen failure occurred. The mechanisms of dwell fatigue crack growth were then examined in a scanning electron microscope.

In the second type of dwell fatigue experiments, the mechanisms of sub-surface and surface crack growth were investigated in the same type of smooth hour-glass specimens that were used in the normal fatigue experiments (Figure 2). The specimens were subjected to an initial ramp to a peak load corresponding to ~ 0.8 of the yield stress in 1/6 second. A dwell load was then applied for 60 seconds before ramping down to minimum load in 1/6 second. A stress ratio, $R = \sigma_{min}/\sigma_{max}$, of ~ 0.1 was used in all the dwell fatigue experiments. The tests were continued until specimen failure occurred. However, periodically, beachmarks were introduced in an effort to track the crack shape evolution. Beachmarking was effected by increasing the minimum load to ~ half the maximum load, and fatigue cycling between the maximum load and minimum load (Figure 3b). The resulting beachmarking profiles were used to track both the sub-surface and depth growth rates. The second set of dwell crack growth experiments were continued until specimen failure occurred. The underlying mechanisms of sub-surface and surface crack growth were then elucidated via scanning electron microscopy.

Results and Discussion

(a) Fatigue of Long Through Thickness Cracks

The beachmarks observed on the fracture surfaces of the through-thickness cracks are shown in Figures 4a – 4c. These show clearly that the beachmarking procedures work well for all three microstructures. The beachmarks also reveal bowed crack shapes (Figures 4a – 4c) that are consistent with transitions in stress state from near plane stress (at the surface) to plane strain conditions in the middle of the specimens [15].

(a) (b) (c)

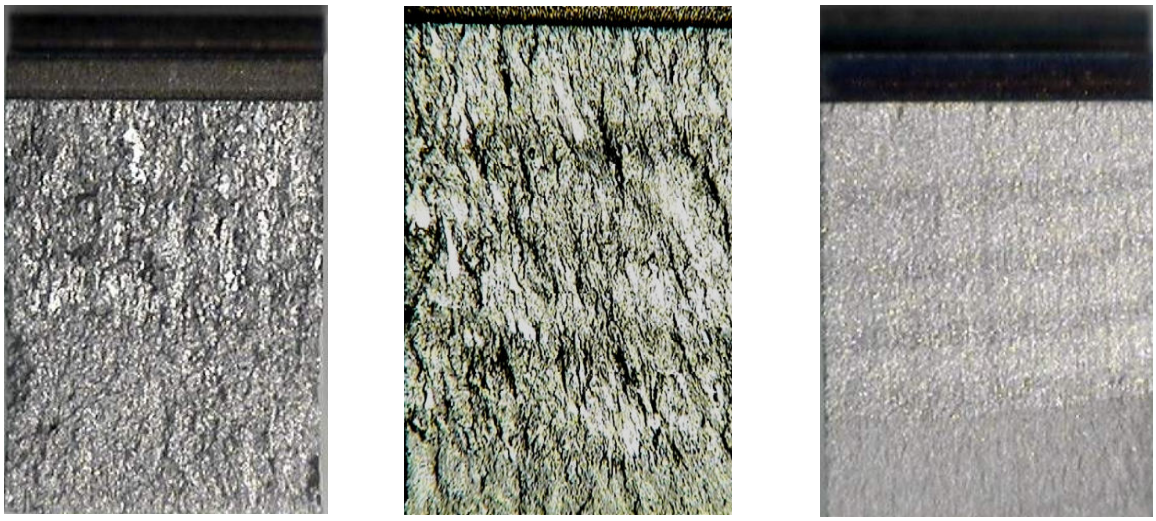

Figure 4 – Beachmarks on Long Through-Thickness Cracks in: (a) Equiaxed Structure (Microstructure 1); (b) Elongated Structure (Microstructure 2), and (c) Colony Structure (Microstructure 3)

The measured long crack growth rate data are presented in Figure 5 for the three microstructures. The results show that Microstructure 1 (the equiaxed microstructure) exhibits the fastest fatigue crack growth rates, while Microstructure 3 (the colony microstructure) exhibits the slowest fatigue crack growth rates across the three regimes of crack growth. Microstructure 2 (the elongated structure) has comparable fatigue crack growth resistance to Microstructure 3 in the near-threshold and Paris regimes. However, crack growth rates in Microstructure 2 are faster than those in Microstructure 3 in the high ΔK regime.

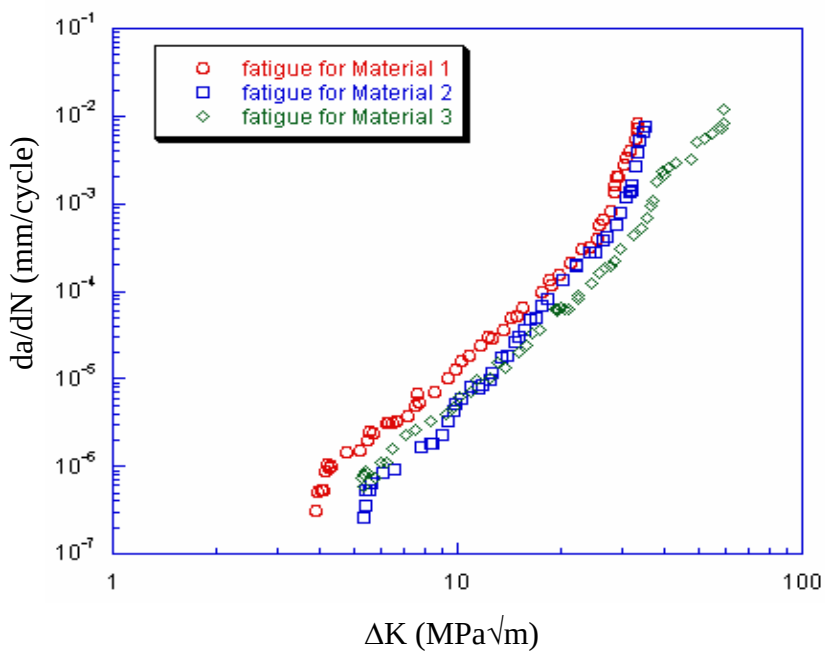

Figure 5 – Comparison of Long Fatigue Crack Growth Rate Data Obtained from SENB Specimens

The trends in the above fatigue crack growth rates are consistent with the results obtained from prior studies of fatigue crack growth in α/β titanium alloys [7-10,16-24]. These studies show that colony (Widmanstatten or basket weave) microstructures generally have superior fatigue crack growth resistance to equiaxed microstructures [22-24]. The improved fatigue crack growth resistance of the colony microstructure has been attributed largely to the role of crack deflection and roughness-induced closure [20,22]. However, the reasons for the observed effects of micro-texture on fatigue crack growth are less well understood.

(b) Sub-Surface/Surface Fatigue Crack Nucleation and Growth

The fatigue fracture modes are presented in Figures 6-8 for microstructures 1-3, respectively. High magnification SEM examination revealed that sub-surface fatigue crack nucleation occurred on cleavage facets, as shown in Figures 6a,b and 8 a,b) for the three microstructures. The orientations of the cleavage facets are yet to be determined. However, extensive prior work has shown that sub-surface cleavage is most likely to occur on basal planes (0001) in α/β titanium alloys [5]. The occurrence of sub-surface cleavage has also been explained by a Stroh-type model (Figure 1)[6]. In this model, sub-surface crack nucleation is induced by dislocation pile-up against grain boundaries. This results ultimately in the nucleation of cleavage cracks when local critical conditions are reached. In this case, it is not clear whether the growth of the cleavage crack (across a single facet) occurs suddenly in one step, or incrementally by cycle-by-cycle fatigue crack growth.

(a)

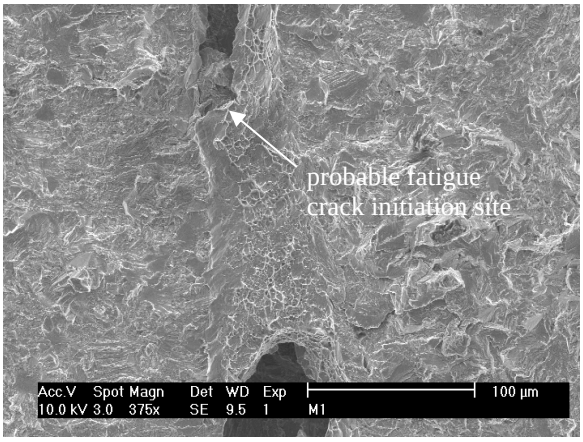

(b)

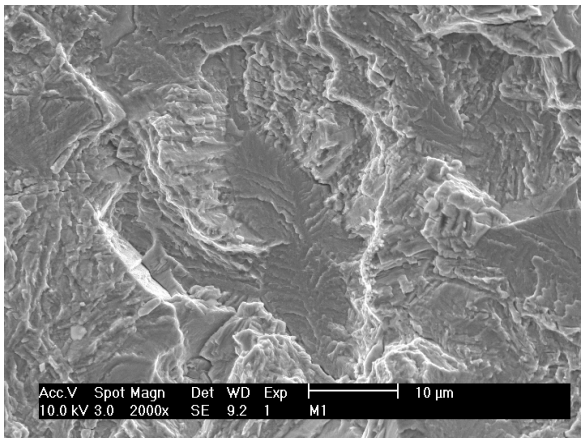

(c)

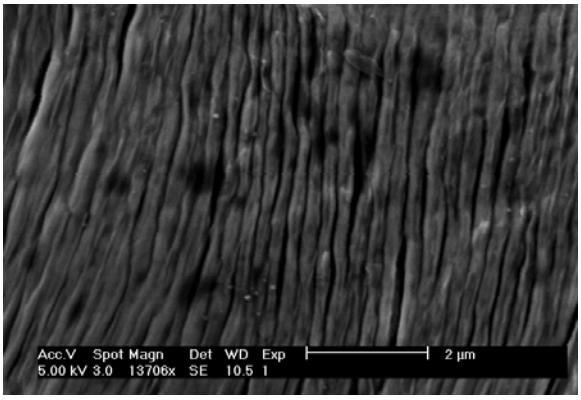

(d)

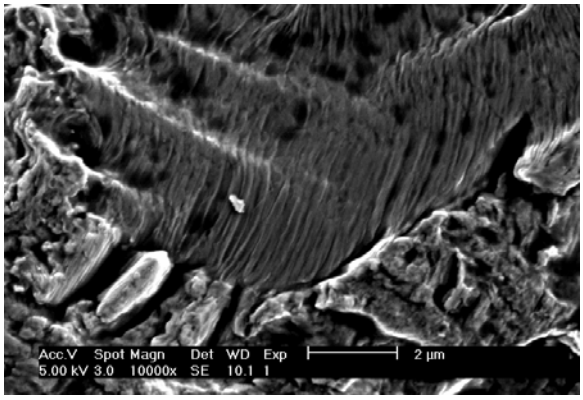

(e)

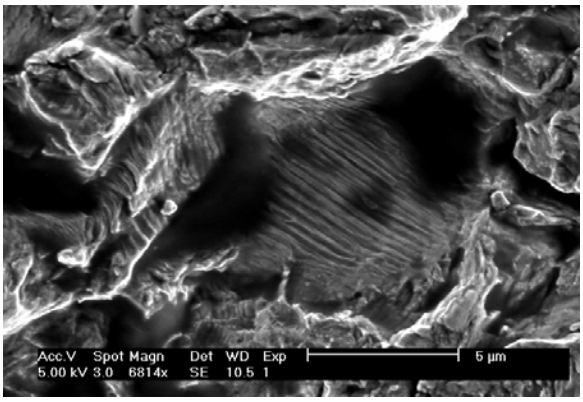

(f)

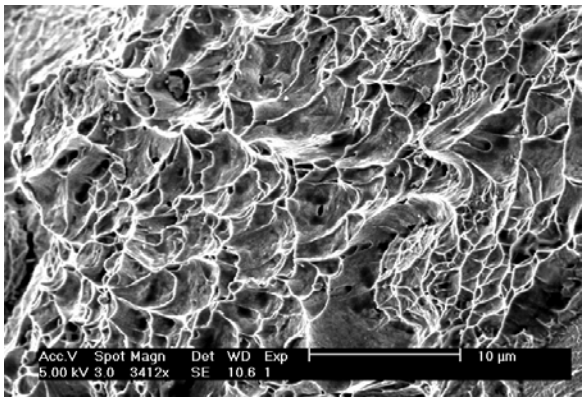

Figure 6 – Fatigue Fracture Modes in Microstructure 1: (a) Sub-surface Crack Nucleation; (b) Crack Growth by Cleavage; (c) Transition from Cleavage to Striation; (d) Fatigue Striations; (e) Fatigue Striation plus Dimples; (f) Final Fracture

(a)

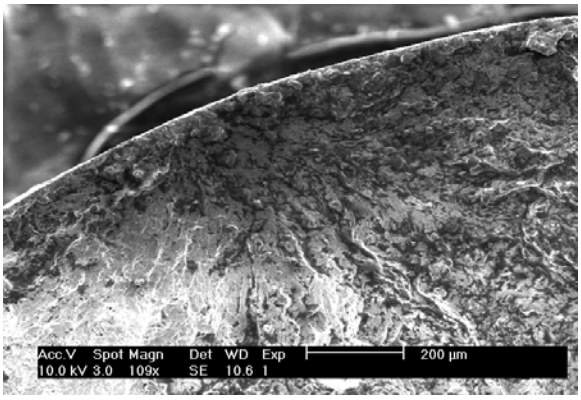

(b)

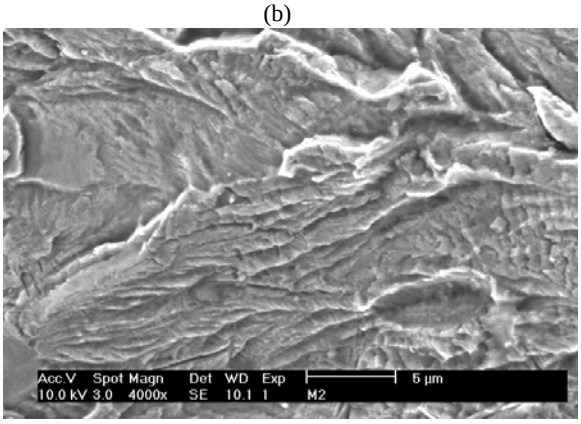

(c)

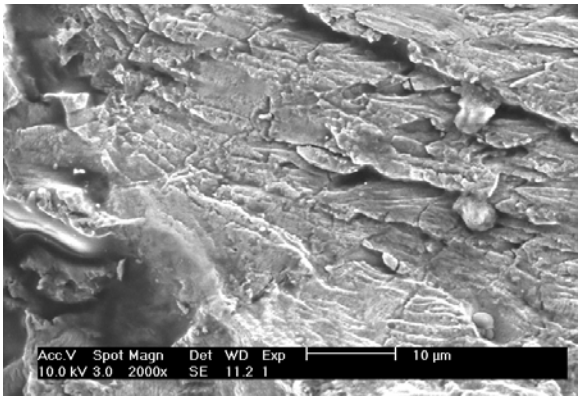

(d)

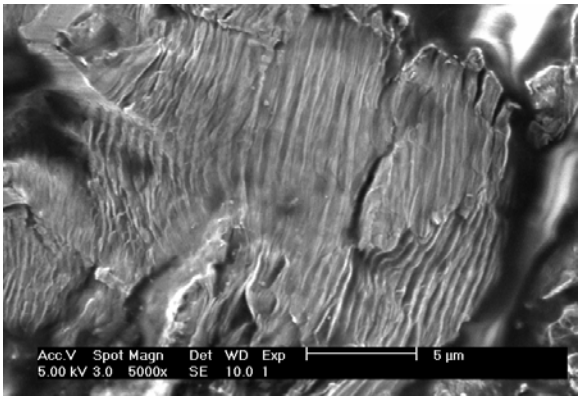

(e)

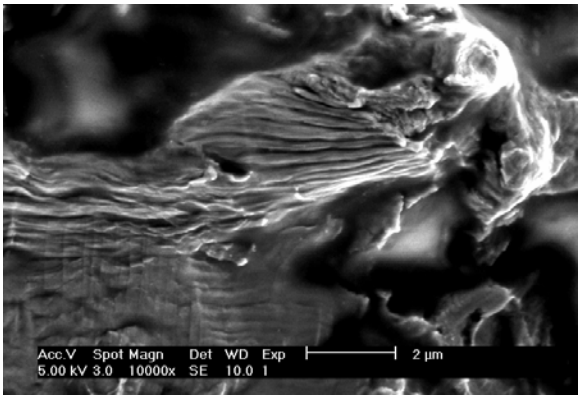

(f)

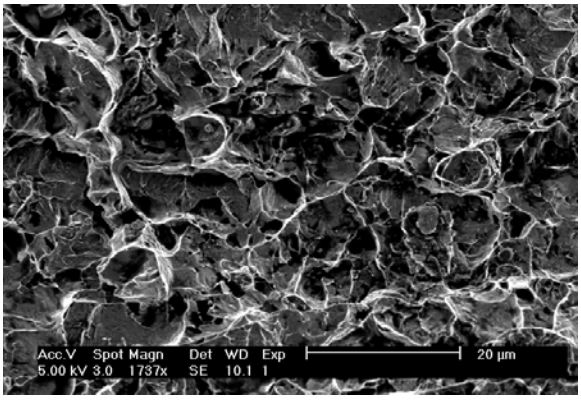

Figure 7 – Fatigue Fracture Modes in Microstructure 2: (a) Sub-surface Crack Nucleation; (b) Crack Growth by Cleavage; (c) Transition from Cleavage to Striation; (d) Fatigue Striations; (e) Fatigue Striation plus Dimples; (f) Final Fracture

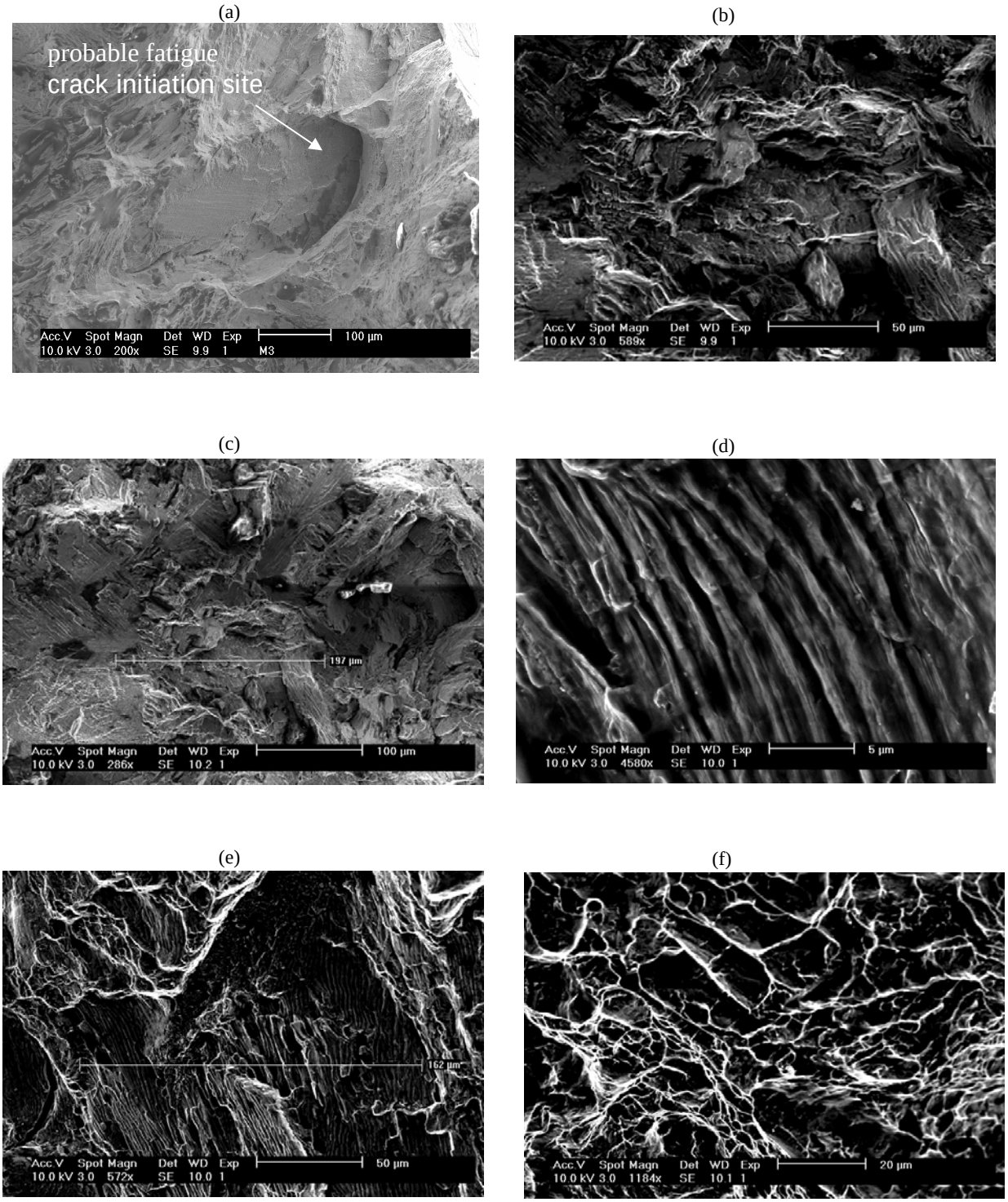

Figure 8 - Fatigue Fracture Modes in Microstructure 3: (a) Sub-surface Crack Nucleation; (b) Crack Growth by Cleavage; (c) Transition from Cleavage to Striation; (d) Fatigue Striations; (e) Fatigue Striation plus Dimples; (f) Final Fracture

Following the initial growth of sub-surface nearly elliptical cleavage cracks (Figures 6b 7b and 8b), the fatigue fracture modes were similar to those reported earlier for α/β Ti alloys [16-22]. In the case of Microstructure 1 (the equiaxed microstructure), fatigue striations (Figure 6c and 6d) were observed in the mid-ΔK/Paris regime. A combination of fatigue striations and ductile dimples was also observed in the region of transition from stable fatigue crack growth to overload fracture (Figure 6e). Final overload failure occurred by ductile dimpled fracture (Figure 6f).

In the case of Microstructure 2 (the elongated textured microstructure), the initial cleavage facet was ~ 25 μm from the surface (Figure 7a). This is surrounded by a region containing a mixture of cleavage facets (Figure 7b and c) and fatigue striations (Figure 7d).

Finally, in the case of the Microstructure 3 (the colony microstructure), a rough fatigue fracture mode is observed, with evidence of a flat faceted fatigue crack nucleation site (Figure 8a). A faceted cleavage fracture mode is observed in the near-threshold regime (Figures 8b and 8c). This transitions to a fatigue striation mode in the grid-ΔK regime (Figure 8d). As before, a combination of fatigue striations and ductile dimples was observed in the high ΔK regime (Figure 8e), before final overload failure occurred by ductile dimpled fracture (Figure 8f).

It is important to note here that the beachmarks on the sub-surface cracks were more difficult to reveal. However, beachmarks on the surface-breaking cracks were much easier to reveal. These are shown in Figure 9a for microstructure 1. The figure shows an asymmetric crack profile that is almost semi-elliptical. The possible asymmetric crack profiles are illustrated schematically in Figure 9b. Actual plots of aspect ratio, c/a, for each side of the semi-elliptical cracks, are presented in Figures 10 and 11. Note that the aspect ratios are different for each side of the crack (Figures 10a-10c). However, the extent of the asymmetry is limited. Hence, an average aspect ratio may be used to represent the crack shape evolution (Figures 11a-11c).

Both halves of the surface cracks evolve towards “Preferred Propagation Paths” (PPPs), as observed in prior work on surface cracks [25,26]. However, the magnitudes of the aspect ratios along the PPPs are different from those reported for square or rectangular cross-sections under tension or bending loads [25-27]. Prior work has shown that the aspect ratios are ~ 0.9 [27] under tensile loading, and between ~ 0.6 and 0.9 along the PPPs under bending loads. In contrast, the aspect ratios are between 0.8 and 2.5 for cracks evolving along circular cross-sections within the hour-glass specimens that were used in the current study of crack shape evolution under tensile loading (Figures 10 and 11).

A summary of the fatigue crack growth rate data obtained for the different regimes of semi-elliptical fatigue crack growth is presented in Figures 12-14. Note that the stress intensity factor solutions (for the semi-elliptical cracks) were computed using solutions by Newman and Raju [28], while the crack growth rates were estimated from beachmarked crack profiles. The crack growth rates were estimated from plots of crack length (obtained from the beachmarked crack profiles) and the number of fatigue cycles in which a stress ratio, $R = \sigma_{min}/\sigma_{max}$, of 0.1 was applied.

(a)

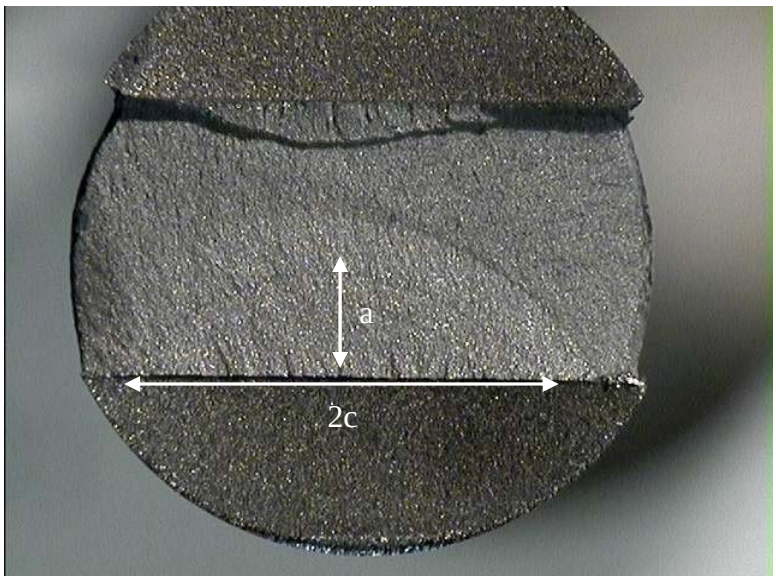

(b)

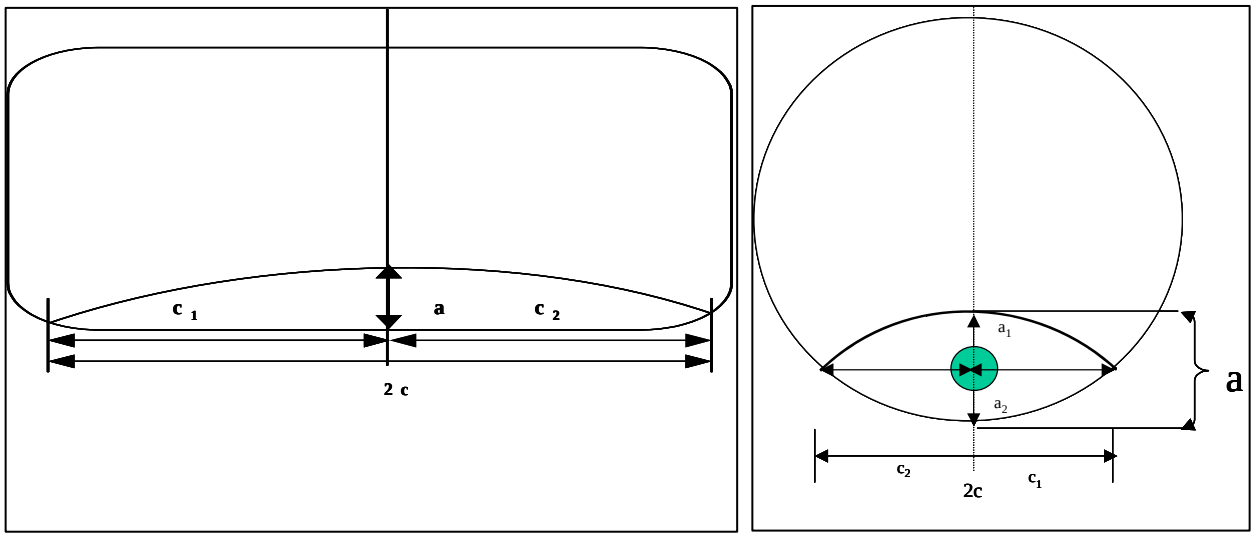

Figure 9 – Possible Crack Profiles and Crack Shape Parameters: (a) Typical Optical Photomicrograph; (b) Schematics of Possible Crack Profiles

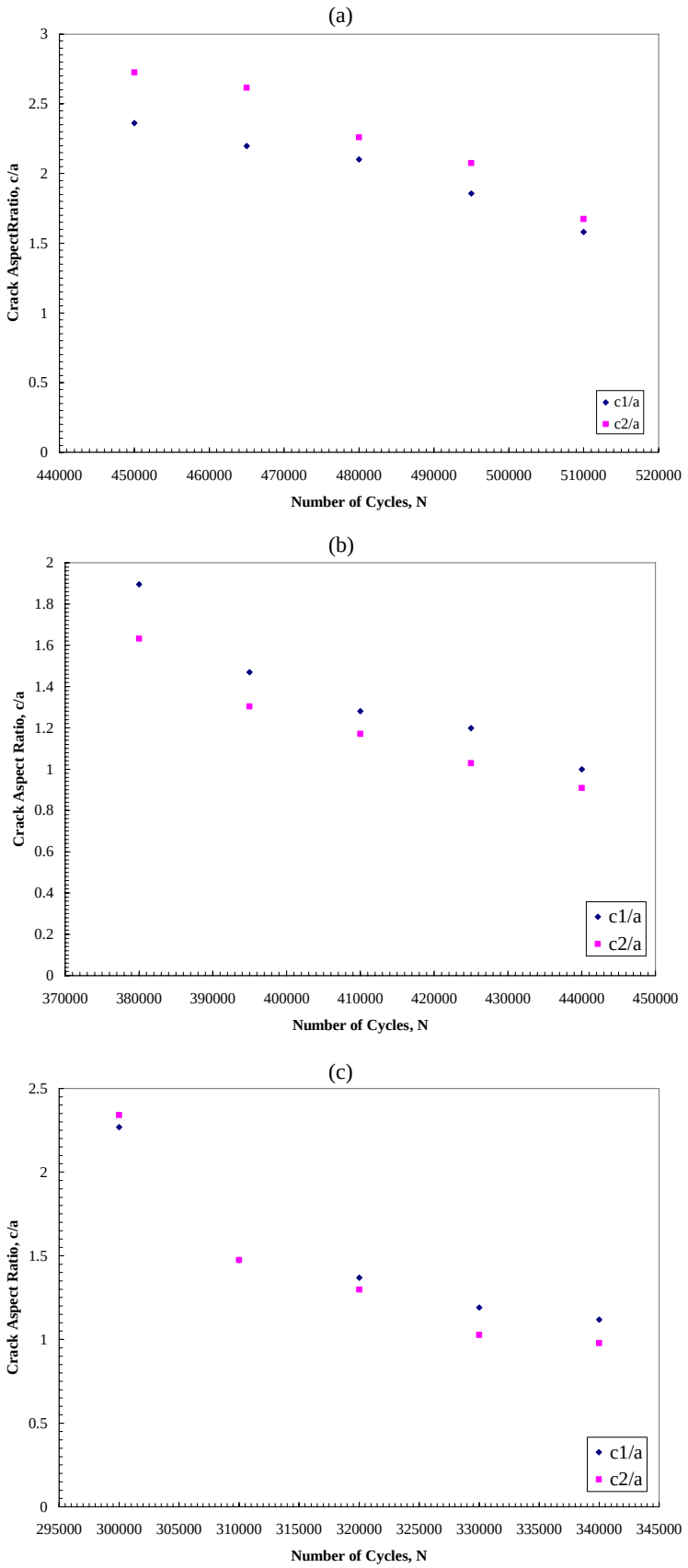

Figure 10 – Asymmetries in Crack Shape Evolution: (a) Equiaxed Microstructure; (b) Elongated Microstructure and (c) Colony Microstructure

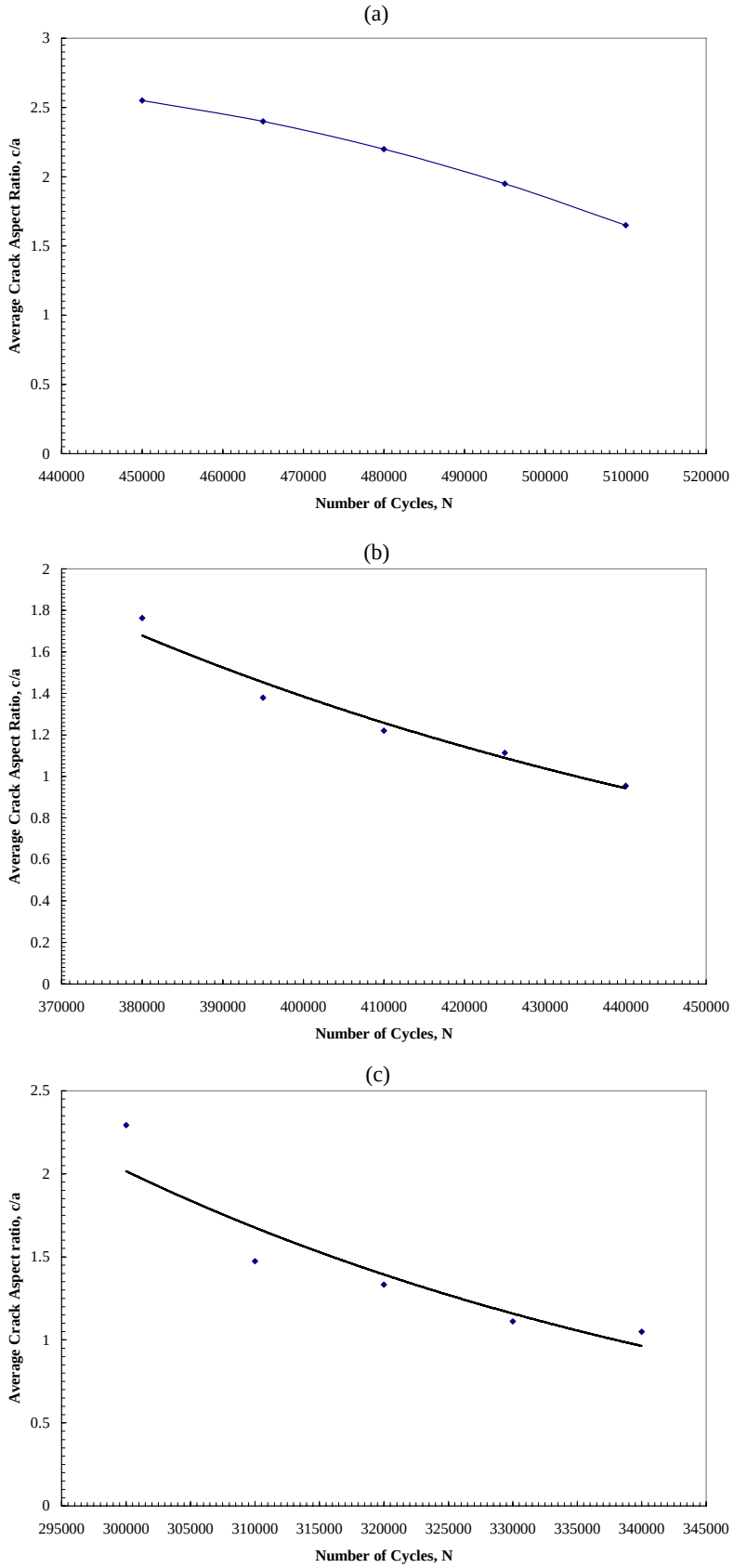

Figure 11 – Average Crack Shape Evolution: (a) Equiaxed Microstructure; (b) Elongated Microstructure and (c) Colony Microstructure

For comparison, the data obtained for through-thickness cracks (Figure 5) are included in Figures 12-14. The surface growth rate data are generally comparable to the through-crack growth rate data in the long crack growth regime. However, the depth crack growth rates are somewhat slower than the through-crack growth rates. The differences may be attributed, at least partly, to the differences in access to the environment (laboratory air) in the crack tips, and differences in the levels of plasticity-induced crack closure at the surface and the depth positions.

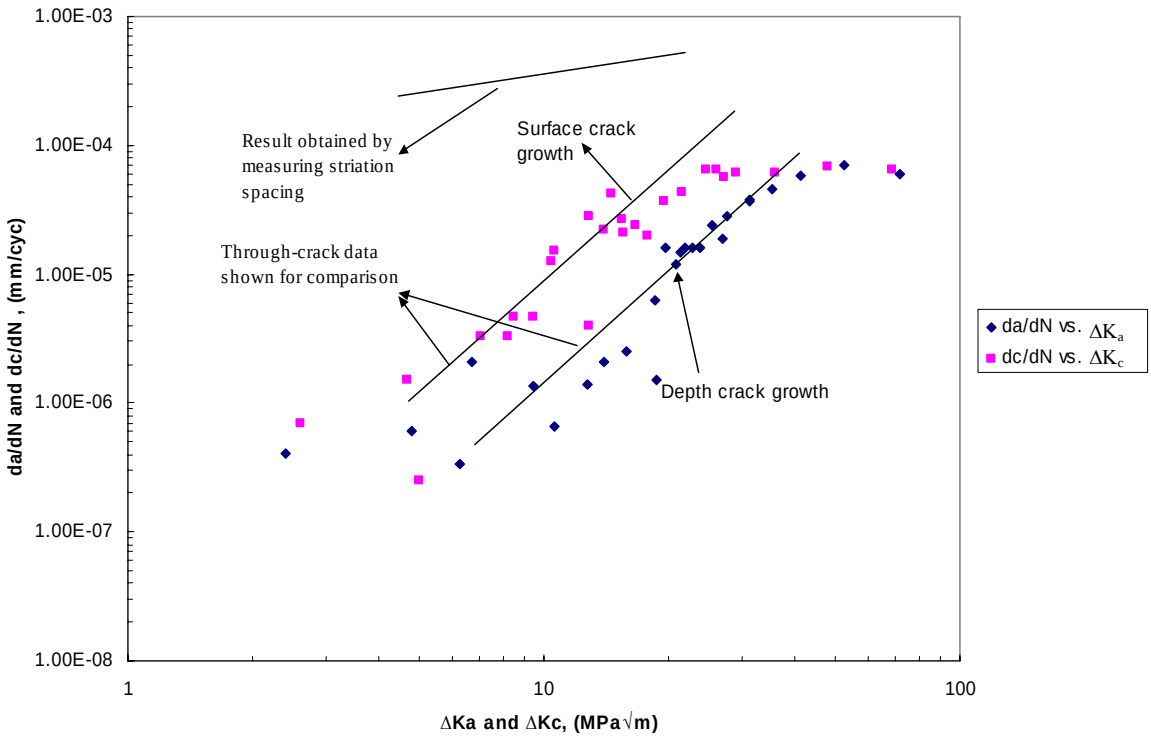

Figure 12 – Comparison of Semi-Elliptical and Through Thickness Crack Growth Rate Data Obtained for Microstructure 1

It is particularly of interest to compare the short and long crack growth rate data in the surface and depth positions. In all the three microstructures, anomalous short crack growth behavior was observed for surface crack lengths or crack depths between 0.4 and 2 microstructural unit sizes (Table 2). This is somewhat lower than prior suggestions by Taylor and Knott [30], who suggest a transition from short to long crack growth at crack lengths that correspond to ~ 5 microstructural units. Before the transition, the significant variations in crack growth rates are attributed to local variations in micro-texture, microstructural/chemical inhomogeneities [7,8,10] and the evolution of a plastic wake that can give rise to plasticity-induced crack closure [26,27,29,30].

Microstructure	Grain/Colony Size, d/μm	Transition Surface Length, c/μm	Transition Depth, a/μm	$\frac{c}{d}$	$\frac{a}{d}$
Equiaxed	22	40	8	1.8	0.36
Elongated	17	20	31	1.2	1.8
Colony	77	15	30	0.2	0.4

Table 2 – Microstructural Unit Sizes and Transitions from Short to Long Crack Growth

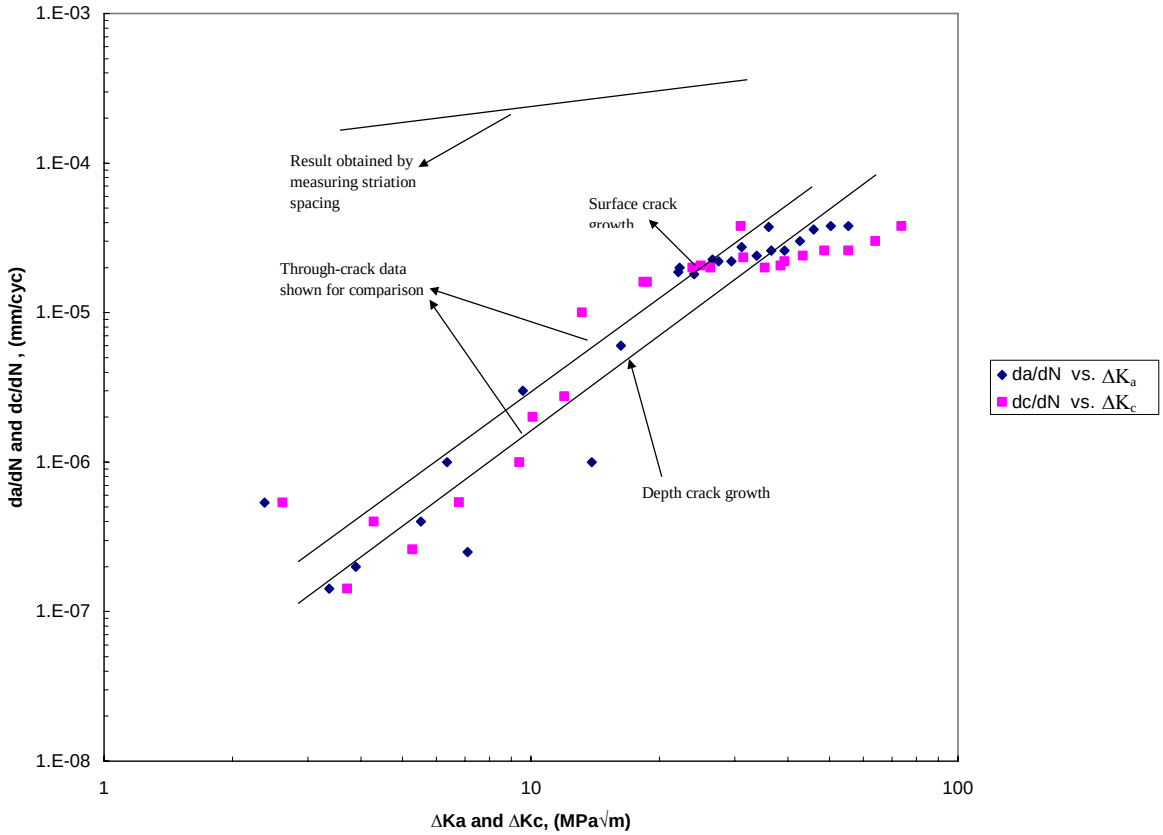

Figure 13 – Comparison of Through-Thickness and Semi-Elliptical Crack Growth Rate Data Obtained for Microstructure 2

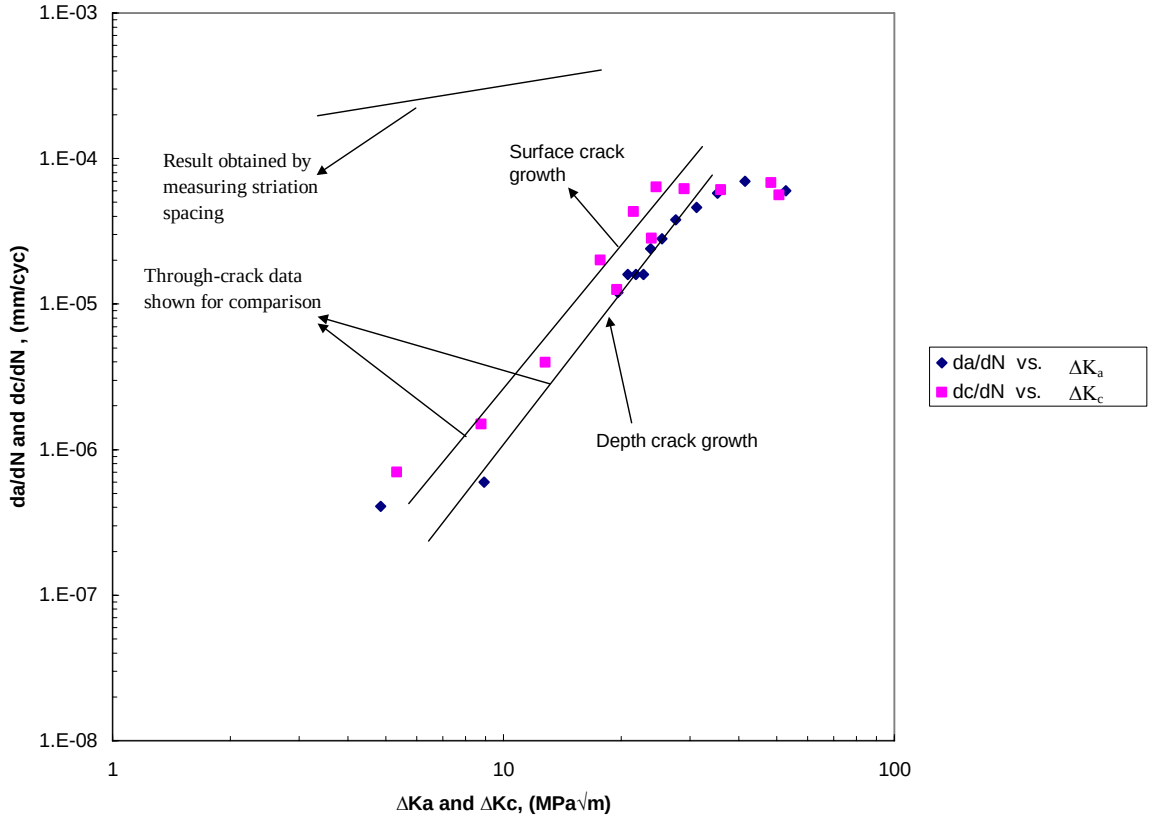

3

Figure 14 – Comparison of Semi-Elliptical and Through-Thickness Fatigue Crack Growth Rate Data Obtained for Microstructure 3

Furthermore, the depth crack growth rates are generally lower than the surface growth rates (Figures 12-14). This is attributed to the possible effects of environment on crack growth along the surface and depth positions. The slower crack growth rates in the depth directions may be explained by the fact that the environment may have limited access to the sub-surface and surface-breaking cracks. In such cases, the depth growth rates may be reduced since fatigue crack growth in air is environmentally-assisted [22,31,32].

(c) Dwell Fatigue of Long Through-Thickness Cracks

The through-thickness dwell-fatigue crack growth rate data obtained for the three microstructures are presented in Figure 15. The plots show the crack growth rate data from stress intensity factor range of around $20MPa\sqrt{m}$. It is shown that crack growth rates are fastest in the elongated structure. The crack growth rates in the equiaxed structure are comparable to those in the elongated structure in the upper Paris regime, and a little smaller than in the high ΔK regime. Furthermore, the colony structure has the best crack growth resistance.

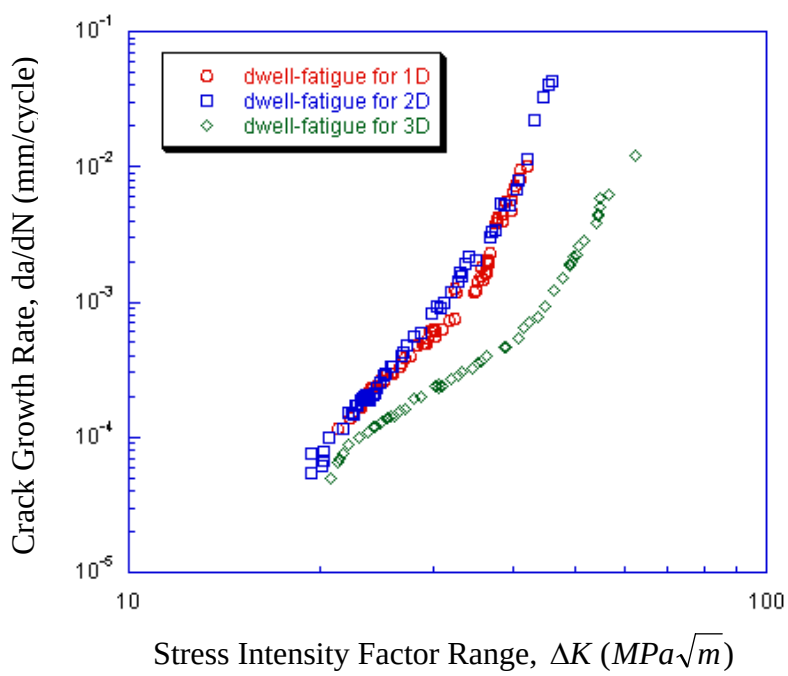

Figure 15 – Comparison of Dwell Crack Growth Rate Data Obtained for Microstructure 1-3

- **Equiaxed Structure**

The dwell-fatigue crack growth data in the equiaxed structure are compared with the normal fatigue crack growth rate data in Figure 16. In this figure, only crack growth data corresponding

to stress intensity factor range, ΔK, larger than $20\,MPa\sqrt{m}$ were collected because of the long test durations (approximately one month per test). It shows that in the upper Paris regime, the fatigue crack growth rates are a little higher than the dwell-fatigue crack growth rates while in the very high ΔK regime, the fatigue crack growth rates are much faster than dwell-fatigue crack growth rates. This is caused by that the instability of fatigue crack growth increases with the stress intensity factor range, ΔK. The final stress intensity factor range, ΔK, at which specimen fractured ($42.2\,MPa\sqrt{m}$) is comparable to its fracture toughness ($47.1\,MPa\sqrt{m}$).

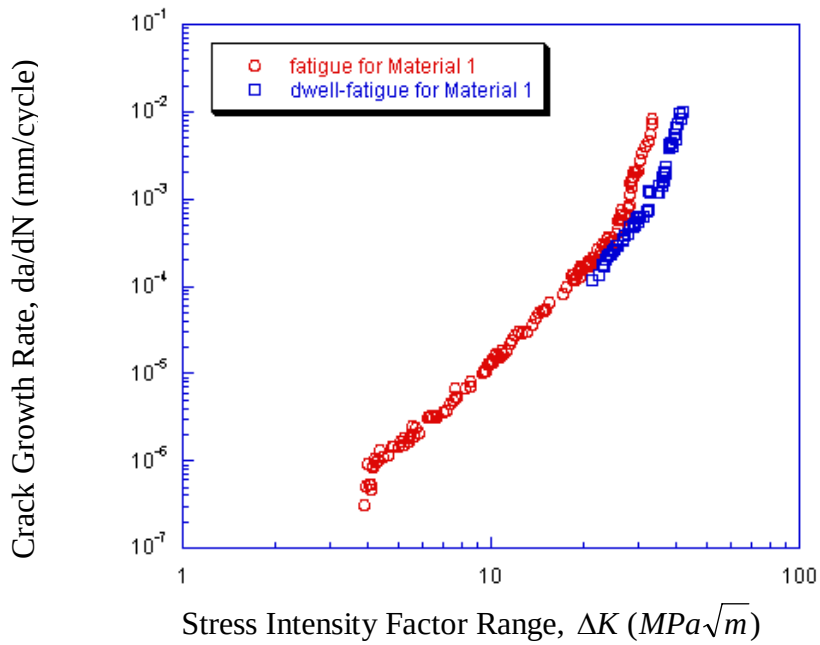

Figure 16 – Comparison of Through-Thickness Fatigue and Dwell Fatigue Crack Growth Rate Data for Microstructure 1

- **Elongated Structure**

The dwell-fatigue crack growth data obtained from the elongated structure are compared with the normal fatigue crack growth data in Figure 17. Due to the long test durations required for the dwell-fatigue tests, only crack growth data corresponding to stress intensity factor ranges, ΔK, larger than $19\,MPa\sqrt{m}$ were obtained. The results suggest that the fatigue and dwell-fatigue crack growth rates based on log-scale are almost comparable (Figure 17), except at the highest ΔK levels where the fatigue crack growth becomes unstable. It is interesting to find that the stress intensity factor range, ΔK, at the moment of specimen failure ($46.23\,MPa\sqrt{m}$) is exactly same as specimen fracture toughness ($46.2\,MPa\sqrt{m}$).

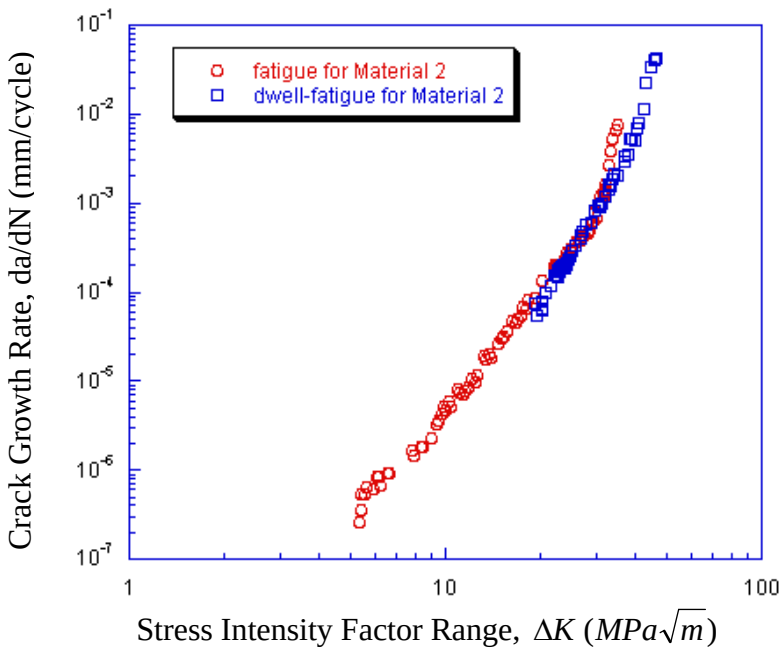

Figure 17 – Comparison of Through-Thickness and Dwell Fatigue Crack Growth Rate Data for Microstructure 2

- **Colony Structure**

The dwell-fatigue crack growth data obtained from the colony structure are compared with the normal fatigue crack growth data in Figure 18. In this figure, only crack growth data corresponding to stress intensity factor range, ΔK, larger than $20\,MPa\sqrt{m}$ were collected. It shows that in the upper Paris regime and the high ΔK regime, the fatigue and dwell-fatigue crack growth rates are comparable based on log-scale (Figure 18). The deviation of fatigue crack growth rates at around stress intensity factor range of 35 $MPa\sqrt{m}$ was most probably caused by some unexpected experimental factors. The final stress intensity factor range, ΔK ($62.2\,MPa\sqrt{m}$), at which specimen fractured is comparable to the fracture toughness ($56.2\,MPa\sqrt{m}$).

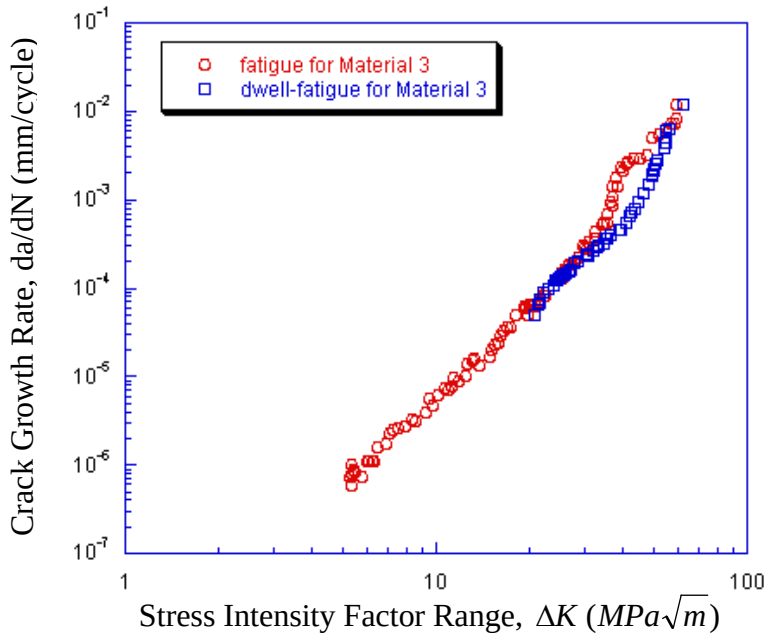

Figure 18 – Comparison of Through-Thickness and Dwell Fatigue Crack Growth Rate Data for Microstructure 3

6.3 Fracture Modes

- **Equiaxed Structure**

The fracture surfaces of the failed specimens were examined in SEM. Typical fracture modes are presented in Figure 19. When ΔK is within the range of $20 \sim 30\, MPa\sqrt{m}$, the main fatigue fracture mechanism is striations (Figure 19a and 19b). At higher ΔK levels, fatigue fracture occurs by a combination of striations and ductile dimples (Figure 19c and 19d). The striation spacing increases with ΔK, and is comparable to the crack growth rate.

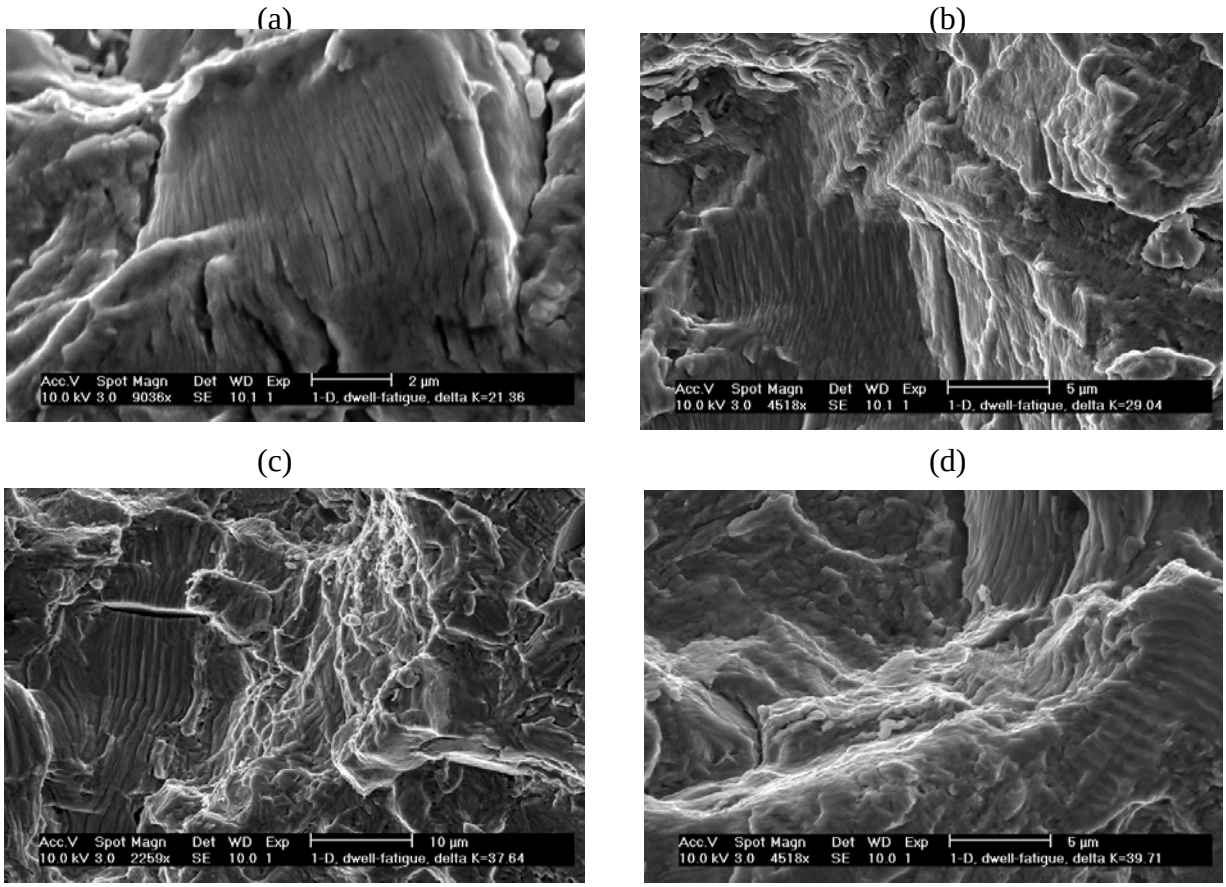

Figure 19 – Through-Thickness Dwell Fatigue Fracture Modes for Microstructure 1: (a,b) Fatigue Striation in Mid-ΔK Regime; (c,d) Ductile Dimples and Fatigue Striations at Higher ΔK Levels

- **Elongated Structure**

The fracture surfaces of the failed specimen were examined in SEM and presented in Figure 20. There are two fracture mechanisms, i.e. cleavage facets (Figure 21a-21d) corresponding to lower ΔK and, void coalescence and ductile dimples (Figure 20e and 20f) corresponding to higher ΔK. At lower ΔK, striations were evident on some facets (Figure 20b) and the facets are comparable in size to primary α grains. Cracks can grow in different directions simultaneously on the same facet (Figure 20b). Decohesion is observed between α grains and β matrix (Figure 20b). Ductile dimples are also observed on the fracture surfaces in the higher ΔK, and then incidence of ductile dimpled fracture increases with increasing ΔK in this regime (Figure 20c-20f). A combination of ductile dimples, fatigue striations and cleavage-like river lines is observed at the highest ΔK levels (Figure 20f).

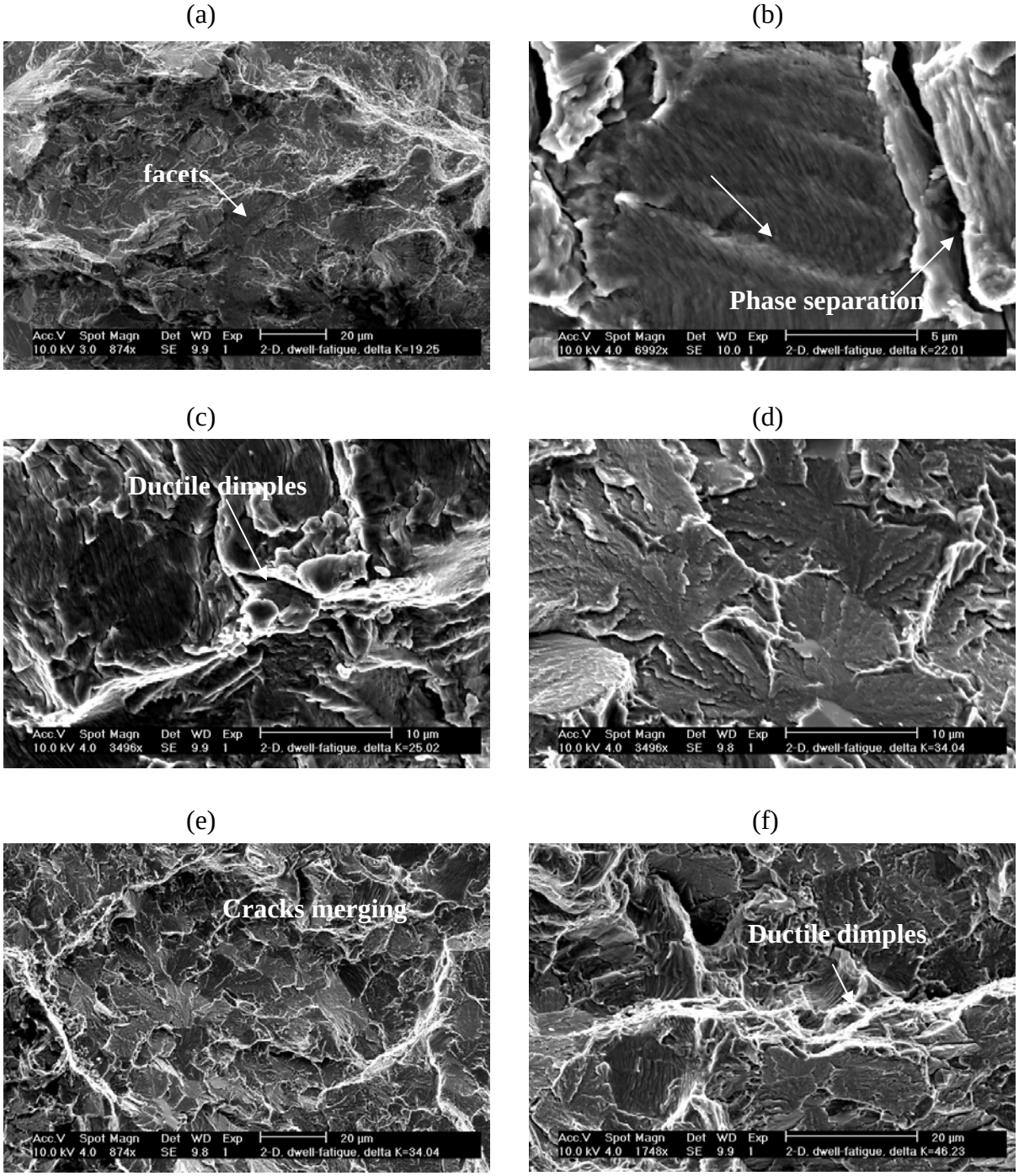

Figure 20 – Through-Thickness Dwell Fracture Modes for Microstructure 2: (a) Cleavage Facets in Near-threshold Regime; (b) Fatigue Striations and Phase Separation; (c) Ductile Dimples and Fatigue Striations at Higher ΔK Levels; (d,e) Cleavage Facets at High ΔK levels; and (f) Cleavage Facets and Ductile Dimples Superimposed on Fatigue Striations.

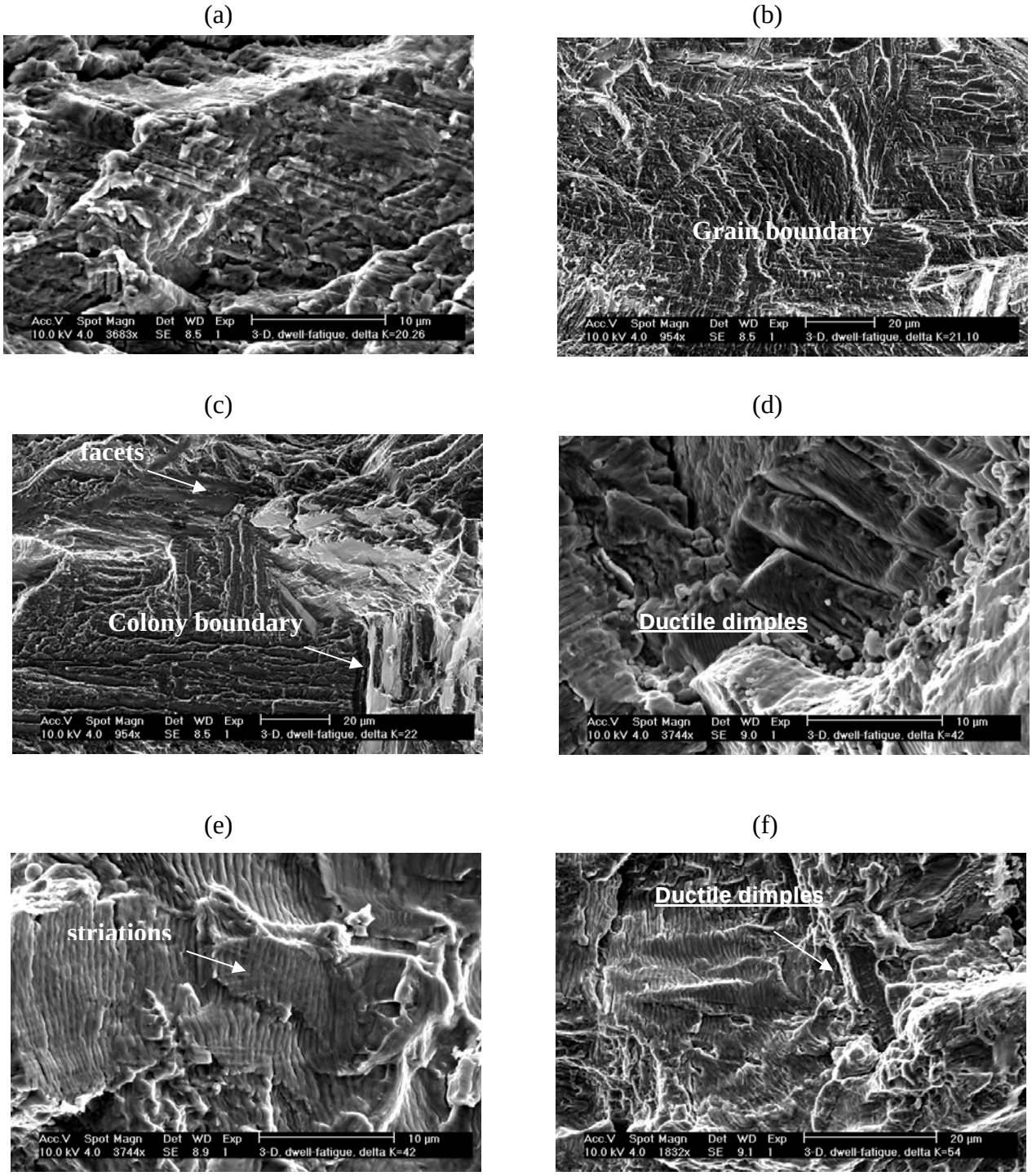

Figure 21 – Through-Thickness Dwell Fracture Modes for Microstructure 3: (a-c) Faceted Fracture Modes in Paris Regime; (d) Secondary Cracks and Striations at Higher ΔKs; (e,f) Fatigue Striations and Ductile Dimples at the Highest ΔK Levels

These mechanisms of dwell-fatigue crack growth are therefore similar to the mechanisms of fatigue crack growth in the elongated structure at the same ΔK levels (Figures 7 and 20). However, in the upper Paris regime, dwell crack growth occurs predominantly by a combination of ductile dimples and fatigue striations, with the incidence of ductile dimpled fracture increasing with increasing ΔK .

- **Colony Structure**

Typical fracture modes observed in the colony structure are presented in Figures 21a-21f. Crystallographic fracture modes were observed in the upper Paris regime (Figure 23a-c). The crack interactions with laths (Figure 21a), colony boundaries (Figure 21c) and grain boundaries (Figure 21b) are apparent. As the stress intensity factor range increases, striations and interfacial separation become evident (Figure 21d and 21e) while colony structures become gradually unclear. Ductile dimples and striations were observed in the high ΔK regime (Figure 21f). It is interesting to note that striation spacing increases with stress intensity factor range from fine to coarse, and are exactly comparable with the corresponding crack growth rate (Figure 15).

(d) Dwell Fatigue Crack Nucleation and Growth

The dwell fatigue fracture modes (Figures 22-24) were similar to the normal fatigue fracture modes (Figures 6-8). As in the case of normal fatigue, sub-surface crack nucleation was generally observed under dwell fatigue loading (Figures 6a and 8a). Furthermore, sub-surface crack nucleation was generally observed to occur at distances of ~ 2-8 microstructural units from the surface (Table 3). This suggests that dwell fatigue crack nucleation occurs by the Stroh-type nucleation mechanism shown schematically in Figure 1.

Microstructure	Microstructural Unit Size/μm	Distance from Surface (h/μm)	$\frac{h}{d}$
Equiaxed (1)	22	148	6.7
Elongated (2)	17	40	2.3
Colony (3)	77	613	8

Table 3 – Positions of Dwell Fatigue Crack Nucleation Sites: Effects of Microstructure

Similar conclusions have been reached by Evans and Bache [5] in prior work on the dwell fatigue behavior of near α Ti alloys. The onset of sub-surface cleavage is attributed to dislocation pile-up and subsequent dislocation reactions that give rise to sub-surface cleavage fracture. However, it is currently unclear whether the sub-surface nucleation is instantaneous across a grain, or if it occurs by incremental dwell fatigue crack growth processes, i.e. by “cyclic cleavage”. Further work is clearly needed to reveal the processes involved in the earliest stages of sub-surface dwell or fatigue crack growth.

However, the subsequent mechanisms of short and long crack growth are consistent with prior reports of crack growth in α/β titanium alloys [7,8,16-22]. The dwell fatigue fracture modes observed in the smooth hourglass specimens (Figures 22-24) are also similar to those presented earlier for the growth of surface/sub-surface cracks initiation. Hence, in the near-threshold

regime, cleavage-like facets were observed (Figures 22a,b, 23 a,b, and 24 a,b). In the mid/ΔK or Paris regimes, fatigue striations were observed in the equiaxed and elongated microstructures (Figures 22 c,d, 23 c,d and 24 e,f). The striation spacings also increased with increasing ΔK. A combination of fatigue striations and ductile dimples was observed in the high ΔK regime (Figures 22e, 23e and 24e) before final overload failures occurred by ductile dimpled fracture in all three microstructures (Figures 22f, 23f and 24f).

(a)

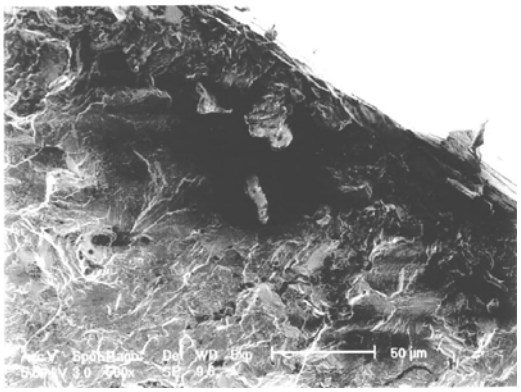

(b)

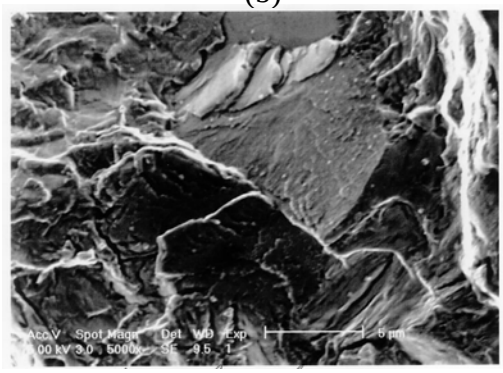

(c)

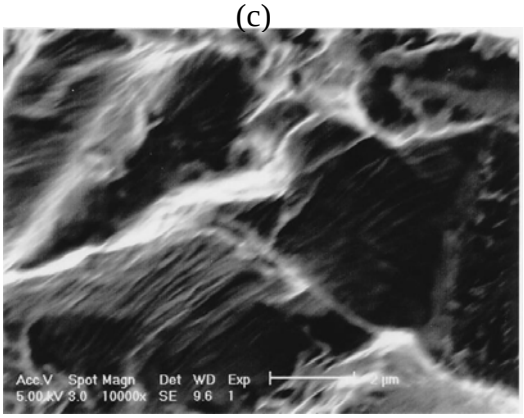

(d)

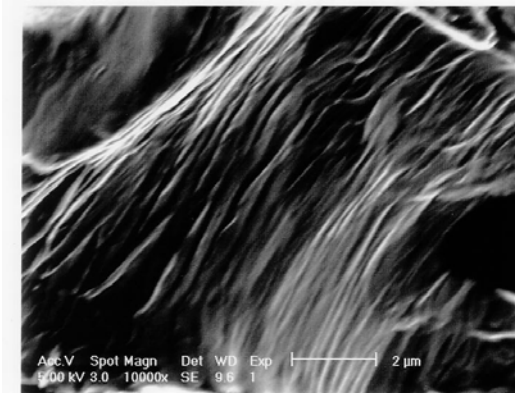

(e)

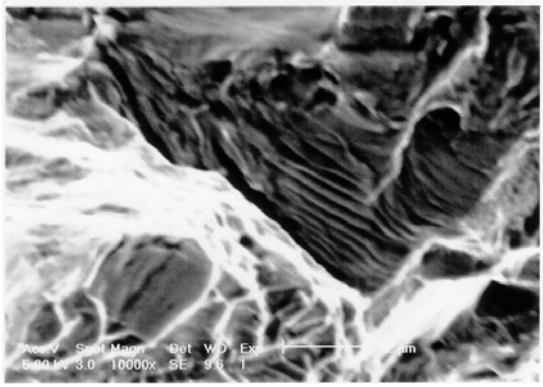

(f)

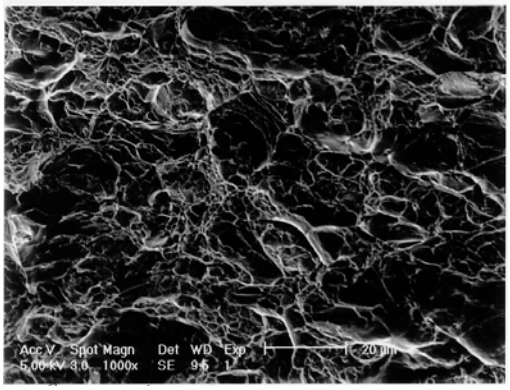

Figure 22 – Typical Dwell Fatigue Fracture Modes in Equiaxed Microstructure 1: (a) Subsurface Crack Nucleation; (b) Crack Growth by Cleavage; (c) Transition from Cleavage to Striation; (d) Fatigue Striation; (e) Fatigue Striation Plus Dimples; (f) Final Fracture

(a)

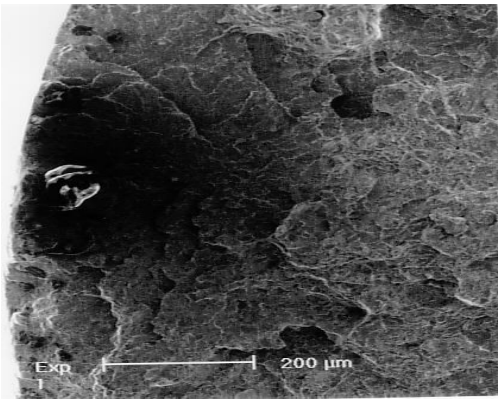

(b)

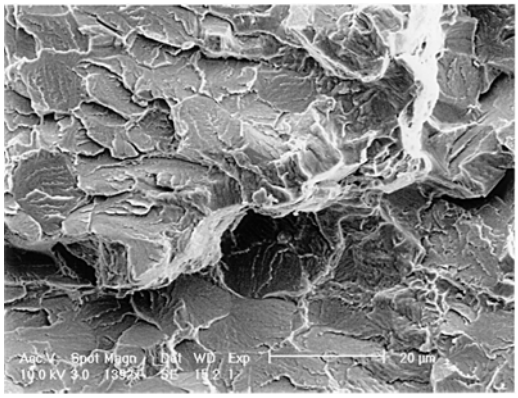

(c)

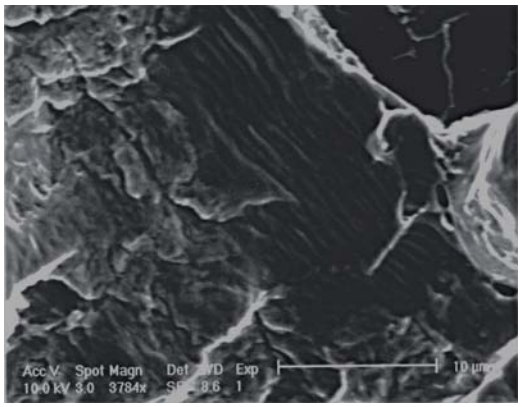

(d)

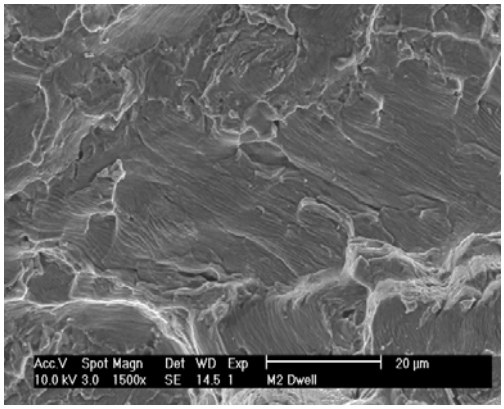

(e)

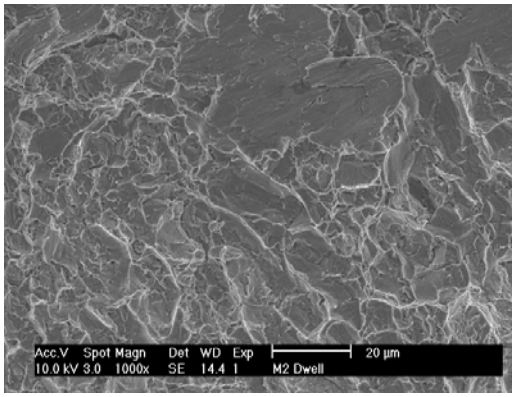

(f)

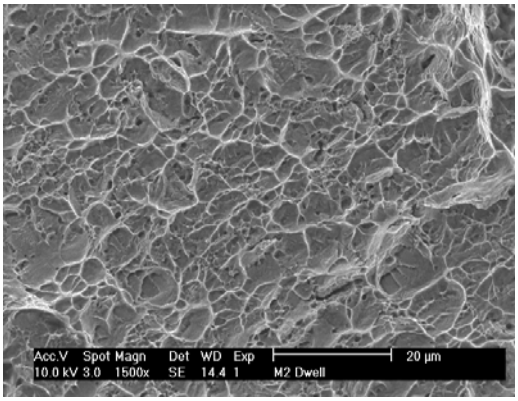

Figure 23: Dwell Fatigue Fracture Modes in Microstructure 2: (a) Sub-surface Crack Nucleation; (b) Crack Growth by Cleavage; (c) Transition from Cleavage to Striation; (d) Fatigue Striations; (e) Fatigue Striation plus Dimples; (f) Final Fracture

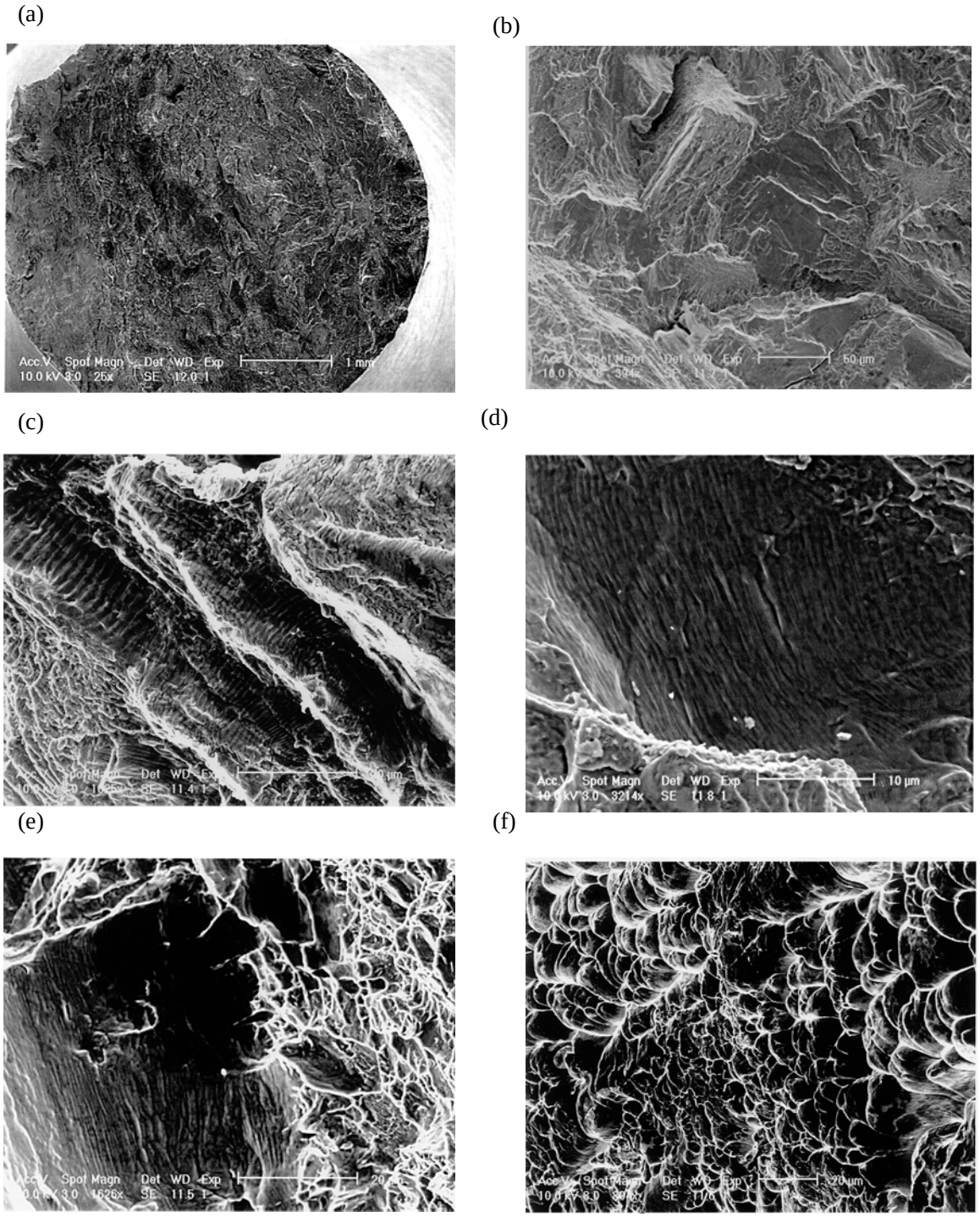

Figure 24: Dwell Fatigue Fracture Modes in Microstructure 3: (a) Sub-surface Crack Nucleation; (b) Crack Growth by Cleavage; (c) Transition from Cleavage to Striation; (d) Fatigue Striations; (e) Fatigue Striation plus Dimples; (f) Final Fracture

The dwell fatigue fracture modes were, therefore, comparable to those described earlier for through-thickness cracks (Figures 19-21) under dwell fatigue loading conditions. They are also comparable to fracture modes presented earlier in Figures 6-8 for surface and depth crack growth under normal fatigue loading. This suggests that the dwell period of 1 minute does not significantly alter the mechanisms of crack growth in the three microstructural conditions (equiaxed, elongated and colony) of Ti-6242 that were examined in this study.

However, unlike the normal fatigue crack growth rate data obtained at cyclic frequency of 10 Hz, the crack growth rate in the dwell specimens corresponded to the striation spacings (Figures 19-24). In contract, the striation spacings on the normal fatigue specimens did not correspond to the measured crack growth rates. This suggest that normal fatigue crack growth at 10 Hz occurs in bursts, while dwell fatigue occurs by cycle-by-cycle fatigue crack growth mechanisms.

(e) Implications

The results obtained from the current study provide some insights that may be used to guide future modeling and experimental efforts. First, the fractographic evidence suggests a cleavage-type crack nucleation mechanism that is somewhat akin to the Stroh-type mechanism (Figure 1)[4-6]. Such crack nucleation phenomena may occur due to dislocation pile-up against obstacles, such as grain boundaries and inclusions. Such dislocation interactions need to be modeled to develop physically-based concepts for the prediction of crack nucleation.

Secondly, the beachmarking profiles provide much needed information on crack shape evolution and surface and depth crack growth rate data (Figures 9-11). However, further work is needed to develop beachmarking methods that will better reveal sub-surface cracking and the earliest stages of crack growth. These may include the use of heat-tinting methods [8]. Nevertheless, the measured crack growth rate data obtained in this study provide an initial basis for the modeling of long crack growth in microstructure 1. In general, the measured crack growth rates may be incorporated into fracture mechanics approaches for the modeling of fatigue crack extension [9,11-13]. These rely on estimates of crack extension, Δa_i, that are given by:

$$\Delta a_i = \int_{a_i}^{a_{i+1}} da = \int_{N_i}^{N_{i+1}} f(\Delta K, R)\, dN \qquad (1)$$

where a is the current crack length, a_i is the initial crack length, a_{i+1} is the crack length after the crack extension, a_i, the function f (ΔK,R) is a function that characterizes the dependence of da/dN on ΔK and R, and N is the number of fatigue cycles.

Various schemes have already been developed to incorporate Equation 1 into the modeling of fatigue crack growth of three-dimensional semi-elliptical/nearly elliptical cracks [11-13]. These rely on: the detailed computation of stress intensity factors around the crack front (using existing stress intensity factor solutions or finite element computations); orthogonal extensions of points

along the crack front by crack length increments given by Equation 1; recharacterization of the crack profile, and repetition of the above sequence to simulate fatigue crack growth.

Quite clearly, the above sequence describes a framework for a fracture mechanics simulation of long fatigue crack growth. Further insights are needed to develop mechanism-based approaches for the prediction of crack nucleation [35] and short crack growth [3,10,36-38].

Conclusions

1. The initial experiments on SENB specimens were used to establish the conditions for beachmarking, as well as the long crack growth rate data for the three microstructures. The experiments revealed bowed through-thickness crack fronts that are consistent with transitions in stress state (from plane stress near the surface to plane strain conditions in the middle of the specimens).

2. The through-thickness fatigue crack growth rate data show that the equiaxed α microstructure (Microstructure 1) has the weakest long fatigue crack growth resistance. The elongated microstructure (Microstructure 2) and the colony microstructure (Microstructure 3) have comparable fatigue crack growth resistance in the near-threshold and Paris regimes. However, the colony microstructure has the best fatigue crack growth resistance in the high-ΔK regime.

3. The stress-life fatigue tests revealed that surface and sub-surface fatigue crack nucleation occurs in the three microstructures. In all cases, sub-surface cleavage facets are associated with the crack nucleation. The initial cleavage facets are ~ 10 μm in diameter, and microstructural unit size away from the surface. Subsequent fatigue crack growth occurs by crack-tip blunting mechanism that gives rise to fatigue striations in microstructures observed before final failure occurs by ductile dimpled fracture in all three microstructures.

4. The beachmarking of the hourglass specimens reveals the evolution of crack profiles in the case of surface-breaking defects. It shows the evolution of crack aspect ratios towards preferred propagation paths (PPPs) in circular cross sections. The aspect ratios along the PPPs are different from those reported previously for square or rectangular cross-sections.

5. A combination of fractography and beachmarking was used to estimate the fatigue crack growth rates of the surface/sub-surface cracks. These show that the surface growth rates are comparable to those of through-thickness cracks in the long crack regime. However, the depth growth rates are slower.

6. Dwell-fatigue crack growth rates are fastest in the elongated structure and slowest in the colony structure. The dwell-fatigue crack growth rates in the equiaxed structure are comparable to that in the elongated structure. The onset of catastrophic failure during dwell crack growth occurs when the final stress intensity factor range, ΔK, is comparable to the measured fracture toughness.

7. The dwell-fatigue crack growth rates are similar to the fatigue crack growth rates at ΔK levels between ~19 and 25 $MPa\sqrt{m}$. However, at higher ΔK levels, the fatigue crack growth rates appear to be somewhat faster than the dwell-fatigue crack growth rates in regions close to the onset of crack growth rate instability in the equiaxed structure and the elongated structure. The fracture modes observed under dwell-fatigue crack growth conditions appear to be similar to those under normal fatigue crack growth conditions. Dwell-fatigue crack growth in the elongated structure and the colony structure occurs by a combination of crystallographic fracture and fatigue striations in the upper Paris regime, and striations together with ductile dimpled fracture in the high ΔK regime.

8. One-minute dwell-fatigue crack growth tests at constant ΔK levels show that: for the equiaxed structure, a one-minute dwell between fatigue cycles increases the crack growth rate at low and mid-ΔK ($\leq 20 MPa\sqrt{m}$). With increasing of ΔK, fatigue crack growth becomes faster and faster until crack growth becomes unstable; for the elongated structure, the dwell effect is less obvious when ΔK is in the low- and middle-ΔK regime ($\leq 20 MPa\sqrt{m}$). With increasing of ΔK, the creep effect plays a significant role in crack growth; for the colony structure, the creep ΔK effect does not become evident until ΔK reaches $30 MPa\sqrt{m}$ and the crack growth ΔK increasing extent is small.

9. The colony structure has the best fatigue and dwell-fatigue creep resistance, the equiaxed structure has lowest fatigue resistance and intermediate dwell-fatigue resistance (fatigue sensitivity), and the elongated structure has the lowest dwell-fatigue resistance and intermediate fatigue resistance (dwell-fatigue sensitivity). The colony structure is most sensitive to the interaction between fatigue and creep while the elongated structure is most sensitive to the time dependent strain accumulation.

References

1. P. Shankar and K.S. Ravichandran, Fatigue of Beta Annealed Ti-10V-2Fe-3Al Alloy: Effects of Aging and Mechanisms of Crack Nucleation, Proc. Fatigue 2002, A.F. Blom, Editor, pp. 1789-1796.

2. S.H. Spence, W.H. Evans and M. Cope, Advances in Fracture Research, Proc. 9th International Conference on Fracture, Pergamon, 1997, pp. 1571.

3. K.S. Ravichandran, S.K. Jha and P.S. Shankar, Fatigue of Beta Titanium Alloys: Crack Initiation, Growth and Fatigue Life, Proc. Fatigue 2002, A.F. Blom, Editor, Vol. 3, EMAS, Warley, Cradley Heath, U.K., pp. 1751-1762.

4. A. N. Stroh, Proc. Roy. Soc. London, 1954, 223, 404.

5. W.J. Evans and M.R. Bache, Int. J. Fatigue, 16, 1994, pp. 443-452.

6. J.F. Knott, Fundamentals of Fracture Mechanics, Butterworth, 1973.

7. J.O. Peters, B.L. Boyce, X. Chen, J.M. McNaney, J.W. Hutchinson and R.O. Ritchie, Eng. Fract. Mech., Vol. 69, 2002, pp. 1425-1446, 2002.

8. M.J. Hicks and A.C. Pickard, Int. J. Fracture, Vol. 20, pp. 91-101, 1982.

9. S. Suresh, Fatigue of Materials, Cambridge University Press, U.K., 1991.

10. V. Sinha and W.O. Soboyejo, 2000, Materials Science and Engineering, Vol. A287, pp. 30-42.

11. W.O. Soboyejo and J.F. Knott, Fat. Fract. Engng. Mater. Struct., Vol. 14, pp. 37-49, 1991.

12. W.O. Soboyejo, K. Kishimoto, R.A. Smith and J.F. Knott, Fat. Fract. Engng. Mater. Struct., Vol. 12, pp. 167-174, 1989.

13. W.O. Soboyejo, R.C. Reed and J. F. Knott, Int. J. Fract., Vol. 44, pp. 27-41, 1990.

14. W.O. Soboyejo and J.F. Knott, Int. J. Fatigue, Vol. 12, pp. 403-407, 1990.

15. J. Zhou and W.O. Soboyejo, Int. J. Fracture, Vol. 115, pp. 287-304, 2002

16. J. Chesnutt, A.W. Thompson and J.C. Williams, 1980, Titanium 80: Science and Technology, AIME, p. 1875.

17. G.R. Yoder, L.A. Cooley and T.W. Crooker, Metall. Trans., 1977, 8A, pp. 1737.

18. G.R. Yoder and D. Eylon, Metall. Trans., 1979, 10A, 1808.

19. K.S. Ravichandran, Acta Metall., 1991, 39, p. 401.

20. S. Shademan, Ph.D. Thesis, The Ohio State University, 2000.

21. V. Sinha, Ph.D. Thesis, The Ohio State University, 1999.

22. S. Suresh, 1985, Fatigue Crack Deflection and Fracture Surface Contact: Micromechanical Models, Metal. Trans., Vol. 16A, p. 249-260.

23. H. Sehitoglu and A.M. Garcia, 1997, Contact of Crack Surfaces During Fatigue, Metal. Trans., Vol. 28A, p. 2263-2289.

24. C.J. Beevers and M.D. Halliday, 1979, Non-closure of Cracks and Fatigue Crack Growth in β Heat-Treated Ti-6Al-4V, International Journal of Fracture, Vol. 15, R27-R30.

25. D.L. Corn, Eng. Fract. Mech., 1971, 3, 45.

26. W.O. Soboyejo and J.F. Knott, Int. J. Fatigue, Vol. 17, pp. 577-581, 1995.

27. M. Jolles and V. Tortoriello, Prof. 15th Symp. On Fracture Mechanics, Editor: R.J. Sanford, ASTM STP 833, ASTM, Philadelphia (1983), pp. 300-311.

28. J.C. Newman and I.S. Raju, Eng. Fract. Mech., Vol. 15, p. 185.

29. N.A. Fleck, I.F.C. Smith and R.A. Smith, Fatigue Eng. Mater. Struct. 1983, 6, 225.

30. D. Taylor and J.F. Knott, Fatigue of Engineering Materials and Structures, Vol. 4, p. 147.

31. W.O. Soboyejo, Mechanical Properties of Engineered Materials, Marcel Dekker Publishers, New York, NY.

32. R.C. McClurg, B.H. Lawless, M. Gorelik, Y. Gill and R.S. Piasak, Fatigue Crack Growth of Titanium Rotor Alloys in Vacuum and Air, the Minerals, Metals and Materials Society, pp. 211-218.

33. S. Shademan and W.O. Soboyejo, Materials Science and Engineering, Vol. A335, pp. 116-127, 2002.

34. C. Mercer, S. Shademan and W.O. Soboyejo, Journal of Materials Science, Vol. 38, pp. 291-305, 2003.

35. J.A. Hall, International Journal of Fatigue, Vol. 19, pp. S23-S37, 1997.

36. R.O. Ritchie, B.L. Boyce, J.P. Campbell, O. Roder, A.W. Thompson, W.W. Milligan, International Journal of Fatigue, Vol. 21, pp. 653-662, 1999.

37. K. Nakajima, K. Terao and T. Miyata, Materials Science and Engineering, Vol. A243, pp. 176-181, 1998.

38. Y.M. Hu, W. Floer, U. Krupp and H.-J. Christ, Materials Science and Engineering, Vol. A278, pp. 170-180, 2000.

Pergamon

Available online at www.sciencedirect.com

SCIENCE DIRECT®

Acta Materialia 51 (2003) 4533–4549

Acta MATERIALIA

www.actamat-journals.com

Deformation and creep modeling in polycrystalline Ti–6Al alloys

Vikas Hasija [a], S. Ghosh [a,*], Michael J. Mills [b], Deepu S. Joseph [a]

[a] *Department of Mechanical Engineering, The Ohio State University, Columbus, OH 43210, USA*
[b] *Department of Materials Science and Engineering, The Ohio State University, Columbus, OH 43210, USA*

Received 6 January 2003; received in revised form 15 May 2003; accepted 22 May 2003

Abstract

This paper develops an experimentally validated computational model for titanium alloys accounting for plastic anisotropy and time-dependent plasticity for analyzing creep and dwell phenomena. A time-dependent crystal plasticity formulation is developed for hcp crystalline structure, with the inclusion of microstructural crystallographic orientation distribution. A multi-variable optimization method is developed to calibrate crystal plasticity parameters from experimental results of single crystals of α-Ti–6Al. Statistically equivalent orientation distributions of orientation imaging microscopy data are used in constructing the polycrystalline aggregate model. The model is used to study global and local response of the polycrystalline model for constant strain rate, creep, dwell and cyclic tests. Effects of stress localization and load shedding with orientation mismatch are also studied for potential crack initiation.
© 2003 Published by Elsevier Ltd on behalf of Acta Materialia Inc.

Keywords: Crystal plasticity; FEM; Titanium alloys; Load shedding; Creep

1. Introduction

Titanium alloys based on the α (hexagonal close packed, hcp) phase are attractive materials for structural applications for several reasons. They have high strength (in the range of 700–1000 MPa), relatively low density, as well as good fracture toughness and corrosion resistance [1]. Alloys such as Ti-6242 and Ti–6Al–4V have found utilization in a number of high performance aerospace applications, as well as in orthopedic, dental and sporting goods applications [2] due to their high specific stiffness and strength. Despite these attractive properties, the performance of Ti alloys is often hindered by time-dependent deformation characteristics at low temperatures, including room temperature [3–7]. This "cold" creep phenomenon occurs at temperatures lower than that at which diffusion-mediated deformation is expected (room temperature is about 15% of the homologous temperature for titanium). Consequently, the creep process is not expected to be associated with diffusion-mediated mechanisms such as dislocation climb. Indeed, TEM study has shown that deformation actually proceeds via dislocation glide,

* Corresponding author. Tel.: +1-614-292-2599; fax: +1-614-292-3163.
E-mail address: ghosh.5@osu.edu (S. Ghosh).

1359-6454/03/$30.00 © 2003 Published by Elsevier Ltd on behalf of Acta Materialia Inc.
doi:10.1016/S1359-6454(03)00289-1

where the dislocations are inhomogeneously distributed into planar arrays. The planarity of slip has been attributed to the effect of short range ordering (SRO) of Ti and Al atoms on the hcp lattice [8]. In addition, significant creep strains can accumulate at applied stresses significantly smaller than the yield strength. Consequently, sufficient caution is exercised in the use of titanium alloys in high performance structural applications where dimensional tolerance is a critical factor. The creep process is of transient kind or "exhaustion" type, i.e. the creep rate decreases continually with time [3–7]. There is some controversy in the literature regarding the stress level below which creep does not occur under ambient conditions. However, creep has been reported to occur at stresses as low as 60% of yield strength [6].

This characteristic has previously been attributed to rate sensitivity effects [9]. However, Ti alloys typically exhibit rate sensitivity values that are not very different from those observed in other metallic alloys that do not display a similar low temperature creep behavior [10]. More recently, it has also been recognized that crack initiation in Ti alloys is associated with grains that have their [0 0 0 1] crystal orientations close to the deformation axis. While a number of sources have been speculated for this effect [11], it appears that local load-shedding between grains of differing orientations has a predominant effect on this behavior.

Plastic deformation in pure Ti and its alloys is known to have considerable dependence on the crystal orientation. These hcp materials exhibit complex modes of deformation on account of their low symmetries. The inelastic deformation by slip in hexagonal materials is highly anisotropic due to difference in deformation resistances in different slip systems of the crystals [12]. For example, single crystals of single-phase α-Ti–6Al are significantly stronger when the deformation axis is oriented parallel to the [0 0 0 1] direction of the crystal [11]. In this orientation, $\langle c + a \rangle$ dislocation slip on pyramidal planes is activated, which exhibits a critical resolved shear strength (CRSS) that is 3–4 times larger than the CRSS for $\langle a \rangle$-type slip on prism or basal planes. Also, the strain hardening exponents of Ti alloys are quite small as a consequence of planar slip [8]. This makes the effect of grain boundaries and interfaces on deformation particularly important. With little intrinsic ability to strain harden, planar slip bands propagate across favorably oriented grains upon initial loading. Large local stress concentrations consequently develop in neighboring grains, which are less-favorably oriented for $\langle a \rangle$-type slip. Local stresses are particularly large when favorably oriented grains are adjacent to grain that is oriented with its $\langle c \rangle$-axis parallel to the macroscopic deformation direction.

The major factors in modeling the deformation process in crystalline material are (i) the external process variables such as stress, strain, strain rate, temperature and (ii) the internal microstructural features such as crystallographic texture, deformation localization and its evolution. In order to optimize or improve the performance of a structural component, a complete understanding of these factors is desired [12]. With a view that deformation in polycrystals is intrinsically inhomogeneous, the present paper is aimed at gaining an understanding of the role of material microstructure on the mechanical behavior of α-Ti–6Al alloys through a combination of modeling and experiments.

Rate-dependent and -independent crystal plasticity models have been extensively developed in literature to predict anisotropy due to crystallographic texture evolution, e.g. in [13–15]. Anand et al. have developed experiment based crystal plasticity computational models for OHFC copper (fcc) [16], aluminum (fcc) [12] and tantalum (bcc) [17], where material parameters are obtained by curve fitting to polycrystalline experimental data and then the predictive capability of the model is evaluated by comparing its predictions for stress–strain curve and texture evolution. Robust computational and experimental effort for titanium (hcp) at high temperatures has also been reported by Balasubramanian and Anand [12,18]. Slip system data for crystal plasticity parameters have been calibrated from single crystal experiments with polysynthetically twinned γ - TiAl + α_2 - Ti_3Al by Grujicic and Batchu [19]. Kad et al. [20] have used these single crystal based parameters to model polycrystalline material behavior.

The goal of the present research is to develop

an experiment-based computational modeling capability which can account for the large strains, material anisotropy and time-dependent nature of plasticity, integral to creep and dwell phenomena. A time-dependent crystal plasticity formulation is employed with the purpose of including microstructural information such as crystallographic texture, which has a major influence on deformation. A multi-variable optimization method is used to calibrate crystal plasticity parameters for basal $\langle a \rangle$, prismatic $\langle a \rangle$ and pyramidal $\langle c + a \rangle$ slip systems, from a limited set of constant strain rate tests of single crystals of α-Ti–6Al (hcp). The polycrystalline model is constructed by constructing equivalent orientation distributions of those measured via electron-backscattered diffraction (EBSD) techniques. Results of the polycrystalline model are then compared with experimentally measured constant strain rate and creep tests for different orientations.

2. Material description and model

The material studied in this work is single-phase α-Ti–6Al which has a hcp crystal structure. The material basis vectors corresponding to the hcp lattice structure are denoted by a set of nonorthogonal base vectors, $\{\mathbf{a}_1, \mathbf{a}_2, \mathbf{a}_3, \mathbf{c}\}$, with the constraint $\mathbf{a}_1 + \mathbf{a}_2 + \mathbf{a}_3 = 0$, as shown in Fig. 1. For computational simplicity, an orthonormal basis $\{\mathbf{e}_1^c, \mathbf{e}_2^c, \mathbf{e}_3^c\}$ can be derived from these crystallographic vectors [12,18]. The hcp crystals consist of five different families of slip systems, namely the basal $\langle a \rangle$, prismatic $\langle a \rangle$, pyramidal $\langle a \rangle$, first order pyramidal $\langle c + a \rangle$ and second order pyramidal $\langle c + a \rangle$ slip systems with a total of 30 possible slip systems, as shown in Fig. 1. For elasticity, a transversely isotropic response with five independent elastic constants is used to model the anisotropy.

The deformation behavior of Ti–6Al is modeled using a rate-dependent, isothermal, elastic–viscoplastic, finite strain, crystal plasticity formulation following the work of Anand et al. [12,16,18,21]. In this model, crystal deformation results from a combination of the elastic stretching and rotation of the crystal lattice and plastic slip on the different slip systems. The stress–strain relation in this model is written in terms of the second Piola–Kirchoff stress ($\mathbf{S} = \det\mathbf{F}^e\mathbf{F}^{e^{-1}}\boldsymbol{\sigma}\mathbf{F}^{e^{-T}}$) and the work conjugate Lagrange Green strain tensor ($\mathbf{E}^e \equiv (1/2)\{\mathbf{F}^{eT}\mathbf{F}^e - \mathbf{I}\}$) as

$$\mathbf{S} = \boldsymbol{C}:\mathbf{E}^e \tag{1}$$

where $\boldsymbol{C}$ is a fourth order anisotropic elasticity tensor, $\boldsymbol{\sigma}$ is the Cauchy stress tensor and $\mathbf{F}^e$ is an elastic deformation gradient defined by the relation

$$\mathbf{F}^e \equiv \mathbf{F}\mathbf{F}^{p^{-1}}, \ \det\mathbf{F}^e > 0 \tag{2}$$

$\mathbf{F}$ and $\mathbf{F}^p$ are the deformation gradient and its plastic component, respectively, with the incompressibility constraint $\det\mathbf{F}^p = 1$. The flow rule governing evolution of plastic deformation is expressed as in terms of the plastic velocity gradient

$$\mathbf{L}^p = \dot{\mathbf{F}}^p\mathbf{F}^{p^{-1}} = \sum_\alpha \dot{\gamma}^\alpha \mathbf{s}_0^\alpha \tag{3}$$

where the Schmidt tensor is expressed as $\mathbf{s}_0^\alpha \equiv \mathbf{m}_0^\alpha \otimes \mathbf{n}_0^\alpha$ in terms of the slip direction ($\mathbf{m}_0^\alpha$) and slip plane normal ($\mathbf{n}_0^\alpha$) in the reference configuration, associated with the αth slip system. The plastic shearing rate $\dot{\gamma}^\alpha$ on the αth slip system is given by the power law relation:

$$\dot{\gamma}^\alpha = \dot{\tilde{\gamma}}\left|\frac{\tau^\alpha}{g^\alpha}\right|^{1/m} \mathrm{sign}(\tau^\alpha), \quad \tau^\alpha \equiv (\mathbf{C}^e:\mathbf{S})\cdot\mathbf{s}_0^\alpha \tag{4}$$

Here $\dot{\tilde{\gamma}}$ is the reference plastic shearing rate, τ^α and g^α are the αth slip system resolved shear stress and the slip system deformation resistance, respectively, m is the material rate sensitivity parameter and $\mathbf{C}^e$ is the elastic stretch. The slip system resistance is taken to evolve as:

$$\dot{g}^\alpha = \sum_{\beta=1}^{nslip} h^{\alpha\beta}|\dot{\gamma}^\beta| = \sum_\beta q^{\alpha\beta}h^\beta|\dot{\gamma}^\beta| \tag{5}$$

where $h^{\alpha\beta}$ corresponds to the strain hardening rate due to self and latent hardening, h^β is self-hardening rate and $q^{\alpha\beta}$ is a matrix describing the latent hardening. The evolution of the self-hardening rate is governed by the relation:

$$h^\beta = h_0^\beta\left|1 - \frac{g^\beta}{g_s^\beta}\right|^r \mathrm{sign}\left(1 - \frac{g^\beta}{g_s^\beta}\right), \quad g_s^\beta = \tilde{g}\left(\frac{\dot{\gamma}^\beta}{\dot{\tilde{\gamma}}}\right)^n \tag{6}$$

where h_0 is the initial hardening rate, g_s^β is the satu-

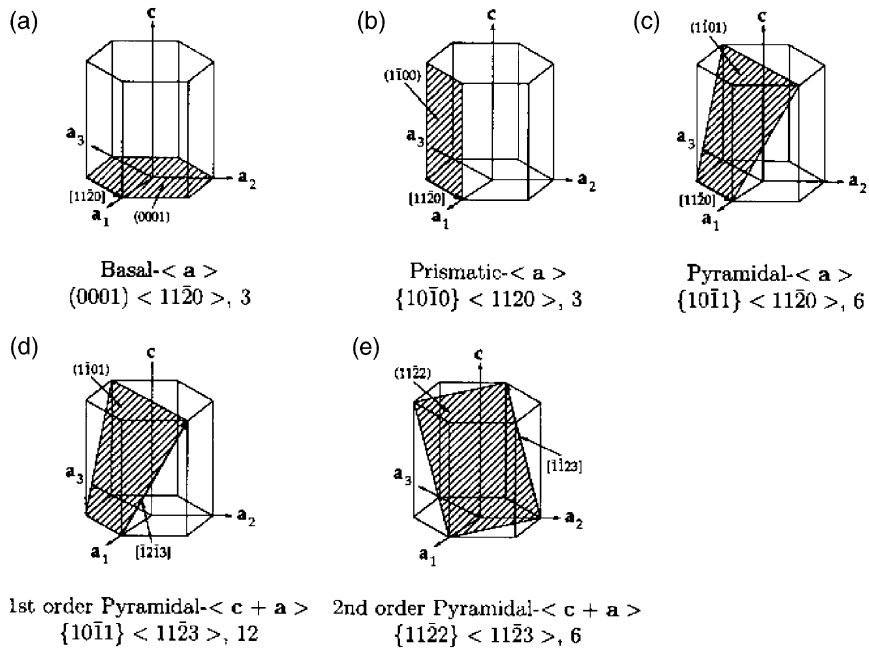

Fig. 1. Schematic showing the nonorthogonal basis $\{\mathbf{a}_1, \mathbf{a}_2, \mathbf{a}_3, \mathbf{c}\}$ and the slip systems in hcp materials.

ration slip deformation resistance, and r, $\tilde{g}$ and n are the slip system hardening parameters. For modeling cyclic deformation, it is important to include kinematic hardening. This has been done by including a backstress in the power law equation (4) as in [22,23]. Consequently, the rate of crystallographic slip on a particular slip system is expressed as:

$$\dot{\gamma}^{(\alpha)} = \dot{\gamma}_0 \left| \frac{\tau^{(\alpha)} - \chi^{(\alpha)}}{g^{(\alpha)}} \right|^{1/m} \operatorname{sgn}(\tau^{(\alpha)} - \chi^{(\alpha)}) \tag{7}$$

where $\chi^{(\alpha)}$ is the backstress on the αth slip system. As in [22,23], an Armstrong–Frederick type nonlinear kinematic hardening rule is chosen for the evolution of backstress as

$$\dot{\chi}^{(\alpha)} = c\dot{\gamma}^{(\alpha)} - d\chi^{(\alpha)}|\dot{\gamma}^{(\alpha)}| \tag{8}$$

Here c and d are the direct hardening and the dynamic recovery coefficients, respectively.

2.1. Time integration and implementation in ABAQUS Standard

An implicit time integration scheme is implemented for integrating the rate-dependent crystal plasticity equations (1)–(8). Various effective implicit schemes have been proposed in literature, e.g. by Kalidindi, Anand and others [16–18], Cuitino and Ortiz [24] using the backward Euler time integration methods. Both of these algorithms are based on the solution of a set of nonlinear algebraic equations in the time interval $t \le \tau \le t + \Delta t$ using Newton Raphson or quasi-Newton solvers. However, the algorithm proposed in [16–18] requires the solution of six equations corresponding to the number of second Piola stress components, while that in [24] solves equations equal to the number of slip systems. Since this is larger than 6 for the hcp systems considered, the integration algorithm proposed in [16–18] is adopted in this paper. The time integration and incremental update routine is incorporated in the user subroutine UMAT. Known deformation variables like deformation gradient $\mathbf{F}(t)$, plastic deformation gradient $\mathbf{F}^p(t)$, backstress $\chi^\alpha(t)$, and the slip system deformation resistance $g^\alpha(t)$ at time t, and the deformation gradient $\mathbf{F}(t + \Delta t)$ at $t + \Delta t$ are passed to the material update routine in UMAT. The integration algorithm in the UMAT subroutine updates stresses, plastic strains and all slip system internal

variables to the end of the time step at $t + \Delta t$. The second Piola–Kirchoff stress is first evaluated in this algorithm by solving the following set of nonlinear equations iteratively:

$$\mathbf{S}(t+\Delta t) - \boldsymbol{C}:\left[\frac{1}{2}\{\mathbf{A}(t+\Delta t)-\mathbf{I}\}\right] = -\sum_{\alpha}\Delta\gamma(t+\Delta t)(\mathbf{S}(t+\Delta t),\ g^{\alpha}(t+\Delta t),\ \chi^{\alpha}(t+\Delta t))\ \boldsymbol{C}:\left[\frac{1}{2}\{\mathbf{A}s_0^{\alpha} + s_0^{\alpha T}\mathbf{A}\}\right] \tag{9}$$

$$g^{\alpha}(t+\Delta t) = g^{\alpha}(t) + \sum_{\beta} h^{\alpha\beta}|\Delta\gamma^{\beta}| \tag{10}$$

and

$$\chi^{\alpha}(t+\Delta t) = \frac{\chi^{\alpha}(t) + c\Delta\gamma^{\alpha}}{1 + d|\Delta\gamma^{\alpha}|} \tag{11}$$

where $\mathbf{A}(t+\Delta t) = \mathbf{F}^{p^{-T}}(t)\mathbf{F}^{T}(t+\Delta t)\mathbf{F}(t+\Delta t)\mathbf{F}^{p^{-1}}(t)$ and $\Delta\gamma^{\beta}$ is the increment of plastic shear on the slip plane β. The solution is executed using a two-step algorithm, in which the stress $\mathbf{S}(t+\Delta t)$, the slip system resistance $g^{\alpha}(t+\Delta t)$ and the backstress $\chi^{\alpha}(t+\Delta t)$ are each updated iteratively, holding the other unchanged during each iterative cycle. After convergence of the nonlinear equation is achieved, the plastic deformation gradient and the Cauchy stress in each integration point of the element are computed using equations

$$\mathbf{F}^{p}(t+\Delta t) = \left\{1 + \sum_{\alpha}\Delta\gamma^{\alpha}\mathbf{s}_0^{\alpha}\right\}\mathbf{F}^{p}(t) \tag{12}$$

and

$$\boldsymbol{\sigma}(t+\Delta t) = \frac{1}{\det\mathbf{F}(t+\Delta t)}\mathbf{F}(t+\Delta t)\ \mathbf{F}^{p^{-1}}(t+\Delta t)\ \mathbf{S}(t+\Delta t)\ \mathbf{F}^{p^{-T}}(t+\Delta t)\ \mathbf{F}^{T}(t+\Delta t) \tag{13}$$

These are then passed on to the ABAQUS main program [25] for equilibrium calculations. In addition, the Jacobian or tangent stiffness matrix given as $W_{ijkl} = \partial\sigma_{ij}/\partial\varepsilon_{kl}$ is computed in UMAT as well and returned to ABAQUS. Details of this tensor are presented in [12]. In this paper, 3D eight-noded brick elements with reduced integration (C3D8R) are used for all the simulations.

3. Mechanical tests with single and polycrystalline Ti–6Al

The computational models in this work are both calibrated and validated using results of mechanical tests, conducted with samples of single-phase α-Ti–6Al. The nominal composition of the alloy, provided by Duriron Co., is given in Table 1. The single crystals of Ti–6Al were grown utilizing a vertical float zone technique in a Crystalox furnace at Air Force Research Labs in Wright Patterson Air Force Base. In this process, crystal growth of 12 mm rods was performed in an inert Ar atmosphere (3–4 psi) to reduce contamination. A molten zone (approximately 12 mm high) was created in the rods using inductive R.F. heating and was held at approximately 15–25 °C above the melting temperature utilizing an optical pyrometer for temperature measurement. The molten zone was then translated along the sample's longitudinal axis by pulling the rod through the RF heating coils using stepper motors for accurate control at a rate of 2.16 mm/h. Successfully grown crystals ranged in size from 5 to 25 mm. Compression samples of size 4 mm × 4 mm × 12 mm were machined with all surfaces ground to 600 grit. Prior to mechanical testing, the samples were all subjected to a conventional heat treatment schedule to produce a known SRO state of Ti and Al atoms [8]. The samples were encapsulated in quartz glass tubes that had been evacuated to 10^{-6} torr and backfilled with 99.995% Ar gas. The samples were then heat treated at 900 °C for 24 h and air-cooled.

Two types of mechanical tests in a compression cage, viz. uniaxial constant strain rate tests and creep tests are performed for the single crystals and polycrystalline alloys. For polycrystals, the strains are measured using a strain gauge of resolution ~ 5×10^{-6} mm/mm, mounted directly on one sample face. The strain and load data are acquired

Table 1
Nominal chemical composition of as received Ti–6Al material

Alloy	Al (wt%)	Fe (wt%)	O (wt%)	N (wt ppm)	C (wt%)	H (wt%)
Ti–6Al	6.5	0.06	0.08	0.01	0.01	0.003

using a high speed LabView computer-based data acquisition system. The constant strain rate tests are executed in an electro-mechanical, screw-driven Instron 1362 machine, in which the strain rate is controlled using a linear variable displacement transducer (LVDT) mounted on a rod and with a tube extensometer across the compression cage. The strain rate sensitivity is measured from strain rate jump tests. The tests are done for three different rates, viz. 8.4×10^{-4}, 1.5×10^{-4} and 1.68×10^{-5} s^{-1}. On the other hand, a dead-load creep frame is used for the creep tests.

Compression tests are conducted with single crystals, in which samples are each oriented to maximize the resolved shear stress on one of the three $\langle a \rangle$-type slip directions on the prism and basal planes. In addition, tests are conducted with samples for which the [0 0 0 1] axis coincides with the compression direction. The crystallographic orientation is determined in these tests using the Laue back-reflection X-ray techniques. A SiC abrasive saw is used to extract square cross-sectional compression samples of nominal dimensions 3 mm × 3 mm × 8 mm from the single colony rod. The sample faces are ground flat by mounting them in epoxy and hand grinding in a fixture to ensure orthogonal faces, with a final grit size of 1200 (6 μm). Each face is then polished on a vibratory polisher in 1 and 0.25 μm slurries to provide a suitable final surface finish to facilitate slip line analysis after mechanical testing. The constant strain rate compression testing is performed at room temperature using an Instron™ model 1362 mechanical test frame equipped with a compression cage. All tests are performed at a constant strain rate of 1×10^{-4} s^{-1} to a total of 5% nominal plastic strain. An LVDT coupled to the compression platens via a rigid rod and tube assembly provides displacement data and strain rate control feedback to ensure an accurate and constant strain rate. All strain measurements from constant strain rate testing reported are made from the LVDT system.

4. Determination of material parameters from experiments

Systematically calibrated material parameters from experimental results are critical to the meaningful simulation of deformation processes of crystalline materials. Important material parameters include anisotropic elastic constants and crystal plasticity parameters for individual slip systems in each crystal. For calibration purposes, constant strain rate uniaxial compression tests at a rate of 1.0×10^{-4} s^{-1} are conducted with single crystal α-Ti–6Al alloys. Three experiments are set up for maximum slip system activity (Schmid factor of 0.5) along the basal $\langle a \rangle$, prismatic $\langle a \rangle$ and pyramidal $\langle c + a \rangle$ slip systems, respectively. The computational model for the single crystal Ti–6Al is developed with ABAQUS Standard [25], in which a rectangular block of dimensions 1×1×5 is meshed into 2000 eight-noded brick elements with reduced integration and hourglass control (element C3D8R in ABAQUS Standard). The elastic–plastic constitutive relation for finite deformation is incorporated in ABAQUS with the UMAT user interface. A velocity field corresponding to the compressive strain is applied on the top surface, and nodes on the boundary are constrained to suppress all rigid body modes of the block.

The elastic constants are calibrated by comparing the slope of the experimental stress–strain curve in the constant strain rate test for single crystals with that obtained from the finite element simulations. The material coordinate system is defined by orthonormal basis $\{\mathbf{e}_1^c, \mathbf{e}_2^c, \mathbf{e}_3^c\}$, where the 1, 2, 3 directions are aligned with the $[\bar{1}\,2\,\bar{1}\,0]$, $[\bar{1}\,0\,1\,0]$ and [0 0 0 1] directions of the hcp crystal lattice, respectively. In this system, the components of the elastic stiffness tensor $\boldsymbol{C}_{\alpha\beta}$ (α = 1,…,6, β = 1,…,6) for a transversely isotropic material are determined from the experimental observations to be: $\boldsymbol{C}_{11} = \boldsymbol{C}_{22} = 136.0$ GPa, $\boldsymbol{C}_{12} = 78$ GPa, $\boldsymbol{C}_{13} = \boldsymbol{C}_{23} = 68$ GPa, $\boldsymbol{C}_{33} = 163$ GPa, $\boldsymbol{C}_{44} = 29$ GPa, $\boldsymbol{C}_{55} = \boldsymbol{C}_{66} = 40.0$ GPa and all other $\boldsymbol{C}_{\alpha\beta}$'s = 0. The stiffness components also compare well with values obtained by time resolved line focus acoustic microscopy experiments [26].

Determination of the crystal plasticity parameters involves a more complex process due to the number of parameters required to describe the slip system flow rule and shear resistance evolution, and the nonlinearity of these equations. Of the various parameters calibrated using the experimental results are (i) the material rate sensitivity m, (ii)

the reference plastic shearing rate $\dot{\tilde{\gamma}}$, (iii) the initial slip system deformation resistance g_0^α, (iv) the initial hardening rate h_0 and (v) various shear resistance evolution related parameters r, $\tilde{g}$ and n. A continuous function optimization method is deployed to minimize the difference between experiments and model predictions for the set of design variables, defined as $\mathbf{\Phi}_{\mathrm{DV}}(m,\dot{\tilde{\gamma}},g_0^\alpha,h_0,r,\tilde{g},n)$.

Material parameter calibration is conducted in two stages. In the first stage, a sensitivity analysis of key response variables with respect to $\mathbf{\Phi}_{\mathrm{DV}}(m,\dot{\tilde{\gamma}},g_0^\alpha,h_0,r,\tilde{g},n)$ is conducted to determine which parameters affect the response significantly. The key response variables are considered to be the proportional limit (σ_{p}), initial macroscopic yield strength (σ_{y}), and the post yield slope ($\boldsymbol{H}$) in the stress–strain curve. Table 2 depicts the result of the sensitivity analysis for the three different slip systems considered. For the basal and prismatic $\langle a\rangle$ systems, higher sensitivity is observed with respect to m, $\dot{\tilde{\gamma}}$, g_0^α, h_0 and r. For the pyramidal $\langle c+a\rangle$ systems, higher sensitivity is observed with respect to m, $\dot{\tilde{\gamma}}$ and g_0^α. Higher sensitivity is associated with a higher order representation in the minimization.

The second step in the calibration process is associated with the minimization of a suitably chosen objective function with respect to the design variables to obtain parameters for the crystal plasticity constitutive equations for the different hcp slip systems. The objective function is chosen as

$$\boldsymbol{OF} = \sum_{i=1}^{3} w_i \left(\frac{S_i^{\mathrm{experimental}} - S_i^{\mathrm{simulation}}}{S_i^{\mathrm{simulation}}} \right) \tag{14}$$

where S_1, S_2 and S_3 correspond to the macroscopic key variables σ_{p}, σ_{y} and $\boldsymbol{H}$, respectively, and w_i are the corresponding weights. Equal weights are assigned in this work. Since a direct function dependence of the objective function on the constitutive parameters is not obvious, computational simulations are used to formulate a systematic procedure for the minimization process. For each slip system, i.e. for basal $\langle a\rangle$, prismatic $\langle a\rangle$ and pyramidal $\langle c+a\rangle$ systems, the major steps involved in this process are as given in [27].

1. An initial guess for the set $\mathbf{\Phi}_{\mathrm{DV}}$ is made from a physically reasonable and expected range of parameters. A complete finite element simulation of the constant strain rate compression test is done with each set of constitutive parameters using ABAQUS Standard.
2. The key variables S_i (i = 1, 2, 3) are each represented as polynomial functions of the constitutive parameters for each slip system as shown in Eq. (15). This procedure provides a continuous function representation of the key variables, necessary for gradient-based optimization.

Table 2
Sensitivity of different slip systems with reference to design variables

Design variables changed	Key response variable (angle)					
	Basal $\langle a\rangle$ slip system		Prismatic $\langle a\rangle$ slip system		Pyramidal $\langle c+a\rangle$ slip system	
	Yield strength	Post yield slope	Yield strength	Post yield slope	Yield strength	Post yield slope
$\dot{\tilde{\gamma}}$	0.0	89.9997	89.9994	0.0	89.9996	0.0
m	0.0	89.9994	89.9530	0.0	89.9777	0.0
g_0^α	0.0	89.6878	54.2873	0.0	40.3645	0.0
h_0	0.0	86.4258	0.0	85.2272	0.0	0.0
r	0.0	89.9791	0.0	89.8861	0.0	0.0
n	0.0	0.0	0.0	0.0	0.0	0.0
$\tilde{g}$	0.0	0.0	0.0	0.0	0.0	0.0

$$S_i = (a_{i0} + a_{i1}m + a_{i2}m^2) \times (b_{i0} + b_{i1}\dot{\tilde{\gamma}} + b_{i2}\dot{\tilde{\gamma}}^2) \times (c_{i0} + c_{i1}g_0^{\alpha} + c_{i2}g_0^{\alpha 2}) \times (d_{i0} + d_{i1}h_0 + d_{i2}h_0^2) \times (e_{i0} + e_{i1}r + e_{i2}r^2) \times (f_{i0} + f_{i1}n) \times (g_{i0} + g_{i1}\tilde{g}) \quad (15)$$

3. Approximately 150 ABAQUS simulations with different parameters sets are conducted to evaluate the coefficients of the polynomial expansion. The computed values of S_i (i = 1, 2, 3) are recorded from the stress strain plots for each simulation. The coefficients are evaluated by a least square method using MATLAB [28]. Using these coefficients, the functions S_i (i = 1, 2, 3) can be constructed.
4. The crystal plasticity constitutive parameters are finally obtained by minimizing the objective function stated in Eq. (14), stated as

$$\text{Minimize} \quad \boldsymbol{OF} \qquad \text{wrt} \quad \boldsymbol{\Phi}_{\mathrm{DV}} \quad (16)$$

The corresponding calibrated parameters for the three different slip systems are shown in Table 3. Stress–strain plots, comparing the experimental and computational results with the calibrated parameters, are shown for the three slip systems in Fig. 2.

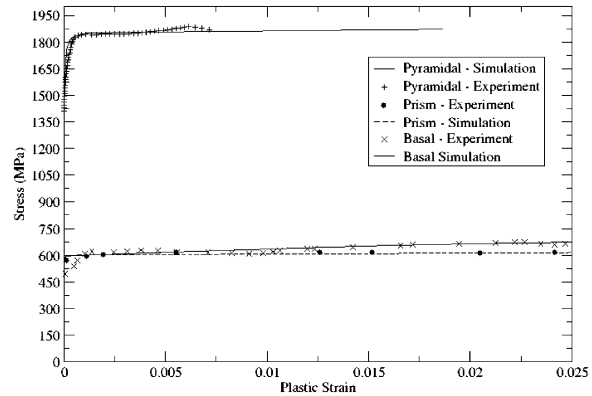

Fig. 2. Experimental [35] and calibrated curves for basal ⟨a⟩, prismatic ⟨a⟩ and pyramidal ⟨$c + a$⟩ slip systems.

5. Orientation assignment to the finite element mesh

Each grain in the polycrystalline aggregate of α-Ti–6Al is considered to be an element in the finite element model. Since deformation and creep response of α-Ti–6Al is observed to be highly sensitive to the overall texture, it is important to assign appropriate crystallographic orientation to the elements prior to FE simulation. For physically meaningful simulations, crystallographic orientations that are statistically equivalent to those obtained from orientation imaging microscopy (OIM) techniques, involving EBSD in scanning electron microscopy, are assigned to the FE model. The orientation probability assignment method discussed in [29,30] is used for this purpose.

In this method, crystallographic orientations, represented by Euler angles, are first generated from transformed pole figures, in which points in discretized regions of the projected plane are extracted from contour plots of the pole figures in X-ray diffraction analysis. This process generally generates a large number of Euler angles that are considerably in excess of the orientations assignable to the finite element model. For example, a

Table 3
Calibrated parameters for basal ⟨a⟩, prismatic ⟨a⟩ and pyramidal ⟨$c + a$⟩ slip systems

Parameters	Basal ⟨a⟩ slip system	Prismatic ⟨a⟩ slip system	Pyramidal ⟨$c + a$⟩ slip system
m	0.02	0.02	0.02
g_0 (MPa)	322	320	846
$\tilde{\gamma}$ (s^{-1})	0.0023	0.0023	0.0023
h_0	100.0	100.0	350.0
r	0.5	0.5	0.55
n	0.14	0.1	0.1
$\tilde{g}$ (MPa)	450.0	550.0	1650.0

total of 19 620 discrete orientations are obtained from the experimental pole figure in Fig. 3. The finite element model in ABAQUS for a polycrystalline model is assumed to contain 512 grains with a total of eight elements per grain. Since the number of grains is far less than the number of orientations, statistically equivalent orientations with similar probability density distributions $f(g)$ of the crystallographic orientations are assigned to the finite element mesh. The steps in this process are:

(i) An Euler angle space, in which the three coordinate axes are represented by three Euler angles (ϕ_1,ϕ,ϕ_2), is discretized into n cubic orientation space elements and the discrete orientation data are recorded.

(ii) From the definition of probability density function, $f(g)\mathrm{d}g = \mathrm{d}V_g/V$ is the probability of observing an orientation G in the interval $g \leq G \leq g + \mathrm{d}g$, where $\mathrm{d}V_g$ is the volume of crystals with the orientation between g and $\mathrm{d}g$ and V is the total volume of all grains. Therefore, the volume fraction of crystal orientations in the ith orientation space element ranging in coordinate space from (ϕ_1,ϕ,ϕ_2) to $((\phi_1 + \mathrm{d}\phi_1,\phi + \mathrm{d}\phi,\phi_2 + \mathrm{d}\phi_2))$ is determined as

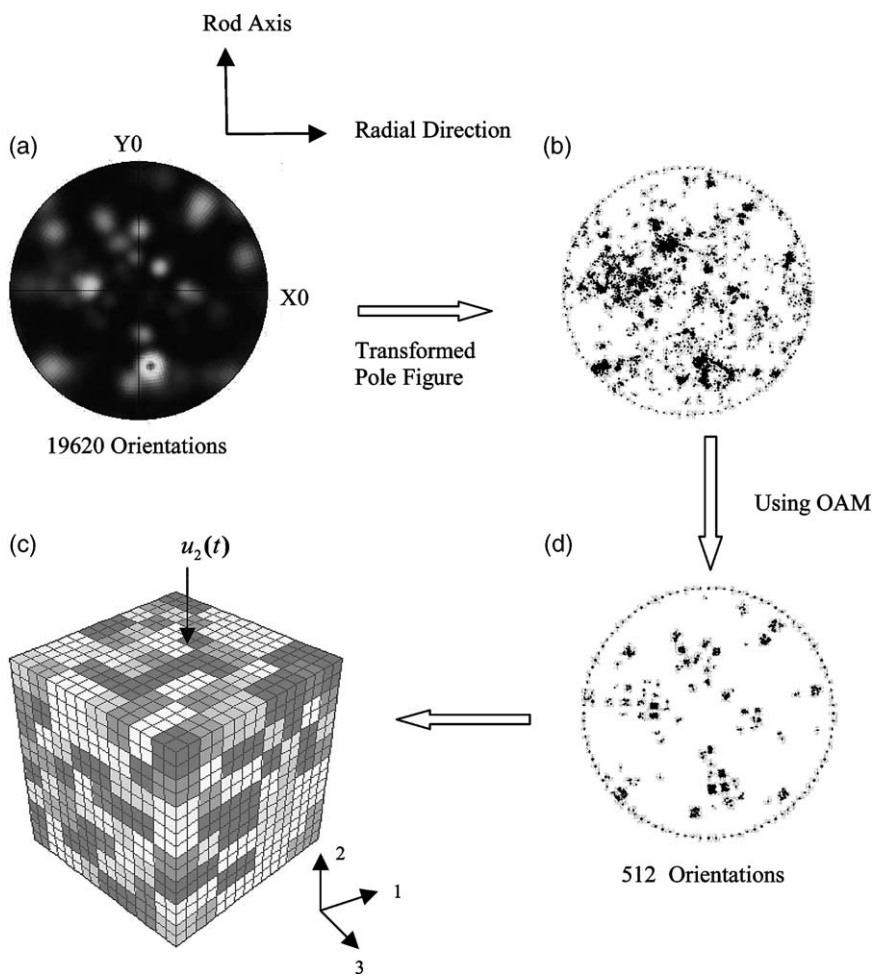

Fig. 3. (a) Contour plot of the experimental (0 0 0 1) pole figure. (b) Transformed experimental pole figure [35] from contour plot to points in the discretized regions of the projected plane. (c) Statistically equivalent orientations obtained from the orientation assignment method, put into the finite element model. (d) Orientation distribution for the FEM simulations of polycrystalline Ti–6Al.

$$V_f^{(i)} = \frac{V^{(i)}}{V} = \int_{\phi_2}^{\phi_2 + d\phi_2} \int_{\phi}^{\phi + d\phi} \int_{\phi_1}^{\phi_1 + d\phi_1} \frac{f(g)}{8\pi^2} \sin\phi \, d\phi_1 \, d\phi \, d\phi_2 \tag{17}$$

(iii) An orientation probability factor (P_i) for each orientation space element is obtained as

$$P_i = K \times V_f^{(i)} \tag{18}$$

where K corresponds to a number that is equal to or larger than the number of orientations to be assigned to the finite element mesh. The complete set of statistically equivalent orientations is then given as

$$P = \sum_{i=1}^{n} P_i \tag{19}$$

where P is equal to or larger than the number of grains in the finite element model.

(iv) Q ($\leq P$) sets of Euler angles are randomly selected from the orientation population P and are assigned to the integration points of the different grains. The computational model with this assigned orientation represents a statistically equivalent polycrystalline aggregate.

6. Simulation of deformation and creep in polycrystalline Ti–6Al

The simulations are for two different types of mechanical tests, (i) constant strain rate tests and (ii) creep tests which have been conducted with the polycrystalline Ti–6Al in [10]. As mentioned in Section 3, constant strain rate tests are with strain rates of 8.4×10^{-4}, $1.5\times10^{-4}\text{s}^{-1}$ and 1.68×10^{-5} s^{-1}. From these tests, it has been observed in [10] that the strain rate sensitivity of this material is not very high in comparison with other metallic materials like steel and copper. Additionally, a comparison of the post yield hardening shows that the strain rate has little influence on hardening. The overall hardening in these polycrystalline Ti–6Al alloys is also found to be low. This is attributed to the planar slip due to the presence of SRO of Ti and Al atoms, which reduces the rate of hardening as well as the interaction between the different slip systems. The creep tests are conducted at two different stress levels viz. 606 and 716 MPa. They enable the study of strain accumulation phenomenon, which can be significant with time. Higher creep strains are observed at higher stress levels. The creep strain accumulation follows a power law behavior in time, with monotonically decreasing creep rates.

The finite element model for the polycrystalline aggregate consists of a cubic domain of unit dimensions that is discretized into 4096 eight-noded brick elements (C3D8R) in ABAQUS. A total of 512 grains, for which the crystallographic orientations are assigned using the orientation assignment method of Section 5, are assumed to be contained in this model. The model texture is statistically equivalent to the actual orientation distribution obtained from the OIM results as shown in Fig. 3. Fig. 3d shows the distribution of orientations in the polycrystalline finite element model. To simulate the experimental conditions, no symmetry constraints are imposed in the model. Only the constraints that are necessary to prevent the rigid body modes are applied to the model. The material parameters for both elasticity and crystal plasticity are the same as those for the single crystals that have been calibrated in Section 4.

For simulation of the constant strain rate tests, the strain rate boundary condition is applied using the DISP subroutine in ABAQUS. Consistent with the constant strain rate $\dot{\varepsilon}_c$, a displacement boundary condition is applied on the top face of the cube as

$$u(t) = l_0(\exp(\dot{\varepsilon}_c t) - 1) \tag{20}$$

where l_0 is the initial dimension (=1) of the cube. The average stress–plastic strain response in the direction of the applied displacement (X_2) is plotted in Fig. 4. The average stress ($\bar{\sigma}_{22}$) and average plastic strain ($\bar{\varepsilon}^{\text{p}}_{22}$) are calculated as

$$\frac{\sum_{i=1}^{nel}\sum_{j=1}^{npt}(\sigma_{22}J)_{ij}}{\sum_{i=1}^{nel}\sum_{j=1}^{npt}(J)_{ij}}, \quad \frac{\sum_{i=1}^{nel}\sum_{j=1}^{npt}(\varepsilon^{\text{p}}_{22}J)_{ij}}{\sum_{i=1}^{nel}\sum_{j=1}^{npt}(J)_{ij}} \tag{21}$$

where σ_{22} and $\varepsilon^{\text{p}}_{22}$ are the Cauchy stress and the

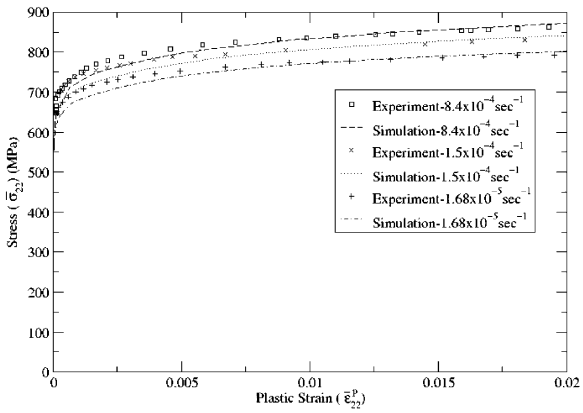

Fig. 4. Constant strain rate test for strain rate = 8.4×10^{-4}, 1.5×10^{-4} and 1.68×10^{-5} s^{-1}.

true plastic strain at each element integration point and J is the determinant of the jacobian matrix at these integration points. The number of elements in the model are designated as *nel*, and *npt* corresponds to the number of integration points per element. These plots in Fig. 4 compare the experimental and the computational results for the different strain rates. The results show a remarkably close match between the experiments and computations for all the three strain rates, even though the material parameters are calibrated with the single crystal tests. It is noted that the orientation plays a significant role in these overall stress–strain plots and corresponding simulations appears to catch the overall behavior rather well. The small discrepancies in Fig. 4 may be attributed to various aspects, such as the orientations and material parameters. The orientation assignment for the 3D models from 2D OIM maps is a potential source of error. Additionally, the crystal plasticity parameters are calibrated using a nonlinear function minimization of the overall material response. The lack of more detailed experiments for better calibration of individual parameters could lead to nonuniqueness in their values. For example, the latent hardening parameter, which is taken to be 1, could benefit from isolating experiments.

For the simulation of creep, the boundary condition is applied in two steps. In the first step, uniform pressure load is applied on the top face using the DLOAD option in which the pressure is ramped from zero to the final value in a interval of 1 s. In the subsequent step, the load is held at the desired level and the material is allowed to creep using the STATIC option in ABAQUS. Average plastic strains as defined in Eq. (21) are plotted as a function of time in Fig. 5. The plots are on a log–log scale and are for the two stress levels, 606 and 716 MPa. Considering the variabilities in the model and the range of time over which the experiments are conducted, the agreement between the experimental and simulated results are found to be quite good. The total strain in the plots is found to follow a power law in time of the form as described in [5–7]:

$$\varepsilon = A\, t^{\alpha}. \tag{22}$$

The experimental and simulated creep constants A

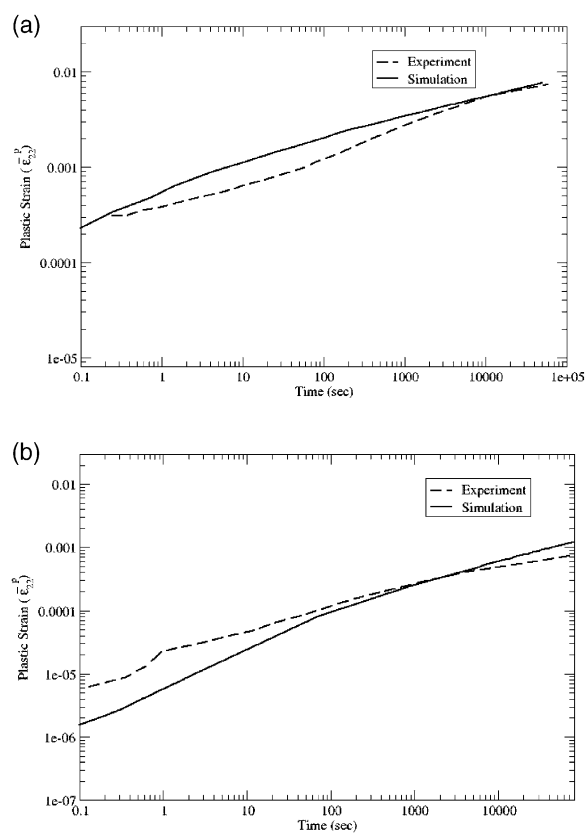

Fig. 5. Log–log plot for creep showing the experimental curve and the simulated curve for stress levels of (a) 716 MPa and (b) 606 MPa.

and a for both stresses are calculated and shown in Table 4. It is observed that the value of the coefficient A depends on the applied stress, with lower creep stresses leading to smaller A values. There is some discrepancy observed in the value of A between the experiments and the simulations for the two stress levels. The time exponent a is seen to compare well between the experiments and the simulations. The fact that the value of the time exponent a is less than unity demonstrates that steady state creep is not observed in these experiments.

7. Creep and cyclic deformation with strength mismatch

7.1. Load shedding with creep

This section discusses a finite element model that is created to reflect the effects of heterogeneity in the crystal structure on the local material response to compressive creep loading. The model consists of two regions that have distinctly different orientations to reflect mismatch in strength characteristics. The first region is constructed as a cube of dimensions 0.2 m × 0.2 m × 0.2 m for which the c-axis in the crystallographic structure is aligned with the global loading axis. The second is a cubic region of external dimensions 1 m × 1 m × 1 m that surrounds the inner cube. The basal plane in the crystallographic structure of this region is parallel to the global loading axis. The crystallographic orientations are depicted by the pole figure in Fig. 6b. It has been observed from the previous calibration exercise that the critical resolved shear stress for the pyramidal $\langle c + a \rangle$ slip systems is about 2.7 times that for the $\langle a \rangle$-type slip systems. Since only the $\langle c + a \rangle$ slip systems will be active in the inner region for the given loading, it represents a region with a considerably higher strength response in comparison with the outside region. The inner cube, as shown in Fig. 6a, is uniformly discretized into a mesh of 512 eight-noded brick elements (C3D8R). The outside region consists of a graded mesh with 4608 eight-noded brick elements, to create more refined elements near the interface. Such resolution is necessary to adequately represent the high gradients in stress and strains. The material properties for elasticity and all the crystallographic slip systems correspond to the calibrated values in Section 4. The model is subjected to a compressive creep loading with a constant applied pressure of 606 MPa held over a period of 1000 s. This loading is applied on the outer face of the model. All other boundaries

Table 4
Creep constants for applied stress of 716 and 606 Mpa

Power law creep constants	Simulation		Experiment	
	716 MPa	606 MPa	716 MPa	606 MPa
A	0.000642	2.26e−05	0.00037	1.84e−05
a	0.26	0.35	0.275	0.36

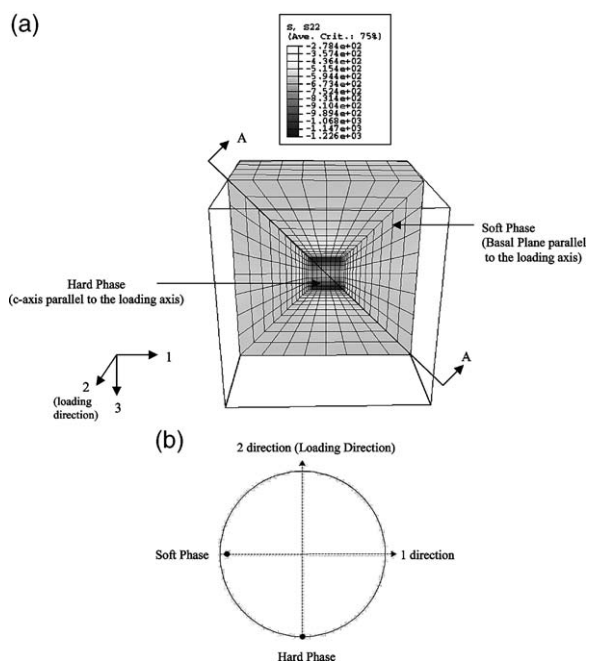

Fig. 6. (a) Contour plot showing the stress concentration around the hard phase for value of rate exponent $m = 0.05$; (b) (0 0 0 1) pole figure showing the orientation of the hard phase and the soft phase.

are free to deform subject to the constraint of rigid body motion. A total of 100 equal time steps are used to simulate the creeping process.

The results of the creep simulation are shown in Figs. 6–8. Fig. 6a shows the contour plot of the dominant stress (σ_{22}) in the loading direction at the end of the creep process. It can be seen from this figure that while the stress is generally uniform in the outer region away from the interface, there are significant gradients near the interface in both phases. The compressive stress just outside the interface dips below the average but rises considerably near the interface in the inner phase. This is further illustrated in the graphs of the evolving stress as a function of location in Fig. 7a. The stress is plotted along the diagonal A–A. Both the minimum peak stress in the lower-strength phase (outer region) and the maximum peak stress in the higher-strength phase (inner region) increase with

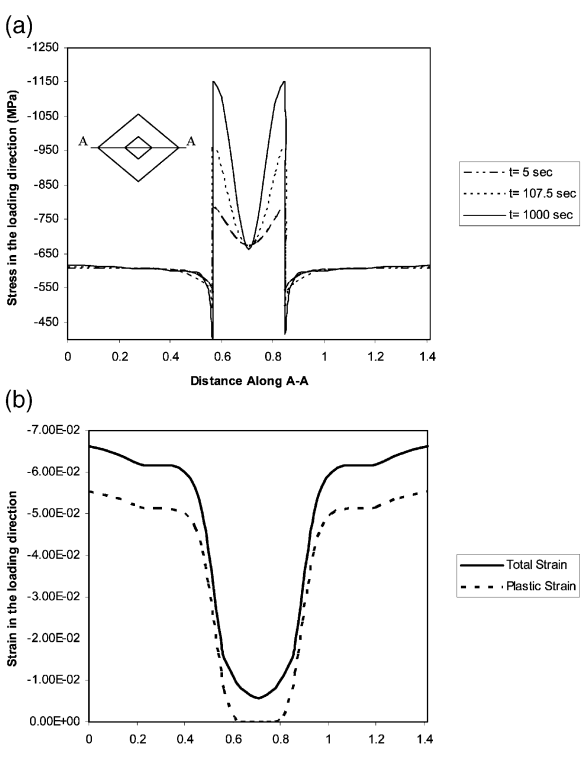

Fig. 7. (a) Evolution of dominant stress (σ_{22}) as a function of time along the line A–A for rate exponent $m = 0.05$ and (b) total strain (ε_{22}) and plastic strain (ε^p_{22}) at the end of the creep process, for rate exponent $m = 0.05$.

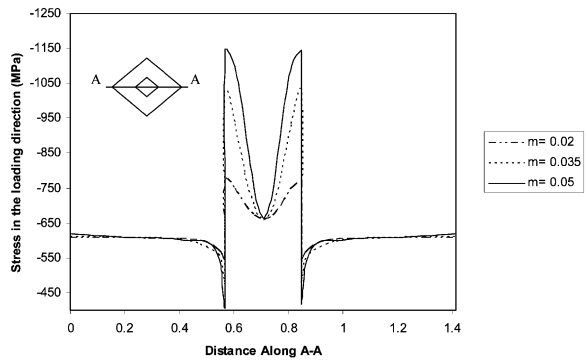

Fig. 8. Stress (σ_{22}) along the line A–A for different values of the strain rate sensitivity exponent, plotted at the end of the creep process.

creep and time. With the onset of plastic deformation in the lower-strength phase, the outer region sees an increase in the total strain due to plastic creep. The compatibility constraint at the interface, however, requires the local strain near the interface to be lower than the rest of the outer region. This causes a drop in the lower-strength phase stress near the interface. Likewise, the compatibility requirement in the high-strength phase causes the strain near the interface to be higher than that away from it. This gives rise to the high stress concentration near the interface. With increasing creep, the strain increases and hence the local stress also increases as a function of time. Fig. 7a, which corresponds to a strain rate exponent $m = 0.05$ clearly shows that the local peak stress rises significantly as a function of time. However for $m = 0.02$, the rise in the peak stress for the same interval is small. This result clearly points to the significant effect of strain rate sensitivity on local peak stress as a function of time. This phenomenon has been termed as load shedding in creeping heterogeneous materials. It is particularly relevant in the context of fatigue crack initiation because the regions of high stress concentration are potential nucleation sites. It is interesting to note that the stress at the center of the stronger phase does not change with increasing creep. This may be explained from the plastic strain plot at the end of the creep process in Fig. 7b. The total logarithmic strain (ln V, V is the left stretch tensor) and the plastic strain ($1/2(\mathbf{F}^{p^T}\mathbf{F}^p-$

I)) are plotted along the diagonal A–A in this figure. For the times considered, the material in a considerably large area around the center of the stronger phase does not yield and hence the strain is entirely elastic and unchanged with creep. The stress behavior follows from its dependence on the elastic strain.

To understand the effect of the material rate sensitivity on the load shedding due to creep, the above simulations are conducted with three different rate sensitive exponents i.e. m = 0.02, 0.035 and 0.05 in Eq. (4). The corresponding stresses (σ_{22}) at the end of the creeping process are plotted along the line A–A in Fig. 8. The effect of load shedding reflected in the stress concentration at the interface reduces considerably with reducing rate exponent. The lower bound of the stress discontinuity will occur for the rate-independent material behavior. It is evident through this example that mismatch interfaces have a high potential of crack nucleation for creeping materials, especially with increasing rate sensitivity.

7.2. Load shedding for various load histories

In this example, the effect of overall load histories on the local evolution of stresses and strains is examined for the polycrystalline material with discrete orientation mismatch. The computational domain consists of a large cubic grain of dimension 0.25 m × 0.25 m × 0.25 m contained in an aggregate of 4032 grains occupying the external cubic domain. The inner grain represents a higher-strength phase with c-axis parallel to the loading axis while the 4032 outside grains have random orientations as shown in Fig. 9. In the finite element model, the inner grain is discretized into a mesh of 64 eight-noded brick elements while each grain in the outer region is modeled using a single eight noded brick element.

Four different overall loading conditions have been considered in this example. They are (a) creep loading with a peak load of 606 MPa, (b) cyclic loading with a peak load of 606 MPa and cycle time of 2 s, (c) dwell cyclic loading with a peak load of 606 MPa and a cycle time of 62 s with 60 s of dwell period and 2 s of unloading and reloading period, (d) dwell cyclic loading with a peak load of 606 MPa and a cycle time of 122 s with 120 s of dwell period and 2 s of unloading and reloading period. All the cyclic loading cases are run with a stress ratio of 0. The dwell load cycles have been chosen from data on experiments performed on dwell fatigue of Ti alloys at the Ohio State University. All the loadings are run for a total time of 370 s. Since the loading considered in these cases are cyclic and include unloading, the kinematic hardening terms discussed in Section 2 are included in the material model. The kinematic hardening parameters are chosen to be c = 500 and d = 100 MPa for all the slip systems. The boundary conditions and all the material parameters except m are the same as those discussed in Section 7.1. The value of m is chosen to be 0.02, corresponding to that calibrated from experiments.

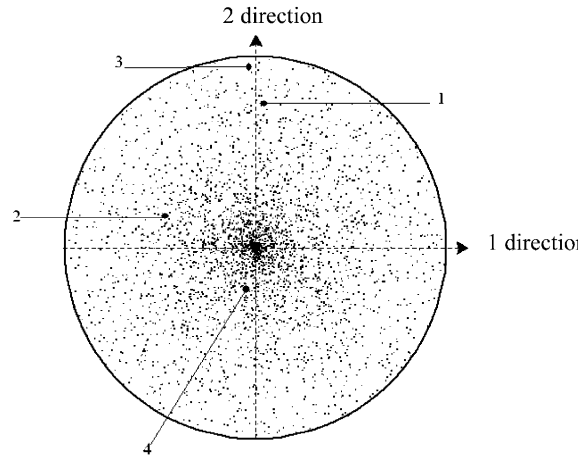

Fig. 9. (0 0 0 1) Pole figure showing the random orientation distribution.

The results of simulations for the four load histories are shown in Fig. 10. Fig. 10a shows the plastic strain in a representative grain as a function of time. The plastic strain (ε^{p}_{22}) in the loading direction shows a continual increase with time indicating plastic ratcheting. There is a significant difference in the plastic strain accumulation for the cyclic loading case and the other cases, while the response is very similar for the creep and the dwell cyclic loading cases. Plastic strain accumulation is seen to increase slightly with increasing dwell time as shown in the inset of Fig. 10a. This may be attributed to the fact that no plastic strain is added

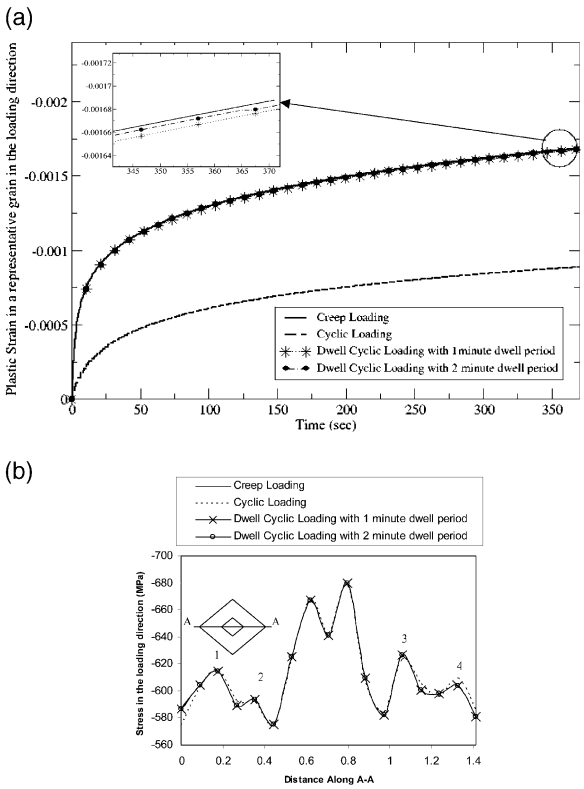

Fig. 10. (a) Plastic strain plot in a representative grain in the loading direction for the four load cycles as a function of time. (b) Stress (σ_{22}) plot for the four load cycles along the line A–A at the end of 370 s.

during unloading–reloading phase of the cyclic loading. Fig. 10b shows the σ_{22} stress plot along the diagonal A–A plotted at the end of the loading for the four different histories considered. Higher stresses are observed in the higher-strength phase near the interface whereas for the outside region near the interface, the stresses are low. This is due to load shedding as discussed in Section 7.1. Since the outside region consists of grains with random orientations, local peaks (1, 2, 3, 4) are observed away from the interface. However, these peaks are considerably smaller than those at the interface. The higher of these peaks at points 1 and 3 correspond to orientations which are close to *c*-axis orientation as seen from Fig. 9. Since the value of *m* chosen is small (0.02), the time-dependent rise of the peak stress is not very significant. This is consistent with the results obtained with the same rate exponent in Section 7.1.

8. Conclusion

Cold creep has been observed to be the dominant mode of deformation in Ti alloys at low temperatures, where significant strains can accumulate with time. In an attempt to understand this behavior, the material response of α-Ti–6Al is analyzed using a rate-dependent elastic crystal plasticity model in this paper. The model accommodates the plastic anisotropy that is inherent to the Ti alloys and accounts for time dependence that is observed under deformation and creep behavior, with crystal plasticity parameters calibrated from experiments. For modeling polycrystalline aggregate of α-Ti–6Al, a statistically equivalent orientation distribution is assigned to the finite element model through a special orientation assignment method from OIM images of polycrystalline α-Ti–6Al. The model with the calibrated parameters is tested by comparison with the experimental results of constant strain rate and creep tests with excellent agreement. It is observed that the model can account for changes of many orders of magnitude in strain rate. It is also observed that the power law in time (i.e. Andrade creep) is a direct consequence of load shedding from soft- to hard-oriented grains. Previous explanations for the power-law creep transient have been proposed in the literature [6]. Several dislocation-based models attempting to explain exhaustive creep at lower temperatures have been forwarded—some rather recently by Cottrell and Nabarro [31−33]. These models argue that primary creep is due to the operation of dislocation sources with a distribution of energies, but make the assumption that polycrystals deform homogeneously. In fact, the extended power laws in time naturally arise rather remarkably from the crystal plasticity model simulations. Slip occurs first in the most favorably oriented grains for prism and basal slip. As these grains deform, load is shed to neighboring grains, which are not as favorably oriented, in order to ensure compatibility and equilibrium between the grains. It is therefore the evolving distribution of internal stresses which

leads to the creep transients observed. A conceptually similar explanation for these transients has been offered by Daehn [34] who has used a simpler cellular automata (CA) modeling approach to produce transients. The apparent "hardening", or reduction in strain rate with time, is not due to any change in material structure, but instead is the result of load redistribution. With time, a larger fraction of the load is borne by higher-strength grains, whereas load is evenly distributed at shorter times. The shape of the transient is intimately related to the distribution of strengths of individual grains. Thus, this single-phase material is essentially deforming in a manner similar to a composite with relatively "soft" and "hard" regions produced by the inherent plastic anisotropy of hcp grains.

An understanding of load shedding and local stress rising in polycrystalline aggregates of Ti alloys is also developed from this study. This is important because creep and dwell cyclic loading can lead to local crack initiation at critical locations within the microstructure with large orientation mismatch. A model is created to understand this phenomenon by assigning large orientation mismatch in the constituent grains of the aggregate. It is observed that the stress concentration is significantly affected by the material rate sensitivity and the peaks increase considerably with time, especially for higher values of m. An interesting observation is that even though the applied macroscopic stress (606 MPa) is only about 88% of the yield strength of the polycrystalline aggregate (693 MPa in the constant strain rate test) and about 33% of the axial stress necessary to activate $\langle c + a \rangle$ slip in single crystals of the same composition (shown in Fig. 2), considerable local yielding leading to plastic strain is realized in the microstructure. Significant local stress concentrations evolve with time in the material microstructure. For example, the stress amplification in the c-axis oriented grain with respect to the applied stress is ~2, for $m = 0.05$ at time 1000 s. The compatibility constraint at the interface causes the development of these high local stress concentrations. Alternatively, this can be explained by considering the planar slip bands, which can propagate across the favorably oriented grains. Higher local stresses will develop due to dislocation pile-ups when these slip bands are impinging upon an adjacent grain that is oriented with c-axis parallel to the macroscopic deformation direction. This is clearly a potential location of crack nucleation in creep or dwell fatigue loading for Ti alloys. The effect of cyclic loading with different dwell periods is studied by incorporating kinematic hardening in the material model. The phenomenon of plastic ratcheting is observed in these materials when subjected to cyclic loading. The time-dependent rise of the peak stress is small for the value of rate exponent considered. In conclusion, the paper provides a good understanding of the plastic behavior of Ti alloys from a local standpoint which is helpful to set up guidelines for the study of their fatigue failure behavior.

Acknowledgements

This work has been supported by the Federal Aviation Administration through grant No. DTFA03-01-C-0019 (Program Director: Dr. Bruce Fenton). This support is gratefully acknowledged. The authors are grateful to Drs. A. Woodfield, A. Chatterjee, J. Hall and J. Schirra for their insightful suggestions. The authors are also grateful to Dr. Vikas Sinha for providing the experimental data. Computer support by the Ohio Supercomputer Center through grant # PAS813-2 is also acknowledged.

References

[1] Donachie Jr MJ. Titanium—a technical guide. Metals Park (OH): ASM International, 1998.
[2] Froes FH, editor. Non-aerospace applications of titanium. Warrendale (PA): TMS; 1998.
[3] Adenstedt HK. Metal. Progress 1949;65:658.
[4] Inman MA, Gilmore CM. Metall. Trans. 1979;10:419.
[5] Chu HP. J. Mater. 1970;5:633.
[6] Odegard BC, Thompson AW. Metall. Trans. 1974;5:1207.
[7] Miller WH, Chen RT, Starke EA. Metall. Trans. 1987;18A:1451.
[8] Neeraj T, Mills MJ. Mat. Sci. Eng. A-Struct. 2001;319:415.
[9] Thompson AW, Odegard BC. Metall. Trans. 1973;4:899.
[10] Neeraj T, Hou DH, Daehn GS, Mills MJ. Acta Mater. 2000;48:1225.
[11] Paton NE, Baggerly RG, Williams JC. AFOSR Report SC526.7FR. 1976.

[12] Balasubramanian S. Polycrystalline plasticity: application to deformation processing of lightweight metals. Ph.D. dissertation. Cambridge (MA): MIT; 1998.
[13] Peirce D, Asaro RJ, Needleman A. Acta Metall. Mater. 1983;31:1951.
[14] Asaro RJ, Needleman A. Scripta Metall. Mater. 1984;18:429.
[15] Harren SV, Asaro RJ. J. Mech. Phys. Solids 1989;37:191.
[16] Kalidindi SR, Bronkhorst CA, Anand L. J. Mech. Phys. Solids 1992;40:537.
[17] Kothari M, Anand L. J. Mech. Phys. Solids 1998;46:51.
[18] Balasubramanian S, Anand L. Acta Mater. 2002;50:133.
[19] Grujicic M, Batchu S. J. Mater. Sci. 2001;36:2851.
[20] Kad BK, Dao M, Asaro RJ. Mat. Sci. Eng. A-Struct. 1995;193:97.
[21] Bronkhorst CA, Kalidindi SR, Anand L. Philos. Trans. R. Soc. London A 1992;341:443.
[22] Morrissey RJ, McDowell DL, Nicholas T. Int. J. Fatigue 2001;23:S55.
[23] Goh CH, Wallace JM, Neu RW, McDowell DL. Int. J. Fatigue 2001;23:S423.
[24] Cuitino AM, Ortiz M. Model. Simul. Mater. Sci. 1993;1:225.
[25] ABAQUS reference manuals. Providence (RI): Hibbit, Karlsson and Sorenson, Inc, 2001.
[26] Kim JY, Yakovlev V, Rokhlin SI. CP615, vol. 21. American Institute of Physics, 2002.
[27] Ghosh S, Ling Y, Majumdar BS, Kim R. Mech. Mater. 2000;32:561.
[28] Matlab. Version 6.2, 2001.
[29] Xie CL, Nakamachi E. J. Mater. Process Tech. 2002;122:104.
[30] Xie CL, Nakamachi E. Mater. Design 2002;23:59.
[31] Cottrell AH. Philos. Mag. Lett. 1996;74:375.
[32] Cottrell AH. Philos. Mag. Lett. 1997;75:301.
[33] Nabarro FRN. Philos. Mag. Lett. 1997;75:227.
[34] Daehn GS. Acta Mater. 2001;49:2017.
[35] Sinha V, Savage M, Tatalovich J. Unpublished research, 2001.

Appendix L

A Crystal Plasticity Based Model of Polycrystalline Ti-6242

Dhyanjyoti Deka[a], Deepu Joseph[a], Somnath Ghosh[a], Michael Mills[b].

[a] *Department of Mechanical Engineering, The Ohio State University, Columbus, OH, 43210, USA*

[b] *Department of Materials Science and Engineering, The Ohio State University, Columbus, OH, 43210, USA*

1. Introduction

1.1 Objective

The aim of this work is to simulate the behavior of the alloy Ti-6Al-2Sn-4Zr-2Mo (Ti-6242) using a crystal plasticity model. The parameters in the model are to be calibrated using the experiments for single colony results. The model is then used to simulate the behavior of the polycrystal alloy containing both primary α and transformed β phases and the results compared to experiments. Since the explicit modeling of all the features of Ti-6242 could prove to be computationally expensive, an equivalent model is developed and used in all the simulations.

1.2 Background

The transformed β regions consist of α/β colonies. In these colonies there is a definite orientation relation between the α and the β phase[1] which is seen to follow the Burger's Orientation relation given by[2]:

$$(101)_\beta \parallel (0001)_\alpha, [1\bar{1}\bar{1}]_\beta \parallel [2\bar{1}\bar{1}0]_\alpha$$

This crystallographic relationship brings one of the hcp (hexagonal closed packed) directions into coincidence with the bcc (body centered cubic) slip direction. The major slip which takes place in these colonies is along the α/β interface which provides little resistance to slip in the colony structure. For the transformed β phase, anisotropy in the critical resolved shear stress is observed in the three (a1, a2 and a3) basal planes and also in the three (a1, a2 and a3) prism planes. The observed anisotropy for the three basal slips and

for the three prism slips has been attributed to the differing ease of α/β slip transmission for a1, a2, a3 basal and prism slip caused by the Burger's orientation relation.

1.3 Scope of the report

The first section following this summarizes the experimental results available for Ti-6242. This is followed by a description of the computational models, including the development of the equivalent model for the β phase, used in the simulation. Also described are the steps taken to calibrate the model using the experiments, so as to obtain the various crystal plasticity parameters. This is followed by descriptions about polycrystal simulations and comparison with the experiments. The technique used to obtain a statistically equivalent orientation and misorientation distribution with the experiment will also be discussed.

2. Approach, Results and Discussion

2.1 Summary of Experiments

2.1.1 Micro-Tensile Testing of Ti-6242 single colonies

Single α/β colonies of Ti-6AI-2Sn-4Zr-2Mo-O.ISi were grown utilizing a vertical float zone technique in a Crystalox furnace at Wright Patterson Air Force Base, Dayton, OH by J.M. Scott and M.D.Uchic. Successfully grown colonies ranged in size from 5 to 25 mm. All samples for mechanical testing were extracted from the single colony rod used for the chemical analysis, results given in Table 1. Scanning Electron Microscopy (SEM) observations were made in a Philips XL30 SEM using backscattered electrons to determine the relative alignment of the broad face of the α/β interface, allowing for the unambiguous identification of the three a-type {11-20} slip directions. Thin sections containing both the desired Burgers vector to be activated and the tensile axis (45° from the desired slip plane) were cut from the single colony rod using a SiC abrasive saw. Tensile testing was performed under strain control in a piezo-driven microsample testing machine at The Johns Hopkins University. During constant strain rate testing, load is applied to the system using a piezoelectric actuated drive. Strain is measured directly from the microsample using a non-contact ISDG measurement system.

2.1.2 Compression Testing of Ti-6242 single colonies

Single- α/β colonies of Ti-6AI-2Sn-4Zr-2Mo-O.ISi were prepared using a vertical float zone technique. Compression test samples in the form of rectangular parallelpipeds with a final dimension of nominally 3mm x 3mm x 8mm were sectioned from the single colony rod using an SiC abrasive saw. The compression samples were each oriented to maximize the resolved shear stress on one of the three a-type slip directions on the basal plane. The orientations used in this study are identical to those used for the micro tensile testing of the basal slip orientations. Each compression sample was oriented with the basal plane at 45° to the tensile axis, and one of the faces of the compression sample was parallel to the prism plane containing the a-type slip direction to be activated. This results in a zero resolved shear stress for the motion of the primary Burger's vector on its corresponding prism slip plane. A resolved shear stress of 0.5 is applied to the a-type slip Burger's vector to be activated on the basal plane. Table 2 lists the Schmid factor for each orientation for the three a-type slip directions (a1, a2 or a3) on basal, prismatic or first order pyramidal planes plane. Constant strain rate compression testing was performed at room temperature using an Instron™ model 1362 mechanical test frame equipped with a compression cage. All tests were performed at a constant strain rate of $1 \times 1\ 0^{-4}$ to a final plastic strain of nominally 5%.

2.2 Computational Modeling of Ti-6242

Computational modeling of polycrystalline Ti-6242 is a non-trivial process owing to the heterogeneity present in the microstructure. A systematic approach towards solving the problem is necessary. As a first step, a crystal plasticity based finite element model to represent the transformed β regions considering the exact morphology of the lamellar structure is constructed namely the explicit model. The constitutive parameters for the slip systems on the bcc phase are calibrated using this model. As can be easily imagined the explicit model is an expensive option for modeling polycrystalline Ti-6242. Hence an equivalent model is developed to represent the transformed β regions. This is a homogenized representation of the lamellar structure and thus less computationally expensive. In the equivalent model, each point in the continuum has hcp as well as bcc slip system activity. The parameters for the bcc phase are taken to be the same as calibrated

from the explicit model calibrations while calibration of the hcp crystal plasticity parameters is done to match single colony Ti-6242 results. The next step involves the simulation of polycrystalline Ti-6242. The finite element model of the polycrystalline model consists of 70% primary alpha grains which are purely hcp and 30% transformed β which are represented using the equivalent model. Statistically equivalent orientation as well as misorientation distribution is assigned to the finite element model. The above-mentioned procedure is illustrated in the form of a flow chart in fig 2.

2.2.1 Explicit Modeling of the transformed β region

The explicit modeling of the alpha and beta phase in the transformed beta regions is done in an effort to find the bcc crystal plasticity parameters. In this model the alpha and beta lamellae are spatially separated with the alpha regions having an hcp crystal structure consisting of 30 slip systems and the beta phase having a bcc crystal structure consisting of 48 slip systems. A unit cube discretized into 343 eight nodded brick elements (C3D8 in ABAQUS/Standard) serves as the computational model. Minimum constraint boundary conditions just enough to prevent rigid body motions are used(fig 3).. The model accommodates the Burger's Orientation relationship between the alpha and the beta phase as described in section 1.2.

Crystal plasticity parameters used for the basal and prism slip systems of the hcp phase are shown in table 3. The parameters for the pyramidal systems of hcp are taken to be the same as for Ti-6Al [3].

2.2.2 Characterization of BCC Constitutive Parameters

Calibration of the BCC crystal plasticity parameters is done using the explicit finite element model to optimally match the micro-tensile experimental curves available [4]. The experimental curves are available for six different orientations namely a1 basal, a2 basal, a3 basal, a1 prism, a2prism and a3 prism. For these six orientations, the schmid factor is maximum on the respective slip plane. Simulations are conducted for these six orientations at a strain rate of 10^{-4} sec^{-1} applied to the top face. The computational model and boundary conditions are same as described in section 2.2.1. A genetic algorithm (fig 4) is used to

minimize the difference between the experimental and simulation results in a least square fashion. The fitness function is given by

$$f = \min \sum_{i=1}^{ndata} \left\| \sigma_i^* - \sigma(\varepsilon_i^*, v) \right\|^2$$

Stress-plastic strain plots comparing the experimental and computational results are shown in figs 5 through 7.

2.2.3 Equivalent Model for the transformed beta region

Since the explicit model is computationally very expensive to be feasibly used to model polycrystalline Ti-6242, an equivalent model of the transformed beta regions is used in polycrystalline Ti-6242 simulations (fig 8). Each point in this homogenized representation consists of both hcp and bcc slip systems. The stress at a point in the equivalent model is a weighted average of the hcp and bcc response according to their volume fractions.

$$\sigma_{ij}^{equivalent} = vf^{hcp} \times \sigma_{ij}^{hcp} + vf^{bcc} \times \sigma_{ij}^{bcc}$$

In the above equation, σ_{ij}^{hcp} and σ_{ij}^{bcc} are the stresses due to hcp and bcc slip systems respectively, vf^{hcp} and vf^{bcc} are the volume fractions of hcp and bcc phases respectively and $\sigma_{ij}^{equivalent}$ is the net stress at a point. In all simulations, vf^{hcp} = 0.88 and vf^{bcc} = 0.12.

This model accommodates the observed tension/compression asymmetry by switching parameters based on the sign of the macroscopic hydrostatic stress. The bcc constitutive parameters are the ones that have been calibrated using the explicit model while the hcp crystal plasticity parameters are calibrated using a genetic algorithm (GA) to match the experimental micro-tensile and compression curves of Ti-6242 single colonies [4]. The micro-tensile experimental curves are the same as discussed in section 2.1.1. Experimental data is available for a1 basal, a2 basal and a3 basal in compression (section 2.1.2) and the compression parameters for basal hcp slip systems in the compression direction are calibrated from this data. Very good match has been obtained through the GA as can be seen in figs 9 through 13. The calibrated parameters are depicted in table 4.

To gain confidence in the ability of the equivalent model to represent the microstructure of the transformed beta regions, a comparison in the values of the accumulated shear strain on the bcc slip systems between the equivalent model and the explicit model has been done for

all basal and prism oriented simulations. In case of the explicit model, averaging of the slip system shear is done over all bcc elements. The microscopic shear strains were measured when the macroscopic strain in the loading direction equaled 0.024. It has been observed that the predominant bcc slip systems were the same in both the models and the shear strain values on these slip systems compared well (table 5,6). This study validates the equivalent model as an acceptable representation of the transformed beta regions.

3. Polycrystal Ti-6242 simulation

3.1 Material Properties

The polycrystalline material consists of 70% primary alpha and 30 % transformed beta. The computational model accounts for this volume fraction with the transformed beta phase being treated as equivalent grains. For modeling the transformed beta regions of the polycrystalline material, the calibrated data on the Ti-6242 single colonies is used. However owing to the much finer lathe size of the transformed beta regions compared to the single colonies, an increase of around 150 MPa in the slip system initial deformation resistance in the tension direction and around 25 MPa in the compression direction has to be applied to account for the Hall-Petch effect.

The primary alpha regions have a purely hexagonal close packed structure. The properties for this phase are taken to be the same as that for the <a1> type slip systems in the transformed beta regions. Owing to the size difference between the globular primary alpha in the polycrystalline material and the coarse single colony structure of the <a1> oriented single colonies, an increase in the slip system initial deformation resistance of around 90 MPa in tension direction and around 30 MPa in compression direction has to applied to account for the Hall-Petch effect.

3.1.1 Statistically equivalent orientation distribution.

The experimental orientations are provided in the form of Euler angles. Large numbers of Euler angles are obtained from the experimental procedure, which involves Orientation Imaging Microscopy (OIM). In order to get the reduced number of orientation input for the finite element model, the orientation distribution method is used which provides statistically equivalent orientations as shown in figure 14.

3.1.2 Statistically equivalent misorientation distribution.

Misorientation refers to the amount of misalignment between two neighboring grains. The misorientation angle between two grains is generally given as the smallest angle needed to transform one orientation to the other. In most crystal systems, such as FCC and HCP, there are many equivalent transformations, so the one with the lowest angle is used.

It is common to describe the misorientation in terms of a rotation axis vector $\vec{n}$ and an angle θ. The axis $\vec{n}$ represents a common crystallographic lattice or slip direction for both crystal lattices. The angle θ is the rotation about $\vec{n}$ required to bring the two crystal lattices into coincidence. Using the axis/angle description, the misorientation angle θ between two neighboring grains is described in [5] as

$$\theta = \min\left|\cos^{-1}\left\{\frac{tr\left(\mathbf{g}_A\mathbf{g}_\mathbf{B}^{-1}\mathbf{O}-\mathbf{1}\right)}{2}\right\}\right|$$

where $\mathbf{g}_A$ and $\mathbf{g}_B$ are the orientation matrices of grain A and B, respectively, expressed as

$$\mathbf{g}_i = \begin{pmatrix} \cos\varphi_1\cos\varphi_2 - \sin\varphi_1\sin\varphi_2\cos\Phi & \sin\varphi_1\cos\varphi_2 + \cos\varphi_1\sin\varphi_2\cos\Phi & \sin\varphi_2\sin\Phi \\ -\cos\varphi_1\sin\varphi_2 - \sin\varphi_1\cos\varphi_2\cos\Phi & -\sin\varphi_1\sin\varphi_2 + \cos\varphi_1\cos\varphi_2\cos\Phi & \cos\varphi_2\sin\Phi \\ \sin\varphi_1\sin\Phi & -\cos\varphi_1\sin\Phi & \cos\Phi \end{pmatrix}_i, \ (i=A,B)$$

The angles φ_1, φ_2 *and* Φ are the Euler angles in each grain and $\mathbf{O}$ is the crystal symmetry operator.

The method for matching the misorientation distribution is noe desribed. First, the orientation distribution is matched and then grains are only moved around, so that this orientation distribution is not spoiled. A computer program is used to calculate and export the misorientation value for each neighbor of every element in the FE model. For each element there are either 3,4,5,or 6 values of misorientation, depending on the location of the element. (i.e. 3 for corner elements, 4 for edge elements, 5 for face grains, and 6 for bulk elements)

The first step is to add all the misorientations of an element's neighbors together and divide by the number of neighbors it has, simply yielding the average misorientation with its neighbors. These misorientation values are then divided into bins according to their

average misorientation values. Experimental misorientation distribution is shown in fig 15. The initial misorientation distribution in the Finite Element Model is shown in fig 16. It can be easily observed that they don't compare well. The next step is to to determine which bins are most wrong and select elements that have values in these bins. At the same time, if a bin is correct we would not allow any elements that has a value in that bin to be moved so that it is essentially locked in. This process can be iterated until satisfactory results are obtained (Fig 17).

3.1.3 Results of the polycrystalline sample

The mesh used to represented the polycrystalline model consists of 343 elements and is depicted in fig 18 and the orientation distribution in the mesh is shown in fig 19. The computational model is constrained from moving by using minimum boundary conditions described in section 2.2.1. The compression constant strain rate simulation is done through the application of a velocity load of 0.0001 sec^{-1} applied to the top face. For the tension constant strain rate simulation, a strain rate of 0.000114 sec^{-1} is applied. Creep simulation is done through the application of a constant pressure load of 907 MPa on the top face in compression and 897 MPa in tension. Good agreement has been obtained between experiment and simulation results for all the cases considered.(fig 20-23).

4. Study of the stress normal to the basal plane as a criterion for crack initiation

In this section, the stress normal to the basal plane of hcp is studied as a mechanism for crack initiation. The element on which the stress is calculated represents the hardest grain in the polycrystalline material. The choice of the hardest grain is done systematically as follows. Initially all grains which have their [0001] axes aligned at an angle not greater than 10° with the loading axis are short-listed. These grains are typically hard owing to strong <c+a> activity and low <a>-type activity. Among these grains, the one which has the highest average misorientation with its neighbours is chosen as the strongest element owing to load-shedding effects. Fig 24 represents the stress evolution on the hardest grain and a typical soft grain in a constant strain tension test. It can be observed that the stress on

the hard element is much higher than the soft element which is indicative of a crack nucleation site.

5. Conclusion

An efficient computational model for modeling the behavior of Ti-6242 polycrystalline material has been developed. This includes an explicit model which represents the exact morphology of the α-β lathe structure in the transformed beta region. An equivalent model to represent the same is constructed to reduce the computational cost involved in simulating the explicit model. An extensive set of calibrations against single colony experimental results are done to obtain the crystal plasticity parameters. Following this the behavior of polycrystalline Ti-6242 is simulated and compared with constant strain rate and creep experiments. In addition this model has the scope of being used for the prediction of crack nucleation sites based on the values of the stress normal to the basal plane.

	Composition (Wt. %)	Error (+/-)
Al	6.01	0.005
Mo	1.96	0.0035
Sn	1.96	0.0035
Zr	4.01	0.005
Si	0.10	0.005
O	0.131	0.008
N	0.012	0.003
Ti	Balance	

Table 1 Composition of Ti-6242

	Slip System	a_1 **Basal** (2-1-13)	a_2 **Basal** (-12-13)	a_3 **Basal** (-1-123)	a_1 **Prism** (3-410)	a_2 **Prism** (-3410)	a_3 **Prism** (1-430)
Basal	**a/3**[-2110](0001)	**0.50**	0.25	0.25	0.00	0.00	0.00
	a/3[-12-10](0001)	0.25	**0.50**	0.25	0.00	0.00	0.00
	a/3[-1-120](0001)	0.25	0.25	**0.50**	0.00	0.00	0.00
Prism	**a/3**[-2110](01-10)	0.00	0.23	0.23	**0.50**	0.26	0.26
	a/3[-12-10](10-10)	0.23	0.00	0.23	0.26	**0.50**	0.23
	a/3[-1-120](-1100)	0.23	0.23	0.00	0.23	0.23	**0.50**
Pyramidal	**a/3**[-2110](0-111)	0.24	0.32	0.32	0.44	0.23	0.21
	a/3[-2110](0-11-1)	0.24	0.08	0.08	0.44	0.23	0.21
	a/3[-12-10](10-11)	0.32	0.24	0.32	0.23	0.44	0.20
	a/3[-12-10](-1011)	0.08	0.24	0.08	0.25	0.44	0.24
	a/3[-1-120](1-101)	0.32	0.32	0.24	0.20	0.20	0.44
	a/3[-1-120](1-10-1)	0.08	0.08	0.24	0.17	0.20	0.44

Table 2 Schmid factor on different slip planes for six different orientations

	Basal	Prism
m	0.02	0.02
so	300	240
a	0.0023	0.0023
ho	2000	4153
r	0.3	0.2935
n	0.14	0.148
s	504	504

(a)

	{101}	{112} Soft	{112}Hard	{123}Soft	{123}Hard
m	0.02	0.02	0.02	0.02	0.02
so	250.0	209.63	229.82	200.67	251.28
a	0.0023	0.0023	0.0023	0.0023	0.0023
ho	1500	1979.82	1371.6	1634.8	2311.95
hinf	25.0	25.0	25.0	25.0	25.0
go	500.0	500.0	500.0	500.0	500.0
ginf	200.0	200	200.0	200.0	200.0

(b)

Table 3 (a) Parameters for the basal and prism slip systems of hcp phase (b) Calibrated parameters for the five bcc slip families.

Tensile Parameters	A1 basal	A2 basal	A3 basal
m	0.02	0.02	0.02
so	290	315	243
a	0.0023	0.0023	0.0023
ho	1500	2540	8000
r	0.3	0.3	0.4
n	0.14	0.1	0.05
s	450	634	371

(a)

Tensile Parameters	A1 prismatic	A2 prismatic	A3 prismatic
M	0.02	0.02	0.02
so	240	220	240
a	0.0023	0.0023	0.0023
ho	3453	6000	4000
r	0.2935	0.201	0.3
n	0.148	0.2	0.1
s	504	583	504

(b)

Compressive Parameters	A1 basal	A2 basal	A3 basal
m	0.02	0.02	0.02
so	400	470	480
a	0.0023	0.0023	0.0023
ho	350	350	750
r	0.5	0.5	0.5
n	0.1	0.1	0.1
s	504	504	654

(c)

Table 4 (a) Calibrated parameters of basal slip systems in tension direction. (b) Calibrated parameters of prism slips systems in tension direction. (c) Calibrated parameters of basal slip systems in compression direction.

A1 basal

BCC Slip System	Strain in explicit model	Strain in equivalent model
[-111](101)	3.22e-2	3.5e-2
[111](21-3)	7.47e-3	4.38e-3
[-111](312)	1.76e-3	1.65e-3
[-111](2-13)	1.59e-3	1.65e-3
[-111](211)	1.35e-3	9.72e-4
[-111](1-12)	1.23e-3	1.04e-3

(a)

A2 basal

BCC Slip System	Strain in explicit model	Strain in equivalent model
[11-1](112)	2.19e-2	9.11e-3
[11-1](101)	2.10e-2	2.23e-2
[11-1](213)	4.82e-3	2.49e-3
[-111](211)	3.92e-3	4.86e-3
[-111](101)	2.17e-3	2.15e-2
[1-11](121)	1.52e-3	9.27e-4

(b)

A3 basal

BCC Slip System	Strain in explicit model	Strain in equivalent model
[11-1](101)	2.13e-2	2.57e-2
[111](-312)	1.44e-2	1.01e-2
[11-1](2-11)	5.71e-3	4.49e-3
[11-1](3-12)	2.46e-3	1.96e-3

(c)

Table 5 Comparison of shear strain values on prominent bcc slip systems (shear strain > 10^{-3}) for (a) a1 basal (b) a2 basal and (c) a3 basal oriented simulations.

A1 prism

BCC Slip System	Strain in explicit model	Strain in equivalent model
[-111](12-1)	3.8e-2	3.85e-2
[111](2-31)	2.06e-3	1.8e-3
[1-11](132)	2.06e-3	1.8e-3

(a)

A2 Prism

BCC Slip System	Strain in explicit model	Strain in equivalent model
[1-11](31-2)	1.13e-2	2.5e-2
[111](-312)	6.5e-3	1.89e-2
[111](11-2)	5.02e-3	7.63e-3
[-111](23-1)	3.27e-3	2.14e-3
[-111](13-2)	3.14e-3	7.35e-3
[1-11](32-1)	1.98e-3	1.63e-4

(b)

A3 Prism

BCC Slip System	Strain in explicit model	Strain in equivalent model
[11-1](-132)	1.69e-2	1.5e-2
[11-1](-231)	1.68e-2	1.64e-2
[11-1](-121)	6.63e-3	6.38e-3

(c)

Table 6 Comparison of shear strain values on prominent bcc slip systems (shear strain > 10^{-3}) for (a) a1 prism (b) a2 prism and (c) a3 prism oriented simulations.

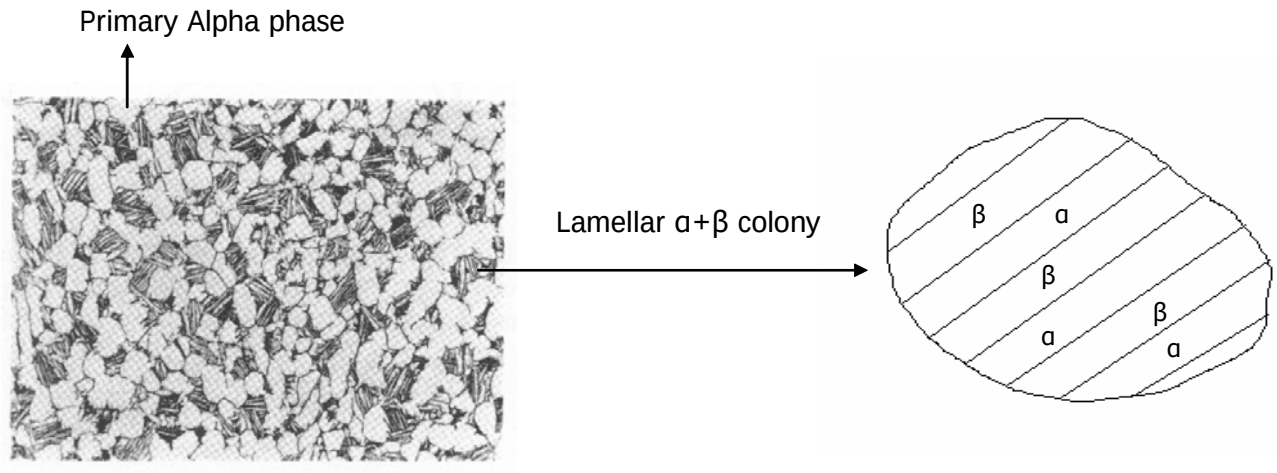

Figure 1. Microstructure of Ti-6242 after forging in the α+β regime. The microstructure consists of transformed β (dark phase) colonies in a matrix of equiaxed primary α grains (light phase).

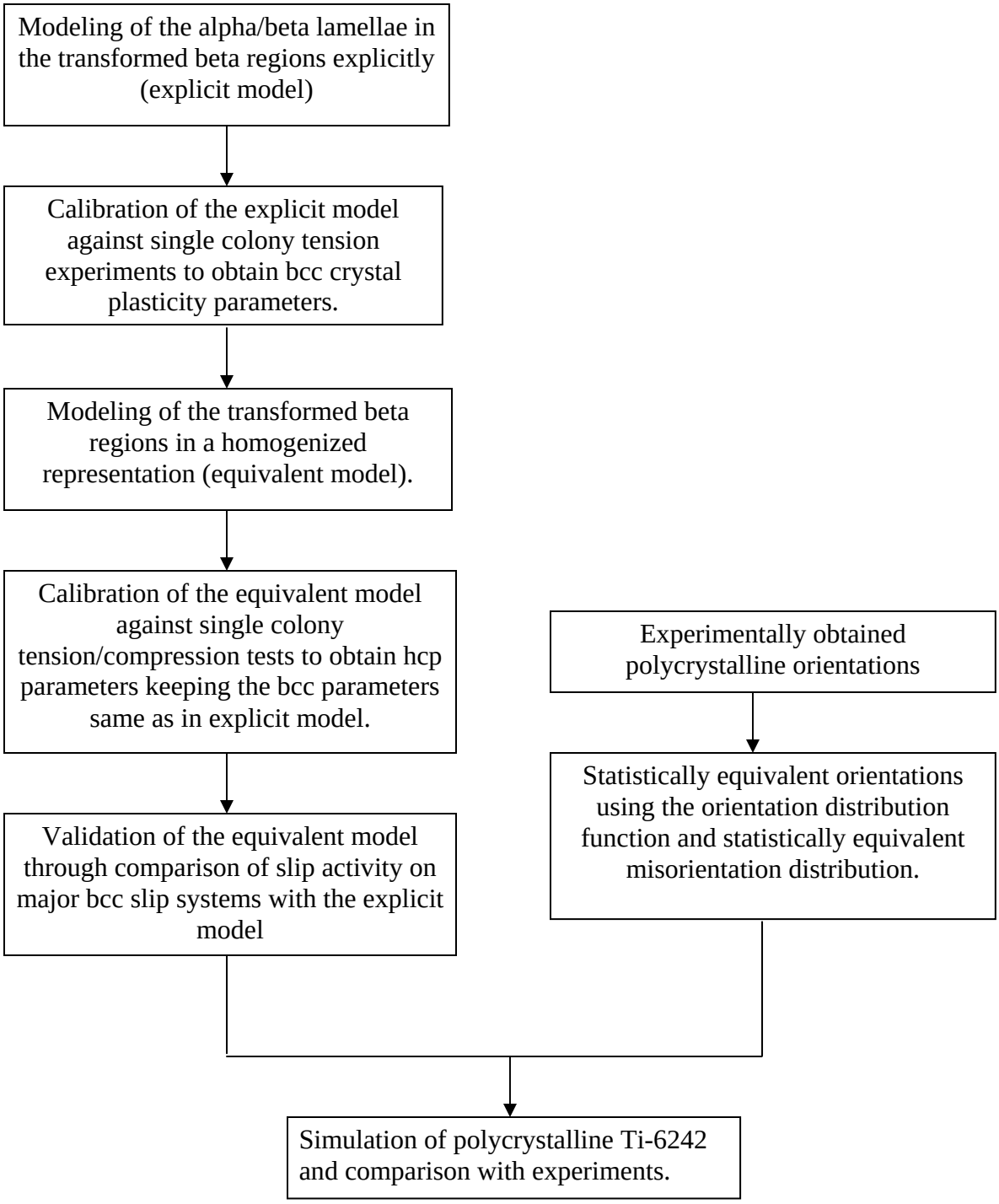

Figure 2. Computational modeling framework for polycrystalline Ti-6242.

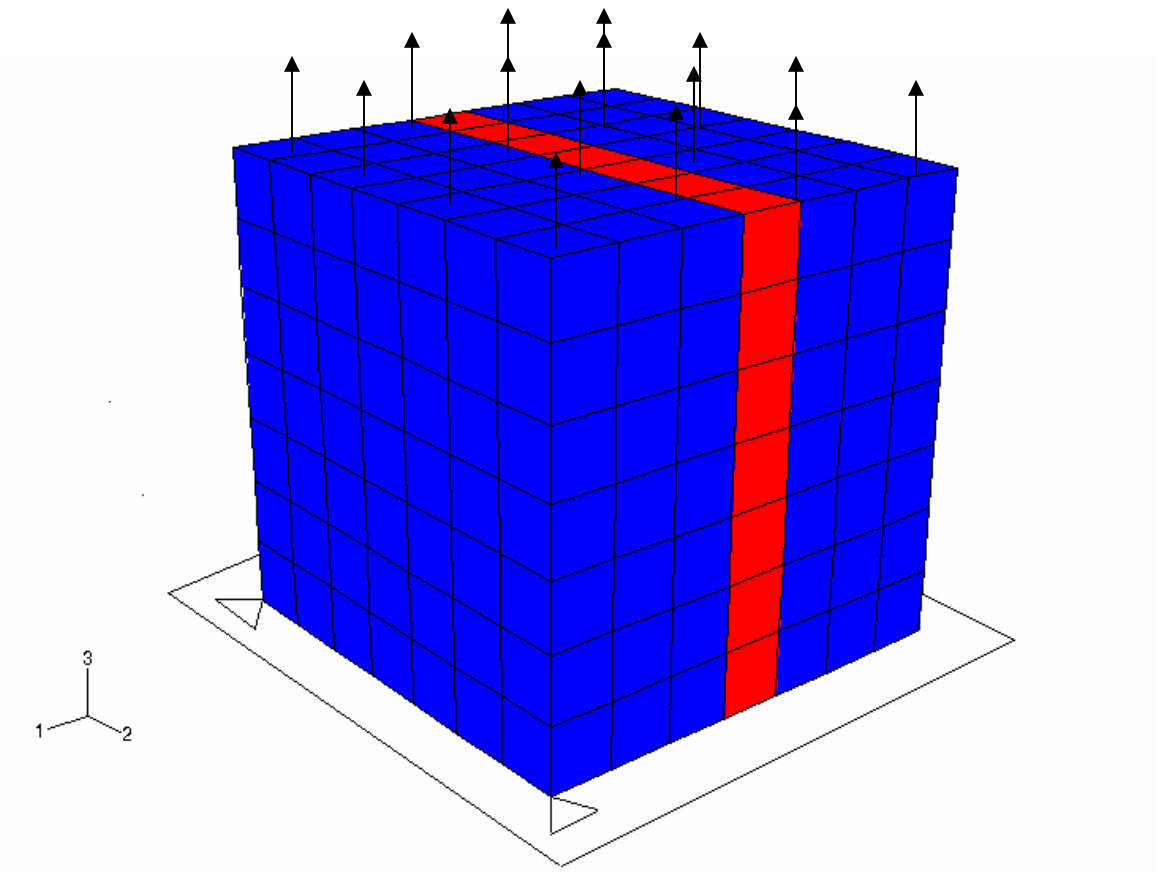

Figure 3. Explicit Model for the transformed beta region depicting the alpha phase (**blue**) and the beta phase (**red**).

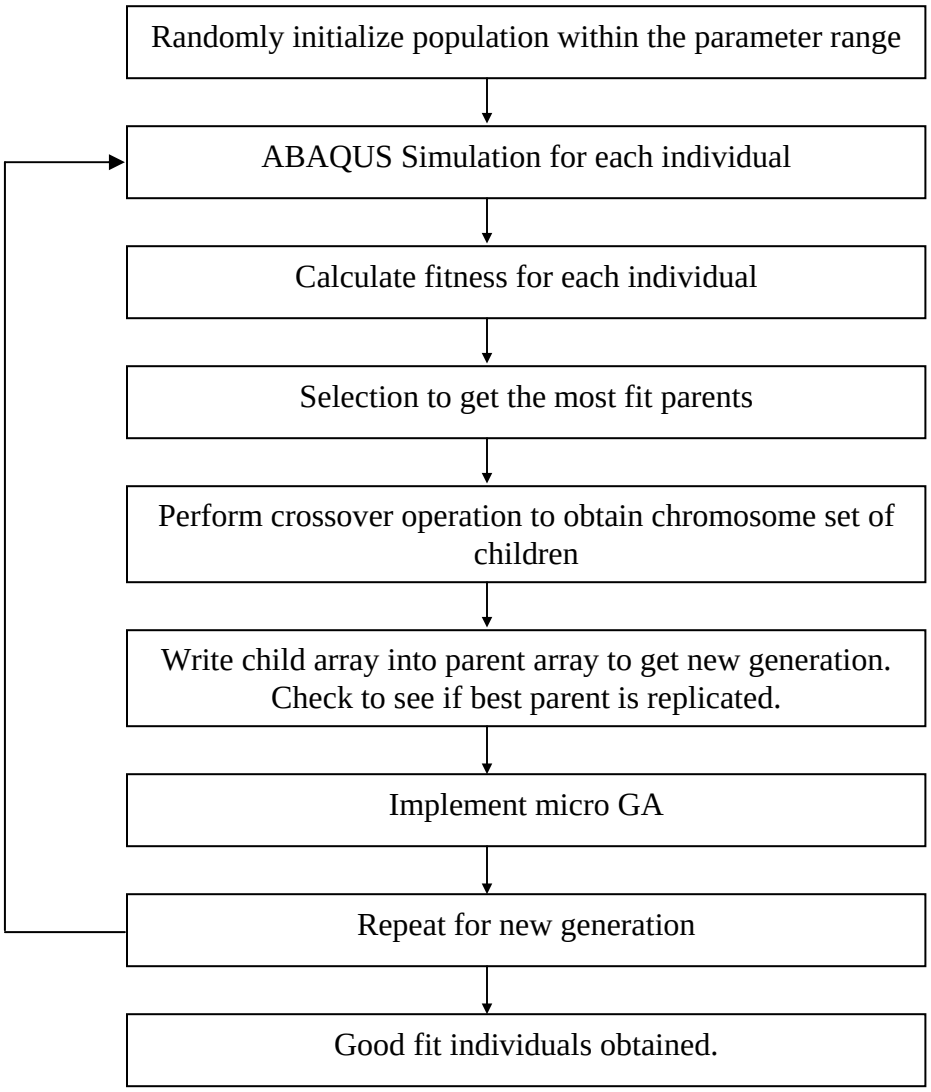

Figure 4. Flowchart depicting the Genetic Algorithm used in the optimization process.

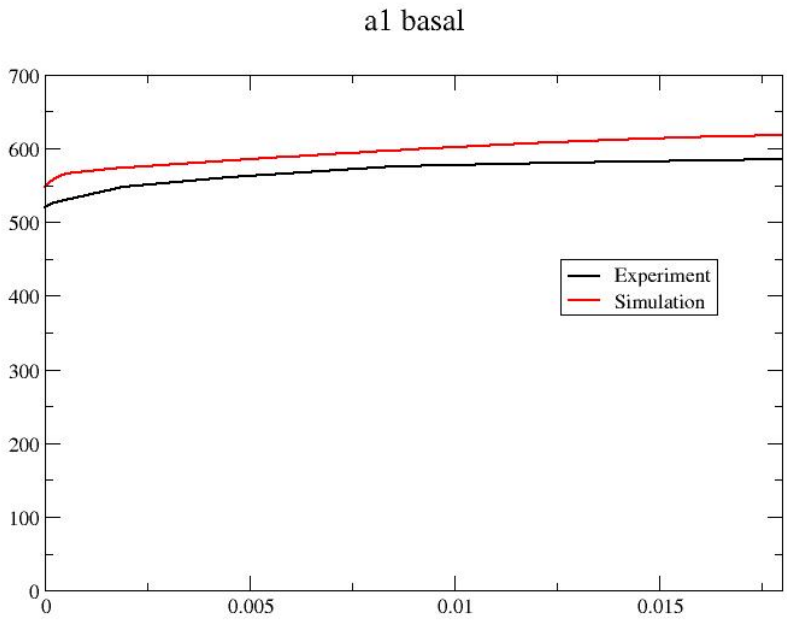

(a)

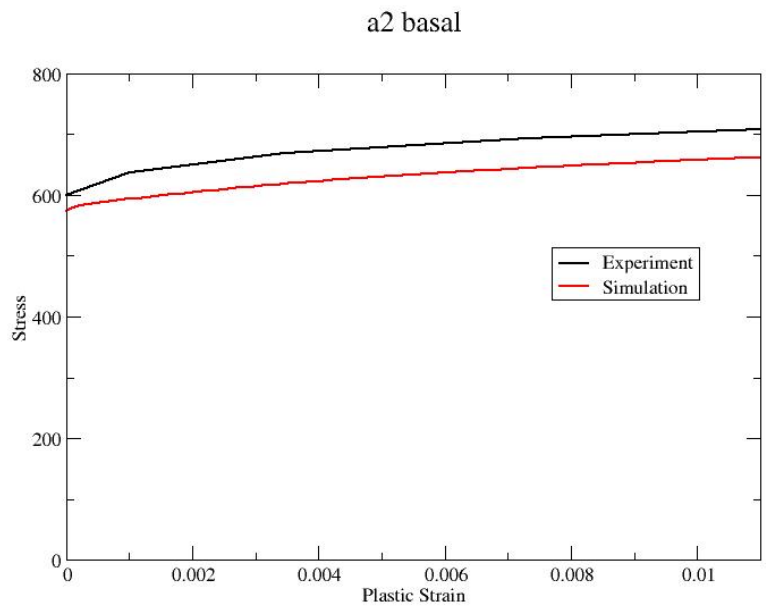

(b)

Figure 5. Constant Strain rate tensile testing on Ti-6242 single colony sample oriented for (a) a1 basal slip and (b) a2 basal slip.

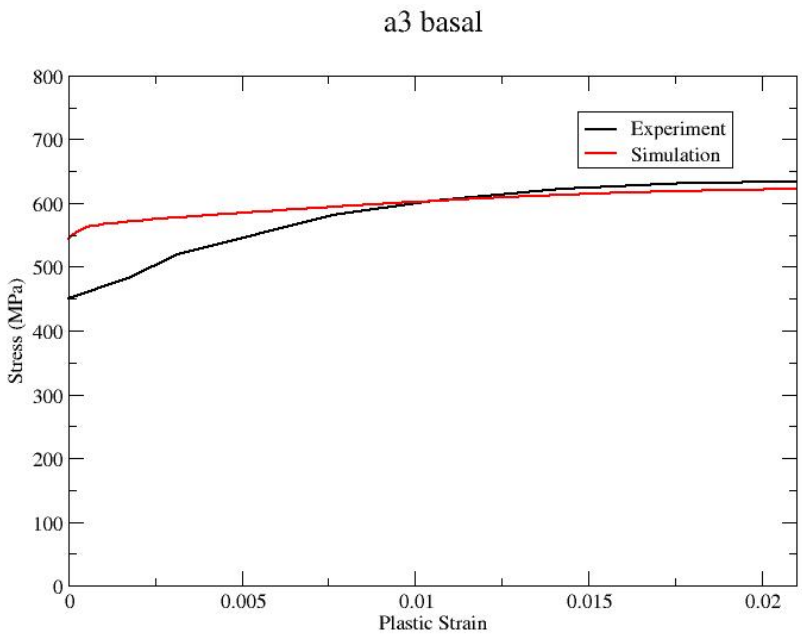

(a)

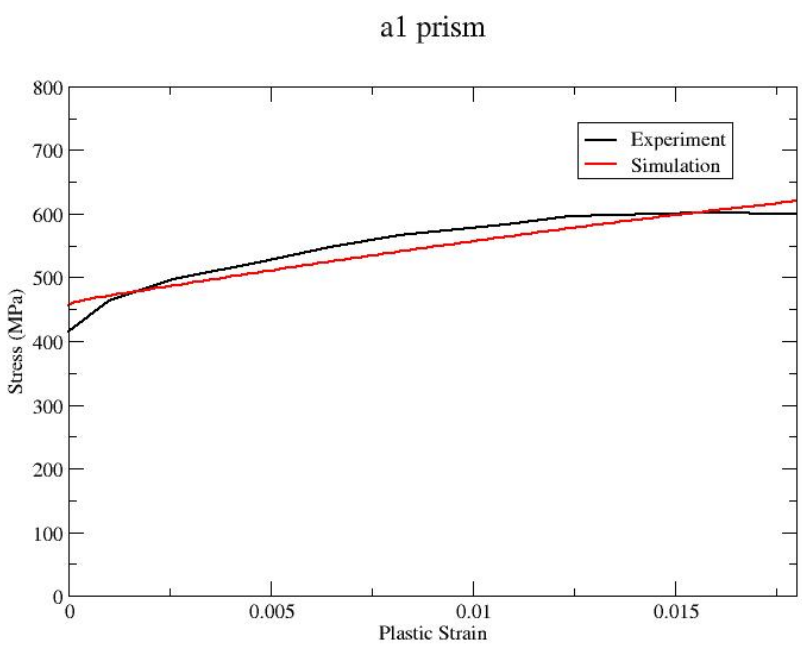

(b)

Figure 6. Constant Strain rate tensile testing on Ti-6242 single colony sample oriented for (a) a3 basal slip and (b) a1 prism slip.

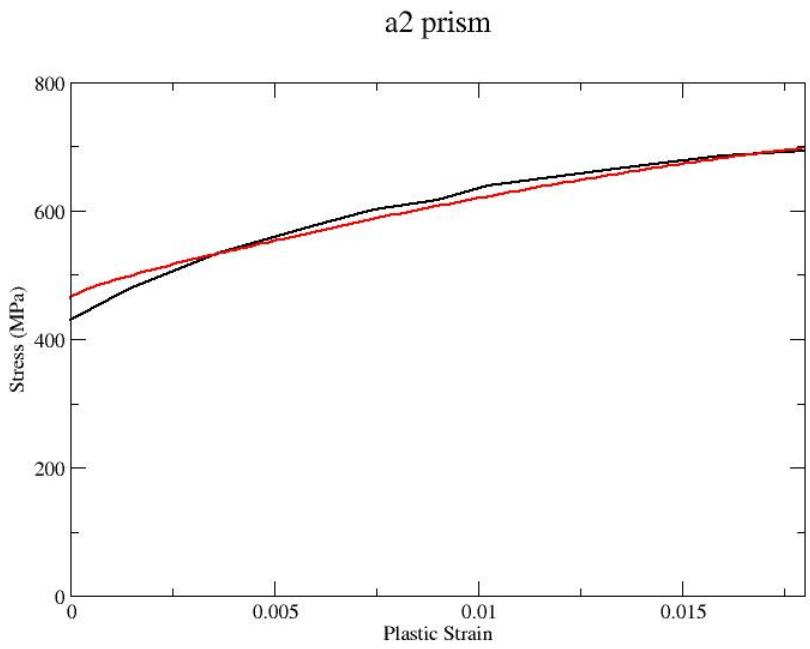

(a)

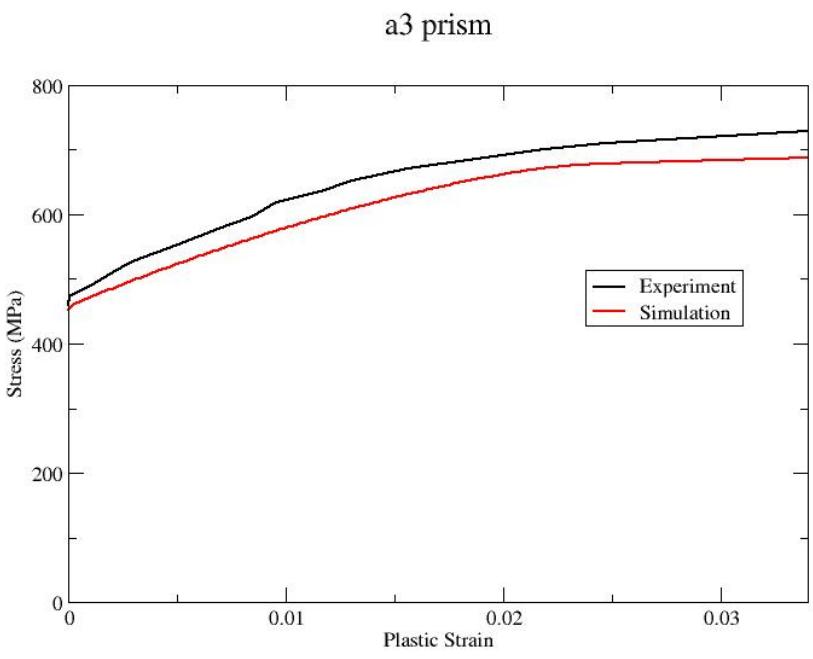

(b)

Figure 7. Constant Strain rate tensile testing on Ti-6242 single colony sample oriented for (a) a2 prism slip and (b) a3 prism slip.

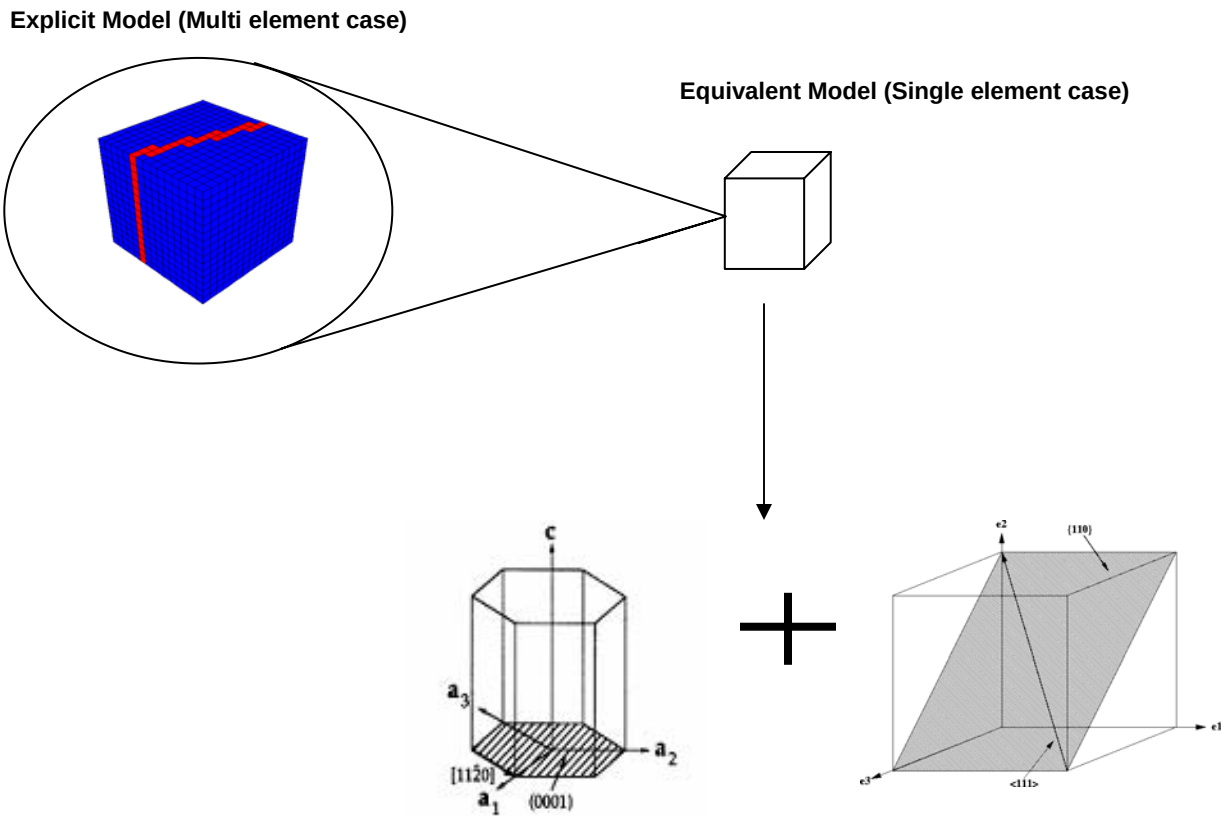

Figure 8. Ti-6242 single colonies can be represented by a single element using the equivalent model.

(a)

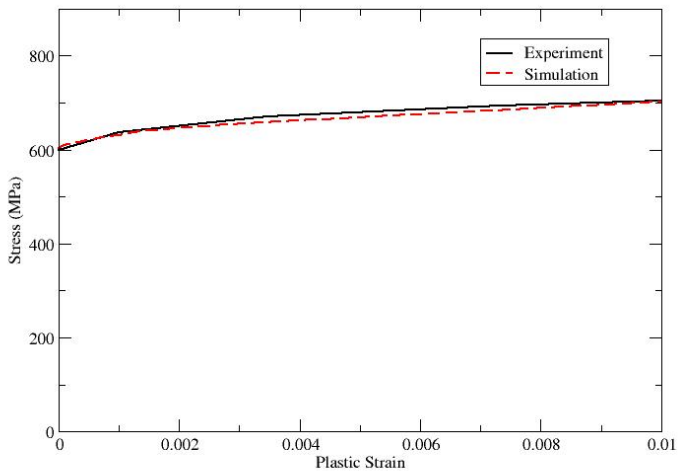

(b)

Figure 9. Constant Strain rate tensile testing on Ti-6242 single colony sample oriented for (a) a1 basal slip and (b) a2 basal slip.

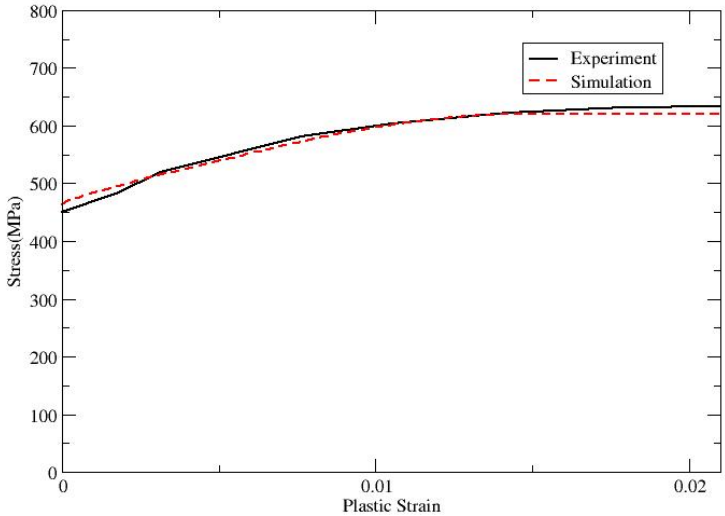

(a)

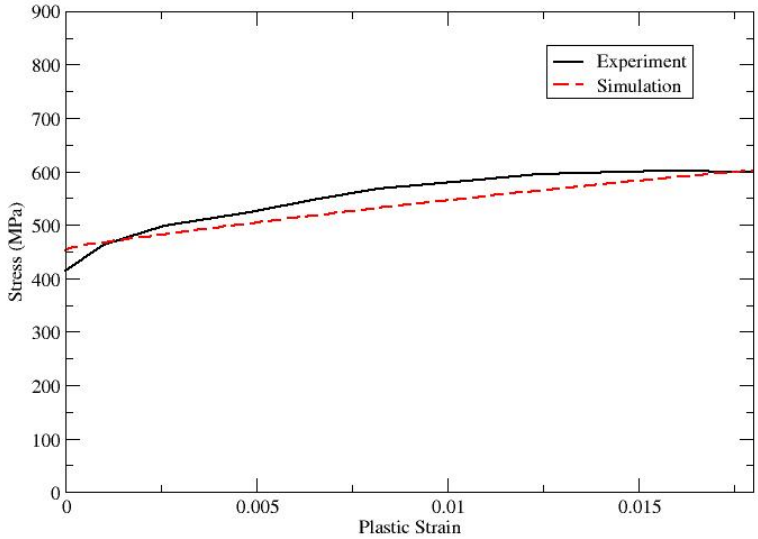

(b)

Figure 10. Constant Strain rate tensile testing on Ti-6242 single colony sample oriented for (a) a3 basal slip and (b) a1 prism slip.

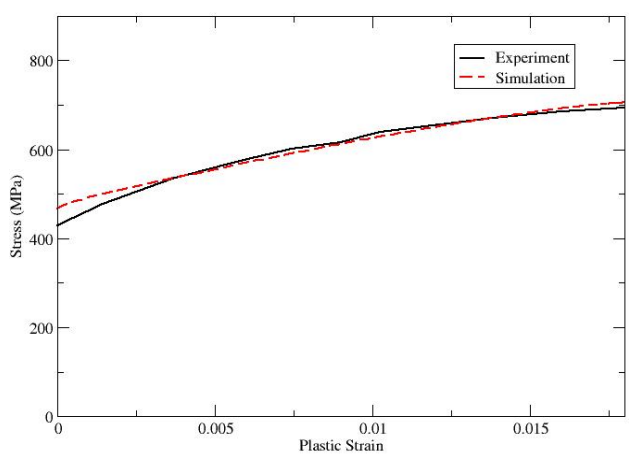

(a)

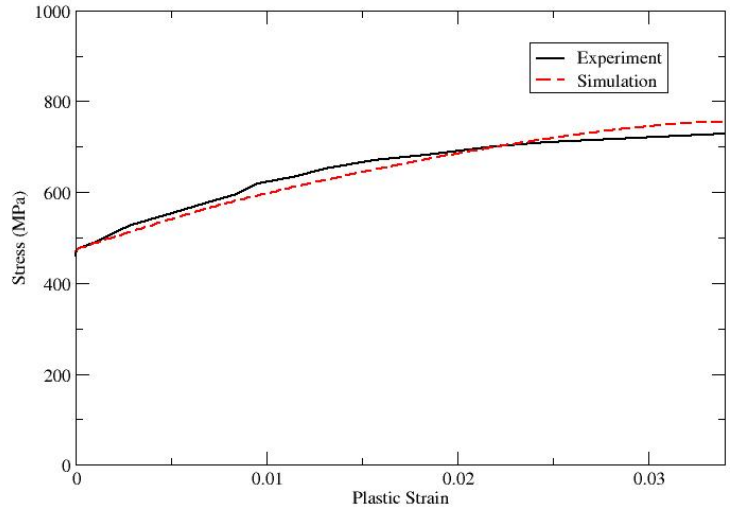

(b)

Figure 11. Constant Strain rate tensile testing on Ti-6242 single colony sample oriented for (a) a2 prism slip and (b) a3 prism slip.

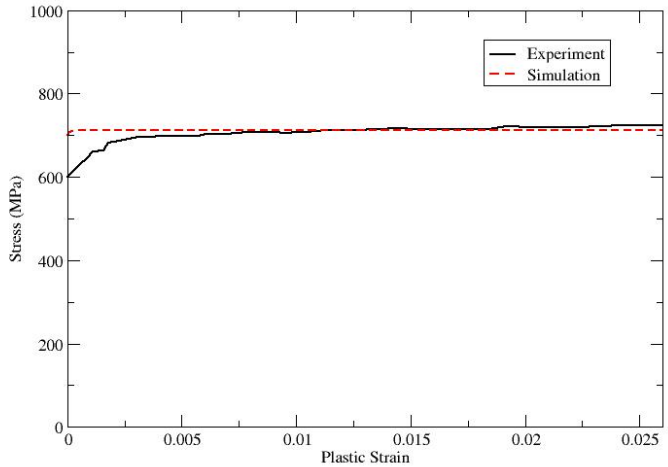

(a)

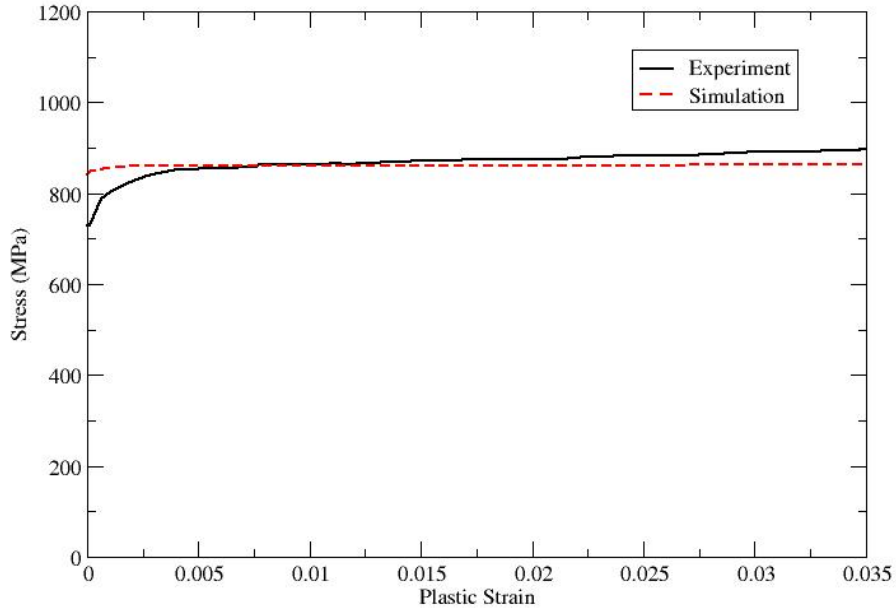

(b)

Figure 12. Constant Strain rate compression testing on Ti-6242 single colony sample oriented for (a) a1 basal slip and (b) a2 basal slip.

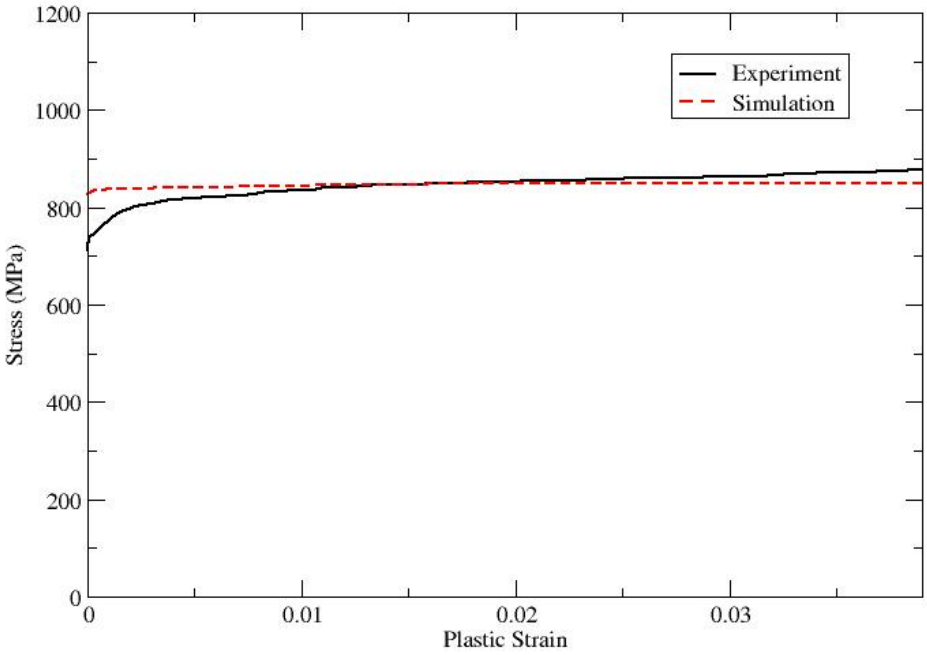

Figure 13. Constant Strain rate compression testing on Ti-6242 single colony sample oriented for a3 basal slip.

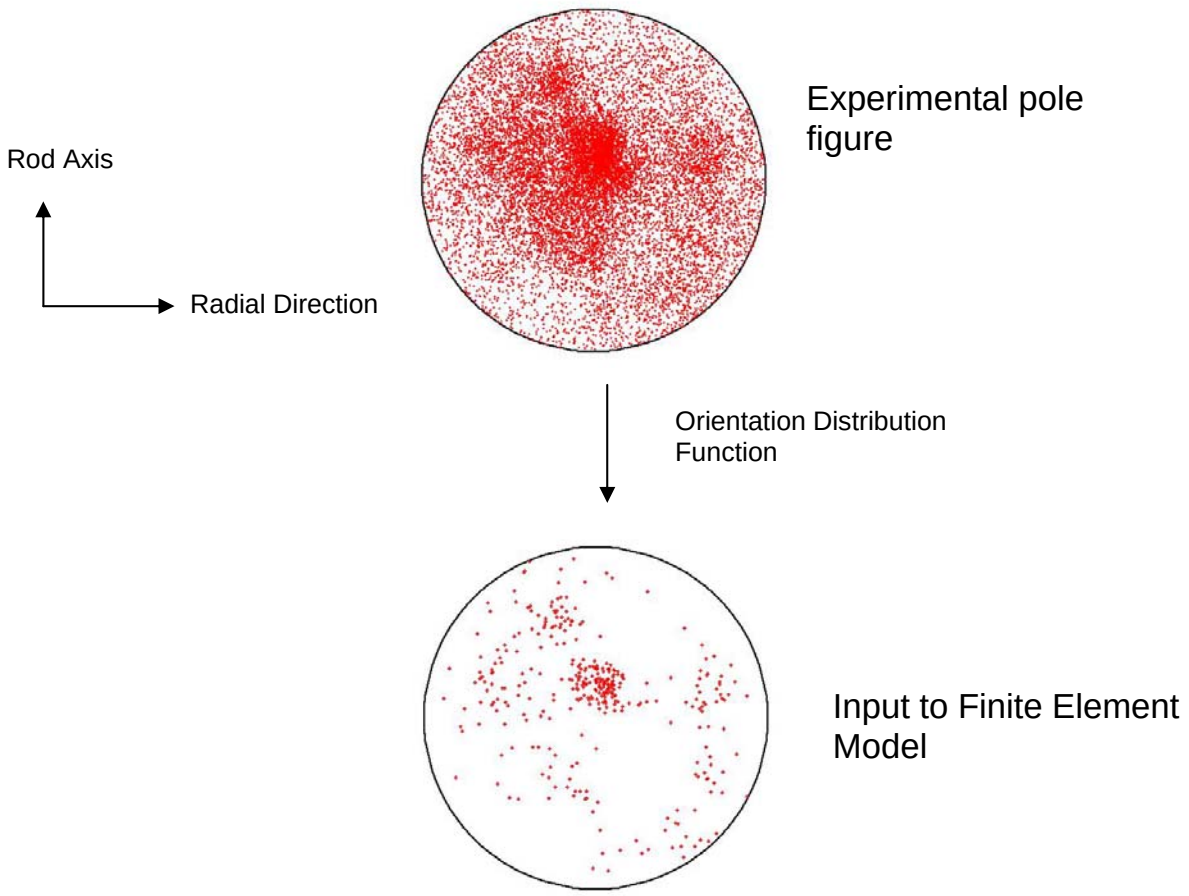

Figure 14. (0001) pole figure shown for the α/β Forged polycrystalline sample (pancake2)

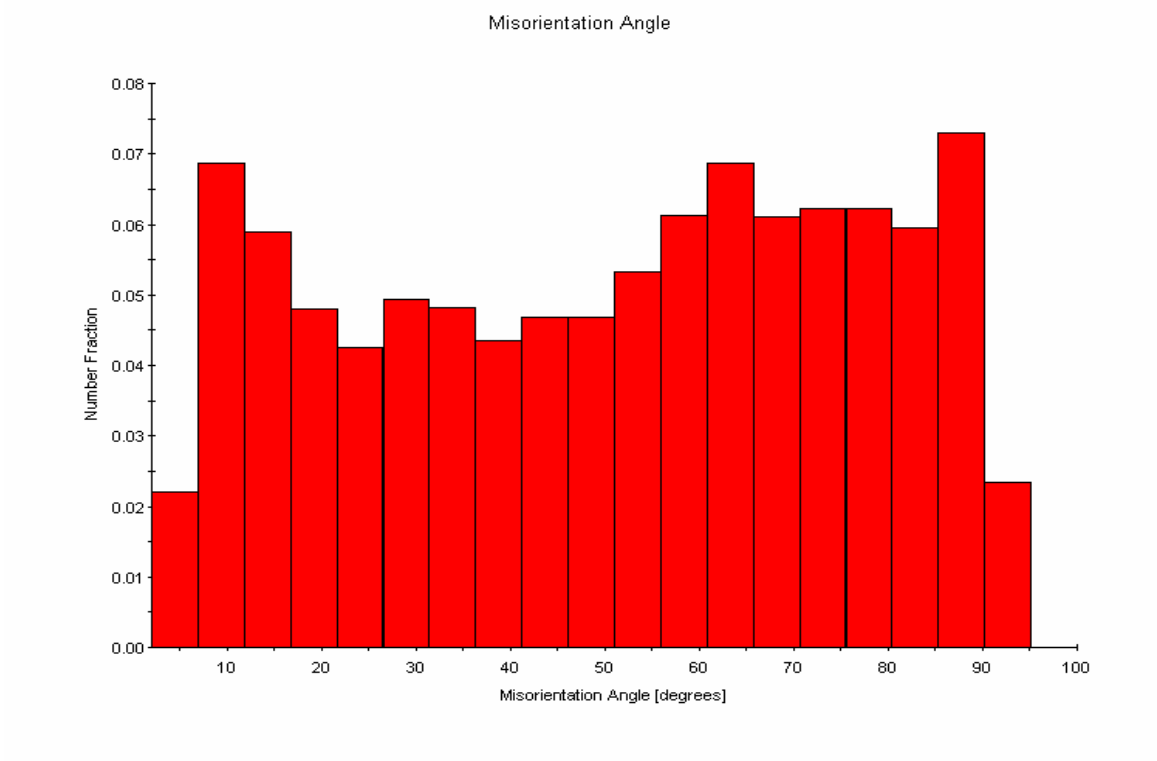

Figure 15. Experimental misorientation distribution.

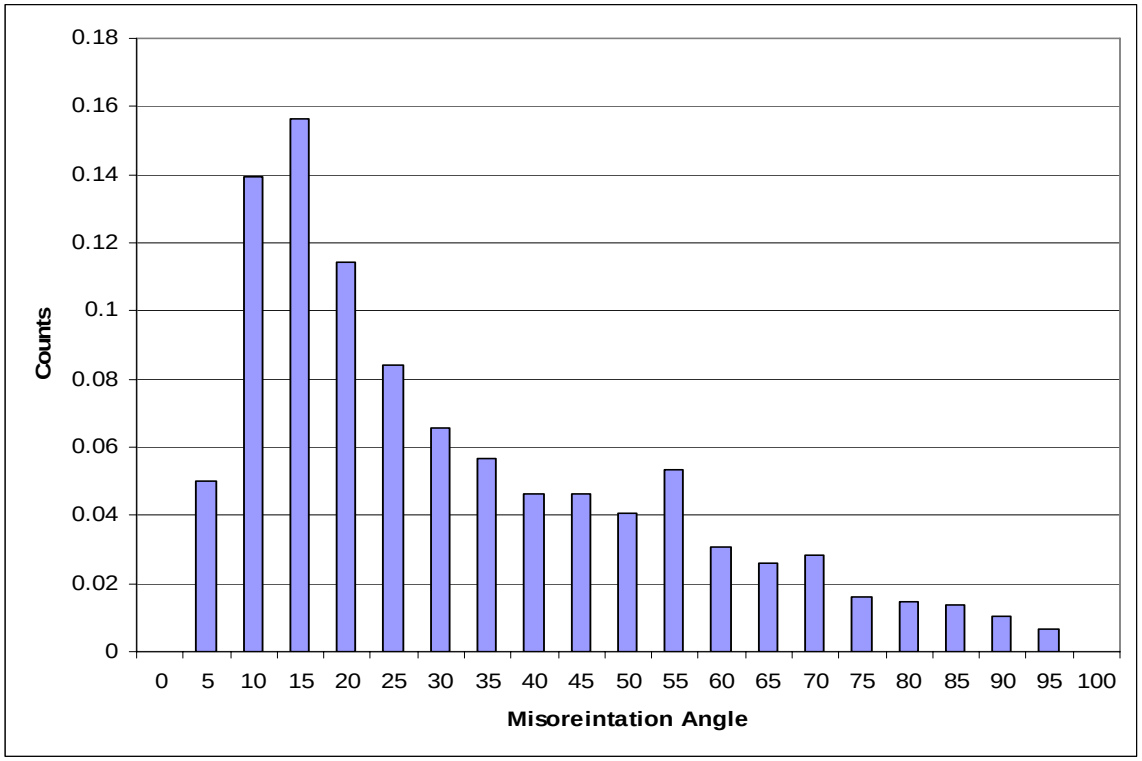

Figure 16. Initial misorientation distribution.

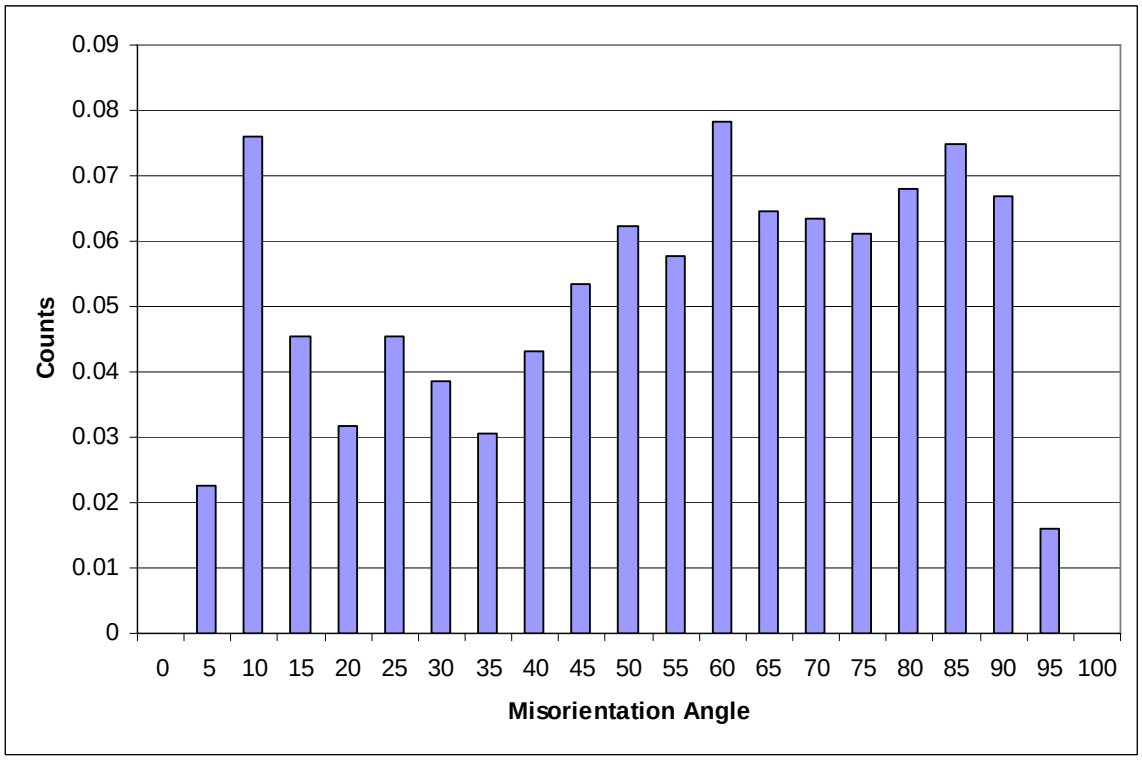

Figure 17. Final misorientation distribution in the FE Model.

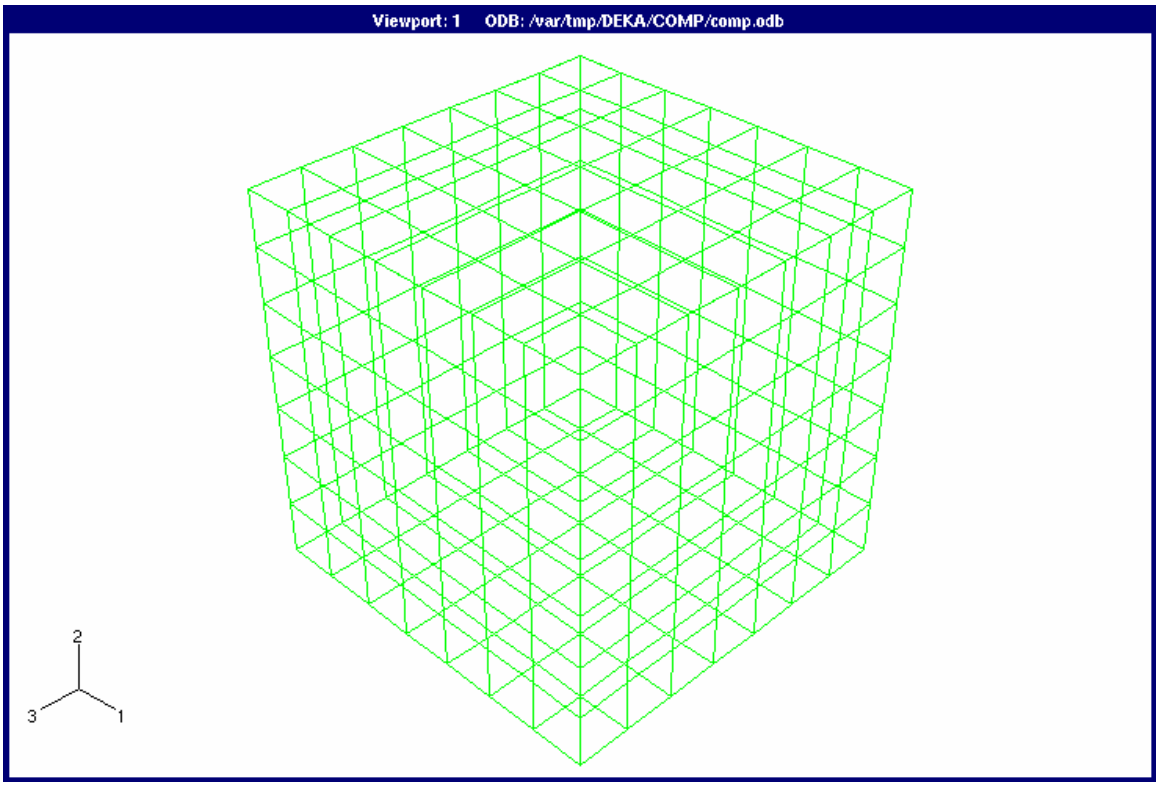

Figure 18. Mesh used for the polycrystalline material.

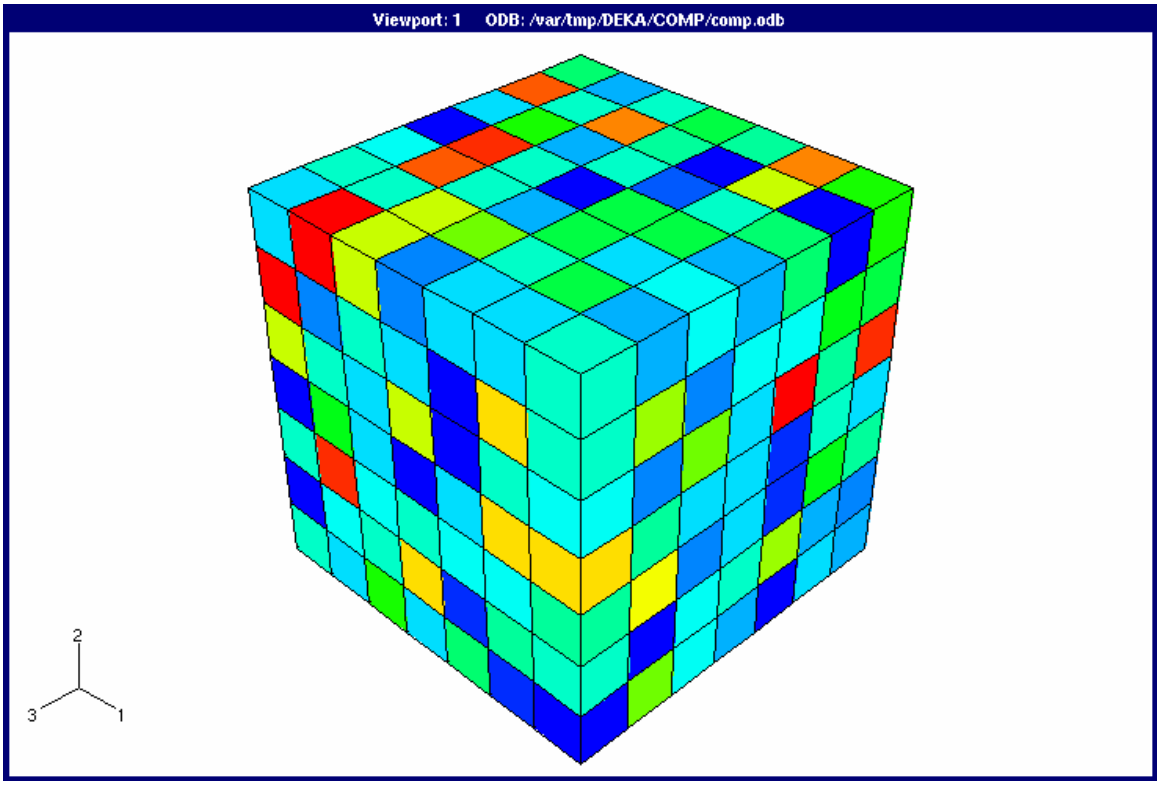

Figure 19. Orientation distributions for the polycrystalline material.

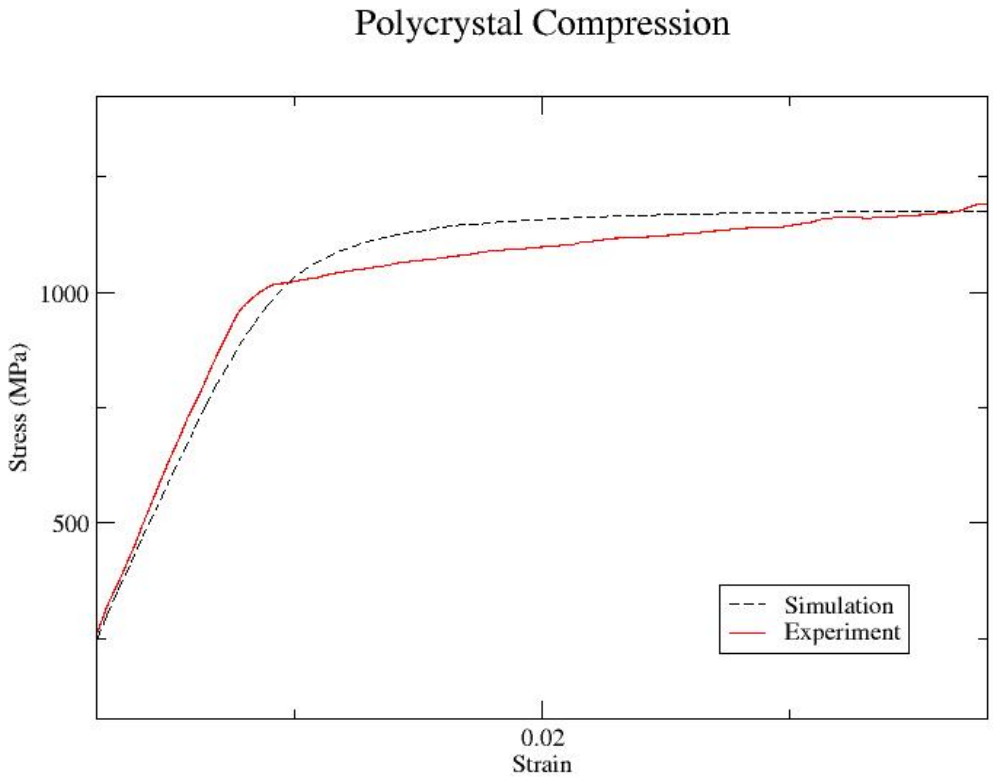

Figure 20 Polycrystalline simulation result for compression constant strain rate test.

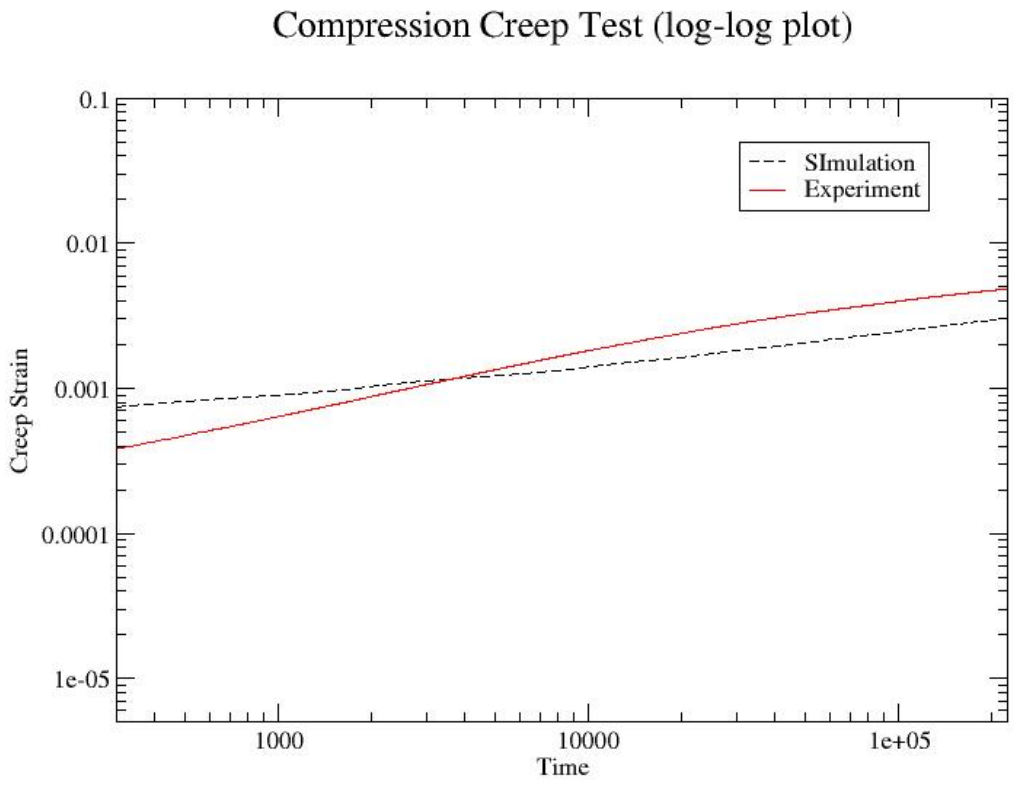

Figure 21 Polycrystalline simulation result for compression creep test (log-log plot).

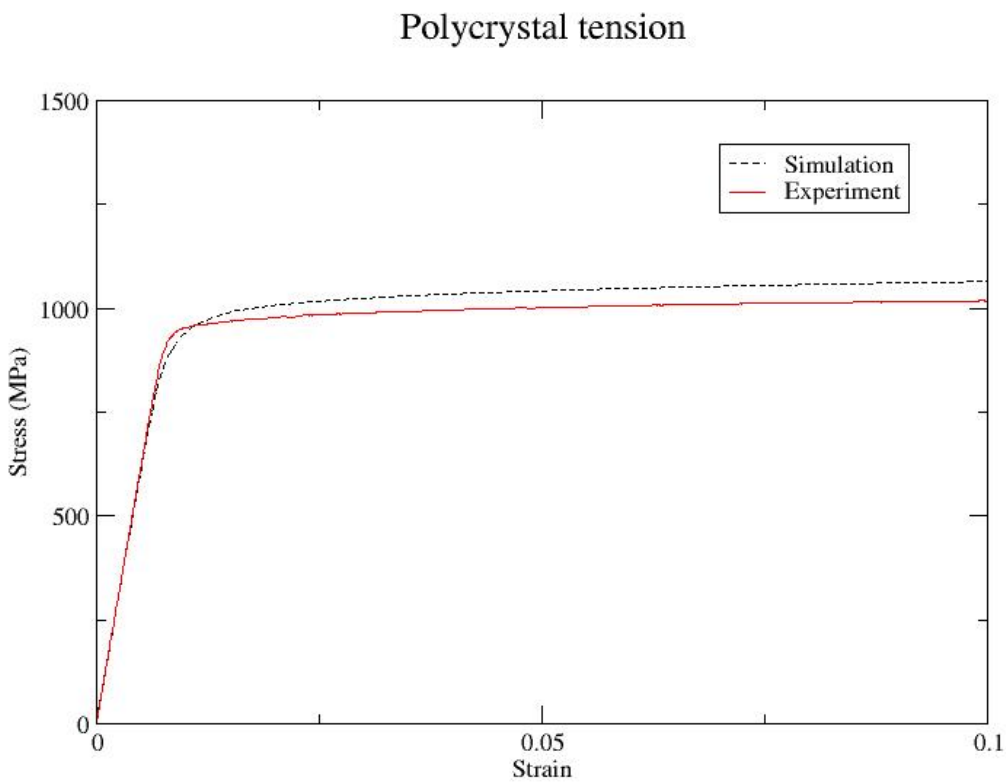

Figure 22 Polycrystalline simulation result for tension constant strain rate test.

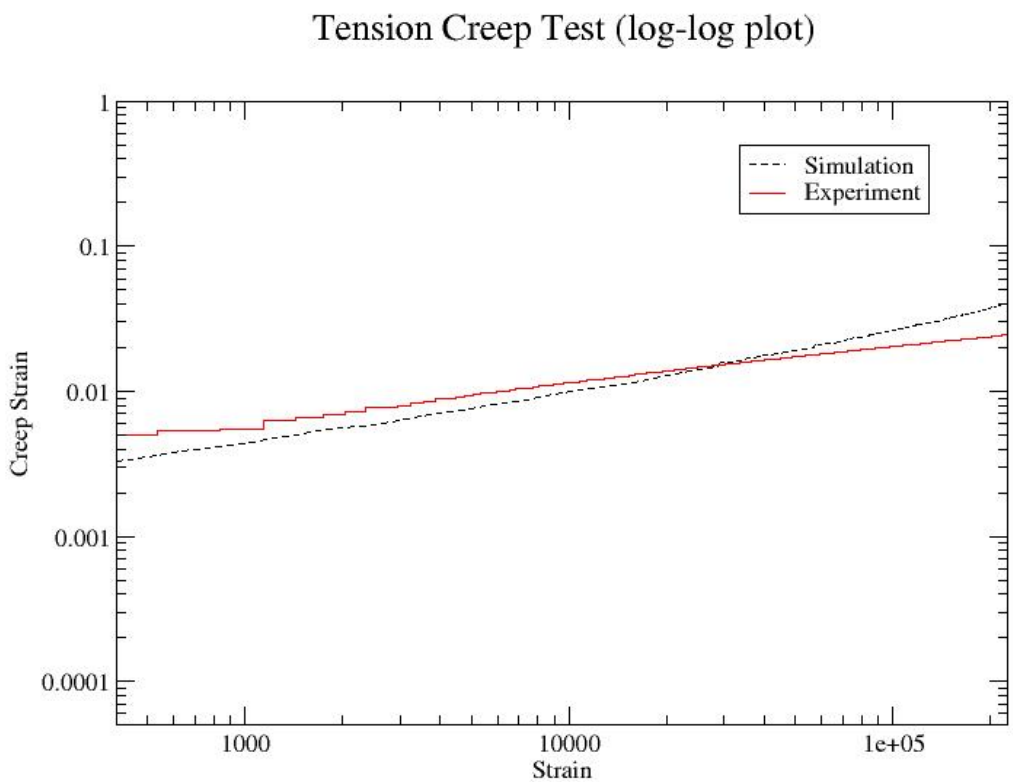

Figure 23. Polycrystalline Simulation Result for Tension Creep (log-log plot)

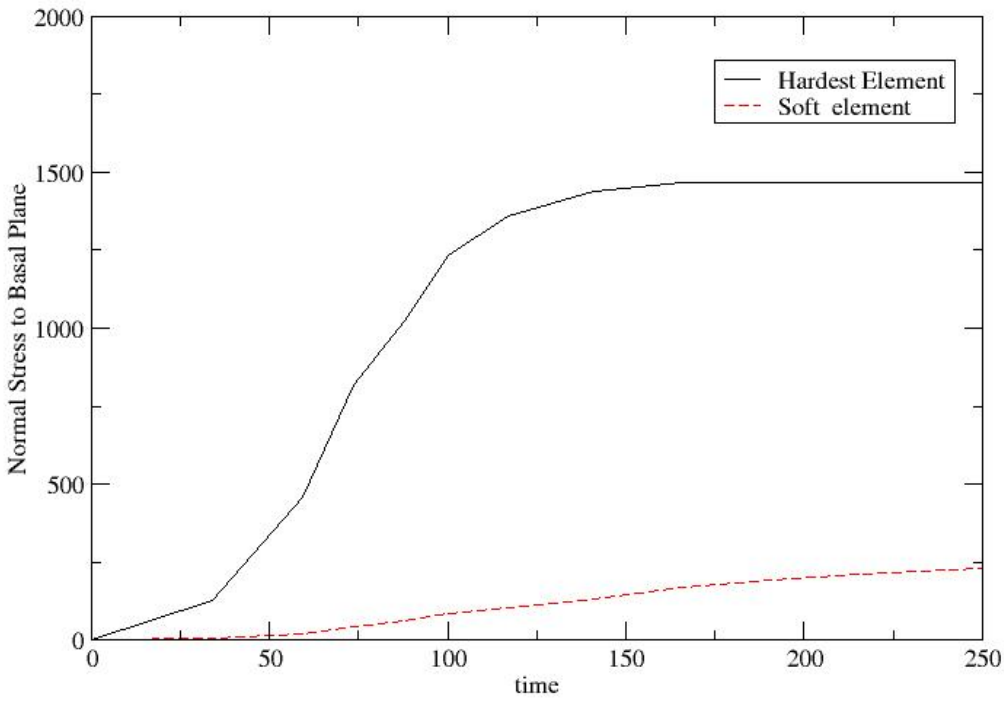

Figure 24. Comparison of the stress normal to the basal plane between a soft and the hardest grain in the polycrystalline model.

BIBLIOGRAPHY

[1] Burgers, W.G., Physica, 1934; pp 1:561

[2] Williams, A.J., Cahn, R.W. and Barret, C.S., Acta Metallurgica, 1954; pp 2:117.

[3] Hasija, V., Ghosh, S., Mills M. J. and Joseph, D. S., "*Modeling Deformation and Creep in Ti-6Al alloys with Experimental Validation*", Acta Materialia, 2003(51); pp. 4533-4549.

[4] Savage M, "*Polycrystalline Plasticity: Microstructural and Mechanistic study of low temperature creep and dwell fatigue in single colony alpha/beta titanium alloys*", 2000, Doctoral dissertation. Columbus (OH): The Ohio State University.

[5] Kocks, U. F., Tomé, C. N., and Wenk, Texture and Anisotropy: Preferred Orientations in Polycrystals and Their Effect on Materials Propertie, 1998, Cambridge University Press, Cambridge.